

# UNIVERSITÉ DE STRASBOURG

ÉCOLE DOCTORALE DES SCIENCES DE LA TERRE ET DE L'ENVIRONNEMENT (ED 413)

INSTITUT TERRE et ENVIRONNEMENT de STRASBOURG (UMR 7063)

**THÈSE** présentée par :

**Carole Glaas**

soutenue le : **19 février 2021**

pour obtenir le grade de : **Docteur de l'Université de Strasbourg**

Discipline / Spécialité : **Sciences de la Terre / Géologie**

## **Mineralogical and structural controls on permeability of deep naturally fractured crystalline reservoirs**

### **Insights from geothermal wells (Upper Rhine Graben)**

**THÈSE dirigée par :**

**M GIRARD Jean-François**

Professeur, Université de Strasbourg

**Mme PATRIER Patricia**

Professeure, Université de Poitiers

**RAPPORTEURS :**

**Mme BUATIER Martine**

Professeure, Université de Besançon

**M LIOTTA Domenico**

Professeur, Università di Bari

**AUTRES MEMBRES DU JURY :**

**Mme SCHILL Eva**

Professeure, Karlsruher Institut für Technology

**M MANATSCHAL Gianreto**

Professeur, Université de Strasbourg

**M GIBERT Benoît**

Maître de Conférences, Université de Montpellier

**M GENTER Albert**

Directeur Général Adjoint, ÉS-Géothermie, Strasbourg





ÉCOLE DOCTORALE DES SCIENCES DE LA TERRE ET DE L'ENVIRONNEMENT (ED 413)  
INSTITUT TERRE et ENVIRONNEMENT de STRASBOURG (UMR 7063)

**THÈSE** présentée par :

**Carole Glaas**

soutenue le : **19 février 2021**

pour obtenir le grade de : **Docteur de l'Université de Strasbourg**

Discipline / Spécialité : **Sciences de la Terre / Géologie**

**Mineralogical and structural controls on  
permeability of deep naturally fractured  
crystalline reservoirs  
Insights from geothermal wells (Upper Rhine Graben)**

**THÈSE dirigée par :**

**M GIRARD Jean-François**

Professeur, Université de Strasbourg

**Mme PATRIER Patricia**

Professeure, Université de Poitiers

**RAPPORTEURS :**

**Mme BUATIER Martine**

Professeure, Université de Besançon

**M LIOTTA Domenico**

Professeur, Università di Bari

**AUTRES MEMBRES DU JURY :**

**Mme SCHILL Eva**

Professeure, Karlsruher Institut für Technology

**M MANATSCHAL Gianreto**

Professeur, Université de Strasbourg

**M GIBERT Benoît**

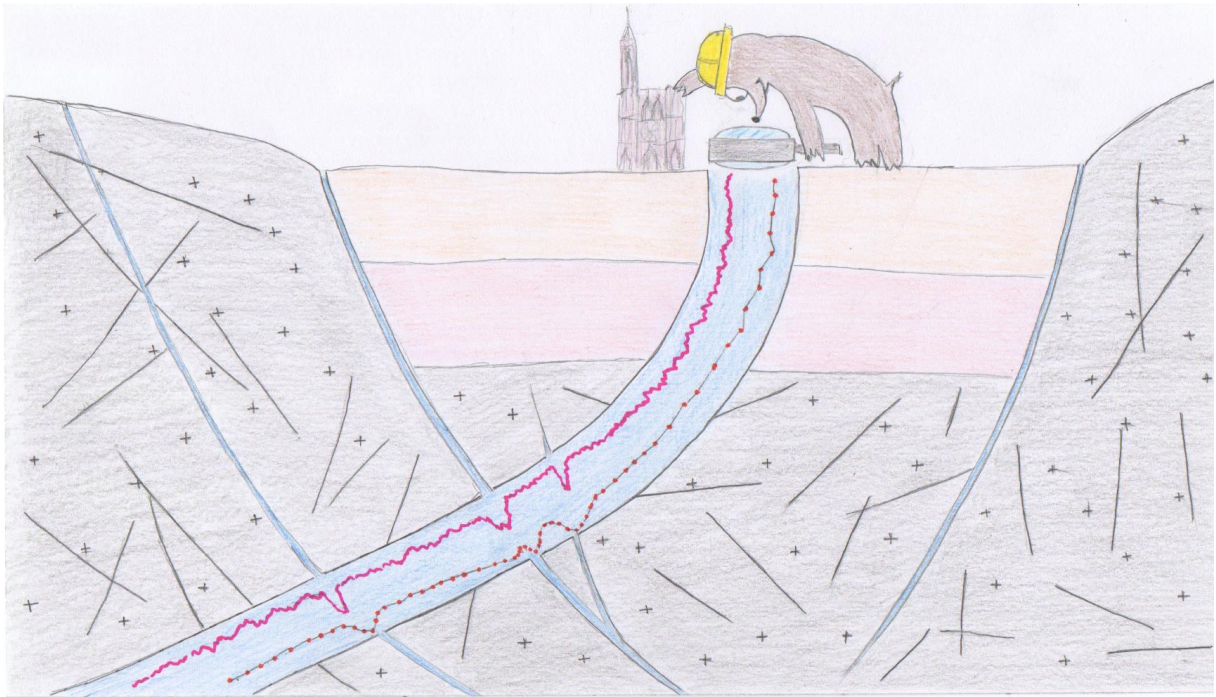
Maître de Conférences, Université de Montpellier

**M GENTER Albert**

Directeur Général Adjoint, ÉS-Géothermie, Strasbourg

How to cite this thesis:

Glaas C., (2021), Mineralogical and structural controls on permeability of deep naturally fractured crystalline reservoirs, Insights from geothermal wells (Upper Rhine Graben), PhD thesis, University of Strasbourg, France.



Slide pour « Ma thèse en 180 secondes », 2019



## Preface

I came into the office of Jeanne Vidal (PhD student at university of Strasbourg) and told her I wanted to work in deep geothermal. I did not understand a lot about it at this time but I wanted to be part of it, or more precisely to use my geological knowledge for developing this renewable energy. End of summer 2017 I finished my internship in the framework of a master's project at ÉS-Géothermie (Strasbourg), about the link between the permeability, the mineralogy observed on cuttings, and the geophysical logs in the fractured granite intersected by Rittershoffen wells. As I was searching for a PhD or job opportunities, Albert Genter had the idea to build a PhD research project in collaboration with Jean-François Girard (University of Strasbourg) and Patricia Patrier (University of Poitiers). It was too late: I was already trapped into a marvellous journey to the center of the Earth. A journey where the exploration of fractures and secondary minerals in granite led me to scrutinize borehole images, geophysical logs, and drill-cuttings for secondary hydrothermal quartz, illites, or other species that rule the fracture permeability at more than 2 km depth in the Upper Rhine Graben ...

More seriously, my PhD work is based on the dataset of three geothermal sites: Soultz-sous-Forêts, Rittershoffen and Illkirch, gathering ancient and recent well-data from 8 geothermal wells. I had the opportunity to follow the drilling of Illkirch GIL-1 well and its geophysical logs acquisition. I performed the petrographic observation of cuttings samples on-site during drilling operations in the granite, and could participate in the injection tests.

This PhD benefitted from grant calls a CIFRE (Convention Industrielle de Formation par la Recherche) convention and was co-funded by ÉS-Géothermie company. This PhD was also carried out in the framework of several national public funded projects like EGS Alsace (ADEME), Cantare Alsace (ANR) and DEEP EM (ADEME).

This PhD is also the result of a fruitful collaboration between industry and academy. At the University of Strasbourg, Jean-François Girard supervised the PhD work about geophysical logs and more precisely electrical resistivity logs. At the University of Poitiers, Patricia Patrier provided supervision on the various laboratory measurements done on cuttings for the petrographical characterization of clay minerals. At ÉS-Géothermie, Albert Genter supervised the core of the work, provided all the dataset and their history, and shared his rich geothermal experience.

The PhD work has been presented at the European Geothermal Workshops 2017, 2018 and 2019 (partnership between Karlsruhe Institute of Technology and Ecole et Observatoire des Sciences de la Terre de Strasbourg), at the European PhD days in 2018 (Zurich, Switzerland), 2019 (Potsdam, Germany) and 2020 (Denizli, Turkey), at the Mid-European Clay Conference in Zagreb (Croatia) in 2018, at the European Geothermal Congress in Den Haag (Netherlands) in 2019, and was accepted to be presented at the World Geothermal Congress in Reykjavik (Iceland) in 2021. The results have been published or submitted in 6 international papers whose 4 in first author in peer-reviewed journals; Journal of Volcanology and Geothermal Research, Geothermal Energy Journal, Geofluids Journal, Journal of Structural Geology and Minerals Journal.

This thesis is structured based on the scientific production of the 3 years of PhD.



## Avant-propos

J'ai déboulé dans le bureau de thèse de Jeanne Vidal en lui disant : je veux faire de la géothermie. Je n'y comprenais pas grand-chose, mais j'avais très envie d'en être. Ou plutôt, j'avais très envie de mettre à profit ma formation de géologue pour aider à développer cette énergie renouvelable. Et c'est ainsi qu'à la fin de l'été 2017, je terminais mon stage de master 2 à ES-Géothermie, à propos du lien entre perméabilité, minéralogie à partir d'échantillons de forage, et diagraphies géophysiques dans le granite fracturé recoupé par les deux puits du projet de Rittershoffen. Alors que je postulais à des offres d'emplois et de thèse diverses et variées, Albert Genter eut l'idée de monter un projet de thèse en collaboration avec Jean-François Girard (Université de Strasbourg) et Patricia Patrier (Université de Poitiers). C'était déjà trop tard : j'étais déjà lancée dans un merveilleux voyage au centre de la Terre. Un voyage qui m'a menée à scruter imageries de parois, diagraphies géophysiques et échantillons de forage à la recherche de quartz hydrothermal, d'illites et autres espèces qui régissent la perméabilité à plus de 2 km de profondeur dans le Fossé rhénois...

Plus sérieusement, mon travail de thèse se base sur les données de trois projets de géothermie : Soultz-sous-Forêts, Rittershoffen et Illkirch, rassemblant des données de 8 puits géothermiques, anciennes ou plus récentes. J'ai eu l'opportunité de suivre le forage du puits GIL-1 d'Illkirch, ainsi que l'acquisition de ses diagraphies géophysiques, j'ai pu y réaliser l'observation pétrographique des échantillons de cuttings sur site durant le forage, et j'ai aussi pu participer aux tests d'injection de ce puits.

Cette thèse a bénéficié d'une convention CIFRE (Convention Industrielle de Formation par la Recherche), co-financée par ES-Géothermie. Cette thèse a aussi été réalisée avec le support financier de différents projets nationaux subventionnés comme EGS Alsace (ADEME), Cantare Alsace (ANR) et DEEP EM (ADEME).

Cette thèse résulte aussi d'une collaboration fructueuse entre industrie et académie. En effet, à l'Université de Strasbourg, Jean-François Girard a encadré le travail de thèse sur les diagraphies géophysiques et plus précisément les logs de résistivité électrique. A l'Université de Poitiers, Patricia Patrier a encadré les différentes préparations d'échantillons et mesures en laboratoire sur les cuttings pour l'analyse des minéraux argileux. A ES-Géothermie, Albert Genter a encadré le cœur du travail, renseigné les données et leur histoire, et partagé sa riche expérience géothermique.

Ce travail de thèse a été présenté aux European Geothermal Workshops 2017, 2018 et 2019 (partenariat entre le Karlsruhe Institut of Technology et l'Ecole et Observatoire des Sciences de la Terre de Strasbourg), aux European PhD days de 2018 (Zurich, Suisse), 2019 (Potsdam, Allemagne) et 2020 (Denizli, Turquie), à la Mid-European Clay Conference à Zagreb (Croatie) en 2018, à l'European Geothermal Congress à La Haye (Pays-Bas) en 2019, et a été accepté pour être présenté au World Geothermal Congress à Reykjavik (Islande) en 2021. Les résultats ont été publiés ou soumis dans 6 revues internationales dont 4 en premier auteur dans des journaux à comité de lecture ; Journal of Volcanology and Geothermal Research, Geothermal Energy Journal, Geofluids Journal, Journal of Structural Geology and Minerals Journal.

Cette thèse est structurée sur la base de la production scientifique des 3 années de thèse.



## Remerciements

Je remercie sincèrement Martine Buatier et Domenico Liotta d'avoir accepté d'être rapporteurs de ma thèse, ainsi que Eva Schill, Gianreto Manatschal et Benoît Gibert d'avoir accepté d'être examinateurs lors de ma soutenance orale.

Ma thèse a bénéficié d'un contrat de collaboration CIFRE entre les Universités de Strasbourg et de Poitiers, et l'entreprise ES-Géothermie, où j'ai été dirigée et encadrée par Jean-François Girard, Patricia Patrier, et Albert Genter, respectivement.

Jean-François, merci pour toutes les discussions passionnées à propos des logs électriques, pour ton encadrement et ta présence.

Patricia, merci de m'avoir accueillie à Poitiers, et de m'avoir fait confiance pour toutes les analyses en laboratoire. Merci pour toutes ces discussions fructueuses à propos des interprétations des données, là où souvent je ne voyais rien, tu m'as appris à décerner et comprendre les réponses.

Albert, merci pour tout le temps que tu m'as accordée, merci surtout pour ton organisation exemplaire qui a permis à ce travail d'être si bien cadré. Merci pour ton enthousiasme et ton dévouement pour la géologie et la géothermie, qui sont communicateurs et ont oeuvré pour toujours maintenir ma motivation à flots ! Merci pour toutes les relectures d'abstracts, d'articles, et tes conseils avisés.

Jeanne, celle qui m'a lancée, inspirée et soutenue au cours du stage de master, puis de la thèse et qui est tout naturellement devenue une amie. Tu as su me redonner le courage lorsque c'était difficile, me faire rire avec ta bonne humeur contagieuse. Toujours à fond, je me souviens de tous ces matins où tu me disais "cette nuit j'ai pensé que tu devrais faire ça ...". Je me souviens des premiers traitements SWIR, et depuis on a fait tellement de travaux et parcouru tant de chemin ensemble ! Les apéros chez toi, au Supertonic, chez Albert, les nuits blanches sur le forage d'Illkirch ...

Merci à toute la magnifique team d'ÉS-Géothermie: Eléonore la géologue sur tous les fronts, Clément le manager géosciences balistos, Régis l'hydrogéologue pianiste chanteur et multi-tool à ses heures, Benoît l'informaticien guitariste, Jean-Jacques le DG happy-culteur, Mumu l'assistante magicienne des galères administratives, Manue l'assistante blagueuse et face-swappeuse, Guillaume l'ingénieur surface accros au chocolat et aux gâteaux, Olivier l'ingénieur surface rockstar, les géophysiciens Alex et Vince les cyclistes et Nico le géophysicien sultzien, Jean-Mi le manager surface anglophone, Justine la géochimiste footballeuse, Abi la talentueuse créatrice, et Clio la géochimiste rigolote. Merci à tous d'avoir fait de nos moments de travail des instants légers sur base de bonne humeur.

Les moments passés à Poitiers furent toujours d'une grande richesse. Alain merci de m'avoir prise sous ton aile pour m'initier aux argiles, Daniel merci d'avoir toujours été prêt à regarder mes résultats, et pour les discussions très instructives. Merci à toute l'équipe de doctorants : Marine, Thomas, Jérémie, et Grace pour avoir détendu l'atmosphère pendant et après des journées intenses, que ce soit autour d'un repas au RU ou au Palais de la Bière !

Astu, my sunshine, my dear friend ! I can easily remember the first time we met at ESG, as stagiaires sitting at the same office: the beginning of an incredible friendship between Indonesia and Alsace ! Moments with you are always so natural and the way we can share our passion for food (mainly eating), but the intensity with which we can debate about every subject, has made working times easily liveable.

Merci à toute la fine équipe de copains de la vallée de Munster pour tous ces week-end de folie et de détente qui faisaient oublier la semaine et permettaient d'aborder les lundis avec plein d'espoir ! Augustin merci d'être toujours prêt à faire les 400 coups avec moi, net ! La dream-team des randocuites : Pierre, Alexis, Charly, Emilie, Cécile, Antoine, Romain, Marc et Clément. Jack et Nassim toujours prêts à partager une bière. Charlotte et ses vins délicieux. Tom le roi des bolides. Sophie, Thomas, Charlotte, et Julien les musiciens de folie ! Et bien sûr Jeanne et Erwann et les soirées au chalet. Emma la reine des vignes qui a plus d'une bouteille dans son sac.

Merci à ma famille. Papa pour la confiance que tu as en moi, le fait que tu n'ai jamais douté de moi m'a sûrement beaucoup aidé à croire moi-même en ma thèse. Martin mon frère chéri, mon idole, petit savant fou tu m'auras fait rêver avec tes projets, toujours prêt à me distraire avec ta folie, tes entourloupes, tes câlins et ton sourire. Merci Papi et Mamie pour les moments doux à vos côtés, autour d'un repas partagé après une longue journée. Mado merci d'être cette personne passionnée, rêveuse et cette cuisinière hors pair. Vous m'avez tous ouvert l'esprit et tant appris. Je vous porte un amour inestimable.

Aurélien, merci pour ton soutien, ta présence à tout instants mais surtout ta patience. Merci pour tes talents culinaires qui m'ont souvent redonné le sourire après de longues journées.

## Abstract

With climate change and increasing pollution of our environment, reducing the consumption of energies, raw materials, and developing renewable energies have become major issues, and the development of geothermal energy is one of the ways to contribute. Although geothermal has numerous advantages like to be a local resource, decentralized, continuously available and emitting very low CO<sub>2</sub>, there are still challenges for its development. Among them, the high drilling costs, the understanding of the fractured reservoirs and in urbanized areas the public acceptance and the control of the induced seismicity. The high temperature gradients encountered in the European Cenozoic Rift Systems (ECRIS) are targets with high geothermal potential. The Upper Rhine Graben (URG) is one of these rifts, resulting from Tertiary extension and is subject to geothermal exploration since the 80's. In this tertiary basin, the geothermal reservoir is mainly located in the Hercynian crystalline basement and in the Triassic sedimentary formations. Furthermore, an industrially viable geothermal project requires a hot (>150°C) and sustainable reservoir at drillable depth (2-5 km). In this graben, the circulation of the highly saline fluid is mainly supported by the natural fracture network inherited from the complex and polyphasic tectonic history of the URG. Convection in these reservoirs has been observed in the wells and is characterized by convection cells using the natural fractures. The fracture network is multi-scale: from the regional border faults that are plurikilometric, to local faults, plurimetric fractures, and microcracks. The fractures connectivity, but also their connection with the well trajectories, are determining the access to the geothermal resource.

This PhD aims to characterise the mineralogical and structural controls on the permeability of the naturally fractured deep crystalline reservoirs. That for, a rich dataset from the geothermal wells is investigated. 8 wells were studied (5 on Soultz-sous-Forêts, 2 on Rittershoffen and a first well drilled on Illkirch) were cuttings samples and geophysical logs are available. All those wells targeted local normal faults and crossed the Triassic sandstones before reaching the Palaeozoic granites hosting geothermal reservoirs.

The geothermal project of Soultz-sous-Forêts was intended for developing an artificial heat exchanger in the granite, finally demonstrated the pre-existence of natural circulations in a complex fracture network, composed of hydrothermally altered zones, secondary mineralisations, deformation zones and open pathways. The geothermal project of Rittershoffen, realized 20 years later, derived from the experience gained on the Soultz-sous-Forêts project and is a success story with the achievement of industrially viable flow rates (70 L/s) and temperatures (165°). In fact, both wells of the site intersected the intra-granite Rittershoffen fault, oriented N-S, highly dipping westward and with an apparent vertical offset of 200 m. This fault and its associated damage zone are major fluid pathways intersected by both wells, characterized by intense hydrothermal alterations. At Illkirch, the first well intersected the Eschau fault at the interface between Triassic sandstones and the granite. This fault is oriented N-S with a kilometric apparent vertical offset. However, hydraulic tests seem to show that the permeable fracture zones are mostly located deep fractured granite than in this faulted sediments-granite interface.

Based on several thousands of cuttings samples, secondary clay minerals resulting from hydrothermal alteration were firstly analysed with standard mineralogic and petrographic methods like the macroscopic observation of the cuttings with magnifying loupe, X-ray diffraction (XRD), scanning electron microscope (SEM) coupled with energy dispersive spectroscopy (EDS), optical microscopy, and geochemical analyses on bulk rock. These analyses allowed to first characterize the secondary mineralogy of the samples before interpreting secondly the spectra resulting from Short Wave Infrared spectroscopy (SWIR).

The SWIR analysis appears a promising method, as it is rapid and innovative for the quantification of secondary clay minerals. However, a calibration of the SWIR spectra with the encountered mineralogy has to be realized previously. In the granite of the URG, Illite and illite-smectite mixed-layers (<10% smectite) (I/S ml) were identified to be the main clay minerals resulting from hydrothermal alteration, corresponding to the illitization of the primary minerals (biotite, feldspars), and of the earlier secondary minerals (chlorite). The semi-quantification of these phases with the SWIR method on 3000 cuttings samples from the 3 granitic reservoirs of Soultz-sous-Forêts, Rittershoffen and Illkirch and their correlation with the XRD, SEM and binocular observations proved the reliability and accuracy of the SWIR method on the several alteration facies encountered.

Granitic fractured reservoirs of the URG are composed of fracture zones (FZ) made of fault core (FC) and associated damage zones. The secondary minerals that are Illite and I/S ml are systematically associated to paleo or present-permeable circulations associated to fracture zones. SWIR results from Rittershoffen and Soultz-sous-Forêts wells suggested that intense illitization (quantitatively) is a good proxy of permeability in the FZ. However, the SWIR results from Illkirch well suggest also that an intense illitization widely distributed in the rock mass and notably around FC can also clog circulation channels. These observations underline a fragile equilibrium between dissolution and precipitation processes that can clog or preserve natural fluid pathways in FZ.

The natural fracture network has been deeply investigated from geophysical data (borehole images) and geological data (core samples) from the 8 geothermal wells studied. The natural fractures at Soultz-sous-Forêts and Rittershoffen have been compared to new structural dataset of the Illkirch well. The fracture network was characterized in terms of orientation, fracture spacing, fracture density, fracture thickness and spatial distribution. These natural fractures inherited from the polyphasic tectonic history of the URG since the Visean are steeply dipping and are oriented NNW-SSE to N-S. The highest fracture densities and thicknesses that are the most suitable for hydrothermal circulations are localized at the top of the fractured granitic basement.

The comparison of the secondary clay minerals and the natural fractures on the three geothermal sites of Soultz-sous-Forêts, Rittershoffen and Illkirch highlighted the following aspects:

- The integrated application of the SWIR measurements to several wells intersecting the same secondary minerals underlines the need of quantifying the clay minerals and allowed to calibrate and demonstrate the efficacy of the SWIR method.
- The distribution of the illitic material resulting from argillic alteration in the FZs was found to be a determining factor in the permeability of the reservoir in the URG. Above the intensity of the hydrothermal alteration, the way that it is distributed in the mass allows to preserve or not the permeability in the FZs.
- Fluid circulation is distributed in complex pathways inside the different components of FZs: damage zones, wallrocks, and fault core(s).
- Observations in geothermal wells highlight a fragile equilibrium between dissolution and precipitation processes that can clog or preserve natural fluid pathways in FZ.
- To achieve suitable flowrates, the connection between the wells and the permeable fracture network should be maximised by smart well trajectories cross-cutting local faults at the top basement.

The results obtained in this thesis underline the added value of the combination of the geological and geophysical methods for the understanding of fluid circulations in the naturally

fractured granite of the URG. These results allow to propose a revised version of the conceptual model of fluid circulation in fault and fracture zones intersected by the wells and underline the interest of integrating the SWIR method in the exploration process for deep geothermal.

This thesis is structured into three main parts: 1) State of the art and objectives of the thesis, 2) Permeable fracture zones at well scale, and 3) Conclusions and perspectives, which are further divided into nine chapters.



## Résumé

Avec le constat du réchauffement climatique et d'une pollution croissante de notre environnement, réduire la consommation d'énergie, de matières premières et développer les énergies renouvelables sont devenus des enjeux primordiaux et le développement de la géothermie profonde est l'un des moyens d'y contribuer. Bien que la géothermie possède de nombreux avantages tels être une ressource locale, décentralisée, disponible en continu, d'émettre très peu de CO<sub>2</sub>, il y a encore de nombreux freins à son développement. Parmi eux, les coûts élevés de forage, la compréhension des réservoirs fracturés et dans les zones urbanisées l'acceptabilité par la population et la maîtrise de la sismicité induite. Les gradients de température élevés à de faibles profondeurs rencontrés dans les systèmes de rifts cénozoïques ouest-européens font de ces environnements des cibles à fort potentiel géothermique. Le Fossé rhénan est l'un de ces grabens liés à l'extension Tertiaire, et fait l'objet d'exploration géothermique depuis les années 80. Dans ce bassin tertiaire, le réservoir géothermal est situé dans le socle cristallin hercynien et dans les formations sédimentaires triasiques. Pour qu'un projet de géothermie profonde soit économiquement rentable, il requiert la présence d'un fluide chaud (>150°C), qui circule dans un réservoir pérenne à des profondeurs facilement atteignables (2-5 km). Dans ce graben, le fluide géothermal sursalé circule essentiellement dans le réseau de fractures hérité de l'histoire tectonique complexe et polyphasée du Fossé rhénan. Le phénomène de convection dans les réservoirs géothermiques a pu être observé dans les puits à ces profondeurs, via le fonctionnement de boucles de circulation utilisant le réseau de fractures naturelles. Ce réseau de fractures est multi-échelle allant des failles bordières régionales plurikilométriques, à des failles locales, des fractures plurimétriques, et des microcracks. La connectivité des fractures, mais aussi leur connexion avec les trajectoires de puits, vont être déterminants pour l'accès à la ressource géothermique.

Le travail de cette thèse vise à caractériser les contrôles minéralogiques et structuraux qui influent sur la perméabilité des réservoirs cristallins profonds naturellement fracturés. Pour ce faire, cette thèse s'appuie sur un jeu de données de puits géothermiques réalisés en Alsace (France). Huit puits ont été spécifiquement étudiés (5 sur Soultz-sous-Forêts, 2 sur Rittershoffen et un premier forage sur Illkirch) pour lesquels étaient disponibles des échantillons de roche ou débris de forage (cuttings) ainsi que de diagraphies géophysiques. Ces 8 puits ont intersecté des failles normales d'échelle régionale à locale, ont traversé les grès triasiques, avant d'atteindre les granites paléozoïques hébergeant les réservoirs géothermiques.

Le projet de géothermie de Soultz-sous-Forêts d'abord destiné à développer un échangeur artificiel dans le granite a finalement démontré l'existence de circulations naturelles de fluide géothermal dans un réseau de fractures complexe, composé de zones altérées, de minéralisations secondaires, de zones déformées et de drains ouverts. Le projet de géothermie de Rittershoffen, réalisé une vingtaine d'années plus tard, a découlé du retour d'expérience acquis sur le projet de Soultz-sous-Forêts et constitue un franc succès avec l'atteinte des objectifs en termes de débit (70 L/s) et de température (165°C). En effet, les 2 puits du site intersectent la faille de Rittershoffen intra-granite, orientée N-S avec un fort pendage ouest et un rejet vertical apparent de 200 m. Cette faille et sa zone endommagée associée sont un des drains perméables majeurs intersectés par les 2 puits, et qui sont marquées par d'importantes altérations hydrothermales. A Illkirch, le premier puits a intersecté la faille d'Eschau à l'interface faillée entre les grès triasiques et le granite. Cette faille normale est orientée N-S et présente un rejet vertical apparent de l'ordre du kilomètre. Toutefois, les

tests hydrauliques réalisés ont tendance à montrer que les zones fracturées perméables sont davantage localisées dans le granite fracturé profond qu'à l'interface faillée socle-sédiments.

Avec à disposition plusieurs milliers d'échantillons de roche (cuttings), les minéraux argileux secondaires résultant des altérations hydrothermales ont dans un premier temps été analysés avec des méthodes minéralogiques et pétrographiques classiques telles que l'observation macroscopique des cuttings à la loupe binoculaire, la diffraction des rayons X (DRX), la microscopie électronique à balayage (MEB) équipée d'un spectromètre X, et des analyses chimiques sur roche totale. Ces premières analyses ont permis de caractériser la minéralogie secondaire des échantillons avant de pouvoir interpréter, dans un second temps, les spectres résultant des analyses en spectroscopie infra-rouge à courte longueur d'onde (SWIR pour Short Wave InfraRed). L'analyse SWIR apparaît comme une méthode prometteuse de par sa rapidité d'exécution et novatrice pour la quantification des minéraux argileux secondaires. Toutefois, une calibration des spectres SWIR par rapport à la minéralogie rencontrée doit être réalisée en amont. Dans le granite du Fossé rhénan, l'illite et les interstratifiés de type illite-smectite (<10% smectite) (I/S ml) ont été identifiés comme étant les principaux minéraux argileux résultant de l'altération hydrothermale laquelle s'exprime par une illitisation des minéraux primaires (biotite, feldspaths) et des minéraux secondaires plus précoces (chlorite). La semi-quantification de ces phases par l'analyse SWIR appliquée sur plus de 3000 échantillons dans les 3 réservoirs granitiques de Soultz-sous-Forêts, Rittershoffen et Illkirch et leur corrélation avec les résultats DRX, MEB et observations binoculaires ont permis de prouver la fiabilité et la précision de la méthode SWIR sur les différents faciès d'altération rencontrés.

Les réservoirs fracturés granitiques du Fossé rhénan sont composés de zones de fracture (FZ) qui comprennent un ou plusieurs cœur(s) de faille (FC) et des zones endommagées associées. Les minéraux argileux secondaires que sont les illites et les I/S ml sont systématiquement corrélés aux circulations de fluides anciennes ou récentes associées aux zones fracturées. Les données SWIR à Soultz-sous-Forêts et Rittershoffen peuvent laisser penser qu'une illitisation intense (importante quantitativement) est un bon marqueur de la perméabilité actuelle dans les FZ. Dans cette configuration, le rôle perméable des cœurs de failles pourrait être supplanté par la perméabilité due à la porosité secondaire résiduelle résultant de la dissolution des minéraux primaires, dans les zones endommagées. Toutefois, les résultats des analyses SWIR à Illkirch suggèrent également qu'une forte illitisation largement répartie dans la masse, et notamment autour des cœurs de faille, peut aussi colmater les chenaux de circulation. Ces observations soulignent donc un équilibre fragile entre les processus de dissolution et de précipitation qui peuvent soit préserver, soit colmater les drains naturellement perméables au sein d'une FZ.

L'analyse structurale des réseaux de fractures naturelles dans les réservoirs géothermiques est fondée sur un jeu de données géophysiques (imagerie de parois) et géologiques (carottes) provenant des 8 puits étudiés. La fracturation naturelle de Soultz-sous-Forêts et Rittershoffen a été comparée à celle d'Illkirch. Le réseau de fractures naturelles a été caractérisé en termes d'orientation, d'espacement inter-fractures, de densité, d'épaisseur et de distribution spatiale. Ces fractures naturelles héritées de l'histoire tectonique polyphasée du Fossé rhénan depuis le Viséen sont très pentées et orientées NNW-SSE à N-S. Les densités et épaisseurs de fractures les plus élevées qui sont les plus propices aux circulations hydrothermales sont localisées au toit du socle granitique fracturé.

La comparaison des minéraux argileux secondaires et de la fracturation naturelle sur les trois sites de géothermie de Soultz-sous-Forêts, Rittershoffen et Illkirch a permis de mettre en lumière les points suivants :

- L'application intégrée des mesures infra-rouges à plusieurs puits recoupant la même minéralogie secondaire souligne l'intérêt de la quantification des minéraux argileux et a permis de calibrer et de démontrer l'efficacité de la méthode SWIR.
- La distribution du matériel illitique résultant de l'altération argillique dans les FZs semble être un facteur déterminant pour la perméabilité du réservoir dans le fossé Rhénan supérieur. Au-delà de l'intensité de l'altération hydrothermale, c'est la manière dont elle est répartie dans la masse qui permet de préserver, ou non, la perméabilité dans les FZ.
- Les circulations fluides sont distribuées dans des drains complexes dans les différentes parties des FZs : *damage zones*, *wallrocks*, et *fault core(s)*.
- Les observations dans les puits géothermiques ont souligné un équilibre fragile entre les processus de dissolution et de précipitation qui peuvent boucher ou préserver les drains de circulations naturelles dans les FZs.
- Pour atteindre des débits exploitables, la connexion entre les puits et le réseau de fractures perméable peut être maximisée avec des trajectoires de puits recoupant les failles locales au toit du socle granitique de manière optimale.

Les résultats obtenus dans cette thèse soulignent la valeur ajoutée de la combinaison des méthodes géologiques et géophysiques pour la compréhension des circulations fluides dans le granite naturellement fracturé du Fossé rhénan. Ils permettent de proposer une révision du modèle conceptuel des circulations fluides dans les zones de faille et de fracture intersectées par les puits et soulignent l'intérêt d'intégrer l'approche SWIR dans le processus d'exploration pour la géothermie profonde.

Cette thèse est structurée en trois parties : 1) État de l'art et objectifs de la thèse, 2) Zones de fractures perméables à l'échelle des puits, et 3) Conclusions et perspectives, lesquelles sont divisées en neuf chapitres.

# Contents

Preface.....	1
Avant-propos .....	2
Remerciements.....	3
Abstract.....	5
Résumé.....	9
Contents.....	12
List of Figures .....	14
List of Tables .....	23
Abbreviations .....	25
PART 1:.....	27
STATE OF THE ART AND OBJECTIVES OF THE THESIS .....	27
1. Geothermal energy .....	28
1.1. Concepts.....	28
1.2. Production.....	30
1.3. Targets of the European Commission .....	35
1.4. Deep geothermal energy in the URG.....	36
2. Geological setting.....	40
2.1. Tectonic phases and associated mineralisations in the URG .....	40
2.2. Fluid circulation in the URG .....	44
2.3. Soultz-sous-Forêts .....	46
2.4. Rittershoffen .....	51
2.5. Illkirch.....	52
3. Fracture zones complexity .....	53
3.1. Muschelkalk limestones .....	53
3.2. Buntsandstein sandstones .....	55
3.3. Palaeozoic granite .....	57
4. Motivation .....	63
4.1. Socio-economic framework.....	63
4.2. Scientific motivation.....	64
PART 2:.....	67
PERMEABLE FRACTURE ZONES AT WELL SCALE .....	67
5. Structural geology and geophysical signatures of permeable fracture zones .....	68

5.1.	How do the geological and geophysical signatures of permeable fractures in granitic basement evolve after long periods of natural circulation? Insights from the Rittershoffen geothermal wells (France). Published in Geothermal Energy Journal.....	69
5.2.	Structural characterization of naturally fractured geothermal reservoirs in the central Upper Rhine Graben. Submitted to the Journal of Structural Geology. ....	92
6.	Argillic and geophysical signature of permeable fracture .....	121
6.1.	Clay mineralogy: a signature of granitic geothermal reservoirs of the central Upper Rhine Graben. Submitted to Minerals Journal. ....	122
6.2.	How do secondary minerals in granite help distinguish paleo- from present-day permeable fracture zones? Joint interpretation of SWIR spectroscopy and geophysical logs in the geothermal wells of Northern Alsace. Published in the Geofluids journal. ..	147
6.3.	Contribution of SWIR to the Clay Signature of Permeable Fracture Zones in the Granitic Basement. Overview of Soultz and Rittershoffen wells. Presented at the European Geothermal Congress 2019.....	175
6.4.	Impact of secondary clay minerals quantity on the permeability of granitic geothermal reservoirs. Insights from the GIL-1 well, coupled interpretation of SWIR and electrical induction logs.....	192
PART 3: .....		211
CONCLUSIONS AND PERSPECTIVES .....		211
7.	Major outcomes for research .....	212
8.	Major outcomes for industrial exploitation .....	217
9.	Perspectives.....	222
References.....		223
APPENDICES .....		244

# List of Figures

Figure 1.1: Non-magmatic active geothermal system in active extensional terrains with different types of reservoirs (1, 2a and 2b) from Moeck, (2014). Type 1 is a convection cell from infiltration to discharge along one fault. Temperature gradient is very low at well site 1. Types 2a and 2b are fault controlled activity. The temperature of a well drilled into such an area increases up to the permeable layer and drops below the layer (2a and 2b). ..... 29

Figure 1.2: Generic URG geothermal plant for co-production of energy and lithium. Schematical 3D block diagram of deep geothermal wells in a fractured basement and view of the surface installations for electricity and heat production, and lithium extraction (source ES-Géothermie)..... 30

Figure 1.3: Map of the geothermal power plants repartition in the world in 2020 (Huttrer, 2020). ..... 31

Figure 1.4: Country leaders in power generation from geothermal energy a) worldwide comparison with Europe and France, b) European comparison. Datasets are from (1) Huttrer, (2020), dataset of 2020; (2) International Energy Agency, dataset of 2018; (3) EGEC, dataset of 2019..... 31

Figure 1.5: Map of the underground heat resources in France and a) geothermal heat plants operating for direct use of heat, from BRGM. The Rittershoffen plant is the only project providing heat to industry. b) geothermal power plants operating for electricity production, from EGEC country report 2019..... 32

Figure 1.6: Estimates of lifecycle GHG emissions (gCO<sub>2eq</sub>/kWh) for broad categories of electricity generation technologies (Edenhofer et al., 2012). CCS: carbone capture and storage..... 33

Figure 1.7: Levelized cost of energy (LCoE) comparison per MWh after Ray, (2019)..... 34

Figure 1.8: European REmap case electricity mix by 2050. .... 35

Figure 1.9: a) Map of the European Cenozoic rift system (ECRIS) after Dèzes et al., (2004), black lines specify the Cenozoic faults, grey zones represent the sedimentary basins, black zones represent volcanism, marks represent the basement and the dotted line represents the Alpine push. BF= Black Forest, BG = Bresse Graben, EG = Eger (Ohre) Graben, FP = Franconian platform, HG = Hessian Graben, LG = Limagne Graben, LRG = Lower Rhine Graben, URG = Upper Rhine Graben, OW = Odenwald, VG = Vosges. The red frame represents the map on Figure 1.10 b) Map of the Temperatures extrapolated at 5 km depth after Hurtig et al., (1992). ..... 36

Figure 1.10: Map of the deep geothermal sites operating or under development in 2020, also representing the major oilfields and the isotherms at 2000 m depth. Isotherms were re-drawn based on a joint-interpretation of those proposed by Baillieux et al., (2013), GeOrg, (2017) and Vidal et al., (2019). ..... 38

Figure 1.11: Evolution of deep geothermal concepts through time. Overview of the URG geothermal projects..... 39

Figure 2.1: Geodynamic evolution of the URG and its several tectonic phases, with the orientations of faults and stresses in the URG along the geological timescale, on the left. On the right, associated mineralisation episodes are presented from the Palaeozoic to the Cenozoic ages, modified after Bossennec et al., (2020) and other references: (1) (Baatartsoqt et al., 2007), (2) (Burisch et al., 2017a), (3) (Walter et al., 2016), (4) (Bartier et al., 2008), (5)

(Dezayes and Lerouge, 2019), (6) (Clauer et al., 2008), (7) (Lippolt and Seibel, 1991), (8) (Burisch et al., 2017b), (9) (Pfaff et al., 2010), (10) (Walter et al., 2017), (11) (Schleicher et al., 2006), (12) (Cathelineau et al., 2012), (13) (Walter et al., 2019), (14) (Bons et al., 2014), (15) (Staude et al., 2012), (16) (Walter et al., 2018), (17) (Boiron et al., 2010), (18) (Cathelineau et al., 2004), (19) (Schwinn et al., 2006)..... 43

Figure 2.2: Temperature distribution in the 112 boreholes of Soultz-sous-Forêts area. Database from Agemar et al., (2012) and Pribnow and Schellschmidt, (2000). Figure is from Baillieux, (2012)..... 44

Figure 2.3: Temperature anomalies at top basement, distribution of temperature measurements in boreholes and their distance to top basement, and fault traces and dip directions (black lines) at top basement. A temperature gradient of 39.2°C per km, corresponding to the lowest temperature gradient observed in the area, is subtracted from the temperature field at the top basement to obtain this temperature anomaly map at top basement. Temperature database from (Pribnow and Schellschmidt, 2000) and (Agemar et al., 2012). Temperature anomalies of Soultz-sous-Forêts and Rittershoffen and local faults. Figure is from (Baillieux et al., 2014). ..... 45

Figure 2.4: Fluid flow scenarios visualized via a modelling of the central area along a section through Soultz-sous-Forêts and Rittershoffen. On top, the topography and the assigned hydraulic head are shown. Figure is the model D with high permeable faults from Freymark et al., (2019). ..... 46

Figure 2.5: a) Structural map of the center of the URG with isotherms at 2 km depth from the geoportal (GeOrg, 2017), the geothermal anomaly in the Strasbourg area is from the dataset of Baillieux et al., (2013). Geothermal power plants in operation are represented by green stars, and the geothermal projects under drilling operations by blue stars. On the left and right sides, N-S sections with simplified geology are presented: b) through the Soultz-sous-Forêts wells, c) through the Rittershoffen wells, c) through the Illkirch well. The thick line represents the cased section of the wells, and the thin line the open hole. Production wells are in red, and injection wells are in blue. GPK-1 well is today an observation well, and GIL-1 well is not yet in operation..... 47

Figure 2.6: Type of geological and well-logging data used or collected, in the deep geothermal wells of Soultz-sous-Forêts, Rittershoffen and Illkirch. BHTV: BoreHole TeleViewer, CEC: Cation Exchange Capacity, FMI: Formation Micro-Imager, FMS: Formation Micro-Scanner, GR: Gamma-Ray, UBI: Ultrasonic Borehole Imager, SWIR: Short-Wave Infrared spectroscopy, XRD: X-Ray Diffraction. .... 50

Figure 3.1: Core samples from EPS-1 well. a) in the Muschelkalk: on the left dolomite strongly folded with fractures at 955 m depth, on the right hydraulic breccia at 965 m depth. Picture is from (Aichholzer et al., 2019). b) FZ and secondary precipitations in the Vosgian sandstone at 1204 m depth, and c) FZ and its related argillic alteration in the granite at 2160 m depth. ... 55

Figure 3.2: Different architectures and structural elements of fault zones in a) porous sandstones with fault core (FC) composed of clay and a damage zone (DZ) with deformation bands. As a third fault zone part mixed zones (MZ) with deformed and mixed sediments where established (Heynekamp et al., 1999; Rawling and Goodwin, 2006), and in b) crystalline rocks with fault core (FC) composed of breccia and fault gouge and damage zone (DZ) with increased fracture density (Caine et al., 1996). Figure is from (Bauer et al., 2015). ..... 56

Figure 3.3: Porosity profile and fracture density in a conceptual zonation of lithofacies related to hydrothermally altered and fractured granite. Figure from Genter et al., (2000). ..... 58

Figure 3.4: Examples of composite logs for a fracture zone in GPK-1. UBI: acoustic borehole image; Legend of facies: red crosses: monzogranite; green hatches: argillic altered granite; blue hatches: cataclased granite; blue crosses: brecciated granite; black: quartz vein. Figure is from (Dezayes et al., 2010). ..... 61

Figure 3.5: Complexity of a fracture zone (FZ). Three zones are distinguished: a) the fault core, which can be a pathway for fluid if illite and quartz veins do not totally seal the zone, b) the damage zone, which can be sealed or opened with small-scale fractures that act as fluid pathways, and c) the unaltered granite, which generally shows very low matrix and fracture permeability. .... 63

Figure 4: Synthetic representation of the methods used in the thesis to address the mineralogical and structural controls on the permeability of deep naturally fractured crystalline reservoirs with well logs, borehole images and cuttings analyses from the geothermal wells of Soultz-sous-Forêts, Rittershoffen and Illkirch. .... 66

Figure 5.1: Location of the Rittershoffen geothermal site. a Simplified geological and structural map of the Rittershoffen and Soultz-sous-Forêts (SsF) area. The isotherms at the top of the basement are from Baillieux et al. (2014). b Geological cross section through the Rittershoffen and Soultz-sous-Forêts geothermal sites with the Rittershoffen well trajectories, after the GeOrg Team (2017). The dashed lines are schematic trajectories of the GRT-1 (blue) and GRT-2 (red) geothermal wells (Vidal et al., 2018). .... 71

Figure 5.2: Composite log of the GRT-2 granitic basement, including alteration mineral quantities from cutting observations and the following geophysical logs: resistivity, temperature, mud losses, rate of penetration (ROP), gamma ray, porosity, and density. The permeable fracture zones (in red) were deduced from the complete data set presented here and were based on the previous studies (Vidal et al., 2017). The gray areas represent loss of data due to well temperatures that were too high. The facies are as follows: GRAN: granite, HLOW: low hydrothermal alteration grade, HMOD: moderate alteration grade, HHIG: high alteration grade, VEIN: quartz vein, RED: reddish granite. .... 72

Figure 5.3: Geological logs of both the GRT-1 and GRT-2 wells, based on the mineralogical quantities observed in cuttings. The reference depth is TVD for both wells. The facies are as follows: GRAN: granite, HLOW: low hydrothermal alteration grade, HMOD: moderate alteration grade, HHIG: high alteration grade, HEXT: extreme hydrothermal alteration, VEIN: quartz vein, GRAN\_OX: oxidized granite, RED: reddish granite, PERM: Permian sandstone. .... 74

Figure 5.4: Correlation between the mineralogy observed in cores (left) and the mineralogy observed in cuttings (right), defining the several granitic alteration facies (middle). The conceptual fracture zone architecture and its corresponding alteration grades is not at scale and links mineralogy observed in cores with the mineralogy observed in cuttings (middle) (Genter et al., 2000). .... 76

Figure 5.5: Identification of fractures from geophysical logs in the GRT-2 well. a) Major permeable fractures identified at 2900 m MD in the caliper log. The black arrows indicate the cave visible in the hole radii (left) in the oriented caliper log (right) to fit a sinusoid with at least three points. b) Acoustic image log with visible sinusoids representing natural fractures, identified and interpreted from Vidal et al., (2017). .... 78

Figure 5.6: Wells GRT-1 and GRT-2 with geology, temperature, and gamma ray data at the same depth. The cumulative number of fractures is from acoustic images for both wells and from the caliper data for the GRT-2 well. The fracture analysis was performed using stereographic diagrams, specifically, Schmidt lower hemisphere plots realized with the Kamb method; 2 specifies the initial contouring interval and 3 specifies the number of standard deviations that define the expected count for a uniform distribution. The stereographic diagrams were constructed based on both caliper and acoustic image log data for four major fracture zones in the granitic basement of the GRT-2 well. The black areas represent zones where UBI data was not acquired, and the gray areas represent zones where fractures from the caliper log were not computed. The UBI fracture datasets are from (Vidal et al., 2016a). The facies are as follows: GRAN: granite, HLOW: low hydrothermal alteration grade, HMOD: moderate alteration grade, HHIG: high alteration grade, HEXT: extreme hydrothermal alteration, VEIN: quartz vein, GRAN\_OX: oxidized granite, RED: reddish granite, PERM: Permian sandstone. .... 81

Figure 5.7: Comparison of the measured and calculated electrical logs. a) From left to right: measured apparent resistivity, contribution of the porosity to the calculated resistivity (Archie term), contribution of the clays to the calculated resistivity, and recalculated synthetic resistivity. Red zones indicate permeable fracture zones. b) Consequences of the independent weighting of the Archie term (y-axis) and the clay term (x-axis) for the fit of the resistivity model [RMS in log(ohm m)]. The optimal solution includes two independent coefficients (red cross) and produces the lowest RMS value (dark blue). After correction, the “clay term” resistivity log is in fact 10 times higher (and the contribution to the conductivity is 10 times lower). ..... 86

Figure 5.8: Conceptual model of fracture zones and their geophysical and geological signatures linked to hydrothermal alteration grades in the granitic basement of Rittershoffen. Red zones represent the depth extent of permeable fracture zones. a) Specific geological and geophysical signatures of a permeable fracture. b) Specific geological and geophysical signatures of a plugged fracture with low residual permeability. The geophysical log anomalies are true anomalies that were found in the GRT-2 well as well as the quartz, illite, and chlorite samples. The hydrothermal alteration facies are as follows: HLOW: low hydrothermal alteration grade, HMOD: moderate alteration grade, HHIG: high alteration grade, HEXT: extreme hydrothermal alteration, and VEIN: quartz vein. .... 88

Figure 5.9: a) Structural map of the centre of the Upper Rhine Graben showing the faults at a 2 km depth from the geoportal GeOrg, (2017). The locations of the geothermal power plants under exploitation and under drilling are also shown. Two cross sections in reference to Figures 5.12 and 5.13 are represented on the map. b) The orientations of faults and stresses in the URG during the several tectonic phases are presented along the geological timescale from the Palaeozoic to the Cenozoic ages. .... 94

Figure 5.10: a) Type of data available in each geothermal well, specifying the depth of the logged interval, the depth of the main geological interfaces, the drilling date and the logging date. b) Stereoplots (Schmidt lower hemisphere) per lithology in each geothermal well. The main fracture set is in red, the secondary set is in blue and the less represented one is in black. .... 96

Figure 5.11: Examples of borehole imagery methods and continuous cores: a) Core section of the EPS-1 well at 2156 m MD; b) FMI in the GPK-1 well at 2865 m MD; c) UBI in the GRT-1 well at 2321 m MD; d) CMI in the GIL-1 well in the 8"1/2 section at 3226 m MD; and e) CMI in the GIL-1 well in the 6" section at 3330 m MD. .... 100

Figure 5.12: Schematic geological cross-section drawn following the 3D seismic data, through the Rittershoffen geothermal site with the projection of the trajectories of the GRT-1 and GRT-2 wells. Only the local normal Rittershoffen fault is represented. .... 106

Figure 5.13: Schematic geologic cross-section drawn following the 2D seismic data, through the Illkirch geothermal site with the trajectory of the GIL-1 well. Only the local normal Eschau fault is represented. The occurrence of the Permian sedimentary layer is uncertain because it was not intersected by GIL-1 but was observed in the surrounding wells (Aichholzer, 2019). ..... 107

Figure 5.14: Stereoplots (Schmidt lower hemisphere) of the permeable fractures in the sediments (regrouping Buntsandstein sandstones and Muschelkalk limestone) and in the granite; the orientations and dips used in this figure are detailed in the supplementary materials 5.S1. a) Poles of all the permeable fractures. b) Stereoplot of the permeable fractures in the Muschelkalk and Buntsandstein. c) Stereoplots of the permeable fractures in the granite at Soultz-sous-Forêts, Rittershoffen and Illkirch (from left to right); SHmax is the maximum horizontal stress orientation (Valley, 2007; Hehn et al., 2016). ..... 108

Figure 5.15: a) Cumulative fracture density along the depth for all the geothermal wells. The cumulative fracture density is presented only in the granite, and the depth scale was normalized to begin at the top of the granite for all the wells. b) Table presenting the global fracture densities (frac/m) in the Buntsandstein sandstones and the granite for each well. 110

Figure 5.16: Fracture spacings presented on a log-log scale, with the type of law fitting the data and its equation, and the coefficient of variation (CV): a) For the EPS-1 well; b) For the GIL-1 well; c) For the GRT-1 well and d) For the GRT-2 well. .... 112

Figure 5.17: Cumulative fracture thicknesses presented along the depth (TVD) for the 3 geothermal sites, with the main petrographical units along the depth showing the alteration grades or mineralogy of the granite,: a) For Soultz-sous-Forêts with the EPS-1 and GPK-3 wells; b) For Rittershoffen with the GRT-1 and GRT-2 wells; and c) For Illkirch with the GIL-1 well..... 114

Figure 6.1: a) Structural and geological map of the central URG with isotherms at a 2km depth from the geoportal (GeOrg, 2017). The location of the geothermal power plants in exploitation and under drilling is also shown; b) cross section through the Illkirch site showing the GIL-1 well trajectory through the sedimentary layers, the Eschau fault and the granitic basement c) episodes of secondary minerals deposition occurring in the URG are presented along the geological timescale from the Palaeozoic to the Cenozoic ages, modified after Bossennec et al., (2020). References are a) (Baatartsogt et al., 2007), b) (Burisch et al., 2017a), c) (Walter et al., 2016), d) (Bartier et al., 2008), e) (Dezayes and Lerouge, 2019), f) (Clauer et al., 2008), g) (Lippolt and Seibel, 1991), h) (Burisch et al., 2017b), i) (Pfaff et al., 2010), j) (Walter et al., 2017), k) (Schleicher et al., 2006), l) (Cathelineau et al., 2012), m) (Walter et al., 2019), n) (Bons et al., 2014), o) (Staude et al., 2012), p) (Walter et al., 2018), q) (Boiron et al., 2010), r) (Cathelineau et al., 2004), s) (Schwinn et al., 2006). ..... 125

Figure 6.2: Compositions of biotite in basement rocks from Soultz-sous-Forêts (SsF), Rittershoffen (Ri) and Illkirch (Ik) in the Upper Rhine Graben compared to those of biotites from the Crêtes and Mayet-de-Montagne granites in the MgO, FeO and Al<sub>2</sub>O<sub>3</sub> diagram after (Parneix and Meunier, 1982; Chèvremont and Genter, 1989; Genter, 1989). ..... 126

Figure 6.3: Composite log from the lower part of the open-hole of the GIL-1 well granitic basement, presenting from left to right: the petrographic log built from the binocular lens

observations; the XRD results from the oriented fractions <5 µm and their interpretation; the gamma-ray log; the permeable zones; the fracture density; the major fractures and the samples for which deconvolution of the peak at 10 Å, and SEM analyses were performed. HLOW, HMOD, HHIG and HEXT: low, moderate, high and extreme argillic alteration, VEIN: secondary drusy quartz veins, KFZ: permeable fracture zones. The granitic basement is divided in four depth sections characterized by a) intense argillic alteration; b) and d) propylitic alteration locally superimposed by argillic alteration and c) fresh biotite-rich granite..... 131

Figure 6.4: Microscopic observations of thin sections of cuttings (a, b, c, d, e, f, g, h, i) and rock sample (j) fixed in epoxy in GIL-1 at a) 3340 m MD (crossed polarized light, CPL), b) 3678 m MD (SEM observations), c) and d) 3482 m MD (CPL and SEM), e) and f) 3071 m MD (CPL), g) and h) 3005 m MD (CPL), i) 3678 m MD (CPL), j) unknown depth (SEM). Anh = anhydrite, Ap = apatite, Bt = biotite, Cal = calcite, Ill = illitic minerals, K-Fsp = potassic feldspar, Pl = plagioclase, Qz = quartz, Ti = non identified titanium oxide; INTCH = interlayer charge; HLOW, HMOD, HHIG and HEXT = low, moderate, high and extreme argillic alteration. .... 134

Figure 6.5: XRD results of oriented samples made on the fraction <5 µm from the GIL-1 well under air dried (AD) and ethylene-glycol (EG) conditions. The sample at 3025 m MD presents a predominance of I/S ml and PCI whereas the sample at 3340 m MD presents a predominance of well crystallized illite (WCI) (+/- micas). Ca = calcite, Chl = chlorite, Ill = illite, I/S ml = illite-rich illite-smectite mixed layers, K-Fsp = potassic feldspar, Pl = plagioclase, Qz = quartz..... 135

Figure 6.6: Decomposition of peak profile in the 7–10° 2θ CuKα domain of the X-ray diffractograms (<5 µm clay fraction) of AD and EG-saturated oriented powder of three samples (3071, 3171 and 3452 m MD). AD = air dry, EG = ethylene glycol, I/S ml: illite-rich illite/smectite mixed layer; WCI: well crystallized illite, PCI: poorly crystallized illite. .... 137

Figure 6.7: Chemical compositions of primary biotite, illite, and chlorite formed during the hydrothermal alteration of the granite at Soultz-sous-Forêts (GPK-1 well), Rittershoffen (GRT-1 & GRT-2 wells) and Illkirch (GIL-1 well) in the M+ 4SI R<sup>2+</sup> diagram ; a) illites, biotites and chlorites in the three sites, b) illites in Illkirch granite affected by argillic fracture-related alteration (2894-2350 m MD); c) illites in Illkirch granite affected by propylitic alteration (3104-3433 & 3513-3686 m MD); Bei +/-: beidellite high/low charge, Ill: illite, Mnt +/-: montmorillonite high/low charge, Ms: muscovite. Soultz-sous-Forêts data are from Genter, (1989) and Rittershoffen data are from Vidal et al., (2018)..... 139

Figure 6.8: Plot of X<sub>Fe</sub> (Fe/(Fe+Mg+Mn)) versus Si/Al content for the chlorites and biotites at Soultz-sous-Forêts, Rittershoffen and Illkirch, Soultz-sous-Forêts data are from Genter, (1989) and Rittershoffen data are from Vidal et al., (2018). .... 140

Figure 6.9: Paragenetic sequence of the granitic basement at Illkirch and schematic representation of the successive hydrothermal alterations that occurred in the fractured granite and sandstone intersected by the GIL-1 well at Illkirch. The (1), (2), and (3) alteration stages were described in this paper. Only the paloweathering that was not observed at Illkirch because of the Eschau fault, but was observed at Soultz-sous-Forêts and Rittershoffen (Just and Kontny, 2011)..... 143

Figure 6.10: Complexity of a FZ after Caine et al., (1996). We can differentiate three zones: a) the fault core, which can be a pathway for fluid if illite and quartz veins are not totally sealing the zone, b) the damage zone, which can be sealed or opened with fractures that are acting as fluid pathways, and c) the unaltered granite, which shows generally very low permeability. .... 148

Figure 6.11: (a) Structural map of the top of the granitic basement from the GeOrg geoportal with the well trajectories (green), the thermal anomalies (Baillieux et al., 2013), and the Soultz-sous-Forêts (SsF) and Rittershoffen localizations. (b) Geological cross section through the GPK-1 and GRT-2 wells crossing the URG sedimentary cover and granitic basement; the well trajectory of the GRT-2 well is a NW-SE projection on the cross section, from the last 3D seismic campaign (Richard et al., 2019)..... 150

Figure 6.12: Examples of mineralogical assemblages of the granitic basement observed in cores (middle) and in cuttings (right); these assemblages define the different hydrothermal alteration grades (left). GRAN: unaltered granite; HLOW: low hydrothermal alteration; HMOD: moderate hydrothermal alteration; HHIG: high hydrothermal alteration; HEXT: extreme hydrothermal alteration; VEIN: secondary drusy quartz vein; Anh: anhydrite; Bt: biotite; Cal: calcite; Chl: chlorite; Hem: hematite; Ill: illite; Kfs: potassic feldspars; Pl: plagioclase; Qz: quartz..... 153

Figure 6.13: (a) Example of an absorption spectrum and a simulated profile in the GRT-2 well at 2800 m. (b) Reference spectra from Pontual et al., (1997) for biotite (Bt), muscovite (Ms), chlorite (Chl), and illite (Ill). ..... 155

Figure 6.14: Composite log of the GRT-2 well at Rittershoffen presenting the mineral quantity, petrographical log, T log, porosity and density logs, drilling tool change, total GR, SWIR results with water and the 2200 nm absorption band areas, and resistivity log. Petrographical facies abbreviations are defined in the legend in Figure 6.12. .... 160

Figure 6.15: Magnified view of the four (a, b, c, and d) main permeable FZs of the GRT-2 well at Rittershoffen, presenting the mineral quantity, petrographical log, T log, porosity and density logs, total GR, SWIR results with water and the 2200nm absorption band areas, and resistivity log (low values to the right). Petrographical facies abbreviations are defined in the legend in Figure 6.12. .... 161

Figure 6.16: Composite log of the GPK-1 well at Soultz-sous-Forêts, presenting the mineral quantity, petrographical log, T log, porosity and density logs, drilling tool change, gas species, spectral GR-K, SWIR results with water and 2200 nm absorption band areas, and resistivity log. Petrographical facies abbreviations are defined in the legend in Figure 6.12. .... 163

Figure 6.17: Magnified view of two (a and b) main permeable FZs of the GPK-1 well at Soultz-sous-Forêts, presenting the petrographical log, T log, porosity and density logs, spectral GR-K, SWIR results with water and 2200 nm absorption band areas, and resistivity log. Petrographical facies abbreviations are defined in the legend in Figure 6.12. .... 165

Figure 6.18: Correlation of the SWIR water and 2200 nm absorption band area for (a) the GRT-2 and GPK-1 wells, (b) XRD results for the slightly altered granite and the hydrothermally altered granite in the GRT-2 well, and (c) XRD results for the unaltered granite and the hydrothermally altered granite in the GPK-1 well. .... 167

Figure 6.19: Model showing the variation in the 2200 nm absorption band area and its correlation with geophysical logs (gamma ray, temperature, and electrical conductivity) in response to different grades of hydrothermal alteration of the granite and different FZ architectures..... 170

Figure 6.S1: Composite log of the GPK-1 well presenting the secondary minerals, the petrographical log built from the mineralogical observations, the temperature log, the spectral K-GR log and the SWIR results. The successive measurements realized for each cuttings bag are represented by black full circles and the error bounds calculated from these successive

measurements are represented by the distance between red squares for each cuttings bag. .....	172
Figure 6.S2: Composite log of the GRT-2 well presenting the secondary minerals, the petrographical log built from the mineralogical observations, the temperature log, the GR log and the SWIR results. The successive measurements realized for each cuttings bag are represented by black full circles and the error bounds calculated from these successive measurements are represented by the distance between red squares for each cuttings bag. .....	173
Figure 6.S3: Composite log of the GPK-1 well presenting the secondary minerals, the petrographical log built from the mineralogical observations, the temperature log, the spectral K-GR log and the SWIR results that were free-fitted with the TSS software (blue and yellow full circles for water and 2200 nm absorption band areas, respectively). The light green full circles represent the SWIR results manually fitted. ....	174
Figure 6.20: NW-SE Geological cross section through the Soultz-sous-Forêts GPK-4 well and the Rittershoffen GRT-1 well. ....	176
Figure 6.21: XRD diffraction patterns a. of the clay fraction in the GRT-1 well main FZ, after Vidal et al., (2018). b. of a vein alteration facies in the GPK-4 well (untreated sample), after Dezayes et al., (2005). c. of a vein alteration facies in GPK-4 (untreated sample). The chlorite peaks are still visible despite the occurrence of illite, indicating percentage of mixing rock, after Dezayes et al., (2005). ....	178
Figure 6.22: Mineralogy and its corresponding alteration facies. Observed from cores (left, Soultz-sous-Forêts) and from cuttings (right, Rittershoffen). ....	180
Figure 6.23: a) Example of an absorption spectra and the simulated profile in the GRT-1 well at 2420 m MD. b) Reference spectra from literature of illite, chlorite and biotite. ....	182
Figure 6.24: Composite log of the GRT-1 well presenting the petrography observed on cuttings with the associated minerals quantity, the SWIR results with the water feature, 2200wvl and the total area, the potassium (K) from the spectral gamma ray (GR), the temperature log acquired at temperature equilibrium and the drilling tool change. ....	184
Figure 6.25: Zoom on the main permeable FZ of the GRT-1 well, showing the petrography, the SWIR results with the water feature, 2200wvl and the total area, and the potassium (K). a. acoustic image log of the open fracture at 2328 m. b. acoustic image log of the open fracture at 2359 m c. acoustic image log of the open fracture at 2328 m. ....	185
Figure 6.26: Composite log of the GPK-4 well presenting the petrography observed on cuttings with the associated minerals quantity, the SWIR results with the water feature, 2200wvl and the total area, the potassium (K) from the spectral gamma ray (GR), the temperature log acquired at temperature equilibrium and the drilling tool change, (GR2M: two mica granite, MELA: biotite rich granite, INT: granite artificially enriched in biotite due to drilling process). .....	187
Figure 6.27: Zoom on a FZ of the GPK-4 well, showing the petrography, the SWIR results with the water feature, 2200wvl and the total area, the potassium (K), and the temperature log. a. acoustic image log of the fracture at 2234 m MD. b. acoustic image log of the fracture at 2273 m MD. ....	188
Figure 6.28: Zoom on a FZ of the GPK-4 well, showing the petrography, the SWIR results with the water feature, 2200wvl and the total area, the potassium (K), and the temperature log. a.	

acoustic image log of the fracture at 4780 m MD. b. acoustic image log of the fracture at 4802 m MD.....	189
Figure 6.29: Model of variation of the area of the 2200wvl in response to the different grades of hydrothermal alteration of the granite and to FZ. ....	190
Figure 6.30: Composite log of GIL-1 well at Illkirch showing on the left the raw petrographical log (1) based on the mineralogy deduced from binocular observations and the clay minerals occurrence from XRD. On the right, the petrographical log based on SWIR observations and the clay content (water and 2200 nm absorption band areas).....	197
Figure 6.31: Correlation of the water and 2200 nm absorption bands areas from SWIR spectroscopy in the granitic basement of GIL-1 well. Samples have been sorted according to the petrographic log (2) shown in Figure 6.30, quartz veins are shown in the Figure 6.30..	198
Figure 6.32: Correlation plot between the 2200 nm absorption band area and the electrical resistivity. Interpolation was realized by affecting electrical resistivity values to the closest SWIR values. a) the samples have been sorted according to the petrographical log (3) shown in Figure 6.33, and b) quartz veins depths are shown in the Figure 6.30. ....	199
Figure 6.33: Composite log of the GIL-1 well presenting the mineralogy (binocular observations, XRD and SWIR), the geophysical logs (electrical induction, gamma-ray, porosity and density), natural fractures (fracture density, major fractures, ROP, caliper) and the permeability evidences (gas occurrences, T anomalies, and mud losses).....	201
Figure 6.34: Correlation plot between the 2200 nm absorption band area and the electrical resistivity. Interpolation was realized by affecting electrical resistivity values to the closest SWIR values. The samples represented are the ones corresponding to the thermal anomalies shown in red in Figure 6.33, and to the quartz veins shown in the Figure 6.30. ....	207
Figure 7.1: Evolution of a permeable fracture zone (KFZ) through time, forming a complex architecture resulting from several deformation and hydrothermal alteration cycles, determining the permeability distribution, DZ: damage zone, WR: wallrock, FC: fault core.	215
Figure 8.1: Conceptual model of the granitic section intersected by GIL-1 well at Illkirch. ..	218
Figure 8.2: 2D conceptual model of the geothermal reservoirs in the Upper Rhine Graben including horst structure and well trajectories.....	219
Figure 8.3: Innovative drilling techniques applied in the oil and gas industry (Sahu et al., 2020). ....	220



## List of Tables

Table 1: Geothermal and Lithium research permits (PER) and concessions in the URG area in November 2020. Source ES-Géothermie.....	40
Table 5.1: Details of the geological and geophysical data sets available for the granitic basement of the GRT-1 and GRT-2 wells. The first column presents the type of data; columns two and three present the measured depth intervals in the two openhole sections. The fourth column presents the units of the data, and the fifth column presents the resolution of the data according to the log acquisition resolution, both vertically and horizontally (in italic letters)..	73
Table 5.2: Structural analysis of the GRT-2 granitic basement with the caliper. Comparison of the structural analyses and their accuracies as calculated from the caliper and acoustic image logs (zones 1 and 2). Structural analysis from caliper data only (zones 3 and 4).....	82
Table 5.3: Description of the specificities of each method used for the structural data analysis. The well logged, the logging date, the tool configuration, the vertical and azimuthal resolutions, as well as the references are detailed for each method used.....	103
Table 5.4: Fracture thickness densities and mean values of the fracture thicknesses calculated for the EPS-1, GPK-3, GRT-1, GRT-2 and GIL-1 wells. For the GPK-3 well, the top of the granitic section corresponds to the first 800 m of granite intersected by the well, and for the GIL-1 well, it corresponds to the 200 m of granitic section intersected by the well. ....	114
Table 5.S1: Major permeable fractures identified in the wells with their depth (MD), dip direction (°E), dip (°), and thickness (mm). The supposed orientations are given in italics and “-“ means no data available. The following permeability indicators associated with the fractures are reported: temperature anomalies, mud losses or outlets and gaz anomalies. The green lines correspond to fractures in the Muschelkalk; the pink lines to fractures in the Buntsandstein; and the white lines to fractures in the granite. The structural data of Rittershoffen are from Vidal et al., (2017) (1) and Dezayes et al., (2013) (2), the data of Soultz-sous-Forêts are from Dezayes et al., (2010) (3), Vidal et al., (2015) (4), Vidal et al., (2018) (5) and from Vidal et al., (2019) (6). The mud losses or outlets, as well as gaz anomalies were computed from Genter, (1989) (7), Vuataz et al., (1990) (8), Genter et al., (1995) (9), Aquilina et al., (1993) (10), (Genter and Tenzer, 1995)(11), Degouy et al., (1992) (12), Socomine, (1995) (13), and the data from the GIL-1 well are original data and were compiled for this study (*). ....	120
Table 6.1: Chemical compositions of the geothermal fluid sampled in the Palaeozoic granite reservoir at Soultz-sous-Forêts in the GPK-2 well (05.02.2020) and at Rittershoffen in the GRT-1 well (04.11.2020) (Bosia et al., 2021). ....	126
Table 6.2: Chemical compositions of major element oxides of 20 cuttings samples from the GIL-1 well. Samples are sorted by facies and grade of alteration. GRBT: Biotite-rich granite, HLOW, HMOD, HHIG and HEXT: low, moderate, high and extreme argillic alteration, VEIN: secondary drusy quartz veins. ....	135
Table 6.3: Calculations of structural formulae of some illitic minerals at various depths in GIL-1 well. Structural formulas were calculated relative to a structure containing 11 oxygen atoms and assuming that the total iron content is composed of Fe <sup>3+</sup> . n.a.: number of analyses; An. Av.: analytical average; s.d.: standard deviation; OCT: octahedral occupancy; INTCH: interlayer charge; X <sub>Fe</sub> : Fe/(Fe+Mg+Mn). 2960, 3005 m MD: HHIG granite; 3071 m MD: KFZ1; 3340 m MD: KFZ4; 3482 m and 3573 m MD: HHIG granite on both sides of KFZ5; 3678 m MD: HLOW granite.....	138

Table 6.4: Calculations of structural formulae of some chlorite at various depths in the GIL-1 well. The structural formulas were calculated relative to a structure containing 14 oxygens and assuming that the total iron content is composed of Fe<sup>2+</sup>. n.a.: number of analyses; An. Av.: analytical average; s.d.: standard deviation; OCT: octahedral occupancy; INTCH: interlayer charge; X<sub>Fe</sub>: Fe/(Fe+Mg+Mn). ..... 140

Table 6.5: Six permeable fracture zones with their SWIR, geophysical and structural signatures visible on the Figure 6.33 and associated permeability indicators. .... 205

## Abbreviations

BHTV	BoreHole TeleViewer
CCS	Carbone Capture and Storage
CEC	Cation Exchange Capacity
DZ	Damage Zone
ECRIS	European Cenozoic Rift System
EDS	Energy Dispersive X-ray Spectrometry
EGS	Enhanced or Engineered Geothermal System
EPS-1	Old petroleum well deepened and cored for the Soultz-sous-Forêts geothermal project
FC	Fault Core
FMI	Formation MicroImager
FMS	Formation MicroScanner
FZ	Fracture Zone
GHG	Greenhouse Gases
GIL-1	Name of the deep borehole of the Illkirch geothermal project
GPK-1, 2, 3, 4	Names of the deep boreholes of the Soultz-sous-Forêts geothermal project
GR	Gamma Ray
GRT-1, 2	Names of the deep boreholes of the Rittershoffen geothermal project
HDR	Hot Dry Rock
HEXT	Extremely altered granite
HHIG	Highly altered granite
HLOW	Slightly altered granite
HMOD	Moderately altered granite
HRLA	High Resolution Laterolog Array
KFZ	Permeable Fracture Zone
LCA	Life Cycle Analysis
LSP	Line Shaft Pump
MD	Measured Depth
NCG	Non-Condensable Gas
NPHI	Neutron Porosity
ORC	Organic Ranking Cycle
PER	Research Permit (Permis Exclusif de Recherches)
PI	Productivity Index
SEM	Scanning Electron Microscopy
SWIR	Short Wave Infrared Spectroscopy
T log	Temperature log
TDS	Total Dissolved Fluid

TOE	Tonnes of Oil Equivalent
TVD	True Vertical Depth
UBI	Ultrasonic Borehole Image
URG	Upper Rhine Graben
VEIN	Vein of secondary hydrothermal quartz
XRD	X-Ray Diffraction
THC	Thermal, Hydraulic and Chemical
I/S ml	illite-rich illite-smectite mixed layers (<10% smectite)
WR	Wallrock



**PART 1:**  
**STATE OF THE ART AND**  
**OBJECTIVES OF THE THESIS**



# 1. Geothermal energy

“Geothermal” means literally the Earth’s heat. The earth’s heat is generated by the natural disintegration of Uranium, Thorium and Potassium from crustal rocks but also by the initial heat produced by the planetary accretion. The main heat transfers are via fluid circulations through faults, fracture networks and intrinsic porosity. At human scale, this is an endless resource. Hence, in the Earth the heat flux increases regularly with depth and the normal geothermal gradient is 30°C/km in stable intracratonic basin. In some regions along tectonic plates, in volcanic areas or active basins associated to rifts, the geothermal gradient could be higher than 30°C/km and could reach up to 300°C/km (active volcanic field). In the actual environmental crisis and increasing demand for energy, the potential of geothermal energy is considerable, but unfortunately often put aside because of high costs and risks. Hence, geothermal energy involves high CAPEX (capital expenditure) because of high investments due to the drilling, and high risks due to the resource uncertainty, induced seismicity, and public acceptance.

## 1.1. Concepts

Geothermal energy can be provided by different types of natural reservoirs, at different depths and temperatures. Very low enthalpy projects exploit fluids with temperatures below 30°C with heat pumps between 10 and 200 m deep, for domestic heat or air-cooling. Geothermal projects for higher enthalpy are divided in projects with installed capacities below and over 20 MWth. Geothermal projects with installed capacities lower than 20 MWth generally exploit deep aquifers via deep wells (<2 km) located in sedimentary basins, with normal geothermal gradients inducing temperatures between 30 and 150°C. The produced heat can then be used for district heating, agriculture (greenhouses, fish farming...) and balneology. Geothermal projects with installed capacities over 20 MWth exploit deep wells (>2 km) in volcanic or magmatic fractured rocks, affected by abnormal geothermal gradients inducing temperatures higher than 150°C for electrical production or industrial use. These projects are usually named “deep geothermal projects”. The produced heat is directly used for industrial needs or converted into electricity. But geothermal resources can also be classified according to their geological setting: magmatic-volcanic type, magmatic-plutonic type, extensional domain type, intracratonic basin type, orogenic belt/foreland basin type, and basement (hot dry rock) type (Moeck, 2014). The geothermal projects of Soultz-sous-Forêts, Rittershoffen and Illkirch considered in this work are high enthalpy projects, in extensional domain type (Figure 1.1). These projects include at least two subvertical deep wells with a cased hole and an open hole targeting the geothermal reservoir (Figure 1.2).

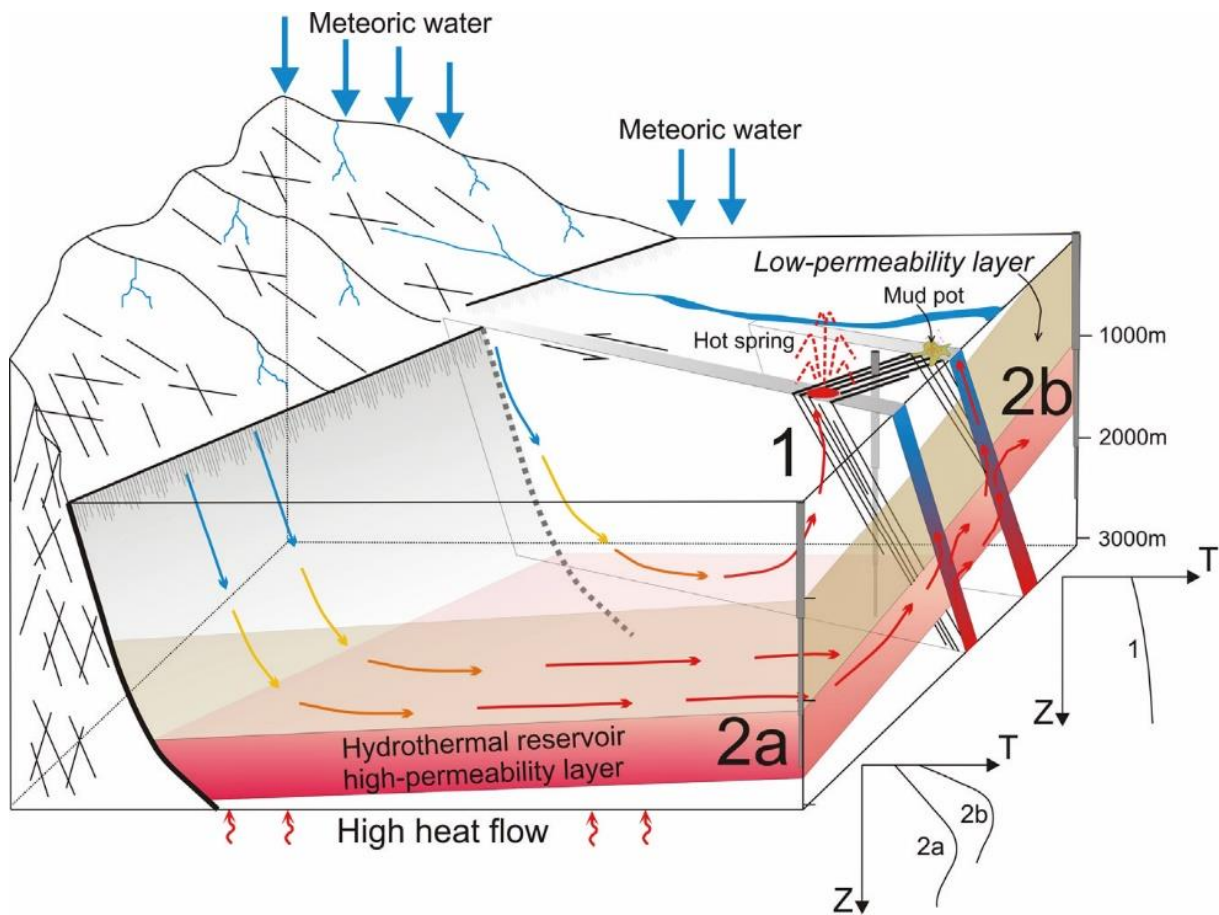


Figure 1.1: Non-magmatic active geothermal system in active extensional terrains with different types of reservoirs (1, 2a and 2b) from Moeck, (2014). Type 1 is a convection cell from infiltration to discharge along one fault. Temperature gradient is very low at well site 1. Types 2a and 2b are fault controlled activity. The temperature of a well drilled into such an area increases up to the permeable layer and drops below the layer (2a and 2b).

The fluid that circulates in the naturally fractured granitic basement is pumped to the surface through the production well. On surface, the produced hot geothermal fluid circulates in a closed loop and, depending on its nature, can be used either directly or through heat exchangers for producing electricity or provide direct heat (Figure 1.2). Then the fluid is reinjected into the injection well and circulates from one well to another through the natural reservoir (Figure 1.2). In France, to be economically viable, a well should reach a productivity index (PI) higher than 2 L/s/bar (Baujard et al., 2017a; Vidal and Genter, 2018). This value is linked to the reservoir properties but also to the well properties (well diameter, depth of the production pump, water level). A well with a PI higher than 2 L/s/bar is considered as hydrothermal. If the natural configuration of the reservoir and the well trajectory does not allow to reach this value, production and injection wells may be enhanced by different stimulation operations. The Enhanced or Engineered Geothermal Systems (EGS) technology consists in thermic, hydraulic and chemical treatments that can be used to (re-)open pre-existing natural fractures, enhance fracture aperture and hydraulic connection or to dissolve mineralisation in order to re-open clogged fractures (Gérard et al., 2006; Schulte et al., 2010; Reinecker et al., 2019). In the Upper Rhine Graben (URG), the highest PI were obtained in hydrothermal projects that do not need any EGS stimulations (Vidal and Genter, 2018). Beyond that, EGS technology often leads to massive fluid injections which can cause induced seismicity that could drastically reduce public acceptance. The optimal way to obtain high PI is then to find natural reservoirs at drillable depth (<3 km) for reducing drilling costs, stimulation costs and risks, with circulating fluids (>70 L/s) at high temperature (>30°C/km, >150°C). Today, another

keen interest is the co-exploitation of lithium (Li) naturally found in the geothermal fluid, and research on Li extraction processes is ongoing with innovative research projects like the European project EuGeLi or the involvement of companies active in this field (ERAMET, Vulcan Energy, Geolith, Cornish lithium). In Europe, the lithium extracted from geothermal plants could supply a significant part of the European demand for lithium and could reduce the dependency on polluting lithium imported from other continents. Beyond this, lithium extraction coupled to geothermal energy production could add value to the geothermal exploitations (Figure 1.2). Finally, lithium extraction from the geothermal fluid would be the first mining exploitation with zero-carbon footprint.

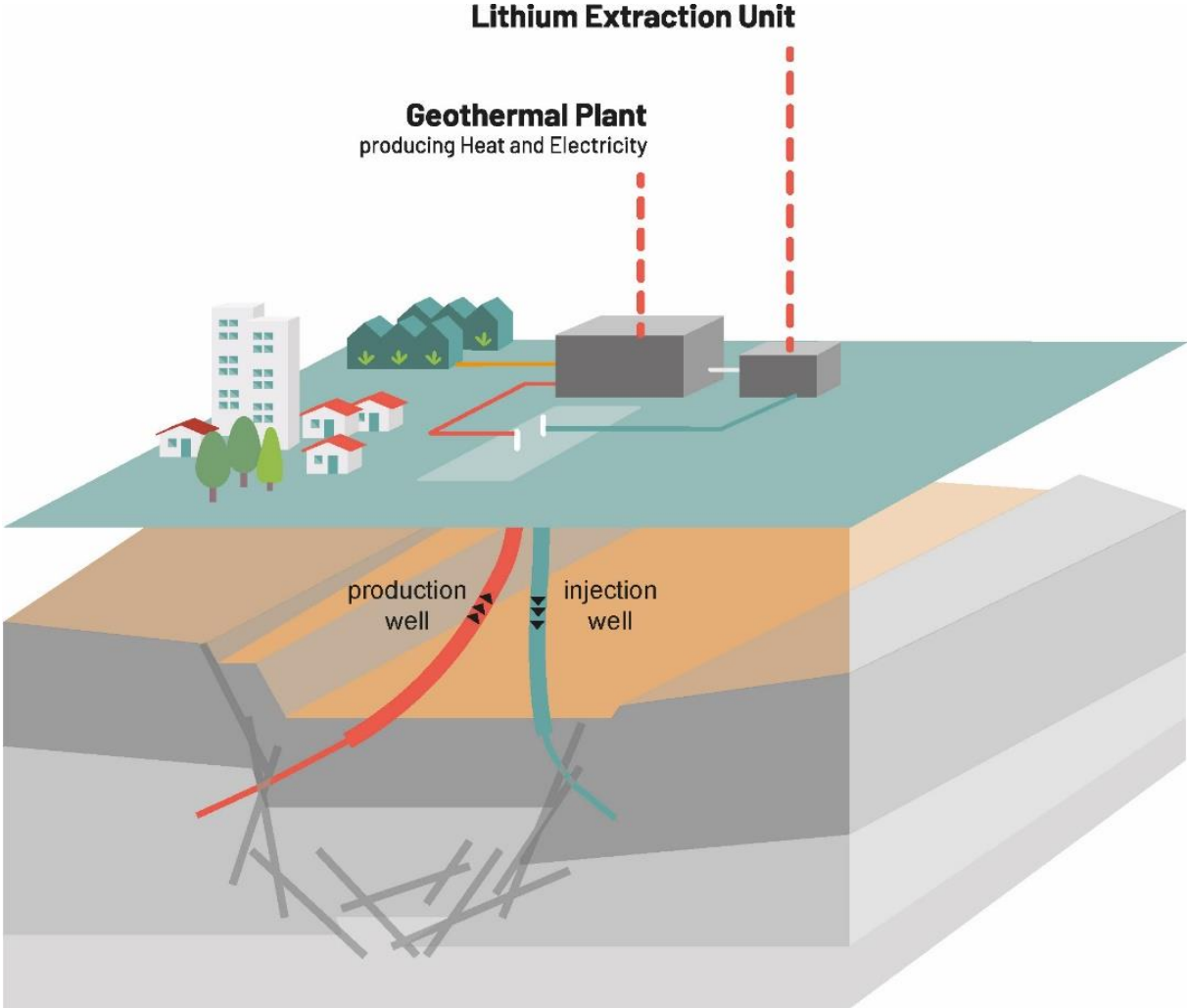


Figure 1.2: Generic URG geothermal plant for co-production of energy and lithium. Schematical 3D block diagram of deep geothermal wells in a fractured basement and view of the surface installations for electricity and heat production, and lithium extraction (source ES-Géothermie).

### 1.2. Production

The first deep geothermal project to generate electricity was initiated in Larderello (Italy) in 1904. In 1921, a geothermal power plant supplied by a deep well was built in the Geysers geothermal field in California (USA); 5 years later, the first greenhouses were heated with geothermal heat in Klamah Falls (USA); and in 1930 the first district heating was constructed in Reykjavik (Iceland). Since then, geothermal installed capacity in the world has increased to reach 15,950 MWe and produce 88 956 GWh of electricity in 2020, but representing only 0.3%

of the global electricity production (Figure 1.3) (Huttrer, 2020). In 2020, countries with the most installed geothermal power capacity are (in descending order): USA, Indonesia, Philippines, Turkey, Kenya, Mexico, New Zealand, Italy, Japan and Iceland (Figure 1.4a) (Huttrer, 2020). The European leader countries with the most installed geothermal power capacity and the highest power generation are Turkey, Italy, Iceland, Germany, Portugal, France, and Croatia (Figure 1.4b).



Figure 1.3: Map of the geothermal power plants repartition in the world in 2020 (Huttrer, 2020).

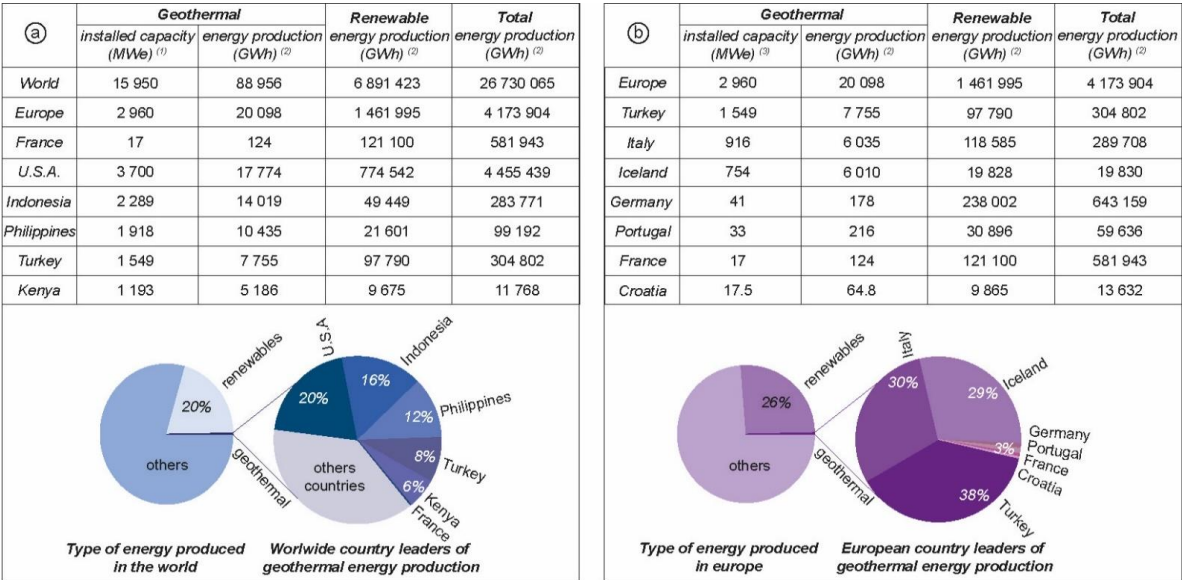


Figure 1.4: Country leaders in power generation from geothermal energy a) worldwide comparison with Europe and France, b) European comparison. Datasets are from (1) Huttrer, (2020), dataset of 2020; (2) International Energy Agency, dataset of 2018; (3) EGEC, dataset of 2019.

In addition, the installed thermal capacity in the world from geothermal plants for direct utilization was estimated to 107,727 MWth in 2020, representing an increase of 52% over the last 5 years, and the thermal energy used was estimated to 283,580 GWh/year (1,020,887 TJ/year), representing an increase of 72% over the last five years (Lund and Boyd, 2020). The major users with more than 20,000 TJ/year are China (246,212 TJ), U.S.A. (145,460 TJ), Sweden (62,400 TJ), Turkey, Japan, Germany, Iceland, and Finland for the year

2019 (Lund and Boyd, 2020). However, the worldwide leaders of direct use in terms of population (per inhabitant) is dominated by Nordic countries with Iceland (99.10 TJ), Sweden (6.22 TJ), Finland (4.23 TJ), Norway (2.34 TJ), and New Zealand (2.12 TJ) (Lund and Boyd, 2020). Besides, the worldwide leaders of direct use in term of land area (per 100 km<sup>2</sup>) is dominated by European countries with Iceland (32.62 TJ), Switzerland (32.18 TJ), Sweden (13.86 TJ), Hungary (11.94 TJ), and Austria (10.30 TJ) (Lund and Boyd, 2020). European leader countries with the most geothermal installed heating and cooling capacities are Turkey (3,587 MWth), Iceland (2,131 MWth), Italy (1,424 MWth), Hungary (908 MWth), France (627 MWth), and Germany (395 MWth) (Sanner, 2019). In France, low to medium enthalpy geothermal systems are massively exploited for the direct use of heat like in the Paris basin or in Aquitaine (Figure 1.5a). However, the Rittershoffen heat plant is the unique high enthalpy project for the direct industrial use of heat in France (Figure 1.5a). In terms of electricity production, France is the last of the European country leaders. Indeed, only 2 geothermal power plants are installed: one at Soultz-sous-Forêts and one in Bouillante. The latter is located in the Guadeloupe department in the Caribbean islands and exploits a very hot fluid (250°C) circulating into the volcanic rocks of the Soufrière volcano, in the Lesser Antilles arc (Figure 1.5b). The power plant of Soultz-sous-Forêts will be largely studied in this manuscript. Soultz-sous-Forêts power plant is situated in the Grand Est region and exploits a hot brine (170°C) circulating in the fractured granitic reservoir of the Upper Rhine Graben, producing 1.7 MWe gross power (Figure 1.5b). A new 12 MWe geothermal power plant was under construction and was expected to be in operation in 2021 at Vendenheim, in the URG at 10 km to the North of Strasbourg. But due to intense seismic activity around this zone the operations were stopped end of 2020 on this site.

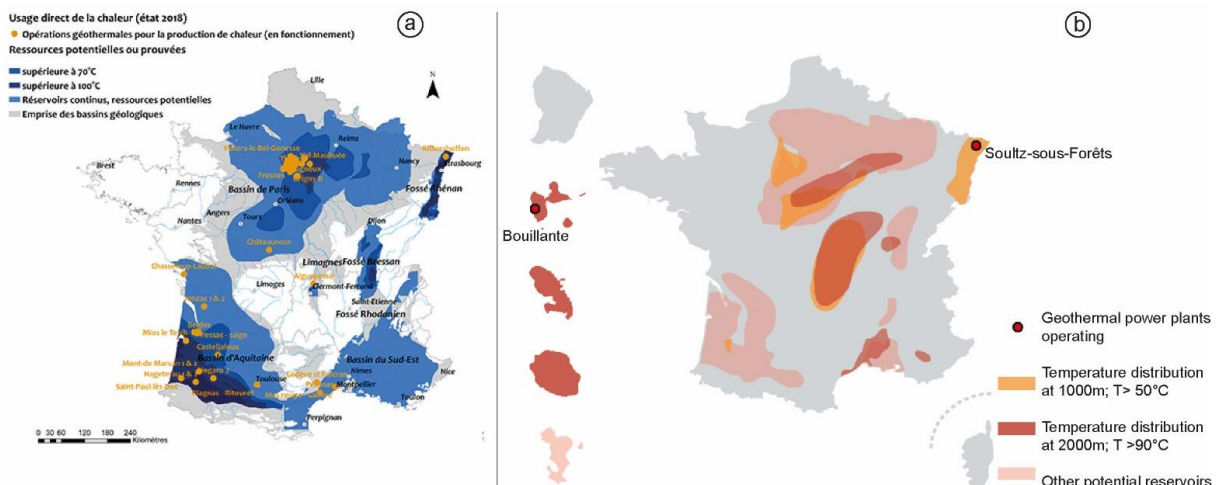


Figure 1.5: Map of the underground heat resources in France and a) geothermal heat plants operating for direct use of heat, from BRGM. The Rittershoffen plant is the only project providing heat to industry. b) geothermal power plants operating for electricity production, from EGEN country report 2019.

Lund and Boyd, (2020) estimated that the direct use of heat from geothermal energy allowed to save in 2019 at least 40.5 million tonnes of oil equivalent (TOE), and about 135 million tonnes of CO<sub>2eq</sub> being released to the atmosphere, considering a CO<sub>2</sub> content of 3.3 tCO<sub>2eq</sub>/TOE. Also, we can estimate that geothermal power generation saved in 2019 about 19.1 million TOE, and 64 million tonnes of CO<sub>2eq</sub> by considering a geothermal energy production of 88,958 GWh, and by applying a thermodynamical efficiency of 40% for electricity generation from oil. These estimations underline that the most gainful energy use from geothermal is the direct use of heat.

Indeed, geothermal energy is a renewable resource exploiting the abundant Earth’s heat, and the fluid, once used and cooled, is reinjected back into the reservoir. However, some geothermal plants operating with flash or even with binary installations are degassing greenhouse gases (GHGs) and toxic elements in the atmosphere. This is a considerable environmental problematic: in Turkey geothermal exploitations release CO<sub>2</sub> in the atmosphere, while elsewhere hydrogen sulphide, ammonia or mercury can also be released, polluting agricultural areas, and causing breathing problems (Figure 1.6) (Bacci et al., 2000; Aksoy et al., 2015). Nevertheless, these aeriform emissions were successfully mitigated in Tuscany and reduced by 95% by ENEL Green Power with an abatement technology allowing to trap H<sub>2</sub>S emissions into solid sulphur (Bonciani et al., 2013). If great part of the geothermal fluid is released to the atmosphere in a flash plant, it can also cause the depletion of the reservoir, inducing subsidence issues as the vapor is not reinjected. But some studies also address the fact that releasing the gases to the atmosphere by geothermal plants decreases the natural release of gases by the natural fumaroles, explaining that this could somehow equilibrate the GHGs emissions (Bertani, 2015; Fridriksson et al., 2017).

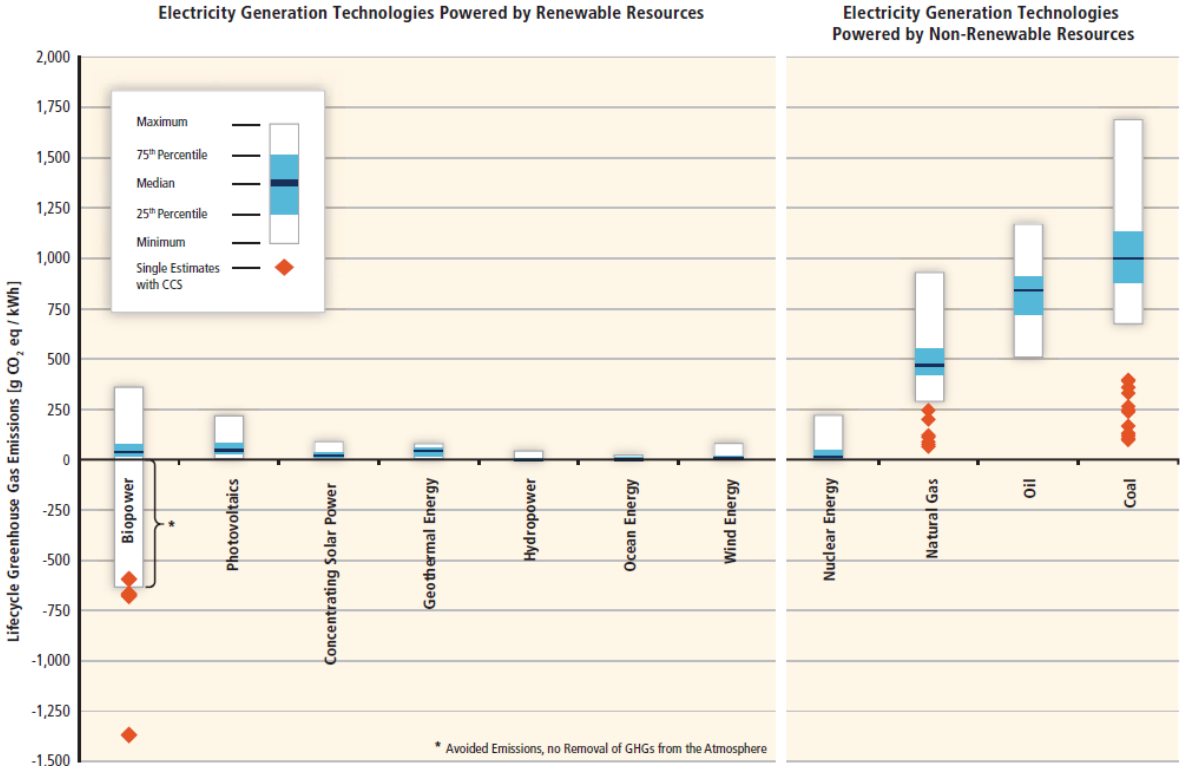


Figure 1.6: Estimates of lifecycle GHG emissions (gCO<sub>2eq</sub>/kWh) for broad categories of electricity generation technologies (Edenhofer et al., 2012). CCS: carbone capture and storage.

To quantify all the emissions that can occur during the exploitation of a geothermal reservoir but also the pollution and emissions due to exploration, construction and deconstruction of geothermal projects, life cycle assessment (LCA) studies are realised (Masanet et al., 2013). LCA of the Illkirch, Rittershoffen and Soultz-sous-Forêts geothermal plants have been made showing that Soultz-sous-Forêts plants’ emissions are of 37 CO<sub>2eq</sub> g/kWh and Rittershoffen plants’ emissions are 8 CO<sub>2eq</sub> g/kWh (Lacirignola and Blanc, 2013; Pratiwi et al., 2018). Based on several LCA analyses, geothermal energy releases considerably less green-house gases (GHGs) in the atmosphere than fossil-fuel based resources, and among renewables, geothermal energy was found to be a good compromise in terms of GHGs emissions (Figure 1.6).

Figure 1.7 presents different levelized costs per MWh of power production from renewable and fossil resources. Average presented costs of geothermal power production are based on flash and Organic Ranking Cycle (ORC) conventional hydrothermal plants. Costs of geothermal power are in the middle range of renewable energy, between 69 and 112 USD/MWh according to Ray, (2019) (Figure 1.7). However, this cost range is not representative of EGS power plants, and can reach 240 USD/MWh (International Renewable Energy Agency and European Commission, 2019). Typical 3 to 5 MW<sub>e</sub> geothermal doublet power plants installed in the URG costs are about 35 to 40 million of euros. Costs per installed capacity is therefore between 7,500 and 9,000 €/kW in the URG and drilling costs can represent up to 50% of total plants costs (Ravier et al., 2016).

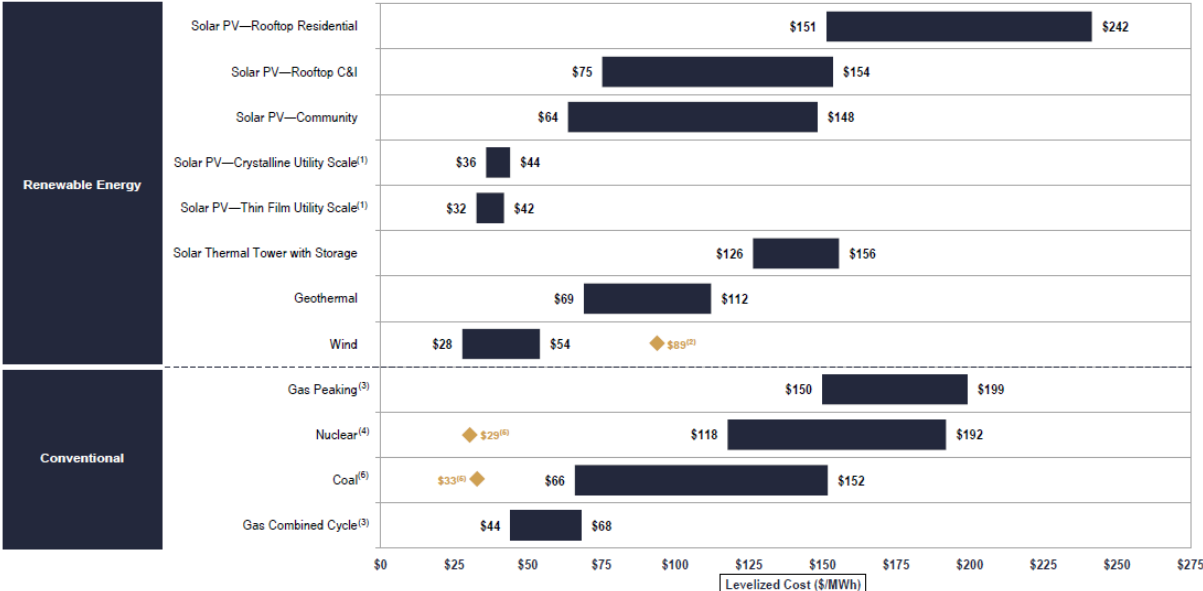


Figure 1.7: Levelized cost of energy (LCoE) comparison per MWh after Ray, (2019).

Contrary to wind power or solar energy, geothermal energy is not an intermittent energy: geothermal plants can produce all year long and all day and night long, excepted during the maintenance times, estimating that geothermal production could be available 93% of the year (7500-8500 hours/year). Thus, the Capacity Factor (ratio of the produced energy over a given period of time to the full capacity over the same period) is much higher than for other renewable energy sources (Bertani, 2018), resulting in a total cost (LCoE) comparable or lower than for other energy sources (International Renewable Energy Agency and European Commission, 2019).

To conclude, geothermal energy is a costly energy but has non-negligible advantages: it is non-intermittent, with costs similar to the fossil energies and even sometimes lower for heat production as it is the case in the Paris Basin. These advantages represent a strong economic interest for geothermal energy which has also a low environmental impact in terms of GHGs emissions. In the present context of energy transition, governments show a growing interest for developing geothermal energy, as it is the case of the European Union which wants to reduce the polluting emissions by 80% by 2050 (Figure 1.8). Under the European Renewable Energy Prospects for the European Union (REmap) program, electricity consumption in end-use sectors would double by 2050 (relative to 2015 levels), while the renewables share of power generation sector would rise to 85%. This means that investments in new renewable energy capacity in Europe should increase to almost 500 billion USD per year over the period to 2050 to meet this REmap target (International Renewable Energy Agency and European

Commission, 2018). Thus, geothermal power should increase from less than 1% of the total European power generation, about 25,000 TWh in 2015 to 3% corresponding to 47,000 TWh in 2050 (Figure 1.8). This increase is a real challenge for the geothermal sector. In order to embrace the geothermal potential of Europe in a coordinated and responsible way, European geothermal stakeholders in the framework of the European Commission's SET-Plan (Strategic Energy Technology Plan of the European Commission) have set in 2016 ambitious targets with respect to efficiency, system integration, cost reduction, transparency and societal inclusion (European Commission, 2016).

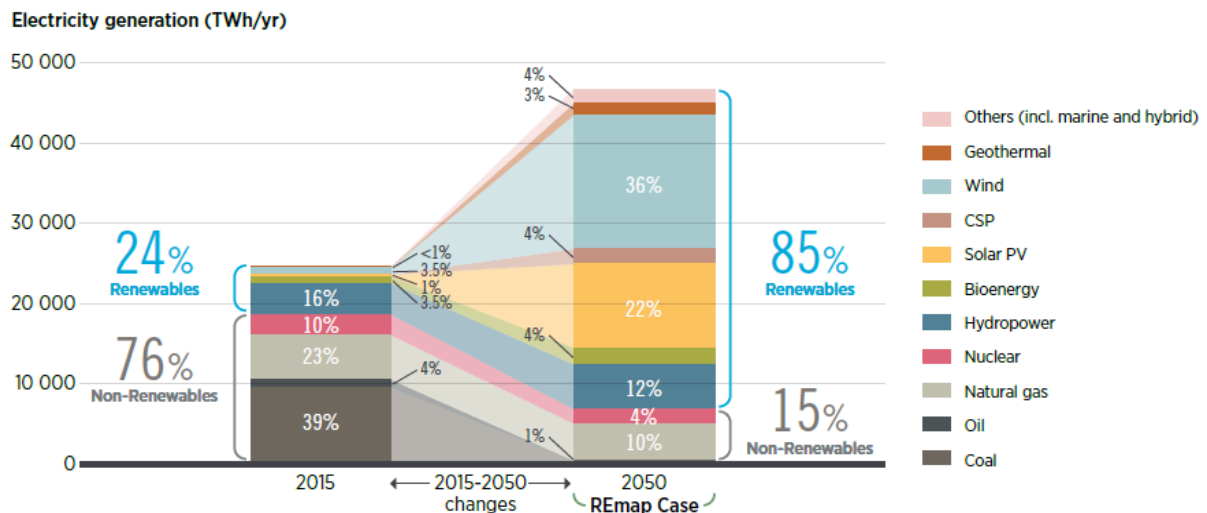


Figure 1.8: European REmap case electricity mix by 2050.

### 1.3. Targets of the European Commission

The development of deep geothermal energy, despite its low costs, low environmental impacts, and 93% availability is still slow, especially given the favourable energetic transition context. The ambitious targets and transversal goals set in 2016 by the European geothermal sector in the framework of the SET-Plan are directly aimed at unblocking the geothermal development by addressing the main constraints (European Commission, 2016):

- The first target is to increase reservoir performance, reducing the power demand of production pumps to less than 10% of gross energy generation and achieving a sustainable yield expected over 30-years or more by 2030.
- The second target is to improve overall conversion efficiency, including the bottoming cycle, of geothermal installations at different thermodynamic conditions by 10% by 2030 and 20% by 2050.
- The third target is to reduce the production costs of geothermal energy to less than 0.10 €/kWh for electricity and 0.05 €/kWh for heat by 2030.
- The fourth target is to reduce exploration costs by 25% in 2025 and by 50% in 2050 as compared to 2015.
- The fifth target is to reduce the unit cost of drilling (€/MWh) by 15% in 2020, 30% in 2030 and by 50% in 2050 as compared to 2015.
- The sixth target is to demonstrate the technical and economic feasibility of responding at any time to demands from a grid operator to increase or decrease output ramp up and down from 60% to 110% of nominal power.

In achieving these six targets, one of the transversal goals is also to develop transparent and harmonized methods and instruments for the management of technical and financial risk, and

another transversal goal is seek greater social acceptability and mitigation of unsolicited side effects (induced seismicity, gas emissions).

#### 1.4. Deep geothermal energy in the URG

The URG extends on 300 km length, from Basel (Switzerland) in the south to Mainz (Germany) in the north and is part of the European Cenozoic rift system (ECRIS) (Figure 1.9 and 1.10). The ECRIS rift system was formed during the Cenozoic and is marked by lithospheric thinning induced by extension and associated mantle uplift (Ziegler, 1992). This is clearly visible on the extrapolated temperatures map at 5000 m depth, which underlines significant temperature increases in the different ECRIS grabens (Figure 1.9).

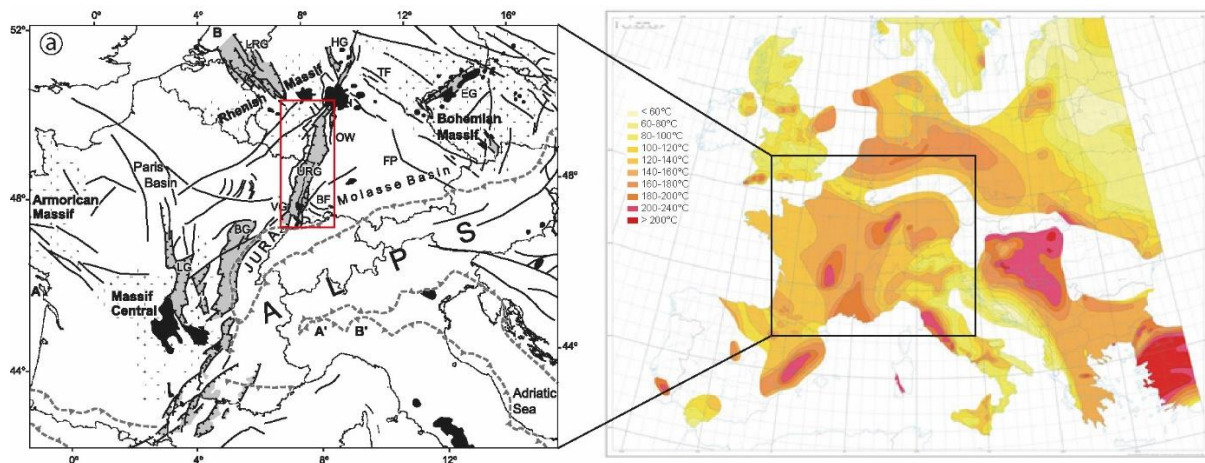


Figure 1.9: a) Map of the European Cenozoic rift system (ECRIS) after Dèzes et al., (2004), black lines specify the Cenozoic faults, grey zones represent the sedimentary basins, black zones represent volcanism, marks represent the basement and the dotted line represents the Alpine push. BF= Black Forest, BG = Bresse Graben, EG = Eger (Ohre) Graben, FP = Franconian platform, HG = Hessian Graben, LG = Limagne Graben, LRG = Lower Rhine Graben, URG = Upper Rhine Graben, OW = Odenwald, VG = Vosges. The red frame represents the map on Figure 1.10 b) Map of the Temperatures extrapolated at 5 km depth after Hurtig et al., (1992).

The URG region benefited from a rich history of geological exploration due to the presence of the Pechelbronn oil field, which was exploited from 1741 to 1970, first for medicinal applications and then for oil extraction (Figure 1.10). Also, the Pechelbronn oil field was the place where the Schlumberger brothers, Conrad and Marcel, acquired the first electrical log in 1927. The correlation between a first map of isotherms at 400 m, based on a rich dataset of 500 thermometric measurements from petroleum exploration wells and mines and a structural map of the Soultz-sous-Forêts site pointed out that temperature anomalies were organized along the NNE direction, which is also the direction of the major normal faults in the region (Haas and Hoffmann, 1929; Schnaebeler, 1948). Later on, Gérard et al., (1984) built a map of the estimated temperatures at 1000 m depth, predicting 110°C and highlighting an abnormally high thermal gradient of 100°C/km. Since then, the temperature anomalies in the URG have been identified and are well-known today (Figure 1.10). Only later, in the early 90's the European geothermal research project of Soultz-sous-Forêts was launched, gathering researchers from France, Germany and Switzerland, (BRGM, CNRS, Strasbourg University, Nancy University, ENSG, Mines de Paris, MeSy, Bochum University, GTC, BGR, Stadt Werke Bad Urach, ETH Zurich, GeoWatt, Neuchatel University) (Figure 1.10). The initial idea was to apply the Hot Dry Rock (HDR) concept which came mainly from pilot projects developed since the early 70's in the USA (Los Alamos), the UK (Cornwall), Japan (Hijiori, Ogachi) and Germany (Falkenberg) (Figure 1.11).

The HDR concept consists in creating an artificial heat exchanger at depth in hard rocks by generating fractures in the rock formation by hydraulic fracturing. A first well is drilled at great depth, before inducing typical penny-shaped fractures around the well by hydraulic fracturing, which can generate induced micro-seismicity. Those fractures represent the basic pillars of the future artificial heat exchanger. Then, a second is drilled in the optimal direction, from which additional induced fractures are generated again by hydraulic fracturing, in order to connect both wells by an artificial fractures network. The process then consists in injecting fresh water at ambient temperature from the surface into the injection well; by circulating in the artificial heat exchanger, the water would absorb the rock's heat by conduction and then be produced at high temperature through a pump in the production well in order to feed a turbine and then generate electricity. In Soultz-sous-Forêts, after the first well was drilled, the main result was the observation of natural geothermal fluid circulating at depth in a pre-existing naturally fractured reservoir. Various chemical and hydraulic treatments based on EGS technology were applied to the natural reservoir of Soultz-sous-Forêts for the first time in France (Figure 1.11). The Soultz-sous-Forêts site has been serving for over 30 years as a full-scale laboratory, for many involved teams from Europe (France, Germany, Switzerland, UK, etc.), the USA and Japan. In 2001, industrial partners joined the project helping to create a first prototype of geothermal power plant. In 2008, the power plant produced electricity for the first time and in 2016 the site became exclusively industrial. Since then, it produces continuously electricity on the grid.

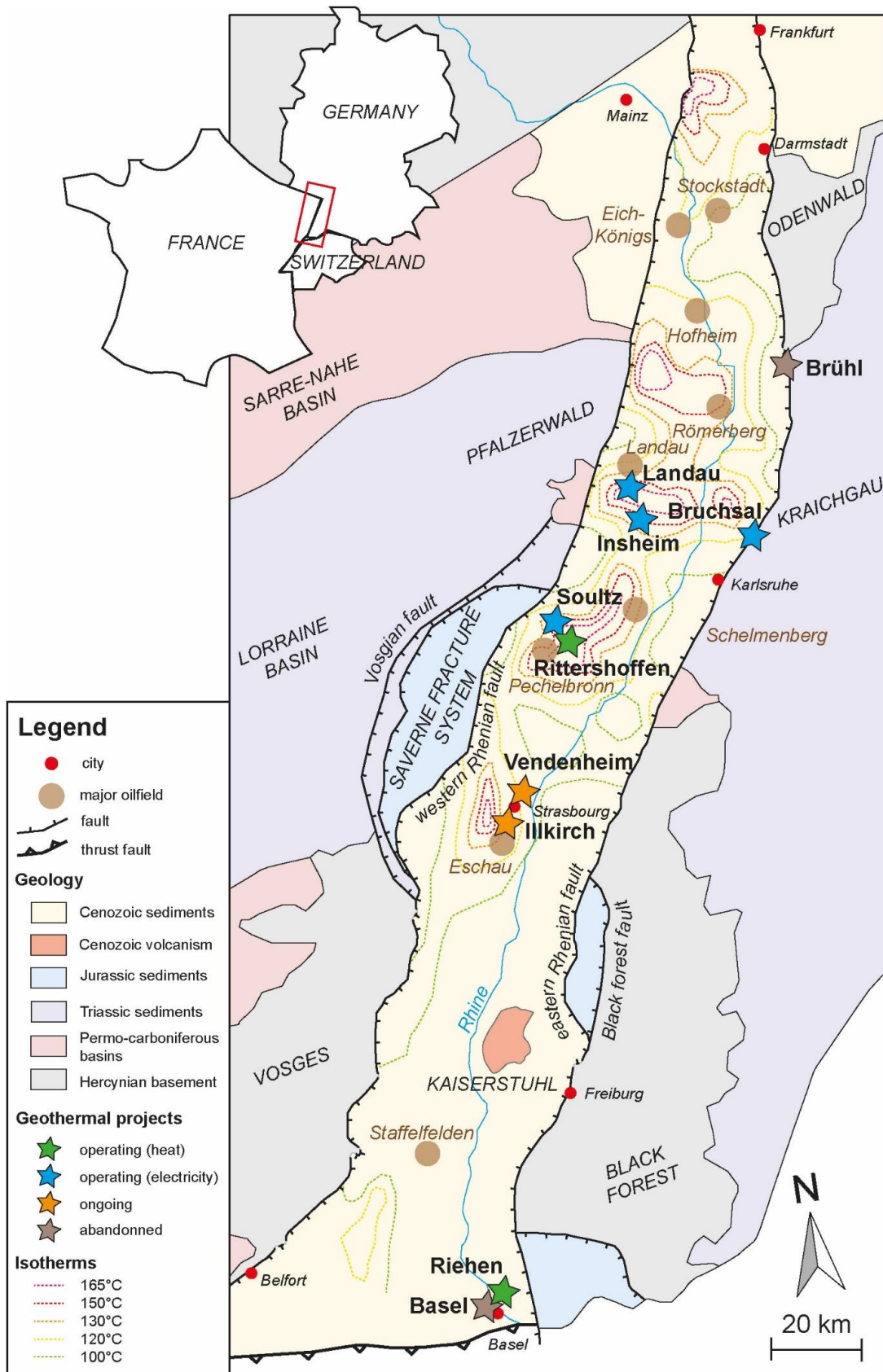


Figure 1.10: Map of the deep geothermal sites operating or under development in 2020, also representing the major oilfields and the isotherms at 2000 m depth. Isotherms were re-drawn based on a joint-interpretation of those proposed by Baillieux et al., (2013), GeOrg, (2017) and Vidal et al., (2019).

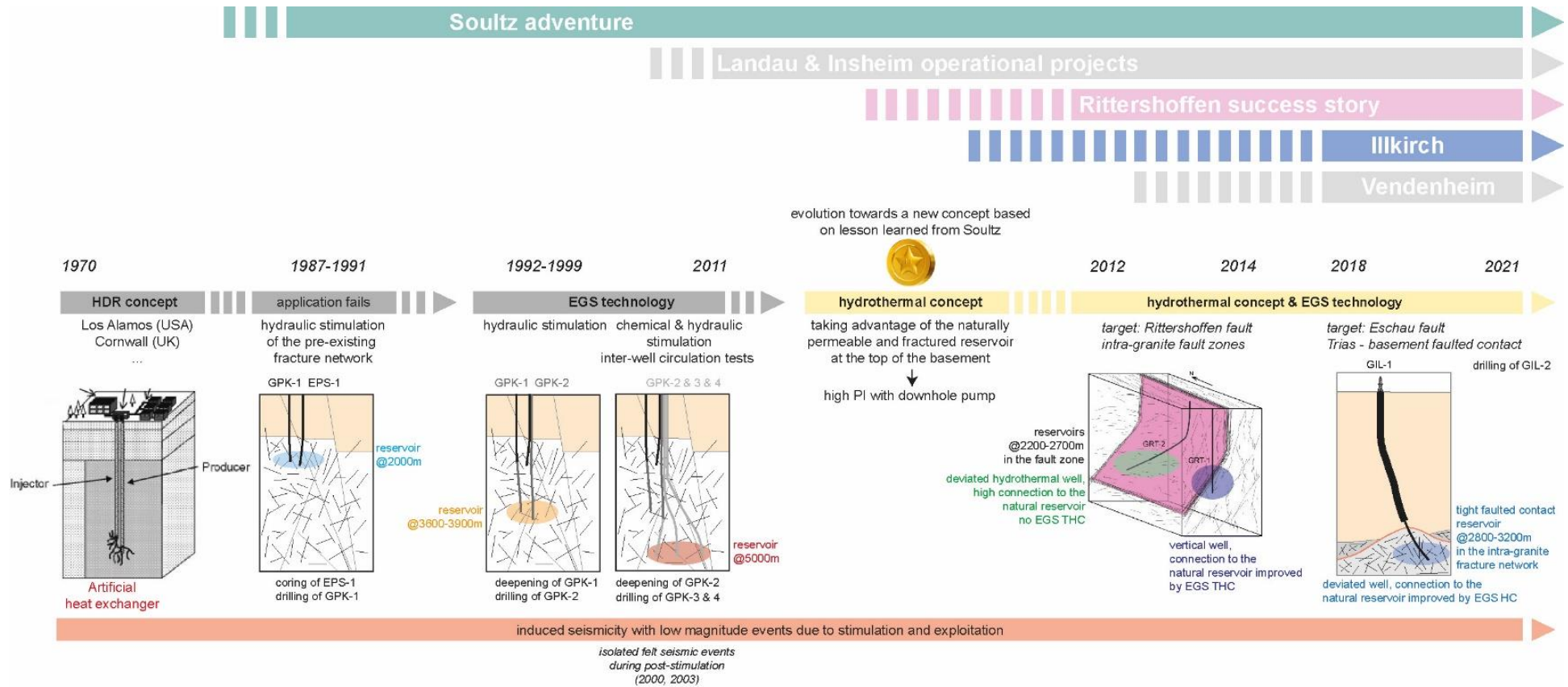


Figure 1.11: Evolution of deep geothermal concepts through time. Overview of the URG geothermal projects.

Based on the Soultz's experience, several geothermal sites have been explored in the URG, where most of the geothermal targets correspond to deep fractured formations. Over the last twenty years, the URG's geothermal activity has continued: on the French, German and Swiss sides of the URG, 9 geothermal projects were launched, totalling up 23 wells and more than 75 km of drilling completed today (Figure 1.10). In 2020, 3 of these geothermal projects produce electricity, and 2 produce heat (Figure 1.10). In the French side of the URG, 2 projects (Vendenheim and Illkirch) are under development and should be operational by the end of 2021 (Figure 1.10). 6 exploration permits for geothermal energy, and 3 for lithium extraction are in progress in Alsace (Table 1).

Name	Sector	Type	Company	Area (km <sup>2</sup> )	Start	End	Status
Hatten-Rittershoffen	Geothermal	PER	Electricité de Strasbourg	52	2008/03/22	2023/03/22	Valid
Illkirch-Erstein	Geothermal	PER	Electricité de Strasbourg	143	2013/06/23	2023/06/23	Valid
Lauterbourg	Geothermal	PER	Electricité de Strasbourg	212	2011/12/03	2019/12/03	On-going modification
Strasbourg	Geothermal	PER	Fonroche Géothermie	573	2013/06/23	2023/06/23	Valid
Wissembourg	Geothermal	PER	Electricité de Strasbourg	116	2011/12/03	2021/12/03	Valid
Soultz-sous-Forêts	Geothermal	Concession	GEIE (Exploitation Minière de la Chaleur)	23.42	2015/09/24	2040/09/24	Valid
Illkirch	Lithium	PER	Electricité de Strasbourg	143	Demand: 2019/05/13		First demand
Outre-Forêt	Lithium	PER	Electricité de Strasbourg	423	Demand: 2019/05/13		First demand
Plaine du Rhin	Lithium	PER	Fonroche Géothermie	572	Demand: 2018/12/28		First demand

Table 1: Geothermal and Lithium research permits (PER) and concessions in the URG area in November 2020. Source ES-Géothermie.

## 2. Geological setting

### 2.1. Tectonic phases and associated mineralisations in the URG

As evoked in the part 1.4, the URG belongs to the ECRIS (Figure 1.9a). The URG extends over 300 km length from Basel (Switzerland) in the south, to Frankfurt (Germany) in the north, with a width of between 30 and 40 km, and follows an SSW-NNE direction (Figure 1.10). In the early-Tertiary, volcanic eruptions occurred and then, the rifting started in the middle Eocene. The URG is thus characterized mostly by normal faults, on its borders and in its internal part. The subsidence of the graben and the uplift of its boundaries resulted in filling the graben with a thick cover of Secondary and Tertiary sediments, reaching up to 3350 m in thickness in the northern part of the graben. Today, the graben subsidence and boundaries uplift are still in progress with annual vertical movements up to 0.7 mm, and seismic activity (Illies, 1972). The boundaries in the southern part of the URG are composed of the Vosges Palaeozoic crystalline massif on the west side and the Black Forest Palaeozoic crystalline massif on the east side, with similar altitudes (<1500 m) (Figure 1.10). To the North, the boundaries of the URG are composed on the western side of the Mesozoic sedimentary series of the Vosges du Nord and the Pfälzerwald, and on the eastern side, of the Odenwald crystalline massif (Figure 1.10). The western limit of the graben is marked by the western Rhenian and Vosgian faults, which both delimitate the Saverne fracture system (Illies, 1972; Sittler, 1992). At its eastern border, the

graben is marked by the eastern Rhenian and Black Forest faults, which both delimitate the eastern fracture system, enclosed between the Black Forest crystalline massif and the Rhine plain (Figure 1.10). The tectonic history of the URG is directly linked to the formation of the Variscan and Alpine orogenesis.

In the Palaeozoic, the Variscan cycle is characterized by the intrusion of Carboniferous granitoids into the crystalline basement from the Visean (340 Ma) and the Permian (270 Ma) eras, in a subduction context. These granitoids were emplaced following a NE to NNE axis along the main weak zones that are collisional or shear zones, such as the Lalaye-Lubine or Baden-Baden fault zones (Lagarde et al., 1992; Altherr et al., 1999, 2000; Edel and Schulmann, 2009). Several tectonic phases occurred during the Variscan cycle: the Sudete phase is the structuration of the orogeny and consists of a N-S compression generating NE-SW sinistral and NW-SE dextral shear faults (Figure 2.1). Then, an extension along an NNE-SSW axis is observed, which reactivated the normal NW-SE to WNW-ESE oriented faults, until the Permian (Figure 2.1). Subsequently, the Saalian phase is marked by compressional and thrusting events in the NE-SW direction, which are associated with NW-SE dextral and E-W sinistral shear faults (Burg et al., 1984). The late Permian is characterized by a N-S to NNE-SSW extension that forms the Permian basins along NE-SW to ENE-WSW oriented faults (Villemin and Bergerat, 1987; Schumacher, 2002; Ziegler et al., 2006).

During the Mesozoic, the extension observed at the late Permian continued until the Jurassic in some parts of the URG, inducing fluid migrations and several mineralisation events (Schleicher et al., 2006; Clauer et al., 2008; Bossennec et al., 2020). Then, an E-W extension affected the Lorraine basin and the western part of the graben (Figure 1.10 and 2.1) (Villemin et al., 1986). During this period, sedimentary series of the Buntsandstein sandstones, Muschelkalk limestones and Keuper evaporites accumulated in the graben (Sittler, 1985). The lithostratigraphy of those series has also been meticulously described on the basis of observations made on cores and cuttings samples as well as the interpretation of gamma ray logs from the geothermal wells of Soultz-sous-Forêts, Rittershoffen and Illkirch (Aichholzer, 2019; Düringer et al., 2019).

The Post-Variscan cycle refers to the tectonic activity associated with the Cenozoic rifting, structurally affecting the Variscan basement but also the Buntsandstein, Muschelkalk and Jurassic sediments. Villemin and Bergerat, (1987) and Schumacher, (2002) propose a structural evolution in 4 tectonic phases. The first phase is a N-S compression under the Alpine thrust, reactivating ENE-WSW and NNE-SSW structures at the early Eocene (Figure 2.1) (Ziegler, 1992; Dèzes et al., 2004). Then, from late Eocene to early Oligocene, an E-W extension with N-S and NNE-SSW faults dominates the rifting phase (Doebel, 1967). At late Oligocene, a NE-SW compression reactivates the border faults with dextral shear (Villemin and Bergerat, 1987; Schumacher, 2002). And at early Miocene, a NE-SW compression influenced by the Pyrenean thrust transforms the graben into a shear zone (Figure 2.1) (Illies and Greiner, 1979; Bergerat, 1985; Edel et al., 2006). The most recent tectonic event corresponds to the Alpine NW-SE compression, which uplifts and erodes the crystalline horsts (Vosges and Black Forest) and reactivates the N-S and NE-SW faults inherited from the Variscan and Tertiary eras, respectively (Illies, 1972; Dèzes et al., 2004; Edel et al., 2007). The current phase reactivates the border faults of the URG in sinistral shear and has a dilation effect on the NNW-SSE structures (Figure 2.1) (Michon et al., 2003).

The URG polyphasic tectonic history results in a rich structural inheritance marked at the regional scale by the large fault zones of Lalaye-Lubine and Baden-Baden and the border faults resulting from the graben formation during the post-Variscan cycle. At the well scale,

local normal faults also associated with the graben formation can also be observed but a smaller-scale fracture network corresponding to the inherited Variscan tectonics is mostly intersected.

This dense network of faults and fractures has been the host of intense hydrothermal circulations leading to various mineralisations (Bossennec et al., 2020 and references therein; Clauer et al., 2008; Schleicher et al., 2006). More precisely, the dating of illites allows to reconstruct the timing of fluid circulation episodes in the granites and Triassic sandstones since the late Palaeozoic. Hence, Clauer et al., (2008) described a complex pre-rift evolution with episodic mineralisations by dating illites from Buntsandstein sandstones. Schleicher et al., (2006), Lippolt and Seibel, (1991), Bartier et al., (2008) described also episodic mineralisations that took place during the Triassic, Jurassic and Cretaceous in the granitic rocks.

An illitization stage in granitic rocks occurred during the Permian, from 270 to 250 Ma (Schleicher et al., 2006). Then, the tectonic activity in the Saverne fracture system induced fluid migrations in the porous sandstones from 210 to 185 Ma or as two distinct events at 210 and at 185 Ma, affecting rocks of the eastern part of the graben (Clauer et al., 2008). In the Jurassic, illitization was evidenced in granitic rocks and sandstones (Schleicher et al., 2006; Clauer et al., 2008) (Figure 2.1). Afterwards, tectonic activity in the Soultz-sous-Forêts region produced two episodes of illitization in the sandstones at 95 and 70 Ma, which were also evidenced in the granite around 94 Ma, and further illitization may have started at 55 Ma (Schleicher et al., 2006; Clauer et al., 2008) (Figure 2.1). The youngest detected illitization age appears older than the main Miocene rifting episode, suggesting that no illite crystallization occurred in the Buntsandstein sandstones during this tectonic event (Clauer et al., 2008).

In plutonic basement rocks, several authors (Brockamp et al., 2003; Hagedorn and Lippolt, 1994; Lippolt and Kirsch, 1994; Lippolt and Seibel, 1991; and Zuther and Brockamp, 1988) reported also Triassic, Jurassic and Cretaceous hydrothermal events associated with illitization all over the Black Forest.

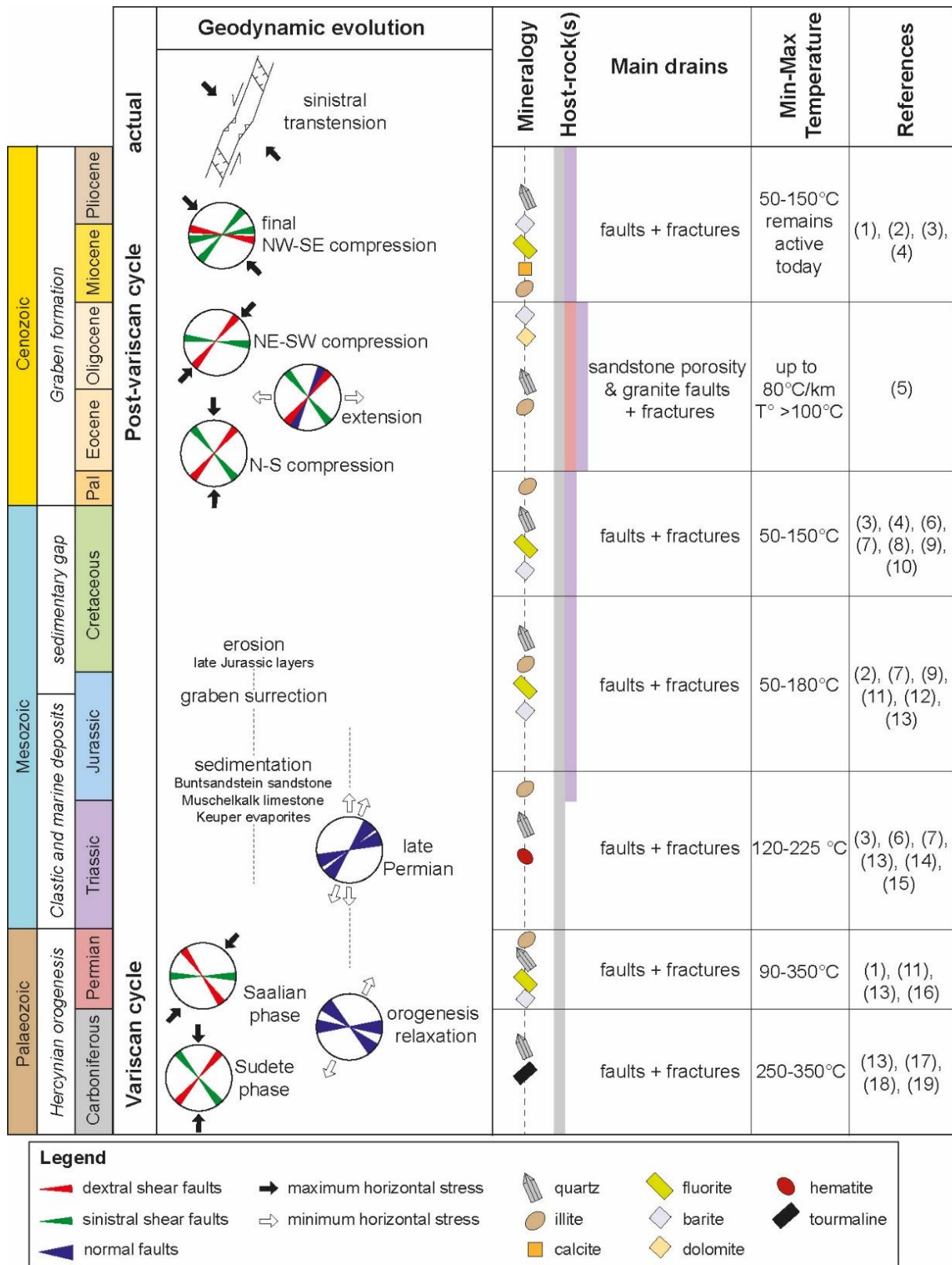


Figure 2.1: Geodynamic evolution of the URG and its several tectonic phases, with the orientations of faults and stresses in the URG along the geological timescale, on the left. On the right, associated mineralisation episodes are presented from the Palaeozoic to the Cenozoic ages, modified after Bossennec et al., (2020) and other references: (1) (Baatartsogt et al., 2007), (2) (Burisch et al., 2017a), (3) (Walter et al., 2016), (4) (Bartier et al., 2008), (5) (Dezayes and Lerouge, 2019), (6) (Clauer et al., 2008), (7) (Lippolt and Seibel, 1991), (8) (Burisch et al., 2017b), (9) (Pfaff et al., 2010), (10) (Walter et al., 2017), (11) (Schleicher et al., 2006), (12) (Cathelineau et al., 2012), (13) (Walter et al., 2019), (14) (Bons et al., 2014), (15) (Staude et al., 2012), (16) (Walter et al., 2018), (17) (Boiron et al., 2010), (18) (Cathelineau et al., 2004), (19) (Schwinn et al., 2006).

## 2.2. Fluid circulation in the URG

Today, the fluid circulation in the URG is still active. It was found that the main supply came from meteoric waters that infiltrated and flowed along and into the graben shoulders that are the Vosges and Black Mountains, and discharged inside the graben, mostly through the border faults (Clauser and Villinger, 1990; Lampe and Person, 2000; Pribnow and Clauser, 2000; Guillou-Frottier et al., 2013; Baillieux et al., 2014; Freymark et al., 2019). At depth, meteoric water mixes with highly saline deep brines formed by the advanced evaporation of seawater and halite dissolution during successive marine transgression-regression cycles from the Triassic to the Oligocene (Sanjuan et al., 2010, 2016; Gardien et al., 2016). According to fluid analyses from Soultz-sous-Forêts, Rittershoffen, Landau and Insheim wells, this fluid mix gives geothermal brines of the Na-Cl type, with pH values close to 5 and reservoir temperatures close to  $225 \pm 25$  °C (Sanjuan et al., 2016). The minimum transit-time of these brines would be about 1000 years (Komninou and Yardley, 1997). The temperature profiles measured in the wells of the URG and especially in the Soultz-sous-Forêts geothermal wells evidence thermal convection in the Palaeozoic basement, Buntsandstein sandstones, and Muschelkalk limestones and thermal conduction in the sedimentary layers above (Figure 2.2).

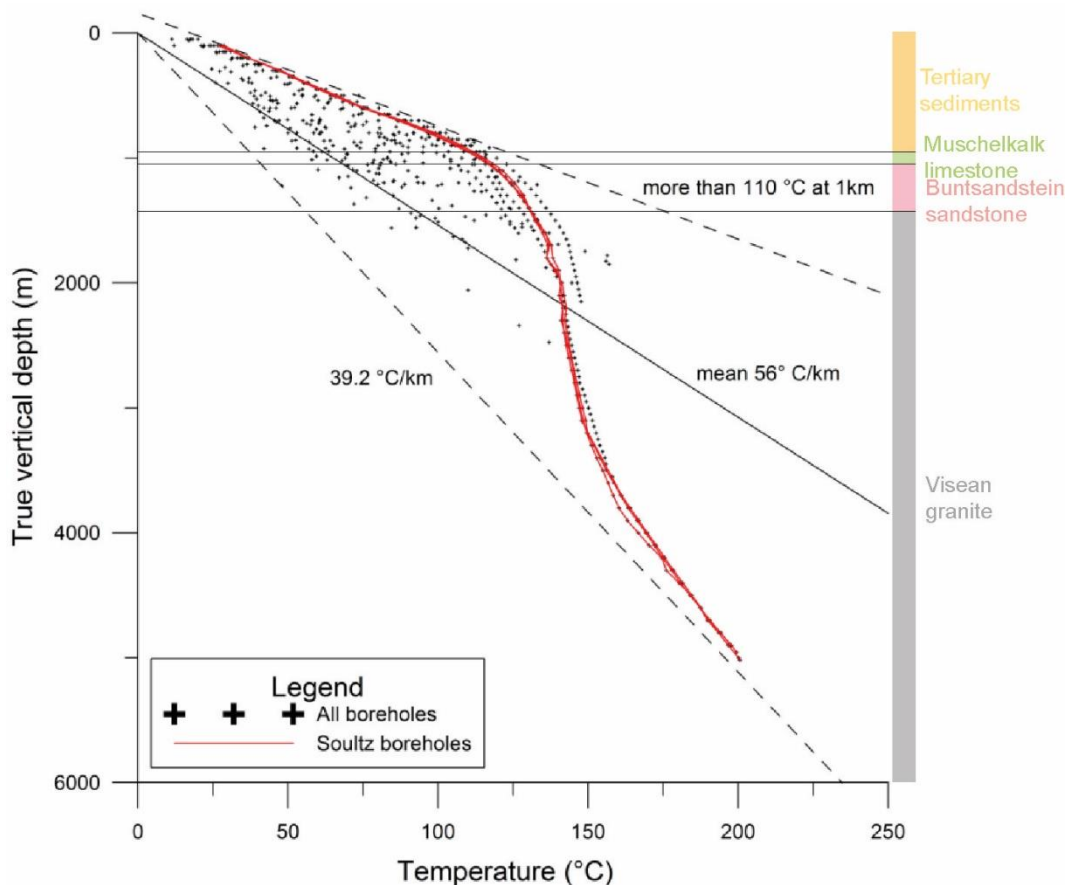


Figure 2.2: Temperature distribution in the 112 boreholes of Soultz-sous-Forêts area. Database from Agemar et al., (2012) and Pribnow and Schellschmidt, (2000). Figure is from Baillieux, (2012).

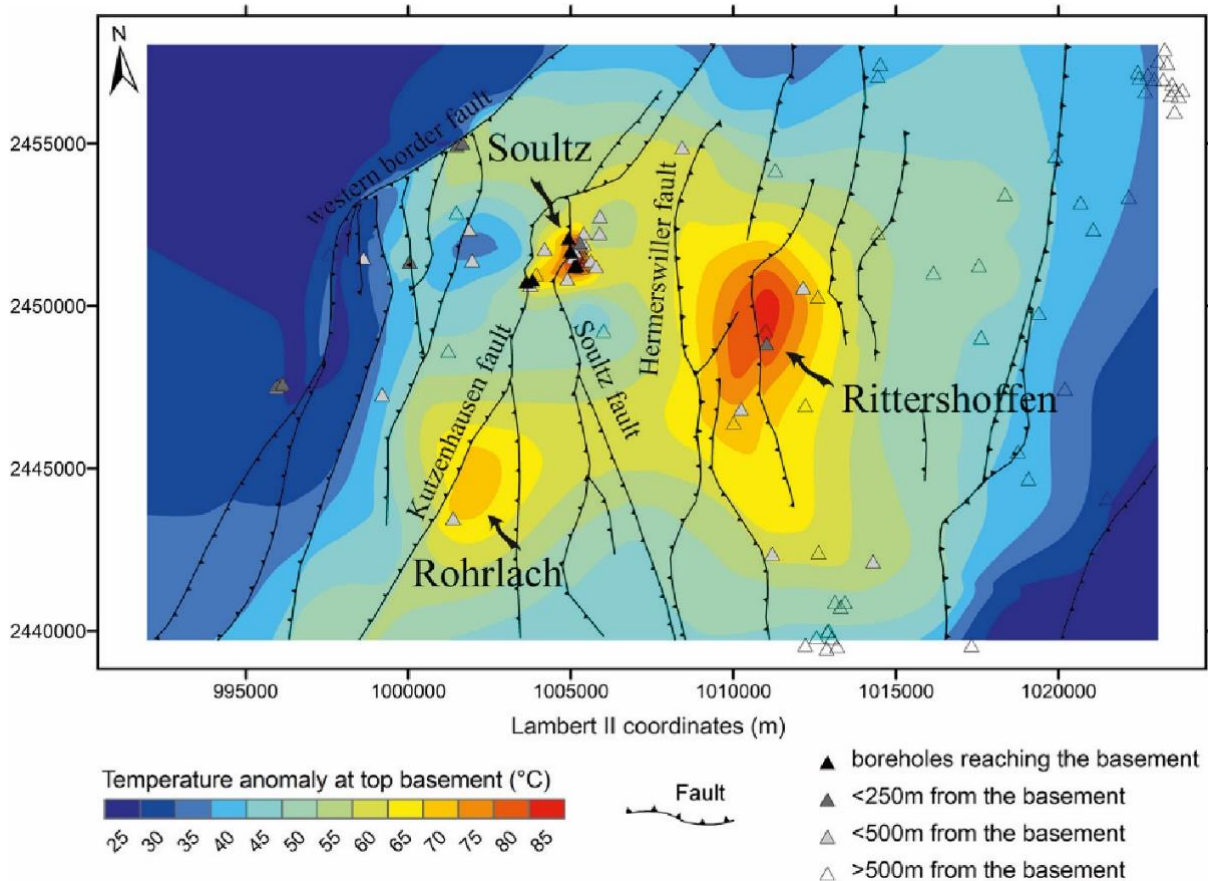


Figure 2.3: Temperature anomalies at top basement, distribution of temperature measurements in boreholes and their distance to top basement, and fault traces and dip directions (black lines) at top basement. A temperature gradient of  $39.2^{\circ}\text{C}$  per km, corresponding to the lowest temperature gradient observed in the area, is subtracted from the temperature field at the top basement to obtain this temperature anomaly map at top basement. Temperature database from (Pribnow and Schellschmidt, 2000) and (Agemar et al., 2012). Temperature anomalies of Soultz-sous-Forêts and Rittershoffen and local faults. Figure is from (Baillieux et al., 2014).

Evidence of fluid convection along local normal faults is given by the distribution temperature anomalies along N-S normal faults (Figure 2.3). These N-S normal faults channelling the fluid circulation were found to be deep faults rooted in the Palaeozoic basement, and dipping westward at Soultz-sous-Forêts and Rittershoffen and eastward at Landau and Insheim (Baillieux, 2012). More to the South in the URG, the Eschau normal fault intersected by Illkirch well is also oriented N-S and dips westward.

At the graben scale, some recent modelling studies indicate that the graben flanks act as a major recharge, leading to a graben-perpendicular flow towards the graben centre (Figure 2.4) (Koltzer et al., 2019). Thus, the Black Forest to the east, the Jura Mountains to the south, and the Vosges Mountains to the west limit the groundwater flow around the southern URG. It has been found that the groundwater dynamic follow a northward trend in the south up to Strasbourg surely due to the high altitude and hydraulic head of the Jura Mountains south of the URG, an eastward trend in the central part between Strasbourg and Heidelberg probably influenced by the top of the Variscan basement, and a more complex flow regime in the North (Koltzer et al., 2019). These local directions are overprinted by a predominant flow from the graben boundaries to the centre of the graben with a pronounced upflow along the rift central axis (Figure 2.4) (Clauser and Villinger, 1990; Freymark et al., 2019; Koltzer et al., 2019). Through modelling studies have also found that the main border faults were the pathways for downward fluid flow (Freymark et al., 2019), and also constrain the temperature anomalies in

the graben (Baillieux, 2012; Dezayes and Lerouge, 2019). The thermal anomalies in the graben are directly related to the fluid flow and could be explained by local forced convective upflow within the Cenozoic sediments in addition to the slightly upward-flowing fluids within the basement (Freyemark et al., 2019).

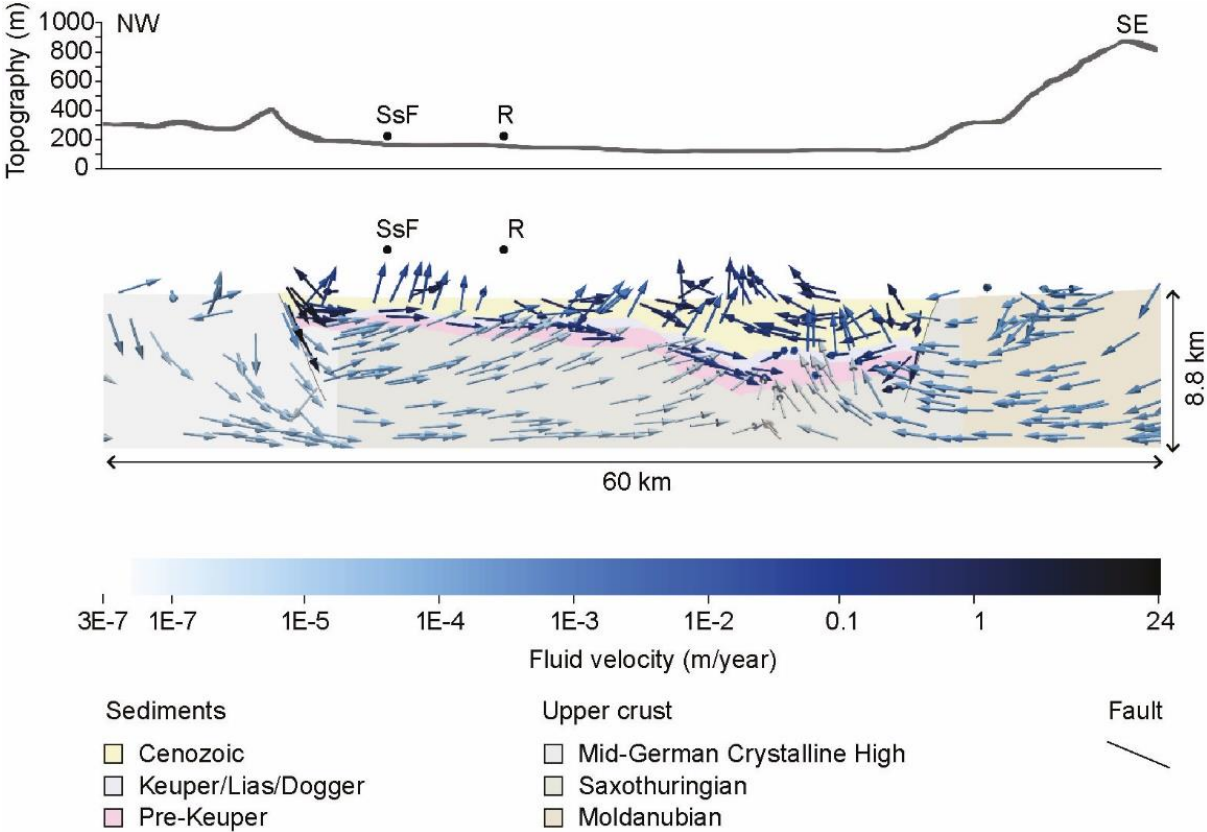


Figure 2.4: Fluid flow scenarios visualized via a modelling of the central area along a section through Soultz-sous-Forêts and Rittershoffen. On top, the topography and the assigned hydraulic head are shown. Figure is the model D with high permeable faults from Freyemark et al., (2019).

### 2.3. Soultz-sous-Forêts

As mentioned in part 1.4, the Soultz-sous-Forêts geothermal site was initially a European research project, where the idea was to apply the HDR concept. The initial concept firstly developed at Soultz-sous-Forêts was to establish hydraulic connections between two or more boreholes within the target reservoir at the top basement to allow the circulation of fluid through the hot rocks at rates of commercial interest. Exploration for the Soultz-sous-Forêts project and site implantation consisted essentially in interpreting the detailed map of temperatures at 400 m depth (Haas and Hoffmann, 1929), and seismic reflexion (Cautru, 1987) originating from the previous oil and gas exploration. The implantation of the Soultz-sous-Forêts site was based on the following criteria: the presence of an important temperature anomaly, a detailed knowledge of the sedimentary cover, the presence of crystalline basement at depth, the recovery of 3 neighbouring oil wells, suitable for the installation of seismic sensors, and the industrialized region in-between the French and German partners of the project (Genter, 1989) (Figure 2.5a).

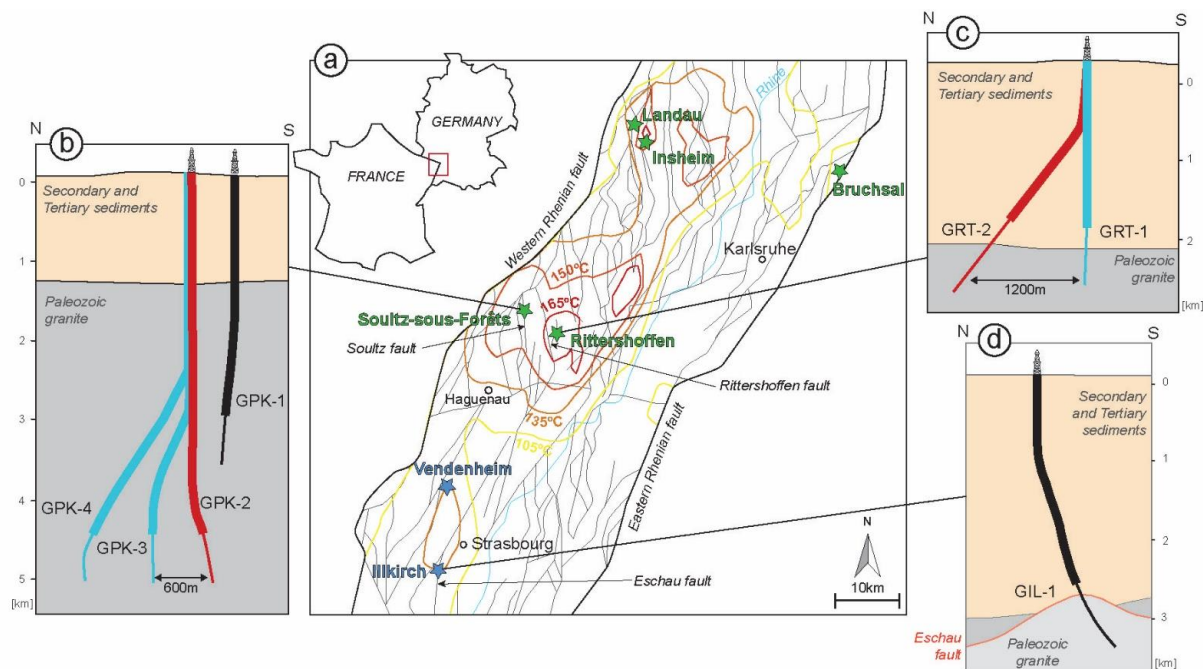


Figure 2.5: a) Structural map of the center of the URG with isotherms at 2 km depth from the geoportal (GeOrg, 2017), the geothermal anomaly in the Strasbourg area is from the dataset of Baillieux et al., (2013). Geothermal power plants in operation are represented by green stars, and the geothermal projects under drilling operations by blue stars. On the left and right sides, N-S sections with simplified geology are presented: b) through the Sultz-sous-Forêts wells, c) through the Rittershoffen wells, c) through the Illkirch well. The thick line represents the cased section of the wells, and the thin line the open hole. Production wells are in red, and injection wells are in blue. GPK-1 well is today an observation well, and GIL-1 well is not yet in operation.

In 1987 began the drilling of GPK-1 well, the first well of the project. Then, until 2004, four wells (GPK-1, 2, 3, 4) were drilled and one petroleum well (EPS-1) was deepened. All the deep wells drilled in Sultz-sous-Forêts (down to 5 km) penetrated a deep granitic basement with pre-existing natural fractures containing natural salty water with associated mineralisations due to massive hydrothermal alteration (Genter, 1989). The site was characterized by the presence of large volumes of natural brine contained in fractured crystalline rocks, whose natural permeability was very low due to the poor hydraulic connection within the natural fracture network. In order to achieve circulation through the rock mass at rates needed for commercial energy production, the permeability of the rock mass had to be increased or “stimulated” by applying various techniques such as thermal, hydraulic or chemical stimulation. Thus, the term of EGS was created to describe this technology which consists of increasing the hydraulic performance of a given geothermal well by applying thermo-hydraulic and chemical treatments. After this intense R&D activity, in 2014, the Sultz-sous-Forêts site was converted into an industrial project, operated by the GEIE (Exploitation Minière de la Chaleur). The current geothermal system involves three wells: a production well named GPK-2 and two injection wells named GPK-3 and GPK-4. The deep fluid is of Na-Cl type with total dissolved solids (TDS) content of 99 g/L and a pH of 4.98 (Sanjuan et al., 2010). The measured temperature in the wells at 5000 m depth is around 200°C and the production temperature on the surface is 150°C. The pumped geothermal fluid reaches the wellhead at a nominal flow rate of 30 kg/s provided by a downhole Line Shaft Pump (LSP) (Baujard et al., 2018a). The geothermal brine is then flows through a system of three consecutive double-pass tubular heat exchangers supplying heat to an ORC, in order to produce electricity. The geothermal brine is then fully reinjected in the reservoir at around 70°C, and the volume of reinjected brine is shared between the two injection wells, one third in GPK-4 and two third in GPK-3 without

using reinjection pumps. The reinjection temperature is linked to the energy conversion process. The geothermal plant has been successfully producing electricity since September 2016 under commercial conditions (Genter et al., 2018). Since 2016, the Soultz-sous-Forêts power plant has been the first EGS plant to produce electricity with a gross power of 1.7MW<sub>e</sub> corresponding to an annual production of 10GWh<sub>e</sub> in France and probably the most well-known in the world. The Soultz-sous-Forêts concession (exploitation authorization given by the French government) is valid until 2040 (Table 1).

The five Soultz-sous-Forêts wells are located in the Soultz-sous-Forêts horst, which is bounded on its western part by a normal fault with a vertical offset of at least 500 m and oriented N20°E (Kappelmeyer, 1991; Genter and Traineau, 1996). The wells are sub-vertical in the sedimentary layers and are slightly inclined in the deepest part of the granite (Figure 2.5b). The wells crossed the Tertiary and Secondary sedimentary rocks (350 m of Buntsandstein and 35 m of Permian layers) before reaching the top of the fractured granitic basement at 1400 m (Figure 2.5b). The granitic basement at Soultz-sous-Forêts is composed of a porphyric monzogranite, dating from 334.0±3.8/3.5 Ma, which consists of biotite, quartz, plagioclase and mega-crystals of potassic feldspar (>1 cm), and locally amphibole (hornblende) (Genter, 1989; Stussi et al., 2002; Cocherie et al., 2004; Hooijkaas et al., 2006). Accessory minerals such as oxides, titanite, apatite, zircon, and allanite (in descending order of abundance) have also been observed (Genter, 1989). The deepest wells (GPK-2, -3 and -4) also reached a fined-grained two-mica granite at 4100 m, dating from 327±7 Ma, and composed of quartz, plagioclase and potassic feldspars but characterized by high amounts of biotite and muscovite (Cocherie et al., 2004; Hooijkaas et al., 2006). Both Viséan ages confirm that the granites were emplaced before the Sudete phase and thus record the structural heritage of the latter. Both granites underwent intense episodes of hydrothermal alteration. First, a pervasive propylitic alteration affected the entire granitic pluton during its emplacement and is characterized by the chloritisation of the biotite. Then, due to the fluid circulation in the fracture network, a second hydrothermal alteration is observed, an argillic alteration occurring in the vicinity of fracture zones due to the fluid circulation in open fractures. This argillic alteration is characterized by several grades of intensity depending on the intensity of the fluid flow, to the fluid-rock ratio, and to the physico-chemical conditions and fluid properties. This argillic alteration resulted from several episodes of fluid-rock interactions and is characterized by the destabilization of primary minerals (biotite and feldspars) and formation of illite, carbonates, sulphates and secondary quartz in the highest grades (Genter, 1989).

The Soultz-sous-Forêts wells intersected several fracture zones characterized by the occurrence of fractures and argillic alteration, correlated with temperature and other geophysical anomalies (gamma-ray, resistivity, porosity, density, gas venue ...) indicating fluid exchanges between the well and the formation at preferential depths. For example, in GPK-1 well, four permeable fracture zones were identified: at 1645 m MD, 1814 m MD, 2818 m MD and 3490 m MD (Vidal et al., 2019). Dezayes et al., (2010) identified three clusters of fractures intersected by the Soultz-sous-Forêts wells with the first one located between 1800 and 2000 m depth in the unaltered porphyritic granite showing the highest natural permeability. The second one is located between 3000 and 3400 m depth within the fractured and altered granite zone and the third one is located between 4500 and 5000 m depth.

Today, GPK-2 well is used as production well and GPK-3 and -4 wells as injection wells, GPK-1 well is kept as an observation well (Figure 2.5a).

The dataset available from the Soultz-sous-Forêts wells is very rich because of the site's history of intense scientific research. Indeed, 810 m of continuous cores were collected during

the deepening of EPS-1 well, and GPK-1 well was also cored discontinuously, providing 50 m of core samples (Figure 2.6). The research carried out at the Soultz-sous-Forêts site covered three decades and tested the evolution of borehole imagery tools and various geophysical logs providing a very rich dataset (Genter et al., 1997a) (Figure 2.6). During my thesis, I had the opportunity to acquire SWIR spectra on all the cuttings samples from the granitic basement of the GPK-1, -2, -3 and -4 wells, totalizing 2905 acquired spectra (Figure 2.6). I also had the opportunity to acquire 23 X-ray diffractograms on GPK-1 samples (Figure 2.6).

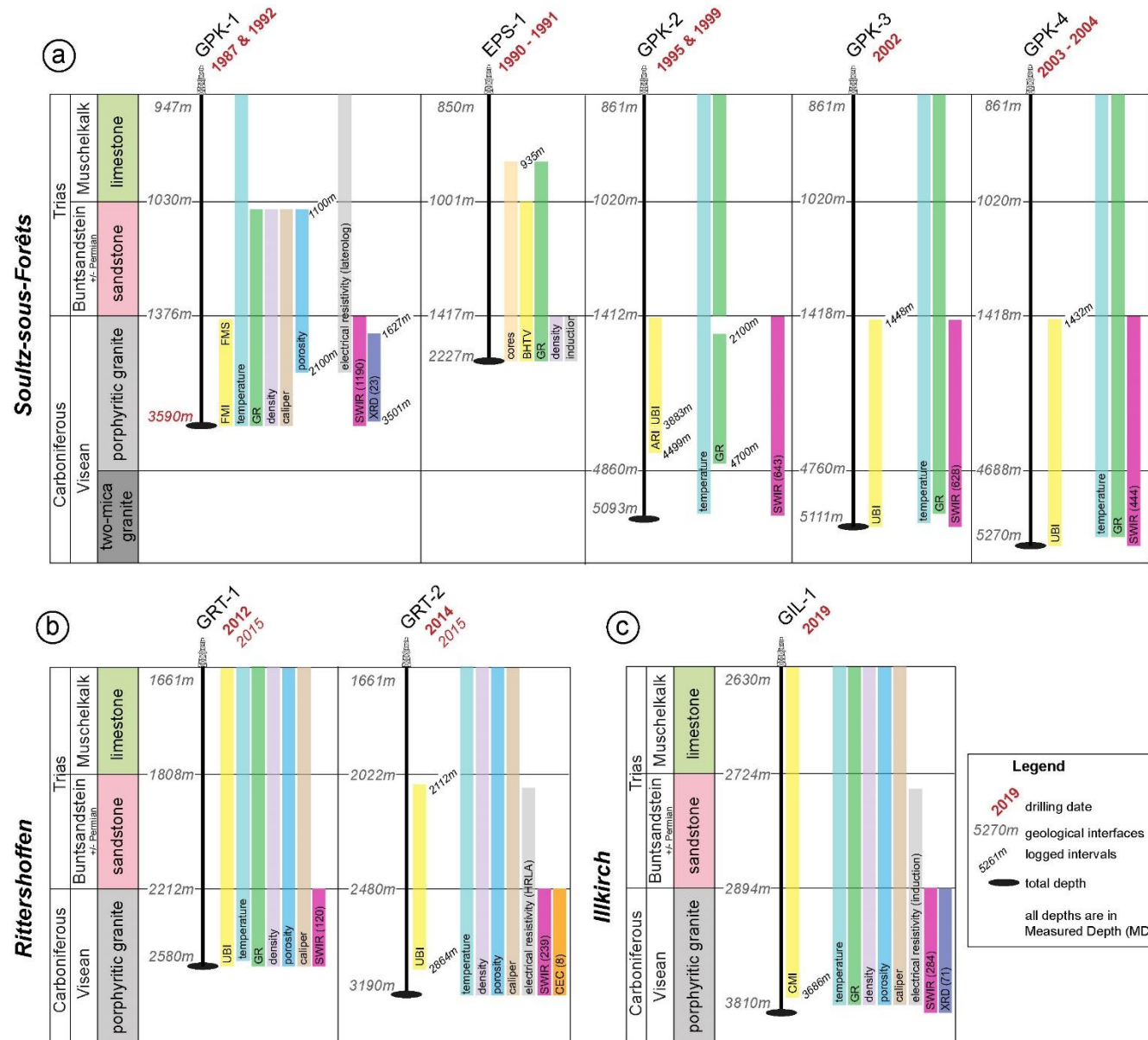


Figure 2.6: Type of geological and well-logging data used or collected, in the deep geothermal wells of Sultz-sous-Forêts, Rittershoffen and Illkirch. BHTV: BoreHole TeleViewer, CEC: Cation Exchange Capacity, FMI: Formation Micro-Imager, FMS: Formation Micro-Scanner, GR: Gamma-Ray, UBI: Ultrasonic Borehole Imager, SWIR: Short-Wave Infrared spectroscopy, XRD: X-Ray Diffraction.

## 2.4. Rittershoffen

The Rittershoffen geothermal heat plant was developed to supply heat to the industrial processes of a starch plant. This industrial user, located in Beinheim, France, totalizes 100 MW<sub>th</sub> of thermal needs. Exploration of the Beinheim area close to the industry was not satisfactory for a suitable geothermal exploitation. Hence, located in the middle of the graben, along the Rhine river, the industry is within the part of the graben where the top of the granitic basement is the deepest. Exploration around the Rittershoffen thermal anomaly, evidenced from bottom hole temperature measurements done in several oil wells, highlighted the potential of the Rittershoffen fault as a geothermal target, where the top of the granitic basement is shallower (2200 m) than in Beinheim (5000 m) (Figure 2.5a). The Rittershoffen project took advantages of the Soultz-sous-Forêts experience, and the target was the Rittershoffen normal fault which is located approximately 15 km east of the western Rhenish border fault and is oriented N5°E based on subsurface geological data. The Rittershoffen fault intersects the Triassic sandstones, and the top of the fractured granitic basement at about 2500 m depth (Figure 2.5a and c) (Baujard et al., 2017a). The first well, GRT-1, was drilled in 2012 to 2580 m MD, and the first testing results after drilling showed a low PI (0.5 L/s/bar). A stimulation program, including thermal, chemical, and hydraulic stimulation, was therefore designed and successfully completed in 2013, increasing the hydraulic yield up to 2.5 L/s/bar (Baujard et al., 2017a). The induced micro-seismicity activity related to the stimulation tests was very low and undetectable by the surrounding populations.

After the drilling of the GRT-1 well, a new 2D seismic campaign was carried out in order to better define the path of the Rittershoffen fault and the trajectory of the second well GRT-2 was optimized according to the orientation of the Rittershoffen fault (Baujard et al., 2017a). GRT-2 well was drilled in 2014 and was slightly deviated but tangent to the local fault over its length of approximately 400 m of open-hole in the granitic basement (Figure 2.5c). Its high productivity index of 4 L/s/bar without any stimulation revealed a good connection between the well and the fracture network (Baujard et al., 2017a). The well probably intersects the fault zone characterized by a high fracture density with optimized natural fluid pathways (Vidal et al., 2017). The hydrothermal concept has been extremely positive for the well GRT-2 (Vidal and Genter, 2018). The geothermal heat plant, with an installed capacity of 27.5 MW<sub>th</sub>, has successfully supplied an average of 22.5 MW<sub>th</sub> and 180 GWh/year of heat to the starch plant since June 2016. The Rittershoffen research permit is valid until 2023 (Table 1) and the concession license is currently examined by the French government. The Rittershoffen geothermal power plant is classified as an EGS due to the stimulation program performed on GRT-1 but also because of the total reinjection of the discharged geothermal fluids in the reservoir inducing a micro-seismicity activity at the reinjection side during geothermal exploitation.

The geothermal brine is a Na-Ca-K-Cl dominated brine with a TDS value of about 100 g/L and a non-condensable gas (NCG) content, mainly CO<sub>2</sub>, of 0.24% in weight mass (Mouchot et al., 2018). As a result, the heat plant was designed with a pressurized geothermal loop. A downhole LSP pressurizes the geothermal brine in the surface equipment over the gas break-out pressure to prevent any NCG emission during operation. The production wellhead temperature at GRT-2 reaches 170°C and the flowrate is regulated at 75-85 kg/s, according to the heat demand of the starch plant. The geothermal heat is transferred to a secondary loop using several tubular heat exchangers and the brine is fully reinjected without additional pumps at 85°C into the GRT-1 injection well. The secondary loop of the heat plant, containing

superheated freshwater, is then connected to a transport loop to transfer the heat to the starch plant located 15 km away (Ravier et al., 2017).

A rich dataset was collected in both wells of the Rittershoffen project. Geophysical logs were acquired in both wells, an electrical log was acquired in the GRT-2 well, of the type “High Resolution Laterolog Array” (HRLA) from Schlumberger company (Figure 2.6). Acoustic borehole images were also acquired in both wells. Both wells of the Rittershoffen project were drilled by crushing the rock by conventional drilling tools, so cuttings samples were collected each 3 meters depth (Figure 2.6). During my thesis, I had the opportunity to acquire SWIR spectra on all the cuttings samples of the granitic basement of both wells, totalizing 359 acquired spectra (Figure 2.6).

## 2.5. Illkirch

The presence of the Strasbourg temperature anomaly along the Eschau fault in Illkirch was the base for the implantation of the GIL-1 geothermal borehole (Figure 2.5a). Prior to the drilling of GIL-1 well, an extensive exploration campaign was conducted including aeromagnetic and gravimetric surveys, as well as a 2D seismic campaign (Richard et al., 2016; Edel et al., 2018). The target of the GIL-1 well was to intersect the Eschau normal fault at the interface between the Buntsandstein and the granite. The Eschau normal fault is oriented N10°E based on 2D seismic interpretation (Figure 2.5c) (Richard et al., 2016). Drilling of GIL-1 well began in 2018, and the target was successfully reached at 2894 m MD (2636 m true vertical depth, TVD). GIL-1 well crosses the Tertiary and Secondary sedimentary formations including 300 m of Buntsandstein but no Permian layers were intersected by the well due to the Eschau fault displacement, which does not allow to determine its thickness at this location, even if it was found to be between 20 and 200 m thick in nearby deep wells (Housse, 1984; Richard et al., 2016; Aichholzer, 2019). The total depth of the well is 3800 m MD (3391 m TVD) and the open-hole crosses the Buntsandstein sandstones and Carboniferous granite from 2762 m MD (2512 m TVD) to 2894 m MD for a total open-hole length of 1038 m MD (879 m TVD) (Figure 2.5c). In the open-hole section of the well, the GIL-1 well trajectory has a NW-SE azimuth in order to intersect the fault with a high angle. In 2020, hydraulic testing of GIL-1 well is still in progress, and reservoir modelling studies for the implantation of the second well are ongoing. The Illkirch research permit is valid until 2023 (Table 1).

The granitic basement intersected by GIL-1 well at Illkirch was observed on cuttings samples. It was found to be a porphyric granite as at Soultz-sous-Forêts and Rittershoffen with the occurrence of a biotite-rich granite. The granite shows intense argillic alteration within 200 m below the faulted interface between the Buntsandstein and granite, and further away a propylitic alteration with occurrence of argillic alteration in the vicinity of fractures zones.

Seven permeable zones were encountered in GIL-1 well. One permeable zone is located in the Buntsandstein at 2780 m MD, and the six other permeable zones are in the granite. Only one of them is located in the granite affected by intense argillic alteration at 3070 m MD, and the five others are located in the granite affected by dominant propylitic alteration at 3220 m MD, 3310 m MD, 3360 m MD, 3540 m MD, and 3635 m MD. These observations define a reservoir that is mainly located in the intra-granite fractures network, further away from the faulted interface. The fluid is a highly saline brine of NaCl type, close to the composition of the fluids circulating in Soultz-sous-Forêts and Rittershoffen reservoirs.

Various standard geophysical logs like gamma-ray, porosity, and density were acquired in GIL-1 well (Figure 2.6). However due to potential wellbore stability issues, borehole electrical

images, electrical induction log as well as temperature profiles were acquired inside the drill strings (Figure 2.6). GIL-1 well was drilled by crushing the rock with conventional drilling tools, so, cuttings samples were collected, each 3 or 5 meters depth. During my thesis, I had the opportunity to acquire SWIR spectra on the cuttings samples, totalizing 284 acquired spectra (Figure 2.6). I had also the opportunity to acquire 71 X-ray diffractograms on the cuttings samples, as well as to observe 8 polished thin-sections with a Scanning Electron Microscope (SEM) coupled with Energy Dispersive X-ray spectroscopy (EDS) (at the University of Poitiers), for chemical measurements on selected minerals (Figure 2.6).

### 3. Fracture zones complexity

The term “fracture zone” (FZ) that is used hereafter and more generally in this thesis is widely used to name zones resulting from faulting and fracturing. These FZs are systematically associated with mineralisation and are generally affected by brittle and semi-ductile deformation facies like cataclasis, breccia, microbreccia and even protomylonite. Schematically, a fracture zone is made of a fault core, which accommodates the fault displacement, and this fault core is surrounded by damage zones. At the well scale, FZs are identified on borehole images, comprise several single fractures and/or faults and have systematic geophysical and mineralogical signatures.

Many parameters are controlling FZ complexity, that is approached here in terms of hydraulic behaviour. Among them, fluid properties (chemistry, temperature, pressure), host rock properties (primary mineralogy, inherited tectonics, stress state, temperature, matrix porosity) but also their evolution versus time. These specific properties will determine the chemical exchanges between the fluid and the rock (fluid-rock ratio), where and how long they occur within the FZ. These chemical exchanges modify the FZ organisation and result in a complex distribution of the resulting physical properties (porosity, density, electrical conductivity, radioactivity, permeability ...) (Bense et al., 2013). In the URG, fluid circulation was evidenced to occur in nearly vertical FZs in the granitic basement and vertically extends upwards to the base of the Triassic sedimentary cover comprising the Muschelkalk and the Buntsandstein units. This part is devoted to the presentation of a brief state of the art and a literature review, to approach the spatial distribution of physical properties of FZs in sedimentary and crystalline rocks based on laboratory experiments, observations from outcrops but also from geothermal or petroleum wells.

#### 3.1. Muschelkalk limestones

##### 3.1.1. Organisation

The FZs observed in the Muschelkalk limestones of the URG presents centimetric to millimetric veins with secondary fillings, but can also present fractures without clogging (Figure 3.1a) (Dezayes et al., 2012). Gouges textures are observed and the surrounding damage zones can present micro-cracks (Dezayes et al., 2012). From outcrop studies, decreasing fracture lengths were observed with distance to the fault cores and it was observed that fracture connectivity at fracture tips was enhanced in proximity of slip surfaces (Meier et al., 2015). Several geothermal wells encountered permeable fracture zones in the Muschelkalk in the URG (Vidal and Genter, 2018). Core samples from EPS-1 well revealed one-meter-thick hydraulic fracture breccias that present mineralisation and totally destroyed the typical sedimentary structures (Figure 3.1a) (Aichholzer et al., 2019). A permeable FZ over 40 m thick was encountered in GRT-1 well at Rittershoffen (Dezayes et al., 2013; Dalmais et al., 2015).

### 3.1.2. Mineralisation

In the Muschelkalk limestones of the URG, carbonates like fibrous calcite, and sparite but also barite, anhydrite, and quartz have been observed as veins and fractures fillings, as well as iron oxides pyrite and siderite (Sizun, 1995; Dezayes et al., 2012). Chalcopyrite, galena and blende have also been observed and often reduce the rock porosity (Sizun, 1995).

### 3.1.3. Physical and hydraulic properties

The matrix porosity measured on cores from the Muschelkalk is low and varies from 0.01 to 0.1 % and the permeability is below  $10^{-18}$  m<sup>2</sup> (Kushnir et al., 2018). A comparative study of hydraulic data in the URG in Germany and France reveals a mean hydraulic conductivity of  $2.0 \times 10^{-6}$  m/s in Muschelkalk limestones (Stober and Jodocy, 2009). At Soultz-sous-Forêts, anomalies of gamma ray, occurrences of gas and mud losses during drilling (indicators of natural permeability) were correlated with the occurrence of FZs observed in the limestones. The FZ intersected by GRT-1 in the limestones was associated with total mud losses during drilling and a temperature anomaly suggesting important natural circulations (Baujard et al., 2017a). In most of the geothermal wells of the URG, convection observed in temperature profiles suggests natural circulations of brine in the Muschelkalk limestones (Vidal and Genter, 2018). Fractures sealed with secondary minerals like carbonates or quartz are indicators of past fluid flow and thus they could act as hydraulic barriers. In these stratabound formations, some authors point out that permeability depends on their internal infrastructure and is enhanced close to the fault core (Meier et al., 2015). In a first stage, fault core may act as a conduit for fluid flow if fractures or pores get interconnected during slip. In a second stage, permeability drops due to the rotation of particles and grain size reduction due to the slip evolution (Meier et al., 2015). The fault core becomes a barrier for fluid flow whereas the damage zone, where the rock is highly fractured, becomes a conduit.

Occurrences of geothermal resources in the Muschelkalk of the URG are mainly supported by the FZs and several geothermal wells present promising results for exploiting this reservoir like in Riehen or Insheim (Mégel and Rybach, 2000; Meier et al., 2015). However, these FZs present an important variability in terms of internal organization with existence of hydraulic breccias, gouge or fault core but also in terms of mineralisation intensity that can lead to reduce the natural permeability.

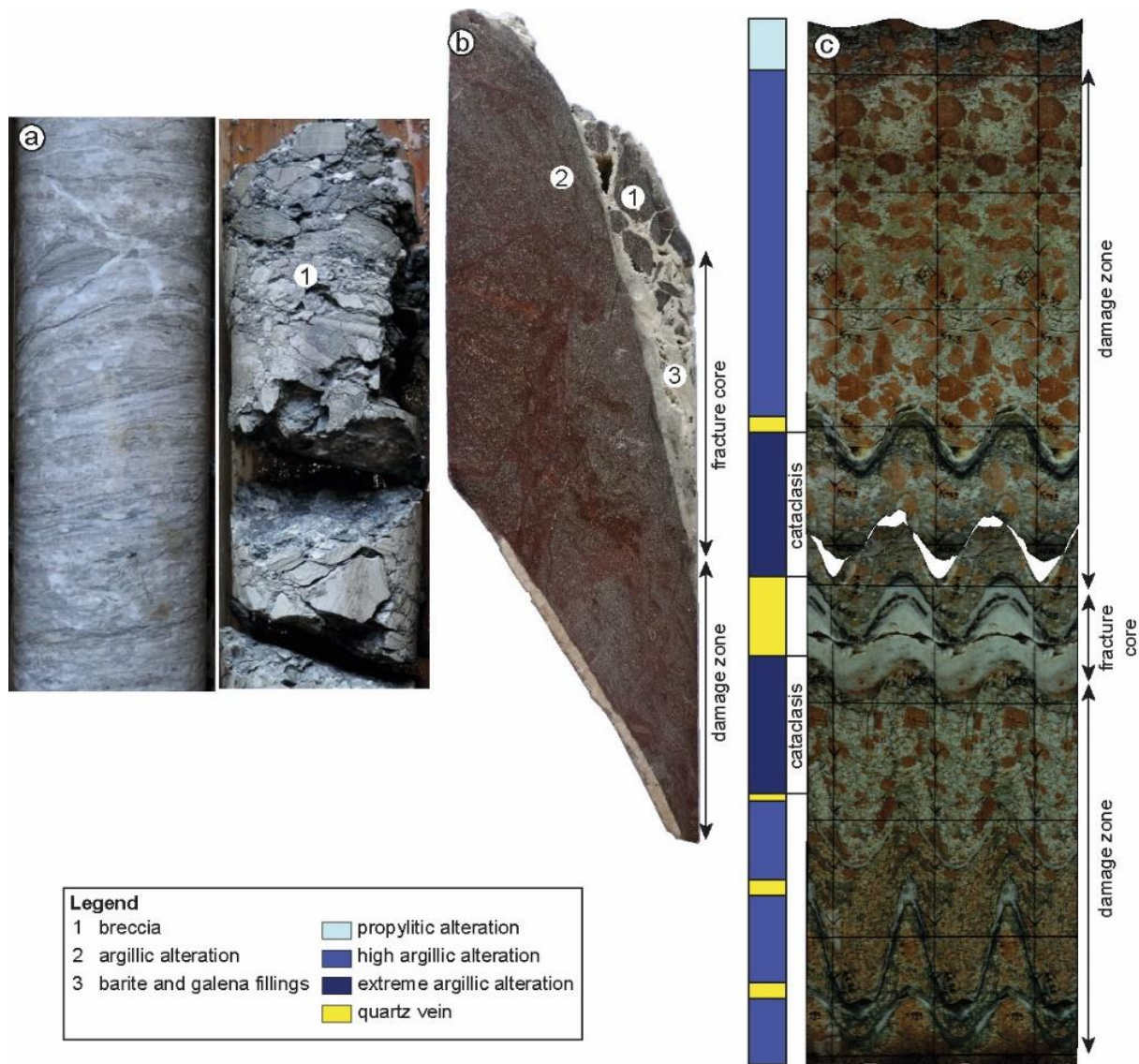


Figure 3.1: Core samples from EPS-1 well. a) in the Muschelkalk: on the left dolomite strongly folded with fractures at 955 m depth, on the right hydraulic breccia at 965 m depth. Picture is from (Aichholzer et al., 2019). b) FZ and secondary precipitations in the Vosgian sandstone at 1204 m depth, and c) FZ and its related argillic alteration in the granite at 2160 m depth.

## 3.2. Buntsandstein sandstones

### 3.2.1. Organisation

The FZs in sandstones generally comport deformation bands or zones of deformation bands that are defined by grain deformation. These deformation bands generally comport zones of reduced porosity (Rawling et al., 2001) (Figure 3.2a). In other geothermal contexts, FZs in siliceous sediments present also a complex architecture comporting damage zones and fault core(s) controlling the permeability distribution (Brogi, 2008). Outcrops studies in the URG indicate a FZ organization with a fault core, a transition zone and a damage zone with fracture orientations between the core and the damage zone that differ (Bauer et al., 2015). The fault core is generally clay-rich, often associated to lower permeabilities (Figure 3.1b and 3.2a) (Heynekamp et al., 1999). FZs in the Buntsandstein sandstones of the URG are associated with cataclasis textures (Dezayes and Lerouge, 2019). Geothermal wells of the URG that

encountered FZs in the Buntsandstein revealed a cluster organization between 10 and 20 m with no obvious displacement (Vidal and Genter, 2018). The most permeable FZ are the ones associated to local fault zone intersected by EPS-1 well and the Brühl geothermal wells and composed by several permeable drains over 50 m thick and 100 m thick respectively (Vernoux et al., 1995; Reinecker et al., 2019).

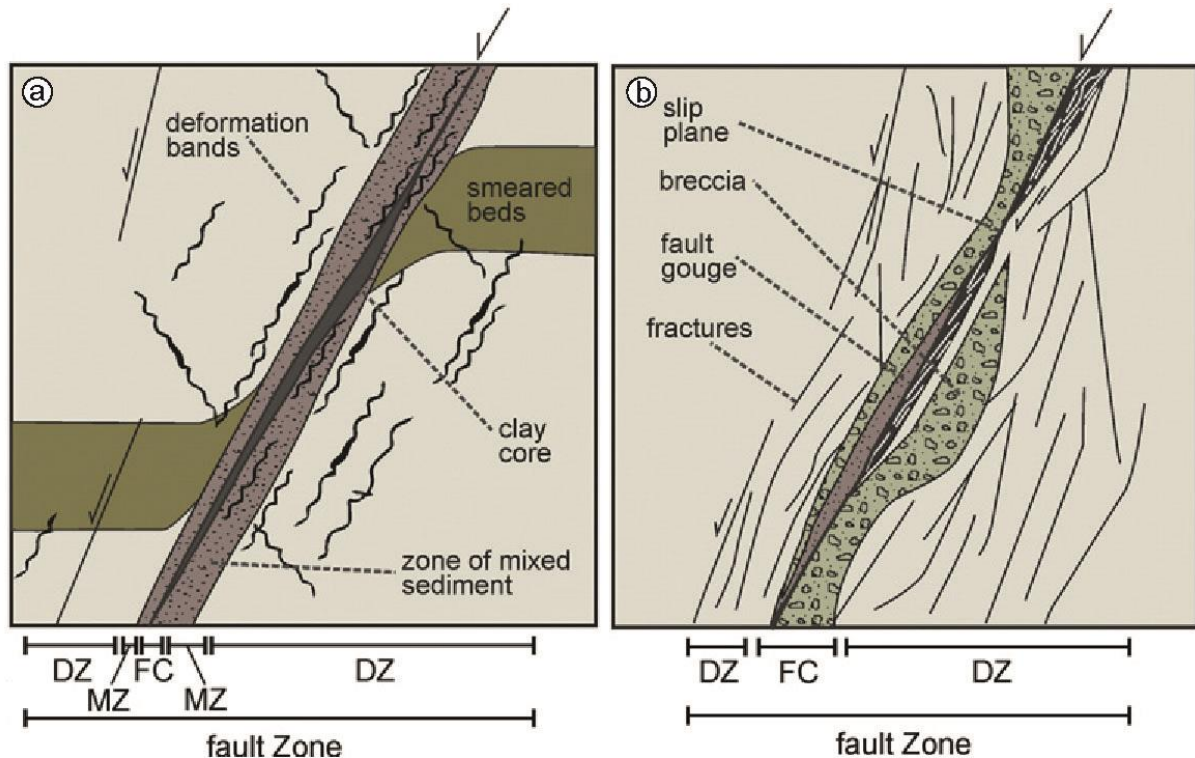


Figure 3.2: Different architectures and structural elements of fault zones in a) porous sandstones with fault core (FC) composed of clay and a damage zone (DZ) with deformation bands. As a third fault zone part mixed zones (MZ) with deformed and mixed sediments where established (Heynekamp et al., 1999; Rawling and Goodwin, 2006), and in b) crystalline rocks with fault core (FC) composed of breccia and fault gouge and damage zone (DZ) with increased fracture density (Caine et al., 1996). Figure is from (Bauer et al., 2015).

### 3.2.2. Mineralisation

In the Buntsandstein sandstones of the URG, the quartz and feldspars located at the edge of the fault core are corroded due to fluid circulation while the fault core can be partially sealed by secondary precipitations like micro-quartz, euhedral quartz, barite, illite, galena associated to pyrite, as well as dolomite, hematite and siderite (Figure 3.2a) (Brockamp et al., 2011; Dezayes and Lerouge, 2019; Sizun, 1995). In the surrounding damage zone, hydrothermal fluids strongly affect potassic feldspars as well as quartz and lithic grains. These dissolutions enable the development of secondary porosities (micro and macro) in the matrix and the precipitation of illite as well as quartz in the inter-grain porosity, in secondary pores related to K-feldspar dissolution (Brockamp et al., 2011; Dezayes and Lerouge, 2019). Pressure-dissolution figures are also observed at the contacts between quartz grains (Dezayes et al., 2012). These processes can tend to, firstly, increase the matrix permeability but, secondly, can reduce it due to a severe silicification.

### 3.2.3. Physical and hydraulic properties

In high matrix porosity sedimentary rocks like sandstones, the fluid circulation is controlled by the primary porosity of the rock in case of absence of fractures and highest permeabilities are

reached in the presence of macroscopic fractures that are as preferential channels for fluid circulation (Heap et al., 2017). From Soultz-sous-Forêts core sample measurements, the matrix porosity of the Buntsandstein varies from 0.03 to 0.2 % (Heap et al., 2017). The permeability of the fractured Buntsandstein ( $8 \times 10^{-14}$  and  $4 \times 10^{-12}$  m<sup>2</sup>) was found to be several orders of magnitude higher than that of the unfractured Buntsandstein ( $10^{-18}$  to  $10^{-13}$  m<sup>2</sup>) (Griffiths et al., 2016; Kushnir et al., 2018). In addition, permeability was found to be one order of magnitude higher when measured parallel to the beddings (Heap et al., 2017). Besides, the secondary pore-filling mineralisation significantly reduces the permeability of the sandstone (Griffiths et al., 2016; Heap et al., 2017). Occurrences of both temperature anomalies and gases and mud losses during drilling are spatially correlated to fracture zones in the geothermal wells (Vidal et al., 2015, 2017). Hydraulic tests in Brühl well reveals the highest PI among the URG wells (Reinecker et al., 2019).

Several geothermal projects in the URG revealed a very positive experience in exploiting the sandstone reservoir like in Insheim, Landau, Bruchsal and Rittershoffen. Permeability is mainly supported by FZs and seems to increase if the intersected FZ is connected to a local normal fault.

### 3.3. Palaeozoic granite

Crystalline rocks are known for their low matrix porosity (< 0.05%) and low matrix permeability rocks ( $< 10^{-19}$  to  $7 \times 10^{-18}$  m<sup>2</sup>), lower than the sedimentary rocks described previously. Natural permeability is therefore mainly controlled by fluid pathways present in the natural fractures (Kushnir et al., 2018). FZs in crystalline rocks were widely investigated for exploitation of several resources such as groundwater, hydrocarbon and geothermal resources. Geothermal wells that intersected the Paleozoic granite in the URG like in Soultz-sous-Forêts, Rittershoffen, Illkirch, Landau and Insheim brought precious data to enrich the conceptual model of intra-granitic FZ presented at the end of this section.

#### 3.3.1. Organisation

FZs are composed of one or several fault cores surrounded by damage zones which are further surrounded by the protolith (Sibson, 1977; Anderson et al., 1983; Chester and Logan, 1987; Davison and Wang, 1988; Forster and Evans, 1991; Byerlee, 1993; Caine et al., 1996; Scholz and Anders, n.d.). The damage zones surrounding both sides of the fault core are not necessarily symmetric and all the components (core, damage zone and protolith) are not necessarily present (Caine et al., 1996 and references therein). The amount and spatial distribution of each component control fluid flow within and near the fault zone. More precisely, the fault core is defined as structurally delimited and is the portion of the FZ where most of the displacement is accommodated, and is the seat of secondary minerals precipitations (Caine et al., 1996). In regard, the damage zones are generally strongly affected by dissolution of primary minerals. Damage zones are composed of microfractures to macrofractures, subsidiary faults, linked segments, splay faults, veins, high strain slip surfaces nested within regions of low strain, Riedel shears, dilational and contractional jogs, and relay ramps (Figure 3.1c and 3.2b) (Bruhn et al., 1994; Rawling et al., 2001; Shipton and Cowie, 2001; Faulkner et al., 2003, 2010). Their width may indicate multiple episodes of slip and the overprinting of successive deformation events. An exponential decrease of the density of macrofractures and microfractures is observed with distance of the fault core, which is linked with decay of stress away from a fault tip (Figure 3.3) (Mitchell and Faulkner, 2012). As most of the displacement is accommodated in the fault core, we observe semi-ductile deformation facies presenting a

planar penetrative orientation like microbreccia, gouge and protomylonite. Generally, the highest slip induces a strong mechanical effect which reduces the grain size. Thus, the granite rock loses its granular texture and structurally evolves to semi-ductile facies in parallel to a severe illitization of the matrix. The resulting facies corresponds to a fine-grained cataclastic facies like a proto-mylonite which has been observed on the Soultz-sous-Forêts cores in GPK-1 well associated to a naturally permeable fracture zone at 1820 m depth (Genter, 1989). Observations conducted on the large dataset of borehole images in Soultz-sous-Forêts and Rittershoffen wells revealed that the thickness of the hereinabove described fracture zones is generally decametric and the thickness of fault cores is generally centimetric to metric (Genter et al., 1995, 1997a; Sausse et al., 1998, 2010; Dezayes et al., 2010; Vidal et al., 2017). At Soultz-sous-Forêts, despite the high porosity values in the damage zone, well tests reveal that 95% of the flow entered the rock mass only at discrete flow points, which correspond to main opened fractures observed on acoustic image logs (Evans et al., 2005). Similar observations were done from hydraulic tests conducted in Rittershoffen wells (Baujard et al., 2017a). Observations conducted on the core samples of EPS-1 borehole revealed fault cores that are 10 cm-thick partly sealed with geodic quartz but acting as main permeable drains and a high density of fracture localized in the core (Fig 3.1a) (Genter and Traineau, 1992; Genter et al., 1995). The surrounding damage zone is highly altered and porous and is composed of hundreds of tiny fractures that are likely connected at the borehole scale (Figure 3.3) (Genter et al., 1997a, 2000). At the URG scale, the thickness of the fracture zones encountered in geothermal wells are between 10 and 40 m in the granitic basement and act as pathways for the geothermal brine (Vidal and Genter, 2018).

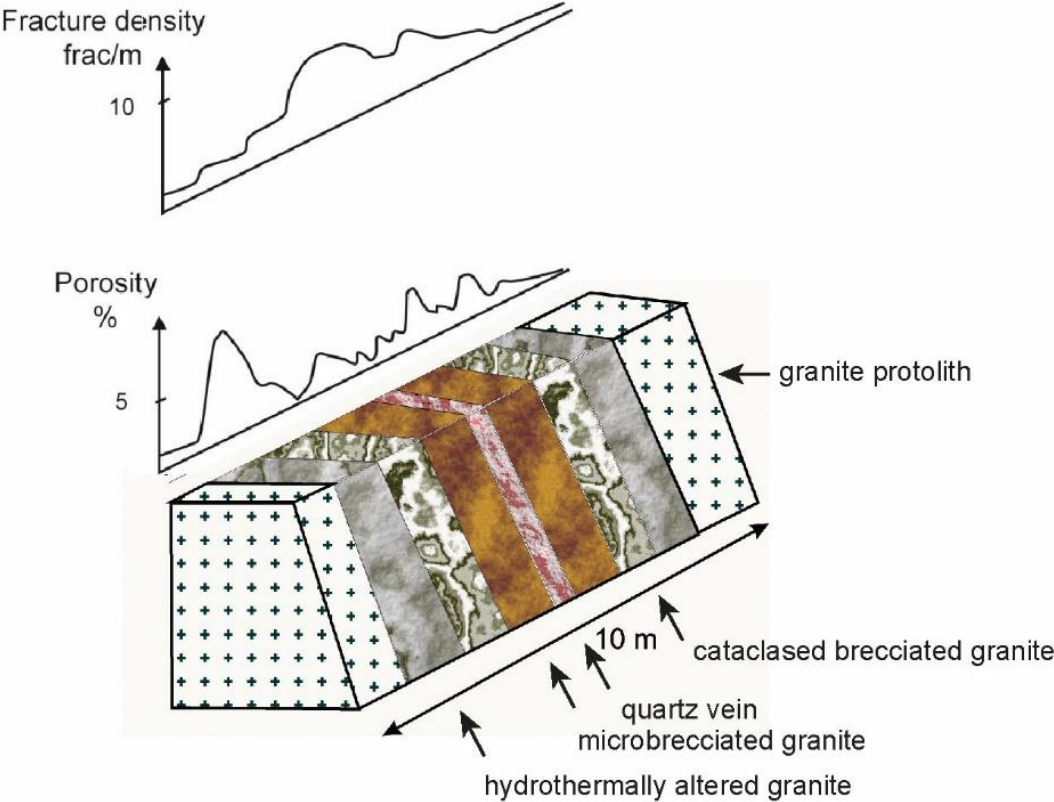


Figure 3.3: Porosity profile and fracture density in a conceptual zonation of lithofacies related to hydrothermally altered and fractured granite. Figure from Genter et al., (2000).

### 3.3.2. Mineralisation

Due to the potential of fault zones to locally increase the rock permeability, variations in fluid-rock ratios, and geochemical composition, and temperature and pressure conditions are generally observed.

In fracture zones in crystalline rocks, these temporary high fluid-rock ratios and associated variations in physical parameters generally lead to partial or complete dissolution of primary minerals in the damage zones and to secondary minerals precipitation in the fault core or the near damage zone. These dissolutions and precipitations are generally the result of pulsed hydrothermal systems (Cathelineau and Boiron, 2010). Multiple phases of alteration can be distinguished in crystalline rocks: alteration related to resident fluids such as propylitic alteration which usually occurs at temperatures at approximately 250-300°C and alteration related to fluid flow such as argillic alteration. The argillic alteration related to the URG basement reservoirs, generally occurs at temperatures between 100 and 200°C. Argillic alteration of deep crystalline basement rocks is characterized by dissolution of primary minerals like biotite, plagioclase and feldspar alteration. These dissolved minerals are then reprecipitating, generally forming phyllosilicates (Schmidt et al., 2018; Fulignati, 2020). Secondary minerals and especially clay minerals are largely studied as they are highly reactive to the system conditions (physico-chemical, temperature) (Velde, 1977; Bettison and Schiffman, 1988; Swanson et al., 2019; Kraal et al., 2021). For example, in the Kojaku granite (Japan), the polytype of illite was found to differ between fractures and gouges (Niwa et al., 2016). In volcanic hydrothermal fields, argillic alteration due to fluid circulation generally occurs at temperatures higher than 200°C. In the Bouillante geothermal field, argillic alteration is characterized by the occurrence of illite/smectite mixed layers (I/S ml), smectite and calcite (Patrier et al., 2013). In the Chipilapa geothermal field (Salvador), argillic alteration is characterized by the occurrence of I/S and chlorite/smectite (C/S) ml (Beaufort et al., 1996). More recently, clay minerals quantification with the SWIR method is of interest, through its application in this thesis but also in other literature studies (Simpson and Rae, 2018; Kraal et al., 2021).

In the URG granite, the secondary mineralisation has been meticulously described from observations conducted on core samples from GPK-1 and EPS-1 boreholes (Genter, 1989; Traineau et al., 1992). Thus, it was found that secondary quartz precipitated in the fault core in its pseudo-hexagonal form, named hereafter geodic, drusy, or hydrothermal quartz (Figure 3.1a). Observations conducted on the core samples of EPS-1 well at Soultz-sous-Forêts revealed a fault core filled with a thickness of 25 cm of secondary quartz, associated with phyllosilicates and sulfides (Genter and Traineau, 1992). Structural and mineralogical analysis of the secondary quartz in this fault core revealed the successive crystallization of 6 quartz generations, revealing a pulsed fluid flow system, probably due to several stress reactivations (Bruhn et al., 1994; Smith et al., 1998). Precipitation of carbonates as well as sulphides in the fault core were also observed. Secondary precipitation of clay minerals can also occur in the fault core, generally associated with the previous minerals described in the fault core, but secondary clay minerals precipitate mainly in the surrounding damage zones, by replacement of the altered primary minerals (Figure 3.1a). In a deep fracture zone of the Soultz-sous-Forêts granite, organic matter originating from the sedimentary layers has also been observed, which explains the existence of large-scale circulations, between the sedimentary cover and the basement (Ledésert et al., 1996). At this particular depth section of the granite at 2170 m, a

primary quartz dissolution was observed as well as the occurrence of a secondary mixed layers of lithium bearing clay (tosudite).

More precisely, the application of the Gresens method demonstrated the major elements transfers that occurred during the alteration of the granite of the URG (Jacquemont, 2002). Thus, the alteration of potassic feldspars released potassium (K) but the brine also enriched the system in K, which was fixed in the plagioclases during the illitisation process (Jacquemont, 2002). The brine also brought some silica (Si) which is fixed in the secondary quartz precipitations. The calcium (CaO) is released by the alteration of plagioclases and fixed by the precipitation of carbonates. The magnesium and iron (MgO & FeO) are released by the dissolution of ferro-magnesian minerals. The MgO is fixed by carbonates precipitation and the FeO is fixed by the precipitation of hematite and ankerite (Jacquemont, 2002).

### 3.3.3. Physical and hydraulic properties

In crystalline fracture zones, a secondary porosity is generally observed in the damage zone surrounding the fault core due to the dissolution of primary minerals. This secondary porosity is not necessarily suitable for a high PI but nevertheless contributes to the fluid flow. Thus, granites that underwent propylitic or argillic alteration vary significantly in terms of porosity (from 0.00 to 0.10%) and permeability (more than five orders of magnitude) (Géraud et al., 2010). The physical response of these effects is readily apparent on the various geophysical and petrographic dataset presented hereafter. Indeed, the physical properties of fracture zones in crystalline basement and especially of permeable fracture zones were described in detail in the URG geothermal wells since the beginning of the Soultz-sous-Forêts experiments in the 90's and continue to evolve. Among all, the anomalies visible on the temperature profiles enable to identify the main conduits in the fracture zone which generally correspond to the core(s) of the fracture zone (Figure 3.4) (Vidal et al., 2019).

Generally, a permeable fault core of a FZ can comport:

- A positive or negative temperature anomaly, respectively due to the venue of hot fluid from the formation, or to the cooling of a fracture zone by the drilling fluid or fluid injection,
- Steps on the flow logs indicating in or out-flow of fluid (Figure 3.4),
- Mud losses during drilling,
- Open fracture(s) visible on the borehole images (Figure 3.4),
- Negative peak in the gamma-ray and potassium curves due to the absence of radioactive elements trapped in potassium bearing clay minerals like illite and occurrences of secondary quartz depleted in potassium (Figure 3.4),
- Negative peak of density correlated to a positive peak of porosity due to the presence of hydrothermally altered granite (Figure 3.4 and 3.5),
- Increase of the caliper diameter due to the cave formed by the open fracture and the occurrence of mechanically softer clay-rich altered facies (Figure 3.4),
- High electrical conductivity surely due to the presence of highly saline circulating brine.

Comparatively, the damage zones in a permeable FZ can comport:

- Small-scale open or clogged fractures visible on the borehole images (Figure 3.4),
- Stable flow logs indicating no detection of fluid flow (Figure 3.4),
- Positive peaks in the total gamma-ray and potassium curves in the wallrocks, due to the presence of radioactive elements in secondary minerals like illitic material rich in K (Figure 3.4),

- Negative peaks of density associated with positive peaks of porosity due to altered facies inducing a secondary porosity (Figure 3.4),
- Positive peaks of density due to zones enriched in secondary minerals like clay minerals (Figure 3.4),
- Undisturbed caliper diameter but increase of the caliper diameter can also be observed due to the cave formed around the open fracture in the wallrock due to the occurrence of mechanically softer clay-rich altered facies (Figure 3.4),
- High electrical conductivity due to the combined effect of highly salted circulating brine and the presence of conductive phyllosilicates.

This description of geophysical logs responses highlighting several physical properties is an example of a given permeable FZ but could vary spatially depending on the FZ architecture and the complex distribution of the permeability. These observations underline the difficulty to differentiate the permeable zones (open fault core, porous damage zone) from the non-permeable zones (damage zones, wall-rocks, clogged core) when no permeability indicator (temperature anomaly, mud losses, gas venue) is present. Indeed, the electrical conductivity that will be investigated in this thesis, is generally higher in FZ than in unaltered granite. Hence, it does not allow to differentiate the high electrical conductivities due to highly salted circulated brine (permeable zone) from the ones due to the presence of conductive secondary clay minerals (clogged zones) but also from the ones due to the combined presence of highly salted circulated brine and secondary clay minerals in the porous damage zones for example. And at a larger scale, permeable FZs and paleo-permeable FZ will also show both high electrical conductivities, which does not allow to differentiate between permeable and paleo-permeable FZs.

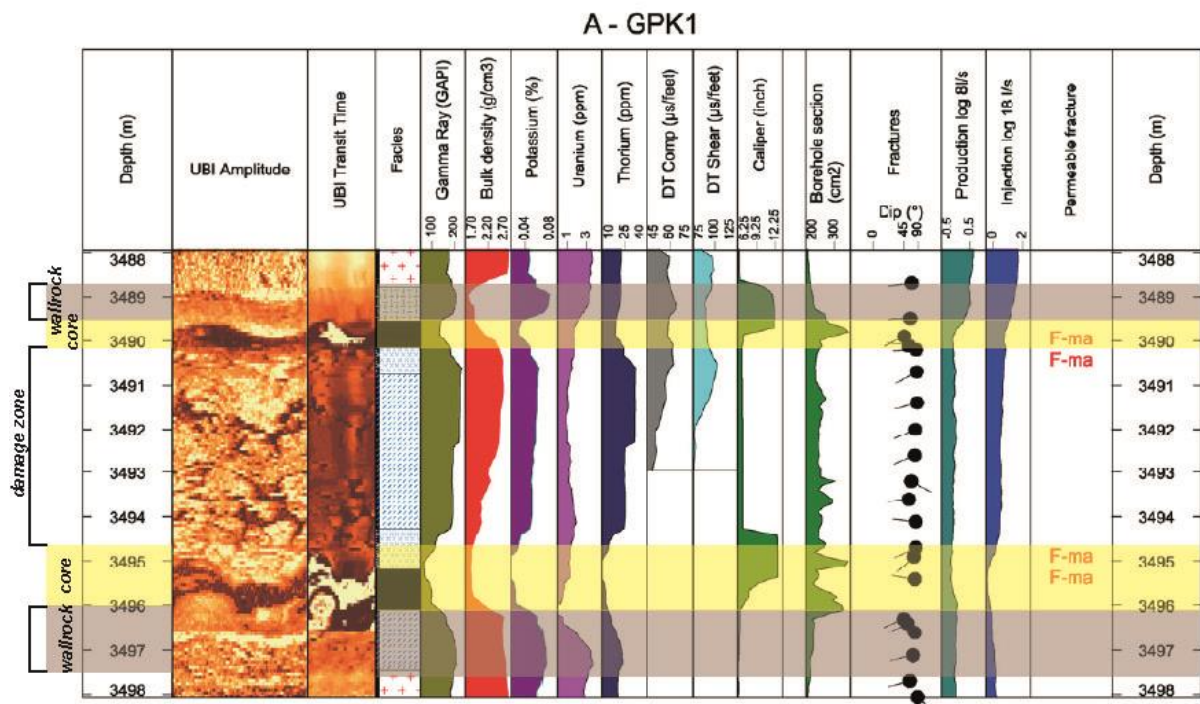


Figure 3.4: Examples of composite logs for a fracture zone in GPK-1. UBI: acoustic borehole image; Legend of facies: red crosses: monzogranite; green hatches: argillic altered granite; blue hatches: cataclased granite; blue crosses: brecciated granite; black: quartz vein. Figure is from (Dezayes et al., 2010).

### 3.3.4. Stress and deformation in crystalline fracture zones

The role of stress in the creation of the fracture zone and its architecture is essential. The evolution of a fracture usually starts with an initial brittle fracture and frictional failure, followed by a fluid-rock interactions period during which permeability increases followed by a period of decreasing permeability due to its sealing with alteration products until the next re-opening of the fractures happens (Davatzes and Hickman, 2005; Stober and Bucher, 2015). Fracture analysis on borehole images in crystalline rocks also highlights a direct link between permeability and stress showing that most permeable fractures were critically stressed shear fractures, compared to the majority of non-permeable fractures that did not appear to be critically stressed (Barton et al., 1995; Evans et al., 2005). Based on the above description, stress appears as a factor for fracture opening and reactivation leading to fluid flow, and thus enhancing the permeability of the fracture zone. It is also observed that chemical alteration of low-porosity crystalline rocks as well as the precipitation of secondary clay minerals modify the deformation processes in terms of mechanics, stress conditions and induced seismicity (Saffer and Marone, 2003; Numelin et al., 2007; Ikari et al., 2009; Meller and Kohl, 2014; Meller and Ledésert, 2017) as well as the distribution of permeability in the fracture zone (Faulkner and Rutter, 2001; Davatzes and Hickman, 2005; Solum et al., 2005, 2010). Thus, secondary minerals can clog the system but are also described to produce dilation due to surface roughness, in case of secondary quartz and calcite (Brown, 1987; Lockner and Beeler, 2002). This “mineralogical effect” changes the petrophysical properties of the rock. Hence, Schmidt et al., (2018) described that the rock can be weakened by mineral–brine interactions, resulting in the propagation of fracture into the adjacent rock, increasing the permeability in the early period of fracture alteration. The presence of phyllosilicates was also found to weaken the FZ. These weakened zones induce a frictional strength lower than the one predicted by Byerlee’s law, resulting in stress-decoupling horizons and faults slipping, and also affecting the evolution of the microseismic cloud measured during hydraulic stimulations (Faulkner et al., 2010; Meller and Kohl, 2014). At Soultz-sous-Forêts, it was demonstrated that clay-rich zones favour the occurrence of aseismic movements on fractures (Meller and Kohl, 2014; Meller and Ledésert, 2017).

### 3.3.5. Towards a conceptual model of FZs in the URG

The fault core generally comports the following components: a free aperture channeling fluid circulations named fault core and a clay-rich gouge, brecciated and geochemically altered zones named damage zone (Figure 3.5a). As described above, fault core is affected by secondary mineralisation like drusy quartz, carbonates, sulfides and damage zones are strongly affected by primary minerals dissolution (biotite, plagioclase, feldspar) generally replaced by secondary phyllosilicates (Figure 3.5a). The resulting architecture of such fracture zone is very complex and lithologically heterogeneous, anisotropic and discontinuous. Due to its complexity, it can act as preferential conduits or as barriers for fluid flow (Barton et al., 1995; Caine et al., 1996). These behaviours were successively observed with laboratory measurements as well as field observations (Caine et al., 2010). For example, fluid circulation in the natural fractures dissolves primary minerals and could create secondary porosity in the surrounding nearby damage zone (Figure 3.5b). In parallel, secondary clay minerals precipitation can partially clog the fracture system (Figure 3.5a). At last, the precipitation of secondary minerals in the fault core like drusy euhedral quartz and carbonates creates rugosity on the fracture planes and could maintain fractures hydraulically open (Figure 3.5a). However, several parameters control the fracture zone evolution: lithology, time, temperature and pressure conditions, fluid chemistry, fluid/rock ratio, and deformation. Over time, due to the

mineralisation, to the successive and episodic stress reactivations and to deformation; the physical and hydraulic properties of a fracture zone may change. Thus, this conceptual model is only valid for a given time and is a transitory representation of a fracture zone and over time this scheme and is subject to evolve. Therefore, attempts have been made to represent linked fault segments that could act as conduits or as barriers for fluid flow (Figure 3.5). Although, the association of conduits and barriers to fluid flow in a single FZ at a given time does also exist (Figure 3.5).

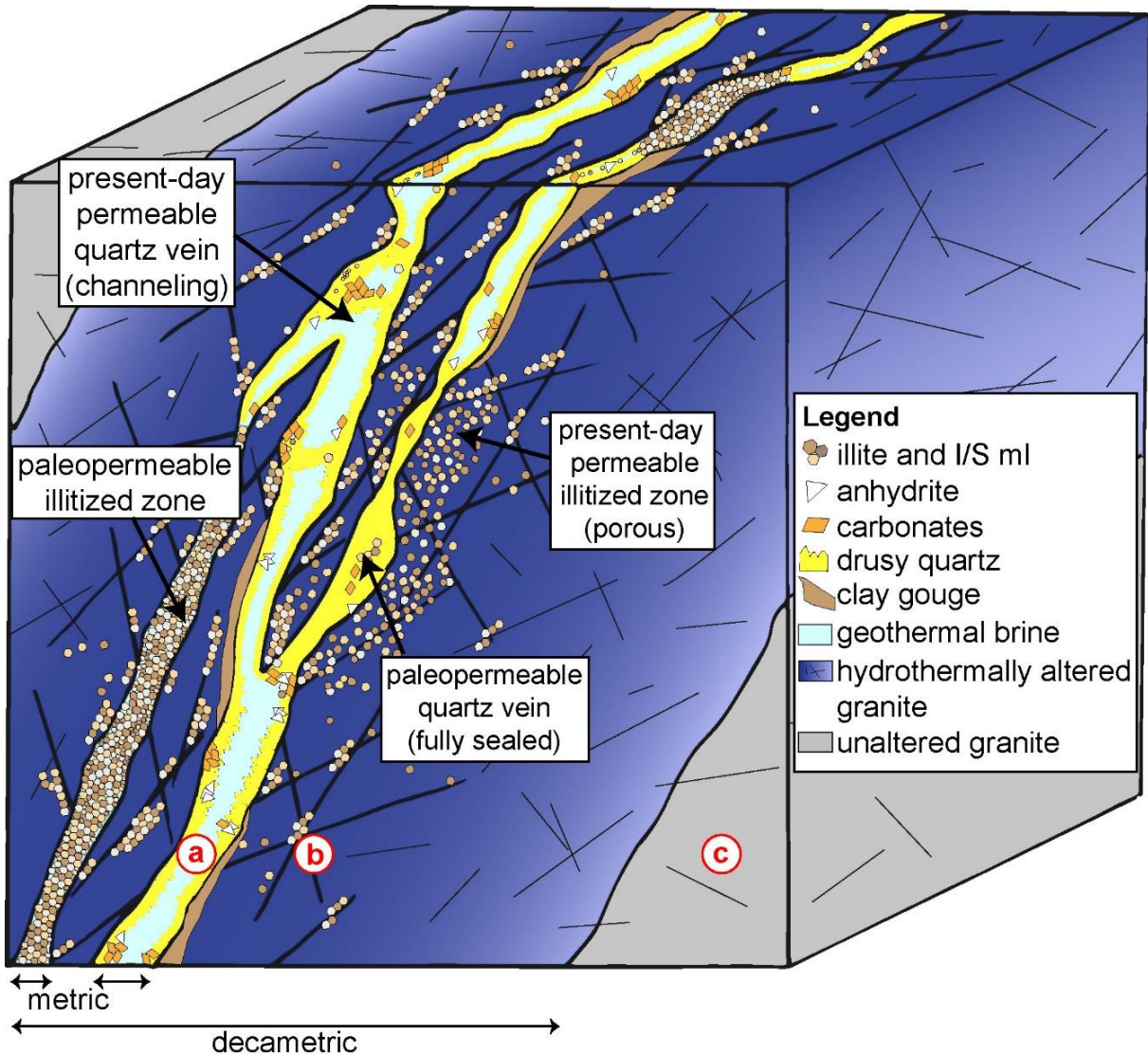


Figure 3.5: Complexity of a fracture zone (FZ). Three zones are distinguished: a) the fault core, which can be a pathway for fluid if illite and quartz veins do not totally seal the zone, b) the damage zone, which can be sealed or opened with small-scale fractures that act as fluid pathways, and c) the unaltered granite, which generally shows very low matrix and fracture permeability.

## 4. Motivation

### 4.1. Socio-economic framework

My research work is directly integrated in the objectives set by the European Commission for the development of geothermal energy. My thesis aims at understanding how the highest permeable zones are distributed in naturally fractured crystalline reservoirs and consequently

how they can be reached by deep drilling in order to improve the access to more geothermal energy resources. More precisely, my thesis aims at contributing to the first target fixed by the European Commission which is to increase the reservoir performance, by better characterizing the permeable pathways, and understanding which geological properties (secondary mineralogy, natural fractures, electrical resistivity) are the signatures of paleo or present permeability (Figure 4). The better understanding of geothermal reservoirs could contribute to design potential stimulations that could improve geothermal production. This better understanding of geothermal reservoirs could also help in determining how the configuration between the well and the reservoir could optimize the production index favouring a hydrothermal concept for future projects (Figure 1.10). The reduction of exploration costs which corresponds to the fourth target is also one key point of my thesis. An innovative, rapid and inexpensive method is developed to identify and quantify clay minerals which are the signature of the past and/or present fluid circulation, directly on the drilling site. The development of this innovative SWIR method also addresses the second goal of the European Commission which is to develop methods and instruments for technical and financial risk management. Hence, SWIR is a rapid and non-expensive method.

## 4.2. Scientific motivation

This research manuscript addresses scientific questions related to the understanding of the natural permeability in the fractured basement rocks of the upper crust. Generally, basement rocks are reputed to be tight with negligible matrix porosity. In Tertiary basins, like the URG, late Variscan basements are hidden by a thick sedimentary cover. They are affected by a complex network of natural fractures inherited from the polyphasic tectonic activity. These inherited faults and fractures are the seat of intense fluid circulation that leads to hydrothermal alteration, modifying the structure and petrophysical properties of granitic rock under specific conditions of pressure and temperature (Figure 4). Hence, the leaching of the granite due to fluid-rock interaction results in the creation of secondary porosity in the surrounding damage zones of faults and fractures due to the dissolution of the primary minerals (Figure 4). Hydrothermal alteration also causes the precipitation of secondary minerals such as carbonates, sulphides, quartz and clay minerals (Patrier et al., 1996; Ledésert et al., 1999; Genter et al., 2000; Mas et al., 2003; Beaufort et al., 2015; Vidal et al., 2018). This association between natural fractures and hydrothermal alteration could contribute to promote fluid flow and thus act as conduits favourable to fluid circulations but could also act as barriers to fluid flow.

Therefore, scientific challenges relying on the analysis of well data could be summarized as follow. How can fractures that are significant hydraulic conduits be identified, located, and characterized? How do flow and transport occur in fracture systems? How to discriminate between sealed conduits and active channels?

The aim of this thesis is to address the couple natural fractures and hydrothermal alterations by developing new tools and methods for identifying permeable fracture zones in geothermal wells, but also for approaching the complexity and the internal architecture of these fracture zones in terms of fluid pathways and clogged zones (Figure 4).

To answer these questions at the well scale, these three main steps are usually performed:

- **Characterization of the natural fractures network** in terms of orientations and dips based on the electrical and acoustic image logs.

- **Correlation of the fracture network with the permeability indicators** which are the following:
  - (1) The occurrence of gases such as CO<sub>2</sub>, helium, and radon, as well as alkanes that are monitored in the well during the drilling by the mud-logger unit. This allows to identify permeable fracture zone at a metric scale. However, permeable fractures are not systematically associated with gas venues.
  - (2) Mud losses and brine outflow, that are monitored during the drilling operation by the mud-logger unit. They allow to identify permeable fracture zone on a decametric scale. However, multiple permeable zones cross-cut by a well could result in a very large zone of mud losses, which could be complicated to interpret in terms of channelling.
  - (3) The most-relevant indicator for the detection of permeable fracture zones is the temperature profile (T logs). These geophysical measurements are inexpensive and are usually acquired at thermal equilibrium, several weeks after drilling operations. But T logs can also be acquired during production or injection. In this case, they need to be coupled with flow logs to estimate the temperature of the fluid circulating in the fracture zone.
- **Understand the permeability distribution.** For this, hydrothermal alteration is a good marker. Hence, clay minerals are the result of hydrothermal alteration due to past and present fluid-rock interactions in the fracture zones of the granitic basement of the URG. At Soultz-sous-Forêts and Rittershoffen, these clay minerals systematically correspond to dioctahedral micas like illitic minerals (illite and illite-rich illite/smectite mixed layers). The identification and characterisation of illitic minerals via common methods enable 1) to identify past or present permeable zones and 2) to understand and anticipate the geothermal reservoir properties like secondary porosity, bulk density, resistivity, and permeability (Mas et al., 2006; Vidal et al., 2018).

Usually, the alteration petrography is characterized by the following methods: clay minerals crystallography is analysed with X-ray diffraction (XRD), chemical composition is analysed with energy-dispersive spectrometry (EDS) and phase relationships by optical and/or electronic microscopy. However, XRD and EDS are time-consuming methods that can be carried out on a few tens of samples, whereas sampling in geothermal wells provides generally one sample every 3 meters of depth. In comparison, the SWIR spectroscopy allows to analyse samples in a very short time, which make it possible to systematically measure all the cuttings samples of a well. Furthermore, SWIR allows a quantitative (or semi-quantitative) approach, essential for the understanding of fluid pathways and clogged zones. However, the SWIR method requires a mineralogical calibration upstream. The SWIR method is already applied in the mining industry but has only been very few applied to geothermal wells, and has never been applied to the URG geothermal wells (Tappert, 2013; Simpson and Rae, 2018; Kraal et al., 2021). This new mineralogical approach, coupled with XRD and EDS data and well log data like temperature, porosity, density, gamma-ray, and resistivity logs, as well as borehole images, should allow to decipher the complexity of permeable fracture zones with a new vision, at the well scale (Figure 4).

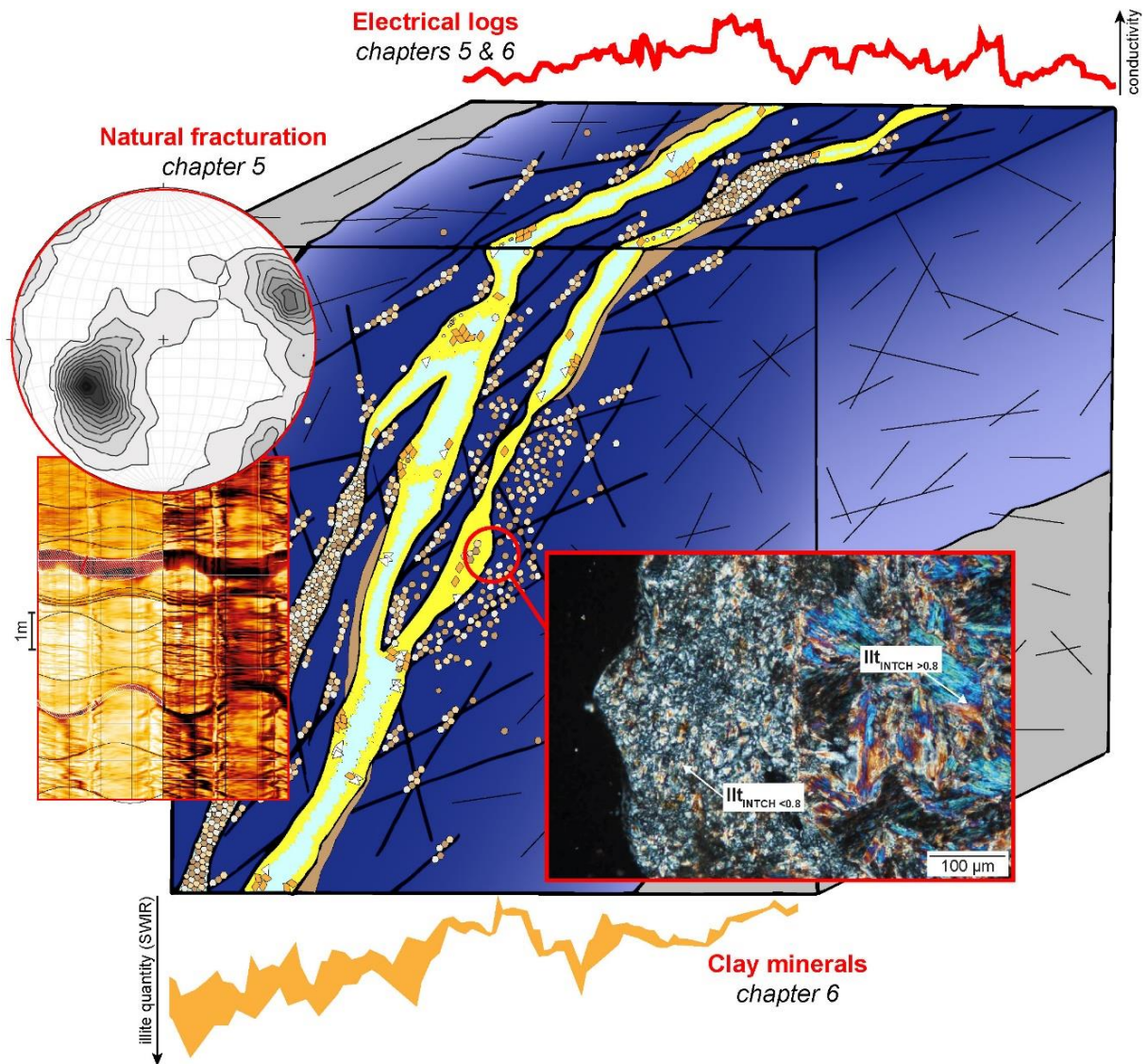


Figure 4: Synthetic representation of the methods used in the thesis to address the mineralogical and structural controls on the permeability of deep naturally fractured crystalline reservoirs with well logs, borehole images and cuttings analyses from the geothermal wells of Soultz-sous-Forêts, Rittershoffen and Illkirch.



PART 2:  
PERMEABLE FRACTURE ZONES AT  
WELL SCALE



## 5. Structural geology and geophysical signatures of permeable fracture zones

This fifth chapter focuses on permeability evidence, geophysical logs and structural network characterization.

The first part 5.1. of this chapter presents an article published in *Geothermal Energy Journal* which aims to complete previous studies carried out at Rittershoffen. Acoustic borehole images were lacking in the deepest part of the GRT-2 well and the structural network was approached by using caliper data. Geophysical logs and structural data were also correlated to the petrographic facies of the granite of the GRT-2 well built from the lens-observation of the cuttings samples.

The second part 5.2. of this chapter presents an article submitted to the *Journal of Structural Geology* that investigates the first well GIL-1 of the Illkirch project, drilled between 2018 and 2019, for which geophysical logs and electrical borehole images and cuttings samples are available. The first goal of this paper is the characterization of the structural network, and the second goal is the integration of these results at the graben scale, by comparing them with the Soultz-sous-Forêts and Rittershoffen wells.

In parallel to these studies, a conjoint work was conducted and published in the peer reviewed *Geofluids Journal* with Jeanne Vidal and co-authors, to refine the interpretation of the thermal signature of permeable fractures, based on data from Soultz-sous-Forêts and Rittershoffen wells. Temperature logs measured at equilibrium and during production coupled with flow logs, were analysed to improve the interpretation of temperature anomalies and fluid circulations at the well scale. This work is presented in Appendix 1.



## 5.1. How do the geological and geophysical signatures of permeable fractures in granitic basement evolve after long periods of natural circulation? Insights from the Rittershoffen geothermal wells (France). Published in *Geothermal Energy Journal*.

C. Glaas<sup>1,2\*</sup>, A. Genter<sup>1</sup>, J. F. Girard<sup>2</sup>, P. Patrier<sup>3</sup> and J. Vidal<sup>1</sup>

<sup>1</sup> ÉS Géothermie, : 5, rue André Marie Ampère, 67450 Mundolsheim, France.

<sup>2</sup> CNRS, UMR 7516 IPGS, University of Strasbourg, 5 Rue René Descartes, 67084 Strasbourg Cedex, France.

<sup>3</sup> CNRS UMR 7285 IC2MP, HydrASA, University of Poitiers, Bat B8, Rue Albert Turpain, TSA51106, 86073 Poitiers Cedex 9, France.

**Keywords:** Granite, Fracture, Hydrothermal alteration, Mineralogy, Caliper, Resistivity, Geothermal field, Upper Rhine Graben

### 5.1.1. Abstract

Two deep wells were drilled at Rittershoffen (Alsace, France) to produce high-temperature fluids to supply heat to a biorefinery. The GRT-2 production well was drilled to a depth of 3196 m MD and was deviated to target a permeable local fault in the granitic basement buried beneath a thick sedimentary cover. The objective of this study is to better understand the permeability of fractured reservoirs within crystalline rocks, focusing on the production well GRT-2. Based on a petrographic and mineralogical analysis of cutting samples, several granitic facies associated with hydrothermal alteration were identified on the basis of the amounts of illite, chlorite, anhydrite, secondary geodic quartz, and oxides. These observations were correlated with various geological and geophysical datasets (gamma ray, porosity, density, electrical resistivity, caliper, borehole image logs, temperature, rate of penetration, and mud losses) to localize and identify permeable fracture zones. In sections where acoustic image logs were not available, such as in the deepest part of the well, the geometries of the fracture zones were interpreted from an oriented caliper log. The caliper log interpretation detected one-third of the fractures detected by acoustic image logs. However, two major fracture sets striking N–S and dipping eastward or westward were observed. Furthermore, a synthetic resistivity log that fits the measured resistivity log relatively well was built using the Archie and Waxman and Smits models. This approach is a proxy for estimating the porosity and the mineralogical changes based on the cation exchange capacity, which is controlled by the chlorite/illite ratio, derived from electrical logs in granitic formations. The correlation of all these results allowed the identification of a resistivity signature of a permeable fracture zone that spatially fits with the temperature signature. The major contribution of this study is the identification of a hierarchy of permeable fractures based on petrophysical signatures. The geophysical signature of fracture zones with low residual permeability exhibits a broad depth extent, whereas the geophysical signature of a highly permeable fracture zone is more localized. Past hydrothermal circulation has enlarged the altered and porous zones around open fractures, and in some cases, intense illitization has plugged these fracture zones and reduced their permeabilities.

### 5.1.2. Background

The economic feasibility of any geothermal project depends mainly on finding the expected resource with a sufficiently high temperature and flow rate to obtain efficient heat production. The sustainability of the geothermal reservoir also needs to be maintained. Geothermal development in Europe and more specifically in the Upper Rhine Graben (URG) has presented

a wide range of hydraulic yields from  $10^{-3}$  L/s/bar to 3.5 L/s/bar (Schill et al., 2017; Vidal and Genter, 2018). This study aims to investigate preferential channels for natural hydrothermal circulation, their contribution to well permeability, and their history and evolution in terms of secondary mineralogy. Based on geothermal development in the URG, the permeability of the granitic reservoir appears to be controlled by fractured zones that act as preferential pathways for natural hydrothermal circulation (Villemin and Bergerat, 1987; Ledésert et al., 1993, 2010; Sausse and Genter, 2005; Rotstein et al., 2006; Dezayes et al., 2010; Sausse et al., 2010; Vidal and Genter, 2018). A large number of studies have tried to characterize permeability, fracture geometry, and hydrogeological systems for geothermal applications or nuclear waste storage, whereas a few studies have addressed the hydrogeology of the deep-seated crystalline rocks (Moreno and Neretnieks, 1993; Stober and Bucher, 2007; Ishibashi et al., 2016). In a volcanic geothermal context, fault zones are also main pathways for fluids (Gudmundsson et al., 2002; Gailler et al., 2014). Fault zones have also been widely studied in outcrops for geothermal applications (Bauer et al., 2015) or at the well or basin scale for oil and gas exploration in sedimentary formations. Deep fracture zones in crystalline rocks have been largely studied with laboratory experiments (Griffiths et al., 2016). However, integrated field examples are lacking (Faulkner et al., 2010). This study proposes field investigations at the well scale, specifically the Rittershoffen GRT-2 production well, in the URG (Figure 5.1). To illustrate how permeable faults are characterized in a geothermal deep-seated granitic reservoir, this study first describes the hydrothermal alterations from mineralogical observations of cutting samples. The structural analysis of fractures with an oriented caliper tool is compared to the structural information from acoustic image logs, and the resistivity response to permeable fault zones and mineralogy is then discussed. Finally, the signature of permeable fractures in the complete well data set is synthesized. This study establishes a hierarchy of fracture zones in terms of permeability based on an original data set from the GRT-2 well.

### 5.1.3. Rittershoffen geothermal reservoir

The Rittershoffen geothermal site is located in the Upper Rhine Graben in northeastern France, 40 km NNW from Strasbourg and 7 km SE from the well-known Soultz-sous-Forêts geothermal site (Figure 5.1). At Rittershoffen, the two deep wells forming the geothermal doublet were designed to supply a biorefinery located close to the Rhine river and to produce 24 MWth (Baujard et al., 2017a). Via a downhole pump, the GRT-2 production well produces a geothermal brine at industrial rates of 70 L/s, with water temperatures of up to 168 °C at the surface and a salinity close to 100 g/L (Sanjuan et al., 2016). In the URG, natural flow rates are low and can be enhanced by thermo-hydro-mechanical-chemical (THMC) stimulation, such as that used in the Soultz wells or at Rittershoffen in the GRT-1 well (Baujard et al., 2017a; Schill et al., 2017). The objective of the enhanced geothermal system (EGS) technology is to improve the connectivity between the well and the reservoir and thus the well productivity. In contrast, the GRT-2 production well is one of the most permeable wells in northern Alsace and is not stimulated after drilling operations, because its natural productivity index was sufficiently high (Baujard et al., 2017a; Vidal and Genter, 2018). The geothermal reservoir is located at the interface between the sedimentary cover and the crystalline basement. At the interface, the sedimentary cover comprises Triassic sandstones. The crystalline granitic basement is composed of muscovite, biotite, K-feldspar, plagioclase, and quartz, and is interpreted to be equivalent to the two-mica granite encountered in the deep reservoir at Soultz (Traineau et al., 1992; Stussi et al., 2002). The formation of the granitic basement has been dated to the mid-

Carboniferous, and it has since undergone pervasive alteration and exhibits several grades of hydrothermal alteration (Genter, 1989; Cocherie et al., 2004). In the granite, the GRT-2 well productivity is supported by four main permeable fracture zones (Baujard et al., 2017a). They were detected in the temperature log at 2533 m measured depth (MD), from 2770 to 2808 m MD, from 2940 to 2980 m MD, and from 3050 to 3072 m MD (Figure 5.2). These zones are strongly supported by the mud loss data, which are correlated with the temperature anomalies. The mud losses increase by approximately 3 m<sup>3</sup>/h at 2530 m MD, approximately 3 m<sup>3</sup>/h at 2795 m MD, approximately 2 m<sup>3</sup>/h at 2810 m MD, and approximately 5 m<sup>3</sup>/h at 2985 m MD (Figure 5.2). In addition, this permeability evidence at the well scale is systematically correlated with increases in the rate of penetration (ROP) at depths of 2535, 2770, 2787, 2800, 2948, and 3050 m MD.

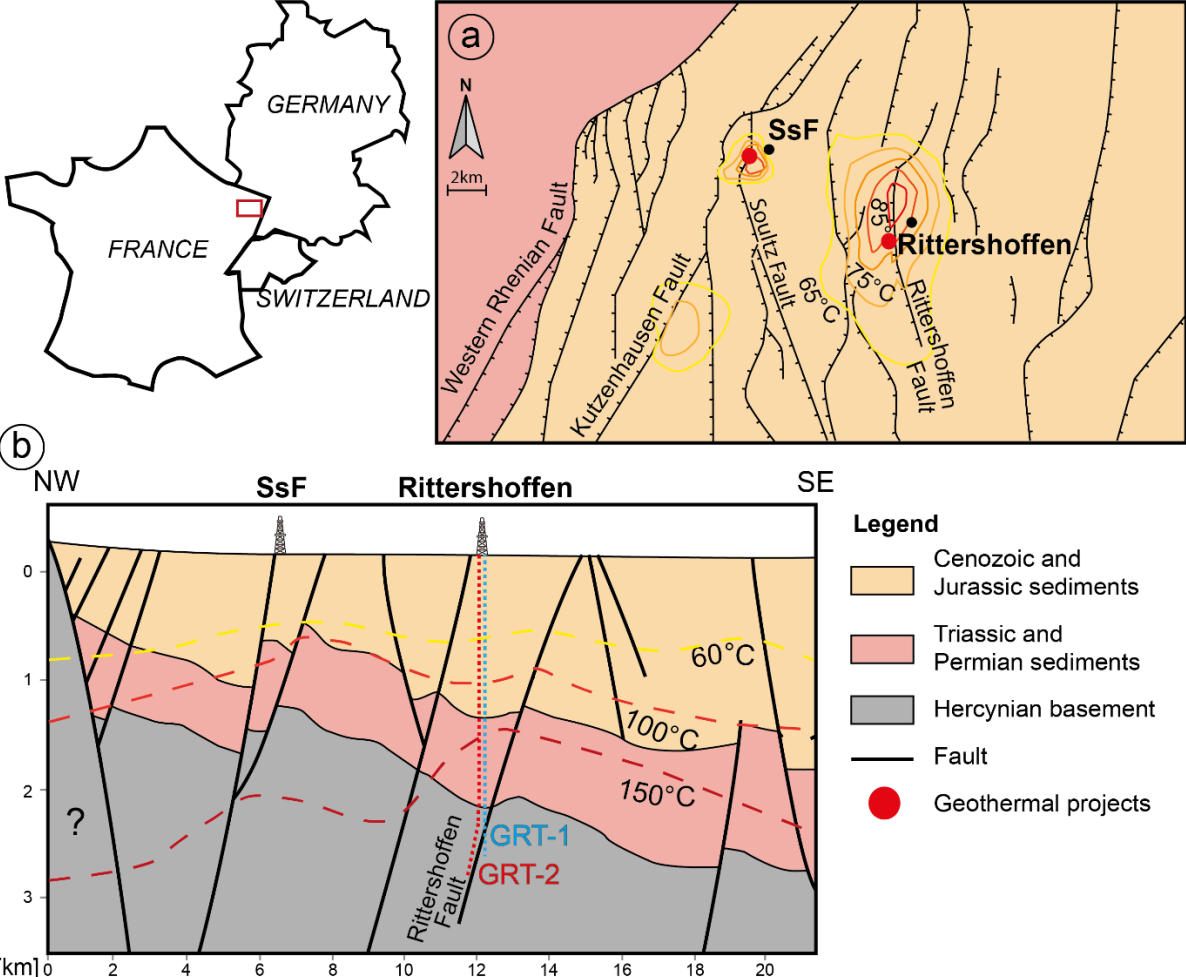


Figure 5.1: Location of the Rittershoffen geothermal site. a Simplified geological and structural map of the Rittershoffen and Soultz-sous-Forêts (SsF) area. The isotherms at the top of the basement are from Baillieux et al. (2014). b Geological cross section through the Rittershoffen and Soultz-sous-Forêts geothermal sites with the Rittershoffen well trajectories, after the GeOrg Team (2017). The dashed lines are schematic trajectories of the GRT-1 (blue) and GRT-2 (red) geothermal wells (Vidal et al., 2018).

## 5.1.4. Borehole data and methods

### 5.1.4.1. Datasets

This study focuses on the open-hole sections of the Rittershoffen wells in the granitic basement and more precisely on the GRT-2 production well, which intersects many permeable fractures. The following table (Table 5.1) presents the available data acquired in the open-hole granitic sections of wells GRT-1 and GRT-2 (Figures 5.2, 5.3, 5.5). The open-hole sections in the granite parts of both wells have lengths of 365 m for GRT-1 and 716 m for GRT-2. Mud logs were acquired during drilling operations and have a spatial resolution between 20 and 50 cm, whereas the geophysical logs were acquired after drilling and have a vertical spatial resolution of approximately 15 cm. The cutting samples were collected at depth intervals of every 3 m during drilling. Because one sample represents 100 L of rock (Table 5.1), the vertical resolution of cutting is thus quite coarse and is not as precise as core samples; in addition, cutting samples provide no information on the rock texture (Figure 5.4).

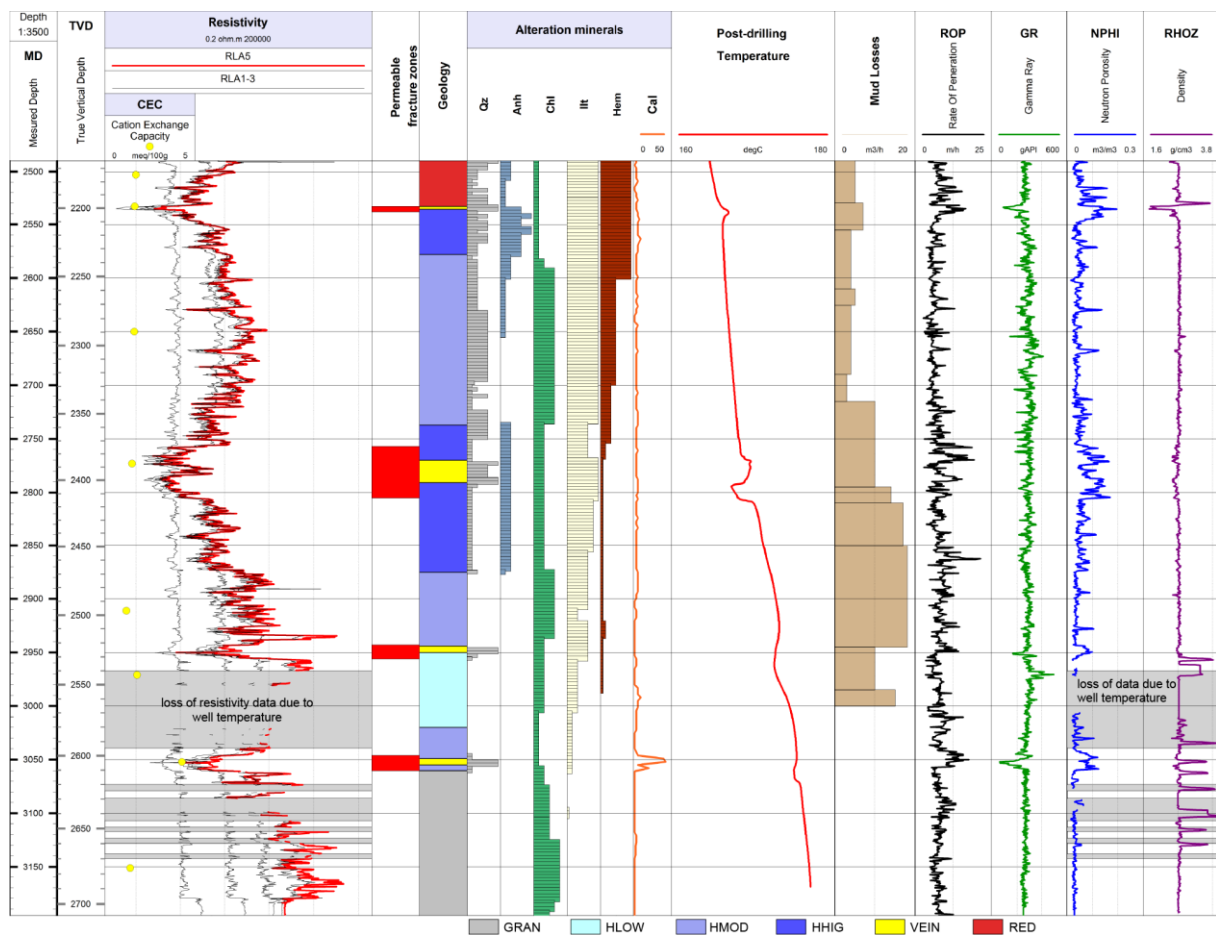


Figure 5.2: Composite log of the GRT-2 granitic basement, including alteration mineral quantities from cutting observations and the following geophysical logs: resistivity, temperature, mud losses, rate of penetration (ROP), gamma ray, porosity, and density. The permeable fracture zones (in red) were deduced from the complete data set presented here and were based on the previous studies (Vidal et al., 2017). The gray areas represent loss of data due to well temperatures that were too high. The facies are as follows: GRAN: granite, HLOW: low hydrothermal alteration grade, HMOD: moderate alteration grade, HHIG: high alteration grade, VEIN: quartz vein, RED: reddish granite.

	Name	Depth (MD) GRT-1	Depth (MD) GRT-2	Unit	Vertical sampling <i>Horizontal sampling</i>
<b>Mud logs</b>	Cuttings	2215-2580 m 122 samples	2480-3196 m 239 samples	no unit	Sampled each 3 m in-depth
	CEC	no CEC measurements in GRT-1	2503-3151 m 8 samples	meq/100 g	CEC measurements were performed on crushed cutting samples
	Calcite	2215-2580 m	2480-3196 m	m <sup>3</sup> /m <sup>3</sup> (expressed in %)	Calcimeter measurements were performed on crushed cutting samples
	Mud Losses	2215-2580 m	2480-3196 m	m <sup>3</sup> /h	Driller observations
	Rate of Penetration (ROP)	2215-2580 m	2480-3196 m	m/h	<b>50 cm</b>
<b>Geophysical logs</b>	Gamma Ray (GR)	2215-2570 m	2480-3196 m	gAPI	<b>15 cm</b>
	Hole Diameter	2215-2580 m	2480-3008 m	inches	<b>15 cm</b> 60°
	BoreHole Image	2480-2865 m	2480-2865 m		<b>1 cm</b> 2°
	Resistivity	no resistivity log in GRT-1	2480-3196 m	ohm.m	<b>15 cm</b>
	Porosity	2215-2577 m	2480-3196 m	m <sup>3</sup> /m <sup>3</sup>	<b>15 cm</b> <i>Depth of investigation: several cm (flushed zone)</i>
	Density	2215-2580 m	2480-3196 m	g/cm	<b>15 cm</b>
	Temperature	2215-2470 m	2480-3169 m	°C	<b>GRT-1 = 20 cm</b> <b>GRT-2 = 50 cm</b>

Table 5.1: Details of the geological and geophysical data sets available for the granitic basement of the GRT-1 and GRT-2 wells. The first column presents the type of data; columns two and three present the measured depth intervals in the two openhole sections. The fourth column presents the units of the data, and the fifth column presents the resolution of the data according to the log acquisition resolution, both vertically and horizontally (in italic letters).

#### 5.1.4.2. Secondary mineralogy from cuttings

The petrographic logs in the open-hole sections of both wells are based on cutting observations with a binocular magnifier. In the GRT-2 well, 240 cutting samples collected in the basement were thoroughly observed and investigated in terms of primary and secondary mineralogy. According to the previous studies on the Soultz-sous-Forêts geothermal site, the hydrothermal alteration grades in the granite are well known from core observations (Traineau et al., 1992; Ledésert et al., 1999; Sausse et al., 2006; Meller and Kohl, 2014; Meller et al., 2014b; Meller and Ledésert, 2017). The core mineralogy and hydrothermal alteration grades were cross-referenced with the minerals observed in the cuttings, although the texture information and the mineral assemblage were not reflected in the cuttings (Figure 5.4).

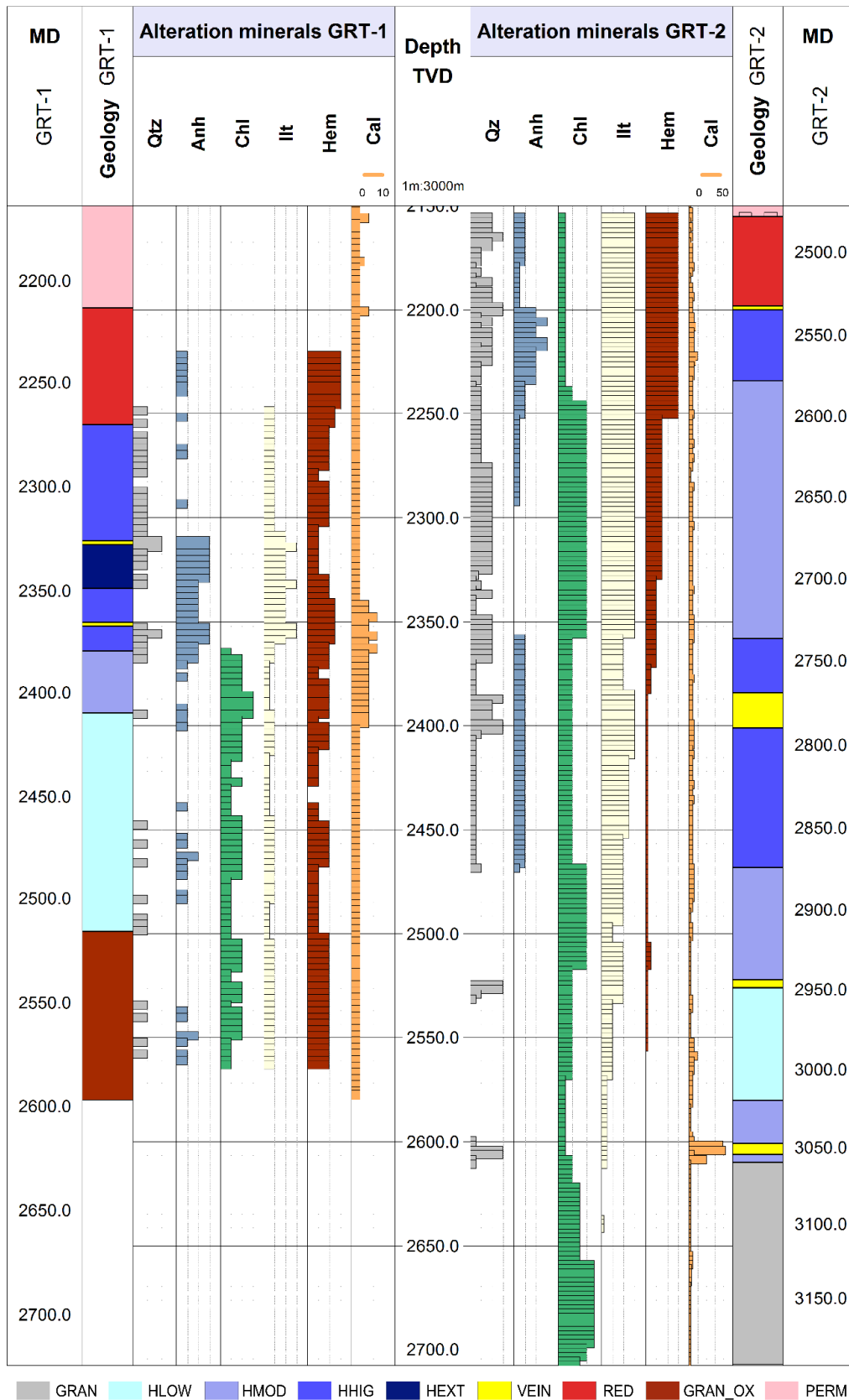


Figure 5.3: Geological logs of both the GRT-1 and GRT-2 wells, based on the mineralogical quantities observed in cuttings. The reference depth is TVD for both wells. The facies are as follows: GRAN: granite, HLOW: low hydrothermal alteration grade, HMOD: moderate alteration grade, HHIG: high alteration grade, HEXT: extreme hydrothermal alteration, VEIN: quartz vein, GRAN\_OX: oxidized granite, RED: reddish granite, PERM: Permian sandstone.

In the cutting samples, several hydrothermal alterations and granite facies were distinguished. The mineralogy was described through a semi-quantitative approach using a three-class scale. The low hydrothermal alteration (HLOW) grade is characterized by more chlorite than primary biotite, the absence or small amount of illite, and intact plagioclase (feldspars). The moderate hydrothermal alteration (HMOD) grade is characterized by the presence of illite due to further alteration of the chlorite and intact feldspars. The high hydrothermal alteration (HHIG) grade is associated with abundant illitic material, very low amounts of chlorite, and altered plagioclase. The extreme hydrothermal alteration (HEXT) grade is characterized by abundant illitic material from biotite and plagioclase transformation and geodic quartz prisms linked to hydrothermal circulation (Traineau et al., 1992; Genter et al., 1997b). The VEIN facies defines the fracture zones identified by the highest amounts of secondary geodic quartz precipitation and is associated with a high calcite content (Hébert et al., 2010). The granitic facies identified in the cuttings include unaltered granite (GRAN), which is characterized by the presence of biotite, hematite, and calcite, and is associated with a propylitic alteration related to the emplacement of the pluton (Genter et al., 2000; Jacquemont, 2002), and reddish granite (RED), which contains a large amount of red K-feldspar megacrysts oxidized through intense exposure to weathering fluids. The oxidized granite (GRAN\_OX) in GRT-1 is a propylitic granite that also presents a pronounced reddish color associated with oxidation and a large amount of hematite. The presence of illite in the granitic basement and as a major signature of hydrothermal alteration was also confirmed by complementary analyses. In the previous studies, X-ray diffraction (XRD) was performed on the clay fraction ( $< 5 \mu\text{m}$ ) of selected cuttings, from which three groups of illitic minerals (well-crystallized illite, poorly crystallized illite, and illite-rich illite/smectite mixed layers) were identified (Vidal et al., 2018). The chemical compositions of the clay minerals (illite and chlorite) were obtained using a scanning electron microscope (SEM) coupled with energy-dispersive X-ray spectroscopy (EDS). This study showed that permeable fractured zones were associated with the occurrence of poorly crystallized illite and illite/smectite mixed layers crystallized during hydrothermal circulation. In the GRT-2 well, some Fe-chlorite was also observed in highly permeable fracture zones that were not totally plugged by small crystallites of illite (Vidal et al., 2018).

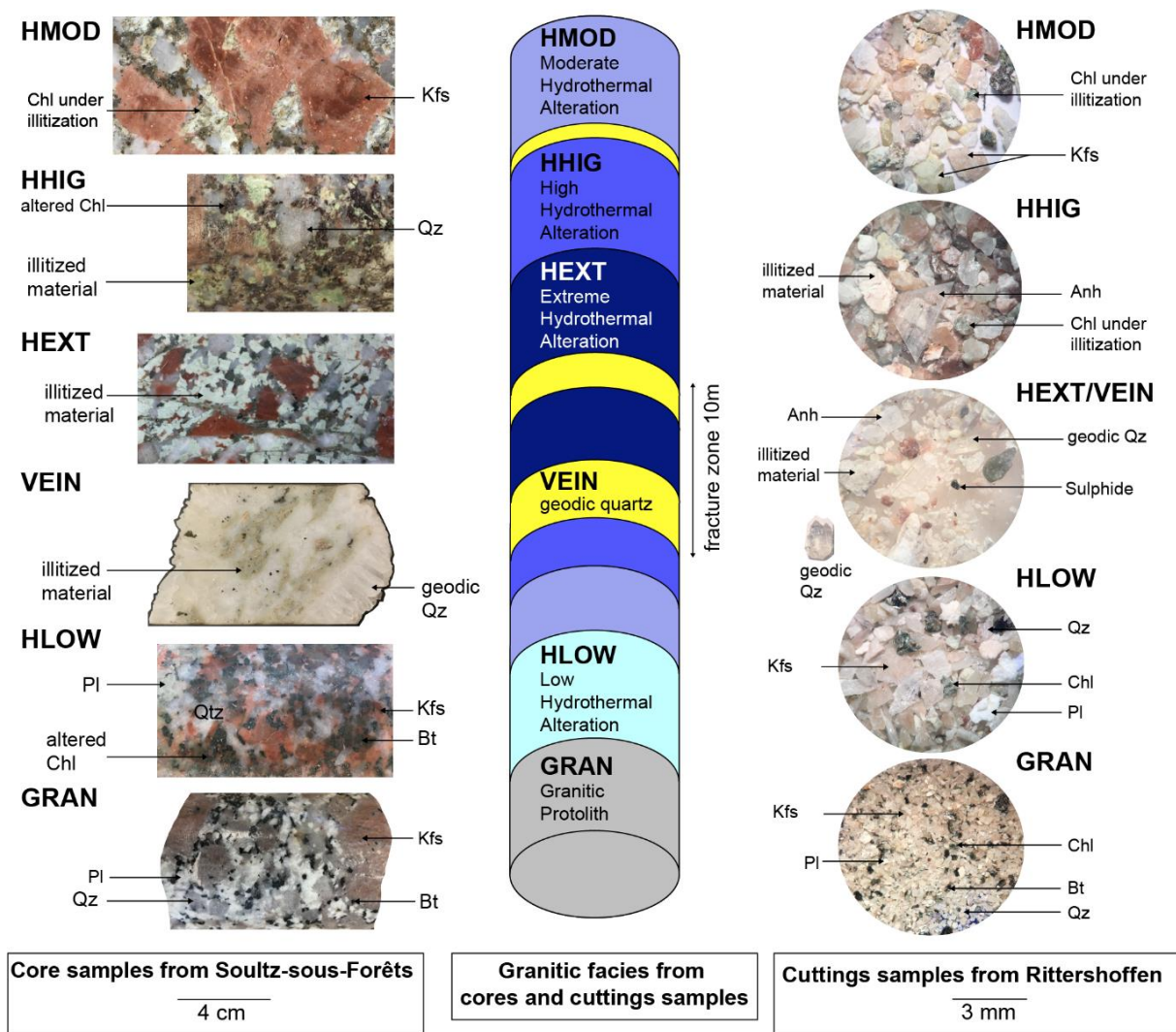


Figure 5.4: Correlation between the mineralogy observed in cores (left) and the mineralogy observed in cuttings (right), defining the several granitic alteration facies (middle). The conceptual fracture zone architecture and its corresponding alteration grades is not at scale and links mineralogy observed in cores with the mineralogy observed in cuttings (middle) (Genter et al., 2000).

The cation exchange capacity (CEC) value is the number of negative sites that can store cations such as K, Ca, Mg, Na, and H<sup>+</sup>. This index provides information about the amount of swelling clays that the rock contains, as the types of clays are known from XRD analyses. CEC analyses were performed on selected cutting samples from the GRT-2 well to quantify the amount of swelling clays (Figure 5.2). The measurement was performed on crushed cuttings with the standard cobaltihexamine chloride method NF X31–130 (1999). Calcimetry was performed on samples from both wells during the drilling and provided information about the relative amount of calcite, dolomite, or total carbonates in the cutting samples (Figure 5.3). More precisely, the use of a calcimeter on the crushed and dried cuttings measures the quantity of CO<sub>2</sub> released by the reaction of the carbonates with HCl. The quantity of CO<sub>2</sub> released after 1 min gives the percentage of calcite, and the quantity of CO<sub>2</sub> released after 15 min gives the percentage of total carbonates. The difference between the total carbonate quantity and the calcite quantity is the amount of dolomite. The two superimposed curves reveal that only calcite is present in the granitic sections of the GRT-1 and GRT-2 wells.

#### 5.1.4.3. Mud logging

Mud logs are instantaneous well logs, and include data on mud losses, gas content, ROP, and many standard drilling parameters. They are the first indicators of the occurrence of permeable zones in a well. In fact, they are acquired during drilling before the other logs. Mud losses provide information on the quantity of mud that is lost through a permeable fractured zone in the well, and they are recorded by the driller and are thus approximations of the fracture zone permeability. The ROP, which provides information on rock softness, has an average value of 3 m/h in the massive granitic Soultz-sous-Forêts basement, indicating a hard granite; values higher than 5 m/h indicate that the granite is fractured and/or altered (Figure 5.2) (Baujard et al., 2017b). In the GRT-2 borehole, especially in the granitic basement, the ROP is very high, with values of approximately 9–10 m/h, due to the hydrothermal alteration that makes the granite easier to drill (Baujard et al., 2017b).

#### 5.1.4.4. Structural analysis from caliper data

The acoustic image log (UBI) (Figure 5.5b) enables the identification of natural and induced fractures as well as their geometries and the determination of the in situ principal horizontal stress orientation. In both wells, GRT-1 and GRT-2, the structural information on natural fractures was derived from the acoustic image log (Vidal et al., 2017). The dip, dip direction, and fracture density were calculated. The GRT-2 well is inclined and crosscuts many fractures, with large cave zones in its deepest part. Stick–slip processes occurred, leading to poor data quality in some zones and the complete absence of data acquisition in the deepest part of the well between 2800 and 3196 m MD (2409–2707 m MD) in the worst case (Vidal et al., 2017). In this study, an additional structural information was derived from the caliper log, which was associated with an orientation system (Figure 5.5a), to complete the structural dataset. A new method was then developed for locating, measuring and orienting the geometry of first-order natural fractures based on a standard tool. The caliper tool measures 6 radii that are spaced approximately 60° from each other in the borehole (Figure 5.5a). In an inclined well like GRT-2, the caliper data must be corrected; in fact, the measured radii are skewed, because the center of the tool is not centered in the borehole. Due to this sampling bias, the radii corresponding to the lower portion of the borehole wall are shorter, and the radii corresponding to the upper portion of the borehole wall are longer. This discrepancy causes enlargements in radii that are due to the sampling bias rather than to natural fractures. Moreover, the tool rotates during the acquisition, and therefore, radius measurements also need to be reoriented. Therefore, calculations and corrections such as centering and data orientation were applied to the caliper data to identify enlargements in the radius due to natural fracture occurrences in the caliper radii curves. More precisely, the centering process was performed by geometrically shifting the caliper tool center to the center of the borehole, and then, the caliper arm lengths were recalculated, thereby avoiding the effects of gravity in an inclined borehole. In addition, the azimuthal positions of the measured radii were calculated using the azimuthal position of the first arm followed by extrapolation to the other arms, as the arms are spaced by approximately 60°. This calculation was performed to avoid artifacts resulting from rotation of the tool in the borehole during data acquisition and enabled plotting of the oriented caliper data with depth to be able to calculate the fracture dip and dip direction. Then, fractures were picked on the corrected caliper log to calculate their dip and dip directions (Figure 5.5). Radius anomalies visible in the six non-oriented curves (Figure 5.5a, left) were identified and then placed at the same depth on the oriented caliper log (Figure 5.5a, right) to fit a sinusoid that represents the fracture based on several identified radius anomalies.

#### 5.1.4.5. Geophysical logs

Once a permeable zone was detected in the mud logs, the geophysical logs' responses corresponding to that zone were also studied (Figure 5.2). The geophysical logs enabled the identification of open permeable fractures at the borehole scale and in the best cases assisted in characterizing the flow contribution of the fracture.

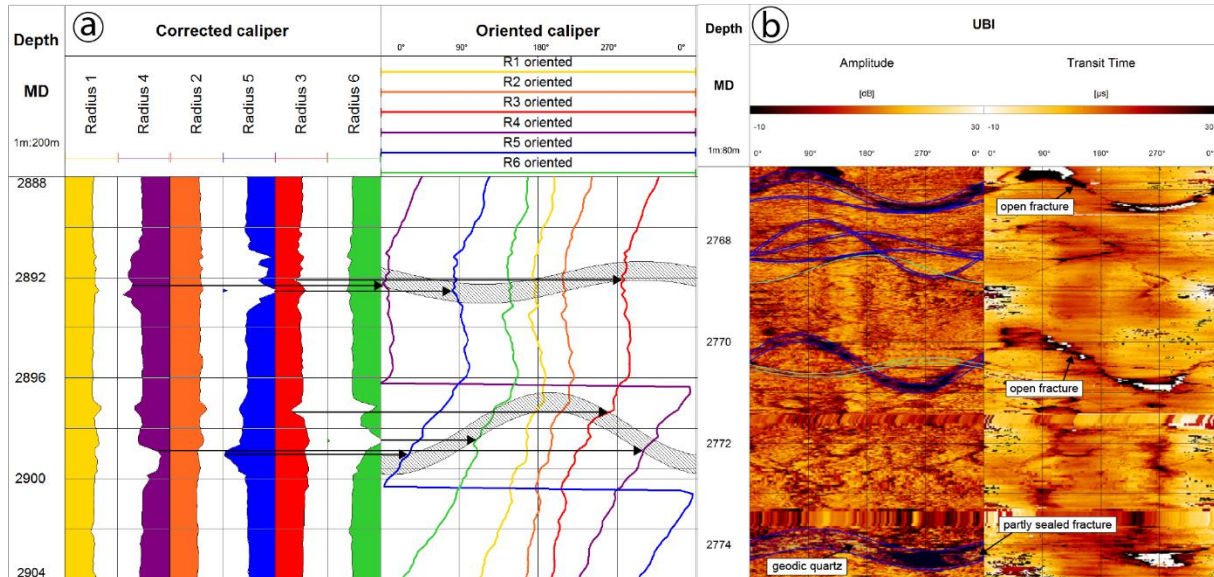


Figure 5.5: Identification of fractures from geophysical logs in the GRT-2 well. a) Major permeable fractures identified at 2900 m MD in the caliper log. The black arrows indicate the cave visible in the hole radii (left) in the oriented caliper log (right) to fit a sinusoid with at least three points. b) Acoustic image log with visible sinusoids representing natural fractures, identified and interpreted from Vidal et al., (2017).

More precisely, negative temperature anomalies reveal permeable fractures that have been cooled during the drilling (Vidal et al., 2017), and positive anomalies are indicators of hot geothermal fluid circulation through a permeable fracture zone. The gamma ray (GR) log measures natural radioactivity (uranium, potassium, and thorium), and aids in interpretations of lithology and rock composition. In the altered crystalline basement, negative GR peaks in the lower positive domain can reflect quartz veins in illitized host rock (Genter et al., 2000). In the studied context, GR data are an indicator of hydrothermal alteration and thus provide information regarding paleopermeability. The porosity log (NPHI) represents measurements of the formation porosity by filling pores with hydrogen and can thus be highly influenced by clay and fluids. Porosity logs do not provide information on permeability but nevertheless provide a global signal for fractured zones to the extent that they are porous and contain clays and fluids. A density log (RHOB) is calculated from nuclear measurements emitted from a chemical source ( $Ce^{137}$  and  $Co^{60}$ ). A negative peak in a density curve could be due to clays and thus reveal alteration associated with a fracture zone, whereas positive peaks are associated with high-density minerals or a change in lithology.

#### 5.1.4.6. Resistivity log

A resistivity log is controlled by the electrical conductivity of the fluid contained in the rock porosity and by the electrical properties of the rock. Resistivity decreases in formations containing water and is even lower for conductive fluids that contain salts, such as brines. Similarly, resistivity is low for clay minerals, pyrite, and hematite, which are conductive

minerals. Laterologs and focused resistivity arrays are common data acquisition tools for hydrocarbon wells carried out in sedimentary formations to find caprock or permeable zones containing oil or gas and to evaluate hydrocarbon saturation (Serra, 1984). It is not possible to use the same petrophysical parameters to directly interpret laterolog resistivity in granite environments, because the contributions of matrix and fracture conductivities can vary by several orders of magnitudes among unaltered and altered granite zones and areas with different clay contents and fracture densities, whether or not sealed. Resistivity was measured with five electrode configurations, yielding five apparent resistivity values (RLA1–5) (Schlumberger, 2018). These configurations are sensitive to different distances beyond the borehole wall. The shallowest resistivity (RLA1) reflects the average resistivity mainly of the borehole mud, and the deepest resistivity (RLA5) reflects the average resistivity of the formation. Some positive peaks in the GR curve can be directly linked to low resistivity values, such as at 2560 m MD [2220 m true vertical depth (TVD)] and 2830 m MD (2433 m TVD) (Figure 5.7), and thus reflect clay properties. To convert apparent resistivity into “true” formation resistivity, borehole caliper data, mud conductivity data, data from several electrode configurations (Schlumberger, 2018), and other parameters have to be combined through an inversion procedure. Strictly speaking, petrophysical relationships should be applied to the inverted resistivity. Nevertheless, apparent resistivity behavior reflects an average of the formation properties except in places with sharp geometrical variations, such as those close to large fractures (Figure 5.2, curves RLA1–5). In the presented work, only trends in the apparent resistivity are compared with the other logs and models. See the detailed discussion later in this paper.

### 5.1.5. Results

#### 5.1.5.1. Mineralogical log

The alteration minerals' distribution in the GRT-2 granitic section (2490–3196 mMD, 2165–2707 m TVD) is characterized by secondary geodic quartz that is well expressed from the top of the granite at 2490 m MD down to 2878 m MD and particularly in two zones at 2950 m MD (2527 m TVD) and 3052 m MD (2604 m TVD) (Figure 5.2). Anhydrite precipitation is visible at the top of the basement to 2653 m MD (2292 m TVD) and from 2737 to 2875 m MD (2358–2469 m TVD) but is not visible in the deepest part of the well. Chlorite is ubiquitous in the GRT-2 borehole but is more concentrated in three zones: 2590–2734 m MD (2243–2356 m TVD), 2872–2935 m MD (2466–2515 m TVD), and 3073–3196 m MD (2620–2707 m TVD). The first and second chlorite zones contain relics of primary biotite that are partially chloritised, precisely corresponding to the HMOD facies, and are thus correlated with hydrothermal alteration. The third chlorite zone contains chloritised biotite that is clearly correlated with the GRAN facies, reflecting propylitic alteration. The illite content is very high at the top of the granitic basement and decreases down to the top of the unaltered granite (3060 m MD, 2610 m TVD), wherein there is no significant trace of illitic material in the cuttings. The oxidation is important in the top of the granitic basement, defining the RED facies unit, but decreases down to 2986 m MD (2955 m TVD). Calcite was measured in high quantities, with especially high values of 40% at 3052 m MD (2604 m TVD), 20% at 3000 m MD (2565 m TVD), and approximately 10% at 2570 and 3052 m MD (2228 and 2604 m TVD) (Figure 5.2). The secondary mineralogy of the GRT-1 well is characterized by globally less chlorite and more hematite than that of the GRT-2 well (Figure 5.3). The alteration grade is also globally higher in the GRT-1 well than in the GRT-2 well; in fact, in the GRT-1 well, the alteration grade HEXT is observed from 2325 to 2350 m MD (2310–2335 m TVD), as evidenced by large amounts of illite and anhydrite.

Secondary geodic quartz is only observed in one major fracture zone from 2357 to 2365 m MD (2341–2349 m TVD) and in one minor zone at 2325 m MD (2310 m TVD). The granitic propylitic basement (GRAN) observed in the GRT-2 well corresponds to a massive and unaltered crystalline rock mass in the deepest part, down to 3196 m MD (Figure 5.2). Above, hydrothermal alteration and a fracture system are highly developed. Fourteen facies zones grouped in three major thicker crystalline units were identified. At the top of the granitic basement, the first unit consists of reddish granite RED from 2479 to 2533 m MD (2155–2198 m TVD) and is characterized by a large amount of hematite and illitic phases. From 2533 to 3060 m MD (2198–2610 m TVD), the second unit is a large fractured zone that contains alteration minerals, such as illitic minerals, geodic quartz, and anhydrite. Four major fracture zones interpreted as quartz veins were delimited, ranging from 3 to 20 m in apparent thickness (at 2533, 2770, 2950, and 3052 m MD, i.e., 2198, 2885, 2527, and 2604 m TVD). These quartz veins contain large amounts of geodic quartz as well as calcite, and are strongly supported by local sharp temperature anomalies, negative GR anomalies, positive neutron porosity anomalies, and occasional low bulk density peaks. Three alteration grades were also observed in the second unit: HLOW, HMOD, and HHIG. The third unit, in the deepest part of the well from 3060 to 3196 m MD (2610–2707 m TVD), consists of a GRAN zone and is characterized by very little hydrothermal alteration and a large amount of chlorite, reflecting the primary pervasive alteration of biotite. The boundary between the fracture zone unit and the deep unaltered granite unit in GRT-2 is characterized by a major permeable quartz zone (Figure 5.2, 3052 m MD). The granitic section in the GRT-1 well (2213–2582 m MD, 2200–2565 m TVD) is composed of oxidized propylitic granite (GRAN\_OX) in the deepest part (2516–2582 m MD; 2500–2565 m TVD) and HLOW granite from 2409 to 2516 m MD (2393–2500 m TVD), which is the lowest alteration grade found in the GRT-1 granite (Figure 5.3). Above, as in the GRT-2 well, a hydrothermally altered and fractured zone comprises four distinct facies zones. At the top of the granitic basement, the reddish granite extends from 2214 to 2274 m MD (2200–2260 m TVD) and contains a large amount of hematite. From 2274 to 2330 m MD (2260–2315 m TVD), a moderate illitic mineral content and sparse geodic quartz define the HHIG facies. A large fracture zone extends from 2330 to 2406 m MD (2315–2390 m TVD) and contains two major quartz veins with geodic quartz from 2366 to 2368 m MD (2350–2352 m TVD) and at 2327 m MD (2312 m TVD). The major quartz vein at 2366 m MD is strongly supported by a negative temperature anomaly, high mud losses, low GR anomaly, high porosity, and low density (Figure 5.6). Surrounding the quartz veins, the HEXT facies are observed from 2330 to 2348 m MD (2315–2333 m TVD), and is characterized by large amounts of anhydrite, illitic minerals, and geodic quartz. From 2348 to 2409 m MD (2333–2393 m TVD), the HHIG facies are characterized by the presence of a large amount of chlorite, small amount of illite, and no geodic quartz.

#### 5.1.5.2. Structural log

##### *Fracture picking*

Structural analysis has already been performed for most of the GRT-1 and GRT-2 wells but is lacking for the deepest part of the GRT-2 well (Vidal et al., 2017). However, new oriented caliper logs have been collected in some sections of the GRT-2 well where the structural analysis was not carried out (Figure 5.6). We then focused on a structural fracture analysis of the GRT-2 well based on comparing only the acoustic image and oriented caliper logs.

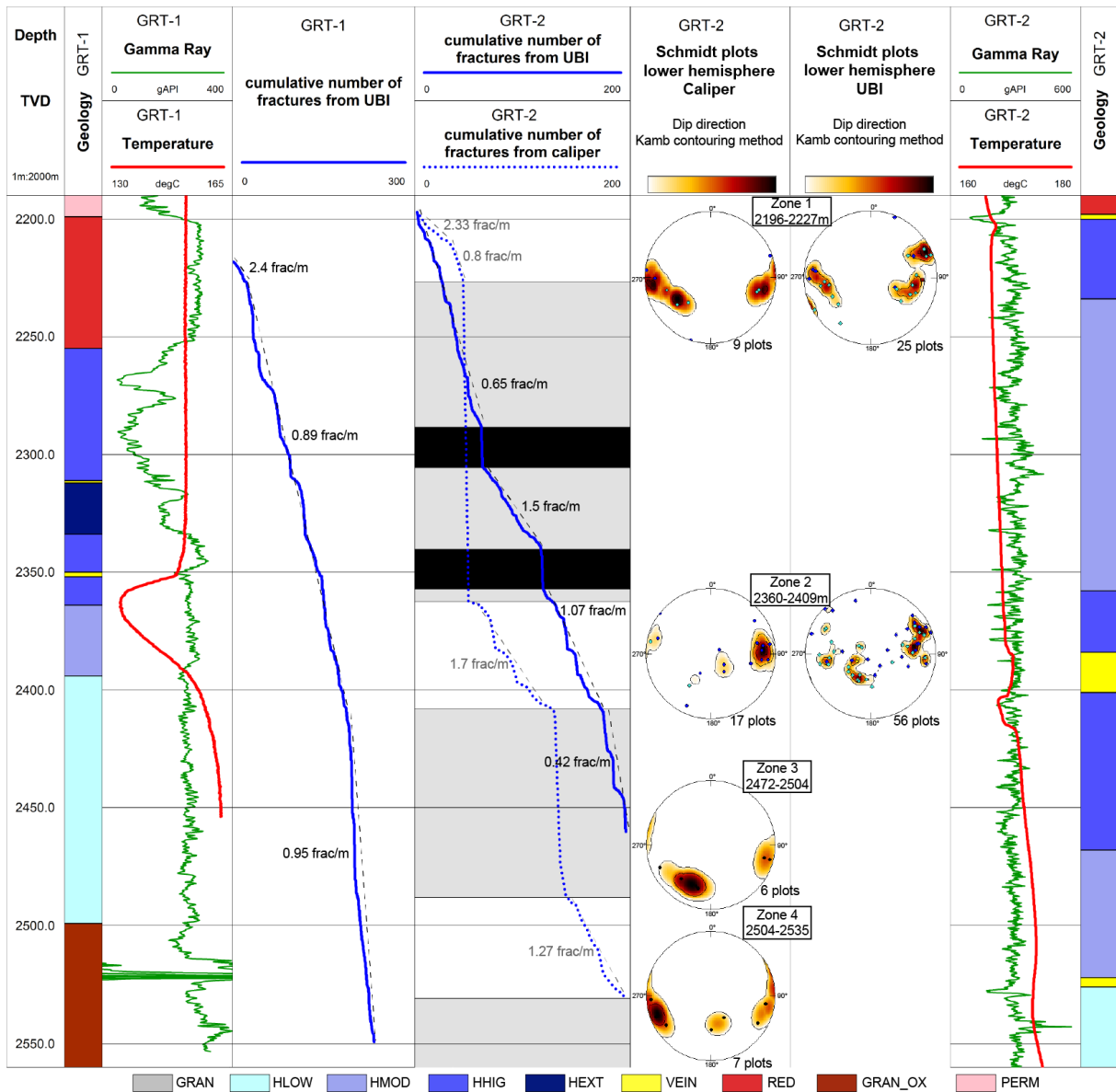


Figure 5.6: Wells GRT-1 and GRT-2 with geology, temperature, and gamma ray data at the same depth. The cumulative number of fractures is from acoustic images for both wells and from the caliper data for the GRT-2 well. The fracture analysis was performed using stereographic diagrams, specifically, Schmidt lower hemisphere plots realized with the Kamb method; 2 specifies the initial contouring interval and 3 specifies the number of standard deviations that define the expected count for a uniform distribution. The stereographic diagrams were constructed based on both caliper and acoustic image log data for four major fracture zones in the granitic basement of the GRT-2 well. The black areas represent zones where UBI data was not acquired, and the gray areas represent zones where fractures from the caliper log were not computed. The UBI fracture datasets are from (Vidal et al., 2016a). The facies are as follows: GRAN: granite, HLOW: low hydrothermal alteration grade, HMOD: moderate alteration grade, HHIG: high alteration grade, HEXT: extreme hydrothermal alteration, VEIN: quartz vein, GRAN\_OX: oxidized granite, RED: reddish granite, PERM: Permian sandstone.

Four zones were studied. In the two first zones located at 2531 and at 2740 m MD (2196, 2360 m TVD) (Table 5.2), caliper results can be compared with UBI observations (Figure 5.6). In zones 1 and 2, 26 fractures were observed in the caliper data, whereas 81 were found in the acoustic images (Figure 5.6). Two major natural fractures were observed in zone 3, at 2895 m MD (2482 m TVD) with a dip direction of N117°E and a dip of 84° and at 2897 m MD (2486 m TVD) with a dip direction of N302°E and a dip of 70° (Figure 5.5). Thus, from this analysis, the corrected caliper data enabled us to identify approximately 34% of the pre-

existing fractures identified with the acoustic image log (Table 5.2). Two sets of fractures dipping towards ca. N50°E in zone 3 and ca. N80°E in zone 4 (with an accuracy of approximately 10°) were identified in the caliper data (Figure 5.6). The fracture picking process was applied to the caliper logs of the two deepest zones in GRT-2, where acoustic image logs were not available (Figure 5.6). Zone 3, between 2880 and 2920 m MD (2472–2504 m TVD), and zone 4, between 2920 and 2960 m MD (2504–2535 m TVD), were selected for structural analysis. In zone 3, six major fractures with a mean dip direction of N52°E and a mean dip of 67° were found (Figure 5.6). In zone 4, seven major fractures with a mean dip direction of N80°E and a mean dip of 87° were found (Figure 5.6).

GRT-2	corrected caliper			acoustic image logs			accuracy	
	density (fract/m)	dip direction		density (fract/m)	dip direction		dip direction	dip
		set 1	set 2		set 1	set 2		
<b>ZONE 1:</b> 38 m (2196-2227m TVD)	0.2	N274°E	N61°E	0.6	N263°E	N74°E	±11°	±5°
<b>ZONE 2:</b> 60 m (2360-2409mTVD)	0.3	N272°E	N70°E	0.9	N265°E	N81°E	±9°	±13°
<b>ZONE 3:</b> 40 m (2472-2504m TVD)	0.15	N52°E		no data				
<b>ZONE 4:</b> 40 m (2504-2535m TVD)	0.17	N80°E		no data			±10	±9°

Table 5.2: Structural analysis of the GRT-2 granitic basement with the caliper. Comparison of the structural analyses and their accuracies as calculated from the caliper and acoustic image logs (zones 1 and 2). Structural analysis from caliper data only (zones 3 and 4).

The two fractures sets in zones 3 and 4 were also found in zones 1 and 2. Furthermore, zone 3 shows significant caves (borehole enlargements) located at approximately 2900 m MD (2488 m TVD), and zone 4, which is located around a quartz zone at 2950 m MD (2527 m TVD), features a negative thermal anomaly (Figure 5.2). The fracture densities in zones 3 and 4 were slightly lower than those in zones 1 and 2. Based on the lower density values, this structural analysis showed that fewer fractures were identified when only the corrected caliper data were used (Table 5.2). However, the two dominant directional fractures sets (east and west) were observed by the caliper and UBI methods. Despite the low density of fractures identified with the corrected caliper data, the major fractures and their structural information for handling the well production were determined. This caliper correction approach enables us to obtain geometrical information from an inclined well and involves lower costs and risks than the collection of acoustic image logs.

*Fracture density*

The fracture densities in the GRT-2 well were compared using the cumulative fracture densities calculated from the acoustic image logs by (Vidal et al., 2016a) and those from the previously corrected caliper log (Figure 5.6). The cumulative fracture density was calculated from the caliper for separated sections in the open-hole section, and the chosen delimitations are inflection points. Moreover, because the sections chosen for this study are not the same as those chosen in Vidal et al., (2016), they cannot be compared. To compare the caliper and UBI cumulative fracture densities for the GRT-2 well, even though the fractures were not sampled throughout the entire open-hole section from the caliper data, the cumulative fracture density calculated with the caliper log was calibrated with the total fracture number observed in the acoustic image log in the GRT-2 well. We observe that the cumulative fracture density from the caliper in GRT-2 seems to follow the same trend as the cumulative fracture density calculated from the acoustic images.

### 5.1.5.3. Electrical logs

#### *Petrophysical observations*

The following discussion is based on the apparent resistivity curve RLA5. As explained in “Resistivity log” section in this work, we did not invert resistivity logs to correct for borehole and mud effects; we used RLA5, as this measurement corresponds to the greatest depth in the surrounding formation and is surely the most representative of the true resistivity of the formation. The other resistivity measurements, RLA1–4, are also shown in Figure 5.2. Although RLA1–4 represent the resistivity closer to the borehole, we show them in the figure for reference, but the work in this article focuses on the RLA5 curve only. Using apparent resistivity implies that geometrical structures, such as a dipping plane of constant resistivity crossing the well, are not interpreted as 2D/3D structures but as zones where the equivalent homogeneous resistivity varies (i.e., a 1D approach). This neglect of geometrical effects is valid far from contacts if the bedding thickness is larger than the sensitive zone of the electrodes’ configuration. Furthermore, this technique is qualitatively valid as long as the geometrical effect does not dominate the electrical response or is almost constant in the studied interval. In the latter case, the logarithm of apparent resistivity is only shifted by a constant value from the true formation resistivity. Finally, note that the apparent resistivity curves show a smaller resistivity range than the true resistivity curves. For all these reasons, we limit our interpretations regarding the trends in the average resistivity data. Inversion of the apparent resistivity curve to true formation resistivity is outside the scope of the data presented in this article. This work is supported by a constant drilling diameter in the studied depth interval. Petrophysical interpretations from the RLA5 apparent resistivity curve behavior and values are made in terms of alteration facies. Indeed, the hydrothermal alteration grades and resistivity seem to be clearly correlated. At the first order, the four permeable quartz veins observed in the GRT-2 well from cuttings yield resistivity responses between 0.2 and 60 ohm.m, which clearly stand out on the electrical log. In terms of facies, the GRAN facies shows a resistivity response of approximately 3000 ohm.m, the HMOD grade shows a resistivity response of approximately 400 ohm.m, and the HHIG grade shows a resistivity response of approximately 60 ohm.m (Figure 5.2). The facies transitions are clearly visible in the resistivity curves, such as at 2740 and 2875 m MD between the HMOD and HHIG grades (Figure 5.2, RLA5). The resistivity log trend is well correlated with the chlorite classes described in “Resistivity log” section, which were scaled from class one (smaller amount) to class three (larger amount) according to the relative amount of chlorite observed in the cuttings. The chlorite class three corresponds to high resistivity values between 200 and 20,000 ohm.m (between 2600 and 2750 m MD for instance), whereas chlorite class one corresponds to lower resistivity values between 20 and 200 ohm.m (Figure 5.2).

#### *Synthetic resistivity*

*Note from the authors: a correction was added to the publication of this article concerning this section. In fact, we used  $B(25^{\circ}C) = 5.19 * 10^{-8} m^2 s^{-1} V^{-1}$  which corresponds to the Na+ ions mobility in bulk water. Instead, as it has been recently published, we should have used a mobility value accounting for the mobility of the counterions in the Stern layer and in the diffuse layer. Following Eq. 2 in Ghorbani et al., (2018), the mobility can be expressed as  $B = \beta_{(+)}(1 - f) + f * \beta_{(+)}^s$ . The value of the mobility of the counterions in the diffuse layer  $\beta_{(+)}$  is the same as in the bulk pore water. The mobility of the counterions in the Stern layer is smaller*

$(\beta_{(+)}^s(\text{Na}^+, 25^\circ\text{C}) = 1.6 * 10^{-9} \text{m}^2 \text{s}^{-1} \text{V}^{-1})$  and a typical value is  $f = 0.95$  (Revil et al., 2017). The correct value is then  $B(25^\circ\text{C}) = 4.2 * 10^{-9} \text{m}^2 \text{s}^{-1} \text{V}^{-1}$ .

*This value is 10 times smaller than the value used in the calculation of the surface conductivity in the article, hence the clay contribution to the resistivity is ten times overestimated in the article. It has several consequences discussed hereafter. Using the wrong value of  $B$ , we evaluated the contribution of the surface conductivity to be of the same order than the volume conductivity (see Figure 5.7a). Then we used Eq. 6 to optimize the weighting of each term through two coefficients (see Figure 5.7b). The optimization of a synthetic log considering only the Archie's term (coef2 = 0) yields a coefficient acting as a geometrical factor, i.e. a rough approach to convert the formation resistivity to the measured (apparent) resistivity RLA5.*

*When we observed which could be the best weighting coefficients (Figure 5.7b), the minimum RMS is obtained when the clay term is emphasized 10 times (coef1 = coef2 with wrong  $B$  value) or 33 times (coef1 = 0.15 and coef2 = 0.56), which is far away from an acceptable range from the nowadays well established model (Eq. 1). The reader should consider the following changes that were added in the text in italic letters.*

A synthetic resistivity log based on observed physical measurements collected in the well was recalculated to study the contribution of electrolytic conductivity in pores (containing brine) and surface conduction (characterized by the CEC value) due to clay content. The resistivity formulas used are derived from the classic Archie, (1942) and Waxman and Smits, (1968) models. More recent and complex models for computing the electrical conductivities of clay rocks have been published (Comparon, 2005). From this overview, models based on different effective media (De Lima and Sharma, 1990), varying in terms of the pore geometries, petrophysics, and surface properties of particles, are of high interest. The electrical conductivity is the inverse of the resistivity  $\sigma = 1/\text{Res}$  (in  $\text{S/m}$ ) and can be calculated as follows:

$$\sigma = \frac{\sigma_f}{F} + \frac{BQV}{F} \quad (1)$$

$$F = \phi^{-m} \quad \text{with } m = 2.2 \quad (2)$$

$$B = B_0 * [1 - 0.6 * \exp\left(-\frac{\sigma_f}{0.013}\right)] \quad (3)$$

$$Qv = \rho_g * \left(\frac{1-\phi}{\phi}\right) * \text{CEC} \quad (4)$$

In Eq. (1), the first term,  $\frac{\sigma_f}{F}$ , corresponds to the Archie law that considers only the contribution of the water that fills the pore space (Archie, 1942).  $\sigma_f$  is the conductivity of the geothermal water contained in the pore space in  $\text{S/m}$ ,  $F$  is the formation factor, which depends on the rock porosity  $\phi$ , and  $m$  is the cementation factor (usually varying between 2 and 3), as shown in Eq. (2).

The second term,  $\frac{BQV}{F}$ , corresponds to the surface conduction introduced in the Waxman and Smits model that considers the clays contribution (Waxman and Smits, 1968; Revil et al., 1998).  $B$  is the ionic mobility of the compensating ions.  $\text{NaCl}$  dominates the brine ionic species, and we used the ionic mobility of sodium by considering that the excess of charges is negative

and that only Na compensates the charge movement due to the flow of electric current.  $Q_V$  depends on rock porosity  $\phi$ , grain density  $\rho_g$ , and the CEC value in meq/100 g (see Eq. 4).

CEC measurements were performed on several cutting samples in which the clay contents were characterized by XRD and were performed on samples from several fracture zones and from the several granitic facies (Figure 5.2). In the presence of clays, the CEC values influence the resistivity through Eq. (4). In total, 8 CEC laboratory analyses were conducted for the granitic basement of the GRT-2 well (Bouchet et al., 2017). The CEC values were found to be inversely proportional to the chlorite quantity. An extrapolated CEC synthetic log was calculated from 2500 to 2900 m MD based on the chlorite classes (Figure 5.2), with values of 4.3 meq/100 g for class one, 3.5 meq/100 g for class two, and 1.9 meq/100 g for class three. Indeed, the CEC values vary between the mineralogical chlorite endmember and the illite endmember (corresponding to higher and lower CEC values, respectively). The ionic mobility is affected by temperature, and consequently, the conductivity of the pore water is also sensitive to temperature. A conductivity increase of approximately 2.3%/°C is widely accepted in the literature. At 1 bar, this empirical pattern is reliable up to temperatures reaching 85 °C. We used the variation trend from Eq. (5) (Revil et al., 1998) to calculate the temperature effect at higher temperatures, because the brine remains liquid under the pressure conditions in the Rittershoffen well:

$$B_0(T) \approx B(25^\circ\text{C}) * [1 + \nu_f * (T - 25)] \text{ and } \sigma_f(T) \approx \sigma_f(25^\circ\text{C}) * [1 + \nu_f * (T - 25)] \quad (5)$$

with  $\nu_f \approx 0.023^\circ\text{C}^{-1}$  and  $B(25^\circ\text{C}) = 4.2 * 10^{-9} \text{m}^2 \text{s}^{-1} \text{V}^{-1}$

In the investigated depth section at Rittershoffen, the temperature ranges between 160 and 180 °C (Figure 5.2). A temperature variation of 20 °C means a resistivity variation of 40 % based on Eq. (5). This variation is moderate compared to the observed range in resistivity values of 0.2 to 10,000 ohm.m (Figure 5.7), and temperature is not the main driver of the resistivity changes observed here.

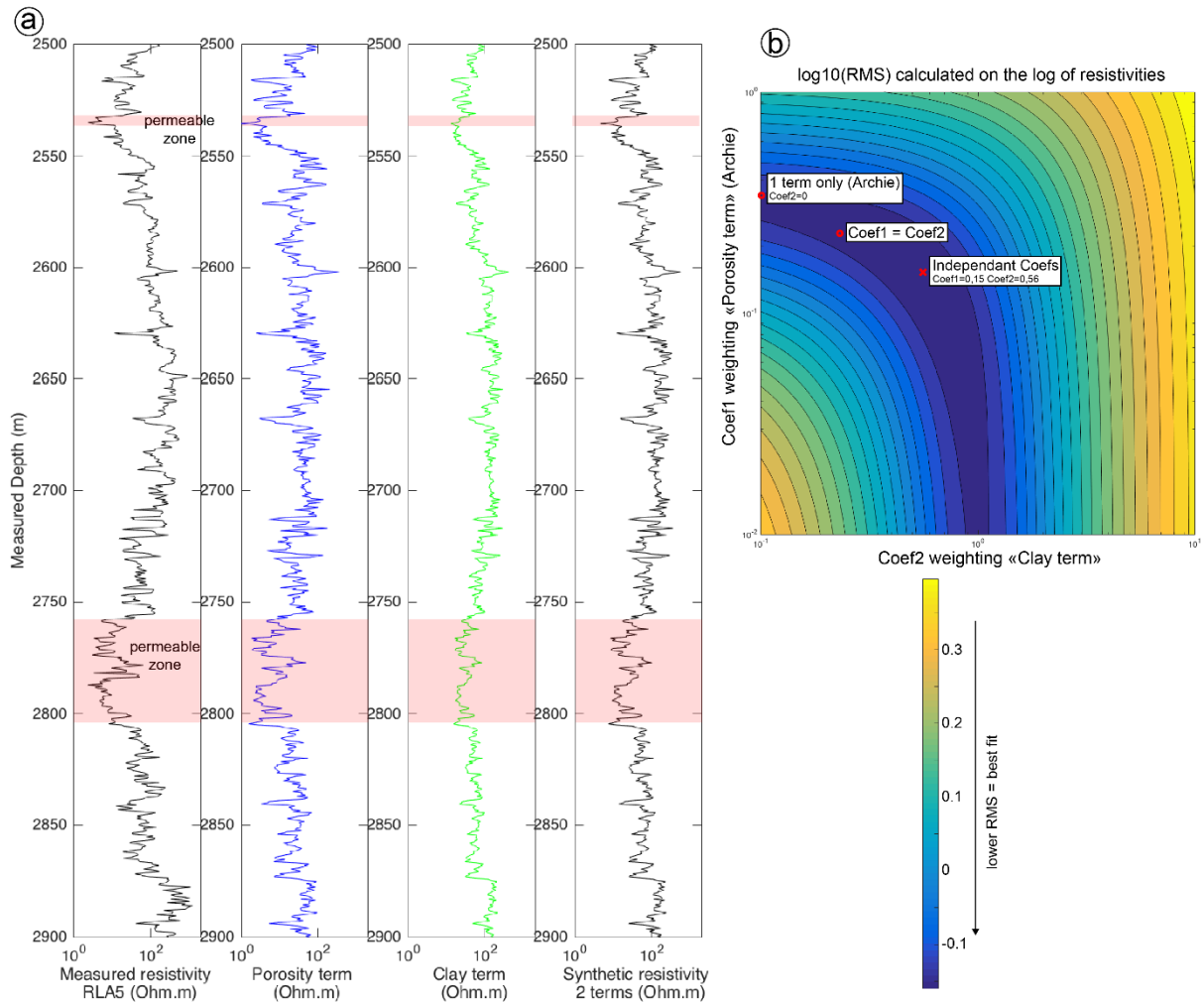


Figure 5.7: Comparison of the measured and calculated electrical logs. a) From left to right: measured apparent resistivity, contribution of the porosity to the calculated resistivity (Archie term), contribution of the clays to the calculated resistivity, and recalculated synthetic resistivity. Red zones indicate permeable fracture zones. b) Consequences of the independent weighting of the Archie term (y-axis) and the clay term (x-axis) for the fit of the resistivity model [RMS in log(ohm m)]. The optimal solution includes two independent coefficients (red cross) and produces the lowest RMS value (dark blue). After correction, the “clay term” resistivity log is in fact 10 times higher (and the contribution to the conductivity is 10 times lower).

The density log (RHOZ) is employed as grain density  $\rho_g$ , and the mean density value measured in the GRT-2 well is 2650 kg/m<sup>3</sup> (Figure 5.2). The cementation factor  $m$  is taken to be 2.2 (Belghoul, 2007). The rock porosity  $\phi$  is taken from the neutron porosity log (NPHI), and it, therefore varies with depth up to 17 %. The fluid conductivity measured at 25 °C is 13.7 S/m in the GRT-1 well, and the fluid salinity is approximately 100 g/L NaCl equivalent in both the GRT-1 and GRT-2 wells (Sanjuan et al., 2016). Thus, based on those values and an extrapolation of a temperature correction derived from Eq. (5), the fluid conductivity is fixed at 30 S/m. Using the model in Eq. (1), we calculated a synthetic resistivity log by weighting the two terms through the coefficients  $coef1$  and  $coef2$  defined in Eq. (6):

$$\sigma = coef_1 * \frac{\sigma_f}{F} + coef_2 * \frac{BQV}{F} \quad (6)$$

$Coef1$  controls the contribution of NPHI through the Archie law term (Figure 5.7a, porosity term).  $Coef2$  controls the weight of the clay contribution based on the extrapolated CEC log and RHOZ (Figure 5.7a, clay term). Synthetic logs were also adjusted using  $coef1$  only (i.e.,

coef2 = 0) to fit the measured resistivity log but could not reach a fit that was as good as that with both terms. We considered the optimization process using the resistivity or the logarithm of resistivity, various depth intervals (> 50 m), and the RLA3–5 data, which provided almost the same results. Hence, only results using RLA5 are presented here. Figure 5.7a shows the logs from 2500 to 2900 m MD used in the calculation, which are, from left to right, the RLA5 data, the porosity term (through the Archie law), the clay term, and finally the sum of these two terms based on Eq. (6), which is the synthetic log that best fits the RLA5 data. A satisfactory model means minimizing the root mean square (RMS) calculated according to Eq. (7) (Figure 5.7b):

$$RMS = \sqrt{\sum(\log(Rho_{calc}) - \log(Rho_{meas}))^2 / N} \quad (7)$$

where  $Rho_{calc}$  is the synthetic resistivity,  $Rho_{meas}$  is the measured resistivity, and  $N$  is the number of resistivity values.

Optimization is illustrated in the cross-plot in Figure 5.7b, which compares the best fits obtained with one term and with two terms. The synthetic curve modelled with two terms has a lower (better) RMS value (0.69 with independent coefficients and 0.71 log(ohm.m) with coef1 = coef2, which correspond to a factor of 2 = exp(0.7) between synthetic and field resistivity values) than the synthetic curve calculated with only the porosity term (1.3 log(ohm.m), which corresponds to a factor of 4 between synthetic and field resistivity values). Thus, a higher correlation coefficient and a lower RMS value are achieved. The resulting correlation coefficient (on the logarithm of resistivity) obtained for the synthetic resistivity calculated with two coefficients is 85 %, compared to 82 % for coef1 = coef2 and 79 % when using only the porosity term (Archie, 1942). Note that optimization with two coefficients decreases the relative weight of the Archie term (related to porosity and water conductivity) and increases the relative weight of the term related to the clay contribution (the respective weights are 0.15 and 0.50). Therefore, when using only the clay term, good fit results are also obtained (Figure 5.7b). *After correction, considering the factor 10 for B, the conclusion is that the clay term should be inappropriately emphasized to have an effective contribution. Then, the surface conductivity plays a negligible role here.*

The permeable fractures were found to correspond to the lowest resistivity peaks, which were controlled by the brine conductivity through the “porosity term” contribution to the resistivity (Figure 5.7a). To better explain the resistivity curve trend in other locations, the clay contribution has to be considered. We will pursue this work on inverted resistivity by combining the RLA1–5 data in other wells in similar contexts and by considering petrophysical measurements on samples.

## 5.1.6. Discussion

### 5.1.6.1. Correlation between well and mud log data

The various datasets enabled characterization of the hydrothermal alteration grades and identification of permeable fracture zones in the granite. The unaltered granite zone is characterized by a steady GR value of approximately 260 gAPI, a neutron porosity of approximately 5 %, a steady bulk density value of approximately 2.65 g/cm<sup>3</sup>, an ROP value of approximately 7 m/h, a high resistivity value of approximately 3000 ohm.m, and a linear temperature profile (Figure 5.2). However, the altered granite (HMOD, HHIG, and HEXT) is

characterized by variable GR values of approximately 320 gAPI, variable ROP values ranging from 4 to 10 m/h, low resistivity values between 60 and 500 ohm m, and calcite contents higher than 5 %. Furthermore, alteration minerals such as illite are abundant, and euhedral quartz is regularly present (Figure 5.2 and 5.8). Permeable fracture zones are associated with the VEIN facies.

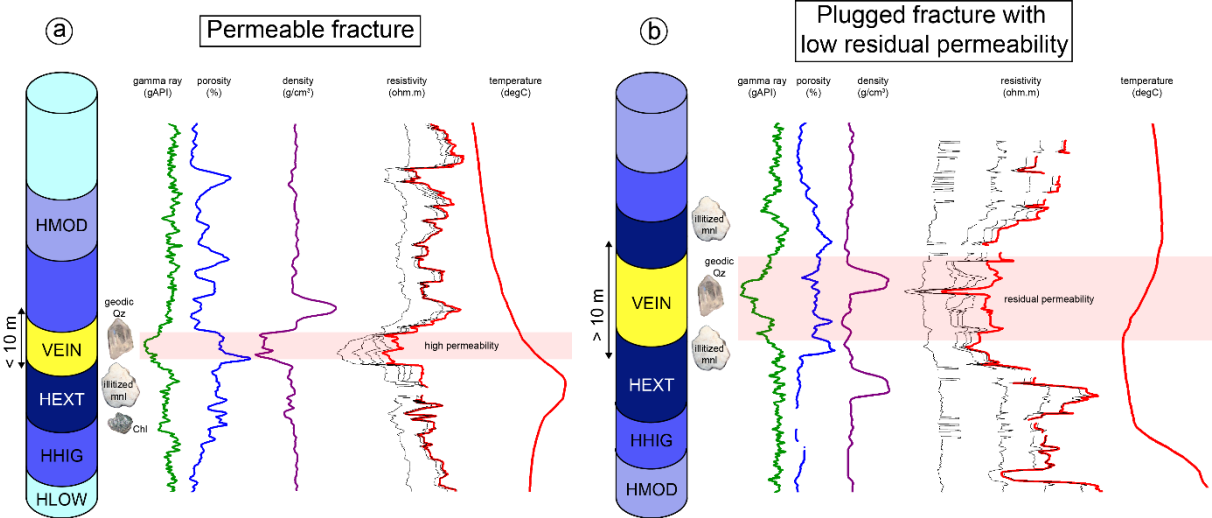


Figure 5.8: Conceptual model of fracture zones and their geophysical and geological signatures linked to hydrothermal alteration grades in the granitic basement of Rittersshoffen. Red zones represent the depth extent of permeable fracture zones. a) Specific geological and geophysical signatures of a permeable fracture. b) Specific geological and geophysical signatures of a plugged fracture with low residual permeability. The geophysical log anomalies are true anomalies that were found in the GRT-2 well as well as the quartz, illite, and chlorite samples. The hydrothermal alteration facies are as follows: HLOW: low hydrothermal alteration grade, HMOD: moderate alteration grade, HHIG: high alteration grade, HEXT: extreme hydrothermal alteration, and VEIN: quartz vein.

An abundance of euhedral quartz is the indicator of past or present hydrothermal circulation. Moreover, temperature anomalies were found to be systematically correlated with the quartz zones (Figure 5.2 and 5.6). For example, from 2770 to 2791 m MD in GRT-2 (Figure 5.2, 2385–2400 m MD), the fracture zone is characterized by a large amount of illite and increasing mud losses from 10 to 13 m<sup>3</sup>/h. This quartz zone is also associated with temperature anomalies, shifting from a positive anomaly at 2772 m MD to a negative anomaly at 2794 m MD (Figure 5.2).

5.1.6.2. Fracture zone detected from well and mud log data

From cutting observations, four quartz zones were found in the GRT-2 well at 2530, 2770–2790, 2950, and 3052 m MD (Figure 5.2), and two were found in the GRT-1 well at 2326 m and 2365 m MD (2311–2349 m TVD) (Figure 5.3). These permeable fracture zones were previously observed by Vidal et al., (2016) in UBI logs. They also match the occurrence of small crystallites of illite and illite/smectite-mixed layers (Vidal et al., 2018). To complete the structural information on fractures, this study attempted to identify fractures in the caliper log in the deepest part of the GRT-2 well (where no acoustic images had been acquired). The resistivity signature was found to correlate with the occurrence of quartz veins in the GRT-2 well (Figure 5.2). For example, at 3052 m MD, the quartz vein extent corresponds to the resistivity anomaly extent in terms of depth (Figure 5.2 and 5.7). This zone also exhibits intense argillization and a high calcite content, which suggest past massive hydrothermal alteration associated with fracture filling. This fracture zone is an interface between the altered and fractured granite and the unaltered granite (Figure 5.2). The fractured and altered granite could

represent the hanging wall of a fault, and the unaltered granite could represent the foot wall. Thus, the interface between them could be interpreted as the local normal fault accommodating the majority of displacement in Rittershoffen, which is the initial geothermal target. This observation is similar to the occurrence of a major permeable fracture zone observed in well GRT-1 from 2326 m to 2365 m MD (2311–2349 m TVD) (Figure 5.3). Due to the geological contrast between the two distinct sections, this interface is assumed to be the trace of a local normal fault with a high degree of natural permeability. A new interpretation of the seismic data with consideration of the results at the well scale could help support this idea.

#### 5.1.6.3. Resistivity signature of permeable fracture zones

The several types of hydrothermal alteration observed in the cuttings are clearly correlated with the resistivity signature (Figure 5.2), and both porosity and clay content/type control the resistivity values, with the clay term dominating (Figure 5.7). *This sentence “with the clay term dominating” is wrong. Based on our available logging data and synthetic models, the influence of clay through the surface conductivity on the resistivity of the studied granites is negligible.* In addition, the responses of fracture zones in the granitic basement in the geophysical logs can also be very different in terms of depth extent and amplitude (Figure 5.2 and 5.8). In GRT-2, temperature anomalies are consistently linked to the occurrence of permeable fracture zones, but they can extend spatially from 3 to 24 m in depth (MD) and vary from + 2 to – 3 °C (Baujard et al., 2017a; Vidal et al., 2017). In addition, there is an evident correlation among the lengths of a temperature anomaly, the fractured zone sampled with the caliper and the resistivity anomaly zone in the electrical logs. For example, in the fracture zone at 2530 m MD, the length of the temperature anomaly, the length of the zone with an enlarged hole diameter, and the length of the resistivity anomaly zone are all approximately 3 m (Figure 5.8). The fracture zones at 2770, 2790, and 3052 m MD exhibit temperature anomaly lengths from 14 to 24 m, which are similar to the lengths of the corresponding resistivity and hole diameter anomalies. For the fracture zone at 2950 m MD, the temperature anomaly is very smooth, and the 1 °C temperature variation extends for more than 50 m in depth; thus, this anomaly is difficult to associate with the resistivity anomaly extent.

#### 5.1.6.4. Hierarchy of permeable fracture zones

A hierarchy of the major permeable fractures in terms of contribution to well productivity was established based on secondary mineralogy, structural information, and geophysical log responses (temperature and resistivity) in the GRT-2 well. The permeable fracture zone at 2770–2790 m MD (2385–2400 m TVD) is assumed to offer the greatest contribution to well productivity, because it exhibits a considerable temperature anomaly (Baujard et al., 2017a). The uppermost permeable fracture at the sediment–basement transition at 2535 m MD (2200 m TVD) presents localized and sharp geophysical anomalies that extend over less than 10 m in depth. A positive temperature anomaly in this area could indicate a hot geothermal outflow through open fractures (Vidal et al., 2017). The GR anomaly at 2535 m MD indicates spatially limited alteration zones around the open fractures. Moreover, chlorite is still observed at this depth, indicating that illitization has not yet plugged the zone. Other fracture zones, such as at 3052 m MD (2604 m TVD), present very low GR peaks, indicating that these zones have experienced more hydrothermal circulation than for the uppermost one. The deepest fracture at the transition between the altered and fractured granite and the unaltered granite at 3052 m MD presents broad extended geophysical anomalies larger than 10 m. The highest porosities and lowest densities are located at the extremities of the GR peak, and this zone

could be interpreted as an altered and porous zone around the open fracture. The large negative GR anomaly could indicate that open fractures in the core of the zone are now plugged by small crystallites of illite. Chlorite is no longer observed, and calcite is present in high proportions (40 %), as a result of long-term hydrothermal circulation leading to chlorite alteration and precipitation of minerals such as illite and calcite (Sausse et al., 1998) (Figure 5.2). Thus, the residual permeability of the fracture zone has likely been reduced by secondary mineralisation. The negative temperature anomaly could be the effect of the remnant cooling of the porous and altered zone after mud circulation during drilling. The cooling of porous zones has also been observed in other geothermal wells (Barton et al., 1995; Davatzes and Hickman, 2005; Bradford et al., 2013). In addition, the fracture zone at 2950 m MD (2527 m TVD) could also be one of the less contributive to the GRT-2 well productivity. In fact, its negative temperature anomaly has a relatively large depth extent, i.e., approximately 50 m, which could indicate a large porous and altered zone around the fracture core. The core of the fracture zone is located at precisely 2950 m MD based on the quartz VEIN facies, a negative GR peak, a higher porosity, and a lower density.

#### 5.1.7. Conclusions

The compilation of various datasets for the GRT-2 geothermal production well has yielded a detailed petrographic log and new permeability estimates, and the geophysical logs can be used to perform structural analyses. In this study on the granitic basement, the major permeable fracture zones associated with high permeabilities were identified. The precision of the cuttings with depth was found to be sufficient to identify fracture cores based on quartz veins and altered and porous zones based on the small size of illite crystallites. The caliper log was improved with geometrical corrections, which resulted in less accurate structural information on fracture zones than the analysis based on UBI data. However, this technique is promising for situations in which other geophysical logs cannot be performed. Furthermore, caliper data are cheaper to obtain and are effective for identifying significant fractures. Petrophysical laws were applied to recalculate a synthetic resistivity log for the granitic basement, which showed a very good correlation with the measured resistivity log. The electrical resistivity model from the Rittershoffen case study will be applied to previously collected and new data sets from other granite-hosted geothermal sites, such as at Soultz-sous-Forêts and Illkirch. Unlike temperature anomalies, the resistivity signature of a fracture zone can provide an accurate, quantitative estimate of the permeability of the granite. At Rittershoffen, an interesting correlation was observed between the depth extents of the temperature and resistivity anomalies. The fractures that contribute most to the actual well productivity are associated with localized anomalies in the geophysical logs. These fractures are also characterized by positive temperature anomalies that are interpreted as hot-water outflows in the well. In contrast, fractures in the deepest part of GRT-2 seem to be plugged by small crystallites of illitic material and calcite due to past massive hydrothermal circulation. These fractures are characterized by broad anomalies in the geophysical logs. The fractures with low residual permeabilities are associated with negative temperature anomalies that are interpreted as cooling of the porous altered zone by mud circulation during drilling.

#### 5.1.8. Acknowledgements

This work is based on data from the ECOGI geothermal project at Rittershoffen, France. This work was undertaken and co-funded by ÉS-Géothermie in the framework of the EGS Alsace project, which is co-funded by ADEME, the ÉS group, and EOST. This work was undertaken

as a contribution to the Ph.D. thesis of Carole Glaas and was co-funded by ANRT (French Research and Technology Agency) and ÉS-Géothermie. The authors want to acknowledge Dr. Philippe Leroy for his help with calculating the clay contribution to electrical conductivity in our model. The authors appreciate the helpful and constructive remarks of Dr. Carola Meller and two anonymous reviewers, which seriously improved the manuscript.



## 5.2. Structural characterization of naturally fractured geothermal reservoirs in the central Upper Rhine Graben. Submitted to the Journal of Structural Geology.

C. Glaas<sup>1,2,\*</sup>, J. Vidal<sup>3</sup>, A. Genter<sup>1</sup>

<sup>1</sup> ÉS Géothermie, : 5, rue André Marie Ampère, 67450 Mundolsheim, France.

<sup>2</sup> UMR 7516 IPGS, University of Strasbourg, CNRS, 5 Rue René Descartes, 67084 Strasbourg Cedex, France

<sup>3</sup> University of Chile, FCFM, Department of Geology, Andean Geothermal Center of Excellence (CEGA), Plaza Ercilla 803, Santiago, Chile

**Keywords:** Geothermal reservoir; natural fractures; hard rocks; borehole images; Rhine Graben

### Highlights:

- Fractures are studied from cores and image logs in the hidden granitic basement
- Fracturation is inherited from tectonic history of the Upper Rhine Graben
- Local normal faults guide the permeability in the geothermal reservoirs
- Better grasp of the matrix/fracture permeability at the sediment-granite interface

#### 5.2.1. Abstract

Image logs and the continuous coring of 8 geothermal wells in the Central Upper Rhine Graben (URG) are used for the structural characterization of 3 geothermal reservoirs at Soultz-sous-Forêts, Rittershoffen and Illkirch (France). The naturally permeable fracture zones (FZs) of the hard rocks are the targets of these wells. Subvertical natural fracture networks are striking NNW-SSE to N-S in the granite (inherited from the late-Variscan orogeny) and N-S/NNE-SSW in the sediments (mainly inherited from the Cenozoic era). The permeable fractures in the granite are subparallel to the main striking values. The fracture densities and thicknesses are the greatest in the first 500-1000 meters of the granite. The fracture thickness surely reflects the intensity of the paleo circulations. The fracture distribution is governed by power laws and negative exponential laws. However, there is no simple relationship between those fracture properties and the present-day fracture permeability. The permeability is related to multiscale fracture networks channelling the fluids. Large-scale fractures within normal fault zones could be a more promising target than wide networks of distributed small-scale fractures affecting the whole granitic batholith. The geometry between the well trajectory and the fracture network, impacts also significantly the resulting permeability.

#### 5.2.2. Introduction

To be economically viable, geothermal projects need to reach a geothermal resource with a heat source, circulating fluids and permeable pathways at a drillable depth. In crystalline rocks with low porosity, permeability is mainly supported by a network of natural fractures (Caine et al., 1996; Faulkner et al., 2010). Fluid is circulated through fracture zones (FZ), which are made of a fault core and damage zones (Caine et al., 1996). The fluid circulation can be enhanced by the presence of active and tensile stresses, normal faults, fracture propagation strike-slip faults and fractures associated with hot springs (Barton et al., 1995; Curewitz and Karson, 1997; Gudmundsson et al., 2002; Faulds et al., 2011; Mitchell and Faulkner, 2012). The occurrence of hydrothermal alteration could contribute to the fluid circulation due to residual channelling occurring inside secondary mineralisation, such as automorphic quartz creating

incomplete clogging in the FZ core. Hydrothermal alteration could also contribute through the dissolving of primary minerals, which creates some residual porosity in the nearby FZ damage zone (Ledésert et al., 1999). Conversely, fluid circulation in the FZ can be decreased by hydrothermal alteration in the case of secondary clay minerals precipitation, which can clog the fracture network (Ledésert et al., 1999).

In Europe, the geothermal development occurring in the last 30 years in the naturally fractured reservoirs of the Upper Rhine Graben (URG) has proven the existence of a resource that is mainly located at the base of the Triassic sedimentary unit and the top of the Palaeozoic basement that has industrial hydraulic yields (with a range of approximately 3 L/s/bar) and appropriate temperatures (>150°C) to produce electricity (3 MWe) and/or heat (25 MWth) (Baumgärtner and Lersch, 2013; Baria et al., 2016; Baujard et al., 2017a; Vidal and Genter, 2018; Reinecker et al., 2019). More recently, industrial interest in exploiting the lithium concentrations of the geothermal fluid circulating in the fracture network of the URG has increased. The knowledge and characterization of this fracture network are of primary importance to exploit geothermal crystalline fractured reservoirs. The experience has shown that pure hydrothermal concepts lead to the most successful projects (Baujard et al., 2017a). Ideally, they do not need Enhanced Geothermal Systems (EGS) technologies, which represent an extra cost and often lead to a loss of public acceptance because of the risk of generating induced seismicity (Häring et al., 2008; Evans et al., 2012).

Generally, fracture networks are studied from relevant outcrops (Brogi, 2008; Bauer et al., 2015). In this paper, we have the opportunity to compare structural data from 3 geothermal sites of the URG, including 8 deep geothermal wells, to understand if there is a structural predisposition to permeability.

More precisely, the aim of this study is to determine how the geometry, scaling law and hydrothermal filling impact the permeability of the reservoir. The studied sites are in the French part of the URG, i.e., Soultz-sous-Forêts and Rittershoffen, which have been exploiting the natural brine since 2016, and the Illkirch site, which is under exploration by drilling and is still under development. The old and new image log and core data come from 8 geothermal wells that intersect the fracture network in the Muschelkalk limestone, the Buntsandstein sandstone and the granitic Palaeozoic basement. The goal is to identify the unvarying and varying structural properties of the multi-scale fracture networks encountered in the studied wells, including the fracture orientation, density, spacing, thickness and permeability indicators. This high-quality dataset will allow for a better understanding of the ideal geothermal target from the structural point of view in the URG or, more generally, in the ECRIS.

### 5.2.3. Structural development of the URG

The URG extends from Frankfurt to Basel, with a maximal width of 30-40 km. It is surrounded by the Vosges mountains forming its western horst and the Black Forest mountains forming its eastern horst, both separated from the graben by local normal faults (Figure 5.9a). These domains belong to the same Saxothuringian unit (Edel and Schulmann, 2009). On both horsts, the basement is outcropping, whereas it is hidden by a thick sedimentary cover within the graben. Thermal anomalies are localized along the normal faults, which are interpreted as thermal convection cells along the faults (Schellschmidt and Clauser, 1996; Pribnow and Schellschmidt, 2000; Baillieux et al., 2013). However, the history of the graben is more complex, and this part presents the main steps of its structural evolution, with a focus on its structural inheritance.

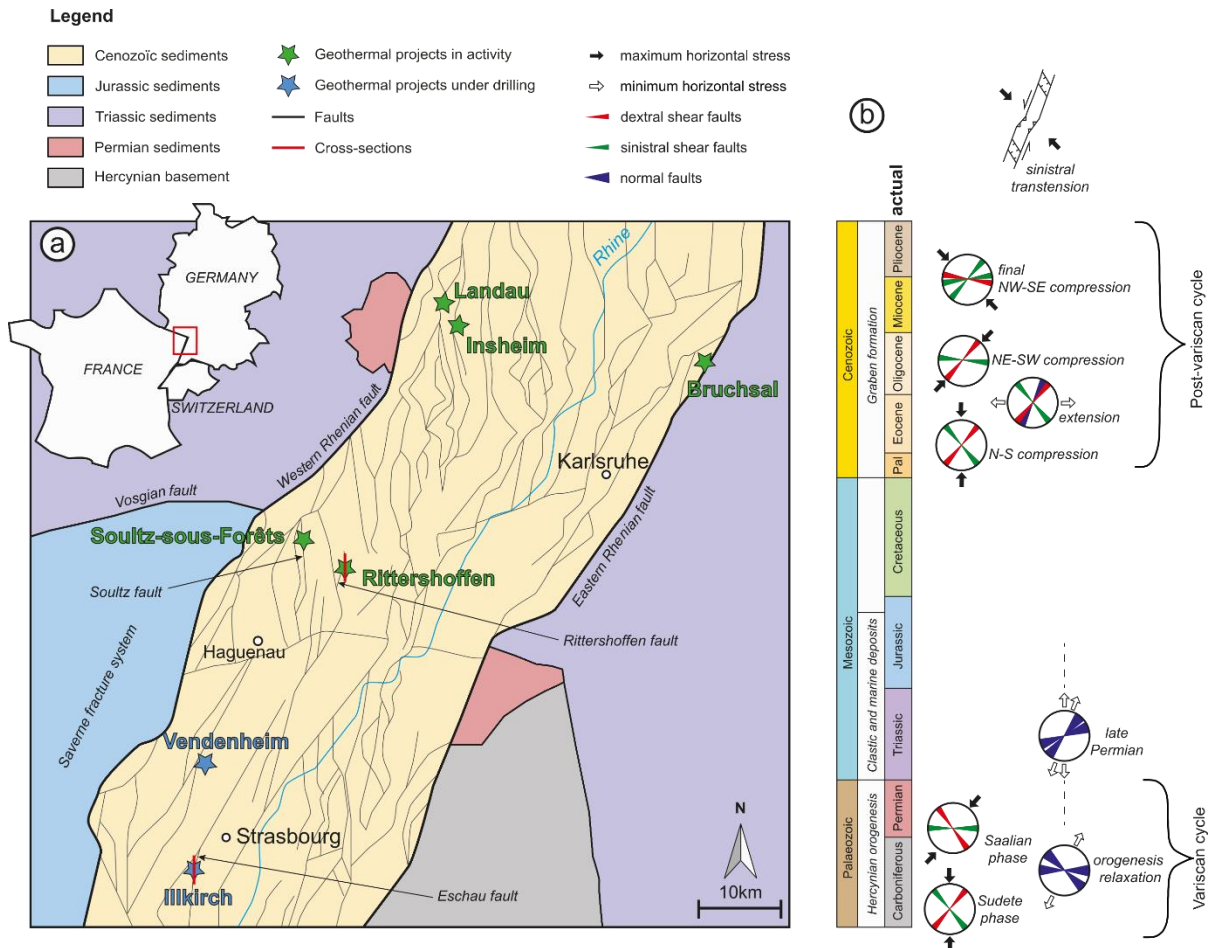


Figure 5.9: a) Structural map of the centre of the Upper Rhine Graben showing the faults at a 2 km depth from the geoportal GeOrg, (2017). The locations of the geothermal power plants under exploitation and under drilling are also shown. Two cross sections in reference to Figures 5.12 and 5.13 are represented on the map. b) The orientations of faults and stresses in the URG during the several tectonic phases are presented along the geological timescale from the Palaeozoic to the Cenozoic ages.

### 5.2.3.1. Variscan cycle

The Variscan cycle is characterized by the intrusion of carboniferous granitoids throughout the crystalline basement from the Viséan (340 Ma) and the Permian (270 Ma) eras. These granitoids were emplaced following a NE to NNE axis along the main weak zones, such as collisional or shear zones (Lagarde et al., 1992; Altherr et al., 1999, 2000; Edel and Schulmann, 2009). The Variscan cycle is also characterized by several tectonic phases (Figure 5.9b). The Sudete phase is the structuration of the orogenesis and consists of a N-S compression generating sinistral NE-SW and dextral NW-SE shear faults (Figure 5.9b). Then, an extension along an NNE-SSW axis is observed, which reactivates the normal faults oriented NW-SE to WNW-ESE until the Permian. The Saalian phase is marked by compression and thrusts in the NE-SW direction, which are associated with sinistral NW-SE and dextral E-W shear faults (Burg et al., 1984). The end of the Permian is characterized by a N-S to NNE-SSW extension that forms the Permian basin along faults oriented NE-SW to ENE-WSW (Villemin and Bergerat, 1987; Schumacher, 2002; Ziegler et al., 2006).

#### 5.2.3.2. Post-variscan cycle

The extension observed at the late Permian continued until the Jurassic in some parts of the URG, inducing fluid migrations and several mineralisation events (Clauer et al., 2008; Bossennec et al., 2020). The Cenozoic rifting affects the Variscan basement but also the sediments of the Buntsandstein, the Muschelkalk and the Jurassic. Villemin and Bergerat, (1987) and Schumacher, (2002) propose a model in 4 tectonic phases (Figure 5.9b). First, at the early Eocene, a N-S compression under the Alpine push reactivates ENE-WSW and NNE-SSW structures (Villemin and Bergerat, 1987; Ziegler, 1992; Schumacher, 2002; Dèzes et al., 2004) (Figure 5.9b). Then, from the late Eocene to the early Oligocene, an E-W extension with N-S and NNE-SSW faults dominates the rifting phase (Doebel, 1967). At the late Oligocene, a NE-SW compression reactivates the border faults with dextral shear (Villemin and Bergerat, 1987; Schumacher, 2002). At the early Miocene, a NE-SW compression influenced by the Pyrenean push transforms the graben in a shear zone (Illies and Greiner, 1979; Bergerat, 1985; Edel et al., 2006). The most recent tectonic event corresponds to the Alpine NW-SE compression, which uplifts and erodes the crystalline horsts (Vosges and Black Forest) and reactivates the N-S and NE-SW faults inherited from the Variscan and Tertiary eras, respectively (Illies, 1972; Dèzes et al., 2004; Edel et al., 2007). The actual phase reactivates the border faults of the URG in sinistral shear and has an opening effect on the NNW-SSE structures (Michon et al., 2003).

## 5.2.4. Materials and methods

### 5.2.4.1. Geothermal reservoir

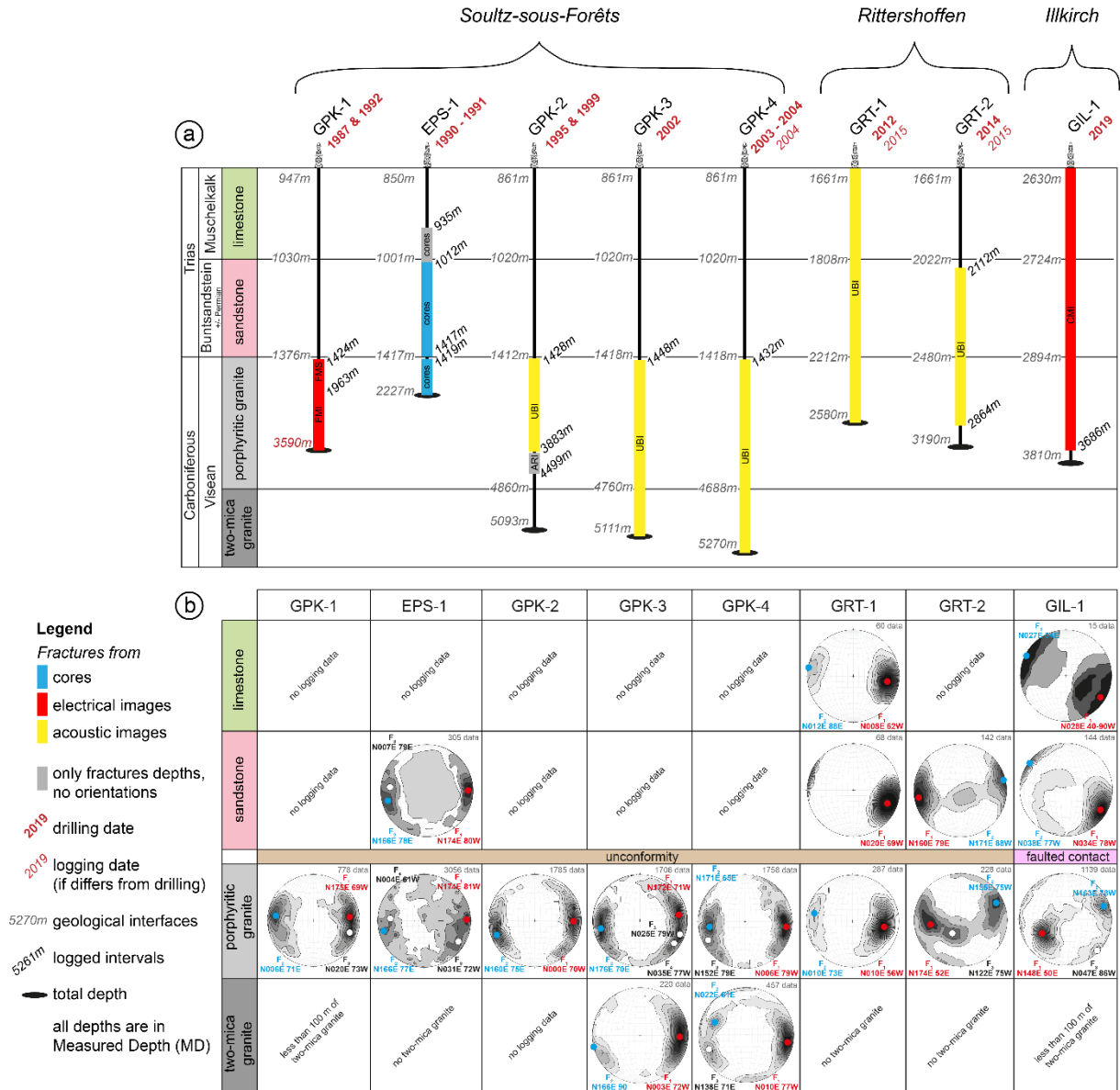


Figure 5.10: a) Type of data available in each geothermal well, specifying the depth of the logged interval, the depth of the main geological interfaces, the drilling date and the logging date. b) Stereoplots (Schmidt lower hemisphere) per lithology in each geothermal well. The main fracture set is in red, the secondary set is in blue and the less represented one is in black.

#### Soutz-sous-Forêts geothermal project

Several deep wells were drilled into the Soutz-sous-Forêts horst structure, which is made of 1.5 km thick tertiary and secondary sediments and a deep crystalline naturally fractured basement (Figure 5.10). The Soutz-sous-Forêts horst is bounded on its western region by a normal fault that shows a vertical offset of at least 500 m and is oriented N20°E (Kappelmeyer, 1991; Genter and Traineau, 1996). In the URG, the sandstones comprise Buntsandstein and Permian. Buntsandstein is deposited in a fluvial environment, is isopach and is approximately 350 m thick in the Soutz-sous-Forêts wells (Aichholzer et al., 2019). The Permian layer, which is a result of continental deposits, is the oldest sedimentary unit in the graben and overlies the

granitic basement by filling the paleo-basins; thus, its presence and thickness are difficult to predict (Aichholzer, 2019). In the Soultz-sous-Forêts wells, it is approximately 35 m thick. The granitic basement at Soultz-sous-Forêts comprises a monzogranite with K-feldspar mega crystals containing locally high amounts of biotite, dating from 334.0±3.8/3.5 Ma and a two-mica granite, which also contains muscovite and dates from 327±7 Ma (Stussi et al., 2002; Cocherie et al., 2004). Both Visean ages confirm that the granites were emplaced before the Sudete phase and, thus, keep the structural heritage of the latter. Even if the Permo-Triassic sandstones revealed some permeable fractured zones, the initial target of the Soultz-sous-Forêts project was to develop an artificial exchanger in the deepest granite, which is located 3.5 km under the top of the basement. Thus, several wells were drilled to 5 km deep and, surprisingly, intersected a permeable natural fracture network that channelized brine (Figure 5.11a & b). A large-scale permeable fault has been identified in the granite with an orientation of N144°E and a dip of 65-70°W (Sausse et al., 2010). The deep well exploration has shown that the highest natural permeability was found in the shallowest reservoirs of the granite, which means between the top basement and 2 km. The lessons learned from Soultz-sous-Forêts lead to an evolution of the concept for the Rittershoffen project, where geothermal wells were drilled a maximum of 1 km below the top basement. To date, the Soultz-sous-Forêts site comprises 5 deep wells (Figure 5.10), with three wells (GPK-2, 3 and 4) that contribute to produce 1.7 MWe for the electrical grid (Mouchot et al., 2019).

#### *Rittershoffen geothermal project*

The Rittershoffen wells, before reaching the granite, intersect approximately 400 m of Buntsandstein and 10 m of Ante-Annweiler Permian sandstone layers. In the granitic basement, the wells intersect only monzogranite, which is remarkably similar to the one encountered in the Soultz-sous-Forêts wells (Figure 5.12). The Rittershoffen site comprises two wells, i.e., GRT-1, the injection well, and GRT-2, the production well, which produces 24 MWth for industrial use (Mouchot et al., 2019). The Rittershoffen project took advantage of the Soultz-sous-Forêts experience, and the target was the Rittershoffen normal fault, which is located approximately 15 km east of the western Rhenish border fault and is oriented N5°E based on subsurface geological data (Baujard et al., 2017a). After the drilling of GRT-1 and the realization of a new 2D seismic campaign, the trajectory of GRT-2 was optimized according to the orientation of the Rittershoffen fault (Baujard et al., 2017a). The second well is therefore slightly deviated but tangent to the local fault over its approximately 400 m length in the granitic basement (Figure 5.12). Its high productivity index of 4 L/s/bar without any stimulation revealed a good connection between the well and the fracture network (Baujard et al., 2017a). The well probably intersects the fault zone characterized by a high fracture density with optimized natural fluid pathways (Vidal et al., 2017). The hydrothermal concept has been extremely positive for the GRT-2 well (Vidal and Genter, 2018).

#### *Illkirch geothermal project*

The Illkirch well, before reaching the basement, intersects 170 m MD (156 m TVD) of Buntsandstein, which is approximately 300 m thick in total (Aichholzer, 2019) (Figure 5.13). No Permian is intersected due to the GIL-1 well trajectory, but the presence of Permian was found to be between 50 and 200 m in the deep wells in the near wells (Housse, 1984; Richard et al., 2016; Aichholzer, 2019). The granitic basement intersected by the GIL-1 well comprises monzogranite, which seems to be similar to the one encountered in the Soultz-sous-Forêts and Rittershoffen wells and is sometimes enriched with biotite. The target of the Illkirch project

was the Eschau normal fault oriented N10°E based on 2D seismic interpretation (Richard et al., 2016), which is intersected by the well at the interface between Triassic sandstone and granite (Figure 5.13). In the open-hole section of the well, the GIL-1 well was drilled in the NW-SE azimuth to intersect the fault at a high angle. To date, hydraulic tests tend to show that the permeability is mostly located in the deepest fractured granite.

These three geothermal sites explored by deep drilling have penetrated from 1 to 3.5 km into a deep fractured basement. To date, the Soultz-sous-Forêts and Rittershoffen sites are exploited for energy production, whereas at the Illkirch site, only one well has been drilled. Various techniques have been used for collecting high quality fracture datasets, such as continuous coring and electric/acoustic borehole images. These datasets have been collected in all the wells, thus providing the opportunity to compare the structural characteristics, such as the fracture orientation, fracture density, fracture spacing, fracture thickness and fracture permeability.

#### 5.2.4.2. Structural analyses

##### *Core samples*

At Soultz-sous-Forêts, in the EPS-1 well, the structural data of 810 m of continuous coring from 1420 to 2230 m was analysed by (Genter and Traineau, 1996) (Figure 5.11a). Approximately 3000 macroscopic natural fractures were identified, and 97% of them were successfully reoriented by comparing the core and acoustic borehole imagery. The orientations, depths and thicknesses of the natural fractures, as well as the type of secondary fillings (quartz, haematite, carbonates, clay minerals, chlorite, epidote, barite, anhydrite, pyrite and galena) were described with great care (Genter and Traineau, 1996).

##### *Acoustic image logs*

The Ultrasonic Borehole Imager (UBI) developed by Schlumberger in 1990 comprises a rotative transducer emitting an acoustic wave towards the borehole wall that records the amplitude and transit time of the wave after its reflexion from the rock (Zemanek et al., 1970). Acoustic imagers allow an image to be obtained that covers 100% of the borehole circumference (Figure 5.11c). The UBI images are presented with an image in amplitude (dB), which provides information on the borehole roughness and quality, and an image in transit time ( $\mu\text{s}$ ), which measures the distance between the tool and the borehole and informs on the borehole geometry (Serra and Serra, 2000). The colour scale shows the borehole expansions due to fractures and caves in dark colours (black), and the unaffected standard borehole diameter appears in light colours (yellow-orange). Natural fractures appear as sinusoids on the unrolled UBI images, which allows the dip, orientation and thickness of the fractures to be measured (Figure 5.11c). The UBI log is oriented and the natural fractures measured on the images are then corrected with the borehole trajectory.

##### *Electrical image logs*

Resistivity image logs were developed by Schlumberger in 1986 as the Formation Micro-Scanner (FMS), which evolved into the Formation Micro-Imager (FMI) (Figure 5.11b). To date, other companies, such as Weatherford, have developed similar tools, such as the Compact Micro-Imager (CMI). These various tools all comprise dipmeter pads, which comprise electrodes, which allow each pad to record the number of microresistivity curves that corresponds to the number of electrodes (Schlumberger, 1993; Crain, 1998). The number of

pads increased during the evolution of the tool to reach 8 pads today, covering 80% of the borehole circumference in an 8" hole size (Figure 5.11c, Table 5.3). The resistivity images are presented with a static and a dynamic image, where the static image is normalized over the complete depth interval logged; thus, the contrast responds to large-scale variations in lithology, porosity and saturation, whereas the dynamic image is normalized using a sliding window of 0.5 m; this highlights small-scale variations in the electrical contrast due to bedding, fractures, and changes in porosity (Figure 5.11d and e). As on the UBI images, natural fractures appearing as sinusoids are measured and reoriented in the same way. The colour scale shows resistive materials in light colours (yellow-orange), whereas conductive materials appear in dark colours (black). As both the very saline brine and the clay minerals are very conductive, a black fracture on both the static and dynamic images could even be interpreted as an open fracture with very saline and conductive brine, or as a clogged fracture filled by conductive secondary clay minerals.

The Azimuthal Resistivity Imager (ARI) was developed by Schlumberger in the early 90's. It is a dual laterolog array with 12 azimuthal electrodes incorporated in its upper electrode, which provide a dozen deep oriented resistivity measurements in addition to the standard deep and shallow readings (LLD and LLS) (Schlumberger, 1993) (Table 5.3). The data is then displayed as an azimuthal resistivity image (Schlumberger, 1993) (Figure 5.11). This image has much lower spatial resolution than the other acoustic or electrical images, but the interest is to use it as a complement to the other types of imageries, as its sensitivity to features beyond the borehole wall is higher. In the GPK-2 well, the ARI was acquired separately, and thus, only the depth of the fractures could be described.

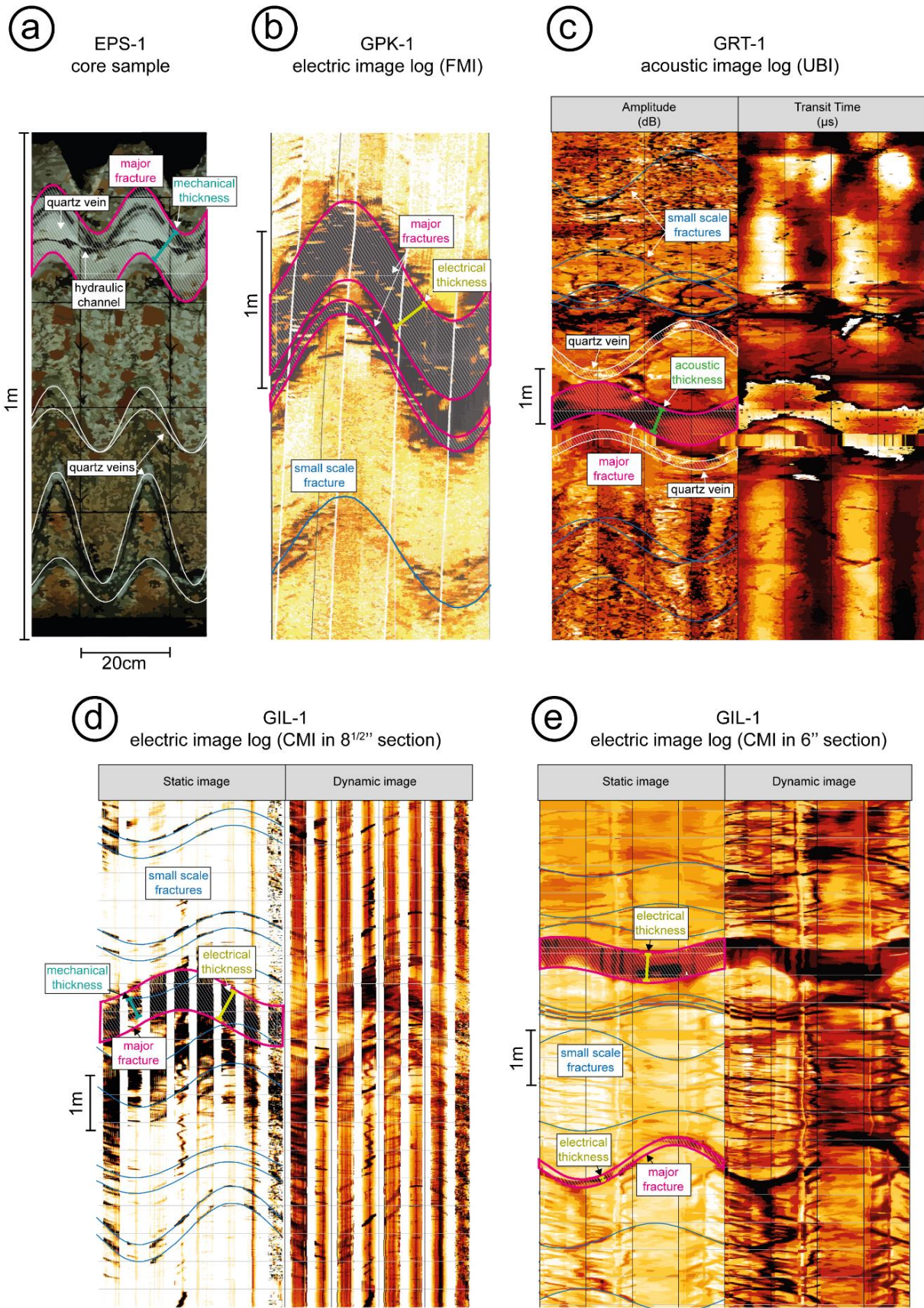


Figure 5.11: Examples of borehole imagery methods and continuous cores: a) Core section of the EPS-1 well at 2156 m MD; b) FMI in the GPK-1 well at 2865 m MD; c) UBI in the GRT-1 well at 2321 m MD; d) CMI in the GIL-1 well in the 8<sup>1/2</sup> section at 3226 m MD; and e) CMI in the GIL-1 well in the 6" section at 3330 m MD.

### *Spatial resolution of fracture analysis*

The different tools used for this study have roughly the same resolution, except for the core samples and the ARI (Table 5.3). It has been shown that even equivalent resolution borehole imagery techniques are not as exhaustive as the core data and cannot provide a complete characterization of the fracture network, as discrete fractures thinner than 1 mm are not properly detected and fractures closer to 5 mm appear only as single traces (Genter et al., 1997a). However, for all techniques, the fracture orientation was shown to be correctly sampled (Genter et al., 1997a). More precisely, Crain, (1998) found that when comparing the same generation tools, the electrical images are more accurate than the acoustic images, even if the electrical images only cover 80% of the borehole circumference. The ARI is also the imagery method with the lower resolution, but it allows the detection of features and perturbations beyond the borehole wall; there is interest in using this in parallel with other electric or acoustic images. Usually, fractures from the Soultz-sous-Forêts and Rittershoffen datasets are classified according to their visibility on the image logs, for example, if they are visible on 100%, 50%, or 30% of the image, or if they are uncertain (Dezayes et al., 2010; Vidal et al., 2016b, 2019). For this study, all the fractures classified as “uncertain” or visible on less than 50% of the image logs were not considered.

### *Fracture thickness*

During the drilling, a mechanical erosion of the surface of the fracture rims would usually occur. Regardless of the imagery technique, this effect overestimates the natural fracture thickness because the fractures appear larger on the image than in reality. This effect does not exist on core samples, especially with a core recovery close to 100%, as we had in EPS-1 (Figure 5.11) (Genter and Traineau, 1996). Then, the different imagery and coring techniques do not precisely consider the same fracture thicknesses scale.

- For the core samples, we measure the mechanical thickness, which corresponds to the normal distance between the two consecutive walls of a given fracture (Figure 5.11a). All the natural fractures observed at Soultz-sous-Forêts are mineralised with secondary minerals, such as quartz, clay minerals, barite, and calcite. Thus, the fracture thickness corresponds to the clogged thickness and could include the residual fracture hydraulic aperture if the clogging is incomplete (Figure 5.11a). On EPS-1 cores, less than 1 % of the natural fractures present incomplete clogging by hydrothermal minerals. From the EPS-1 core analyses, 3000 fractures are characterized, and all the natural fractures are systematically filled by at least one or several secondary hydrothermal minerals (Genter and Traineau, 1996).
- Regarding the electrical images, the electrical thickness includes the clogged fracture and its nearby hydrothermally altered environment, corresponding to the beginning of the damage zone (Figure 5.11b, d and e). It matches our geothermal wells in basement rocks to clay minerals, such as illites, that have the same electrical signature as the fracture itself, generally filled by illite or a conductive fluid. Thus, it becomes quite difficult to differentiate the precise trace of the fracture on the borehole wall. If we add potential mechanical erosion due to the drilling processes, we assume that the fracture thicknesses observed on the electrical images are potentially larger than those on the core samples. The hydraulic aperture, if it exists, is included in this electrical thickness. The electrical thickness tends to be larger than the mechanical thickness.
- Regarding the acoustic images, the acoustic thickness includes the clogged fracture closer to the mechanical thickness but does not systematically include its nearby

altered environment (Figure 5.11c). The hydraulic thickness, if it exists, is included in this acoustic thickness. According to the cases, the acoustic aperture can be larger or smaller than the mechanical aperture (Genter et al., 1992; Vidal et al., 2017).

Tool name	Core	UBI	ARI	UBI	UBI	FMS	FMI	CMI
<b>Well logged</b>	EPS-1	GPK-2	GPK-2	GPK-3 GPK-4	GRT-1 GRT-2	GPK-1	GPK-1	GIL-1
<b>Logging date</b>	1990-1991	1995	1999	2002 2004	2015	1987	1992	2019
<b>Tool configuration</b>	Core mining Diameter: 78 mm from 930 to 1995 m and 56 mm from 1995 to 2230 m	Transducer inserted in a rotating sub	12 azimuthal electrodes	Transducer inserted in a rotating sub	Transducer inserted in a rotating sub	2 pads with 29 sensors/pad and 2 pads with 2 sensors/pad = 62 sensors	8 pads with 16 sensors/pad = 64 sensors	8 pads with 22 sensors/pad = 172 sensors
<b>Vertical resolution</b>	< 1 mm	10 mm	200 mm	10 mm	10 mm	3 mm	2.5 mm	5 mm
<b>Azimuthal resolution</b>	< 1°	1.6°	30°	2°	2°	2.2°	1.5°	+/-5°
<b>References</b>	(Genter and Traineau, 1996)	(Genter et al., 1997a)	(Schlumberger, 1993; Sausse and Genter, 2005)	(Valley, 2007)	(Vidal et al., 2017)	(Genter et al., 1997a; Sausse and Genter, 2005)	(Genter et al., 1997a; Sausse and Genter, 2005)	(Schlumberger, 1993)

Table 5.3: Description of the specificities of each method used for the structural data analysis. The well logged, the logging date, the tool configuration, the vertical and azimuthal resolutions, as well as the references are detailed for each method used.

## 5.2.5. Results

### 5.2.5.1. Fracture orientation

#### *Soultz-sous-Forêts*

The orientation of the natural fracture set is quite similar in the Soultz-sous-Forêts wells to a conjugate fracture set striking  $N000^{\circ}E \pm 10^{\circ}$  and highly dipping (Figure 5.10b) (Dezayes et al., 2010). In all the Soultz-sous-Forêts wells and in all the formations, the main fracture set dips to the West. In the Buntsandstein, the fracture data available are exclusively from the core samples of the EPS-1 well and express a conjugate set comprising fractures striking  $N170^{\circ}E$  and steep dips of  $80^{\circ}$  (Figure 5.11). In the monzogranite, the fracture data are from the 5 wells and behave in the same way as the conjugate set in the Buntsandstein but with less steep dips of  $75^{\circ}$  (Figure 5.11). In the deeper two-mica granite, the fracture set striking  $N000^{\circ}E \pm 10^{\circ}$  and dipping to the West is more visible (Figure 5.11).

#### *Rittershoffen*

In both the GRT-1 and GRT-2 wells, the fractures roughly strike in the N-S direction, but a divergence of dip is observed between both wells (Figure 5.10b & Figure 5.12). In the GRT-1 well, the main set dips to the West, whereas in the GRT-2 well, the main set dips to the East (Figure 5.10b & Figure 5.12). In the Muschelkalk, fracture data are only available in the GRT-1 well and show a main fracture set oriented  $N006^{\circ}E$  and dipping  $62^{\circ}W$  (Figure 5.11b). In the Buntsandstein, fracture data for both wells are available, in the GRT-1 well a fracture set strikes  $N020^{\circ}E$  and dips  $69^{\circ}W$ , which is quite different from the conjugate fracture set observed in the GRT-2 well, which strikes  $N160-170^{\circ}E$  and steeply dips  $88^{\circ}W$  and  $79^{\circ}E$  (Figure 5.11b). In the granite, the GRT-1 well presents a conjugate fracture set that strikes  $N010^{\circ}E$  and dips  $56^{\circ}W$  and  $73^{\circ}E$ ; the GRT-2 well also presents a conjugate fracture set, but it is oriented  $N155-174^{\circ}E$  and has dips  $75^{\circ}W$  and  $52^{\circ}E$ , which are associated with a minor fracture set striking  $122^{\circ}E$  and dipping  $75^{\circ}W$  (Figure 5.11b).

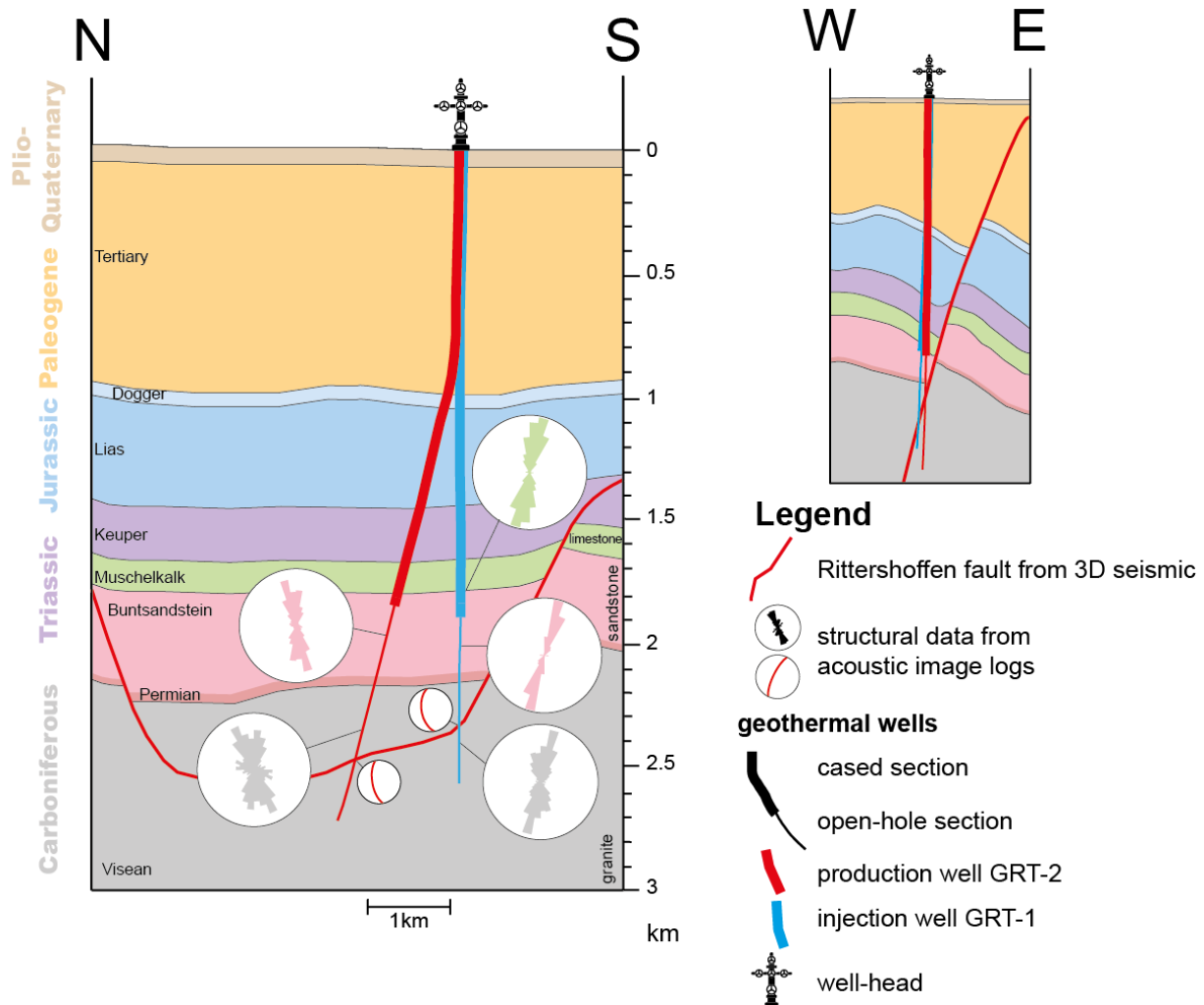


Figure 5.12: Schematic geological cross-section drawn following the 3D seismic data, through the Rittershoffen geothermal site with the projection of the trajectories of the GRT-1 and GRT-2 wells. Only the local normal Rittershoffen fault is represented.

### Illkirch

At Illkirch, the fracture data results from the GIL-1 well, where the fracture orientation in the sediments strikes NE-SW, but differs from those observed in the granite that strikes NW-SE (Figure 5.10b & Figure 5.13). In the sediments, the main fracture set dips to the West whereas in the granite, it dips to the East (Figure 5.10b & Figure 5.13). The fractures in the Muschelkalk are highly dispersed due to the small amount of data collected and present a nearly-vertical conjugate set striking N028°E (Figure 5.10b & Figure 5.13). In the Buntsandstein, the fractures also present a conjugate set but strike approximately N035°E with a steep dip of 80° (Figure 5.10b). In the granite, a conjugate set striking N148-163°E and dipping 76°W and 48°W is observed (Figure 5.10b). Note that the Eschau fault was intersected by the well with a local orientation of N30°E and a general orientation of N10°E from the 2D seismic data.

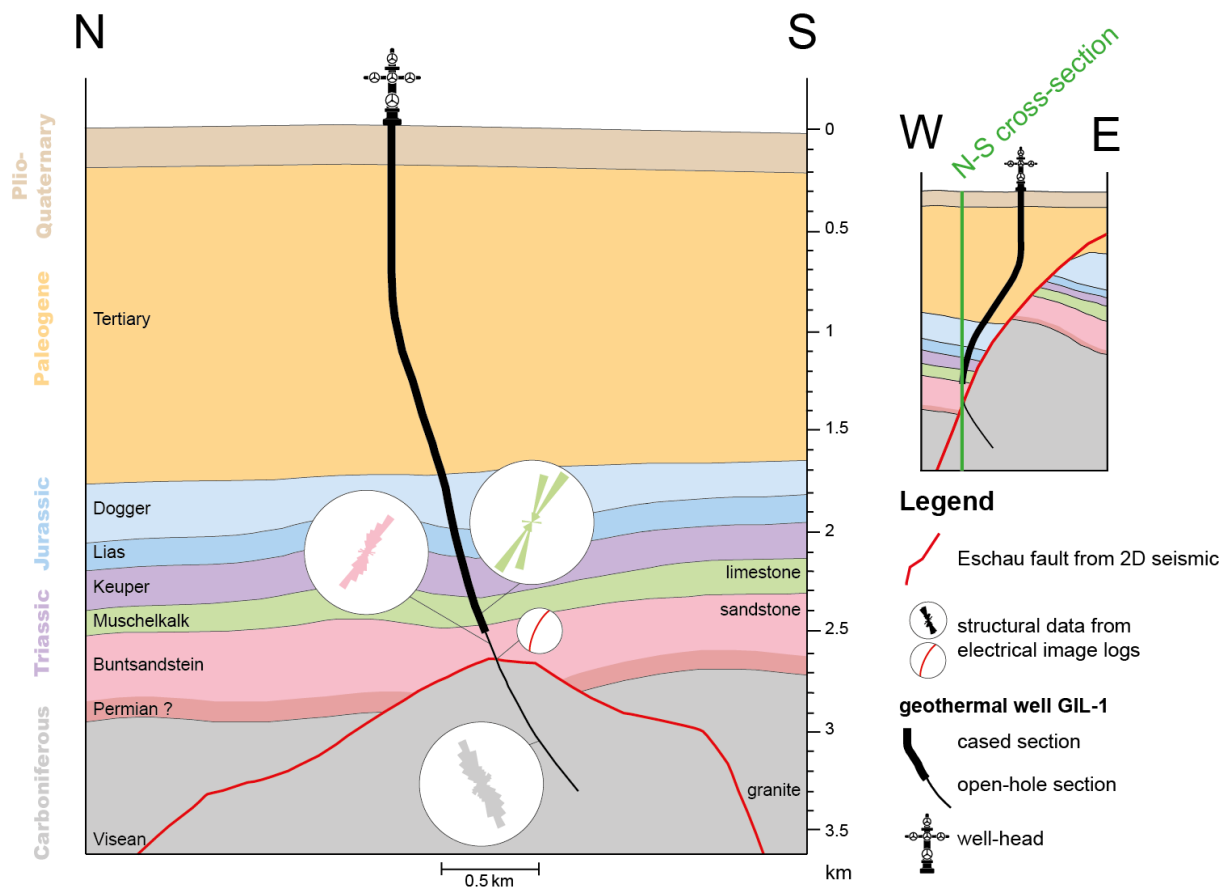


Figure 5.13: Schematic geologic cross-section drawn following the 2D seismic data, through the Illkirch geothermal site with the trajectory of the GIL-1 well. Only the local normal Eschau fault is represented. The occurrence of the Permian sedimentary layer is uncertain because it was not intersected by GIL-1 but was observed in the surrounding wells (Aichholzer, 2019).

### 5.2.5.2. Permeable fractures

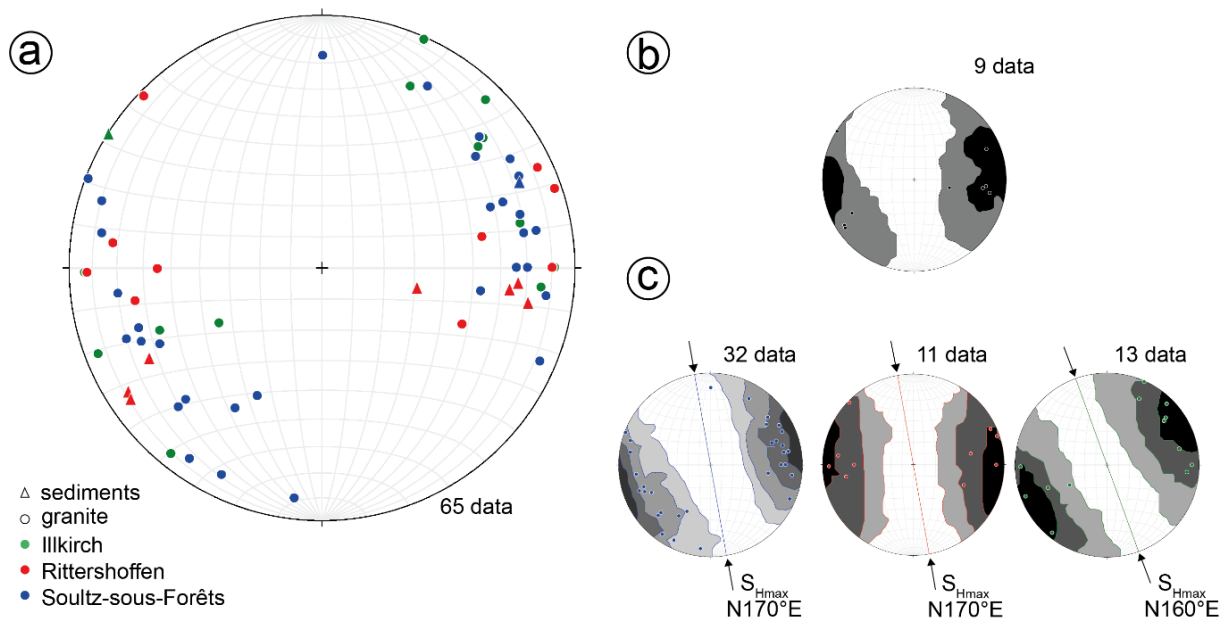


Figure 5.14: Stereoplots (Schmidt lower hemisphere) of the permeable fractures in the sediments (regrouping Buntsandstein sandstones and Muschelkalk limestone) and in the granite; the orientations and dips used in this figure are detailed in the supplementary materials 5.S1. a) Poles of all the permeable fractures. b) Stereoplot of the permeable fractures in the Muschelkalk and Buntsandstein. c) Stereoplots of the permeable fractures in the granite at Soultz-sous-Forêts, Rittershoffen and Illkirch (from left to right);  $S_{Hmax}$  is the maximum horizontal stress orientation (Valley, 2007; Hehn et al., 2016).

All the geothermal wells presented in this paper intersected natural fractures considered as permeable. A natural fracture was considered permeable if there was at least a temperature anomaly and another permeability indicator, such as mud losses or outlets, and gas anomalies (Evans et al., 2005; Vidal et al., 2017, 2018, 2019). In this study, we only included natural fractures that were already permeable prior to any type of stimulation. The permeable fractures with their structural data and the associated permeability indicators are presented in the supplementary materials. However, it is important to consider that these permeable fractures are most often within a larger fracture zone (FZ). They generally act as the main fluid pathways of the FZ, are easily detected on core samples or in image logs and are surrounded by a damage zone (Figure 5.11) (Genter et al., 2000; Vidal et al., 2017; Vidal and Genter, 2018). The permeable FZs in the granite from Soultz-sous-Forêts and Rittershoffen were deeply developed by Vidal et al., (2019) and Dezayes et al., (2010) and those in the sediments were developed by (Vidal et al., 2015, 2017).

At Soultz-sous-Forêts, in the GPK-1 well, 4 permeable FZs were detected in the granite, 1 in the Buntsandstein, 2 permeable but partly sealed FZs were also observed in the Muschelkalk and the Keuper. In the EPS-1 well, 1 permeable FZ was detected in the granite and 1 in the Buntsandstein. In the GPK-2 well, 6 permeable FZs were detected in the granite, 1 in the Buntsandstein and 2 in the Muschelkalk. In the GPK-3 well, 5 permeable FZs were observed in the granite, 2 in the Buntsandstein and 2 in the Muschelkalk. In the GPK-4 well, 7 permeable FZs were detected in the granite, 1 in the Buntsandstein and 1 in the Muschelkalk.

At Rittershoffen, in the GRT-1 well, 2 permeable FZs were detected in the granite and 1 in the Muschelkalk. In the GRT-2 well, 4 permeable FZs were observed in the granite, 1 in the Buntsandstein and 1 in the Permian.

At Illkirch, in the GIL-1 well, permeable FZs were detected in the electrical image logs. In the granite, 6 permeable FZs were detected from 3050 to 3090, 3210 to 3230, 3309 to 3315, 3330 to 3390, 3500 to 3575, and 3625 to 3645 m MD. They are all associated with a temperature anomaly (Glaas et al., 2021b). Surprisingly, the fracture considered as the intersection of the Eschau fault does not present a temperature anomaly and, thus, is not considered as naturally permeable. On the other hand, a temperature anomaly is associated with the intrusion of the biotite-rich granite structures inside the batholith and suggests that dyke or sill could represent a heterogeneity and a localized permeability. Only one permeable FZ was intersected within the Buntsandstein in GIL-1 from 2780 to 2785 m MD.

More generally, in the 3 geothermal sites, we lack oriented data in the sedimentary part. Due to this lack, only 9 permeable fractures could be represented in Figure 5.14b.

Permeable fractures are globally striking NNW-SSE (Figure 5.14a). In the sediments, the permeable fractures present a conjugate set striking N175°E and dipping 75°E and W (Figure 5.14b). In the granitic basement of Soultz-sous-Forêts, the permeable fractures intersected by the wells present a conjugate set striking N164°E and dipping 85°E and W (Figure 5.14c). In the granitic basement of Rittershoffen, the permeable fractures intersected by the wells present a conjugate set striking N003-168°E and dipping 82°E and W (Figure 5.14c). In the granitic basement of Illkirch, the permeable fractures intersected by the well present a conjugate set striking N149°E and dipping 86°E and W (Figure 5.14c). For the three sites, the maximum horizontal stress direction is sub-parallel to the permeable fracture strike  $\pm 10^\circ$  (Valley and Evans, 2007; Hehn et al., 2016).

#### 5.2.5.3. Fracture density

In the granite, the EPS-1 fracture set from the core samples presents the highest fracture density of 3.85 (Figure 5.15b). The EPS-1 well presents two main sections; the first 150 m are highly fractured (6.7 frac/m), and the deepest section is less fractured (4.7 frac/m) (Figure 5.15a).

The other wells present fracture datasets from the acoustic and electric image logs collected from the 3 geothermal sites. In the sandstone of the Buntsandstein, the fracture densities are low, from 0.40 to 0.66 frac/m, whereas in the granite, they show a wide range of fracture density values from 0.36 to 1.60 frac/m. In the granitic basement, the cumulative fracture densities were separated in several depth interval sections, which are roughly the same for all the wells (Figure 5.15a & b). More precisely, GIL-1 and GPK-2 show quite similar fracture density values, i.e., 1.6 frac/m for GIL-1 and 1.2 frac/m for GPK-2 in the first 900 m of the granitic basement. GIL-1 does not descend deeper into the granitic basement, but below, in GPK-2, two different sections are observed, as follows: from 900 to 1800 m and from 1800 to 3000 m below the top of the granitic basement, where the fracture densities are of 0.6 and 0.2 frac/m, respectively. GPK-3 and GPK-4 show exactly the same depth interval sections with similar ranges of fracture densities (Figure 5.15). Both wells can be separated into 4 distinct depth sections, as follows: the first 450 m show fracture densities of 0.8 and 0.9 frac/m, respectively; from 450 to 1350 m below the top basement, the fracture density is of 0.4 frac/m; from 1350 to 1920 m below the top basement, the fracture density is of 0.8 frac/m for both wells; and from 1920 to 3000 m below the top basement, the fracture density values are of 0.4 and 0.2 frac/m, respectively. This last depth interval is also observed in the GPK-2 well, which also has a fracture density of 0.2 frac/m. However, the deepest part of GPK-2, representing a length of approximately 600 m, was never characterized with borehole image logs due to the borehole

conditions. GPK-1, which is characterized by fracture data interpreted from former electrical image logs (FMS & FMI), presents the lowest fracture density value of 0.36 frac/m in the granite (Figure 5.15b).

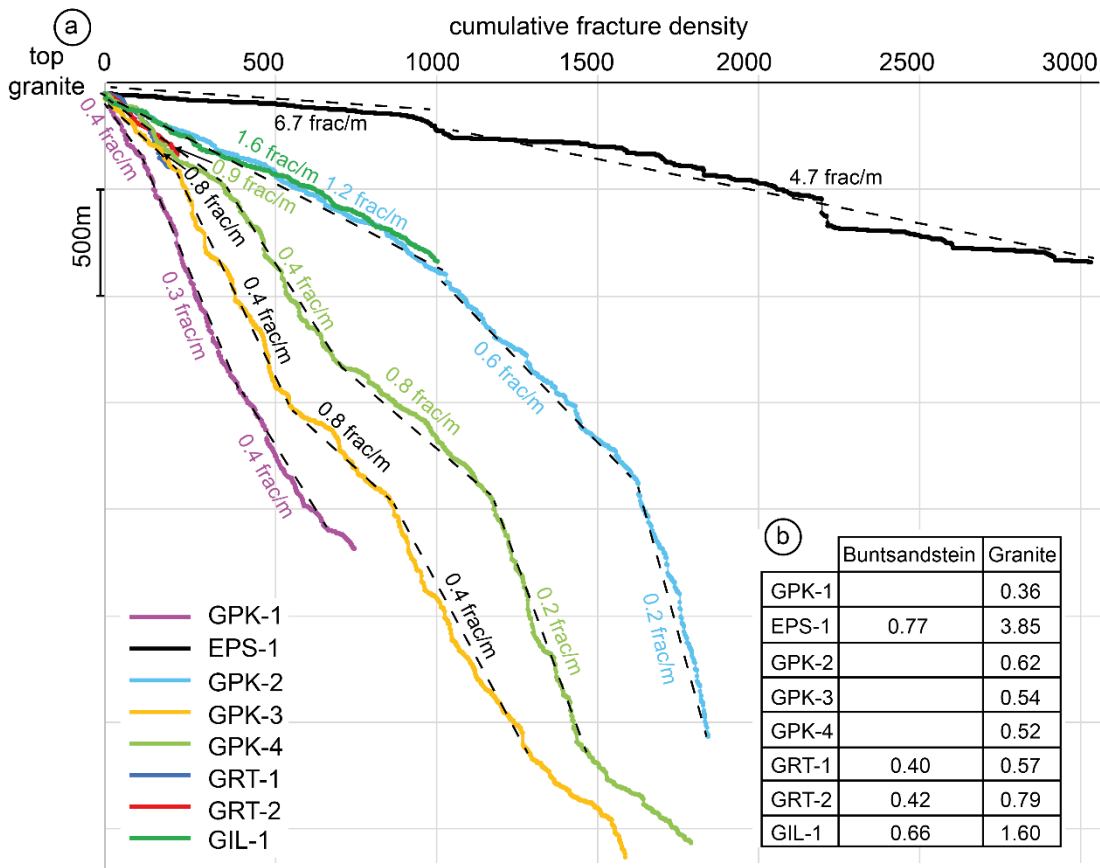


Figure 5.15: a) Cumulative fracture density along the depth for all the geothermal wells. The cumulative fracture density is presented only in the granite, and the depth scale was normalized to begin at the top of the granite for all the wells. b) Table presenting the global fracture densities (frac/m) in the Buntsandstein sandstones and the granite for each well.

From a general point of view, we observe that the fracture density versus depth is higher in the first 500-1000 m of the granitic basement and that from 1900 to 3000 m below the top basement of Soultz-sous-Forêts, the fracture density is lower. GRT-1 presents a fracture density very similar to GPK-2, 3 and -4 in the granitic section (0.57), whereas it is slightly higher for GRT-2 (0.79) (Figure 5.10b).

#### 5.2.5.4. Fracture spacing

To facilitate a comparison, the fracture spacing curves in the granite were normalized for all the wells by applying a correction factor that was determined by dividing each well section by the longest available well section in the basement. The longest well section where fracture data are available is the GPK-4 well granitic section, which is 3831 m. For each well, this correction factor was applied to the fracture spacing distribution plotted on a log-log scale (Figure 5.16). The maximal spacing can be estimated by the projection of the distribution curve on the horizontal axis. We observe that all the largest fracture spacings converge towards a pluridecamic value ranging between 20 and 80 m, except for EPS-1, GPK-2 and GRT-1,

where the largest spacing tends to converge to values higher than 100 m (Figure 5.16). The coefficients of variation (CV) were also calculated for each well by dividing the standard deviation by the average (Figure 5.16). All the wells present CV values higher than 1, which is usually associated with a clustered organization of spacing, meaning a heterogeneous distribution of the fractures along the depth, with closely spaced fractures alternating with large spaces between the fractures. The higher the CV, the more the organization is clustered (Odling et al., 1999; Gillespie et al., 2001).

The fracture spacing distribution for EPS-1 fits a perfect straight line on the log-log graph for more than two decades (Figure 5.16a), which means that the fracture spacings are governed by a power law having an exponent of -1.07. As the resolution of the fracture analysis with core samples is the highest, it means that the sampling biases are minimized. Thus, the power law distribution and the highest CV for fracture spacings, which is 5.56 in the basement, reflects a highly heterogeneous fracture distribution in the rock mass (Figure 5.16).

With the example of the Rittershoffen wells where the same UBI was used, we can also compare the results obtained in terms of the fracture spacing distribution (Figure 5.16c and d). GRT-2 presents a negative exponential law with the lowest CV (1.21), which reflects a low clustered organization of fractures in the well (Figure 5.16d), whereas GRT-1 presents a power law, which reflects a fracture distribution in clusters (Figure 5.16c). Geologically, it is assumed that GRT-2 tangentially intersects the local Rittershoffen normal fault at a 400 m thick section through its damage zone. This assumption means that an intermediate density of fractures of 0.79 frac/mm (Figure 5.15b) over several hundreds of metres in accordance with the distribution law is encountered. In contrast, GRT-1 crosses the fault perpendicularly to enter the low altered granite associated with a lower fracture density (0,57 frac/mm, Figure 5.15b), which could validate the heterogeneous fracture distribution and cluster organization, as observed in Figure 5.16c and d. Note that a truncation bias is visible at the end of the curve of GRT-1 because the length of the studied section is not long enough for a complete sampling (Figure 5.16c). The other bias is the censoring, which is visible at the beginning of the curve and is explained because fractures that are too closely spaced cannot be sampled with the borehole imagery technique, unlike with the core sample (Odling et al., 1999; Gillespie et al., 2001). In fact, censoring is visible on all the curves excepted on the EPS-1 curve, where all the closely spaced fractures are correctly detected and sampled (Figure 5.16a). Due to the effects of truncation and censoring, the power law of GRT-1 fits approximately one decade (Figure 5.16c). Surprisingly, GRT-1 fits a power law but has a low CV (1.84), which could be explained by the fact that the effects of censoring and truncation are important. These observations show that the fracture distribution is well represented by the law but that the tool resolution can influence the CV value.

In GIL-1, the fracture distribution fits a negative exponential law quite well, which means that the fracture spacings are more homogeneously distributed, as in the GRT-2 well (Figure 5.16b and d). Maybe the fit between the raw curve and the extrapolated law is not perfect because of the electrical tool resolution for GIL-1, which is higher than for the acoustic tool for the other wells, enabling the sampling of the closest fractures. It could more accurately reflect the "natural system" in GIL-1 than in GRT-2, for example. In the case of GIL-1, the low CV (1.74) is in agreement with its fit with a negative exponential law, reflecting a low clustered fracture distribution of spacings (Figure 5.16b).

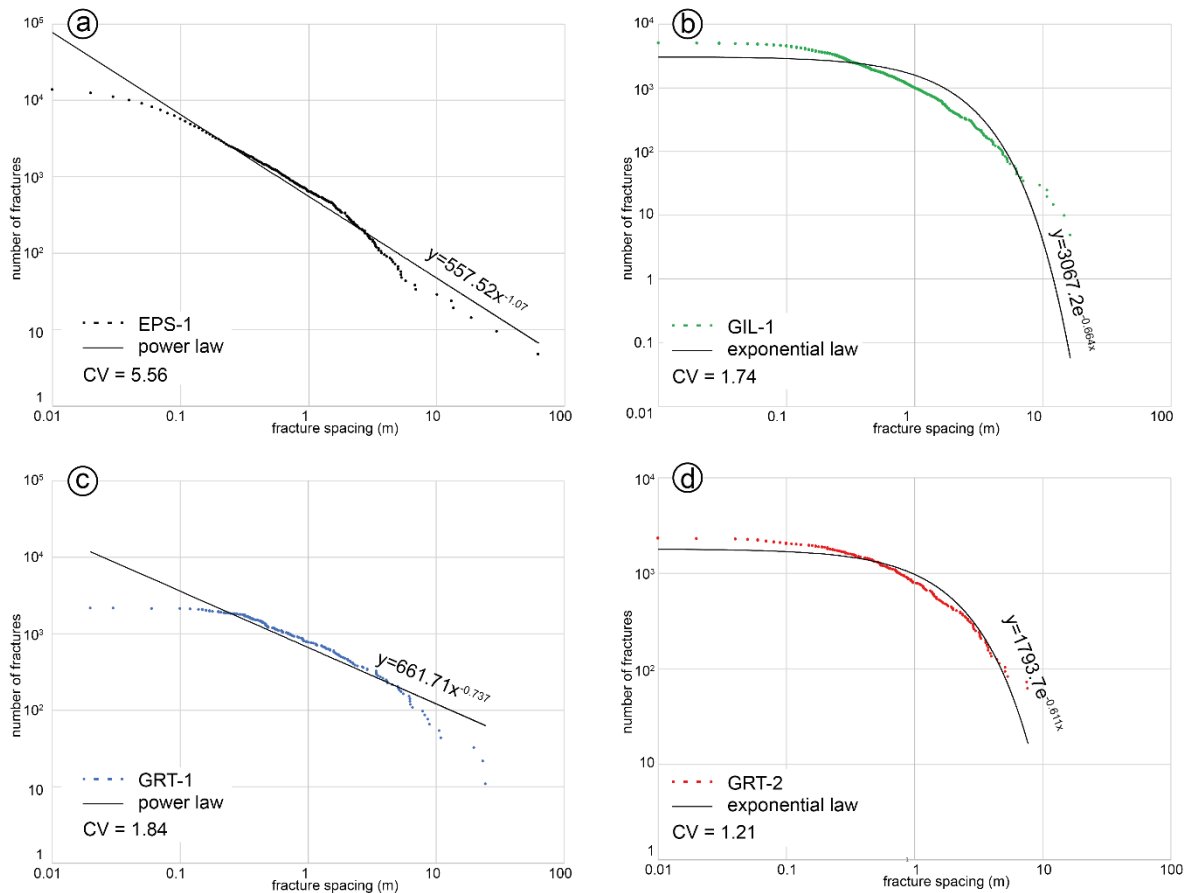


Figure 5.16: Fracture spacings presented on a log-log scale, with the type of law fitting the data and its equation, and the coefficient of variation (CV): a) For the EPS-1 well; b) For the GIL-1 well; c) For the GRT-1 well and d) For the GRT-2 well.

### 5.2.5.5. Fracture thickness

In the Figure 9, the fracture thickness is represented as cumulated along the depth for the three geothermal sites. The permeable fractures identified by various techniques in the corresponding wells were superimposed on the curves as coloured disks (Figure 5.17).

In GPK-3, GRT-1 and GRT-2, the curves show stair-like trends, with the plateau parts showing zones with high cumulated fracture thicknesses and the vertical parts showing zones with lower cumulated fracture thicknesses (Figure 5.17a and b). This indicates the existence of a fracture thickness distribution in clusters of intensively clogged fractures and zones depleted in fractures with very high clogging. For EPS-1, some steps are also observed (Figure 5.17a) that correspond to high fracture thickness zones that were observed on cores (Sausse et al., 1998). For the GIL-1 well, the curve trend is slightly different, with a fracture thickness distribution that shows a rather regular slope with depth. It could correspond to a regular distribution with depth of thicker natural fractures (Figure 5.17c).

At Soultz-sous-Forêts, in the EPS-1 well, the fracture thickness curve presents two plateaus, i.e., one at 1600 m TVD and one at 2150 m TVD, which are associated with permeable FZs (Figure 5.17a). The thickest secondary quartz filling was observed in a permeable FZ with an apparent fracture thickness of 40 cm, located at 2174 m, and it is found in the deepest plateau (Figure 5.11a & Figure 5.17a) (Genter et Traineau, 1996). In the GPK-3 well, there are at least 10 plateaus, and we observe that the permeable FZs are systematically related to the thickest fractures (plateau) (Figure 5.17a). In contrast, thicker fractures are not systematically naturally

permeable, for example, at 3200 m TVD. In the GPK-3 well, from the top basement to 2100 m TVD, the fractures are thicker and 4 of the 5 permeable fractures are concentrated in these 600 first metres of the granitic basement (Figure 5.17a). The most permeable FZ is located in GPK-2 at 2100 m TVD and shows hydraulic index of 20 L/s/bar (Jung et al., 2010; Schill et al., 2017). In GPK-3, below this FZ, there is a drop in the fracture thickness, except at 4770 m TVD, where there is a cluster of thick fractures associated with high natural permeability controlling 70% of the natural flow (Gentier et al., 2005; Sausse et al., 2010).

At Rittershoffen, in the GRT-1 well, we observe a dozen plateaus, and slightly less are observed in the GRT-2 well (Figure 5.17b). In the GRT-1 well, both the permeable FZs are associated with plateaus, and in the GRT-2 well, the permeable FZs are not systematically linked to plateaus. In the GRT-1 and GRT-2 wells, until 2300 m TVD, the fracture thickness is small, except at 2270 m TVD in GRT-1 and 2260 m TVD in GRT-2. From 2300 to 2400 m TVD, we observe a thick fracture filling, which means between 100 and 200 m below the top basement. The Rittershoffen fault is supposed to be intersected by the GRT-1 well at 2328-2368 m MD (2312-2352 m TVD) and by the GRT-2 well at 2766-2800 m MD (2382-2410 m TVD) (Vidal et al., 2017). In the granite in the GRT-2 well, 5 of the 7 permeable fractures are located in this interval. In the granite of the GRT-1 well, both permeable fractures are also located in this interval. Another interesting observation is that between 2200 and 2300 m, the cumulative fracture thickness is extremely low for these 2 wells. This interval corresponds to the propylitic monzogranite, which is very slightly altered. The fracture thickness is extremely low in this interval, except for the top basement, which is a reddish granite from 2170 to 2200 m TVD in GRT-2 and from 2215 to 2222 m TVD in GRT-1. The top of the reddish granite contains thicker fractures and is altered with a reddish colour, which is clearly because of paleo weathering (Glaas et al., 2018; Vidal and Genter, 2018).

At Illkirch, GIL-1 shows a quite regular fracture thickness distribution with depth, and there is no plateau trend, contrary to the Soultz-sous-Forêts or Rittershoffen wells (Figure 5.17c). The permeable fractures are not related to the thickest fractures (Figure 5.17c). However, we can observe a slightly higher fracture thickness from 2700 to 2830 m TVD, which means between 40 and 200 m below the top basement. Although a high fracture thickness is observed in the GIL-1 well, only 2 of the 13 permeable fractures are located in these first 200 meters of the granitic section. The 11 other permeable fractures are located far below the first 200 meters of the granitic basement. All permeable fractures are localized in sections where there is a high cumulative fracture thickness, except at 3185 and 3189 m TVD.

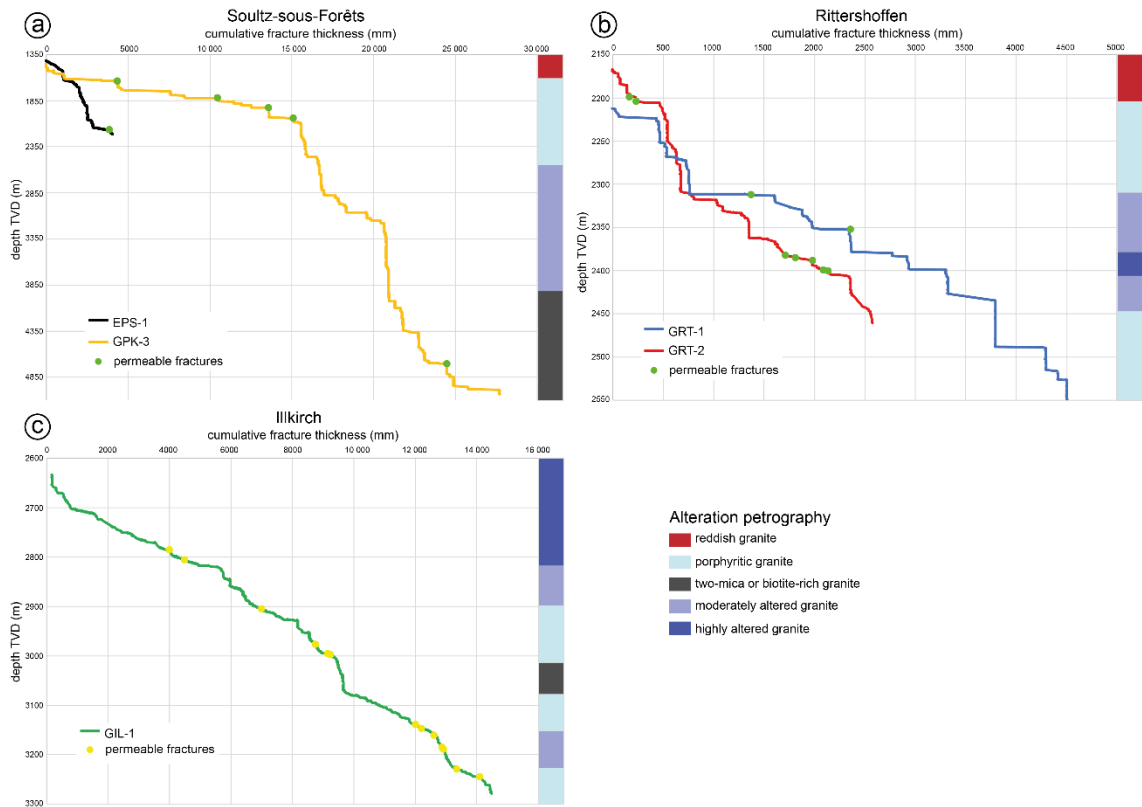


Figure 5.17: Cumulative fracture thicknesses presented along the depth (TVD) for the 3 geothermal sites, with the main petrographical units along the depth showing the alteration grades or mineralogy of the granite.: a) For Soutz-sous-Forêts with the EPS-1 and GPK-3 wells; b) For Rittershoffen with the GRT-1 and GRT-2 wells; and c) For Illkirch with the GIL-1 well.

		EPS-1	GPK-3	GRT-1	GRT-2	GIL-1
Fracture thickness density (mm/m)	Granitic section		7.8 mm/m			22.5 mm/m
	Top of the granitic section	5.1 mm/m	20 mm/m	13.4 mm/m	8.8 mm/m	29 mm/m
	Deepest granitic section		4.3 mm/m			20 mm/m
Mean fracture thickness (mm)	Granitic section		14.4 mm			14 mm
	Top of the granitic section	4 mm	33.6 mm	18.5 mm	11.3 mm	19.8 mm
	Deepest granitic section		8.3 mm			12.4 mm

Table 5.4: Fracture thickness densities and mean values of the fracture thicknesses calculated for the EPS-1, GPK-3, GRT-1, GRT-2 and GIL-1 wells. For the GPK-3 well, the top of the granitic section corresponds to the first 800 m of granite intersected by the well, and for the GIL-1 well, it corresponds to the 200 m of granitic section intersected by the well.

We calculated the fracture thickness densities expressed in mm/m for each well (Table 5.4). Surprisingly, the fracture thickness density is the lowest in EPS-1, with approximately 5 mm/m. This could be due to the method of measuring the fracture thickness, which is very accurate on cores compared to the electrical or acoustical methods, which could overestimate the fracture thickness. GRT-2 presents the lowest fracture thickness density (8.8 mm/m), and the GRT-1 density is slightly higher (13.4 mm/m). The GPK-3 and GIL-1 wells show quite similar fracture thickness density values of approximately 2 mm/m in the first 800 m; this is the highest value and is 4 times higher than that of EPS-1 and is approximately 2 times higher than that of the GRT-1 well. In the GPK-3 and GIL-1 wells, we see that the fracture thickness density is higher in the top portions of the granite (20 and 29 mm/m respectively) than in its

deepest sections (4.3 and 20 mm/m respectively). The mean values of the fracture thicknesses were also calculated (Table 5.4). In the first 800 m of the granite, the EPS-1 well presents the lowest value (4 mm), the GIL-1 and GRT-2 wells present average values (between 11 and 14 mm) and the GRT-1 and GPK-3 wells present higher values (18.5 and 33.6 mm, respectively).

## 5.2.6. Discussion

### 5.2.6.1. Is the permeability linked to the structural and hydrothermal inheritance?

We observe a vertical clockwise rotation of the fracture orientation in the studied wells from NNW-SSE/N-S in the underlying granitic basement to N-S/NNE-SSW in the overburden sediments (Figure 5.10b). The nearly vertical fracture network intersected in the granite could be inherited from the late-Variscan tectonic history of the URG, whereas the sediments could be affected by more recent regional stress fields, mainly from the Cenozoic era. The direction of the fractures in the granite could correspond to that of the Variscan era. They could belong to a larger network of Variscan normal faults reactivated under the Pyrenean compression that took place at the Eocene era (Villemin and Bergerat, 1987). In the granite, a change of the dominating dip direction (E or W) depending on the wells and the depths is observed (Dezayes et al., 2010). It is interesting to notice that the geometry of the permeable fractures in the granite is well constrained with the main striking values; NNW-SSE for Soultz-sous-Forêts, N-S for Rittershoffen and NNW-SSE for Illkirch. These directions could correspond to structures with dips approximately 70° (Figure 5.10b), which could be associated with Variscan normal faults. They could be reactivated into shear faults under the Pyrenean compression at the Eocene or into normal faults under the Rhine Graben extension at the Oligocene (Villemin and Bergerat, 1987). However, in the sediments, the fracture orientation is slightly different from that in the granite but is more consistent with the Cenozoic stress field (Figure 5.10b). In the sediments and the granite, permeable fractures strike from NW-SE to NNW-SSE, which could suggest that their present-day permeability is directly linked to the trans-tensional horizontal stress field because they are critically stressed (Evans et al., 2005) (Figure 5.9b & Figure 5.14c). They could tend to open both by dilatancy and by shearing, which are favourable conditions for permeability. Structural inheritance is guided by the geological tectonic history, which reactivated the same structural directions (NW to NNW). The ENE direction is poorly represented by the drilling data or other outcrop studies, while it is suggested to be a permeable direction by other large scale geophysical studies (Dezayes and Lerouge, 2019; Bertrand et al., 2020). This direction is interpreted as structures delimiting large blocks (Bertrand et al., 2020).

The inherited fracture directions and the actual stress orientation and magnitude are not the only factors that could explain the fracture permeability. In fact, it was observed in all the geothermal wells that the fractures in the granite are more permeable than those in the Triassic sandstones. For example, in GRT-2, it was demonstrated that the main hydraulic contribution comes from a FZ in the granitic basement, even if FZs with the same orientation were also intersected in the sediments (Baujard et al., 2017a; Vidal et al., 2017). This could be linked to the internal organization of the FZ. Indeed, at the borehole scale, the FZs in the granite present a core with cm-thick open fractures that channelize the geothermal resource. These fractures systematically correspond to the thickest fractures encountered in the wells (Figure 5.17). In addition to this structural inheritance, a hydrothermal inheritance is also predisposing the

fracture permeability. The hydrothermal inheritance is due to the successive hydrothermal events that occur in the fracture network and provoke primary mineral dissolution and secondary mineral precipitation cycles. The residual effect is complex FZs with hydrothermally altered and porous damage zones of several m-thick, where intense fluid-rock ratios occurred and led to mineral infillings that could block the permeability over time. In the sediments, the fault core generally comprises thinner fractures and lower fracture densities. Thus, the resulting connectivity of the fractures is less important and hinders reaching interesting hydraulic properties from sedimentary hard-rocks for geothermal exploitation (Vidal and Genter, 2018). According to our extensive core observations, we consider the fracture thickness to be a good proxy for the fracture hydrothermal filling rate. In the Soultz-sous-Forêts and Rittershoffen wells, the cumulative fracture thickness versus the depth shows the occurrence of the thickest fractures partly filled by hydrothermal minerals, which alternates with FZs depleted of thick fractures. The occurrence of permeable fractures is systematically associated with the thickest fractures with residual channels. In contrast, in the Illkirch well, the fracture thickness is regularly distributed along the depth and there is no clear relation between the permeable fractures and their thicknesses. Our observations could then show that the permeability in the granite is associated with the thickest fractures with channels where an intense fluid-rock ratio occurred, producing thick fracture infillings but where the permeability is maintained over time. The most permeable well of this study (GRT-2, Rittershoffen) presents an average fracture density (0.79 frac/m) and the lowest mean fracture thickness (11.3 mm). This shows that the relation between permeability and fracture thickness is valid for a given wells but is less robust for inter-site well comparison. Indeed, the lowest permeable well of this study (GIL-1, Illkirch) presents the highest fracture density (1.60 frac/m) and a fracture thickness (14 mm) higher than GRT-2. The residual permeability of the fracture depends on the competing geochemical equilibrium between the dissolution and precipitation processes, which allows to preserve, or not, natural fluid channels. The local normal fault at the interface between the sandstone and the granite encountered at Illkirch probably underwent a very intense fluid/rock ratio, which generated primary mineral dissolution and secondary clay precipitation and clogged the residual permeability. The reason of a higher fluid/rock ratio in the Illkirch reservoir could be due to the local thermal or geochemical disequilibrium between the brine and the faulted rocks, including the Buntsandstein sandstone and granitic basement. In fact, the sandstone-granite fault at Illkirch could influence the nature and the amount of the clogging differently than the intra-granite faults, such as those in Soultz-sous-Forêts and Rittershoffen. Additionally, the km-length vertical offset of the Eschau fault could explain the mineral clogging due to the high fluid/rock ratio, as well as the smearing induced by the clayey Permian layers.

#### 5.2.6.2. Which is the most permeable reservoir?

The dataset studied in this paper reveals that the initial permeability is very localized and intimately linked to the fractures in both the sediments and granite.

The most permeable reservoir in the URG is the top of the granitic basement (Vidal and Genter, 2018). The highest fracture density and thickest fractures are located in the first 500-1000 m of the hidden granitic basement (Figure 5.15 & Figure 5.17). By excluding the bias of the tool resolution, the highest fracture density values are observed in GIL-1 and GPK-2 (1.6 and 1.2 frac/m, respectively). Even if GIL-1 has a higher fracture density than GRT-2 (0.79 frac/m), the natural permeability of GIL-1 is lower. GRT-2 also presents a lower fracture thickness density and a lower fracture thickness average compared to GIL-1. For example, the trajectory

of the deviated GRT-2 well intersects the Rittershoffen fault zone over a length of more than 400 m and provides the best hydraulic productivity index due to connection between the well and the fracture network in the near-well field (Baujard et al., 2017a). Indeed, this fracture network intersected (NNW-SSE) is colinear to the local fault roughly N-S. The fracture distribution in GRT-2 is quite regular, with a negative exponential law (Figure 5.16d) but with a high concentration of localized permeable fractures at the intersection of the Rittershoffen fault zone extending throughout the entire granitic part of the well (Figure 5.15). These observations tend to show that more than the fracture density, it is the connection of the fractures intersected by a larger fault zone that contributes to the natural permeability (Neuman, 2008).

At Soultz-sous-Forêts, the local Soultz-sous-Forêts fault oriented N020°E was intersected in the Triassic formations and revealed natural permeability (Traineau et al., 1992; Vidal et al., 2015). However, the permeable fracture network intersected in the granite, which is oriented NNW-SSE, is probably more connected to a series of highly connected local-scale faults, with the largest one being oriented N145°E (Sausse et al., 2010). Between the top basement and 5000 m depth, several depth sections with variable fracture densities are observed (Figure 5.15a). The hydraulic studies showed that there are 3 superimposed reservoirs in the granite: the upper one in the first 850 meters of the granite (1400-2200 m MD), the middle one between 1550 and 2450 m (3000-3900 m MD) and the deepest one between 3650 and 3950 m (4000-5400 m MD) (Dezayes et al., 2010; Schill et al., 2017). In the first 500 meters and from 1500 to 2000 m in the granite, the fracture density is higher (0.4-1.2 and 0.4-0.8 frac/m respectively) corresponding to the upper and middle reservoirs. These 3 reservoirs are also reflected by the cumulative fracture thicknesses along the depth (Figure 5.15). Hence, in GPK-3, we observe 3 plateaus, as follows: from 1530 to 2040 m MD, corresponding to the upper reservoir; from 3000 to 3200 m MD, corresponding to the top of the middle reservoir; and from 4350 to 5000 m MD, corresponding to the deepest reservoir (Figure 5.17). The fracture spacings distribution in the EPS-1 well indicates a quite clustered spatial fracture network distribution in the upper reservoir, which could promote fracture connectivity and then higher permeability (Figure 5.16). The most permeable FZ is located in the upper reservoir, i.e., in the GPK-2 well at 2120 m MD, which showed total mud losses during drilling operations (Sausse et al., 2010). Its injectivity index is 20 L/s/bar, which is three orders of magnitude higher than in the middle and deepest reservoirs (Schill et al., 2017). For example, the highest hydraulic yield before stimulation in the deepest reservoir observed in GPK-3 corresponds to the path of a local fault, which bears 70% of the flow (Dezayes et al., 2010).

Indeed, at Illkirch, the local Eschau fault oriented N30°E at the borehole scale was intersected at the interface of the sedimentary cover and the granitic basement, but the permeable fractures are oriented NNW-SSE, which is quite different from the local fault orientation. The local fault was probably intersected in GIL-1 but does not present permeability evidence at the borehole scale, which may be due to the intense mineral clogging linked to paleo-circulations around this fault. The permeability seems more linked to the intra-granite fractures in the deepest part of the well (>3100 m MD), thus far away from this main faulted interface (2894 m MD). The permeability is lower in GIL-1 than in GRT-2, which is probably because the local normal fault zone intersected in GRT-2 exploits a first-order permeability that responds locally and rapidly. The Illkirch well is probably connected to a wide and regular network of small-scale fractures affecting the whole granitic batholith and corresponding to a distributed permeability. By considering a second geothermal well at the Illkirch site close to the first GIL-1 well, as there is no local intra-granite fault, the goal would be to maximize the connection between the intra-granite fractures and this future targeted well. As they are always the same

inherited NNW-SSW to N-S fractures that are encountered in the granitic basement, the well trajectory should favour a W-E direction with an inclination normal to the nearly vertical fractures planes, which means inclinations between 20 and 40°.

The geothermal experience in the Central URG reveals that the most permeable reservoir is located in the first 500-1000 m (TVD) of the granitic basement, which is characterized by high fracture densities and high fracture thicknesses. The trajectory of future wells should be optimized towards local intra-granite fault zones with deep dips. The inclination of the well should allow the intersection on the permeable fault zone over a greater length to maximize the connection between the well and the fracture network. The reservoir should present significant but not too important traces of fluid/rock interactions, such as secondary clay minerals and geodic quartz. Inherited fault zones from the Variscan period, probably channelize the natural hydrothermal circulations and are ideal structural targets, particularly when they are intra-granite. The trajectory tangent to the fault zone, such as in the GRT-2 well, allowed a hydrothermal well to be obtained that did not need any stimulations and that produces 3.5 L/s/bar (Baujard et al., 2017a).

#### 5.2.7. Conclusion

In geothermal reservoirs of the Central URG, we have analysed the structural characteristics of fractured networks based on borehole images and extensive coring from 8 geothermal wells at 3 sites: Soultz-sous-Forêts, Rittershoffen and Illkirch.

- In the three sites, the fractures follow the Rhenish direction (NNE-SSW) in the Buntsandstein sandstones and Muschelkalk limestones. In the granite, fractures strike NNW-SSE to N-S following the late-Variscan inherited directions.
- Few permeable fractures were observed in the Triassic sediments. At Illkirch, the faulted interface between sandstone and granite is tight and does not present interesting permeability. In the granite, the permeable fractures intersected by the Soultz-sous-Forêts and Rittershoffen wells present a conjugate set striking N-S, close to the Illkirch striking direction which is NNW-SSE. For all sites, all the permeable fractures are steeply dipping (85°E and W) and striking sub-parallelly to the maximum horizontal stress direction +/-10°.
- In the granitic basement, the fracture spacings distribution is governed by power laws and negative exponential laws, reflecting a clustered organization of the fractures. Hence, these closely spaced fractures define connected FZs, which are potential fluid pathways.
- In the three sites, the fracture density and the fracture thickness are the greatest in the first 500-1000 m of the basement; this depth section is spatially correlated with the most permeable reservoirs. However, high fracture thickness and high fracture density are not systematically related to high permeabilities. In fact, the permeability depends mainly of the connectivity of the fractures and requires a good equilibrium between the dissolution and precipitation processes to preserve the natural fluid channels.

The structural inheritance predisposes the organization of fractures in the reservoir and governs the hydrothermal inheritance. The permeability is mainly controlled by nearly vertical fracture networks intersecting both the Triassic sandstone and the crystalline Palaeozoic basement. In the Central URG, the most promising target is to intersect and run tangent to highly dipping local normal faults intra-top granite.

### 5.2.8. Acknowledgements

This manuscript was prepared as a contribution to the PhD thesis (University of Strasbourg) of Carole Glaas which is cofounded by ES-Géothermie and ANRT (French Agency for Research and Technology). The authors acknowledge the EGS Alsace project funded by ADEME (French Agency for Environment), as well as the Cantare Alsace project funded by ANR Programme under the grant agreement ANR-15-CE06-0014. The authors also acknowledge GEIE EMC, ECOGI, and ESIG for providing the Soultz-sous-Forêts, Rittershoffen and Illkirch fracture datasets.

### 5.2.9. Supporting information

This supporting information provides the detailed structural data of the permeable fractures in the wells of Soultz-sous-Forêts, Rittershoffen and Illkirch that were used in the stereoplots of Figure 5.14.

Fracture zones	Depth (m)	Dip direction (°E)	Dip (°)	Thickness (mm)	T anomaly	Mud losses or outlets	Gaz anomaly	References
GPK1-FZ1	1646	245	75	-	x			5
GPK1-FZ2	1814	27	47	-	x	X	x	6, 8, 9
GPK1-FZ3	2817	240	75	-	x	X	x	6, 9, 10
	2818.5	230	70		x	X	x	6, 10
GPK1-FZ4	3489	250	60	-	x	X	x	3, 6, 10
	3496	260	70	-	x	X	x	3, 6, 10
EPS1-FZ1	1198	247	74	-	x	X		4
EPS1-FZ2	2179	278	53	-		X		12
GPK2-FZ1	1473	68	66	-	x			5
GPK2-FZ2	1870	270	66	-	x		x	5
GPK2-FZ3	2123	70	71	-	x	X	x	5, 11
GPK2-FZ4	3464	7	81	-	x	X	x	5, 13
GPK2-FZ5	3900	270	70	-	X	x		3, 5, 13
GPK2-FZ6	4362	270	70	-	X			3, 5, 13
GPK3-FZ1	1638	46	68	15	X	x		5
GPK3-FZ2	1820	46	64	21	X			5
GPK3-FZ3	1926	210	72	24	X			5
GPK3-FZ4	2042	72	65	30	X	x		5
GPK3-FZ5	4775	234	64	123	X	x		5
GPK4-FZ1	1627	83	70	-	X	x		5
GPK4-FZ2	1735	180	73	-		x	x	5
GPK4-FZ3	1801	26	80	-	X	x	x	5
GPK4-FZ4	2017	99	77	-	X	x	x	5
GPK4-FZ5-FI-1	2068	107	80	-	X	x		5
GPK4-FZ6	2099	35	81	-	X			5
GPK4-FZ7	2270	65	60	-	X			5
GPK4-FZ8-FI-2	4217	293	83	-		x	x	5
GPK4-FZ9-FI-3	4531	111	89	-	X	x		5
GPK4-FZ10	4712	32	55	-		x	x	5
GPK4-FZ11-FI-4	4924	277	78	-		x		5

Fracture zones	Depth (m)	Dip direction (°E)	Dip (°)	Thickness (mm)	T anomaly	Mud losses or outlets	Gaz anomaly	References
GPK4-FZ12-FI-5	5100	255	70	-		x		5
GRT1-FZM1	1664.3	277	64	120	X			2
GRT1-FZM2	1760	283	32	400	X	x		2
GRT1-FZG1	2328	292	50	230	X	x		1
GRT1-FZG1	2368	259	54	240	X	x		1
GRT2-FZB1	2248	280	72	32	X			1
GRT2-FZB1	2248.5	57	80	30	X			1
GRT2-FZB2	2263	275	67	20	X			1
GRT2-FZB2	2263	55	81	18	X			1
GRT2-FZB3	2455	62	66	11	x	x		1
GRT2-FZG1	2534	89	82	62	x	x		1
	2540	97	72	15	x	x		1
GRT2-FZG2	2767	245	83	66	x	x		1
	2770.5	251	87	36	x	x		1
	2774	80	64	170	x	x		1
	2787	134	88	40	x	x		1
	2788	90	55	30	x	x		1
GRT2-FZG3	2950	270	80	-	x			1
GRT2-FZG4	3050	270	80	-	x		x	1
GIL1-FZ1	2783.6	122	89	90	x			*
GIL1-FZ2	3065.1	275	76	172	x	x	x	*
GIL1-FZ2	3089.7	231	71	36	x			*
GIL1-FZ3	3215.5	204	89	43	x	x	x	*
GIL1-FZ4	3309.2	69	84	59	x			*
GIL1-FZ5	3333.2	232	67	189	x	x	x	*
GIL1-FZ5	3336.9	69	58	26	x	x	x	*
GIL1-FZ6	3512	257	69	101	x	x	x	*
GIL1-FZ6	3522	270	81	116	x	x		*
GIL1-FZ6	3540	89	83	80	x	x		*
GIL1-FZ6	3569.5	224	82	11	x	x	x	*
GIL1-FZ6	3574.6	39	84	10	x	x	x	*
GIL1-FZ7	3625	206	69	28	x			*
GIL1-FZ7	3644.4	62	38	225	x			*
4550	1265	260	75	-		x	x	4

Table 5.S1: Major permeable fractures identified in the wells with their depth (MD), dip direction (°E), dip (°), and thickness (mm). The supposed orientations are given in italics and “-“ means no data available. The following permeability indicators associated with the fractures are reported: temperature anomalies, mud losses or outlets and gaz anomalies. The green lines correspond to fractures in the Muschelkalk; the pink lines to fractures in the Buntsandstein; and the white lines to fractures in the granite. The structural data of Rittershoffen are from Vidal et al., (2017) (1) and Dezayes et al., (2013) (2), the data of Soultz-sous-Forêts are from Dezayes et al., (2010) (3), Vidal et al., (2015) (4), Vidal et al., (2018) (5) and from Vidal et al., (2019) (6). The mud losses or outlets, as well as gaz anomalies were computed from Genter, (1989) (7), Vuataz et al., (1990) (8), Genter et al., (1995) (9), Aquilina et al., (1993) (10), (Genter and Tenzer, 1995)(11), Degouy et al., (1992) (12), Socomine, (1995) (13), and the data from the GIL-1 well are original data and were compiled for this study (\*).





## 6. Argillic and geophysical signature of permeable fracture

This sixth chapter focuses on understanding the permeability distribution by investigating hydrothermal alterations.

The first part 6.1. of this chapter presents an article submitted to the peer-reviewed *Minerals Journal*, which aims to identify the clay minerals resulting from the hydrothermal alteration of the Illkirch granite and to integrate these results at the graben scale, by comparing them with Soultz-sous-Forêts and Rittershoffen wells. The preliminary results of this study focusing on the XRD interpretation were also combined in an extended abstract accepted for presentation to the *World Geothermal Congress 2020*. This work is presented in Appendix 3. Additional data about the structural formulae of primary minerals (biotite, feldspars and carbonates) is given in Appendix 5.

The second part 6.2. of this chapter presents an article published in the peer reviewed *Geofluids Journal*, outlining the development of the SWIR method and its application to the geothermal wells of the URG targeting fractured granitic reservoirs with hot circulating fluids. This is demonstrated by applying the SWIR method to Rittershoffen GRT-2 well and to Soultz-sous-Forêts GPK-1 well. This part highlights the added value of the quantification of illitic minerals for a better understanding of clogging due to secondary clay minerals precipitation.

The third part 6.3. of this chapter is an extended abstract presented at the *European Geothermal Congress 2019* which exposes the application of the SWIR method to Rittershoffen GRT-1 well and Soultz-sous-Forêts GPK-4 well. Additional SWIR data in the GPK-2 and GPK-3 wells of Soultz-sous-Forêts are given in Appendix 4.

The fourth part 6.4. of this chapter is original and could constitute a future submission to a scientific journal. It focuses on the permeability signature and understanding of the fluid circulation in the natural reservoir intersected by Illkirch GIL-1 well. This part presents a joint interpretation of the original SWIR results acquired on the cuttings samples and the geophysical logs of GIL-1 well.

In parallel to these studies, a conjoint work was conducted and published in the peer reviewed *Journal of Volcanology and Geothermal Research* during my master internship as a contribution to the PhD thesis of Jeanne Vidal. It is about the mineralogical characterization of the granitic basement intersected by Rittershoffen GRT-1 and GRT-2 wells. This work is presented in Appendix 2.



## 6.1. Clay mineralogy: a signature of granitic geothermal reservoirs of the central Upper Rhine Graben. Accepted for publication in *Minerals Journal*.

C. Glaas<sup>1,2,3,\*</sup>, P. Patrier<sup>2</sup>, J. Vidal<sup>4</sup>, D. Beaufort<sup>2</sup>, A. Genter<sup>1</sup>

<sup>1</sup> ÉS Géothermie, : 5, rue André Marie Ampère, 67450 Mundolsheim, France.

<sup>2</sup> University of Poitiers, UMR 7285 IC2MP, HydrASA, CNRS, Bat B8 Rue Albert Turpain, TSA51106, F-86073 Poitiers Cedex 9, France

<sup>3</sup> University of Strasbourg, UMR 7516 IPGS, CNRS, 5 Rue René Descartes, 67084 Strasbourg Cedex, France

<sup>4</sup> University of Chile, FCFM, Department of Geology, Andean Geothermal Center of Excellence (CEGA), Plaza Ercilla 803, Santiago, Chile

**Keywords:** Geothermal reservoir, illite, illite-rich illite/smectite mixed-layers, hydrothermal alteration, granite, Upper Rhine Graben

### Highlights

- Propylitic and argillic hydrothermal alterations occurred in the Rhine Graben granite
- Both alterations facies are very similar in the three studied geothermal sites
- I/S mixed layers and illite are the signature of paleo or present fluid circulations

#### 6.1.1. Abstract

Clay minerals are the signature of hydrothermal alteration related to fluid circulation in volcanic and crystalline rocks. In the French part of the Upper Rhine Graben, in the deep-seated granites, illitic minerals (illite and I/S mixed layers (ml)) are typical products of the structural-ly-controlled argillic alteration in the Palaeozoic granitic basement. In the new Illkirch geo-thermal well, GIL-1, drill-cuttings were studied with various petrographic methods to determine the characteristics of illite in paleo- and present-permeable zones, and to compare the alteration mineralogy with that of geothermal Soultz-sous-Forêts and Rittershoffen sites. Alteration petrography, crystal structure, and chemical composition of illitic minerals and chemical composition of the altered bulk rocks, were performed all along the well. This complete characterization combined with geophysical logs and structural results, highlighted that the illitic minerals at Illkirch, Soultz-sous-Forêts and Rittershoffen are composed of illite and illite-rich illite-smectite mixed layers (<10% smectite). Two mineralogical assemblages are distinguished: chlorite + illite resulting from the propylitic alteration after the emplacement of the granitic basement under temperatures higher than 350°C, and illite + I/S ml + carbonates + quartz resulting from the argillic alteration due to fluid circulation in the fractures at temperatures between 130 and 160°C. Fracture zones are characterized by the occurrence of illitic minerals (illite and I/S ml), and specifically, by higher quantities of I/S ml in present-day permeable zones than in paleo-permeable zones. A conceptual model of the fracture zones at the interface between the overlying sedimentary rocks and the granitic basement is proposed. The present-day permeability distribution is controlled by the fault and fracture network, which consists of sealed zones and unsealed zones. Fluid convection in the URG implies paleo and present fluids circulating in both fractured sedimentary and crystalline reservoirs. Such circulations develop illitic minerals that could be considered as exploration guides for future geothermal sites in the URG. At Illkirch, the repartition of the present-permeable fracture zones (KFZs) in the GIL-1 well indicates that the moderately argillically altered granite distally situated from the Eschau fault is more permeable than the intensely argillically altered granite close to the Eschau fault.

### 6.1.2. Introduction

Geothermal energy is one of the best compromises in terms of low CO<sub>2</sub> emissions among renewable energy sources (Masanet et al., 2013; Pratiwi et al., 2018). An industrially viable project requires a long-life geothermal resource with hot fluids circulating through permeable fracture networks at a drillable depth. In the Upper Rhine Graben (URG), these geothermal conditions are fulfilled: brines (100g/L, >150°C) are circulating (optimate flowrate 70 L/s) through nearly vertical fracture network at the base of the Triassic sedimentary unit and the top of the Palaeozoic granitic basement (2-3 km depth) (Vidal and Genter, 2018). Even if stimulations could contribute to enhance the initial permeability after drilling operations, thereby developing viable Enhanced Geothermal Systems (EGS) projects like the Rittershoffen wells (Baujard et al., 2017a), the remaining challenge is the implementation of drilling in zones with the best reservoir quality. This requires an understanding of why some fractured zones hosted in fractured granites are more permeable than others. In such granitic geothermal reservoirs in many places like in Japan, Canada, United Kingdom and France, clay minerals have been studied extensively as they are the main products of water-rock interactions like in other high-enthalpy volcanic reservoirs or ore deposits (Storey and Lintern, 1981; Kaminen and Dugal, 1982; Meunier, 1982; Inoue, 1995; Beaufort et al., 1996; Mas et al., 2006; Nishimoto and Yoshida, 2010; Rigault et al., 2010; Buatier et al., 2012; Lévy et al., 2020). In these various hydrothermal systems, clay minerals are reliable markers of the evolution of the conditions of the hydrothermal system through their mineralogy, their crystal-chemistry, their textural properties as well as their quantity (Fulignati, 2020). Illite and illite-rich illite/smectite mixed-layers (namely I/S ml hereafter) both constituting the illitic minerals mentioned in this paper, are typical secondary minerals resulting from hydrothermal alteration of Al-bearing primary minerals in granites such as feldspars (orthoclase, plagioclase) and ferromagnesian minerals (biotite, hornblende) (Peters and Hofmann, 1984; Meunier and Velde, 1989; Nishimoto and Yoshida, 2010). The formation of illitic minerals is the result of alteration under condition of high fluid/rock ratio with dissolution of primary minerals and creation of significant secondary porosity in fracture controlled damage zones (Huang et al., 1986; Genter et al., 2000; Schmidt et al., 2018; Staněk and Géraud, 2019; Drüppel et al., 2020). In case of extreme hydrothermal alteration, the crystallisation of illite could also contribute to a partial or total sealing of the secondary porosity and the fault core, contributing to reduce the permeability of the fracture zone. Other secondary minerals associated with illitic minerals, like drusy quartz, carbonates, sulfides and sulfates may also contribute to the sealing (Gleeson and Yardley, 2002). Several geothermal sites in the URG that have been studied in details in terms of secondary mineralogy (Soulz-sous-Forêts, Rittershoffen) reported the occurrence of illitic minerals systematically associated to fracture zones and their damage zones (Ledésert et al., 1999; Genter et al., 2000; Vidal et al., 2018; Glaas et al., 2019b). These sites show contrasting natural permeability due to the complexity of the fracture zones in terms of structure and secondary mineralogy (Baujard et al., 2017a; Reinecker et al., 2019). The aim of this study is to present the secondary mineralogy related to hydrothermal alteration of the granitic rocks in the following geothermal EGS sites: Illkirch, Soulz-sous-Forêts, and Rittershoffen. This study will focus on the alteration parageneses and clay signatures of the fracture-controlled permeable zones of the Illkirch basement. To meet the above objectives, we utilize the following analytical techniques: binocular observations, chemical analyses on bulk rock, X-ray diffraction, and chemical composition of clay minerals, and geophysical logs such as temperature log, borehole image log, and gamma-ray.

### 6.1.3. Geological setting

The geothermal well of Illkirch (GIL-1) was drilled in 2018-2019 and is located a few kilometers south of Strasbourg (Figure 6.1a). This EGS project located in an urban area was initiated to supply district heating in winter and to produce electricity on the grid in summer, from a geothermal doublet. The second well of the doublet will be drilled after injection tests and reservoir studies. Before the drilling of the GIL-1 well, a large exploration campaign was conducted including aeromagnetic and gravimetric surveys, as well as a 2D seismic survey (Richard et al., 2016; Edel et al., 2018). The target of the GIL-1 well was to intersect the large-scale Eschau normal fault oriented N10°E, at the interface between the Triassic Buntsandstein and the Palaeozoic granite (Figure 6.1a and b). This target was successfully reached at 2894 m measured depth (MD) (i.e. 2636 m true vertical depth, TVD). The total depth of the well is 3800 m MD (3391 m TVD) and the open-hole crosses the Buntsandstein sandstone and Carboniferous granite from 2762 m MD (2512 m TVD) to 3800 m MD for a total open-hole length of 1038 m MD (879 m TVD).

The URG is part of the European Cenozoic Rift System (ECRIS) and is composed of Palaeozoic granites overlaid by Secondary and Tertiary sediments (Figure 6.1). Its morphology is today still controlled by NNE-SSW normal faults and fractures that are the trace of its tectonic activity. Within the URG, gravity and magnetic data delineated intrusive granitic bodies resulting from a magmatic activity of the late-Variscan age. Such intrusions were confirmed by deep drilling and they were classified as porphyritic monzogranite and two-mica granite, both of which were observed at Soultz-sous-Forêts and Rittershoffen. Geochronological data indicate that the massive porphyritic monzogranite and the two-mica granite were emplaced and cooled down at 333 and 327 Ma, respectively (Stussi et al., 2002; Cocherie et al., 2004). Upon granite emplacement, the granitic bodies first underwent a pervasive and wide-spread propylitic alteration, which transformed primary minerals to secondary chlorite, carbonates and epidote (Stussi et al., 2002) at temperatures higher than 350°C (Dubois et al., 1996). The next argillic alteration, characterized by illite and illite-smectite mixed layers (I/S ml), carbonates, euhedral quartz, and sulphides, was controlled by fracture networks (Figure 6.1c). The structural and hydrothermal histories of the URG lead to several argillic events (Figure 6.1c). However, dating of illite is rare and shows scattered ages, showing that this alteration type recurred several episodes from Permian to Cretaceous (Schleicher et al., 2006; Bartier et al., 2008). Fluid inclusions studies indicated that this argillic alteration occurred at 130-160°C, and that a deep penetration and large scale fluids movements took place between the sedimentary cover and the granitic basement (Dubois et al., 1996). Within a fractured zone, 6 generations of euhedral quartz were observed and were interpreted as the short pulses of hydrothermal fluid flow through the fracture network possibly due to seismic reactivations (Smith et al., 1998). So far, dating has not been determined for the Illkirch granite, and therefore it is not possible to address the timing of the hydrothermal events. The geological section presents two main unconformities: the Permo-Triassic and Paleocene unconformities reflect large-scale deformation with subsidence, uplift, and erosion (Durringer et al., 2019).

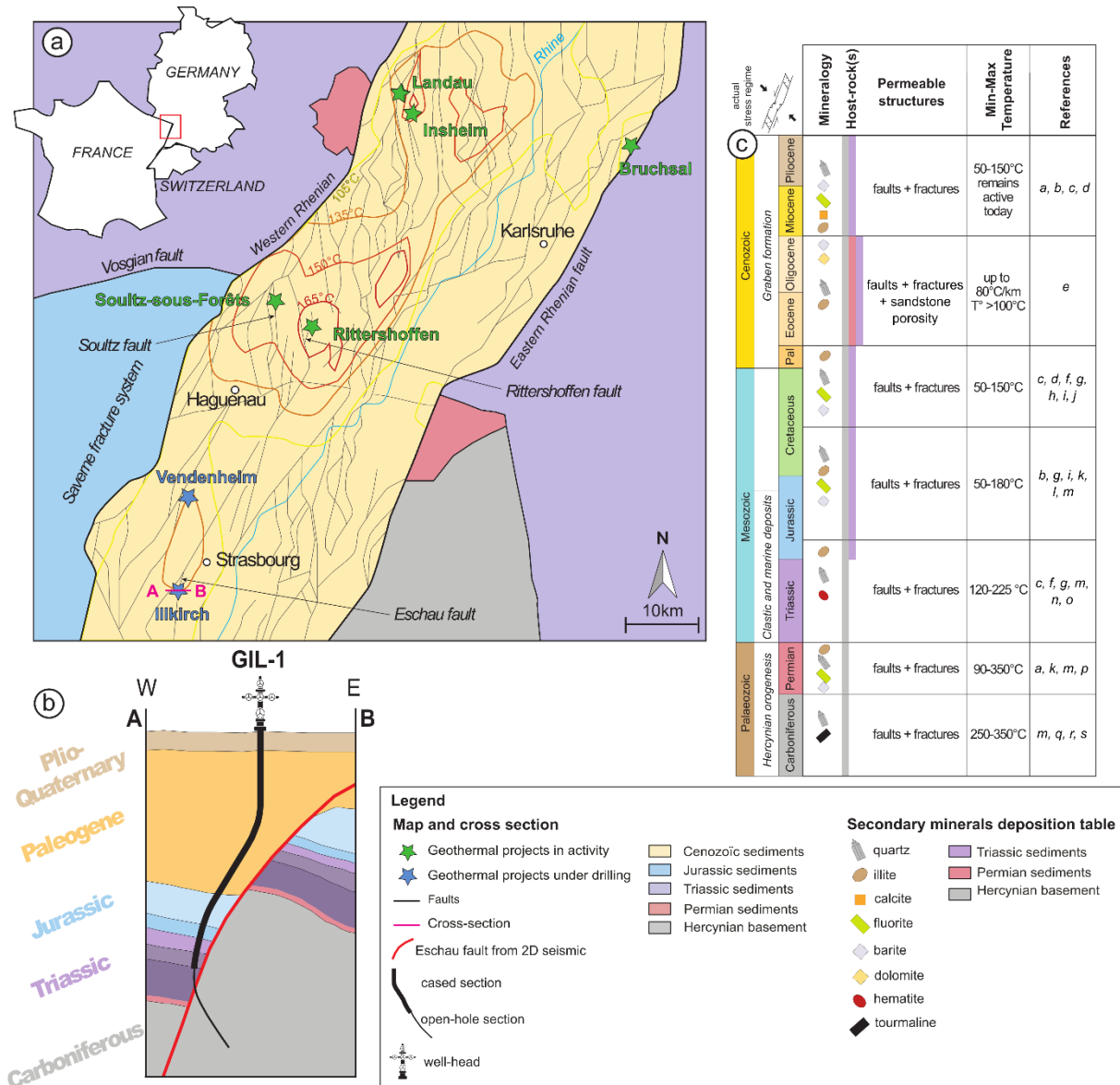


Figure 6.1: a) Structural and geological map of the central URG with isotherms at a 2km depth from the geoportal (GeOrg, 2017). The location of the geothermal power plants in exploitation and under drilling is also shown; b) cross section through the Illkirch site showing the GIL-1 well trajectory through the sedimentary layers, the Eschau fault and the granitic basement c) episodes of secondary minerals deposition occurring in the URG are presented along the geological timescale from the Palaeozoic to the Cenozoic ages, modified after Bossennec et al., (2020). References are a) (Baatartsovt et al., 2007), b) (Burisch et al., 2017a), c) (Walter et al., 2016), d) (Bartier et al., 2008), e) (Dezayes and Lerouge, 2019), f) (Clauer et al., 2008), g) (Lippolt and Seibel, 1991), h) (Burisch et al., 2017b), i) (Pfaff et al., 2010), j) (Walter et al., 2017), k) (Schleicher et al., 2006), l) (Cathelineau et al., 2012), m) (Walter et al., 2019), n) (Bons et al., 2014), o) (Staude et al., 2012), p) (Walter et al., 2018), q) (Boiron et al., 2010), r) (Cathelineau et al., 2004), s) (Schwinn et al., 2006).

Deep fluids in the geothermal reservoirs of Soultz-sous-Forêts and Rittershoffen are of the NaCl type with total dissolved solid (TDS) values close to 100 g/L (Table 6.1) (Sanjuan et al., 2016; Bosia et al., 2021). The pH values of the fluids in the reservoirs are close to 5.0 (Bosia et al., 2021) (Table 6.1). Fluids at Landau, Insheim, Soultz-sous-Forêts, Rittershoffen show a similar chemical composition (Sanjuan et al., 2016, 2021). The geochemical characteristics of the fluids were interpreted based on the chemical analyses for both major and trace elements on the water samples, and the isotopic analyses of the water samples ( $\delta D$  and  $\delta^{18}O$  of the water,  $\delta^{18}O$  and  $\delta^{34}S$  of the dissolved sulphate,  $\delta^{13}C$  of the dissolved carbonate, and the

$\delta^{7}\text{Li}$ ,  $\delta^{11}\text{B}$ , and  $^{87}\text{Sr}/^{86}\text{Sr}$ ), (Sanjuan et al., 2016, 2021). The fluid composition is controlled by the mixing between the recharge of meteoric water along the normal border faults and the primary marine brine (Sanjuan et al., 2010, 2016, 2021).

Geothermal site	$T_{\text{Bottom}}$ °C	pH	TDS g/L	Na mg/L	K mg/L	Ca mg/L	Mg mg/L	Cl mg/L	$\text{SO}_4$ mg/L	$\text{SiO}_2$ mg/L	Br mg/L	Li mg/L	Gas
Soultz-sous-Forêts	200	4.98	99	26400	3360	7020	123	55940	108	179	240	160	$\text{CO}_2$ $\text{N}_2$ $\text{CH}_4$
Rittershoffen	>160	6.27	101	27960	3890	7450	111	65030	76	175	247	203	$\text{CO}_2$ $\text{N}_2$ $\text{CH}_4$

Table 6.1: Chemical compositions of the geothermal fluid sampled in the Palaeozoic granite reservoir at Soultz-sous-Forêts in the GPK-2 well (05.02.2020) and at Rittershoffen in the GRT-1 well (04.11.2020) (Bosia et al., 2021).

Biotite compositions from the propylitically altered granite of Soultz-sous-Forêts, Rittershoffen and Illkirch plot in the subalkaline association of the magnesium-potassium field (Figure 6.2) show geochemical compositions similar to those of the outcropping granites of the Crêtes and of the Mayet-de-Montagne located in the Vosges Massif and the French Massif Central respectively (Parneix and Meunier, 1982; Chèvremont and Genter, 1989; Genter, 1989) (Figure 6.2). The biotites of Rittershoffen are less magnesian than those of Soultz-sous-Forêts, like late Variscan granites (Figure 6.2).

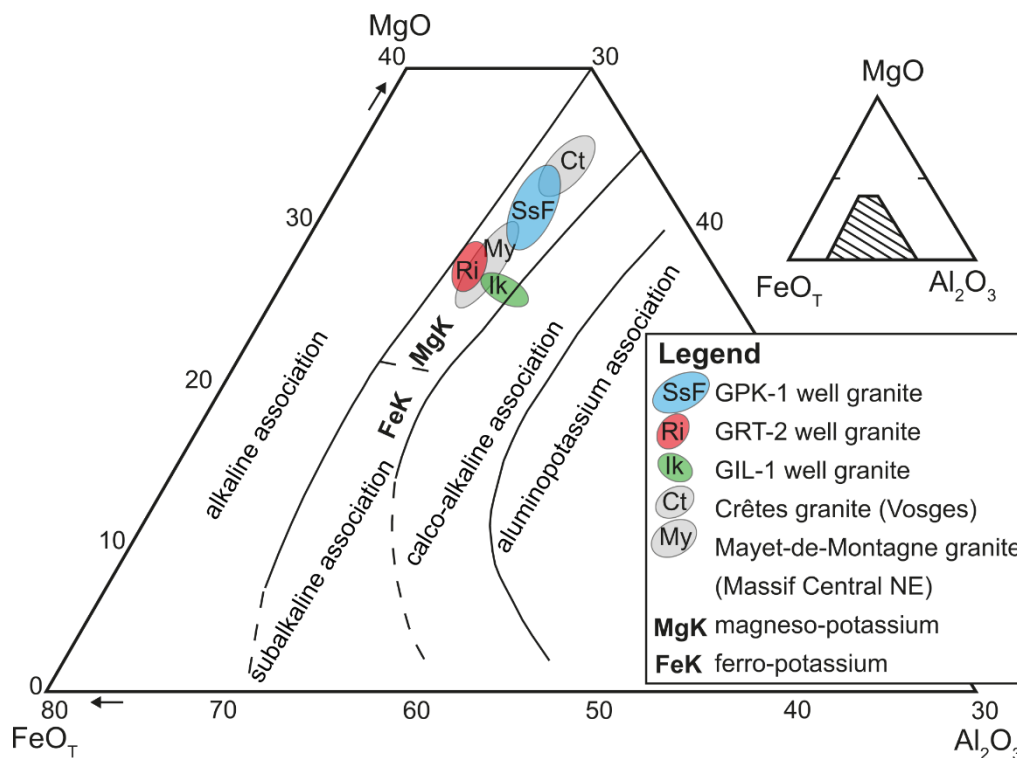


Figure 6.2: Compositions of biotite in basement rocks from Soultz-sous-Forêts (SsF), Rittershoffen (Ri) and Illkirch (Ik) in the Upper Rhine Graben compared to those of biotites from the Crêtes and Mayet-de-Montagne granites in the MgO, FeO and  $\text{Al}_2\text{O}_3$  diagram after (Parneix and Meunier, 1982; Chèvremont and Genter, 1989; Genter, 1989).

The complex tectonic history of the URG was accompanied by several hydrothermal events, which produced secondary minerals that are the records of the paleo-thermal and chemical conditions of the system (Dezayes and Lerouge, 2019; Bossennec et al., 2020). The fluid mostly circulates through the local normal faults and their associated small-scale fracture networks at the sedimentary layers-basement interface (Figure 6.1) through convection cells (Baillieux et al., 2014). Consequently, this results in the formation of several localized temperature anomalies in the URG. The Illkirch project was designed to take advantage of the Strasbourg temperature anomaly (Figure 6.1a). The secondary minerals are mainly composed

of quartz, carbonates, in addition to clay minerals (Figure 6.1c). In Illkirch, the argillic alteration is likely related to the past activity of the Eschau fault (Figure 6.1b) (Dubois et al., 1996; Stussi et al., 2002). Moreover, the dissolution features of the propylitic chlorite and its replacement by illite (argillic illitization) evidence the postdating of propylitic alteration by argillic alteration.

#### 6.1.4. Materials and methods

A detailed petrographic and mineralogical characterization of the granitic reservoir was conducted based on laboratory analyses on cuttings samples and geophysical logs, in the aim to characterize the mineralogical signature of permeable zones.

##### 6.1.4.1. Binocular observations on cuttings

The cuttings (chip samples) collected during the rotary drilling of the GIL-1 well at Illkirch were first washed using sieves and then dried on-site in an oven at 80 °C for 40 minutes, by the mud logger crew. The cuttings were sampled every 5 m depth intervals in the 8 1/2" and 6" drilled sections. Thus, each sample represents approximately 0.1 m<sup>3</sup> of drilled rock in the 6" section and 0.16 m<sup>3</sup> of drilled rock in the 8 1/2" section. The average grain size of the cuttings in each sample varies between 0.5 and 2 mm. The cuttings were observed with a binocular magnifier on-site during the drilling. The presence and abundance of each primary and secondary mineral were initially estimated with a scale of 3 classes from 0-30, 30-70, and 70-100% to build a petrographic log (Figure 6.3) representing the hydrothermal alteration grades according to previous studies on Soultz-sous-Forêts and Rittershoffen wells (Traineau et al., 1992; Ledésert et al., 1999; C. Glaas et al., 2018).

##### 6.1.4.2. Geophysical logs

###### *Gamma-Ray*

The gamma ray (GR) log is indicative of natural radioactivity (cumulative emissions, mainly from uranium (U), potassium (K), and thorium (Th)) in gAPI (American Petroleum Institute); GR measurements of the GIL-1 well were performed every 2.5 cm (Figure 6.3). The GR log is aimed at interpreting lithology and rock composition by detecting clay minerals rich in potassium (mainly illite). In the altered crystalline basement, negative GR anomalies may reflect the occurrence of drusy quartz veins in the host rock (Genter et al., 2000; Dezayes et al., 2010). Generally, the GR data are an indicator of hydrothermal alteration and thus provide information regarding paleo-permeability.

###### *Temperature*

Thermal anomalies identified on temperature profiles are interpreted as the signatures of present-day fluid circulations between the well and the formation and thus reflect the present - permeable fracture zones (KFZs) (Barton et al., 1995; Davatzes and Hickman, 2005; Bradford et al., 2013; Vidal et al., 2019; Kraal et al., 2021). In the GIL-1 well, the temperature profiles of the open hole section were acquired inside the drill strings due to various technical constrains. Because of time constrains during drilling operations, it was not possible to wait until thermal equilibrium for running the temperature profiles. Therefore, in order to help identify the permeable zones, the temperature logs were performed only several hours after substantial cold-water injections. Using this method, the permeable zones cooled down by the injections appear as negative thermal anomalies on temperature profiles (after a short heating period) (Figure 6.3). The thermal anomalies seem to be rather influenced by the absence of thermal

equilibrium than the fact that they were acquired in the drill strings. In the GIL-1 well, one temperature anomaly was identified in the Buntsandstein sandstone and six were identified in the granitic section (Figure 6.3). These temperature anomalies are hereafter named the present-KFZs, as opposed to the paleo-KFZs that largely designate all the zones affected by argillic alteration and do not exhibit temperature anomalies (Figure 6.3).

#### *Fractures from borehole images*

The fractures were extracted from electrical image logs acquired in the open-hole section of the GIL-1 well. Then, the major fractures were selected on the basis of the following criteria:

- The aperture corrected from the borehole orientation >10 mm
- The resistivity <2000 ohm.m on the induction log
- The conductive contrast on the electrical image logs

The fracture density curve is also presented in Figure 6.3.

#### 6.1.4.3. Chemical analyses on bulk rock

Nineteen cuttings samples were selected in the granitic section of GIL-1 well, covering the several alteration facies and permeable zones, for chemical analyses of major oxides. Chemical analyses were conducted at the CRPG laboratory in Nancy (France). Samples with cuttings sizes larger than 1 mm were grinded. Analyses of the major elements oxides (SiO<sub>2</sub>, Al<sub>2</sub>O<sub>3</sub>, Fe<sub>2</sub>O<sub>3</sub>, MnO, MgO, CaO, Na<sub>2</sub>O, K<sub>2</sub>O, TiO<sub>2</sub>, P<sub>2</sub>O<sub>5</sub>) were carried out on samples initially melted in LiBO<sub>2</sub> and put in acidic solution. Analyses were done with ICP-OES instrument (Carignan et al., 2001). These chemical analyses were performed in order to follow the chemical differences between the several alteration grades (Table 6.2).

#### 6.1.4.4. X-Ray Diffraction

X-ray diffraction analyses were carried out on 71 samples of granitic cuttings of the GIL-1 well to identify the clay minerals and associated secondary minerals. The sampling was concentrated in the permeable and altered fracture zones (FZs), as well as in the unaltered granite (GRAN and GRBT). 15 of the 71 samples were also selected to analyze the bulk rock mineralogy. These 15 cuttings were grinded with an ring and agate mills and prepared as disoriented powders. Analyses were carried out on a Phillips X'Pert Pro (Panalytical B.V.) diffractometer (CuK $\alpha$  radiation, 40kV, 40mA). The analytical conditions were as follows: angular domain: 2-65° 2 $\theta$ ; step increment: 0.0235 2 $\theta$  and counting time per step: 0.90 s. The 71 cuttings were used for clay minerals identification were dispersed in distilled water by ultrasonic vibration without any preliminary grinding to avoid contamination of the <5 $\mu$ m fraction by primary micas. Oriented powders were prepared from the <5 $\mu$ m fraction size separated from suspension in water by sedimentation. Clay minerals were identified by XRD of air-dried (AD) and ethylene-glycol (EG)-saturated oriented powders carried out on the same diffractometer. The analytical conditions were as follow: angular domain: 2-35° 2 $\theta$ ; step increment: 0.0235 2 $\theta$  and counting time per step: 0.73 s. XRD data acquisition and treatment were conducted using the X'Pert HighScore software (PANalytical B.V.) at the IC2MP laboratory at the University of Poitiers, France. X-ray identification of clay minerals, which is based on the d-values and the relative intensity of their 00 $\ell$  reflections, has been done by reference to the works of Brindley and Brown, (1980) and Moore and Reynolds, (1997). After background stripping, the peak profiles of illite-like minerals were decomposed in the range 6-11 °2 $\theta$ , as a sum of gaussian curves using the Fityck software (Wojdyr, 2010).

#### 6.1.4.5. Optical microscope and Scanning Electron Microscope coupled with Energy Dispersive Spectroscopy

7 samples were selected in the granitic section to prepare polished thin sections for scanning electron microscope (SEM) analyses. These 7 samples are composed of 6 cuttings samples and 1 rock sample of which its depth is unknown as it came to the surface within the drilling tools. These 7 polished thin sections were first observed with an optical microscope to previously select microsites for SEM analyses (Figure 6.4). These samples were selected to cover permeable and non-permeable zones as well as the several alteration grades of the granite:

- in 2 permeable zones at 3071 m and 3340 m,
- in 4 non-permeable zones at 3005, 3482, 3573 and 3678 m.
- in the HEXT grade at 3005 m,
- in the HHIG grade at 3071 m,
- in the HMOD grade at 3482 and 3573 m,
- in the HLOW grade at 3340 and 3678 m.

For the 6 cuttings samples, the thin sections are made of grains in a resin matrix, thus the texture of the rock as well as the continuity of veinlets are lost. The SEM observations were conducted on a JEOL JSM-IT500 SEM equipped with a BRUKER linxeye Energy dispersive spectrometer EDS associated with SPIRIT software at the IC2MP laboratory, University of Poitiers, France. These analyses were conducted in order to obtain chemical composition of preselected minerals. The analytical conditions were as follows: 15kV; 1nA; counting time: 50 s; and working distance: 11 mm. Analyses were calibrated using natural standards: albite for Na, Al, Si; almandine for Fe, Mg; diopside for Ca, orthoclase for K; spessartine for Mn and Ti metal for Ti and corrected by PhiRhoZ method. Before measurement, thin sections were coated with carbon.

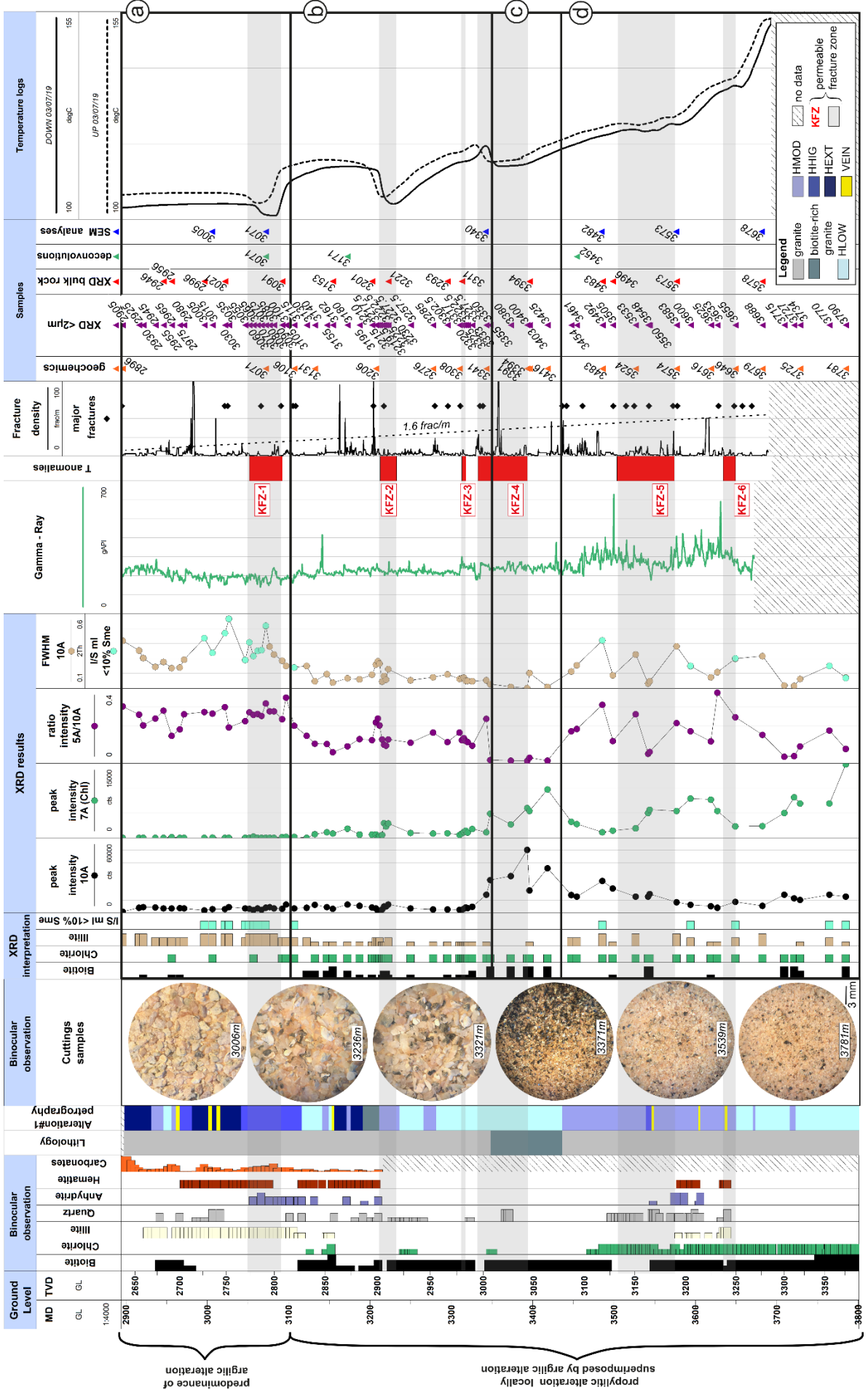


Figure 6.3: Composite log from the lower part of the open-hole of the GIL-1 well granitic basement, presenting from left to right: the petrographic log built from the binocular lens observations; the XRD results from the oriented fractions <5 µm and their interpretation; the gamma-ray log; the permeable zones; the fracture density; the major fractures and the samples for which deconvolution of the peak at 10 Å, and SEM analyses were performed. HLOW, HMOD, HHIG and HEXT: low, moderate, high and extreme argillic alteration, VEIN: secondary drusy quartz veins, KFZ: permeable fracture zones. The granitic basement is divided in four depth sections characterized by a) intense argillic alteration; b) and d) propylitic alteration locally superimposed by argillic alteration and c) fresh biotite-rich granite.

## 6.1.5. Results

### 6.1.5.1. Petrographic log - Mineralogy

Two types of granite were crosscut by the GIL-1 well. First, a porphyritic monzogranite containing biotite, oligoclase, perthitic orthoclase and quartz corresponds to the porphyritic monzogranite encountered in the Soultz-sous-Forêts and Rittershoffen wells, which is named “GRAN” (Genter and Traineau, 1993; C. Glaas et al., 2018). Second, a biotite-rich granite was also encountered on a depth interval between 3346 and 3433 m MD (this facies is named “GRBT”). Argillic alteration is pervasive in the upper part (from 2894 to 3104 m MD, Figure 6.3a) of the drill hole whereas propylitic alteration occurs mostly in the bottom part (from 3104 to 3800 m MD, Figure 6.3b and d). Nevertheless, weak argillic alteration is also observed around permeable fractures in the granitic basement (Figure 6.3b and d). On the basis of petrographic and mineralogical considerations, we can divide the petrographical log into 3 different domains.

The first one corresponds to granite between 3104 and 3350 m MD and between 3433 and 3801 m MD (Figure 6.3b and d), in which pervasive propylitic alteration has been overprinted only locally by argillic fracture-controlled argillic alteration. Illitic minerals associated with quartz veinlets (VEIN) and anhydrite infilled the fractures (Figure 6.4i and Figure 6.3b and d) and feldspars are variably replaced by illite in wallrocks (Figure 6.3a, b, c and d). Apatite is also locally observed, associated to chloritized and illitized biotites with Ti-oxide inclusions (Figure 6.4j). Calcite is not recorded below 3200 m MD but we cannot exclude its presence under the form of local veins in the vicinity of permeable fractures. Large size illite crystals (10-20 µm, Figure 6.4d) appear to have crystallized earlier than the fine grained illitic matrix and could be related to the propylitic alteration event (Genter, 1989; Ledésert et al., 1996, 1999, 2010; Jacquemont, 2002; Schleicher et al., 2006; Bartier et al., 2008; Gardien et al., 2016; Vidal et al., 2018). The presence of two populations of illitic minerals based on their crystal size suggests that at least two alteration events affected these primary minerals. In addition to these large size illitic phases, the propylitic alteration consists of disseminated secondary Fe-Mg chlorite which crystallized as replacement of the igneous biotites. Nevertheless, relicts of primary biotite are still visible in some places (Figure 6.5a). This pervasive chloritization did not precipitate from the fluids, and is not spatially related to fractures or veins but occurs essentially as a biotite pseudomorph in association with inclusions of Ti-oxides and micro-lens of carbonates, feldspars and quartz. These observations characterize the slightly and moderately altered granite (low and moderate hydrothermal alterations, respectively: HLOW and HMOD).

The second petrographical domain is related to an intense argillic alteration observed all around the past and present permeable fractures. This alteration dominates at the upper granite (2894 to 3104 m MD) with very high amounts of illitic minerals in the core of faults as well as in the surrounding damage zones, where it infills fractures in the fault gouge and

secondary pores formed by dissolution of feldspars and chlorite in the altered wall-rocks (Figure 3a). Based on crystal size, two populations of illite can be recognized (Figure 6.4f, g and h), among which fine grained illitic matrix is predominant (<5 µm, Figure 6.4e, f, g and h). Secondary hematite and anhydrite (Figure 6.4i and Figure 6.3a) as well as drusy quartz (VEIN) are observed locally in small amounts (Figure 6.4i and Figure 6.4a). Calcite is present in substantial amounts (Figure 6.3). This second domain reflects a granite highly and extremely altered (+/-HMOD, high and extreme hydrothermal alterations, respectively HHIG and HEXT).

The third petrographical domain corresponds to the fresh biotite-rich granite. Preservation of primary biotite and muscovite evidence an unaltered granite rich in biotite (Figure 6.3c). This biotite-rich granite (GRBT) is observed from 3350 to 3433 m MD.

#### 6.1.5.2. Geophysical logs

##### *Gamma-ray*

The top of the granite (from 2900 to 2940 m MD) is characterized by high values around 230 gAPI, plausibly due to the abundance of illite at the faulted interface between sandstone and granite (Figure 6.3). In the intense argillic alteration domain that extends from 2940 to 3100 m MD, the GR values are around 190 gAPI. At deeper zones from 3100 to 3433 m MD the GR values oscillate between 225 and 245 gAPI in both domains of propylitic alteration and fresh biotite-rich granite. Then, in the deepest part, the GR values are very disturbed, showing two hips from 3450 to 3530 and from 3560 to 3670 m MD where the values oscillate between 180 and 511 gAPI. Below this zone, the GR was not measured. Generally, the GR intervals fit well with the vertical distribution of the different mineralogical assemblages as defined previously (Figure 6.3). However, in the Illkirch well no clear correlation exists between the grade of alteration and the GR values.

##### *Permeable fracture zones*

27 major fractures were identified in the granitic section (Figure 6.3). In addition to these major fractures described above, smaller-scale fractures are also observed on electrical image logs. The density of fractures measured in the Illkirch well (average 1.6 frac/m) is higher than that measured with equivalent techniques of electrical and acoustic borehole images in the Soultz-sous-Forêts (average 0.6 frac/m) and Rittershoffen (average 0.7 frac/m) wells. In the granitic open-hole of the GIL-1 well, six temperature anomalies were interpreted as permeable zones and were linked to major fractures observed on the electrical borehole images. These permeable fracture zones (KFZ) are numbered as follows (Figure 6.3):

- KFZ-1 from 3050 to 3090 m MD,
- KFZ-2 from 3210 to 3230 m MD,
- KFZ-3 from 3310 to 3315 m MD,
- KFZ-4 from 3330 to 3390 m MD,
- KFZ-5 from 3500 to 3570 m MD,
- KFZ-6 from 3630 to 3645 m MD.

Only one (KFZ-1) is in the granite strongly affected by vein alteration and the five other KFZs are located in the granite affected predominantly by propylitic alteration but are generally close to quartz veins or HMOD alteration grade. The particularity of KFZ-4 is its position at the interface between the pervasively altered granite and the fresh biotite-rich granite (Figure 6.3b and c). It appears that the occurrence of KFZ is systematically associated with the occurrence of clusters of major fractures (Figure 6.3), regardless of fracture densities.

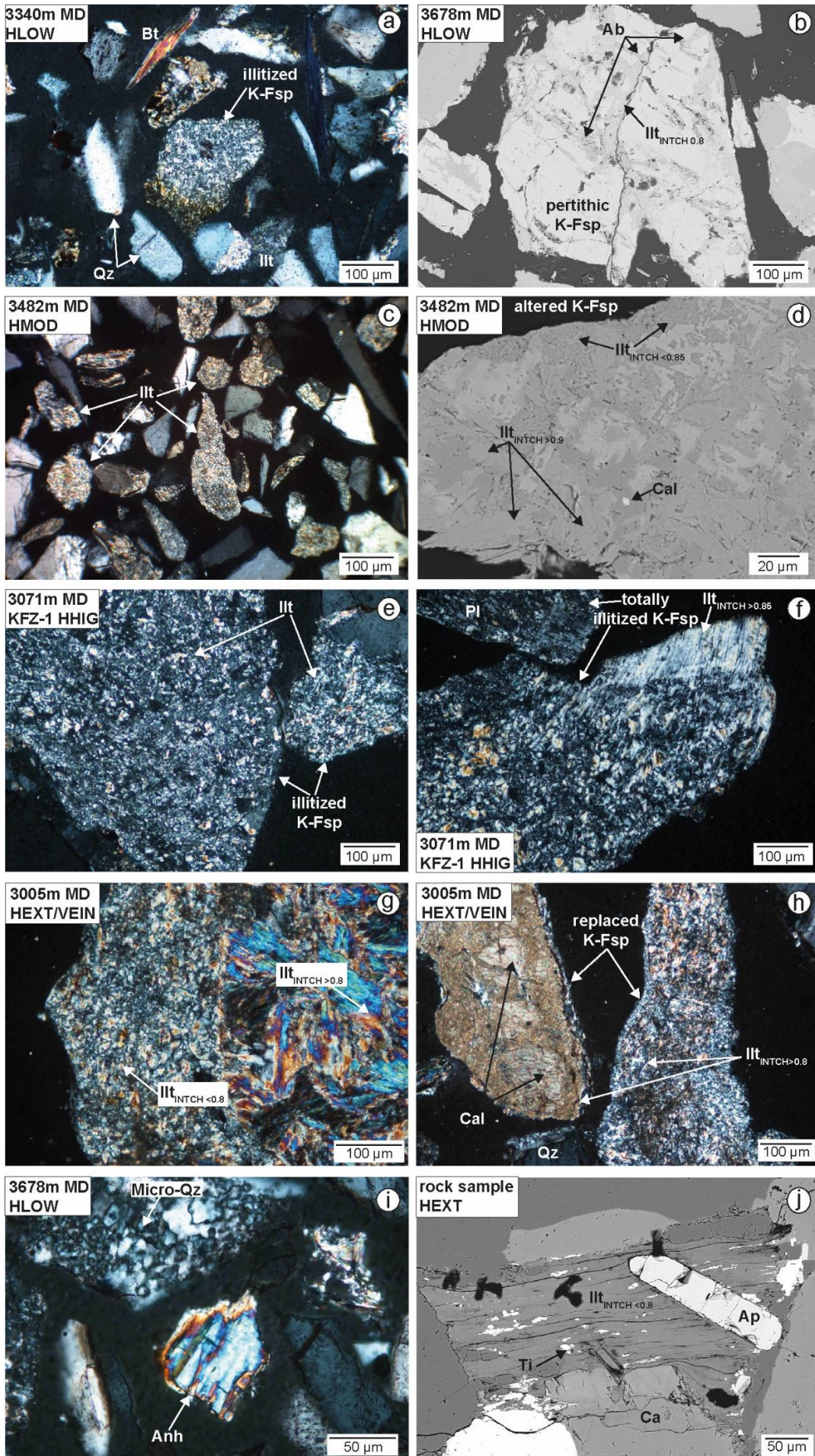


Figure 6.4: Microscopic observations of thin sections of cuttings (a, b, c, d, e, f, g, h, i) and rock sample (j) fixed in epoxy in GIL-1 at a) 3340 m MD (crossed polarized light, CPL), b) 3678 m MD (SEM observations), c) and d) 3482 m MD (CPL and SEM), e) and f) 3071 m MD (CPL), g) and h) 3005 m MD (CPL), i) 3678 m MD (CPL), j) unknown depth (SEM). Anh = anhydrite, Ap = apatite, Bt = biotite, Cal = calcite, Ill = illitic minerals, K-Fsp = potassic feldspar, Pl = plagioclase, Qz = quartz, Ti = non identified titanium oxide; INTCH = interlayer charge; HLOW, HMOD, HHIG and HEXT = low, moderate, high and extreme argillic alteration.

### 6.1.5.3. Bulk rock chemical analyses

The chemical compositions of the bulk rock major element oxides on bulk rock are presented in Table 6.2. The loss of ignition (LOI) value includes H<sub>2</sub>O (corresponding to hydroxyl group of clay minerals), and CO<sub>2</sub> corresponding to carbonates. We observe that the LOI values increase with the hydrothermal alteration grades (Table 6.2). This observation is generally valid for all samples except for quartz vein-bearing alteration zones at 3005 and 3724 m MD (Table 6.2). Considering that LOI is due to the dehydroxylation of the clay minerals (5.5-13% H<sub>2</sub>O according to (Wilson, 2013)) and the decarbonation of calcite (44% of CO<sub>2</sub>), and that calcium is mostly contained in the calcite, then it is possible to estimate the LOI value reflecting only the secondary clay minerals (illite and chlorite). Hence, the Ca amount in primary feldspars can be neglected because CaO in oligoclase is between 3 and 5% and as feldspars represent 19% of the granite mass. When the samples are hydrothermally altered, the CaO and K<sub>2</sub>O values in mass % increase, reflecting the presence of carbonates and illite. SiO<sub>2</sub> value in mass % varies according to the frequency of quartz veins intersected. The mean LOI value for unaltered biotite-rich or porphyritic monzogranite or even HLOW is 2 %, for HMOD it is around 4 %, for HHIG it is around 6 %. Thus, the LOI seems to be a good proxy for alteration grade. The K<sub>2</sub>O and CaO values follow the same evolution that the LOI values, which confirms that illite and calcite are the main mineral phases of the argillic alteration in the wall rocks. Variation of the SiO<sub>2</sub> values is more erratic than that of the K<sub>2</sub>O, CaO and LOI values, due to the heterogeneous distribution of quartz veins.

Depth MD GL	Facies and alteration	SiO <sub>2</sub> (%)	Al <sub>2</sub> O <sub>3</sub> (%)	Fe <sub>2</sub> O <sub>3</sub> (%)	MnO (%)	MgO (%)	CaO (%)	Na <sub>2</sub> O (%)	K <sub>2</sub> O (%)	TiO <sub>2</sub> (%)	P <sub>2</sub> O <sub>5</sub> (%)	LOI (%)	Total (%)
3391 m	GRBT	66.89	13.91	4.24	0.14	1.99	1.98	2.78	4.77	0.59	<L.D.	2.02	99.32
3394 m	GRBT	69.07	14.17	3.14	0.11	1.48	2.07	2.99	4.65	0.42	<L.D.	1.94	100.02
3416 m	GRBT	65.94	14.23	4.52	0.15	2.45	1.81	2.87	4.73	0.65	<L.D.	2.26	99.62
	MEAN GRBT	67,30	14,10	3,97	0,13	1,97	1,95	2,88	4,72	0,55	<L.D.	2,07	97,58
3131 m	HLOW	65.39	15.23	2.32	0.10	1.20	3.36	2.73	5.28	0.25	<L.D.	4.03	99.88
3308 m	HLOW	65.83	17.13	2.55	0.08	1.09	3.00	4.11	4.44	0.33	0.11	1.54	100.20
3341 m	HLOW	70.38	11.04	2.51	0.07	0.73	2.75	1.54	4.62	0.29	<L.D.	4.85	98.77
3679 m	HLOW	69.95	12.74	2.13	0.08	0.91	2.19	3.60	4.46	0.21	<L.D.	4.14	100.40
3781 m	HLOW	72.94	13.08	2.16	0.09	0.82	1.89	2.77	4.68	0.23	<L.D.	2.04	100.69
	MEAN HLOW	68,90	13,84	2,33	0,08	0,95	2,63	2,95	4,70	0,26	0,11	3,32	96,67
3276 m	HMOD	65.48	16.47	2.64	0.08	1.18	2.78	3.84	4.62	0.34	0.11	2.06	99.59
3483 m	HMOD	70.39	12.27	1.95	0.08	0.94	2.75	1.00	5.66	0.23	<L.D.	4.14	99.41
3524 m	HMOD	72.77	11.90	1.87	0.07	0.88	2.36	0.81	5.38	0.22	<L.D.	4.05	100.31
3574 m	HMOD	69.43	12.26	2.11	0.09	1.10	2.00	3.11	4.89	0.29	<L.D.	4.42	99.69
3644 m	HMOD	71.35	13.14	2.11	0.07	0.84	1.96	2.13	5.17	0.25	<L.D.	3.52	100.53
	MEAN HMOD	69,88	13,21	2,14	0,08	0,99	2,37	2,18	5,14	0,27	<L.D.	3,64	96,27
3725 m	HMOD/VEIN	73.61	13.24	1.75	0.06	0.70	1.43	3.22	4.67	0.20	<L.D.	1.86	98.89
3071 m	HHIG	60.36	14.75	2.90	0.15	1.81	4.74	1.79	6.07	0.22	<L.D.	7.36	100.16
3106 m	HHIG	65.25	13.32	2.46	0.11	1.50	3.96	1.75	5.58	0.20	<L.D.	5.76	99.90
3206 m	HHIG	61.76	14.47	5.35	0.11	1.11	3.91	2.16	5.14	0.27	<L.D.	5.37	99.65

	MEAN HHIG	62.46	14.18	3 ;57	0.13	1.48	4.20	1.90	5.60	0.23	<L.D.	6.16	93.74
2896 m	HEXT	59.66	2.57	1.52	0.29	0.96	17.61	0.05	1.31	0.06	<L.D.	15.68	99.71
3006 m	HEXT/VEIN	64.27	14.72	2.42	0.10	1.08	3.70	1.45	5.90	0.24	<L.D.	6.06	99.94

Table 6.2: Chemical compositions of major element oxides of 20 cuttings samples from the GIL-1 well. Samples are sorted by facies and grade of alteration. GRBT: Biotite-rich granite, HLOW, HMOD, HHIG and HEXT: low, moderate, high and extreme argillic alteration, VEIN: secondary drusy quartz veins.

#### 6.1.5.4. Identification of clay minerals

The clay minerals in the GIL-1 well are dominated by potassic dioctahedral TOT (tetrahedral-octahedral-tetrahedral) clay minerals including illite and I/S ml, related either to argillic alteration in the vicinity of fractures (the dominant contribution) or to the propylitic alteration in the poorly altered granite in which chlorite and coarse grained illite replaced biotite and feldspars, respectively.

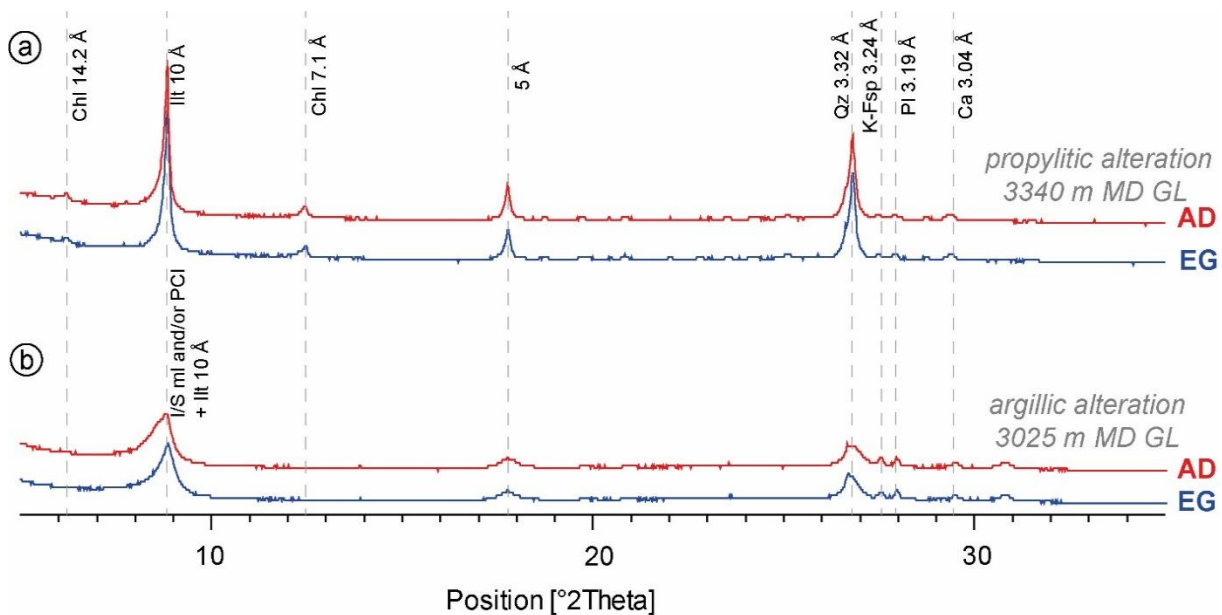


Figure 6.5: XRD results of oriented samples made on the fraction <math>< 5 \mu\text{m}</math> from the GIL-1 well under air dried (AD) and ethylene-glycol (EG) conditions. The sample at 3025 m MD presents a predominance of I/S ml and PCI whereas the sample at 3340 m MD presents a predominance of well crystallized illite (WCI) (+/- micas). Ca = calcite, Chl = chlorite, Ill = illite, I/S ml = illite-rich illite-smectite mixed layers, K-Fsp = potassic feldspar, Pl = plagioclase, Qz = quartz.

#### Illite and illite-rich I/S ml

The XRD pattern of air-dried (AD) as well as ethylene-glycol (EG) saturated powder-prepared illite is characterized by the reflections at 10, 5 and 3.33 Å whereas, due to their swelling behavior, XRD reflections of illite-rich I/S ml slightly shift after EG saturation so resulting in asymmetrical broadening of the peak at 10 Å. As the XRD reflections of illite are similar to those of micas, a combination of several parameters such as the ratio I002/I001 and the FWHM of the peak at 10 Å can be used to differentiate illite from primary biotite.

The value of I002/I001 is lower than 0.10 for trioctahedral micas (biotite here), whereas dioctahedral clays (illite here) will have a value of I002/I001 between 0.37 and 0.55 (Brindley and Brown, 1980) (Figure 6.3). Biotite was identified when the value of I002/I001 was lower than 0.10, and the full width at half maximum (FWHM) of the peak at 10 Å lower than  $0.2^\circ 2\theta$

suggesting the predominance of biotite (in the <5  $\mu\text{m}$  fraction) in the zone from 3350 to 3433 m MD GL, consistent with the binocular observations (Figure 6.3 and 6.5). Biotite occurrence in the fine fraction is due to relicts of biotite layers after incomplete chloritization, essentially in the propylitic altered zones (Figure 6.3b and c).

The FWHM calculated on the XRD reflection at 10  $\text{\AA}$  reflects crystallinity along the c axis. The FWHM of the peak at 10  $\text{\AA}$  higher or close to  $0.2^\circ 2\theta$  is considered as a major contribution of illitic minerals (Brindley and Brown, 1980) (Figure 6.3). Thus, the FWHM values ranging between 0.2 and 0.6  $^\circ 2\theta$  indicated in the log (Figure 6.3) are indicative of the predominance of illite and/or illite rich I/S ml. The XRD patterns in Figure 6.5a show that illite is the main aluminous clay associated with the propylitic alteration as no swelling is observed after EG saturation. The deconvolution of the 10  $\text{\AA}$  peak in sample at 3171 m MD (propylitic granite – Figure 6.6a & b) shows that this peak is in fact more complex including a well crystallized illite (WCI) contribution associated with a poorly crystallized illite (PCI) contribution (Figure 6.6a & b). The XRD of illitic minerals associated with argillic alteration displays broader peaks with a slight swelling behavior after EG saturation as illustrated by the peak at 10  $\text{\AA}$  in Figure 6.5b. The deconvolution of the peak at 10  $\text{\AA}$  for the sample affected by argillic alteration superimposed on propylitic alteration (3452 m MD) shows the presence of an I/S ml phase coexisting with WCI and PCI (Figure 6.6c and d). The deconvolution of the peak at 10  $\text{\AA}$  for the sample affected by argillic alteration (3071 m MD) indicates the coexistence of at least two I/S ml phases in addition to PCI (Figure 6.6e and f). These two I/S phases have their peaks around 10.91  $\text{\AA}$  (I/S ml1) and 10.23  $\text{\AA}$  (I/S ml2) under AD conditions and separate into 2 other peaks around 10.98  $\text{\AA}$  and 9.88  $\text{\AA}$  for the first phase (I/S ml1) and around 10.45  $\text{\AA}$  and 9.93  $\text{\AA}$  for the second phase (I/S ml2) (Figure 6.6e and f). Also, the existence of heterogeneous illites in terms of crystallinity (PCI and WCI) is consistent with the petrographic observations showing a fine-grained matrix postdating large illite crystals. The WCI contribution seems predominant in the propylitic illite (Figure 6.6a and b) whereas the PCI contribution predominates in the argillic illite (Figure 6.6c, d, e and f). The illitic minerals related to argillic alteration differ from those related to propylitic alteration by the presence of I/S mixed-layer minerals (Figure 6.6). It can be noted that the amount of I/S ml is significantly higher with at least two phases in samples from the present KFZ (3071 m MD) than in those from the paleo KFZ with one phase (3452 m MD). The 00l peak positions of I/S ml, is interpreted that the amount of smectite in the I/S ml does not exceed 10% (Brindley and Brown, 1980).

In the GIL-1 well the FWHM of the non-deconvoluted 10  $\text{\AA}$  peak varies with the grade of argillic alteration: in the top of the granite from 2984 to 3100 m MD where argillic alteration occurs, it is close to  $0.28^\circ 2\theta$ , whereas in the weakly altered part of the granite from 3100 to 3800 m MD the FWHM is of 0.18  $2\theta$ . Similarly, the highest values around 0.55  $2\theta$  were observed at 3026 and 3071 m MD in the argillic alteration whereas the lowest values around 0.13  $2\theta$  were observed in the biotite-rich granite (Figure 6.3a & c). This variation could be due to an increase of I/S ml contributions in argillic illitic minerals (as illustrated by the deconvoluted peaks Figure 6.6). No I/S ml were observed in the biotite-rich granite. Illite and more sparsely I/S ml, but similar to the one identified in the Illkirch well, were reported in the Rittershoffen (Vidal et al., 2018) and Soultz-sous-Forêts wells (Genter, 1989; Ledésert et al., 1996, 1999, 2010; Jacquemont, 2002; Schleicher et al., 2006; Bartier et al., 2008; Gardien et al., 2016; Vidal et al., 2018).

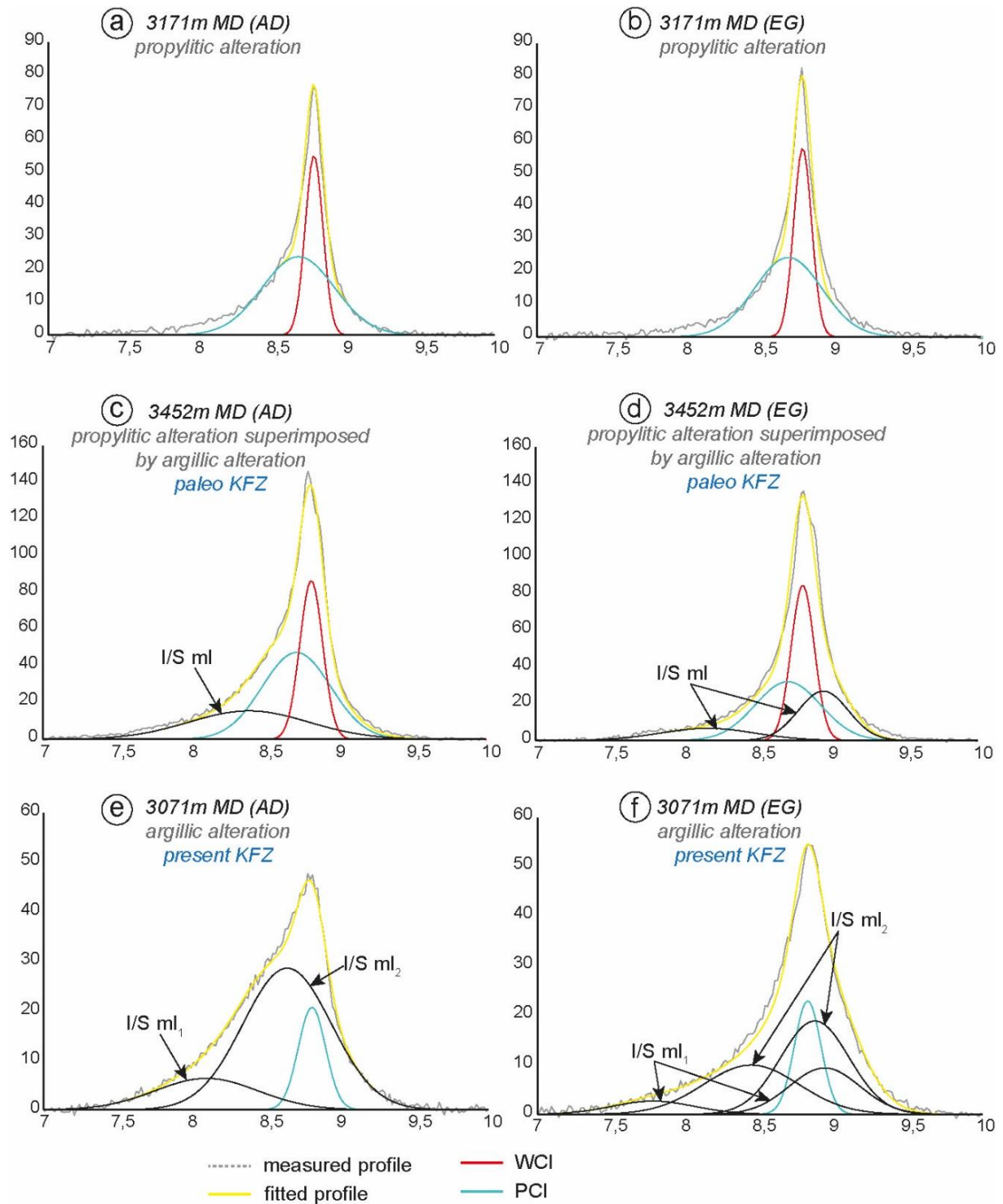


Figure 6.6: Decomposition of peak profile in the 7–10° 2 $\theta$  CuK $\alpha$  domain of the X-ray diffractograms (<5  $\mu$ m clay fraction) of AD and EG-saturated oriented powder of three samples (3071, 3171 and 3452 m MD). AD = air dry, EG = ethylene glycol, I/S ml: illite-rich illite/smectite mixed layer; WCI: well crystallized illite, PCI: poorly crystallized illite.

### Chlorite

Chlorite was identified as a non-expandable phyllosilicate with reflections at 14.2 Å, 7.1 Å, 3.73 Å and 3.54 Å. The 001/002 ratio is homogeneous around 0.55 suggesting a homogeneous population of ferromagnesian chlorite (Figure 6.5). Chlorite is present in the

predominantly propylitically altered granite from 3104 to 3800 m MD, with intensities of the 001 peak increasing with depth (Figure 6.3).

#### 6.1.5.5. Chemical composition of clay minerals (EDS)

Structural formulas for illitic minerals described in this section were calculated relative to a structure containing 11 oxygen atoms and assuming that the total iron content was composed of Fe<sup>3+</sup> (Table 6.3). The structural formulas for chlorites were calculated relative to a structure containing 14 oxygen and assuming that the total iron content was composed of Fe<sup>2+</sup> (Table 6.4).

#### *Illite and illite-rich I/S ml*

Illite and I/S ml are generally characterized by an interlayer charge between 0.7 and 0.9 and lower than 0.7, respectively (Table 6.3 and Figure 6.4). Coupling SEM/EDX and XRD data confirm that the samples with interlayer charges lower than 0.7 contain I/S ml minerals in association with illite. However, due to the low smectite content of the I/S ml, the two populations of illitic minerals cannot be clearly distinguished from their chemical composition (Table 6.3).

Samples	GIL-1 2960m		GIL-1 3005m		GIL-1 3071m		GIL-1 3340m		GIL-1 3482m		GIL-1 3573m		GIL-1 3678m		GIL-1 rock	
n.a.	5		67		32		18		29		29		18		20	
	An.	s.d.	An.	s.d.												
	Av.		Av.		Av.		Av.		Av.		Av.		Av.		Av.	
Si	3.37	0.29	3.28	0.09	3.31	0.09	3.32	0.06	3.27	0.06	3.35	0.10	3.30	0.06	3.37	0.09
Al <sup>IV</sup>	0.63	0.29	0.72	0.09	0.69	0.09	0.68	0.06	0.73	0.06	0.65	0.10	0.70	0.06	0.63	0.09
Al <sup>VI</sup>	1.72	0.14	1.72	0.11	1.70	0.10	1.60	0.08	1.73	0.08	1.67	0.07	1.71	0.04	1.64	0.06
Fe <sup>3+</sup>	0.11	0.05	0.16	0.06	0.16	0.05	0.24	0.07	0.15	0.05	0.15	0.05	0.16	0.04	0.17	0.04
Mg	0.10	0.04	0.13	0.05	0.14	0.06	0.14	0.03	0.11	0.05	0.17	0.05	0.13	0.03	0.19	0.05
Ti	0.03	0.02	0.00	0.01	0.00	0.00	0.01	0.00	0.00	0.01	0.00	0.00	0.00	0.01	0.01	0.02
Mn	0.00	0.00	0.00	0.00	0.00	0.00	0.00	0.00	0.00	0.00	0.00	0.00	0.00	0.00	0.00	0.00
OCT	1.96	0.06	2.01	0.03	2.00	0.03	1.99	0.02	1.99	0.01	2.00	0.03	2.01	0.02	2.01	0.02
Ca	0.01	0.01	0.00	0.01	0.00	0.00	0.00	0.00	0.01	0.01	0.01	0.00	0.00	0.00	0.01	0.00
Na	0.07	0.04	0.01	0.00	0.01	0.00	0.03	0.08	0.01	0.01	0.01	0.01	0.01	0.00	0.01	0.00
K	0.72	0.13	0.80	0.06	0.82	0.06	0.81	0.10	0.84	0.03	0.81	0.05	0.79	0.03	0.75	0.05
INTCH	0.81	0.10	0.81	0.06	0.83	0.05	0.84	0.04	0.86	0.03	0.83	0.05	0.81	0.03	0.78	0.04
XFe	0.53	0.05	0.54	0.09	0.53	0.10	0.63	0.08	0.56	0.09	0.47	0.12	0.55	0.08	0.48	0.12

Table 6.3: Calculations of structural formulae of some illitic minerals at various depths in GIL-1 well. Structural formulas were calculated relative to a structure containing 11 oxygen atoms and assuming that the total iron content is composed of Fe<sup>3+</sup>. n.a.: number of analyses; An. Av.: analytical average; s.d.: standard deviation; OCT: octahedral occupancy; INTCH: interlayer charge; X<sub>Fe</sub>: Fe/(Fe+Mg+Mn). 2960, 3005 m MD: HHIG granite; 3071 m MD: KFZ1; 3340 m MD: KFZ4; 3482 m and 3573 m MD: HHIG granite on both sides of KFZ5; 3678 m MD: HLOW granite.

The chemical composition of the illitic minerals analyzed from the GIL-1 well are reported in Table 6.3, indicating that tetrahedral substitutions range between 0.63 and 0.73 per half formula unit. Divalent cations in the octahedral sheet range from 0.10 to 0.17. In the intense argillic zone, illitic compositions show a small shift towards beidellite (Figure 6.7b & c) but the difference is minor and illitic minerals analysed in the argillically or propylitically altered granites cannot be clearly distinguished by their chemical composition (Table 6.3 & Figure 6.7b & c). Compositionally, the illites from the Illkirch and Rittershoffen sites are similar, whereas illites from the Soultz-sous-Forêts site are closer to the illite pole (Figure 6.7a). Nevertheless, if we compare locally the chemical analyses of illitic minerals obtained as a function of their grain size, it appears that the chemical compositions of coarse grained illitic minerals, related to propylitic alteration, are closer to phengitic compositions. Coarse grained illitic minerals

present higher interlayer charge ( $>0.85$ ) (Figure 6.4b, d, f, g, h) compared to the superimposed fine-grained illitic minerals attributed to argillic alteration with lower interlayer charge ( $<0.85$ ) (Figure 6.4d & g).

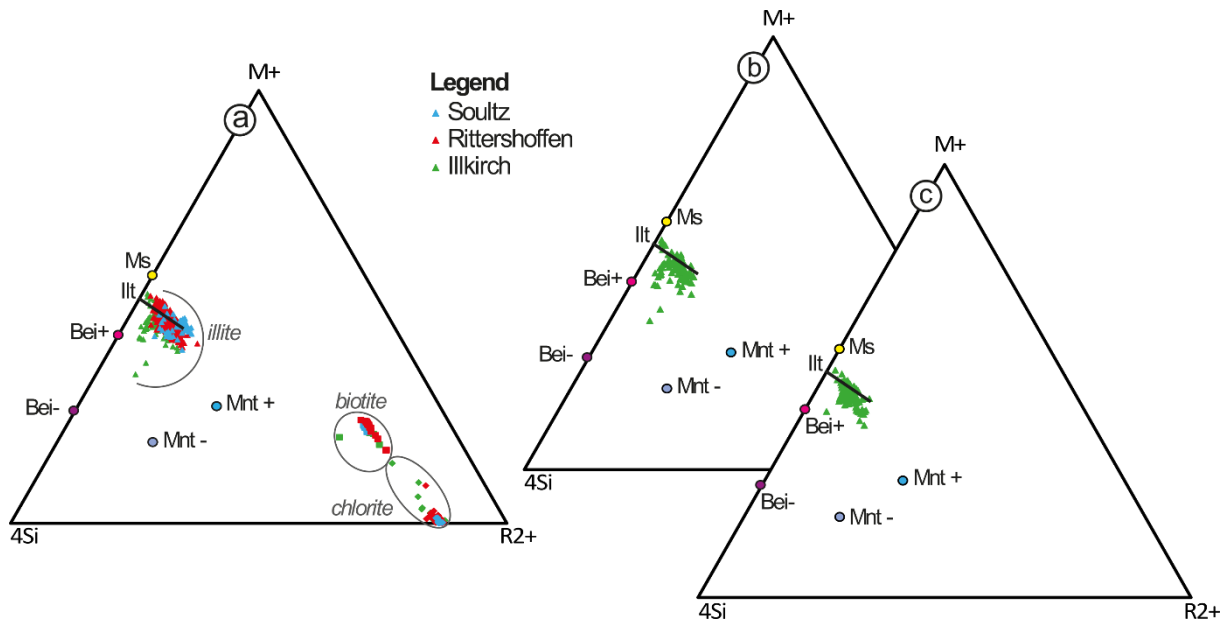


Figure 6.7: Chemical compositions of primary biotite, illite, and chlorite formed during the hydrothermal alteration of the granite at Soutz-sous-Forêts (GPK-1 well), Rittershoffen (GRT-1 & GRT-2 wells) and Illkirch (GIL-1 well) in the M+ 4Si R<sup>2+</sup> diagram ; a) illites, biotites and chlorites in the three sites, b) illites in Illkirch granite affected by argillic fracture-related alteration (2894-2350 m MD); c) illites in Illkirch granite affected by propylitic alteration (3104-3433 & 3513-3686 m MD); Bei +/-: beidellite high/low charge, Ill: illite, Mnt +/-: montmorillonite high/low charge, Ms: muscovite. Soutz-sous-Forêts data are from Genter, (1989) and Rittershoffen data are from Vidal et al., (2018).

### Chlorite

The compositions of chlorite from Illkirch are homogeneous and comparable to those of chlorite in the propylitic zone in the Rittershoffen and Soutz-sous-Forêts fields (Table 6.4 & Figure 6.8) (Vidal et al., 2018). These compositions are controlled by the biotite compositions (Figure 6.8), with similar to slightly lower  $X_{Fe}$  values (due to Fe-Ti exsolution during the chloritization process). Chlorite in the GIL-1 well is ferro-magnesian with an average  $X_{Fe}$  value of 0.45 (Table 6.3, Figure 6.8). Small amounts of potassium as well as the low octahedral occupancy suggest an incomplete chloritization of the biotite layers (GIL-1 3482 m, 3340 m MD) (Table 6.4).

Samples	GIL-1 3340m	GIL-1 3482m		GIL-1 3573m		GIL-1 3678m
n.a.	1	2		9		1
		An. Av.	s.d.	An. Av.	s.d.	
Si	2.97	3.14	0.02	2.99	0.10	2.94
Al <sup>IV</sup>	1.03	0.86	0.02	1.01	0.10	1.06
Al <sup>VI</sup>	1.33	1.33	0.02	1.14	0.19	1.04
Fe <sup>2+</sup>	2.02	1.41	0.03	1.93	0.26	2.08
Mg	2.31	2.68	0.01	2.57	0.21	2.17
Ti	0.00	0.11	0.00	0.08	0.17	0.17
Mn	0.12	0.05	0.00	0.09	0.04	0.12
OCT	5.79	5.57	0.01	5.82	0.13	5.57
Ca	0.01	0.01	0.01	0.01	0.01	0.24
Na	0.01	0.02	0.01	0.01	0.01	0.02
K	0.09	0.14	0.01	0.03	0.03	0.02
INTCH	0.13	0.17	0.01	0.07	0.03	0.53
X <sub>Fe</sub>	0.45	0.34	0.01	0.42	0.04	0.48

Table 6.4: Calculations of structural formulae of some chlorite at various depths in the GIL-1 well. The structural formulas were calculated relative to a structure containing 14 oxygens and assuming that the total iron content is composed of Fe<sup>2+</sup>. n.a.: number of analyses; An. Av.: analytical average; s.d.: standard deviation; OCT: octahedral occupancy; INTCH: interlayer charge; X<sub>Fe</sub>: Fe/(Fe+Mg+Mn).

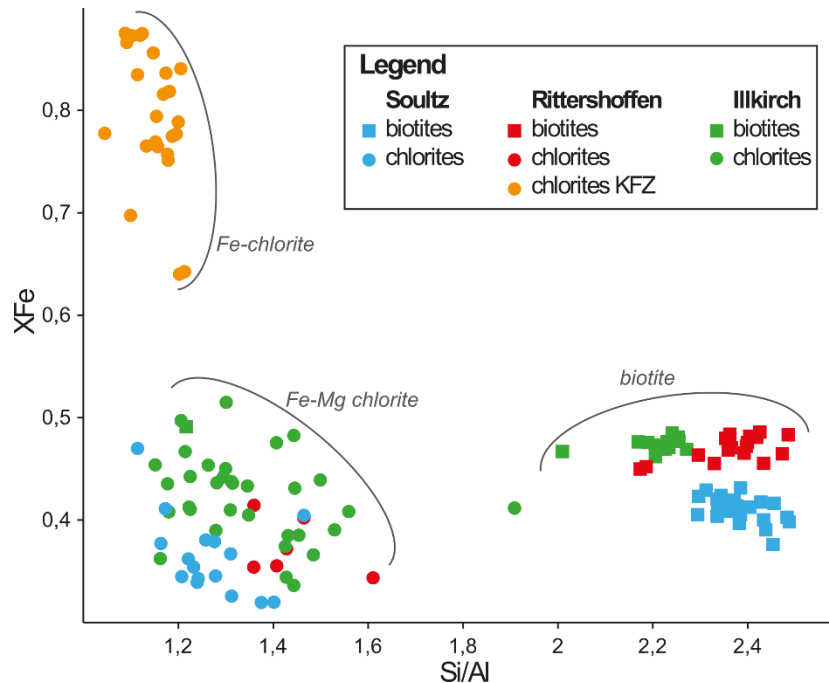


Figure 6.8: Plot of  $X_{Fe} (Fe/(Fe+Mg+Mn))$  versus Si/Al content for the chlorites and biotites at Sultz-sous-Forêts, Rittershoffen and Illkirch, Sultz-sous-Forêts data are from Genter, (1989) and Rittershoffen data are from Vidal et al., (2018).

## 6.1.6. Discussion

### 6.1.6.1. Successive hydrothermal alterations in the Illkirch reservoir

Two types of hydrothermal alteration events were distinguished in the Illkirch granitic basement. First, propylitic alteration developed pervasively in all the granitic basement during its post-magmatic cooling (Figure 6.9). It involved the partial chloritization of the primary biotite and a weak illitization of plagioclases in the GIL-1 well. Based on XRD and EDS analyses, chlorite composition clearly derives from biotite composition (Figure 6.8). This decrease of the ratio Si/Al between the biotite and the chlorite compositions is also observed at Sultz-sous-Forêts and Rittershoffen (Figure 6.8). From SEM and EDS analyses, propylitic illitization is characterized by the occurrence of coarse-grained illite (WCI and PCI) with an interlayer

charge higher than 0.85. According to (Dubois et al., 1996; Jacquemont, 2002; Cocherie et al., 2004; Ledésert et al., 2010), such a propylitic alteration is related to the resident hot and non-saline fluids equilibrating rapidly with the rock during the granite cooling, yielding a minimum age around 320 +/- 8 Ma for the end of the propylitic alteration (maximum 10 Ma after the granite emplacement), and has been active in the granitic basement of the URG at temperatures higher than 350°C and low fluid salinities (Figure 6.9) (Dubois et al., 1996).

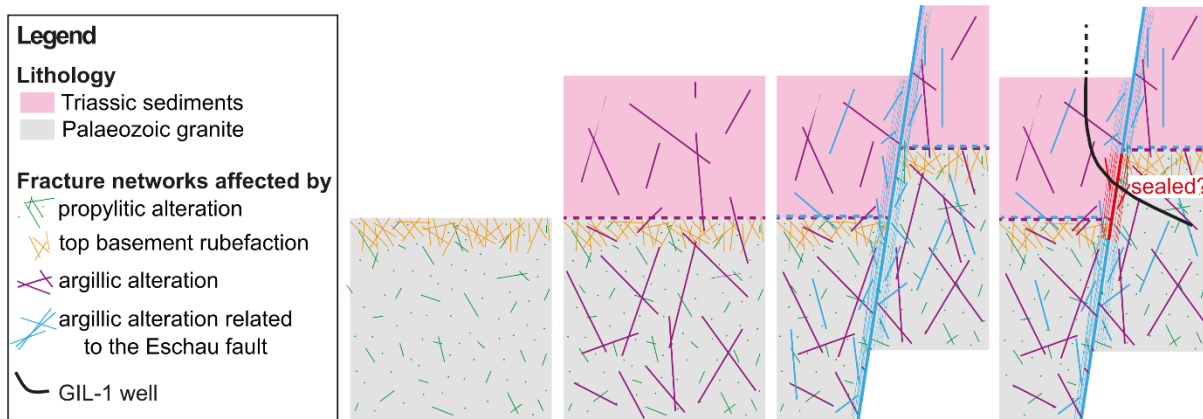
Second, in the GIL-1 well, argillic alteration is characterized by the precipitation of illitic minerals and carbonates in the vicinity of fractures and by secondary quartz veins related to fluid circulation in the fault cores (Figure 6.9). The major illitization stage comports small crystallites of illitic minerals (PCI, and I/S ml) with an interlayer charge lower than 0.85. The strong argillic alteration around the fracture networks replaces the primary minerals of the granite (biotite, feldspars) as well as the secondary minerals formed during the earlier propylitic alteration (chloritized biotite) by illitic minerals. Such chemical process is more prevalent in the upper part of the well from 2894 to 3104 m MD (Figure 6.3a). This argillic alteration in the granitic basement of the URG occurred at temperatures between 130 and 160°C and high fluid salinities close to the actual fluid conditions (100g/L) (Figure 6.9) (Dubois et al., 1996; Sanjuan et al., 2016).

In the biotite-rich granite, the chlorite is preserved and no I/S ml were observed, reflecting a propylitic alteration in which WCI (Well Crystallized Illite) is also observed as a slight early illitization occurring during and after the post-magmatic propylitic alteration (Figure 6.3). The biotite-rich granite is less hydrothermally altered than the porphyritic monzogranite. Hence, no major fractures cut the former rock, and an important small-scale fracture density is observed in the biotite-rich granite, which could be due to differences in mechanical properties between the two granitic bodies.

The propylitic alteration of the granite, related to the resident hot and non-saline fluids is supposed to occur at a minimum age around 320 +/- 8 Ma, and temperatures higher than 350° (Cocherie et al., 2004; Ledésert et al., 2010; Gardien et al., 2016; Sanjuan et al., 2016). The argillic alteration is related to the fluid circulation of a mix of meteoric water and brine of the NaCl type with TDS values close to 100 g/L, pH values close to 5.0, and K content of 3000 - 4000 ppm (Table 6.1) (Sanjuan et al., 2016). This fluid mix is constantly recharged, inducing a continuous argillic alteration (Sanjuan et al., 2016; Freymark et al., 2019; Koltzer et al., 2019). The high content of K in the fluids associated to the liberation of Al, likely originating from the destruction of the primary potassic feldspars and biotite facilitated the formation of illitic minerals. Albeit pervasively distributed, the argillic alteration is the result of pulses of fluid flows in the fracture network as inferred from the presence of at least two types of I/S ml in the argillically altered samples. These ephemeral pulses are most likely related to the development of the fracture networks in the granites and overlying sandstone, which were triggered by the Eschau fault or its splays. During the opening, a drop in the temperature and pressure of the damage zone led to the deposition of clay minerals and quartz that sealed the fractures. These cyclic crack-seal processes resulted in the successive crystallization of illite or I/S ml phases observed in the studied samples that have a close chemical composition in agreement with (Sanjuan et al., 2016) that suggests a rather homogeneous chemical composition of the brine in the Soultz-sous-Forêts, Rittershoffen, and Landau sites in the URG. On a longer time scale, several episodes of illite precipitation in the fractures and in the host rock are evident of several hydrothermal events since the Permian, followed by younger events during the Jurassic and Cretaceous (Schleicher et al., 2006; Bossennec et al., 2020). The occurrence of at least 6 generations of secondary quartz in the EPS-1 well of Soultz-sous-Forêts also support this

hypothesis (Smith et al., 1998). Regardless of the precise ages, we can still affirm that several hydrothermal events occurred on a long timescale, made of a pulsated circulation occurring on a shorter timescale. The argillic alteration took place post-Triassic, as the hydrothermal fluids include a contribution of Triassic marine brines mixed with meteoric water and ore-forming fluids (Sanjuan et al., 2016; Burisch et al., 2017a; Walter et al., 2018, 2019).

In the Illkirch reservoir, the above mentioned fluid circulations were intensively enhanced during the Oligocene by the shearing of the steeply-dipping Eschau fault, which presents a vertical normal apparent offset of kilometric scale (Doebel, 1967; Villemin and Bergerat, 1987; Schumacher, 2002; Edel et al., 2018). Although no dating of illitic minerals in the Illkirch reservoir is available, the intense argillic alteration in the footwall granitic compartment of the Eschau fault (from 2894 to 3104 m MD in the GIL-1 well) is related to the recent hydrothermal activity (late Paleogene period). On the contrary, in the deepest part of the GIL-1 well, further away from the major fault and associated alteration halo, the minerals of propylitic alteration facies (chlorite) and those related to argillic alteration (illitic minerals) during the Permian to Jurassic periods could have been preserved. A detailed mineralogical study of a Mesozoic hydrothermal event on the Buntsandstein sandstone located in the southern Black Forest shows an illite assemblage (illite and I/S) dated at the end of Jurassic (147 Ma) based on K-Ar dating of authigenic illite (Brockamp et al., 2011). The most realistic hypothesis is that the propylitic (1) and Permian-Jurassic argillic (2) alterations are totally overprinted in the top of the well by the late Eocene to early Oligocene Eschau fault-related argillic alteration, whereas the relics of (1) and (2) are preserved in the deepest part of the well, further away from the Eschau fault system.



PARAGENESIS	PROPYLITIC ALTERATION	ARGILLIC ALTERATION	
		<i>paleo</i>	<i>present</i>
Fe, Mg-Chlorite	-----		
Well Crystallized Illite	-----	---	
Carbonates	-----		
Poorly Crystallized Illite	-----		-----
Quartz			
I/S ml		---	$\overline{n}$ $\overline{n+1}$ $\overline{n+2}$ ---
	200-340°C	>200°C	150-180°C
	330+/-8 Ma      320+/-8 Ma	280 Ma	today
	----- cooling stage of granite -----		----- illitization -----

Figure 6.9: Paragenetic sequence of the granitic basement at Illkirch and schematic representation of the successive hydrothermal alterations that occurred in the fractured granite and sandstone intersected by the GIL-1 well at Illkirch. Only the top basement rubefaction was not observed at Illkirch because of the Eschau fault, but was observed at Soultz-sous-Forêts and Rittershoffen (Just and Kontny, 2011).

### 6.1.6.2. Successive hydrothermal alterations in the URG

The whole granitic basement of the URG underwent both propylitic and the argillic alterations. In the three geothermal sites, the main mineralogical signature of the propylitic alteration is chlorite + carbonates ± epidote or hydrogrossular after biotite and amphibole and calcite + clay minerals after plagioclase (Genter, 1989; Ledésert et al., 1996, 1999; Vidal et al., 2018). If corrensite is quite common in Soultz-sous-Forêts in replacement of plagioclases, it has never been identified in Rittershoffen or Illkirch (Vidal et al., 2018). In the latter site, the propylitic alteration produced coarse-grained WCI (+/- PCI), defined by quite high interlayer charge (>0.85 per 11O). In Soultz-sous-Forêts and in the Rittershoffen wells, epidote was observed (Stussi et al., 2002; Vidal et al., 2018) but has not been identified in Illkirch. Hydrogrossular has not been identified in both Rittershoffen and Illkirch sites, but is rare in Soultz-sous-Forêts. In all sites, primary potassic feldspar and quartz are preserved during propylitic alteration. Also, as the fluids are residents, the secondary mineralogy resulting from the propylitic alteration is constrained both by the chemical composition of the most reactive primary minerals of the granite and by the paleo-temperature.

In the three sites, the main mineralogical signature of the argillic alteration is the presence of illite and I/S ml, due to the illitization of primary plagioclase, potassic feldspar, biotite and/or chloritized biotite. However, some differences are observed. In Soultz-sous-Forêts, the secondary minerals like quartz, carbonates (calcite, ankerite, dolomite), barite, tosudite, illite and I/S ml, sulphides, hematite and titanite accompany this illitization stage (Genter and Traineau, 1996; Ledésert et al., 1999) while in Rittershoffen and Illkirch the secondary minerals consist only of quartz, carbonates, anhydrite, and hematite (C. Glaas et al., 2018; Vidal et al., 2018). The Rittershoffen is mineralogically distinguished from Illkirch and Soultz-sous-Forêts sites by the occurrence of additional Fe-chlorite.

The main differences in the argillic secondary mineralogy in the three sites are:

1. The occurrence of tosudite at Soultz-sous-Forêts, which could be related to the presence of organic compounds related to the overlying petroleum field (Ledésert et al., 1996);
2. The sparse occurrence of Fe-chlorite at Rittershoffen associated with reducing conditions and higher temperatures than those of the present-day (Beaufort et al., 2015; Vidal et al., 2018);
3. The occurrence of barite at Soultz-sous-Forêts, compared to the occurrence of anhydrite at Rittershoffen and Illkirch, which could be related to the amount of Barium, liberated by the dissolution of feldspars under acidic conditions.

These small local disparities in the secondary mineralogy related to the argillic alteration seem mostly linked to the fluid properties. Hence, small changes in the chemical composition of the fluid (mixing rate between brine and meteoric waters) as well as its temperature are reflected in the secondary mineralogy, surely due to a reservoir with dynamic fluid circulation and precipitations in conditions of strong chemical disequilibrium. However, the main signature of argillic alteration in the URG, characterized by the presence of illite and I/S ml, is unchanged.

#### 6.1.6.3. Towards an argillic signature in permeable fracture zones?

Previous studies in the Rittershoffen wells suggested that I/S ml are a proxy of the occurrence of KFZs (Vidal et al., 2018). In the Illkirch well, I/S ml are spatially associated with the occurrence of some KFZs (Figure 6.3). However, based on the 3 deconvoluted samples (Figure 6), the present-KFZ exhibits at least two I/S ml populations whereas the paleo-KFZs has one or more populations of I/S ml. This suggests a higher I/S ml content in the present-KFZs. Furthermore, the temperature needed for the formation of I/S ml is similar to the actual temperature (150°C) measured in the GIL-1 well. This suggests that I/S ml could be coeval with the actual thermal regime. Hence, the amount of clay minerals formed during the argillic alteration of the granitic basement was heterogeneous as they show several alteration grades (Figure 6.3, 6.4 and Table 6.2). This suggests that the amount of secondary illitic minerals is enhanced by the quantity of fluid that has been circulating in the FZ, making more or less K available for the formation of secondary illitic minerals and more particularly I/S ml. This observation underscores the relation between the alteration quantity and the fluid-rock ratio (Komninou and Yardley, 1997). The flow quantity depends on the size of the fractured and damaged zone (permeability), and the time during which the rock was exposed to the fluid and the stress field (Bruhn et al., 1994).

As mentioned previously, only one KFZ is present in the upper part of the intensely argillically altered granite (first zone), which corresponds to the footwall of the Eschau fault (Figure 6.2). By contrast, five KFZs occur in the lower part of the propylitically altered (second zone) and biotite-rich granites; the above alteration is superimposed by moderate argillic alteration in the vicinity of the fault zone. From these observations, we propose that in the Illkirch granite basement, the moderately argillically altered granite is situated >200 m from the Eschau fault. There the permeability of the altered granite is greater than that of the intensely altered granite near the fault, because the latter is a sealed zone. Hence the repartition of the illitic minerals quantity in the granitic basement intersected by Soultz-sous-Forêts and Rittershoffen wells was reflected in the short-wave infrared spectroscopy (SWIR) patterns, which we interpret to indicate the past and present fluid circulation (Simpson and Rae, 2018; Glaas et al., 2019b, 2019a; Kraal et al., 2021). In the Soultz-sous-Forêts and Rittershoffen wells, the SWIR data underlined that the KFZs are associated with high quantities of illitic minerals, suggesting a regular re-opening of the associated fractures (Glaas et al., 2019a, 2019b). SWIR was also applied to the Illkirch well and resolved the difference of permeability between the footwall granitic compartment of the Eschau fault and the deepest part of the well.

#### 6.1.7. Conclusion

The newly drilled geothermal well at Illkirch provides an excellent opportunity to study the nature of the primary and secondary minerals of the granitic basement in the URG. Our findings show that the granitic basement, the hydrothermal alteration products and the fluids circulating in the fractures/fault networks at Illkirch are similar to those at Soultz-sous-Forêts and Rittershoffen. Moreover, the repartition of the present-KFZs in the Illkirch well indicates that the moderately argillically altered granite distally situated from the Eschau fault is more permeable than the intensely argillically altered granite close to the Eschau fault.

The present-day fluid temperatures at Illkirch (150°C) correspond with the occurrence of I/S ml rather than illite, generally forms at temperatures  $\geq 200^\circ\text{C}$ . This suggests that illite was probably associated with the paleo-KFZs but at higher temperature, and I/S ml to the present (or more recent)-KFZ but at lower temperature. Thus, the above temperature trend, as indicated by dioctahedral clay minerals, could be interpreted as a retrograde thermal system in this part of the Central URG. High quantities of I/S ml could be linked to present-KFZs. The heterogeneities of the illitic minerals (in terms of textural and structural properties) and the common superimposition of illite (WCI and PCI) with various populations of I/S ml point to several superimposed fluid/rock interaction events linked to the tectonic activities in the URG. Moreover, the Eschau fault targeted by the GIL-1 well was tight in the footwall, suggesting a pervasive and compact sealing by illitic minerals.

The similarities in the secondary mineralogy at the Illkirch, Soultz and Rittershoffen basement granites suggest that fluid-rock interactions at the three sites operate under comparable pressure-temperature conditions and that the fluid chemistries are similar. Drilling at the top basement of the fault system at Soultz-sous-Forêts and Rittershoffen lead to the successful exploitation of geothermal fractured granite reservoirs.

After this complete characterization of the basement mineralogy with classical methods, the Short-Wave infrared spectroscopy, that has been previously applied to all the Soultz-sous-Forêts and Rittershoffen basement, will be conducted at Illkirch, to bring complementary quantitative information on the illitic minerals distribution and its impact on permeability.

In the continental upper crust, hydrothermal ore deposits controlled by fluid flow are fossil analogs of present-day geothermal fractured reservoirs in granite. Therefore, clay mineralogy is a promising exploration tool for mining and geothermal applications.

#### 6.1.8. Acknowledgements

This manuscript was prepared as a contribution to the PhD thesis (University of Strasbourg) of Carole Glaas which is cofounded by ES-Géothermie and ANRT (French Agency for Research and Technology). This work was realized in collaboration with the IC2MP laboratory of the University of Poitiers. The authors acknowledge the EGS Alsace project funded by ADEME (French Agency for the Energy Transition), ES and University of Strasbourg. The authors also acknowledge ESIG for providing access to the Illkirch cuttings rock samples. The authors also want to acknowledge the four anonymous reviewers for their useful advices that improved the manuscript.



## 6.2. How do secondary minerals in granite help distinguish paleo- from present-day permeable fracture zones? Joint interpretation of SWIR spectroscopy and geophysical logs in the geothermal wells of Northern Alsace. Published in the *Geofluids* journal.

C. Glaas<sup>1,2,3</sup>, J. Vidal<sup>2,4</sup>, P. Patrier<sup>3</sup>, J.-F. Girard<sup>1</sup>, D. Beaufort<sup>3</sup>, S. Petit<sup>3</sup>, A. Genter<sup>2</sup>

<sup>1</sup> UMR 7516 IPGS, University of Strasbourg, CNRS, 5 Rue René Descartes, 67084 Strasbourg Cedex, France

<sup>2</sup> ÉS Géothermie, : 5, rue André Marie Ampère, 67450 Mundolsheim, France.

<sup>3</sup> UMR 7285 IC2MP, HydrASA, University of Poitiers, CNRS, Bat B8 Rue Albert Turpain, TSA51106, F-86073 Poitiers Cedex 9, France

<sup>4</sup> FCFM, Department of Geology, Andean Geothermal Center of Excellence (CEGA), University of Chile, Plaza Ercilla 803, Santiago, Chile

### 6.2.1. Abstract

The investigation of permeable hydrothermally altered and fractured zones and their distribution is a key issue for the understanding of fluid circulation in granitic rocks, on which the success of geothermal projects relies. Based on the use of short-wave infrared (SWIR) spectroscopy applied to rock cuttings coupled with interpretation of geophysical logs, we propose an investigation of the clay signature of fault and fracture zones (FZ) inside the granitic basement. This methodology was applied to two geothermal wells: GRT-2 from the Rittershoffen and GPK-1 from the Soultz-sous-Forêts geothermal sites, both located in the Upper Rhine Graben (URG). A total of 1430 SWIR spectra were acquired and analysed. Variations in the 2200 nm absorption band area are correlated with hydrothermal alteration grades. The 2200 nm absorption band area is found to reflect the illite quantity and its variations in the granitic basement. Low, stable values are observed in the unaltered granite facies, showing good reproducibility of the method, whereas scattered high values are associated with high hydrothermal alteration and FZs. Variations in the 2200 nm absorption band area were correlated with the gamma ray and electrical resistivity logs. This procedure allowed us to confirm that illite mainly controls the resistivity response except inside the permeable FZs, where the resistivity response is controlled by the geothermal brine. Thus, the architecture of these permeable FZs was described precisely by using a combination of the 2200 nm absorption band area data and the electrical resistivity log. Moreover, by correlation with other geophysical logs (temperature (T), porosity, and density), paleo-permeable and currently permeable FZs inside the reservoir were distinguished. The correlation of SWIR spectroscopy with electrical resistivity logs appears to be a robust tool for geothermal exploration in granitic reservoirs in the URG.

### 6.2.2. Introduction

The mid-Carboniferous granitic basement of the Upper Rhine Graben (URG) has been affected by several extensional and compressional tectonic phases that developed a multiscale fracture network during the Tertiary (Villemin and Bergerat, 1987; Schumacher, 2002). Today, the network hosts hydrothermal circulations and acts as the main pathway through which the natural brine sustains wide convection cells (Schellschmidt and Clauser, 1996; Baillieux et al., 2013; Dezayes and Lerouge, 2019). More than 30 years of geothermal research in the pilot geothermal project of Soultz-sous-Forêts (Alsace, France) led to a 3D knowledge of those multiscale fault and fracture networks (Sausse and Genter, 2005; Dezayes et al., 2010). Fault and fracture networks will be designated by the general term “FZ” in this paper.

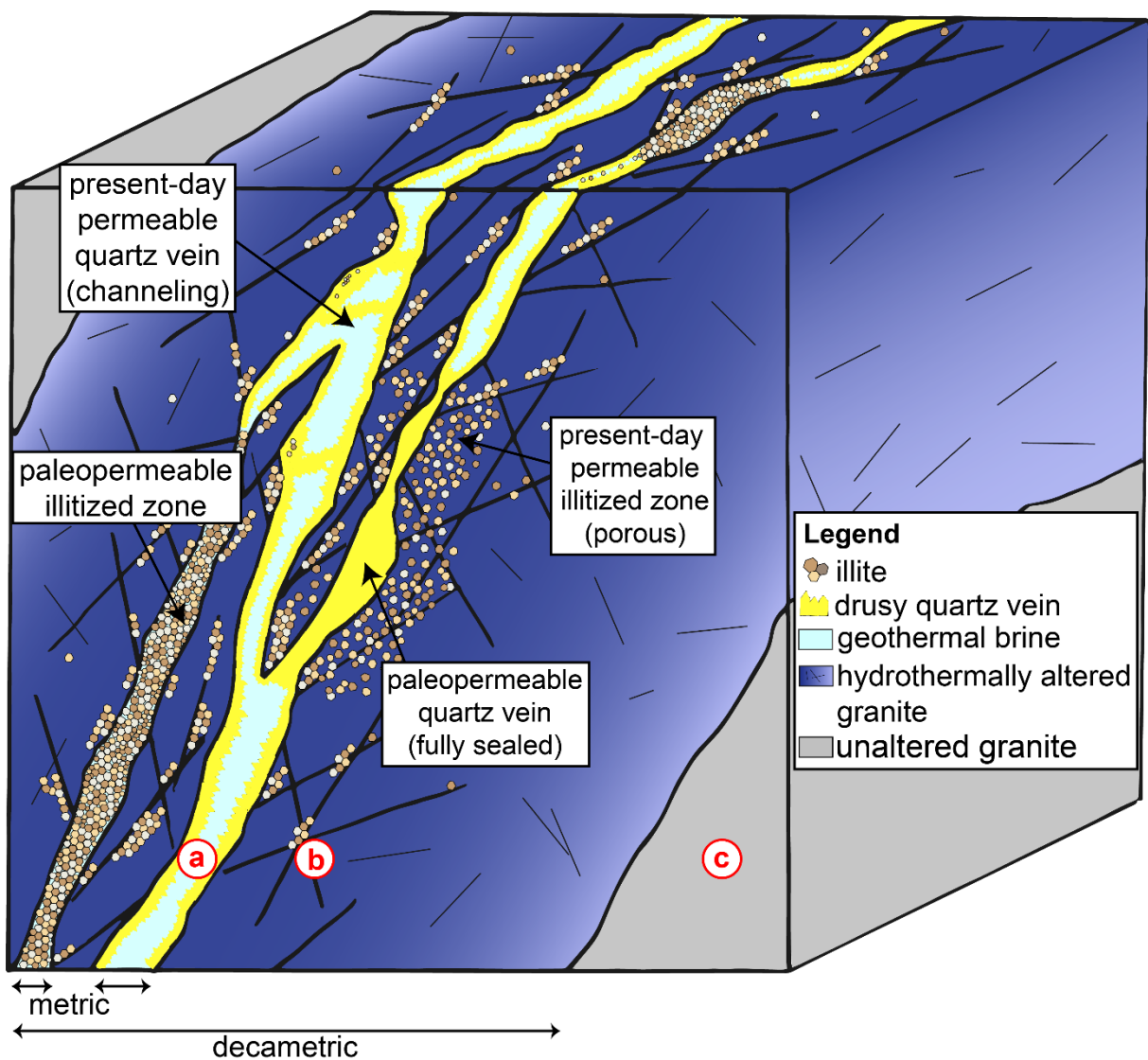


Figure 6.10: Complexity of a FZ after Caine et al., (1996). We can differentiate three zones: a) the fault core, which can be a pathway for fluid if illite and quartz veins are not totally sealing the zone, b) the damage zone, which can be sealed or opened with fractures that are acting as fluid pathways, and c) the unaltered granite, which shows generally very low permeability.

Their internal complexity in terms of architecture and associated permeability is a key question that must be answered when granitic rocks are used as hydrogeological reservoirs, for nuclear waste disposal, or as deep geothermal systems (Figure 6.10) (Manning and Ingebritsen, 1999; Berg and Øian, 2007; Faulkner et al., 2010; Bense et al., 2013; Choi et al., 2016; Dezayes and Lerouge, 2019). In the URG, the current targets for geothermal projects are hydrothermal fractured reservoirs in granitic rocks lying under a thick sedimentary cover (Vidal and Genter, 2018). Benefitting from lessons learned during the Soultz-sous-Forêts project and gained on several deep geothermal wells in Northern Alsace, we decided to avoid drilling subvertical wells in nearly vertical fracture systems to maximize the intersection of permeable FZs. Accordingly, a new drilling approach consisting of targeting deviated well trajectories crosscutting highly dipped FZs in the granitic basement was developed. However, these FZs can act either as permeable conduits and as paleo-permeable barriers for natural fluid transport (Figure 6.10). Therefore, due to primary mineral dissolution and/or secondary mineral

precipitation related to fluid-rock interaction, the resulting permeability of FZs can increase or even decrease, increasing the challenge of obtaining successful geothermal wells (Ledésert et al., 1999; Genter et al., 2000; Hooijkaas et al., 2006; Meller and Kohl, 2014; Vidal et al., 2018). This paper aims to develop a method to both characterize the hydrothermal alteration and evaluate the degree of permeability of the granitic reservoir intersected by geothermal wells in the context of the URG. Hydrothermal alteration of the buried granitic basement in the URG wells is systematically expressed by an illitization process (Sausse and Genter, 2005; Rotstein et al., 2006; Dezayes et al., 2010; Ledésert et al., 2010; Vidal and Genter, 2018). Routinely used for the mining industry, short-wave infrared (SWIR) spectroscopy is an innovative method for geothermal systems (Simpson and Rae, 2018). Here, SWIR spectroscopy was used to detect illitic minerals (illite and illite-rich illite/smectite mixed layers) in the studied geothermal wells. However, the use of SWIR spectroscopy alone does not permit differentiation of whether this high illitization is the clay signature of permeable FZs contributing to the well's productivity or injectivity, or a signature of paleo-permeable FZs that are now sealed by secondary minerals. To distinguish paleo-permeable from currently permeable FZs, we propose an innovative method based on the correlation between SWIR signature, geophysical logs (T, gases, porosity, density, gamma ray, and electrical resistivity), and cuttings observations. After describing the SWIR method and the several geophysical logs used in this study, the SWIR results will be presented for two geothermal wells drilled in Rittershoffen (GRT-2) and Soultz-sous-Forêts (GPK-1), respectively, and the specific signatures and architectures of the FZs will be detailed. In the next step, the geophysical logs and SWIR results will be correlated and used to differentiate paleo- and present-day permeable zones. Finally, we will discuss the applicability of the SWIR method and its implications for the understanding of the mineralogy and the distribution of illitization at the well scale.

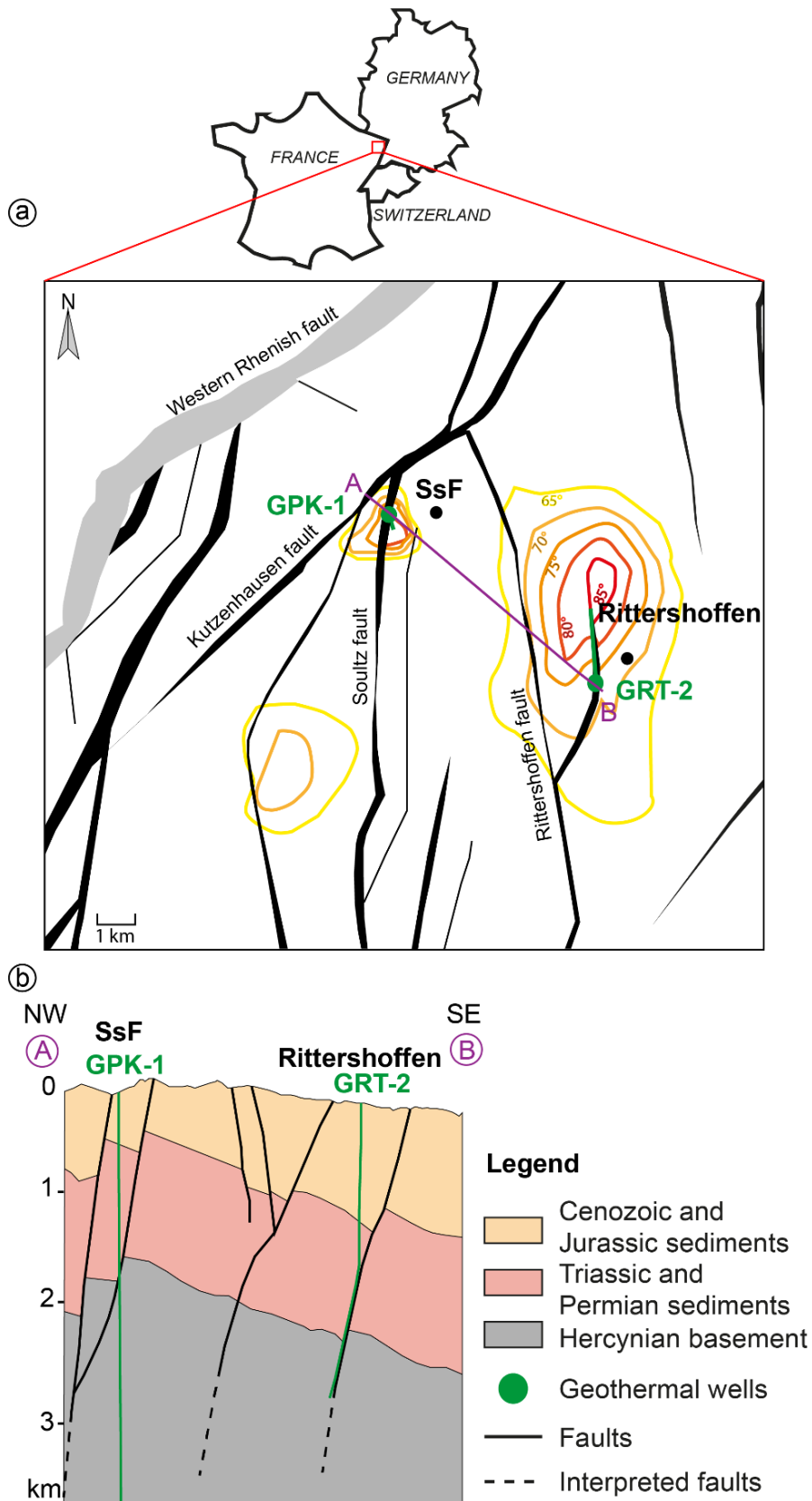


Figure 6.11: (a) Structural map of the top of the granitic basement from the GeOrg geoportal with the well trajectories (green), the thermal anomalies (Baillieux et al., 2013), and the Soultz-sous-Forêts (SsF) and Rittershoffen localizations. (b) Geological cross section through the GPK-1 and GRT-2 wells crossing the URG sedimentary cover and granitic basement; the well trajectory of the GRT-2 well is a NW-SE projection on the cross section, from the last 3D seismic campaign (Richard et al., 2019).

### 6.2.3. Geological setting

#### 6.2.3.1. Soultz-sous-Forêts and Rittershoffen sites

In 2019, two deep geothermal plants exploiting deep fractured granite are operating in France. These plants produce a total of 24 MWth for industrial use at Rittershoffen and 1.7 MWe for the electrical grid at Soultz-sous-Forêts. Both sites are located in the URG approximately 40 km north of Strasbourg and target the hydrothermally altered granitic basement as a geothermal reservoir (Figure 6.11a). The Soultz-sous-Forêts GPK-1 well was drilled vertically from 0 to approximately 2000 m measured depth (MD) in 1987 and was then deepened almost vertically to 3590 m MD in 1992 (Figure 6.11b). It crosses the Cenozoic and Mesozoic sedimentary covers before reaching the top of the Paleozoic granitic basement at 1376 m MD. The drilling of this well in 1987 was conducted according to an old geothermal concept, involving the creation of an artificial heat exchanger by hydraulic stimulation created by vertical wells (Gérard et al., 1984; Garnish, 1985; Gérard and Kappelmeyer, 1987; Kappelmeyer, 1991). The well was hydraulically stimulated several times to enhance the connection between the well and the reservoir (Jung, 1992; Schill et al., 2017). The FZs in the granitic basement are mainly oriented N160-170°E and subvertical, and most of them dip more steeply than 65° eastward or westward (Genter et al., 2000). On drilling, natural very saline brines were encountered in fractured and altered zones bearing secondary minerals of hydrothermal origin (Genter et al., 2010). Five main permeable FZs ranging from 20 to 40 m in apparent thickness are intersected at 1645, 1814, 2000, 2818, and 3495 m MD. In 2004, the Soultz-sous-Forêts site was composed of five deep wells that in fact revealed numerous permeable FZs (Genter et al., 2010). The Rittershoffen project was initiated in 2008, and its target was the Rittershoffen normal fault, which is crossed by two deep wells, GRT-1 and GRT-2. The production well GRT-2 was drilled subvertically from 0 to 2480 m MD crossing the sedimentary cover to the top basement and was highly deviated (40° to the north) down to 3196 m MD crossing the granitic basement (Figure 6.11b). The target was to crosscut the main local fault as long as possible. This normal fault, which is located approximately 15 km east of the western Rhenish border fault, is oriented N5°E based on subsurface geological data (GeOrg, 2017; Vidal et al., 2019). The GRT-2 well is therefore slightly deviated but tangent to the local fault over its approximately 400 m apparent length (Figure 6.11b). The GRT-2 well revealed a high productivity index of 4 L/s/bar without any stimulation; thus, a hydrothermal concept could be implemented (Baujard et al., 2017a; Vidal and Genter, 2018). Achieved in 2016, this Rittershoffen project proved to be a great success, with an operational plant producing a flow rate of 70 L/s at surface T of 168°C (Baujard et al., 2018b). In the granitic section of the open hole of the GRT-2 well, four main permeable FZs ranging from 15 to 40 m in apparent thickness were intersected at 2533, 2770, 2950, and 3052 m MD (Baujard et al., 2017a; Vidal et al., 2017; C. Glaas et al., 2018). Observations conducted on continuous and high-quality coring of the EPS-1 well from Soultz-sous-Forêts highlighted a multiscale fracture network (Genter and Traineau, 1996). Small-scale fractures with no evidence of displacement are filled with carbonates, chlorite, iron oxides, epidote, and sulphides, and faults visible at the core scale are filled with drusy quartz (euhedral quartz crystals as coatings on or infillings in fractures), carbonates, barite, and clay minerals. In the case of the Rittershoffen wells, for which no core was available, only the largest faults could be identified (small-scale fractures were hardly identified) because only cuttings and acoustic image logs were available.

### 6.2.3.2. Alterations of the granitic basement

During the cooling of the crystalline pluton, the granite underwent a pervasive alteration that presents the petrographic and mineralogical features of the propylitic facies. Today, it exhibits several grades of hydrothermal alteration that are also related to fluid circulation (Stussi et al., 2002; Cocherie et al., 2004). The unaltered crystalline granitic basement at Rittershoffen and Soultz-sous-Forêts is composed of primary muscovite, biotite, K-feldspar, plagioclase, and quartz (Traineau et al., 1992; Stussi et al., 2002). This primary mineralogy is affected by hydrothermal alteration, and specific mineralogical associations reflect the various alteration grades encountered. According to previous studies of the Soultz-sous-Forêts geothermal wells, the hydrothermal alteration grades in the granite are well known from core observations (Traineau et al., 1992; Ledésert et al., 1999; Sausse et al., 2006; Meller and Kohl, 2014; Meller et al., 2014b; Meller and Ledésert, 2017). In this study, the core mineralogy and hydrothermal alteration grades were cross referenced with the minerals observed in the cuttings using a binocular magnifier, although the texture information and the mineral assemblage were not reflected in the cuttings (Figure 6.12). The mineralogy of the cuttings was determined through a semi quantitative approach using a three-class scale (C. Glaas et al., 2018; Vidal et al., 2018). The hydrothermal alteration grades—low (HLOW), moderate (HMOD), high (HHIG), and extreme (HEXT)—are described in Figure 6.12 (Genter et al., 1997a, 1997b; Ledésert et al., 2009; Hébert et al., 2010; Nishimoto and Yoshida, 2010). The granitic facies identified in the cuttings include two types of granite, “unaltered” granite (GRAN), affected by a propylitic alteration related to the cooling of the pluton (Genter et al., 2000; Jacquemont, 2002), and the presence of locally reddish granite (RED), containing a large number of red K-feldspar megacrysts that have been oxidized through intense exposure to weathering fluids. The presence of illite in the granitic basement as a major signature of hydrothermal alteration was confirmed by complementary laboratory analyses. In previous studies of the GRT-2 well, X-ray diffraction (XRD) was performed on the <5 µm fraction of selected cuttings; in this way, three groups of illitic minerals (well-crystallized illite, poorly crystallized illite, and illite-rich illite/smectite mixed layers) were identified (Vidal et al., 2018). The chemical compositions of the clay minerals were obtained using a scanning electron microscope (SEM) coupled with energy-dispersive X-ray spectroscopy (EDS). This study showed that permeable FZs were associated with the occurrence of poorly crystallized illite and illite/smectite mixed layers that crystallized during hydrothermal circulation (Vidal et al., 2018). XRD measurements of the GPK-1 well’s cuttings were also performed in this study; the results showed the presence of illite in fractured and altered zones as well as the presence of chlorite and biotite in HLOW and GRAN.

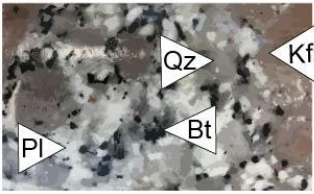
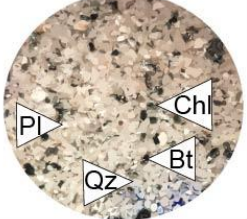
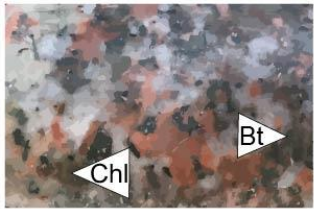
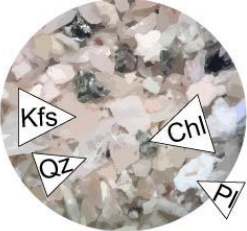
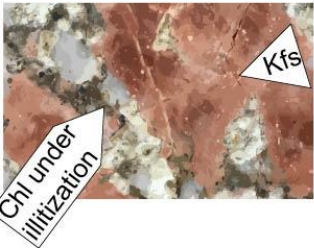
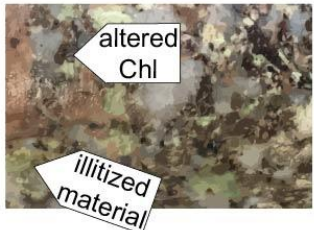
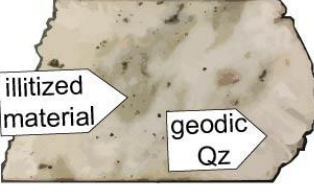
	Granite hydrothermal alteration grades	Core samples Soultz-sous-Forêts 4 cm	Cuttings samples Rittershoffen 3 mm
- hydrothermal alteration - +	<b>GRAN (unaltered granite):</b> - Bt - Hem - Cal - red Kfs megacrysts (large amount)		
	<b>HLOW (low hydrothermal alteration):</b> - Chl - primary Bt (few) - absence/minor amount of secondary Illt - unaltered primary Pl + Kfs		
	<b>HMOD (moderate hydrothermal alteration):</b> - Illt (further alteration of Chl) - Pl + Kfs (weakly altered) - fresh and weakly altered Bt (minor amounts)		
	<b>HHIG (high hydrothermal alteration):</b> - Illt (abundant) - Chl (very few) - Pl + Kfs (strongly altered) - altered Bt (relics)		
	<b>HEXT (extreme hydrothermal alteration):</b> - depletion of Bt - Illt (abundant) replacing primary Bt - Pl + Kfs - drusy Qz linked to hydrothermal circulation		
	<b>VEIN (quartz vein):</b> core of the FZs - highest amount of secondary drusy Qz associated with a high Cal content		

Figure 6.12: Examples of mineralogical assemblages of the granitic basement observed in cores (middle) and in cuttings (right); these assemblages define the different hydrothermal alteration grades (left). GRAN: unaltered granite; HLOW: low hydrothermal alteration; HMOD: moderate hydrothermal alteration; HHIG: high hydrothermal alteration; HEXT: extreme hydrothermal alteration; VEIN: secondary drusy quartz vein; Anh: anhydrite; Bt: biotite; Cal: calcite; Chl: chlorite; Hem: hematite; Illt: illite; Kfs: potassic feldspars; Pl: plagioclase; Qz: quartz.

## 6.2.4. Materials and methods

### 6.2.4.1. SWIR spectroscopy method

#### *Materials*

The cuttings (chip samples) collected during the drilling of the wells were first washed using sieves and then dried on-site in an oven at 80°C for 40 minutes, by the mud logger unit. In the case of the GRT-2 well, the cuttings were sampled every 3 m in depth in the studied 8 1/2" drilled section. Thus, one bag of cuttings represents approximately 0.1 m<sup>3</sup> of rock. For the GPK-1 well, the cuttings were sampled every 1 m in depth; thus in the 9 5/8" drilled section from 1400 to 2850 m MD, one bag of cuttings represents approximately 0.04 m<sup>3</sup> of rock, and in the 7 5/8" drilled section from 2850 to 3590 m MD, one bag of cuttings represents approximately 0.025m<sup>3</sup> of rock. The sampling included in this study encompasses all the facies described in the foregoing section (Figure 6.12). The average grain size of the cuttings chips in each sample varies between 0.5 and 2mm. The chip size can be highly influenced by drilling tool wear. For this reason and because the chip size of the cuttings influences the SWIR intensity (the higher the chip size, the higher the SWIR intensity), the changes of drilling tool are also presented in this work.

#### *Measurement conditions*

The SWIR spectral domain extends from 1000 to 2500 nm. If the wavelength of the infrared radiation is close to the vibrational energy of the eigenmode of the molecule, it causes vibration of some bonds and the infrared radiation energy is absorbed. This is conveyed by absorption bands on the infrared spectrum acquired at the corresponding wavelength in the midinfrared (MIR) domain. In the SWIR domain, we can observe the harmonics and the combinations of these absorption bands (Hunt and Salisbury, 1970). In total, 240 cuttings samples from the GRT-2 well and 1190 cuttings samples from the GPK-1 well were analysed. The SWIR measurements were performed at the same time for each well; thus, the acquisition conditions (hygrometry of the room, ambient temperature) are homogeneous for each well. Because very few expandable clay minerals are present in the granite, even when it has been hydrothermally altered, the SWIR data are not very sensitive to the hygrometry parameter. This is confirmed by the reproducibility of the low values of the 2200 nm absorption band area in the unaltered granite for all the geothermal wells studied in the URG. The spectrometer used is a TerraSpec 4 Standard Res Mineral Analyzer created by Analytical Spectral Devices, Inc. (Malvern PANalytical company) equipped with two SWIR detectors. The spectral domain from 350 to 2500nm is covered at a spectral resolution of 3nm from 350 to 1000 nm and at a spectral resolution of 10 nm from 1000 to 2100 nm. The scanning time of 100 milliseconds made it possible to conduct the measurements rapidly for all granitic sections. The wavelength reproducibility is 0.1 nm with an accuracy of 0.5 nm. The reproducibility of the measurement was tested by measuring the same sample five times; this resulted in a variation of 1% for the 2200 nm absorption band area, by performing five measurements without moving the sample and five measurements after mixing the sample (personal communication). Before measurements are taken, the ASD TerraSpec requires a warm-up period of approximately 30 minutes. It is also necessary to conduct a calibration with the "Spectralon" reference material provided with the machine before the first measurement and thereafter regularly every hour during the measurement period (Hébert, 2018).

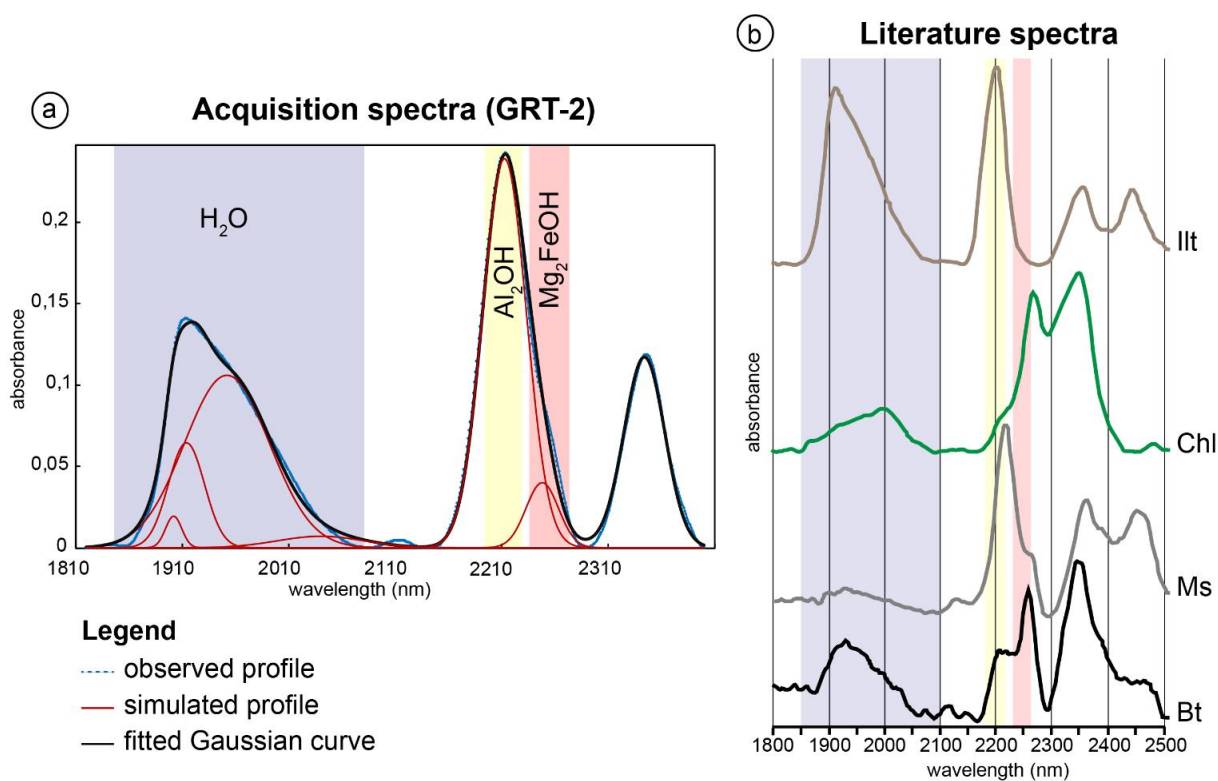


Figure 6.13: (a) Example of an absorption spectrum and a simulated profile in the GRT-2 well at 2800 m. (b) Reference spectra from Pontual et al., (1997) for biotite (Bt), muscovite (Ms), chlorite (Chl), and illite (Ill).

### Processing

After the measurement, the SWIR spectra were processed with “the Spectral Swagger” (TSS), an inhouse Visual Basic Macro developed at Poitiers University that runs on Microsoft Excel (Hébert, 2018). First, the baseline was removed automatically by the software; then, spectra were fitted with few Gaussian curves (four and two for the water and the 2200 nm absorption band areas, respectively). To create a profile simulation, the user must set the position and the half width at half maximum (HWHM). The height parameter is automatically deduced from the baseline-removed spectrum; its initial height equals 90% of the y-axis value of the baseline-removed spectrum at the Gaussian centre wavelength. The user can designate the parameter that will be allowed to change. The final simulated profile is the sum of all Gaussian curves. The quality of the fit between the simulated and observed profile is verified against the weighted profile R-factor (Rwp), which is commonly used in Rietveld refinements (Toby, 2006). In this study, six Gaussian curves were used to fit the spectrum from 1820 to 2300 nm (Figure 6.13). For the GRT-2 well, position and HWHM were locked for each simulation profile. However, different sets of position and HWHM were used. Simulation profiles with a Rwp lower than 0.05 were accepted. For the GPK-1 well, for which a very large number of profiles (1190) were calculated, position and HWHM were free fitted by TSS for each simulation profile. The areas of the water absorption band and the 2200 nm absorption band were also fitted manually for some profiles to determine whether there was a significant deviation in the area with respect to the free fitting. The results showed that there was no significant change in the area between profiles fitted manually and those free-fitted by TSS (see Figure 6.S3 in the supplementary materials). Thus, the results presented in this study for the GPK-1 well are profiles that were free-fitted by TSS.

### *Mineralogical identification*

In the SWIR spectral domain, the phyllosilicates are detected, and they are not influenced by feldspars and quartz, which do not present absorption bands in this domain. Four Gaussian curves were used to fit the absorption band spanning the wavelength range from 1900 to 2060 nm (Figure 6.13); this range corresponds to the stretching and bending vibrations of H<sub>2</sub>O molecules. This absorption band exists not only for the hydrated phyllosilicates but also for some other hydrated minerals such as zeolites, opal, and amorphous silica. This absorption band can also vary according to the humidity of the environment. Hence, not only it is linked to clay minerals but also, under constant humidity conditions, the area of this absorption band will vary according to the quantity of clay minerals present in the sample. This aspect will be discussed in section 6.2.6.1

Two Gaussian curves were used to fit the absorption band spanning the wavelength range from 2200 to 2255 nm, which mainly corresponds to the vibrations of the bonds between the cations of the octahedral sheets and the structural OH groups in the aluminous phyllosilicates, i.e., corresponding to the combination modes of the stretching and bending vibrations of the Al<sub>2</sub>OH groups (Madejová et al., 2017). Thus, the 2200 nm absorption band represents Al-rich dioctahedral clay minerals (Pontual et al., 1997). The shoulder observed between 2247 and 2253 nm is more complex in terms of absorption band and mainly reflects the occurrence of biotite and chlorite trioctahedral clay minerals as well as of muscovite (Figure 6.13a). The Gaussian curves used to fit the spectrum from 2300 to 2400 nm are not presented in this study because we are focusing on the relative quantification of illitic minerals associated with the “Al<sub>2</sub>OH” absorption band. In our study, the mineralogy of the granitic basement in the wells is thoroughly described by binocular magnifier observation of 240 cuttings from the GRT-2 well (Glaas et al., 2018) and 1190 cuttings from the GPK-1 well (Traineau et al., 1992; Genter et al., 1995). Thus, the variation in the relative integrated intensity of the 2200 nm absorption band is considered to represent illite variations, except in the GRT-2 well from 2950 to 3200 m MD, where significant amounts of biotite were observed, and in the GPK-1 well, in which biotite is present in the unaltered granite. Based on a comparison with spectra reported in the literature (Figure 6.13b), the influence of chlorite on the 2200 nm absorption band area is not significant, but the influence of biotite and muscovite could be significant if these minerals were present in high amounts in the studied samples. Beyond the mineralogical signature of the absorption bands, this methodology was used for a broad quantification of clay minerals based on the Beer-Lambert law, which establishes proportionality between the absorbed energy and the concentration of chemical bonds in the analysed material (Duckworth, 1998). In this study, the area of the 2200 nm absorption band is expressed in arbitrary units (a.u.) which represents the area of the absorption band considered.

### *Intrasample variability*

Because each cuttings bag contains sections of the drilled rocks (see Section 6.2.4.1) and because the cuttings could not be homogeneously mixed in the bag, several measurements were performed on each cuttings bag (see Figures 6.S1 and 6.S2 in the supplementary materials). In the GRT-2 well, 10 measurements were performed on the same cuttings bag, whereas only 5 measurements were performed in the GPK-1 well due to the lower amount of cuttings available. Error bars were calculated for each cuttings bag to determine whether the range of variation exceeds the scattering of the data. Because the results were found to be reliable, they are not presented in this study; however, figures showing the results are provided as supplementary materials.

#### 6.2.4.2. X-ray diffraction

X-ray diffraction data were acquired from selected cuttings samples of the GPK-1 well and used to identify the clay minerals present in the samples. The XRD results of Vidal et al., (2018) for the GRT-2 well were also used in this study. Twenty-eight cuttings samples were collected from the GPK-1 well. The sampling was concentrated in the permeable and altered FZs as well as in the unaltered granite that was used as a reference material, as the latter is believed to be representative of rocks preserved from actual fluid circulation. The samples were not ground; they were dispersed in distilled water by ultrasonic vibration. Oriented powders on glass slides were prepared from a <5 µm clay mineral suspension obtained by sedimentation. Clay minerals were identified by XRD of air-dried and ethylene glycol-saturated oriented powders conducted on a Bruker D8 Advance diffractometer (CuK $\alpha$  radiation, 40 kV, 40 mA). The analytical conditions were as follows: angular domain, 2.5-30 2 $\theta$ ; step increment, 0.025 2 $\theta$ ; and counting time per step, 1 s. XRD data acquisition and treatment were conducted using the X'Pert HighScore software (PANalytical B.V.). The clay minerals were identified according to the literature (Brindley and Brown, 1980).

#### 6.2.4.3. Geophysical logs

The geophysical logs and mud logging data are presented in this study to highlight their correlations with evidence of present-day circulation (T log, He, CO<sub>2</sub>, CH<sub>4</sub>, and Rn), FZ evidence (neutron porosity, density, and resistivity), and evidence of the presence of paleocirculation zones rich in illite (total gamma ray, spectral potassium gamma ray (GR-K), and electrical resistivity).

##### *Temperature*

The T log is expressed in °C. Measurements were made every 50 cm and 10 cm in the GRT-2 and GPK-1 wells, respectively. T anomalies are interpreted as the signatures of fluid circulations between the well and the formation (Barton et al., 1995; Davatzes and Hickman, 2005; Bradford et al., 2013; Vidal et al., 2019). For this study, the T log of the GRT-2 well was shifted upwards by 2 m from 2480 to 2650 m MD and upwards by 10 m from 2650 to 3196 m MD because stretching of the cable occurred during the measurement as a function of depth. Moreover, because the T log of the GRT-2 well was acquired separately, it could not be correlated in depth with another reference. Thus, in this study, the T log was correlated with the resistivity and porosity logs because they obviously presented the same types of anomalies preceding the four main T anomalies. For similar reasons, the T log of the GPK-1 well was shifted downwards by 7 m to vertically fit the T anomalies and the permeable FZs (Vidal et al., 2019).

##### *Gas content (He, CO<sub>2</sub>, and CH<sub>4</sub>)*

The occurrence of alkanes as well as of other gas species such as He, CO<sub>2</sub>, and CH<sub>4</sub> indicates permeable FZs (Vuataz et al., 1990; Aquilina et al., 1993). For reference, the abundances of He and CH<sub>4</sub> in the atmosphere are approximately 5.24 ppm and 1.75 ppm, respectively. He, CO<sub>2</sub>, and CH<sub>4</sub> were monitored in GPK-1 (Aquilina et al., 1993). Only CH<sub>4</sub> was monitored in GRT-2 (Vidal et al., 2017).

### *Porosity*

The neutron porosity log (NPHI) which is supposed to quantify the porosity filled with water is deduced from measurements of the hydrogen content of the formation (fast neutrons emitted by the tool are slowed down by elastic scattering, mainly due to collision with hydrogen atoms). Neutron porosity can also be highly influenced by clay minerals, which often contain bound water. It is expressed in m<sup>3</sup>/m<sup>3</sup> and sometimes in %. It was sampled at every 15 cm depth in the GRT-2 and GPK-1 wells. The parameter has an investigation depth of several cm behind the borehole wall, which can correspond to the flushed zone. Porosity logs do not directly indicate true porosity in this context, a specific calibration should be performed, and the influence of the granitic matrix on the neutron porosity can be as high as 7% (Gallé, 1994). Nevertheless, the neutron porosity measured here provides a global signal for FZs to the extent that they are porous and contain fluids and/or clay minerals.

### *Density*

The density log (RHOB) is calculated from returning gamma rays following the interaction of gamma rays emitted from a chemical source (Ce<sup>137</sup> and Co<sup>60</sup>) with the electrons present in the elements in the formation. These gamma rays are related to the electron density of the formation, which itself depends on the formation density. RHOB is given in g/cm and was acquired every 15cm in depth for both the GRT-2 and the GPK-1 wells. A negative peak in a density curve could be due to the occurrence of secondary clay minerals and high porosity and thus should reveal alterations associated with a fracture zone, whereas positive peaks are associated with high-density minerals or changes in lithology.

### *Gamma-ray*

The gamma ray (GR) log measures natural radioactivity (cumulative emissions, mainly from uranium (U), potassium (K), and thorium (Th)) in gAPI; vertical sampling of the GRT-2 and GPK-1 wells was performed every 15 cm. The GR log is aimed at interpreting lithology and rock composition by detecting clay minerals rich in potassium (illite and muscovite). In the altered crystalline basement, negative GR peaks in the lower positive domain can reflect drusy quartz veins in illitized host rock (Genter et al., 2000). In the context under study, GR data are an indicator of hydrothermal alteration and thus provide information regarding paleo-permeability.

### *Electrical resistivity*

In unaltered hard rocks, the electrical resistivity log is mainly controlled by the electrical conductivity of the fluid contained in the rock porosity, a factor that is particularly significant in FZs. Electrical resistivity decreases with water saturation and is even lower for conductive fluids that contain salts, such as brines. Similarly, the electrical resistivity of clay minerals, which are conductive minerals, is low (Lévy et al., 2018). Hence, laterologs and focused resistivity arrays are sensitive to fracturation and alteration. Resistivity laterologs measure an apparent electrical resistivity that needs to be corrected for the probe characteristics, the hole effect, and spatial variations in electrical resistivity (dipping). In the zones in which hydrothermally altered granite may coexist with unaltered granite, electrical resistivity modelling should be applied to obtain the “true” electrical resistivity by taking into account the 2D/3D geometry of the zone (Anderson, 2001). Although petrophysical models are commonly used to evaluate hydrocarbon saturation in sedimentary formations (Serra, 1984); for instance, the estimation of porosity changes from electrical resistivity is not so straightforward in

fractured granitic environments. The electrical conductivity can vary by several orders of magnitudes in zones and areas with different clay mineral contents and fracture densities, whether or not the zones are sealed. In the GRT-2 well, the electrical resistivity was measured with a five-electrode configuration, yielding five apparent resistivity values (RLA1–5) (Schlumberger, 2018). The contribution of the matrix to the electrical conductivity is supposed to be far lower than that of fractures, and it can vary by several orders of magnitude among unaltered and altered granite zones (Glaas et al., 2018). Measurements were obtained every 15cm in depth. These configurations are sensitive to the distance beyond the borehole wall. The shallowest resistivity (RLA1) mainly reflects the average resistivity of the borehole mud, and the deepest resistivity (RLA5) mainly reflects the average resistivity of the formation (granite matrix). In the GPK-1 well, the electrical resistivity was measured in 1989 using a laterolog tool with a two-electrode configuration every 15 cm in depth, yielding a shallow laterolog (LLS) and a deep laterolog (LLD). In this paper, only the most far-reaching resistivity curves (RLA5 and LLD) are presented on an inverted scale with highly resistive values on the left and conductive values on the right, allowing the reader to easily correlate GR, SWIR, and conductive peaks.

## 6.2.5. Results

### 6.2.5.1. GRT-2 well

#### *Dataset*

The petrographical log of the GRT-2 well (Figure 6.14) was built from the macroscopic description of the alteration mineralogy in the cuttings. The hydrothermal alteration grades were determined according to the occurrence of the secondary minerals (chlorite, illite, and drusy quartz) in the cuttings samples. This petrographical log presents three major units: reddish, oxidized granite at the top of the granitic basement, an altered zone from 2535 to 3060 m MD with a highly altered core from 2737 to 2875 m MD, and unaltered granite at the bottom of the well from 3060 to 3196 m MD. These main sections correlate well with the SWIR values; more precisely, we can distinguish four sections in which the variations in the 2200 nm absorption band area are indicative of the alteration grades around the permeable FZs.

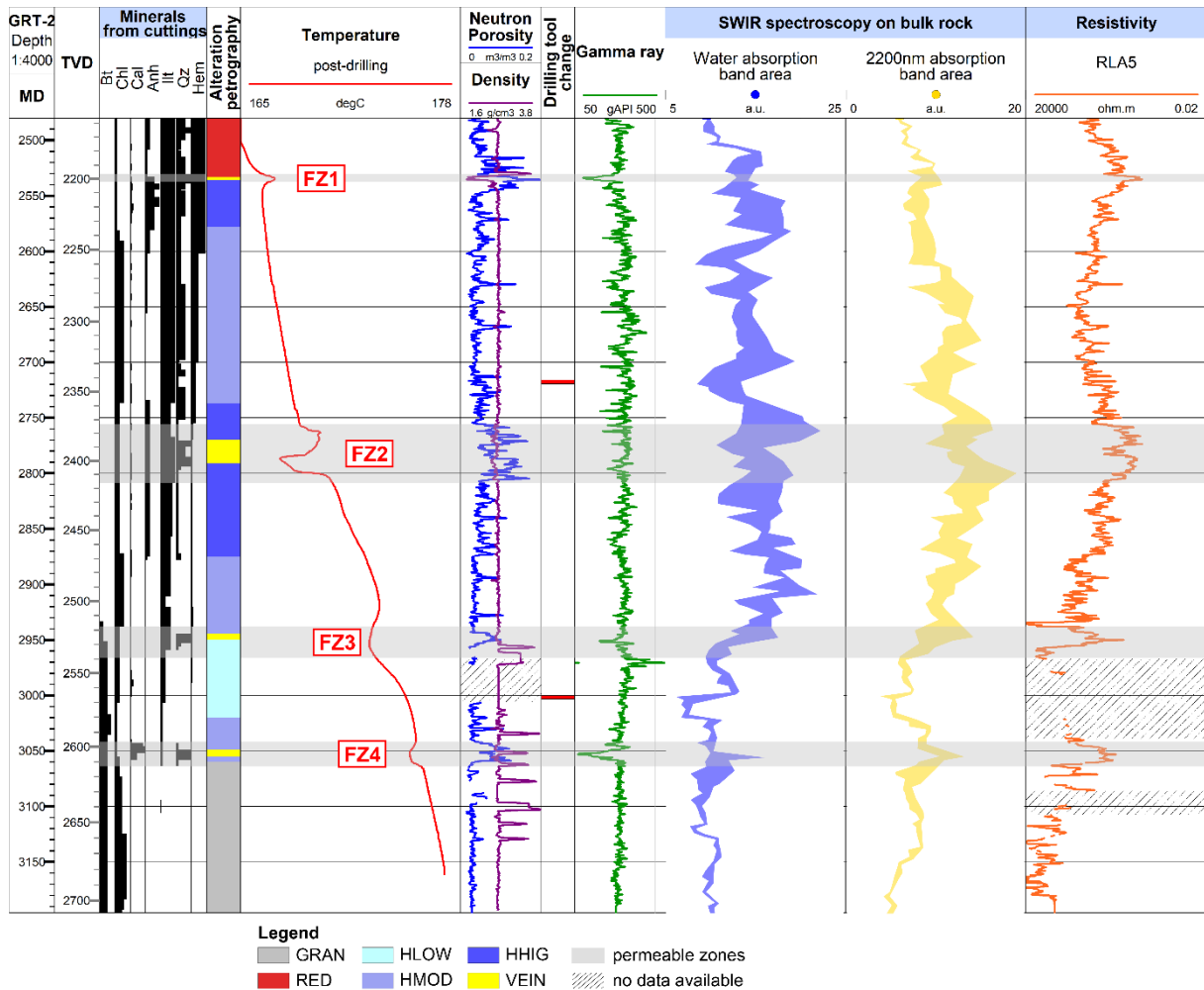


Figure 6.14: Composite log of the GRT-2 well at Rittersshoffen presenting the mineral quantity, petrographical log, T log, porosity and density logs, drilling tool change, total GR, SWIR results with water and the 2200 nm absorption band areas, and resistivity log. Petrographical facies abbreviations are defined in the legend in Figure 6.12.

### SWIR Variations and Hydrothermal Alteration Grades

The first section, from 2514 to 2570 m MD around the FZ1, is characterized by a small increase in the SWIR 2200 nm absorption band area, with scattered values between 6 and 10 a.u. It corresponds to the RED and HHIG facies observed with a binocular magnifier. The second section, from 2570 to 2970 m MD, comprises the FZ2 and the FZ3 and corresponds to the HHIG and HMOD facies observed with a binocular magnifier. This zone is characterized by the highest values of the 2200 nm absorption band area observed for the well. These values are highly scattered between 10 and 20 a.u., and because the acoustic image logs for GRT-2 are of poor quality, it is difficult to correlate the lowest values with opened fractures. The illitization appears to increase with the alteration grade, reaching its highest value (20 a.u.) in the fracture wall (FW) at 2780 m MD. In the FZ2, minimal values of the 2200 nm absorption band area are observed for a few samples located approximately 2773 m MD. In the acoustic image logs, an opened fracture filled with secondary drusy quartz (VEIN) is observed at 2773 m MD. Below, in the deepest section, acoustic image logs are not available. The third section, from 2970 to 3070 m MD, comprises the FZ4. The 2200 nm absorption band area appears to increase with the alteration grade, reaching its highest value (14 a.u.) in the FW at 3055 m MD, associated with a permeable FZ and a quartz vein at 3050 m MD. This zone corresponds to the HMOD and HLOW facies observed with a binocular magnifier. The fourth

section, from 3070 to 3196 m MD, corresponds to the GRAN facies observed with a binocular magnifier. The values of the 2200 nm absorption band area are stable and low, ranging from 5 to 8 a.u. The resistivity log also appears to correlate relatively well with the trend of the SWIR log (2200 nm absorption band area). In the open hole of the GRT-2 well, 500 m is altered granite and 200 m is unaltered granite. Thus, altered granite represents 70% of the open-hole section.

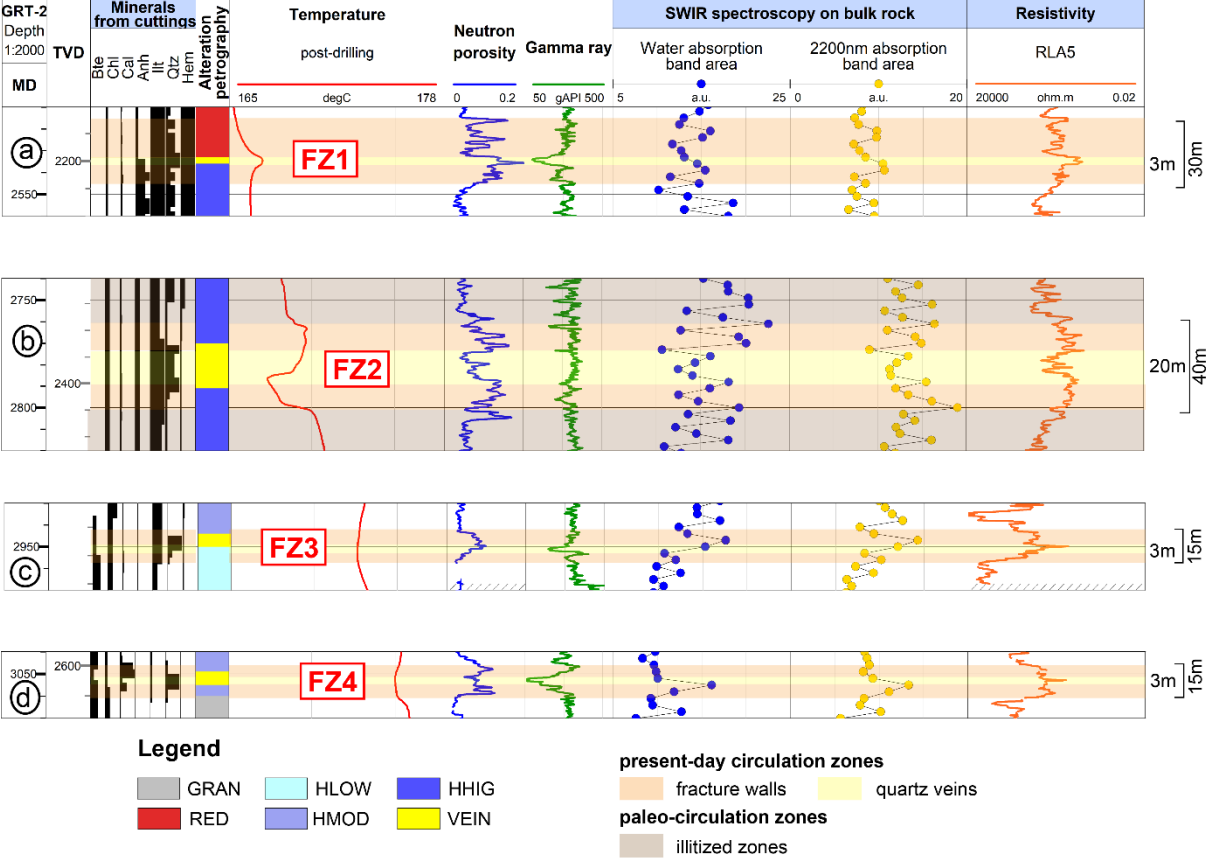


Figure 6.15: Magnified view of the four (a, b, c, and d) main permeable FZs of the GRT-2 well at Rittersshoffen, presenting the mineral quantity, petrographical log, T log, porosity and density logs, total GR, SWIR results with water and the 2200nm absorption band areas, and resistivity log (low values to the right). Petrographical facies abbreviations are defined in the legend in Figure 6.12.

*Permeable FZs*

The four permeable FZs of the GRT-2 well are shown in Figure 6.15 and are discussed below.

- FZ1 (2533 m MD). From the ultrasonic borehole images (UBI), no small-scale fracture is observed around the quartz vein for this FZ (Vidal et al., 2017). The porosity log shows high, scattered values in the entire FZ, the GR log exhibits a low peak correlated with the quartz vein, and the resistivity log shows a high conductivity peak that is also correlated with the quartz vein (Figure 6.15a). The thermal anomaly is localized at the quartz vein depth. The SWIR absorption band area at 2200 nm shows scattered and average values. According to the geophysical logs, the natural flow appears to be spatially correlated with the occurrence of a quartz vein. The observed conductivity peak in this permeable quartz vein could be due to the presence of geothermal brine, which is a very conductive fluid (Sanjuan et al., 2016).

- FZ2 (2770 m MD). The UBI is not available over the entire zone, but open fractures are observed at 2767, 2770, and 2774 m MD and are associated with the occurrence of quartz veins, translating into potential open pathways for fluids. Below these open fractures, smaller sealed fractures are observed from 2786 to 2789 m MD (Vidal et al., 2017). Whereas the GR is quite stable with some small negative peaks, the porosity, electrical conductivity, and SWIR 2200 nm absorption band area present two positive humps extending vertically over a length of 40 m (Figure 6.15b). This zone is the most contributive according to hydraulic tests (Baujard et al., 2017a), but the intra-FZ section reveals a complex architecture. At the centre of the zone, resistive values are observed (from 2776 to 2783 m MD), correlating with low neutron porosity, whereas the GR is unaffected, which goes along with the presence of the quartz vein observed in the cuttings. More generally, the observations in this FZ are consistent with a permeable FZ and brine circulations. The lack of UBI data in this zone does not help support our interpretation. However, the fact that the unavailability of UBI data is due to difficulties in running the tool in this zone because of cavings also suggests the existence of an FZ.
- FZ3 and FZ4 (2950 and 3052 m MD). No UBI is available for this zone; thus, we are unable to describe the architecture of the FZs. The presence of T anomalies implies circulation in both FZs. These two FZs look alike. In fact, they present a neutron porosity increase over 10 m, a low GR, and a sharp peak in electrical conductivity correlated with the quartz veins (Figures 6.15b and c). Two higher resistivity values are observed above and below the FW, surrounding the zone of higher neutron porosity. These peaks appear to be related to the presence of unaltered (or slightly altered) granite, which occurs from 2934 m MD according to the high resistive values and also appears to be correlated with the SWIR values, which are stable and low at this depth. The SWIR 2200 nm absorption band area is high in both of these FZs. For both FZs, the sharp increase in electrical conductivity appears to be linked to brine circulation in the quartz veins, whereas the lower conductive values above and below the quartz veins appear to be linked to the occurrence of illite in the FW. The abrupt decrease in electrical conductivity suggests a closely delimited hydrothermal circulation zone.

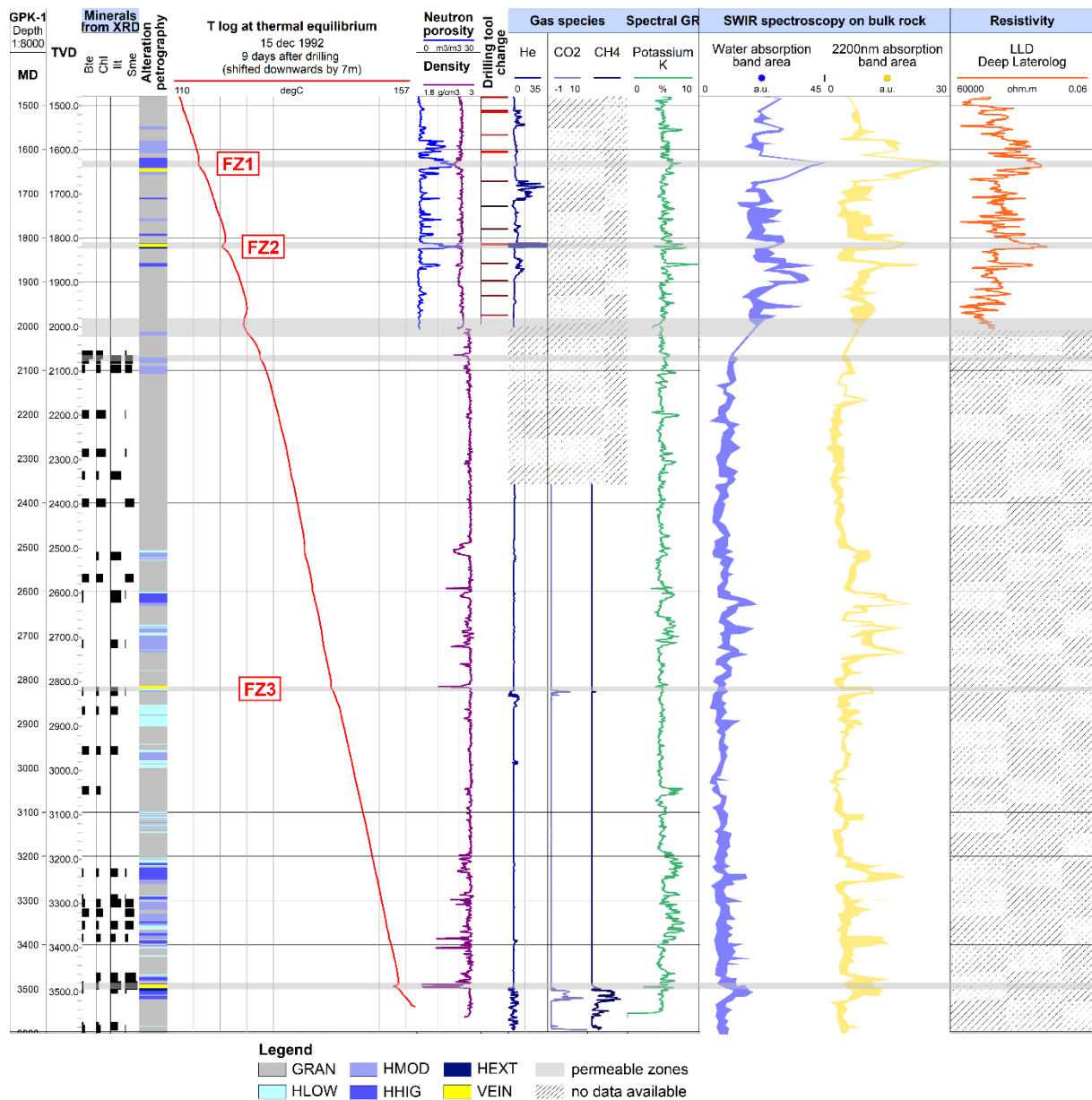


Figure 6.16: Composite log of the GPK-1 well at Soultz-sous-Forêts, presenting the mineral quantity, petrographical log, T log, porosity and density logs, drilling tool change, gas species, spectral GR-K, SWIR results with water and 2200 nm absorption band areas, and resistivity log. Petrographical facies abbreviations are defined in the legend in Figure 6.12.

### 6.2.5.2. GPK-1 well

#### Dataset

The petrographic log of the GPK-1 well was compiled by Genter et al., (1997b, 1997a) and Traineau et al., (1992) from cuttings samples based on macroscopic observations with a binocular magnifier. The grades of hydrothermal alteration were determined according to the occurrence of the secondary minerals (chlorite, illite, and drusy quartz) in the cuttings samples. This petrographical log presents three major hydrothermally altered granite units surrounded by unaltered granite. These three units extend from 1580 to 1830 m MD, from 2600 to 2800 m MD, and from 3200 to 3500 m MD.

### *SWIR Variations and Hydrothermal Alteration Grades*

The first section, from 1580 to 1830 m MD, is characterized by very scattered high values between 3 and 26 a.u. for the 2200 nm absorption band area. The shift of the SWIR values to high values in this section could be due to a granulometry effect, as this section was drilled first and was then deepened, resulting in a change in the cuttings grain size. Based on binocular magnifier observations, this section corresponds to GRAN with hydrothermally altered zones of HMOD/HHIG facies. These altered zones appear to correlate with the SWIR values, which are higher, i.e., between 8-17 a.u. for the 2200 nm absorption band area for HMOD (1547-1553 m MD, 1579-1606 m MD, and 1650-1656 m MD) and approximately 25 a.u. for HHIG (at 1620-1640 m MD). Quartz veins were identified at 1645 m MD (FZ1) and at 1814 m MD (FZ2), where drusy quartz was visible by observations of cuttings. The latter corresponds to a fracture vein that is visible in core samples (Figure 6.16).

The second section, from 2605 to 2827 m MD, is characterized by high, scattered values between 3 and 19 a.u. for the 2200 nm absorption band area. Based on binocular magnifier observations, it corresponds to GRAN with occurrences of low to high hydrothermal alterations. The HLOW grade appears to correlate with the 2200 nm absorption band area, with values between 5 and 10 a.u. at 2600-2603 m MD, 2610- 2612 m MD, 2676-2679 m MD, 2681 m MD, 2693-2701 m MD, and 2731-2733 m MD. Occurrences of HMOD suggest a good correlation with the 2200 nm absorption band area, with values between 7 and 15 a.u. at 2625-2632 m MD, 2679-2681 m MD, 2685-2692 m MD, 2701-2731 m MD, and 2733-2736 m MD. The HHIG occurrences also suggest a good correlation with the stable values of the 2200 nm absorption band area, which range from 14 to 19 a.u. A quartz vein is observed in the cuttings from 2817 to 2818 m MD (FZ3). An open fracture is observed on the FMI log and is characterized by the occurrence of He and CO<sub>2</sub> content, evidencing the presence of geothermal fluid.

The third section, from 3203 to 3523 m MD, is characterized by high, scattered values between 3 and 19 a.u. for the 2200 nm absorption band area. Based on binocular magnifier observations, it corresponds to GRAN with occurrences of hydrothermal alterations of HLOW to HEXT facies. HLOW appears to correlate with values of the 2200 nm absorption band area between 4 and 8 a.u. Two quartz veins are observed in the same fracture zone at 3489 and 3496 m MD in the cuttings. These open fractures, which match the flow log anomalies, are observed on the acoustic image logs at 3490 and at 3495 m MD (FZ4).

Outside of these sections, from 2065 to 2605 m MD and from 2827 to 3203 m MD, we observe low, very stable values between 2 and 9 a.u. for the 2200 nm absorption band area. Based on binocular magnifier observations, these correspond to GRAN, with HLOW-HMOD from 2505 to 2530 m MD. These hydrothermal alteration grades suggest a good correlation with the 2200 nm absorption band area which presents higher values of approximately 9 a.u. In the open-hole section of the GPK-1 well, 500 m is hydrothermally altered granite and 2200 m is unaltered granite; thus, the hydrothermally altered granite represents only 20% of the open hole.

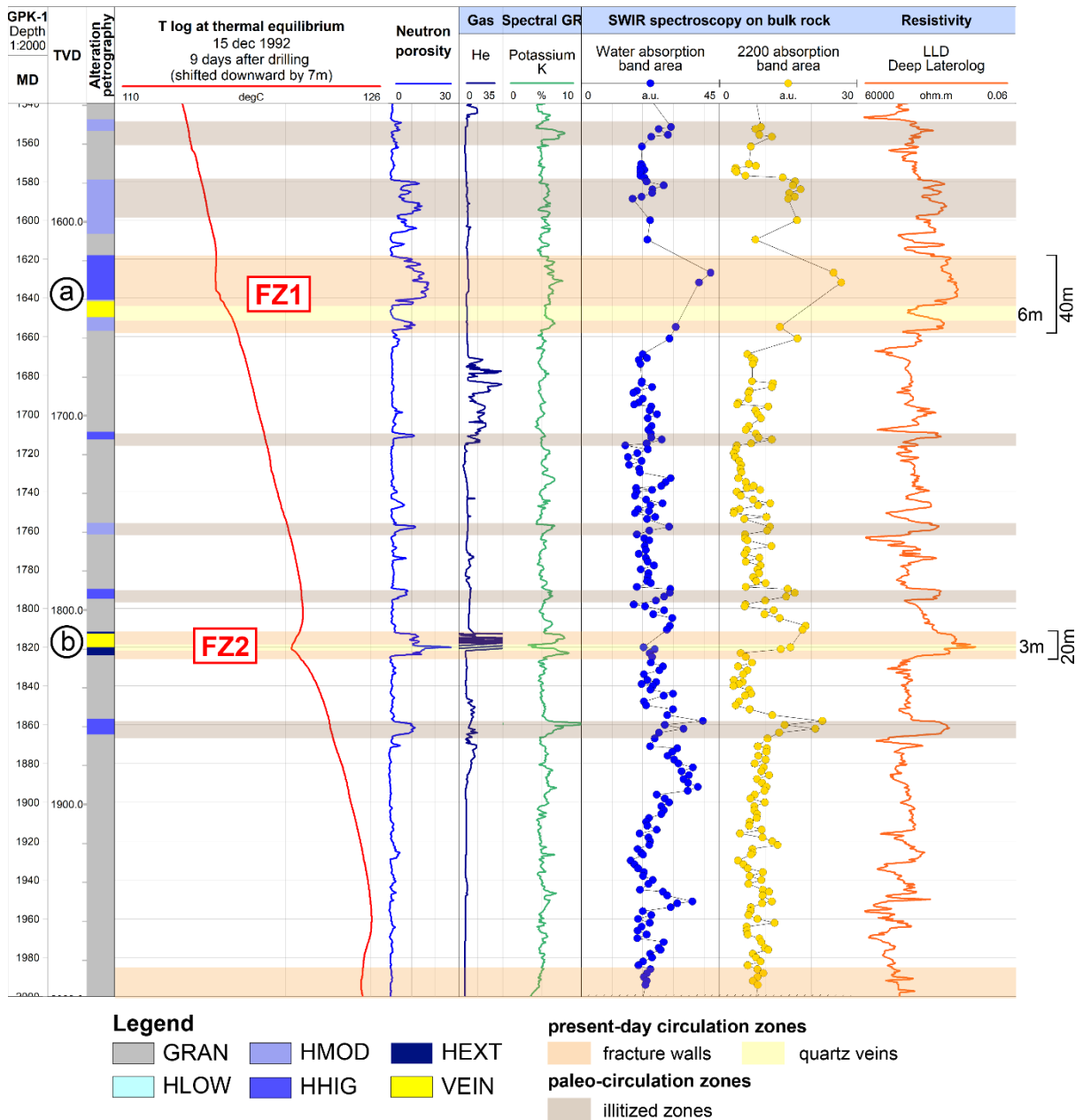


Figure 6.17: Magnified view of two (a and b) main permeable FZs of the GPK-1 well at Soultz-sous-Forêts, presenting the petrographical log, T log, porosity and density logs, spectral GR-K, SWIR results with water and 2200 nm absorption band areas, and resistivity log. Petrographical facies abbreviations are defined in the legend in Figure 6.12.

### Permeable FZs

The two FZs of the upper section of the GPK-1 well (1540-2000 m MD) are shown in Figure 6.17 and are discussed below.

(1) FZ1 (1645 m MD). A quartz vein was observed, and a T anomaly above the quartz vein proves a contributive flow zone (Figure 6.17a). The porosity presents high values above and below the quartz vein, whereas low values are observed at the quartz vein depth. The GR-K is also slightly higher above and below the quartz vein, whereas it is low at the quartz vein. Very small He content is also visible above the quartz vein. The laterolog resistivity (LLD) presents high conductivity values above the quartz vein and high resistivity values at the quartz

vein depth. He content is also observed in this section, indicating the occurrence of dissolved gas in the geothermal fluid (Figures 6.16 and 6.17). The SWIR values are high in the FZ, particularly above the quartz vein. The hydraulic data show that flow anomalies are mainly due to the FZ core (Jung, 1992). However, surprisingly, the quartz vein presents neither a sharp T anomaly nor evidence of fluid circulations from geophysical logs. The geophysical anomalies associated with the FW above the sealed quartz vein could suggest that the FW corresponds to porous granite which allows a good connection between the well and the near-well field. On the other hand, the geophysical anomalies of the FW below the quartz vein could indicate that the FW acts as a tight zone possibly caused by secondary mineral precipitations.

(2) FZ2 (1814 m MD). This FZ presents a localized T anomaly correlated with the quartz vein (Figure 6.17b). According to this T anomaly and considering the section between 1400 and 2000 m, the majority of the fluid flows from this FZ (Jung, 1992; Schellschmidt and Schulz, 1992). The porosity is high and shows a sharp peak in its centre that is correlated with the drusy quartz vein. The GR-K presents a low peak at the quartz vein depth and high peaks in the FW above and below the quartz vein. The resistivity laterolog presents high electrical conductivity values, with a sharp very conductive peak at the quartz vein depth, and lower-than-average resistivity values above and below that are correlated with the FWs. The SWIR 2200 nm absorption band area presents higher values in the FZ. As for FZ3 and FZ4 in the GRT-2 well, the sharp and very high conductivity values could be associated with the brine circulating in the quartz vein since high GR-K and the conductive zone above and below coincide with the high amount of clay minerals (illite) in the FW. The very high He content matching the quartz vein (>200 ppm) evidences the occurrence of permeability indicators such as geothermal gases dissolved in the brine.

## 6.2.6. Discussion

### 6.2.6.1. SWIR as a permeability indicator

The SWIR method showed good reproducibility of the measurements obtained on cuttings samples. Stable and low values appear to be systematically observed in conjunction with the unaltered or slightly hydrothermally altered granite (Figures 6.14, 6.15, and 6.18). The geothermal reservoirs of the Soultz-sous-Forêts and Rittershoffen geothermal sites are highly fractured, with fracture infillings corresponding to secondary drusy quartz and some carbonates, and present hydrothermally altered zones. The heterogeneity of the hydrothermal facies encountered produces heterogeneity in the SWIR signal that appears on the SWIR log as peaks exceeding the mean values, surely reflecting the presence of mineralisations associated with hydrothermal circulations. Because the primary and secondary mineralogy of the deep granites in the URG basement does not vary significantly, the SWIR method is easily applicable to the detection of fluid-rock interaction processes linked to geothermal fluid circulation in the granitic fractured reservoirs of geothermal wells. More generally, the combination of the SWIR 2200 nm absorption band area and the spectral GR-K is a strong illite indicator. On a large scale, the scattering (linked to quartz vein occurrences in the FZs) and the high values of the SWIR 2200 nm absorption band area localize the highly altered zones crossed by the wells. These highly altered zones are linked to the main faults and are interpreted as the permeable zones of the well (Figures 6.15 and 6.17). The vertical extent of this scattering provides in-depth information on the extent of the well volume that is affected by hydrothermal circulations. This initial study applying the SWIR method to the Soultz-sous-Forêts and Rittershoffen geothermal sites will soon be reinforced by an ongoing study in which

the SWIR method is applied to the new Illkirch geothermal site. This will help us confirm our interpretation and extend the interpretation to the URG. Based only on geophysical logs (acoustic image logs were not acquired below 2850 m MD), the main permeable FZ of GRT-2 was identified from 2766-2800 m MD with a true thickness of 35 m by Vidal et al., (2017). Our SWIR method yields new complementary results that provide new information about the FZ architecture, and we observe that the FZ is more extended than was described by Vidal et al., (2017) based on geophysical logs. SWIR helps distinguish the part of the actual FZ that controls the present-day circulations and the part of the FZ that has been affected by paleo-circulations. In fact, this study using SWIR data reveals that this zone presents an intense illitization extending from 2743 to 2884 m MD and thus a true thickness of 112 m. Previous mineralogical studies of the GRT-2 well suggested that a low intensity of illitization could explain the high permeability of the well (Vidal et al., 2018). However, the GRT-2 well presents high values of the 2200 nm absorption band area (20 a.u.); these are higher than the values measured in the GPK-1 well (13 a.u.) and also higher than those measured in other wells such as GRT-1 and GPK-4 (Glaas et al., 2019a). These high SWIR 2200 nm absorption band area values are surprising considering the results of Vidal et al., (2018). The advantage of the SWIR method is that it provides a general and continuous overview of the well in terms of permeability indicators that prevents overinterpretation of punctual localized data.

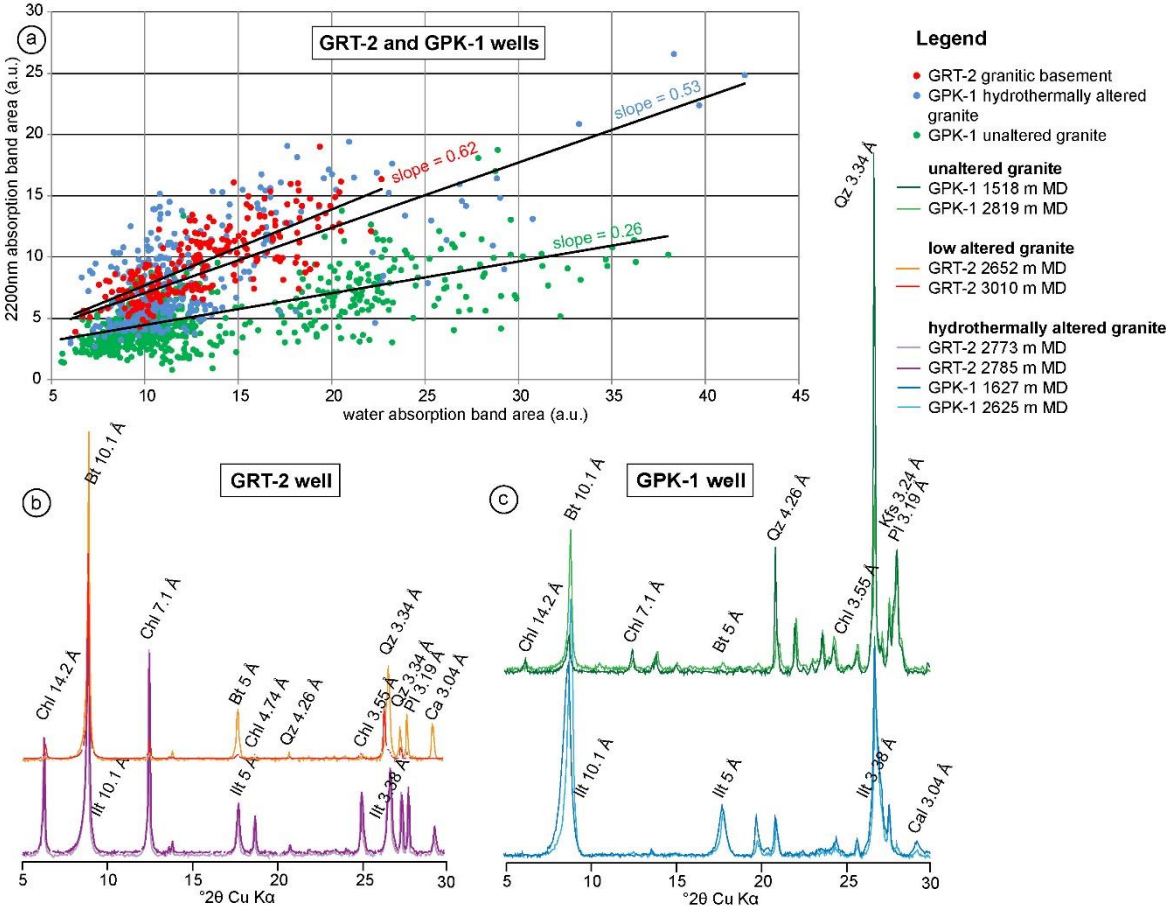


Figure 6.18: Correlation of the SWIR water and 2200 nm absorption band area for (a) the GRT-2 and GPK-1 wells, (b) XRD results for the slightly altered granite and the hydrothermally altered granite in the GRT-2 well, and (c) XRD results for the unaltered granite and the hydrothermally altered granite in the GPK-1 well.

#### 6.2.6.2. SWIR correlation

From simple observations, for both the GRT-2 and GPK-1 wells, the water absorption band area and the 2200 nm absorption band area appear to be correlated (Figures 6.14 and 6.16). In fact, the ratio between the water absorption band area and the 2200 nm absorption band area varies significantly according to the species of aluminous phyllosilicates considered (illite and micas) (Simpson and Rae, 2018). The correlation between these two absorption bands was tested for both wells (Figure 6.18). For the GRT-2 well, the correlation appears to be linear with a correlation coefficient of 0.62 (Figure 6.18a). For the GPK-1 well, the correlation presents two linear tendencies (Figure 6.18a). After classifying the samples into altered and unaltered granite on the basis of petrographic observations, it was found that these two tendencies correspond to hydrothermally altered granite with a coefficient of 0.53 and to unaltered granite with a coefficient of 0.26 (Figure 6.18a). From mineralogical identifications (XRD and binocular magnifier observations), the unaltered granite in both wells is characterized by the presence of biotite and chlorite whereas the altered granite is essentially characterized by the presence of illite and illite-rich illite/smectite mixed layers in considerable amounts (Figures 6.18b and c). Based on the phyllosilicate mineralogy of the unaltered and altered granite, it seems relevant to use the 2200 nm absorption band area as an indicator of the illitization rate of the granitic rocks of Northern Alsace. In the GPK-1 well, we can clearly see that for a similar value of the water absorption band area (e.g., a water absorption band area of 20 a.u.), we observe values of the 2200 nm absorption band area of the illitized granite more than two times higher than those observed for the unaltered granite (17 a.u. and 7 a.u., respectively). Considering the absorption band area at 2200 nm, the lower absorption depth noted for the samples of unaltered granite (Figure 6.18) can be explained by a weak to very weak contribution of both primary biotite and chlorite to the absorption band near 2200 nm (Figure 6.13b). The correlation between the water absorption band area and the 2200 nm absorption band area indicates that the mineralogy of the GRT-2 well is more homogeneous than that of the GPK-1 well (Figure 6.18). From the SWIR results, the GRT-2 well showed a higher degree of hydrothermal alteration all along the well compared to the GPK-1 well. In this well, unaltered granite presents some localized sharp peaks of the 2200 nm absorption band area that correspond to the fracture-controlled altered zones. The interpretation of the two correlation tendencies of the GPK-1 well is consistent along with the petrographic observations: localized FZs are intersected on small apparent depth extents (Figures 6.16 and 6.18). These mineralogical and structural differences between the wells are explained by their different trajectories and concepts. Notably, the GPK-1 well was drilled nearly vertically and intersects few localized FZs at a higher angle, whereas the GRT-2 well is highly deviated but has an orientation parallel to the Rittershoffen local fault over its approximately 400 m apparent length. In fact, the GPK-1 well required stimulation, whereas the GRT-2 well did not, suggesting that intense illitization is a good indicator of permeability.

#### 6.2.6.3. Electrical Logs and SWIR

The similar shapes and tendencies observed for the electrical logs and the SWIR data, outside of brine circulation in FZs, at first show a considerable control of illite on the electrical properties measured in the GRT-2 and GPK-1 wells (Figure 6.19). Very conductive zones are often associated with the SWIR 2200 nm absorption band area and with high GR-K peaks pointing to highly hydrothermally altered zones rich in illite. This type of zone could be observed either associated with a T anomaly, yielding an altered zone that is contributive (in FZ1 at 1620-1640 m MD in GPK-1) (Figure 6.17a), or with a straight T profile, yielding a sealed illitized zone

(at 1550, 1579-1606, 1710, 1758, 1792, and 1860 m MD in GPK-1), which could be paleo-circulation zones (Figure 6.17). Resistive peaks can correlate with negative 2200 nm absorption band area peaks and the occurrence of a quartz vein, suggesting a fracture core plugged with secondary drusy quartz filling with insufficient residual porosity for abundant circulation and no abundant illite (low GR) (FZ1 at 1645 m MD in GPK-1) (Figure 6.17a). At a more restricted level, positive conductivity peaks can also correlate with negative GR-K peaks, low SWIR 2200 nm absorption band area, and T anomalies, translating into the presence of brine such as in the cores of FZs (FZ2 at 1814 m in GPK-1, FZ1 at 2534 m MD, FZ3 at 2950 m MD, and FZ4 at 3050 m MD in GRT-2) (Figures 6.15 and 6.17).

#### 6.2.6.4. FZ signatures

In the GRT-2 well, FZs are always correlated with T anomalies and VEIN facies. This observation is probably related to the drusy euhedral quartz geometry, which keeps the space open and prevents plugging of the fracture. In contrast, the textural organization of illite in the FWs tends to plug the zone (Figure 6.19). A specific signature of the resistivity laterolog is observed in both the GRT-2 and GPK-1 wells (FZ3 and FZ4 in GRT-2 and FZ2 in GPK-1), with very low resistivity values (20 ohm-m) corresponding to the occurrence of geothermal brine within the quartz vein as well as low resistivity values (20 ohm-m) corresponding to illite occurrence in the FW (Figures 6.15, 6.17, and 6.19). We can distinguish three types of FZs (Figure 6.19):

- FZa: permeable FZs with localized brine contributions, such as FZ1, FZ3, and FZ4 in GRT-2 (Figure 6.15a, c, and d) and FZ2 in GPK-1 (Figures 6.15a, c, d, 6.17b, and 6.19)
- FZb: permeable FZs with multiple brine contributions, such as FZ2 in GRT-2 and FZ1 in GPK-1 (Figures 6.15b, 6.17a, and 6.19)
- FZc: paleo-permeable FZs, such as those at 1550, 1579-1606, 1710, 1758, 1792, and 1860 m MD in GPK-1 (Figures 6.17 and 6.19)

Evans et al., (2005) showed that in the open-hole section of GPK-1, the poststimulated flow zones systematically match the permeable and paleo-permeable FZs.

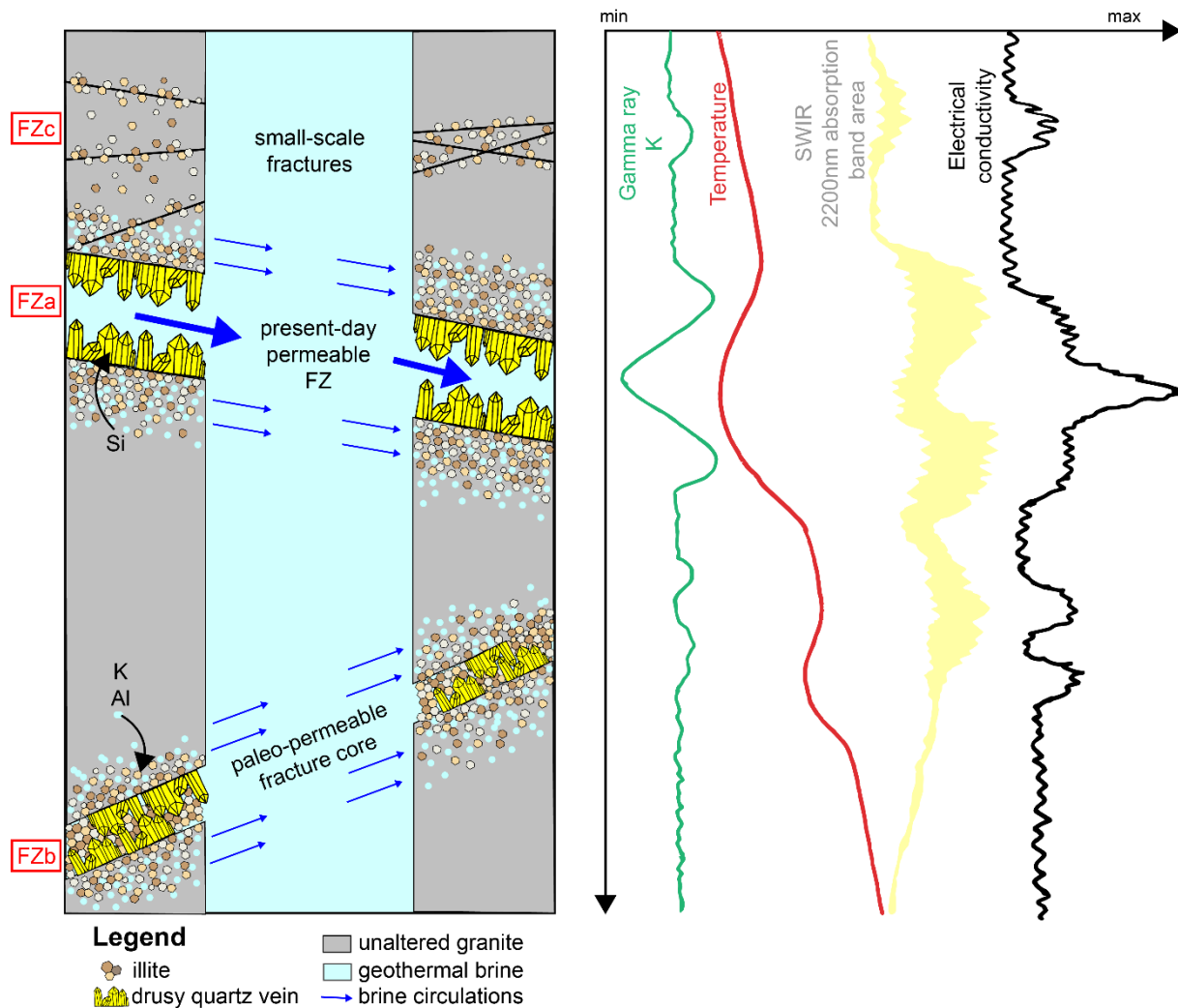


Figure 6.19: Model showing the variation in the 2200 nm absorption band area and its correlation with geophysical logs (gamma ray, temperature, and electrical conductivity) in response to different grades of hydrothermal alteration of the granite and different FZ architectures.

#### 6.2.6.5. Applications

In future geothermal projects in the URG, the SWIR method could be a routine mud logging method. As a matter of fact, along with GR measurements obtained while drilling (MWD), cuttings provide the first data obtained during drilling. The use of SWIR measurements during drilling, when previously calibrated with the granitic analogue signature, could be helpful in determining the extent of the hydrothermally altered fault damage zone and in quantifying the alteration grade encountered in the granite. This could help determine when the exploration well leaves the altered zone and thus when to stop drilling. The SWIR method could be used as a routine mud logging analysis on-site during drilling after washing and drying the cuttings samples. It could also be further refined for the alteration mineralogy identification in geothermal systems (Simpson and Rae, 2018).

In enhanced geothermal system projects, SWIR could be used to target paleo-permeable zones that could be reopened (sealed fractures and damage zones), thereby enhancing the permeability between the well and the reservoir during stimulation operations. In a similar manner, for existing geothermal wells in the URG drilled in granite, SWIR could be used as a

complementary method to precisely characterize the hydrothermal alterations around the FZs and to target potential stimulation zones in cases of decreased productivity.

### 6.2.7. Conclusion

In this paper, the analysis of the correlation between the SWIR water and 2200 nm absorption bands areas confirms the petrography observed in both wells. By showing that the mineralogy is more homogeneous in the GRT-2 well than in the GPK-1 well, the results confirm that the two wells do not crosscut the circulation zones in the same way. Showing that the fluid-rock ratio is higher in the GRT-2 well than in the GPK-1 well, these results are consistent, according to hydrothermal concepts, with the higher productivity of the GRT-2 well compared to the GPK-1 well, which required stimulation. In this study, we observe three types of FZs: FZs with a localized contribution, FZs with multiple contributions, and paleo permeable FZs. In conclusion, the SWIR method is a robust method for the detection of paleo- and present circulation zones for geothermal applications. By the joint interpretation of SWIR data and other geophysical logs, this method could be used to determine whether the studied zone is a currently active circulation zone or a paleo-circulation zone. According to the values of the SWIR 2200 nm absorption band area, grades of alteration as well as the fluid-rock ratio trend can be determined. The similar variations in the SWIR 2200 nm absorption band area and the electrical logs demonstrate a significant influence of the rock clay mineral content (quantity of illitic minerals) on the electrical response. A specific electrical signature is observed in each well, indicating the FZ architecture and brine or illite contributions.

### 6.2.8. Acknowledgements

This manuscript was prepared as a contribution to the PhD thesis (University of Strasbourg) of Carole Glaas which is cofunded by ES-Géothermie and ANRT (French Agency for Research and Technology). The authors warmly thank Benoît Hébert for allowing them to use his in-house Visual Basic software (TSS) and the Poitiers University team for the use of the TerraSpec on the Soultz-sous-Forêts site. They warmly thank Chrystel Dezayes from BRGM for the access to the Soultz-sous-Forêts cuttings samples. The authors acknowledge the EGS Alsace and DEEP-EM projects funded by ADEME (French Agency for Environment), GEIE EMC, and ECOGI for providing the Soultz-sous-Forêts and Rittershoffen cuttings samples and logs. Sophie Funfrock is thanked for improving the manuscript with English revision. Tom Schintgen is also thanked for the review of the manuscript.

### 6.2.9. Supporting information

This supporting information provides details on the SWIR results acquired in both GRT-2 and GPK-1 wells like the intra-sample variability and comparison between manual fit and automatic fit with the TSS software.

#### 6.2.9.1. Intra-sample variability in GRT-2 and GPK-1

For both GRT-2 and GPK-1 wells the intra-sample variability of the granite cuttings was tested. As each cuttings bag represents sections of drilled rocks (see section 6.2.4.1.) and as the cuttings could not be homogeneously mixed in the bag, several measurements were carried out on the same cuttings bag. In the GRT-2 well 10 measurements were done on the same cuttings bag (Figure 6.S1) whereas only 5 measurements were done in the GPK-1 well (Figure 6.S2) because of a lower amount of cuttings available. Error bounds were then calculated for

each cuttings bag in order to observe if the range of variation is not exceeding the scattering of the data. In both wells, we can observe that the variability is low in unaltered granite and higher in the hydrothermally altered granite. Also, the variability observed in the GRT-2 well is higher than in the GPK-1 well. These differences in both wells could be due to the heterogeneity of the mineralogy.

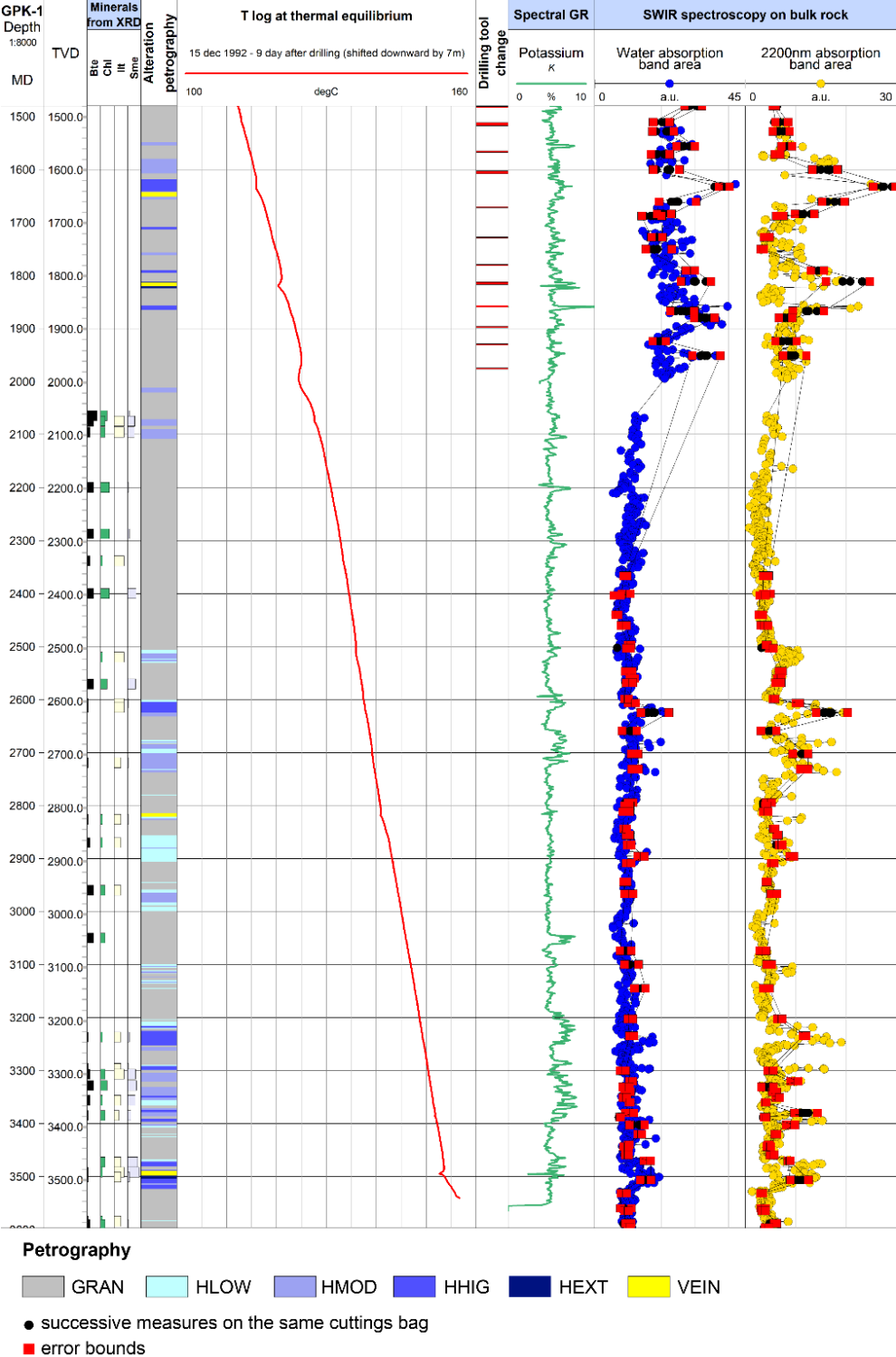
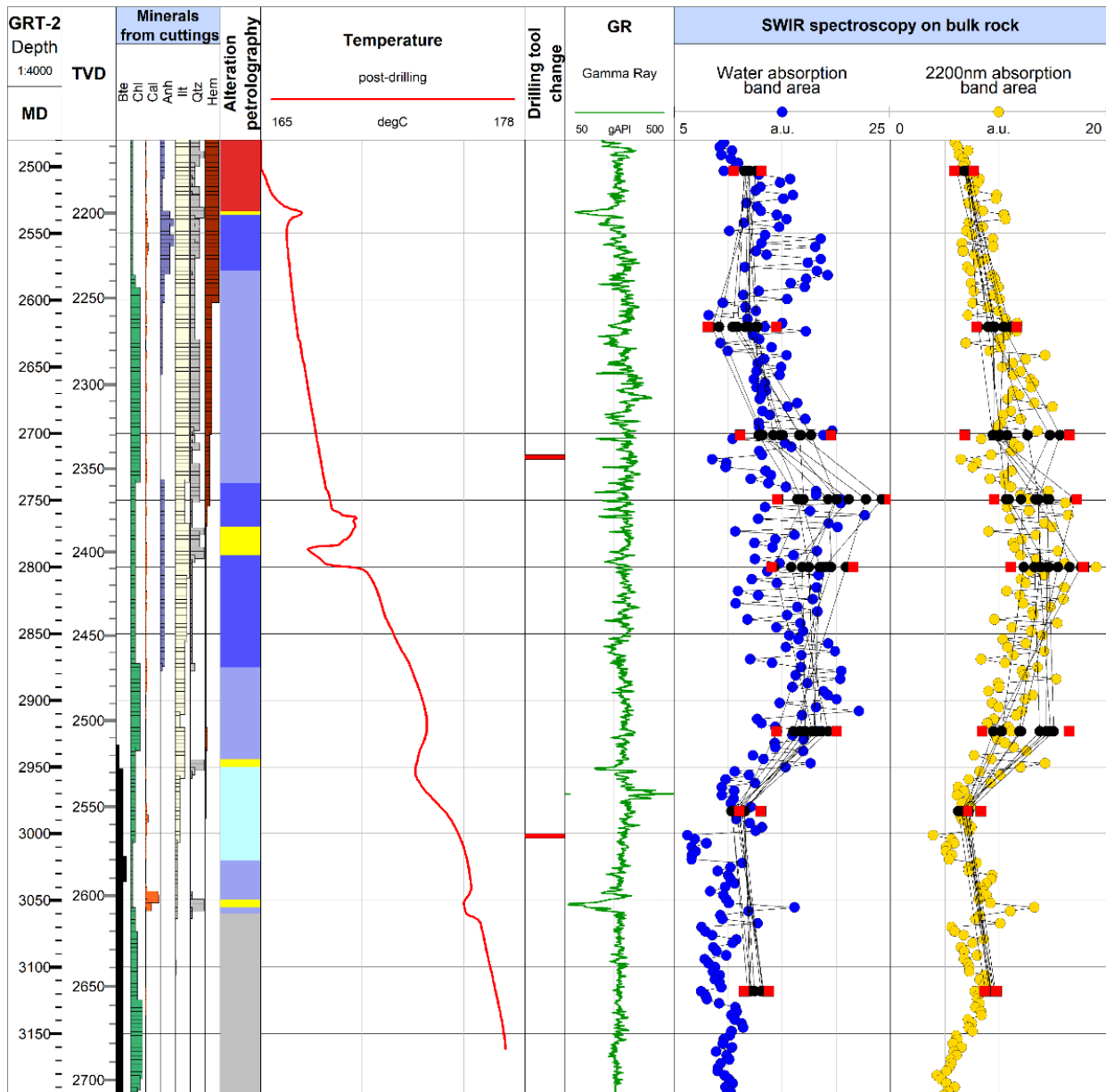


Figure 6.S1: Composite log of the GPK-1 well presenting the secondary minerals, the petrographical log built from the mineralogical observations, the temperature log, the spectral K-GR log and the SWIR results. The successive measurements realized for each cuttings bag are represented by black full circles and the error bounds calculated from these successive measurements are represented by the distance between red squares for each cuttings bag.



#### Petrography

■ RED   
 ■ GRAN   
 ■ HLOW   
 ■ HMOD   
 ■ HHIG   
 ■ VEIN

● successive measures on the same cuttings bag

■ error bounds

Figure 6.S2: Composite log of the GRT-2 well presenting the secondary minerals, the petrographical log built from the mineralogical observations, the temperature log, the GR log and the SWIR results. The successive measurements realized for each cuttings bag are represented by black full circles and the error bounds calculated from these successive measurements are represented by the distance between red squares for each cuttings bag.

#### 6.2.9.2. Auto fit and manual fit

For the GRT-2 well, position and half width at half maximum (HWHM) were locked for each simulation profile. However, different sets of position and HWHM were used. The simulation profiles were accepted with a weighted profile R-factor (Rwp) lower than 0.05. For the GPK-1 well, with regard to the huge amount of profiles calculated (1190), position and HWHM were free fitted by TSS for each simulation profile. The areas of the water absorption band and the 2200 nm absorption band were also fitted manually for some profiles to compare if there is a

significant deviation of the area with the free fitting. Results showed that there was no significant change in the area between profiles fitted manually or free-fitted by TSS for the GPK-1 well (Figure 6.S3).

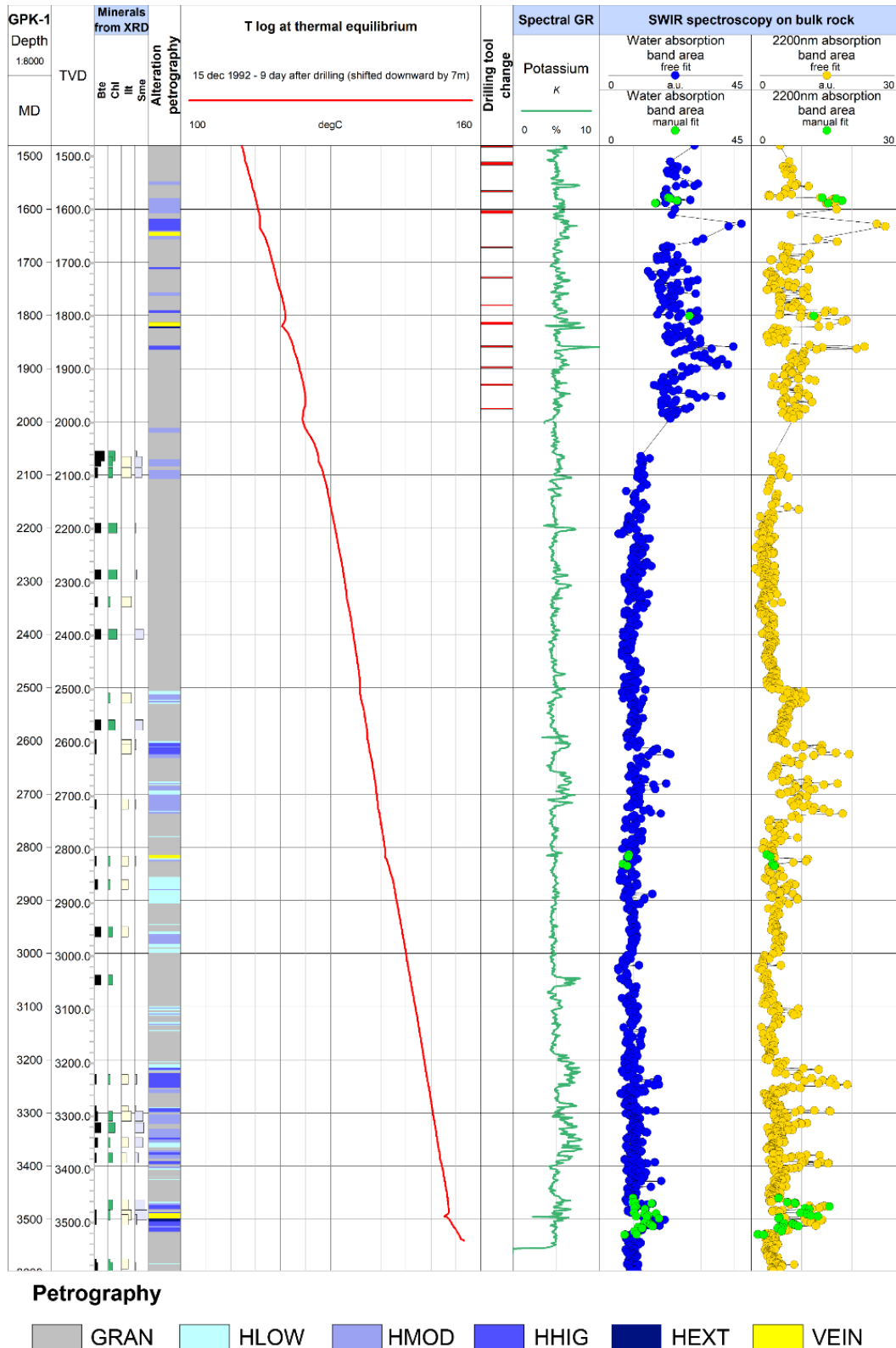


Figure 6.S3: Composite log of the GPK-1 well presenting the secondary minerals, the petrographical log built from the mineralogical observations, the temperature log, the spectral K-GR log and the SWIR results that were free-fitted with the TSS software (blue and yellow full circles for water and 2200 nm absorption band areas, respectively). The light green full circles represent the SWIR results manually fitted.





### 6.3. Contribution of SWIR to the Clay Signature of Permeable Fracture Zones in the Granitic Basement. Overview of Soultz and Rittershoffen wells. Presented at the European Geothermal Congress 2019.

C. Glaas<sup>1,2,3</sup>, J. Vidal<sup>4</sup>, P. Patrier<sup>3</sup>, D. Beaufort<sup>3</sup>, A. Genter<sup>2</sup>

<sup>1</sup> University of Strasbourg, CNRS, UMR 7516 IPGS, 5 Rue René Descartes, 67084 Strasbourg Cedex, France

<sup>2</sup> ÉS Géothermie, : 5, rue André Marie Ampère, 67450 Mundolsheim, France.

<sup>3</sup> University of Poitiers, CNRS UMR 7285 IC2MP, HydrASA, Bat B8 rue Albert Turpain, TSA51106, F-86073 Poitiers Cedex 9, France

<sup>4</sup> University of Chile, FCFM, Dept. of Geology, Andean Geothermal Center of Excellence (CEGA), Plaza Ercilla 803, Santiago, Chile

**Keywords:** geothermal, fractured granite, cuttings, short wave infrared (SWIR) spectroscopy, hydrothermal alteration, illite

#### 6.3.1. Abstract

The high potential of the Upper Rhine Graben (URG) for geothermal relies on more than 30 years of expertise in crystalline geothermal reservoirs developed in Soultz-sous-Forêts (France), the near presence of direct users in the area of the Eurometropolis of Strasbourg and undeniably, the acceptance of the population and the presence of investors. Hence, Strasbourg area is very attractive and is very active in the development of deep geothermal plants. In this context, this study proposes an innovative method of geothermal exploration to detect the highly hydrothermally altered zones corresponding to permeable fracture zones (FZ). They are acting as natural pathways for the fluid in the crystalline rocks of the URG. Applied on cuttings of granite samples with reduced costs and time, the short-wave infrared (SWIR) spectroscopy method was realized on geothermal wells from Northern Alsace (Soultz-sous-Forêts, Rittershoffen) for calibration. Indeed, the FZ of these wells were first characterized by structural and mineralogical studies done from borehole image logs and cuttings analysis, respectively. In the Rittershoffen wells, the occurrence of small crystallites of illite and illite-smectite mixed layers minerals (<10% smectite) were systematically and spatially linked with the occurrence of permeable FZ and thus provide specific clay signatures. In the Soultz wells, mineralogy and FZ structure were deeply studied with core samples descriptions. SWIR spectra were acquired on more than 2400 cuttings in Soultz-sous-Forêts and Rittershoffen wells. The area of the SWIR peak at 2200 nm wavelength correlates with the amount of illitic minerals and can thus be a direct indicator of argilization and alteration. Observations show that SWIR results correlate with the former X-ray diffraction (XRD) results, binocular magnifier or core observations identifying the several granitic facies affected by hydrothermal alteration. Higher the hydrothermal alteration is and higher the SWIR signal is. SWIR spectroscopy is thus a promising tool to estimate the alteration intensity, and could be a complementary tool for the characterization of FZ architecture. Using routinely field SWIR spectroscopy on crystalline cuttings could be a pioneer method to characterize FZ and their permeability at early stages of geothermal exploration wells.

#### 6.3.2. Introduction

The development of the SWIR method as a tool for clay quantification makes sense in the context of developing the deep geothermal expertise in fractured granitic reservoirs. Hence, a better understanding of highly argilized zones corresponding to permeable fracture zones which are acting as natural pathways for the fluid in the crystalline rocks of the URG and their

contribution to the well productivity or injectivity is a key point for geothermal achievement (Ledésert et al., 1993, 2010; Sausse and Genter, 2005; Rotstein et al., 2006; Dezayes et al., 2010; Sausse et al., 2010; Vidal and Genter, 2018). Indeed, a better understanding of permeable zones localization will bring a precise knowledge of the several FZ that the well encounters. This will help to design optimized well implementations for new projects but will also help to precisely plan further chemical stimulations in case of well with reduced injectivity or productivity index. Beyond these objectives, the SWIR method is also rapid in terms of acquisition time and presents reduced costs. Because of mineralogy similarities, the applicability of the method could extend to other geothermal projects under development in the Strasbourg area, projects which both target the granitic fractured basement of the URG as geothermal reservoir.

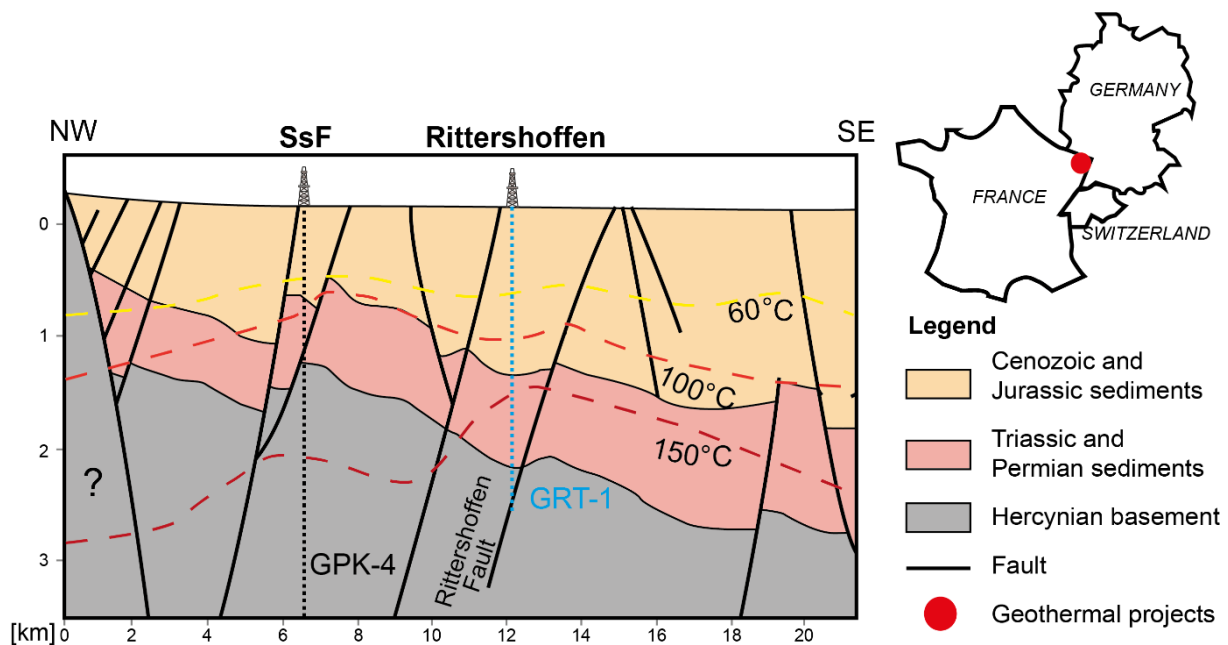


Figure 6.20: NW-SE Geological cross section through the Soultz-sous-Forêts GPK-4 well and the Rittershoffen GRT-1 well.

### 6.3.3. Geological settings

#### 6.3.3.1. Soultz and Rittershoffen sites

In France in 2019, 2 deep geothermal plants exploiting a deep fractured granite are operating (Rittershoffen, Soultz-sous-Forêts), producing a total of 24 MWth for industrial uses and 1.7 MWe for the electrical grid. Both projects target the granitic basement as geothermal reservoir. The Soultz-sous-Forêts research started with the Hot Dry Rock (HDR) concept which deals with the creation of an artificial heat exchanger into massive granitic rocks (Gérard et al., 1984; Garnish, 1985; Gérard and Kappelmeyer, 1987; Kappelmeyer, 1991). By drilling, natural brines were encountered into fractured and altered zones bearing hydrothermal minerals (Genter et al., 2010). Thus, the project slowly evolved from the pure HDR concept to the Enhanced Geothermal System (EGS) concept. That could be characterized as a poorly connected hydrothermal system. The Soultz-sous-Forêts site is now composed of 5 deep wells which in fact revealed numerous permeable FZ (Genter et al., 2010). The GPK-4 well which

will be detailed here was drilled vertically from 0 to about 2100 m and was deviated to the south to 5260 m depth (Dezayes et al., 2005). It crosses the tertiary and secondary covers before reaching the top of the granitic basement at 1418 m depth. Six main permeable FZ associated were found in the granitic section (Dezayes et al., 2010). Then, the Rittershoffen project was initiated in 2008 as an EGS project, and the target was to develop the reservoir through the Rittershoffen normal fault by drilling two deep wells GRT-1 and GRT-2. The production well GRT-2 revealed a high productivity index without any stimulation embracing a hydrothermal concept (Figure 6.20) (Baujard et al., 2017a). Achieved in 2016, this project turned out to be a great success. The GRT-1 injection well which will be detailed here was drilled near-vertical, crossing the sedimentary cover from 0 to 2213 m measured depth (MD) where it reached the granitic basement down to 2580 m MD. Two main permeable FZ are intersected at 2326 and at 2368 m MD (Vidal et al., 2017; Glaas et al., 2018). Observations conducted on the cores of the EPS-1 well from Soultz-sous-Forêts evidence a multiscale fracture network (Genter and Traineau, 1996). Small scale fractures with no evidence of displacement are filled by carbonates, chlorite, iron oxides, epidote and sulphides; and faults visible at core scale are filled by geodic quartz, carbonates, barite and clay minerals. In the case of the Rittershoffen wells, the largest faults are observed because only cutting samples and acoustic image logs are available and thus, small fractures are hardly observed. The term FZ will be generally used in this study for closely spaced fractures of cm-thick observed at borehole scale.

#### 6.3.3.2. Granitic basement

The Cenozoic rift of the URG (Villemain and Bergerat, 1987) is composed of several types of Paleozoic granites covered by secondary and tertiary sediments. In the Soultz-sous-Forêts wells, a porphyritic granite composed of potassic feldspar megacrystals (MFK) as well as biotite, plagioclase, and primary quartz is observed as well as a two-mica granite composed of biotite and muscovite, the most frequently in the deepest part of the wells (Genter, 1989; Traineau et al., 1992; Genter et al., 1999; Dezayes et al., 2005). This fractured granitic basement is the seat of fluid circulations through big convection cells where FZ are the main pathways for fluids. In response to these fluid circulations, the granitic rocks experienced hydrothermal alteration. Several grades of hydrothermal alteration are distinguished, and were observed on core samples and cutting samples (Genter, 1989; Traineau et al., 1992; Genter and Traineau, 1996; C. Glaas et al., 2018) (Figure 6.22). Mineralogy was also deeply studied with XRD analyses (Ledésert et al., 1999, 2009; Dezayes et al., 2005; Hooijkaas et al., 2006; Meller and Ledésert, 2017; Vidal et al., 2018) (Figure 6.21). Based on Soultz-sous-Forêts observations, a low grade alteration is characterized by chlorite (HLOW), a moderate grade is characterized by minor chlorite, illite and the total alteration of biotite (HMOD), the high grade is characterized by higher amounts of illite (HHIG). The extreme alteration grade is characterized by only high amounts of illite and secondary quartz (in the cuttings) which fill veins close to the fracture cores (HEXT). Finally, the VEIN facies is related to the highest amount of secondary quartz due to the presence of a fracture core filled by secondary hydrothermal quartz.

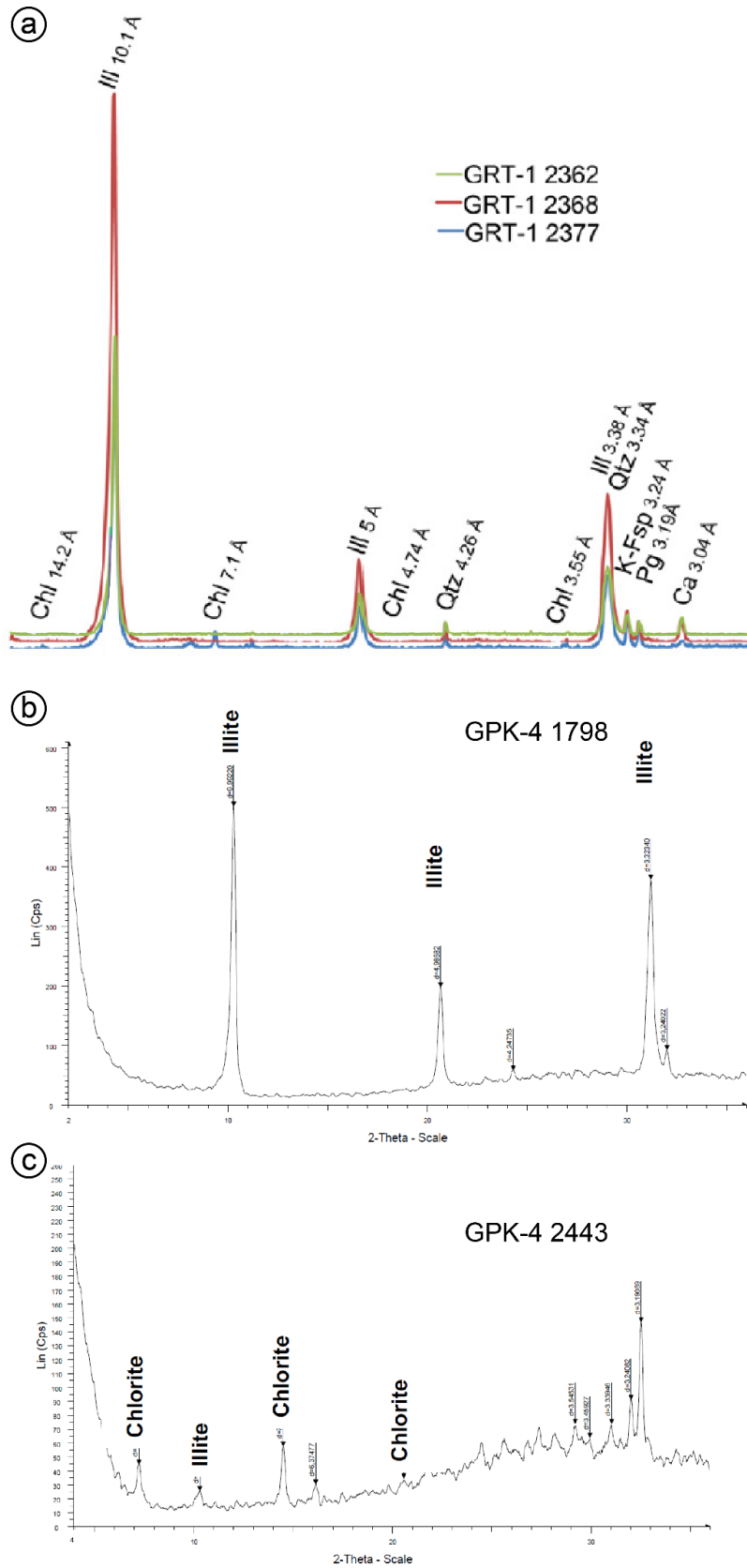


Figure 6.21: XRD diffraction patterns a. of the clay fraction in the GRT-1 well main FZ, after Vidal et al., (2018). b. of a vein alteration facies in the GPK-4 well (untreated sample), after Dezayes et al., (2005). c. of a vein alteration facies in GPK-4 (untreated sample). The chlorite peaks are still visible despite the occurrence of illite, indicating percentage of mixing rock, after Dezayes et al., (2005).

## 6.3.4. Materials and methods

### 6.3.4.1. Materials

The cuttings (chip samples) collected during the drilling of the wells are first washed and then dried on-site, by the mud logger unit. In the case of the GRT-1 well and the GPK-4 well from 4727 to 5260 m, the cuttings were sampled every 3-meters in depth in these 8"1/2 sections. Thus, one bag of cutting represents roughly 100 L of rock. For the GPK-4 well in the 12"1/4 section from 1400 to 4727 m, one bag of cutting represents roughly 200 L of rock. For this study, 122 cuttings were analysed in the GRT-1 well and 610 cuttings were analysed in the GPK-4 well. The sampling presented in this study encompasses all the facies presented in the section before. The average size of the cuttings grains varies between 0.5 and 2 mm in each sample. This cutting size can be highly influenced by other parameters like the drilling tool wear. For this reason and as the cutting size influences the SWIR intensity (higher the grain size is, higher the SWIR intensity is), the changes of drilling tool are also presented in this work (Figure 6.24 and Figure 6.26). In the GPK-4 well, the cutting samples can present low reliability from 1400 to 4700 m because of a high amount of biotite surely due to mixing of the cuttings during their ascent in the well (Dezayes et al., 2005). The occurrence of such bias is represented by an interpretative facies" (INT) (Figure 6.26).

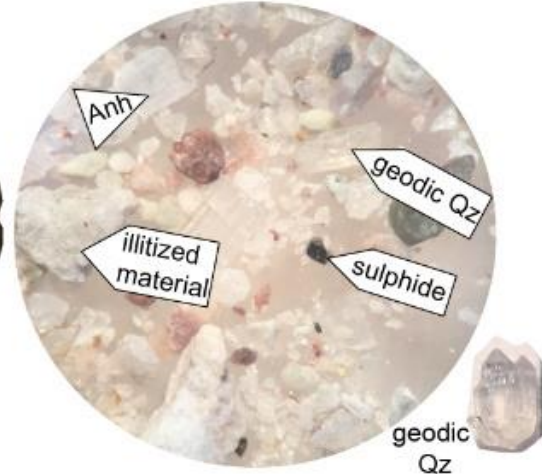
**Core samples  
(Soultz-sous-Forêts)**  
4 cm

**VEIN**

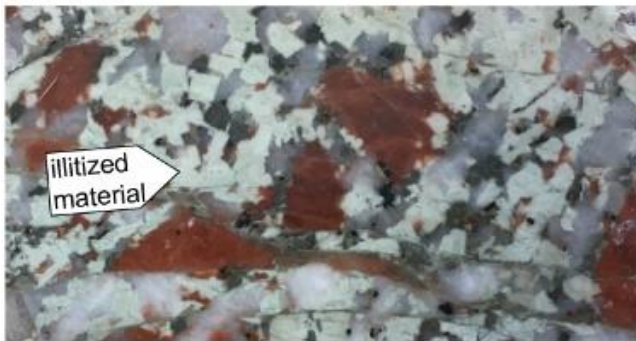


**Cuttings samples  
(Rittershoffen)**  
3 mm

**HEXT/VEIN**



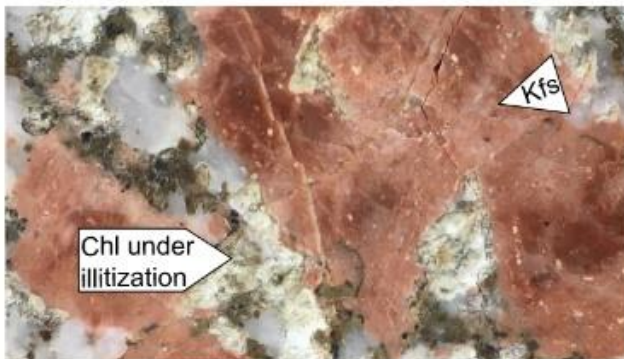
**HEXT**



**HHIG**



**HMOD**



**GRAN**

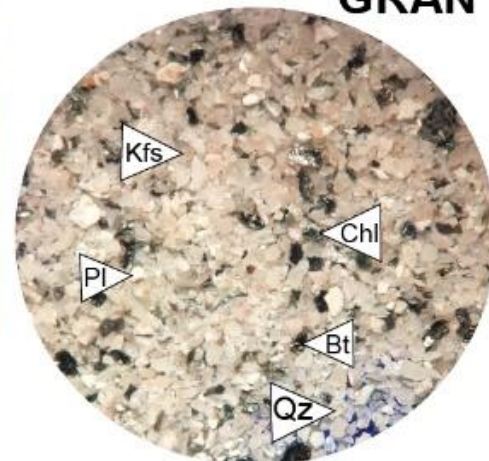


Figure 6.22: Mineralogy and its corresponding alteration facies. Observed from cores (left, Soultz-sous-Forêts) and from cuttings (right, Rittershoffen).

#### 6.3.4.2. Acquisition method

In total, 732 samples were analyzed from GRT-1 well and 239 from GPK-4 well with ASD TerraSpec 4 Standard Res Mineral Analyzer (Panalytical) equipped with two SWIR detectors. The domain of acquisition is 350 nm- 2500 nm with a spectral resolution of 3 nm at 700 nm and 10 nm from 1400 to 2100 nm. The scanning time of 100 milliseconds allows carrying out rapidly the acquisition for the whole the granitic sections. The wavelength reproducibility is 0.1 nm with an accuracy of 0.5 nm. Before acquisition the ASD TerraSpec needs a warming-time around 30 minutes. A calibration with a reference material "Spectralon" provided with the machine needs to be conducted also before the first acquisition but also regularly during the acquisition (every 2 hours) (Hébert, 2018). After acquisition, SWIR spectra were processed with the Spectral Swagger (TSS), an in-house Visual Basic macro that runs on Microsoft Excel (Hébert, 2018). First, the baseline was removed automatically by the software and then, spectra were fitted with few Gaussian curves. To create a profile simulation, the user has to fix the position and the half width at half maximum (HWHM). The height parameter is automatically deduced from the baseline-removed spectra, its initial height equals 90% of the Y-axis value of the baseline-removed spectra at the Gaussian centre wavelength. The user can configure which parameter will be allowed to change. Finally, the simulated profile is the sum of all Gaussian curves. The quality of the fit between simulated and observed profile is also verified with the weighted profile R-factor (Rwp) commonly used in Rietveld refinements (Toby, 2006). For this study, six Gaussian curves were used to fit the spectra from 1820 to 2300 nm (Figure 6.23a). For the GRT-1 well, position and HWHM were locked for each simulation profile. However, different sets of position and HWHM were used. The simulation profiles were accepted with a Rwp lower than 0.05. For the GPK-4 well, with regard to the high amount of profiles calculated, position and HWHM were free for each simulation profile. Four Gaussian curves were used to fit the absorption band from 1900 to 2060 nm (Figure 6.23a). Because this absorption band is related to water, its variation is influenced by the environmental conditions of acquisition (room humidity). Two Gaussian curves were used to fit the absorption band from 2200 to 2255 nm. These absorption bands are associated with mineralogical feature.

#### 6.3.4.3. Mineralogical identification

The main curve, located between 2206 and 2214 nm and called the "2200wvl" is associated with 'AIOH' feature representing Al-rich dioctahedral clays (Pontual et al., 1997). The smaller curve that creates a shoulder, located between 2247 and 2253 nm and called "2250wvl" is more complex in terms of feature. Gaussian curves used to fit the spectra from 2300 to 2400 nm are not presented in this study because it is focused on relative quantification of illitic minerals associated with the 'AIOH' feature. This methodology is only used for a relative quantification of clay minerals. From the comparison with literature spectra (Figure 6.23b), it appears that illite presents a sharp peak at 2200 nm. The influence of chlorite in the 2200 peak is low, but the influence of biotite and muscovite in this 2200 peak is considerable (Figure 6.23b). As the mineralogy of these wells were thoroughly described we can assume that the 2200 nm peak represents illite variations excepted in the GRT-1 well from 2420 to 2515 m where highest amounts of biotite were observed (Figure 6.24) and in the GPK-4 well where high concentrations of biotite were observed in the cuttings from 4400 to 4796 m and where the GR2M was observed from 4814 to 4262 m (Figure 6.26).

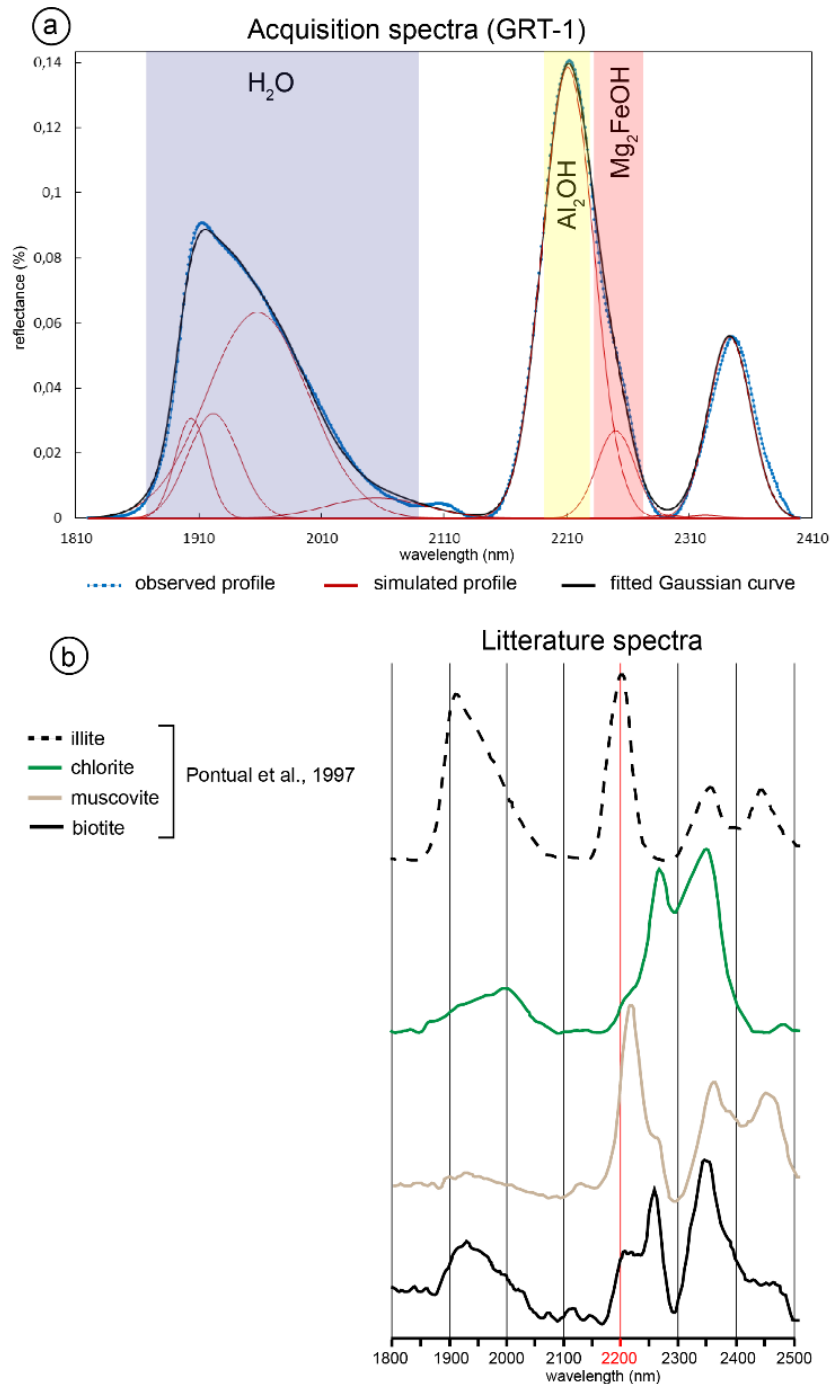


Figure 6.23: a) Example of an absorption spectra and the simulated profile in the GRT-1 well at 2420 m MD. b) Reference spectra from literature of illite, chlorite and biotite.

### *Intra-sample variability*

As each cutting represents sections of drilled rocks (see section 6.3.4.1.) and as the cuttings could not be homogeneously mixed in the bag, several measurements were regularly carried out on the same cutting bag. In the GRT-1 well 10 measurements were done on the same cutting bag while in the GPK-4 well only 5 measurements were done on the same cutting bag as lowest cutting quantities were available. With these several measurements on the same samples, error bars were then calculated in order to observe the range of variation of the data (Figure 6.24 and Figure 6.26).

## 6.3.5. Results

### 6.3.5.1. GRT-1 well

In the granitic part of GRT-1, five zones were distinguished on the basis of SWIR features (Figure 6.24).

The deepest section, from 2580 to 2510 m MD (2563 to 2493 m true vertical depth (TVD)), is characterized by constant values; the total area is around 20 a.u. (arbitrary unit – area of the Gaussian curve), and the 2200wvl around 5 a.u. (Figure 6.24). A local increase is observed for the sample at 2536 m MD (2519 m TVD) for the 2200wvl and the total area. This section corresponds petrographically to the unaltered granite (GRAN\_OX). The origin of the heterogeneity at 2536 m MD still has to be determined.

The second section, from 2510 to 2380 m MD (2493 to 2365 m TVD), is characterized by constant values except from 2470 to 2434 m MD where the curves present small variations (Figure 6.24). The total area is between 17 and 29 a.u. and the 2200wvl between 5 and 10 a.u. This section corresponds to the low to moderately altered granite (HLOW, HMOD) with a low density of natural fractures. The origin of the heterogeneity at 2420 m MD still has to be determined.

The third section, from 2380 to 2330 m MD (2365 to 2315 m TVD), is characterized by scattered values; the total area is between 22 and 40 a.u., and the 2200wvl between 7 and 13 a.u.. This section corresponds to the main permeable FZ. Within this section, from 2354 to 2371 m MD, the total area presents the lowest values, between 21 and 31 a.u. The lowest values for the water feature (9 to 14 a.u.) are observed for samples from 2365 to 2368 m MD. This subsection corresponds to the core of the FZ composed of opened fractures filled by secondary quartz (VEIN). The local decrease for the sample at 2388 m MD (20 a.u. for the total area and 9.5 a.u. for the water feature) correlates an opened fracture observed in the acoustic image logs (Figure 6.25c). Above the core of the FZ, higher values of total area, between 28 to 40 a.u. fit the high values of the water feature (15 to 20 a.u.), corresponding to the damage section of the FZ (HEXT). This section corresponds also to a considerable temperature anomaly (Figure 6.24).

The fourth section, from 2330 to 2255 m MD (2315 to 2241 m TVD), is characterized by quite stable values of the 2200wvl except for samples from 2290 to 2280 m MD. This section corresponds to highly altered granite with a cluster of opened fractures observed in acoustic images from 2290 to 2280 m MD.

The fifth section, from 2255 to 2220 m MD (2241 to 2207 m TVD), is characterized by stable values; around 13 a.u. for the total area, 5 a.u. for the 2200wvl and 1 a.u. for the 2250wvl. It corresponds to the reddish granite (RED) (Figure 6.24).

As a summary, the intra-sample variability of the 2200wvl shows the highest values for the samples at 2536 m, 2418 m and 2358 m, whereas the variability of the water feature shows the highest values for the samples located at 2358 m and at 2350 m, in the main FZ.

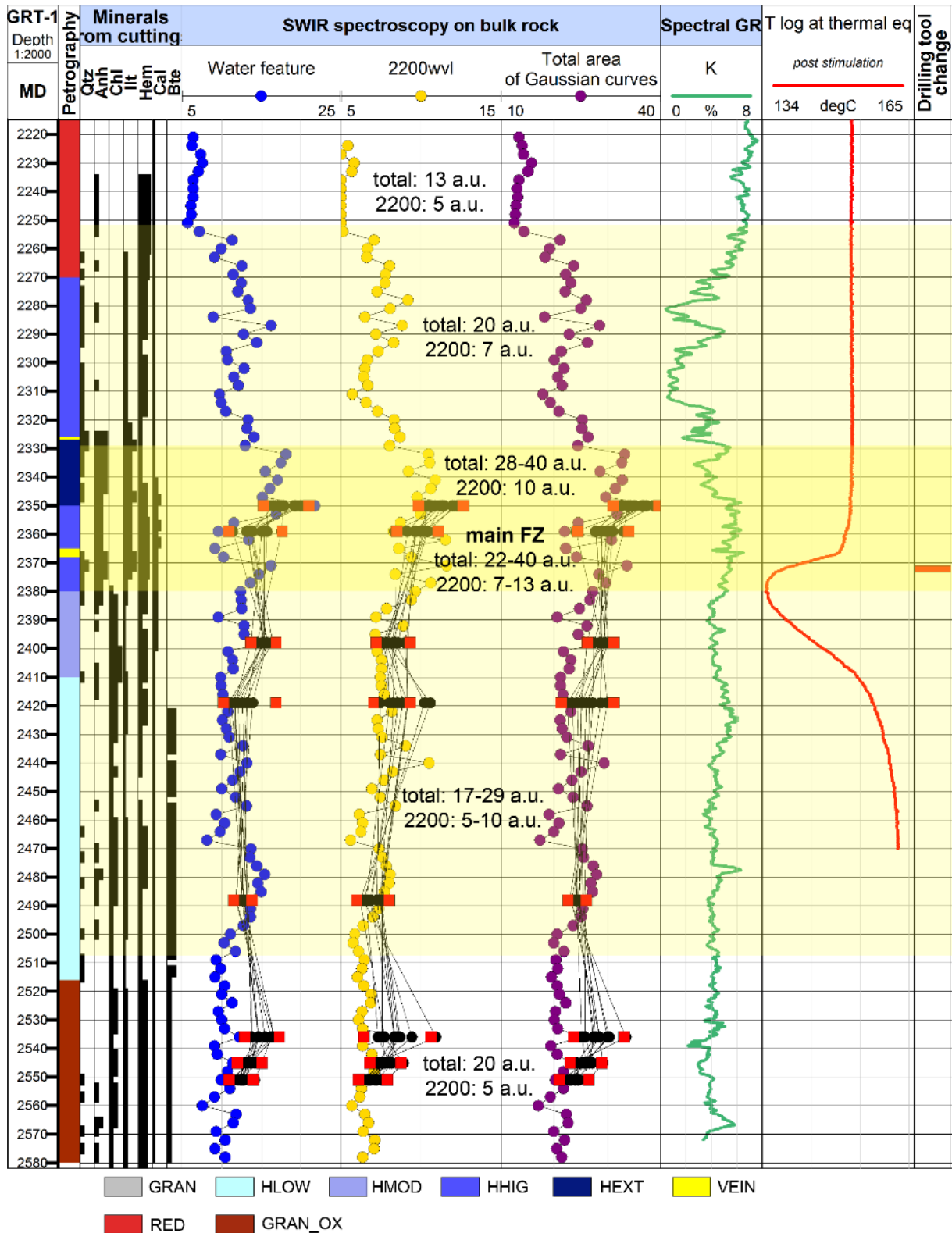


Figure 6.24: Composite log of the GRT-1 well presenting the petrography observed on cuttings with the associated minerals quantity, the SWIR results with the water feature, 2200wvl and the total area, the potassium (K) from the spectral gamma ray (GR), the temperature log acquired at temperature equilibrium and the drilling tool change.

The main FZ of the GRT-1 well from 2350 to 2370 m is composed of several partly opened fractures which are contributing to the well productivity by bearing 70% of the flow (Baujard et al., 2017a; Vidal et al., 2017). With the SWIR signal of illite (2200wvl) we can clearly distinguish

the main FZ from 2350 to 2370 m which is characterized by scattered values of the 2200wvl from 7 to 13 a.u. (Figure 6.25). This main FZ surrounds a quartz vein observed on cuttings which is associated to an open permeable FZ observed on the acoustic image logs (Figure 6.25c). The highest alteration grade (HEXT) is observed above this section, from 2326 to 2350 m and thus is associated with the highest surface area of the 2200wvl (Figure 6.25). We can also clearly distinguish 3 localized fractures at 2328 m (Figure 6.25a), at 2359 m (Figure 6.25b) and at 2368 m (Figure 6.25c). These 3 partly opened fractures are characterized by lowest values of the 2200wvl associated with depleted zones in K and with open factures visible on the acoustic image logs (Figure 6.25). They are associated with a large negative temperature anomaly and mud losses during drilling operations.

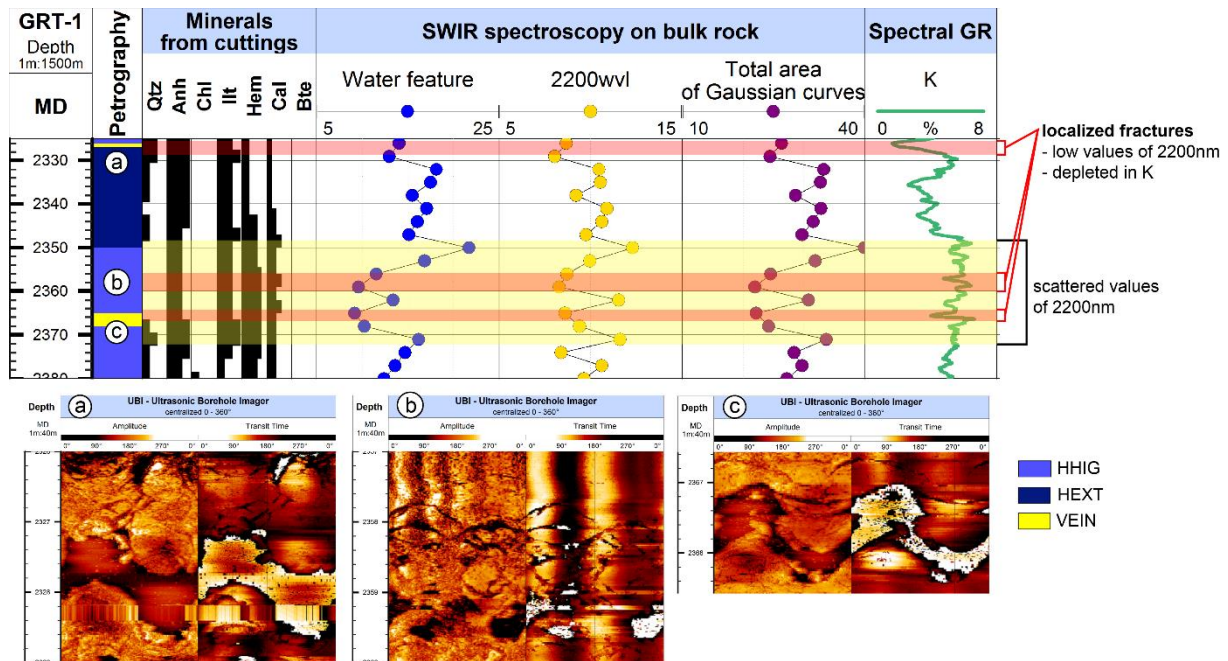


Figure 6.25: Zoom on the main permeable FZ of the GRT-1 well, showing the petrography, the SWIR results with the water feature, 2200wvl and the total area, and the potassium (K). a. acoustic image log of the open fracture at 2328 m. b. acoustic image log of the open fracture at 2359 m c. acoustic image log of the open fracture at 2368 m.

### 6.3.5.2. GPK-4 well

In the granitic part of the GPK-4 well, five sections are distinguished (Figure 6.26). The deepest section, from 5260 to 4740 m MD (4990 to 4475 m TVD), is characterized by scattered values; the total area varies between 5 and 42 a.u., the water feature varies between 2 and 33 a.u. with an important increase from 4742 to 4900 m MD and the 2200wvl varies between 1 and 10 a.u.. This section corresponds to unaltered granite and two micas granite (GRAN, GR2M), with zones abundant in biotite.

The second section, from 4740 to 4000 m MD (4475 to 3823 m TVD) is characterized by stable and low values; around 8 a.u. for the total area, 4 a.u. for the water feature and 1 a.u. for the 2200wvl. This section corresponds to unaltered granite (GRAN).

The third section, from 4000 to 3600 m MD (3823 to 3475 m TVD) presents scattered values; from 8 to 25 a.u. for the total area, from 2 to 14 a.u. for the water feature and from 0.5 to 9 a.u. for the 2200wvl. This section corresponds to unaltered to low altered granite (GRAN, HLOW).

The fourth section from 3600 to 3200 m MD (3475 to 3128 m TVD) presents low and moderately scattered values; from 10 to 25 a.u. for the total area, from 3 to 10 a.u. for the water

feature and from 1 to 4 a.u. for the 2200wvl. This section corresponds to unaltered to low altered granite (GRAN, HLOW).

Between the fourth and fifth section at 3200 m MD, a sharp change in the values of 2200wvl is observed. This is surely due to the change of facies, from unaltered granite to a section of altered granite. This phenomenon could be accentuated by the occurrence of drilling tool change at this same depth (Figure 6.26). A new drilling tool decreases the cutting size and thus the intensity of the SWIR signal is also lowest.

The fifth section from 3200 to 1400 m MD (3128 to 1400 m TVD) presents highly scattered values; from 15 to 60 a.u. for the total area, from 8 to 37 a.u. for the water feature, and from 1 to 19 for the 2200wvl. This section crosses grades of hydrothermal alteration, from low to high altered granite (HLOW, HMOD, HHIG). This section is associated to several temperature anomalies (Figure 6.26). More precisely from 1801 to 1813 m MD correlating to an increase of the 2200wvl, a cluster of opened and sealed fractures is observed with a main fracture at 1801 m MD associated to a temperature anomaly and mud losses (Dezayes et al., 2005).

The variability shows very stable and low values in comparison with the GRT-1 well. The highest variabilities are observed for the samples at 2235 m MD corresponding to a fracture observed on the acoustic image logs in the shallowest section between 1400 and 3200 m MD (Figure 6.27a).

Below this fracture at 2235 m MD, high and scattered values in the SWIR results are observed; from 23 to 55 a.u. in the total area, from 13 to 28 a.u. in the water feature and from 5 to 17 a.u. in the 2200wvl from 2235 to 2300 m MD (Figure 6.27). These high values correlate a FZ of open and sealed fractures observed on acoustic image log with halos of alteration from 2270 to 2273 m MD with the main fracture at 2270 m MD striking N-S and dipping eastward (Figure 6.27a and b). This FZ is associated to a thermal anomaly and permeability indicators.

At the top of the deepest large-scale cluster from 5260 to 4700 m MD, another FZ correlates high peaks in the SWIR results (Figure 6.28). From 4700 to 4900 m MD the total area is from 8 to 43 a.u. and the water feature from 3 to 33 a.u. but very low and stable values around 1 a.u. for the 2200wvl (Figure 6.28). The origin of high values for the water feature still has to be determined. Except at 4725 m where the 2200wvl is slightly higher (from 0 to 3 a.u.). At this depth, acoustic image log present partly opened fractures at 4722.5, 4724.5 and 4726 m MD. These fracture zones are associated with total mud losses observed during drilling operations as well as CH<sub>4</sub> occurrences. But no thermal anomaly was measured.

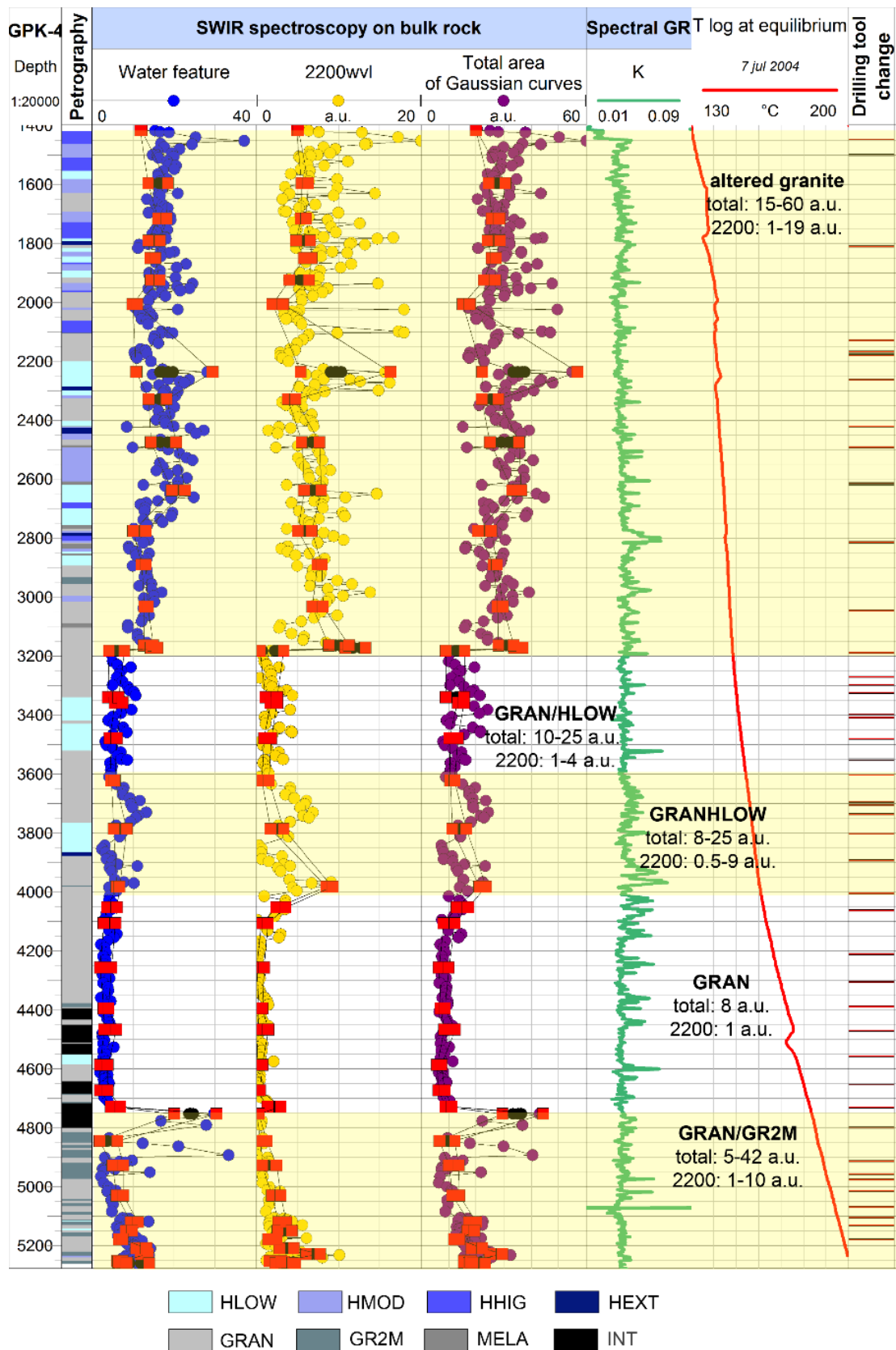


Figure 6.26: Composite log of the GPK-4 well presenting the petrography observed on cuttings with the associated minerals quantity, the SWIR results with the water feature, 2200wvl and the total area, the potassium (K) from the spectral gamma ray (GR), the temperature log acquired at temperature equilibrium and the drilling tool change, (GR2M: two mica granite, MELA: biotite rich granite, INT: granite artificially enriched in biotite due to drilling process).

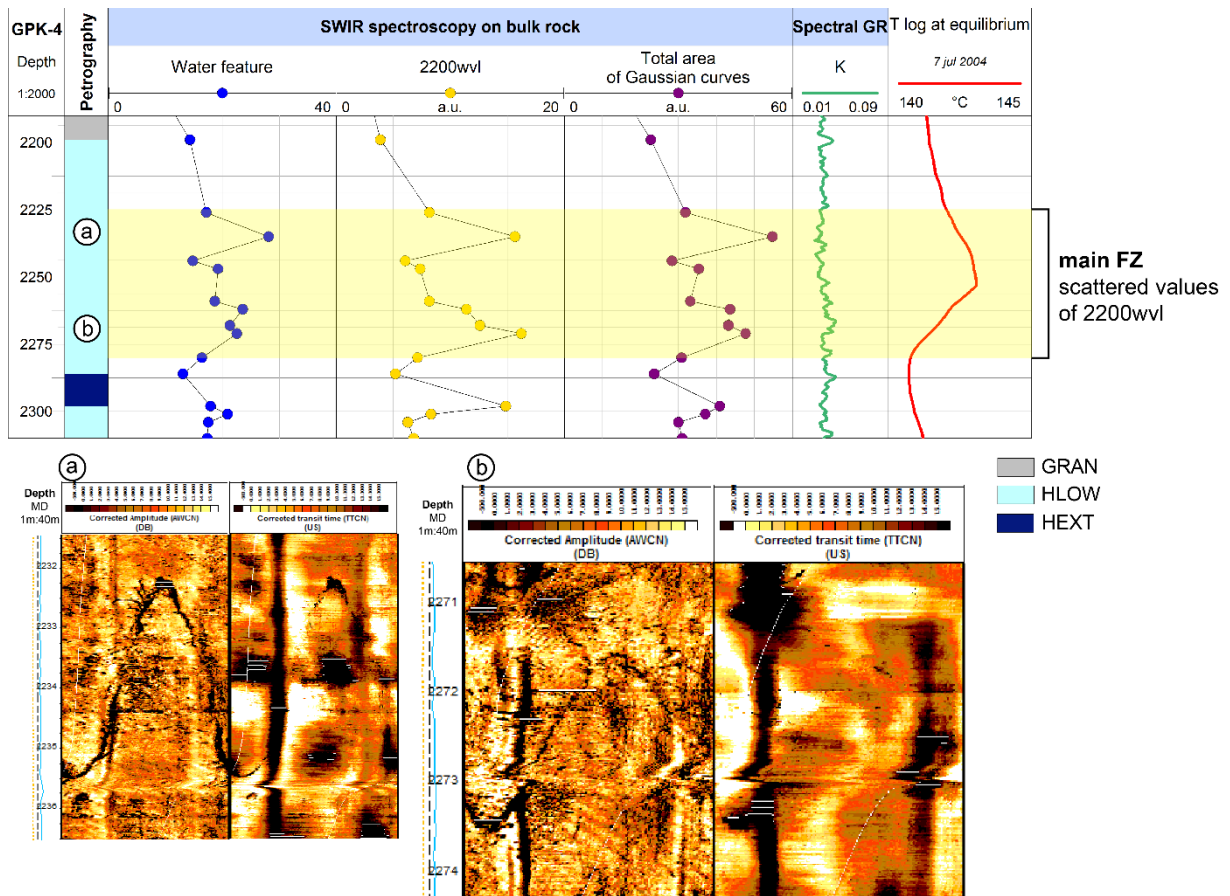


Figure 6.27: Zoom on a FZ of the GPK-4 well, showing the petrography, the SWIR results with the water feature, 2200wvl and the total area, the potassium (K), and the temperature log. a. acoustic image log of the fracture at 2234 m MD. b. acoustic image log of the fracture at 2273 m MD.

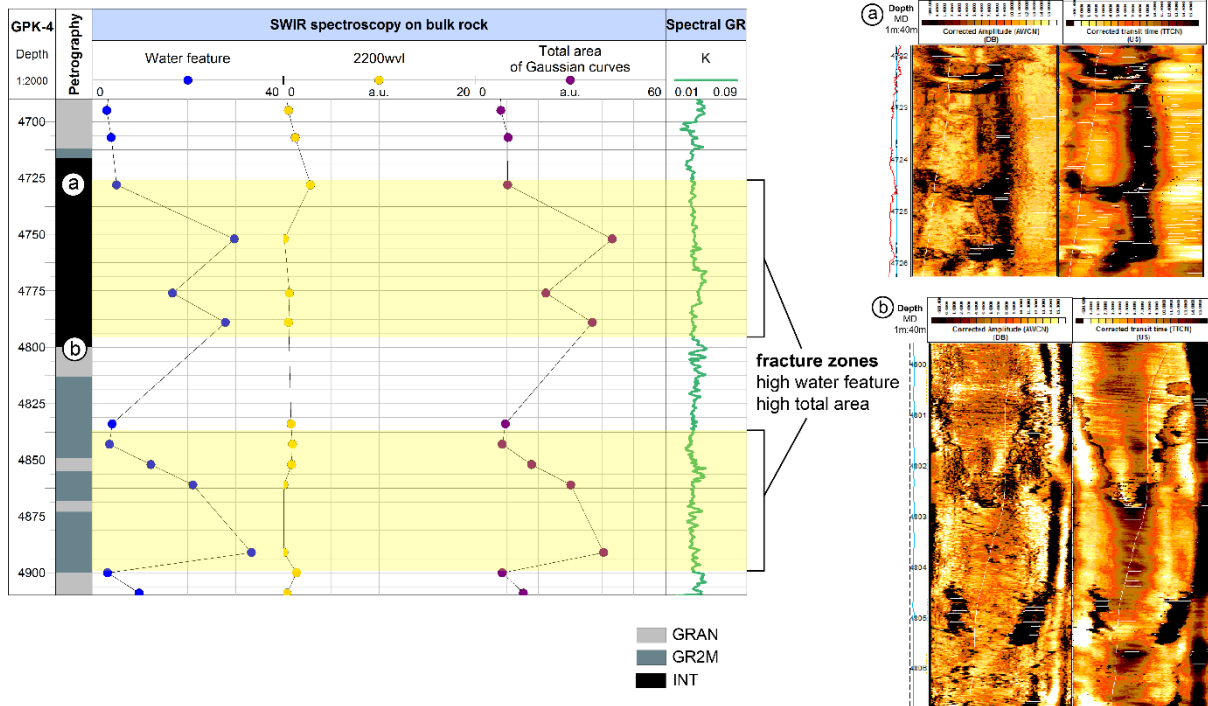


Figure 6.28: Zoom on a FZ of the GPK-4 well, showing the petrography, the SWIR results with the water feature, 2200wvl and the total area, the potassium (K), and the temperature log. a. acoustic image log of the fracture at 4780 m MD. b. acoustic image log of the fracture at 4802 m MD.

### 6.3.6. Discussion

#### 6.3.6.1. SWIR signal and alteration grades

In the unaltered granite, the SWIR signal is homogenous, stable and low, showing thus a good reproducibility of the measurements. Moreover, different responses of the SWIR signal are observed for the several hydrothermal alteration grades (Figure 6.29). In such sections, the scattering of the SWIR signal could mimic the heterogeneity of the altered facies. Hence a highly altered facies containing illite and small scale fractures filled by quartz will have a scattered 2200wvl response, alternating from low values (quartz veins) to very high values (illite) in opposition with the unaltered homogeneous granite (primary biotite partly chloritised). Higher the intensity of the 2200wvl is, higher the illite quantity is.

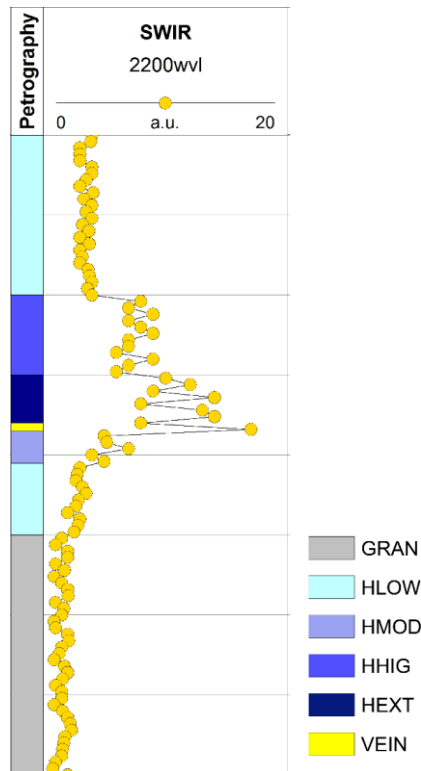


Figure 6.29: Model of variation of the area of the 2200wvl in response to the different grades of hydrothermal alteration of the granite and to FZ.

### 6.3.6.2. SWIR signal in FZs

The highest values of the 2200wvl are most of the time associated with damage zones related to open fractures visible on the acoustic image logs as well as permeable indicators (mud losses, temperature anomaly). At the same time, lowest values of the 2200wvl are associated with fracture cores which are materialized by quartz veins. As a result, FZs (core zone and damage zones) are characterized by great variability in 2200wvl values because of the high heterogeneity of cuttings at this depth (Figure 6.29). It is also observed that the highest values of intra-sample variability are associated with FZs. Illitization is thus in this geothermal system associated to present or fossil hydrothermal circulations.

### 6.3.6.3. Geothermal reservoirs

The GRT-1 well encounters the naturally permeable reservoir from the top of the granitic basement 2250 m MD to 2380 m MD (2236-2365 m TVD) which is characterized by high and scattered SWIR values (Figure 6.24). This section corresponds to a highly altered and fractured damage zone surrounding the main permeable fracture at 2368 m MD associated to a thermal anomaly (Figure 6.25).

The GPK-4 well encounters three permeable reservoirs:

- From the top of the granitic basement 1400 m MD to 3200 m MD (1400-3128 m TVD) a first shallow naturally permeable reservoir characterized by high and scattered SWIR values. Localized very high anomalies of the 2200wvl correlate with permeable FZ as well as temperature anomalies.
- From 3200 to 4700 m MD (3128-4436 m TVD), a lowly permeable reservoir is characterized by very low and stable values corresponding to the unaltered granite (Figure

6.26). Inside this section, from 3600 to 4000 m MD, high values of the 2200wvl correlated with high GR values could correspond to paleo-altered FZ. Hence, there are no thermal anomalies associated because they are sealed by illite. Whereas at 4510 m MD, a thermal anomaly indicates a permeable FZ which is not visible on the SWIR signal at 2200wvl probably because of granite artificially enriched in biotite due to drilling process, INT facies (Dezayes et al., 2005).

- From 4700 to 5276 m MD (4436-5000 m TVD), a third lowly permeable reservoir is encountered. It is characterized by low but increasing SWIR values with depth (Figure 6.26). These values are surely due to the alternation between the two-mica granite (GR2M) and the porphyritic unaltered granite (GRAN) illustrating petrographic facies variations. However some sparse peaks of the 2200wvl are locally observed which could reflect the occurrence of individual partly opened fractures not visible on the temperature log. This lower values of the 2200wvl compared to the shallower reservoir could characterize lower productivity index (Schill et al., 2017). In the deepest granitic section, lower illite alteration could evidence less permeable fractures. It could be interpreted by a lower water-rock ratio and then a lower connection between the FZs and the reservoir. In parallel, in this deep zone, the present-day stress field could tend to close the natural fractures and then reduce the permeability. Moreover, in this deep zone, SWIR signal is higher and thus more impacted by the occurrence of petrographic variations.

From these interpretations, both GRT-1 and GPK-4 wells intersect the top of the most permeable granitic basement. At Soultz-sous-Forêts it is encountered from 1400 to 3128 m TVD and at Rittershoffen it is encountered from 2236 to 2365 m TVD (Figure 5 and 7). This section extending roughly on 1 km in-depth is characterized by a high density of fractures in all the Soultz-sous-Forêts wells (Genter et al., 1997b, 1997a; Valley, 2007; Sanjuan et al., 2010; Dezayes and Lerouge, 2019). At Rittershoffen, in both geothermal wells, the very high values of the 2200wvl are also associated to highly permeable fractures (Vidal et al., 2018). At Soultz-sous-Forêts, the analysis of SWIR data in other wells GPK-1, -2 and -3 is ongoing.

### 6.3.7. Conclusion

In this study, SWIR method has been applied to the Rittershoffen and Soultz-sous-Forêts geothermal wells. The method showed a good correlation between the SWIR signal and the hydrothermal alteration grades. The SWIR at 2200wvl area reflects the occurrence of illite related to FZ. We assume that the intensity of this 2200wvl is an efficient proxy to the quantity of illite. The SWIR method enables to characterize the signature of FZ by distinguishing the nature, extent and intensity of the hydrothermal alteration around permeable and non-permeable FZs.

### 6.3.8. Acknowledgements

The authors warmly thank Benoît Hébert for allowing them to use his in-house Visual Basic software (TSS), and also the Poitiers team for the use of the TerraSpec on the Soultz-sous-Forêts site. They warmly thank Chrystel Dezayes from BRGM for the host and the access to the Soultz-sous-Forêts cutting samples. The authors also acknowledge the EGS Alsace project funded by ADEME (French Agency for Environment), as well as GEIE EMC and ECOGI for providing the samples.



## 6.4. Impact of secondary clay minerals quantity on the permeability of granitic geothermal reservoirs. Insights from the GIL-1 well, coupled interpretation of SWIR and electrical induction logs.

### 6.4.1. Introduction

The GIL-1 well intersects the Eschau normal fault at the transition between Triassic sandstones and Palaeozoic granite. This large fault zone, steeply dipping with a vertical kilometric scale offset was expected to channel the geothermal resource. But this interface turned out to be tight and the main permeable zones where the geothermal resource is exchanged in the GIL-1 well were mainly located in the deepest part of the well, in intra-granite fracture networks. In chapter 6.1., the primary and secondary mineralogy of the GIL-1 well and in particular the clay mineralogy has been detailed. The GIL-1 well turned out to present an intense argillic alteration at the top of the granitic section, from 2894 to 3104 m MD, as a record of intense hydrothermal circulations previously supported by the Eschau fault. In the deepest part of the well from 3104 to 3800 m MD, the propylitic alteration is mostly preserved, but is superimposed by argillic alteration occurring mainly around localized major fracture zones. This preliminary mineralogical analysis was essential before analysing the SWIR response of the GIL-1 well cuttings. Thus, this original chapter will present the SWIR results obtained for GIL-1 samples, how the spectra can be used for a semi-quantitative approach and how the amount of secondary illitic material in the fractured granitic reservoir of Illkirch impacts the permeability distribution. A correlation between the amount of illitic material and the electrical response in the well is proposed. Finally, a revisited petrographic log based on the correlation between the SWIR results and the geophysical logs is proposed.

### 6.4.2. Material and methods

#### 6.4.2.1. Mineralogy

##### *Sampling*

The cuttings collected during the drilling of the well were first washed using sieves and then dried on-site in an oven at 80 °C for 40 minutes, by the mud logger unit. GIL-1 cuttings were sampled every 5 m in depth in the 8" 1/2 and 6" drilled section. Thus, each sample represents approximately 0.1 m<sup>3</sup> of rock in the 6" section and 0.16 m<sup>3</sup> of rock in the 8 1/2" section. The average grain size of the cuttings chips in each sample varies between 0.5 and 2 mm.

##### *SWIR spectroscopy*

For more detailed explanations about the operating principle of SWIR spectroscopy and details on the tool, please refer to section 6.2.4.1. In the granitic section of the GIL-1 well, 284 cuttings samples were measured. It was performed in two distinct times implying distinct acquisition conditions: from 2896 to 3694 m MD in October 2018 and from 3694 to 3801 m MD in October 2019. The absorption band at 2200 nm is due to the presence of the illitic material. The area of this 2200 nm absorption band is used in this study and plotted to represent the variation of the quantity of illitic material along depth in the granitic section of GIL-1 well, it is expressed in arbitrary units (a.u.) (Figure 6.30 and 6.33). The water absorption band area is also plotted in the Figure 6.30, this is the sum of the areas of the four bands from 1850 to 2100 nm, see section 6.2.4.1. Although the acquisition conditions such as room hygrometry and ambient temperature between the two acquisitions may slightly differ, no change in the SWIR values is

observed (Figure 6.30). Chip size can be highly influenced by the drilling tool wear. For this reason and because the chip size of the cuttings influences the SWIR intensity (the larger the chip size, the higher the SWIR intensity), the changes of drilling tool are also presented in this work (Figure 6.30). Nevertheless, the SWIR response does not seem to be influenced by the drilling tool wear (Figure 6.30).

#### 6.4.2.2. Geophysical logs

##### *Induction log*

The electrical resistivity in the GIL-1 well was measured with a “Compact Array Induction Tool” from Weatherford company. Electrical resistivity measurements are provided every 10 cm depth. To avoid problems due to borehole instability, this induction log was acquired in the drilling strings. This induction tool provides raw data from multiple subarrays, which are integrated vertically and radially with environment-dependent processing to produce five depths of investigation (20, 30, 40, 60, and 85 inches) and a “true resistivity” ( $R_t$ ) curve. Figure 6.33 shows the 60 inches, 80 inches and  $R_t$  curves. Its measurement range is comprised between 0.1 and 2000 ohm.m. Since unaltered granite could be highly resistive with values higher than 10.000 ohm.m, this measurement range is supposed to imply a data saturation, which can be observed especially in the propylitic alteration zone from 3104 to 3801 m MD (Figure 6.33). In the argillic alteration zone from 2894 to 3104 m MD, the electrical resistivity is very low and below 2000 ohm.m, implying that it is not affected by the measurement range of the tool (Figure 6.33). The induction log in the open-hole of the GIL-1 well was acquired in two distinct sections, the first one from 2615 m MD to 3316 m MD and the second one from 3176 to 3679 m MD. To avoid the overlap of both datasets on the composite log, and as the bottom of the first acquisition seemed to be disturbed by the measurement conditions, it was chosen to represent the first acquisition only from 2894 to 3176 m MD and the second acquisition below.

##### *Gamma ray, neutron porosity and bulk density logs*

Gamma ray, porosity and density logs were measured every 2.5 cm in the GIL-1 well. For more detailed explanations, please refer to the 6.2.4.3. section.

- The gamma ray log measures natural radioactivity (cumulative emissions, mainly from uranium (U), potassium (K), and thorium (Th)) in gAPI. In altered crystalline basement, negative GR anomalies can reflect drusy quartz veins in illitized host rock (Genter et al., 2000; Dezayes et al., 2010). Occurrences of secondary clays bearing potassium like illite, correspond to positive GR anomalies. Thus here, GR data are an indicator of hydrothermal alteration and thus provide information regarding paleo-permeability.
- The neutron porosity is expressed in % and provides a global signal for FZs, showing that they are porous and could contain fluids and/or clay minerals.
- The bulk density is expressed in  $g/cm^3$ . A negative peak in the density curve could be due to micro-porosity associated with the occurrence of secondary clay minerals and to macro-porosity associated with fractures. A negative peak thus reflects hydrothermal alteration related to a fracture zone. Whereas positive peaks are associated with high-density minerals or changes in lithology.

### 6.4.2.3. Natural fractures

#### *Fracture density and major fractures*

A detailed analysis of the natural fractures was conducted on the electrical borehole images (Compact MicroImager tool hereafter named CMI) acquired in GIL-1 well. For more detailed explanations about the major fractures classification, please refer to the 5.2.4.2 section. In GIL-1 well, 6 major fractures were identified in the Buntsandstein, and 27 in the granitic section (Figure 6.33). A network of small-scale fractures is generally present between localized major fractures. The fracture density curve is presented in Figure 6.33.

#### *Rate of penetration of the drilling tool*

As presented in section 5.1.4.3. the rate of penetration (ROP) provides information on rock hardness. Average values of 3 m/h indicate massive hard rock like unaltered granite; while values above 5 m/h indicate that the granite is fractured and/or hydrothermally altered (Figure 6.33) (Baujard et al., 2017b). As the Weight On Bit (WOB) that is monitored by the driller can influence the ROP value, it was possible to normalize drilling data by calculating the ROP/WOB ratio in order to avoid misinterpretation of drilling rate increases that could be due to higher WOB. Thus, the ROP/WOB ratio peaks presented in the Figure 6.33 show advancement breaks that are surely due to the occurrence of weak zones indicating fractured and/or altered zones due to the occurrence of clays (Baujard et al., 2017b).

#### *Caliper log*

The description of a caliper tool is given in section 5.1.4.4. In GIL-1 well, the caliper tool measuring the borehole radius has 6 arms distributed azimuthally every 60°, and measurements are realized every 10 cm along depth. Two arms of the caliper are represented in the Figure 6.33, in order to visualize caving due to the presence of natural fractures, the indicative nominal diameter of the well was represented.

### 6.4.2.4. Indicators of permeable zones

#### *Gas content (Alkanes, CO<sub>2</sub>, Radon, He et H<sub>2</sub>)*

The occurrence of alkanes (C1 to C5) as well as of other gas species such as CO<sub>2</sub>, Radon (Rn), Helium (He) and Hydrogen (H<sub>2</sub>) indicates permeable FZs (Vuataz et al., 1990). These gases are generally beared by the geothermal fluid that circulates into the fracture network of the granite.

#### *Thermal anomalies*

Thermal anomalies identified on temperature profiles are interpreted as the signatures of fluid circulations between the well and the geological formation reflecting permeable zones (Barton et al., 1995; Davatzes and Hickman, 2005; Bradford et al., 2013; Vidal et al., 2019; Kraal et al., 2021). As detailed in section 6.1.4, permeable zones detected from the negative anomalies of the temperature profiles are presented. Six temperature anomalies were identified in the granitic section of GIL-1 well. Only their depth is presented in Figure 6.33 because of confidentiality of the data.

## *Mud losses*

The term “mud losses” means that the volume of drilling mud brought to the surface is lower than the volume that was injected. In the granitic basement, this is due to the loss of mud in the reservoir through natural fractures. Thus, monitoring the amount of mud losses helps in locating the permeable zones in the well (Figure 6.33).

### 6.4.3. Results

#### 6.4.3.1. Mineralogy from SWIR spectroscopy

The raw petrographic log (1) of GIL-1 well was based on the macroscopic and binocular description of the alteration mineralogy as presented in section 6.1 (Figure 6.30). This petrographic log (1) shows the hydrothermal alteration grades that were determined according to the occurrence of secondary minerals (chlorite, illite, and drusy quartz) in the cuttings samples. The lowest grade (HLOW) corresponds to the propylitic alteration of the granite while the higher grades (HMOD, HHIG, HEXT and VEIN) correspond to the argillic alteration facies. This petrographical log evolved into 2 other versions: the version (2) based on the SWIR correlation detailed hereafter, and the version (3) based on the correlation between the SWIR and geophysical logs results.

The SWIR results and more precisely the area of the absorption band at 2200 nm expressed in arbitrary units (a.u.) globally follows the trend of the alteration grades of the raw petrographical log (1) (Figure 6.30). The same trend is observed for the area of the water absorption band. This can be explained by the fact that the area of the water absorption band and the area of the absorption band at 2200 nm appear to be correlated (Figure 6.30). The ratio between the area of these absorption bands is known to vary significantly according to the nature of the aluminous phyllosilicates considered (I/S ml, illite and micas) (Petit, 1999; Madejová et al., 2010; Simpson and Rae, 2018; Kraal et al., 2021). In order to take this variation into account, the trend between these absorption bands for different facies based on the nature of the dioctahedral clay phases was analysed. The samples were divided in 4 classes: 1) samples affected by argillic alteration, 2) samples affected by propylitic alteration 3) samples from the biotite-rich granite affected by propylitic alteration, on the basis of petrographic observations and 4) samples containing high amount of secondary quartz on the basis of petrographic observations and locally low SWIR peaks (Figure 6.30). It was possible to observe 3 different correlations between the areas of the water absorption band and the band at 2200 nm with the slope of the regression curves varying from 0.21 for the propylitic facies to 0.60 for the argillic facies and to 0.62 for the biotite-rich granite (Figure 6.31). Quartz veins have a similar coefficient than the argillic alteration one 0.63 but present both lower values of the water and 2200 nm absorption band areas than the samples of the argillic facies (Figure 6.31). Coefficients around 0.6-0.7 seem to be representative of the illitic and I/S ml contribution to the total water quantity absorbed in the sample (Figure 6.31) (Glaas et al., 2019b). It was then possible to obtain a semi-quantification of dioctahedral clays for each facies. Based on these data, the distribution of argillic, propylitic and biotite-rich samples was refined and shown in the petrographic log (2) Figure 6.30. This refined petrographic log (2) based on SWIR results follows the tendency of the first established log based on binocular observations and XRD results. Both logs have the same vertical resolution which is about 5 meters, due to the cuttings sampling. This second petrographic log based on the amount of illitic phases, also point out, in the previously defined dominant propylitic alteration zone, diverse locations of superimposition of argillic alteration expressed by high amount of illitic

clays associated to fossil or active fracture zones such as from 3104 to 3236 m MD and from 3433 to 3535 m MD. On the basis of this new log (2) based on SWIR results, the link between the alteration grade and the 2200 nm absorption band area appears clearly as follows:

- The argillic alteration zones observed from 2894 to 3236 m MD and from 3433 to 3536 m MD are characterized by high and heterogeneous values between 7 and 21 a.u. For the main argillic zone from 2894 to 3104 m MD, main values are generally around 17 a.u., although lower values can be observed at 2953 m MD (9 a.u.), 2995 m MD (11 a.u.), 3065 and 3089 m MD (12 a.u.). In the second zone, from 3433 to 3536 m MD, values are more scattered as illustrated by the lower value at 3496 m MD. The scattering of values is linked to the nature of the geothermal reservoir which is fracture controlled. Low values of the 2200 nm absorption band area are linked to the absence of illitic material. They spatially correlate with the occurrences of secondary quartz infilling reflecting partial or total clogging of the fracture zone (i.e. at 2953, 2995, 3153, 3210, and 3496 m MD) (Figure 6.33). Low values also match in depth with major fractures identified from geophysical logs, such as at 3065, 3089, and 3496 m MD.
- The zone dominated by propylitic alteration observed from 3236 to 3350 m MD is characterized by lower values varying between 6 and 14 a.u.. From 3536 to 3801 m MD, values are even lower and constant around 8 a.u (Figure 6.30). Here again, the variation can be explained by the local superposition of localized fractures generating an argillic-type alteration but with a more limited extent than in the previous zone and probably a more limited wall-rock effect (alteration halo).  
The biotite-rich granite observed from 3350 to 3433 m MD is characterized by a depth section with the lowest values around 4.5 a.u, showing a slight scattering. This section characterized by low values is in agreement with a low quantity of illitic material reflecting a propylitic alteration. Occurrences of small scale fractures in all this depth interval can be suggested by the slight scattering of the values.

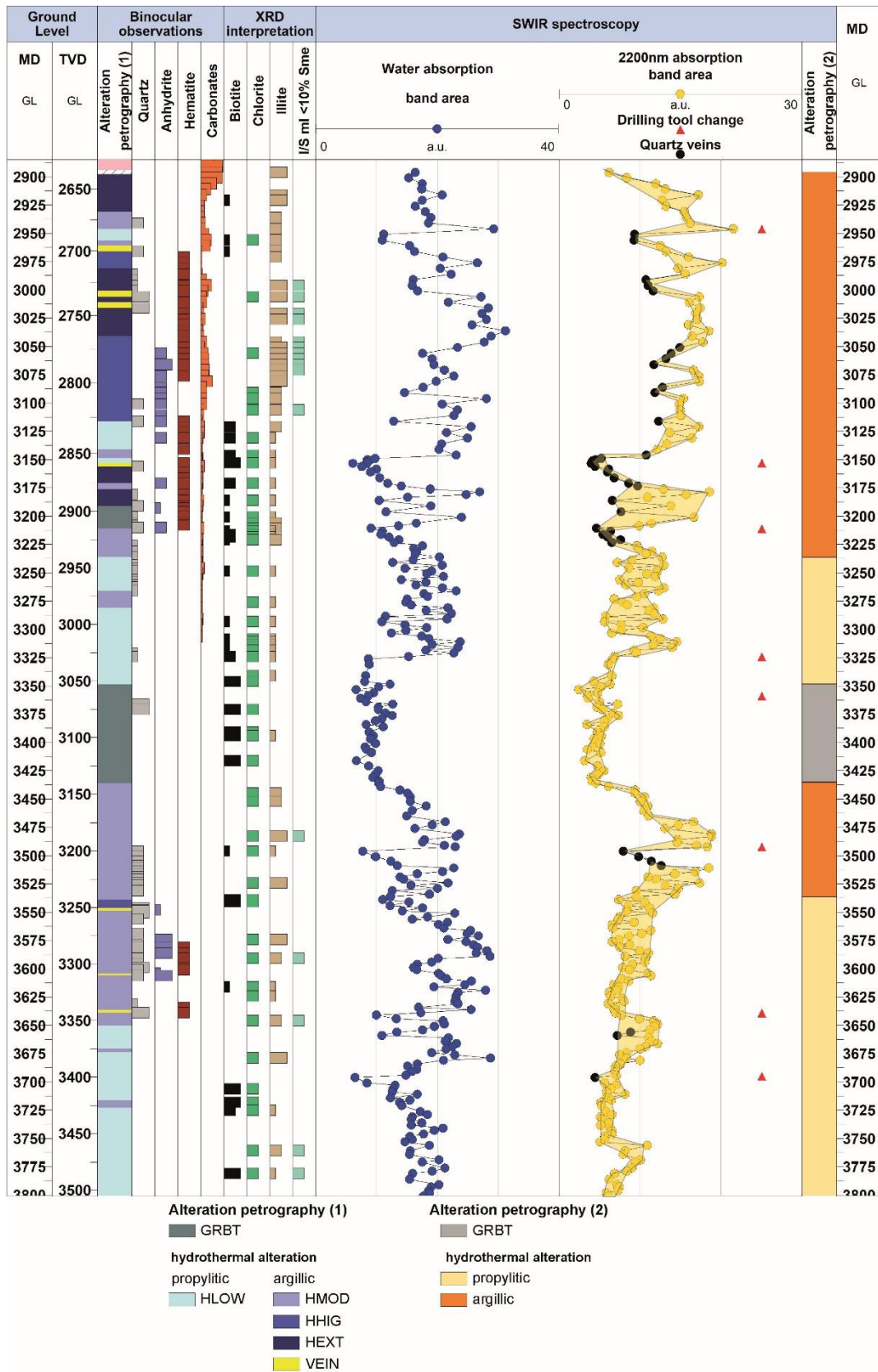


Figure 6.30: Composite log of GIL-1 well at Illkirch showing on the left the raw petrographical log (1) based on the mineralogy deduced from binocular observations and the clay minerals occurrence from XRD. On the right, the petrographical log based on SWIR observations and the clay content (water and 2200 nm absorption band areas).

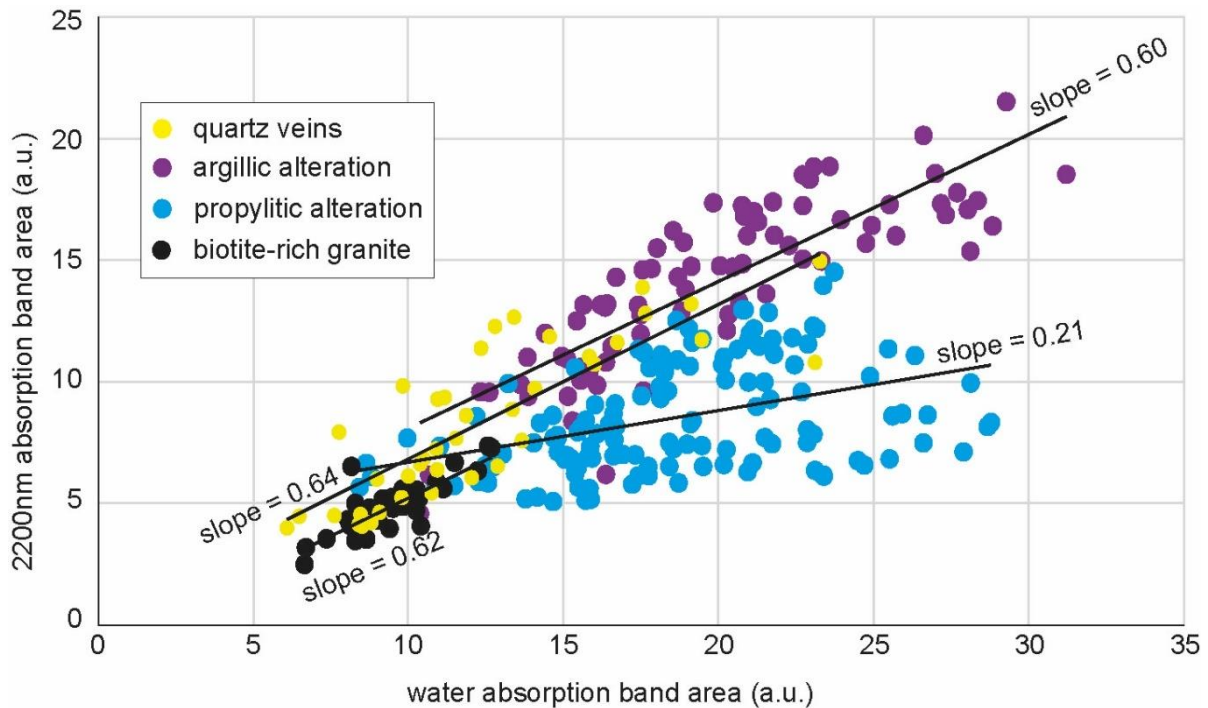


Figure 6.31: Correlation of the water and 2200 nm absorption bands areas from SWIR spectroscopy in the granitic basement of GIL-1 well. Samples have been sorted according to the petrographic log (2) shown in Figure 6.30, quartz veins are shown in the Figure 6.30.

#### 6.4.3.2. Geophysical logs

In this section, alteration grades described are based on the second alteration petrography log refined from SWIR results and named (2) in the figure 6.33.

##### *Induction log*

On the electrical induction log, two main trends can be observed (Figure 6.33).

1. The first one is characterized by low electrical resistivity values indicating highly conductive zones clearly correlated with the predominance of argillic alteration. These low values are observed:
  - in the upper section from 2894 to 3100 m MD with values around 15 ohm.m, corresponding to argillic alteration.
  - from 3314 to 3333 m MD with values around 20 ohm.m, which could reflect the coexistence of both argillic and propylitic alterations.
  - from 3422 to 3500 m MD with values around 6 ohm.m, corresponding to argillic alteration.
  - and from 3600 to 3656 m MD with decreasing resistivity values from 2500 to 4 ohm.m, which could reflect the coexistence of both argillic and propylitic alterations.

In these intervals, local increase of the electrical resistivity can be observed like at 2926, 2934, 2980, and 3047 m MD, that reflect zones depleted in clay minerals, or the absence of conductive brine. These zones could be fault cores clogged by secondary quartz.

2. Elsewhere, a second trend is observed, which is characterized by high resistivity values between 6000 and 14000 ohm.m occurring either in propylitic alteration or biotite-rich granite and seems to be above the resolution of the induction tool. These highly

resistive zones present local decrease of the electrical resistivity like at 3100-3165, 3192, 3206, 3267, 3277-3283, 3340-3360, 3511, 3528, 3544, 3550, 3558 and 3563 m MD, that reflect conductive zones that could be due to the presence of brine or clay minerals.

These two trends are also shown by the correlation between the values of the SWIR absorption band area at 2200 nm and the electrical resistivity (Figure 6.32a). On the left, a group characterized by low resistivity values and high SWIR values is mainly composed of samples from argillic alteration, whereas on the right, a group characterized by higher resistivity values and lower SWIR values is mainly composed of samples from propylitic alteration and biotite-rich granite. In the left group, samples above  $10^4$  ohm.m are underlining the saturation of the tool (Figure 6.32a). The samples from the argillic alteration superimposed to the propylitic alteration are distributed in both groups (Figure 6.32a).

The lower SWIR values are supposed to be due to the presence of veins filled with secondary quartz and are represented in the Figure 6.32b. If these low SWIR peaks are correlated with low resistivities, they are potential fluid pathways. Hence, as seen on the Figure 6.33, the KFZs are generally characterized by lower resistivity peaks in both argillic and propylitic alterations. More precisely, these SWIR or resistivity peaks are considered lower in comparison to the mean value of SWIR or resistivity in the near section (argillic, propylitic, biotite-rich).

Surprisingly, these quartz veins are not systematically correlated with the lowest resistivity values as it could be supposed if brine is circulating in these quartz veins (Figure 6.32b). This could be due to the sampling difference between SWIR that is measured on the cuttings every 3 to 5 meters depth and electrical resistivity that is measured every 10 cm depth. To provide the correlation graphs, it was chosen to affect the closest electrical resistivity values to the SWIR values. In the propylitic alteration, quartz veins are systematically presenting the lowest SWIR values, whereas in the argillic alteration, another group of values are presenting lower SWIR values than the quartz veins (Figure 6.32b). These values are mostly contained in the argillic superimposed to propylitic alteration facies and their low resistivity values should be linked to the presence of circulating brine. However, these values were not identified as quartz veins in the SWIR log (Figure 6.30).

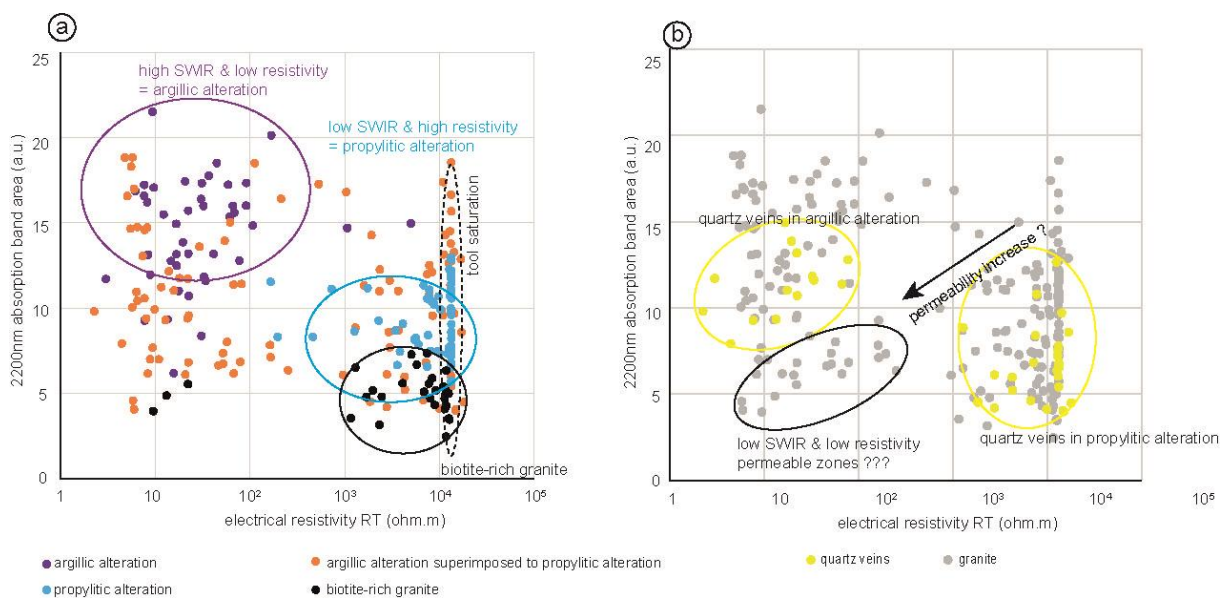


Figure 6.32: Correlation plot between the 2200 nm absorption band area and the electrical resistivity. Interpolation was realized by affecting electrical resistivity values to the closest SWIR values. a) the samples have been sorted

according to the petrographical log (3) shown in Figure 6.33, and b) quartz veins depths are shown in the Figure 6.30.

#### *Gamma-ray, porosity and density*

The top of the granite (from 2894 to 2940 m MD) is characterized by high values around 230 gAPI, probably due to the abundance of illite at the faulted interface between sandstone and granite (Figure 6.33). In the intense argillic alteration domain below (from 2940 to 3100 m MD), GR values are around 190 gAPI. Deeper, from 3100 to 3433 m MD, GR values oscillate between 225 and 245 gAPI in both propylitic alteration zone and fresh biotite-rich granite. Then, in the deepest part, GR values are very disturbed and show two shoulders from 3450 to 3530 and from 3560 to 3670 m MD where values oscillate between 180 and 511 gAPI. Below, GR was not measured.

The porosity and density curves show very similar trends with each other but also with the electrical induction logs (Figure 6.33).

1. The first trend is characterized by high porosity and low density values, correlated with the occurrence of argillic alteration:
  - from 3894 to 3100 m MD, where porosity varies between 3 and 20 % while density varies between 2.1 and 2.6 g/cm<sup>3</sup>. In this interval, a peak of 26 % of porosity and 1.5 g/cm<sup>3</sup> of density is observed at 3056 m MD.
  - from 3422 to 3500 m MD with increasing porosity values from 2 to 18 % and decreasing density values from 2.6 to 2.4 g/cm<sup>3</sup>;
  - from 3600 to 3656 m MD with increasing porosity values from 1 to 3 % and decreasing density values from 2.6 to 2.5 g/cm<sup>3</sup>.

In these zones, local anomalies are observed at 3418, 3422, 3448, 3613, 3633, 3642 and 3654 m MD, surely due to the occurrence of FZs.

2. The second set is characterized by low porosity (2-2.6 %) and high density (2.6 g/cm<sup>3</sup>) values, correlated with the occurrence of the propylitic alteration. It is observed elsewhere in the granitic basement of GIL-1 well, spatially correlated with local anomalies such as at 3206, 3321, and 3528 m MD, surely due to the occurrence of FZs.

#### 6.4.3.3. Natural fractures

Local increases in the fracture density can be correlated to electrical induction peaks in highly fractured zones hosting intense brine circulations and/or affected by argillic alteration (i.e. at 2980, 3161, 3192, 3206, 3277-3283, and 3356 m MD) (Figure 6.33). Advancement breaks observed on the ROP are systematically observed in argillic alteration zones (at 3020, 3052, 3065, 3325, and 3640-3660 m MD) (Figure 6.33). The caliper log shows important cavings in the upper part of the well from 2894 to 3104 m MD and from 3445 to 3513 m MD. Both sections are affected by argillic alteration (Figure 6.33).

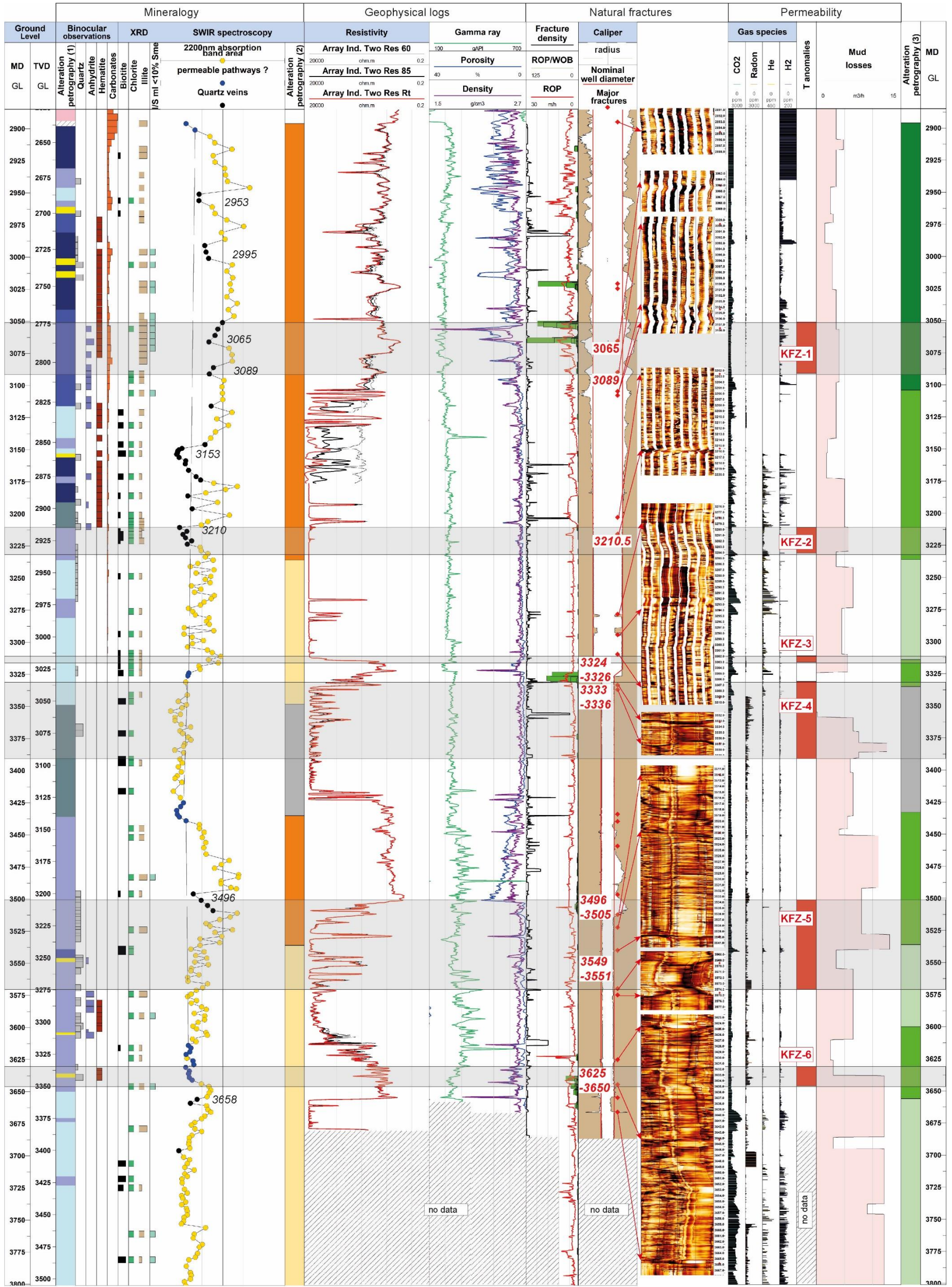


Figure 6.33: Composite log of the GIL-1 well presenting the mineralogy (binocular observations, XRD and SWIR), the geophysical logs (electrical induction, gamma-ray, porosity and density), natural fractures (fracture density, major fractures, ROP, caliper) and the permeability evidences (gas occurrences, T anomalies, and mud losses).



### 6.4.3.3. Permeable FZs

In this section, the alteration grades are the ones of the petrographic log (2). Globally, in the granitic section of GIL-1 well, the mud losses increase with increasing depth from 3 m<sup>3</sup>/h in the upper part to 12 m<sup>3</sup>/h in the deepest part. This could indicate that the deepest part of the granitic section intersected by GIL-1 well is probably more permeable than the upper part. In the granitic section, six temperature anomalies were interpreted as permeable zones. These permeable zones are of decametric scale and are named permeable fracture zones (KFZ) (Figure 6.33). The KFZs match major fractures observed on the CMI and several indicators of permeability and typical signatures of geophysical logs described in the Table 6.5. In the following section, an interpretation of the possible open fractures that are main fluid pathways of centimetric scale inside these 6 KFZs is proposed:

- The permeability of the KFZ-1 seems related to the occurrence of 2 major fractures at 3065 and 3089 m MD, presenting high electrical conductivity peaks surely due to the occurrence of circulating brine, and SWIR low peaks indicating the absence of secondary illitic material (Figure 6.34 & Table 6.5). Also, the correlation plot between SWIR and electrical resistivity suggests that these 2 major fractures are respectively comprised in 2 zones from 3051 to 3065 m MD and from 3086 to 3089 m MD that could contribute to the permeability of the KFZ as they present the lowest SWIR values and lowest electrical resistivity values of the KFZ (Figure 6.34).
- The KFZ-2 comports 2 major fractures at 3202 and 3215 m MD, the first one at 3202 m MD shows high conductivity but high SWIR value which could reflect a clogged zone, the second one at 3215 m MD shows no significant conductivity peak and seems to be partially clogged by secondary quartz like it is suggested by the low SWIR value and the occurrence of secondary quartz in the cuttings at this depth (Figure 6.34 & Table 6.5). But the correlation plot between SWIR and electrical resistivity suggests that at 3210.5 m MD, a smaller scale fracture with low SWIR and electrical resistivity values could contribute to the permeability of the KFZ-2 (Figure 6.34).
- 5 major fractures are located above or at the top of the KFZ-3 and 4 at 3278, 3294, 3309, 3333, and 3336 m MD (Table 6.5). The first one at 3278 m MD shows significant electrical conductivity but is not included in KFZ-3 or 4. The ones at 3294 and 3309 m MD do not present significant electrical conductivity that could be related to brine circulations, and from 3305 to 3314 m MD high SWIR values indicate the occurrence of secondary illitic material. However, the fracture at 3294 m MD fits with an increase of GR value that could be due to argillic alteration. Below from 3314 to 3321 m MD, a high electrical conductivity is observed, as well as a low GR, which could indicate the absence of illitic material. Secondary quartz is observed in the cuttings in this depth section. This zone does not include major fractures but, a high porosity and low density are observed at 3321 m MD, which could indicate brine circulations in this zone via the small-scale fracture network and its associated secondary porosity. Moreover, the correlation plot between SWIR and electrical resistivity suggests that the zone from 3324 to 3326 m MD could contribute to the permeability (Figure 6.34). Furthermore, two major fractures are correlated with high electrical conductivity at 3333 and 3336 m MD. Both major fractures are located at the interface between the propylitic alteration zone developed in the monzogranite and the biotite-rich granite. These 2 fractures are also presenting low SWIR values as it is shown by the correlation plot (Figure 6.34). This interface could constitute a geological weakness and thus, a

preferential pathway for fluids. Also, the correlation plot highlights the existence of a zone from 3351 to 3361 m MD comporting low SWIR values but high resistivity, which could reflect paleo-permeable drains clogged by secondary drusy quartz (Figure 6.34).

Permeable fracture zones	Depth interval	Alteration petrography (3)	Mineralogy (cuttings and XRD)	SWIR 2200 nm absorption band area	Electrical induction	Gamma-ray	Porosity and density	Major fractures	Advancement breaks (AB), fracture density, caving in the caliper	Fracture orientation (strike)	Mud losses	Gas occurrence
<b>KFZ-1</b>	3050-3090 m MD	argillic	Illite and I/S ml	peaks of low values at 3065 and 3089 m MD	high electrical conductivity at 3065 and 3089 m MD	low peaks at 3061, 3065 and 3075 m MD, and high peak at 3080 m MD	peaks of low density and high porosity at 3056, 3065 and 3080 m MD	3065, 3089, 3104 and 3107 m MD	AB at 3052 and 3065 m MD, Important caving in the caliper from 3050 to 3110 m MD, Fracture density: 1.1 frac/m	 N030E 83E N085E 78N N027E 87W	4m <sup>3</sup> /h	H <sub>2</sub> from 3033 to 3066 m MD
<b>KFZ-2</b>	3210-3230 m MD	argillic	Illite, secondary quartz from 3200 to 3210 m MD	peaks of low value at 3210 m MD	high electrical conductivity at 3192 and 3206 m MD	High peak at 3206 m MD	high porosity at 3192 and 3206 m MD	3202 and 3215 m MD	High fracture density from 3202 to 3206 m MD Fracture density 1.6 frac/m	 N153E 50E	5.7 m <sup>3</sup> /h	CO <sub>2</sub> , He and H at 3209 m MD
<b>KFZ-3 &amp; 4</b>	3309-3315 m MD and 3330-3390 m MD	interface between argillic superimposed to propylitic alteration and biotite-rich granite	Illite, secondary quartz at 3322 and from 3365 to 3371 m MD	high values around 3309 m MD, and low but scattered values from 3340 to 3360 m MD	high electrical conductivity from 3314 to 3333 m MD and high conductivity peaks from 3340 to 3360 m MD	Low values from 3315 to 3322 m MD	high porosity and low density peaks at 3315 and 3322 m MD	3309, 3333 and 3336 m MD	AB at 3325 m MD High fracture density at 3331 and 3356 m MD Fracture density KFZ-3: 2.4 frac/m Fracture density KFZ-4: 1.7 frac/m	 N156E 75E N156E 80W N147E 45E	5.5 m <sup>3</sup> /h at 3312 m MD and 12 m <sup>3</sup> /h at 3382 m MD	CO <sub>2</sub> , Radon and He

Permeable fracture zones	Depth interval	Alteration petrography (3)	Mineralogy (cuttings and XRD)	SWIR 2200 nm absorption band area	Electrical induction	Gamma-ray	Porosity and density	Major fractures	Advancement breaks (AB), fracture density, caving in the caliper	Fracture orientation (strike)	Mud losses	Gas occurrence
<b>KFZ-5</b>	3500 to 3575 m MD	argillic and propylitic	Illite, Secondary quartz from 3496 to 3530 m MD and from 35546 to 3556 m MD	peak of low value from 3496 to 3509 m MD, surrounded by two peaks of higher values and scattered values in the rest of the KFZ-5	high electrical conductivity at 3496-3500, 3511, 3518, 3528, 3544, 3550, 3558, 3563, and 3570 m MD	Low peaks at 3496 and 3531 m MD, high peaks at 3501, 3512, 3556, 3563 and 3570 m MD	high porosity and low density at 3501, 3528, 3544 m MD	3496, 3512, 3522, 3539, 3570, and 3574 m MD	High fracture density at 3563 and 3670 m MD, important caving in the caliper from 3465 to 3511 m MD Fracture density 1.4 frac/m	 N170 84W	13 m <sup>3</sup> /h at 3530 m MD	CO <sub>2</sub> , He and H <sub>2</sub> at 3539 m MD and Radon at 3570 m MD
<b>KFZ-6</b>	3625 to 3645 m MD	argillic superimposed to propylitic alteration	Illite, Secondary quartz at 3638 m MD	peak of low value at 6568 m MD surrounded by higher values	global increase with depth of the electrical conductivity with high peaks at 3614, 3633, 3643 and 3654 m MD	High peaks at 3614, 3617 and 3630 m MD, low peak at 3654 m MD	global increase with depth of the porosity and global decrease of the density. Peaks of high porosity and low density at 3614, 3633, 3643 and 3654 m MD	3625, 3644, 3654 m MD	AB from 3640 to 3650 m MD High fracture density from 3610 to 3613 m MD Fracture density: 1.6 frac/m	 N152E 79W	12 m <sup>3</sup> /h	Radon

Table 6.5: Six permeable fracture zones with their SWIR, geophysical and structural signatures visible on the Figure 6.33 and associated permeability indicators.

- The KFZ-5 is correlated with the occurrence of 6 major fractures at 3496, 3512, 3522, 3539, 3569, and 3574 m MD (Table 6.5). The first ones at 3496 and 3512 m MD are correlated to high electrical conductivity, low SWIR values, high porosity and low GR peak. This agrees with open fractures containing circulating brine. The correlation plot suggests a permeable pathway localized between 3496 and 3505 m MD, in fact, at 3509 m MD the electrical resistivity is higher, which does not suggest the presence of brine (Figure 6.34). Around this zone characterized by low SWIR values from 3496 to 3505 MD, two shoulders of higher SWIR values are observed, that could reflect the presence of highly argillized wallrocks around a permeable fault core. The four major fractures below are systematically correlated to electrical conductivity and porosity peaks and show scattered SWIR values on the depth interval. This could reflect the alternation of several fractures with circulating brine and more or less secondary quartz (high conductivity, high porosity, low SWIR value) with illitized damaged zones (lower conductivity and porosity, high SWIR values). There, the correlation plot suggests the contribution of a zone between 3549 and 3551 m MD to the permeability, in fact, these points present quite low electrical resistivities and moderate SWIR value (Figure 6.34).
- The KFZ-6 is correlated with the occurrence of 3 major fractures at 3625 and 3644 and 3654 m MD. The first one at 3625 m MD shows a slight peak of high resistivity but the correlation plot suggest that it could contribute to permeability, as it presents also low SWIR values (Figure 6.33 and 6.34). Both fractures at 3644 m MD and 3654 m MD correlate with higher conductivity anomalies, and density and porosity anomalies. But these anomalies are slightly shifted to the bottom of the fracture at 3654 m MD. In fact, the correlation plot shows that this fracture is more resistive, which suggests that the surrounding damage zones could contribute to permeability more than the fracture cores (Figure 6.34). The fracture at 3644 m MD could be permeable as it is suggested by its low resistivity and quite low SWIR values in the correlation plot (Figure 6.34). A peak of low SWIR value from 3654 to 3659 m MD could be due to the absence of illitic material in the fracture core, but secondary quartz that clogged the pathway as it is observed in the cuttings at this depth, and suggested by the correlation plot that shows high resistivities (Figure 6.34). In the same manner than around 3500 m MD in the KFZ-5, the low peak of SWIR values from 3654 to 3659 m MD is surrounded by two shoulders of higher SWIR values, that could reflect the argillized wallrocks around the fault core composed at least of one major fracture at 3654 m MD (Figure 6.33). Also, the correlation plot underlines the presence of a cluster of permeable drains from 3625 to 3650 m MD as it is shown by high conductive values with low SWIR values (Figure 6.34). These observations suggest that the KFZ-6 is composed of numerous small-scale fractures visible on the CMI, that contribute to the permeability of the zone (Figure 6.33).

These preferential fluid pathways contained in the 6 KFZs described above can be depleted in illitic material as shown by low SWIR value like at 3065, 3089, and 3496 m MD, or can present an amount of illitic material similar to that of the surrounding rock.

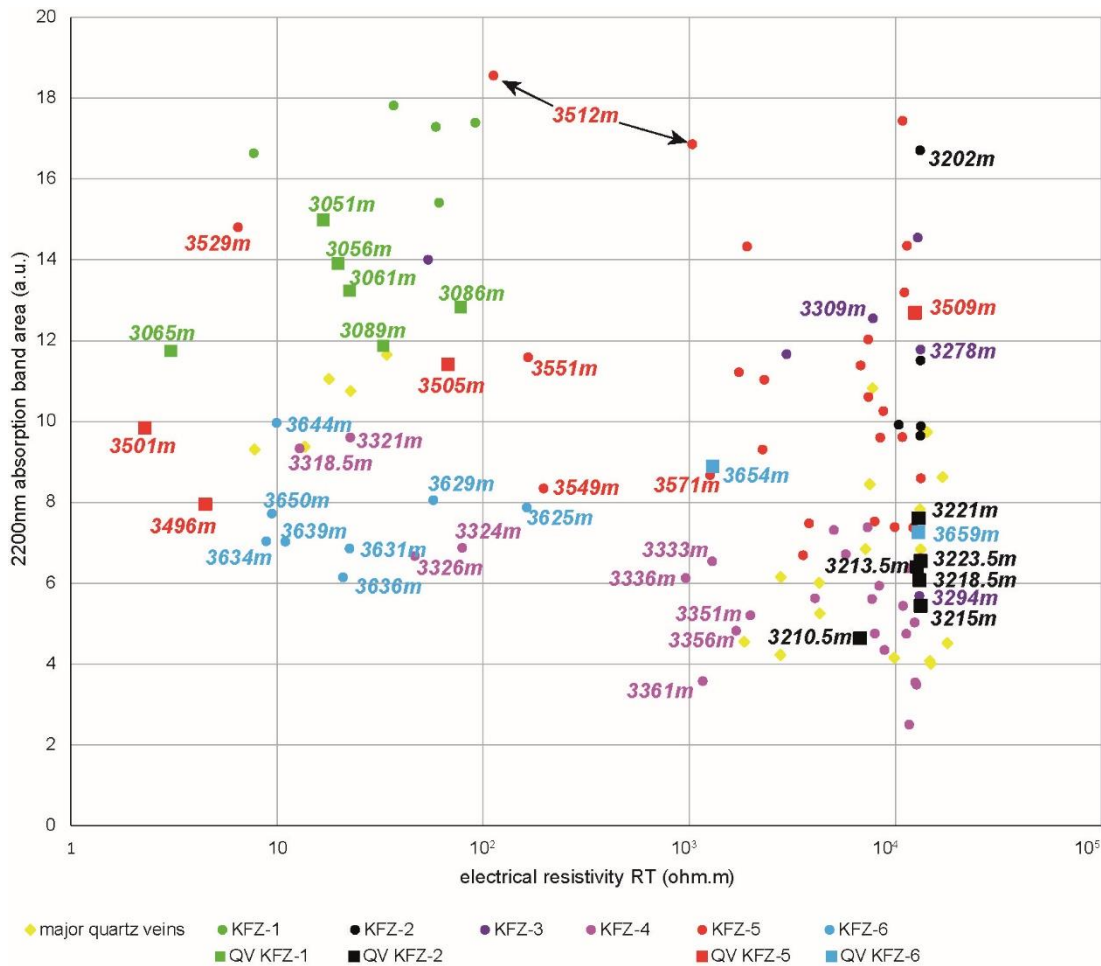


Figure 6.34: Correlation plot between the 2200 nm absorption band area and the electrical resistivity. Interpolation was realized by affecting electrical resistivity values to the closest SWIR values. The samples represented are the ones corresponding to the thermal anomalies shown in red in Figure 6.33, and to the quartz veins shown in the Figure 6.30.

#### 6.4.4. Discussion

##### 6.4.4.1. Towards a refined alteration petrography

The area of the 2200 nm absorption band obtained from SWIR spectroscopy appears to be representative of the hydrothermal alteration grade. This was already observed in the wells GRT-1 and GRT-2 of Rittershoffen and the wells GPK-1 and GPK-4 of Soultz-sous-Forêts, see chapter 6.2 (Glaas et al., 2019b). In the same way, in GIL-1 well, the highest values highlight zones of argillic alteration while the lowest values indicate zone of propylitic alteration and the lowest and stable values in GIL-1 well indicate the presence of the biotite-rich unaltered granite. The refinement of the samples classification into propylitic, argillic alteration zones and biotite-rich granite after the correlation of the water and 2200 nm absorption band areas proposes a second petrographic log (2). This second petrographic log (2) is very close to the first one (1): the interpretation of alteration grades based on the SWIR correlation (2) superimposes perfectly on the first interpretation compiling binocular observations and XRD results (1). Both interpretations and petrographic logs underline the presence of argillic alteration in the top of the granitic section and propylitic alteration in the rest of the section, comprising the occurrence of a biotite-rich granite. However, the second petrographic log (2) refines the alteration distribution by suggesting the adding of two sections of argillic alteration

that were not identified before and that could reflect a lowest grade of argillic alteration than in the top of the granitic section but still superimposes the propylitic alteration. This underlines the importance of the SWIR contribution for the interpretation: SWIR allows to build a petrographic log in a very short time, allows to quantify the alteration, and allows to refine zones that were not detected with bonicular and XRD results. The correlation of the various geophysical and structural information from the logs with the SWIR response also allows to refine this second petrographic log and suggests a third version of the petrographic log (3), presented in the Figure 6.33, where the granitic basement is divided into three major alteration paragenesis.

- 1) The first one is the argillic alteration observed at the top of the granitic section from 2894 to 3104 m MD seems to be linked to the paleo activity of the Eschau fault. This section which is highly fractured is characterized by the occurrence of illite and I/S ml, in high amount according to SWIR, high electrical conductivity, low GR, high porosity and low density.
- 2) The second one is the propylitic alteration observed from 3104 to 3350 and from 3433 to 3801 m MD. This propylitic alteration is characterized by the occurrence of chlorite, low amount of illite according to SWIR, high electrical resistivity, medium GR values, low porosity and high density. This propylitic alteration is sometimes overprinted by argillic alteration (especially from 3104 to 3236, from 3314 to 3335, from 3433 to 3536 and from 3600 to 3656 m MD), that shows responses similar to the ones of the upper hydrothermally altered facies.
- 3) The third one is the biotite-rich granite observed from 3335 to 3433 m MD characterized by the occurrence of biotite, the lowest and constant SWIR values of GIL-1 well, high electrical resistivity, low porosity and high density.

#### 6.4.4.2. Signature of paleo and present permeable fracture zones

Fluid circulations at the well scale in GIL-1 are controlled by 6 KFZs. Detailed observations reveal a complex permeability distribution inside KFZs. It can vary according to the intensity of the present & paleo fluid circulations, leading to a more or less clogging with secondary quartz and illitic material in fault core and/or in damage zones. Nevertheless, the correlation of the different methods allows to estimate the location of major fluid pathways in the KFZs and to define their systematic mineralogic, geophysical and structural signatures. The correlation between these several methods enables to address the complexity of fracture zones in terms of permeability distribution:

- A first order permeability was related to the main drains in the KFZs that are characterized by high electrical conductivity and low SWIR values. In the Illkirch well, it was observed that major fractures acting as fluid pathways in KFZs are systematically characterized by peaks of a consequent higher conductivity than the baseline conductivity of the surrounding host rock. These fluid pathways can be depleted in illitic material as shown by low SWIR value, or present an amount of illitic material similar to that of the surrounding rock. Low SWIR value indicate that fault cores are depleted in illitic material but may be partially or totally clogged with quartz or carbonates. Thus, lower SWIR values cannot directly be interpreted as fluid pathways. However, the combination of low SWIR value with high electrical conductivity will surely indicate a fluid pathway in a KFZ.
- A second order permeability related to small-scale fractures and the secondary porosity in the damage zones due to the dissolution of the primary minerals during hydrothermal

alteration, these zones are characterized by peaks of electrical conductivity and scattered SWIR values that oscillate between low values (quartz veins or small scale drains) and high values (highly argillized wallrocks).

Around 3500 and 3654 m MD, permeable pathways are characterized by low SWIR values surrounded by argillized wallrocks characterized by higher SWIR values. This signature is very characteristic and was also described based on the spectral gamma-ray log with high potassium sections (Genter et al., 2007). Moreover, relocated induced micro-seismicity during injection tests, seems to be correlated with the orientation of the major fracture at 3512 m MD in the KFZ-5.

At the reservoir scale, the mud losses increase with depth suggesting a higher connection between the well and the near-well field in the deepest part of the granitic section. The top of the granitic section is the footwall of the Eschau fault intersected at 2894 m MD and that was revealed to be tight. This zone, from 2894 to 3104 m MD, presents an intense argillic alteration as shown by the presence of I/S ml (see chapter 6.1) (Glaas et al., 2021a), and confirmed by SWIR results in this zone that show high and quite homogeneous values with a low scattering. This SWIR tendency suggests an intense argillic alteration that clogged entirely the zone intense in the whole rock mass, not only limited to the wallrocks in the vicinity of fractures, and including the early permeable drains. In Rittershoffen wells, it has been shown that the greater the alteration the higher the SWIR values, and the higher the fracture density, the greater the scattering. This scattering between low and high SWIR values is interpreted as the alternation between fractures without illitic material that can be potential fluid pathways, and illitized zones in the edges of the fractures that are probably clogged or paleodrain with no circulation anymore because of clogging. This network was shown to be highly permeable at Rittershoffen (Vidal et al., 2018; Glaas et al., 2019b).

The Eschau fault zone at the sediment-basement interface could have been a preferential path for fluid circulation. This interface could have hosted sedimentary brines from the basin floor (+/- meteoric water) leading to intense clogging due to fluid/rock interaction. This permeability distribution reveals a new conceptual model of reservoir at Illkirch, where fluids are not directly exploited in the fault zone, but deeper in the granitic fracture network. The fault zone at the interface is now a paleo-drain as already suggested by (Glaas et al., 2020) (see chapter 5.2).

The correlation coefficients calculated between the SWIR water and 2200 nm absorption band areas for the propylitic and argillic alterations are very similar to the ones that were calculated in the GRT-2 well of Rittershoffen and in the GPK-4 well of Soultz-sous-Forêts (Glaas et al., 2019b). These trends which show mean correlation coefficients for the 3 wells of 0.6 for argillic alteration, and of 0.24 for the propylitic alteration suggest a similar intensity of the hydrothermal alteration at a regional scale in the granitic basement. This suggests also that below the quantity of argillic alteration underwent by the rock, it is mostly the repartition of this alteration in complex fracture zones that controls the reservoir permeability. This is supported by the different conceptual models of the geothermal reservoirs encountered at Soultz-sous-Forêts, Rittershoffen and Illkirch despite a similar intensity of argillic alteration. Below these considerations in terms of permeability, these similar intensities of argillic alteration suggest that with similar fluid conditions (chemical, temperature) and a similar rock protolith, a similar chemical-mineralogical equilibrium was achieved at a regional scale.



**PART 3:**  
**CONCLUSIONS AND**  
**PERSPECTIVES**



## 7. Major outcomes for research

The granitic basement of the URG is hosting natural geothermal reservoirs suitable for geothermal energy production. These reservoirs are characterized by fluid circulation in the natural fracture network, inherited from the multiphase tectonic history that occurred in the upper crust since the emplacement of the granite at the Carboniferous period. Since this period, various episodes of natural fluid circulation have generated strong geochemical interactions between geothermal fluids and basement rocks producing hydrothermal alterations.

### 7.1. Natural faults and fractures

The natural fractures were investigated in 8 geothermal wells from electrical and acoustic borehole image logs, and from core samples. In the 3 geothermal sites (Soultz-sous-Forêts, Rittershoffen, Illkirch), natural fractures are mainly NNW-SSE to N-S oriented, steeply dipping and generally expressing conjugate sets (Glaas et al., 2020) (see chapter 5.2). These fractures were reactivated by the different stress fields that varied over time in this area. Thus, they are inherited from several tectonic episodes such as the late Variscan extension, the Jurassic extension, Eocene Pyrenean compression and Oligocene extension (Villemin and Bergerat, 1987). The present-day stress field presents favourable conditions for maintaining hydrothermal circulation in the vertical fracture system (Evans, 2005). Fractures are connected in clusters that are potential pathways for fluid circulation. These clusters of fractures form FZs that comprise fracture core(s) surrounded by fracture wallrocks (WR) and damage zones (chapter 3.3. Figure 3.4). Fracture properties like fracture density and fracture thickness show the highest values in the first 500-1000 m of the basement, which correspond to the most permeable reservoirs (Dezayes et al., 2010; Vidal and Genter, 2018; Glaas et al., 2020) (see chapter 5.2).

Fault zones are three-dimensional structures also composed of fault cores and damage zones such as the smaller scale FZ described above (Caine et al., 1996; Brogi, 2008, 2011; Faulkner et al., 2010). Due to their heterogeneous mechanical properties, fault zone could develop a local stress field that could be very different from the surrounding regional stress field (Valley, 2007). Then, the relationship between the fault geometry and the stress field determines how the fault could behave and slip with shearing and/or dilation (Evans, 2005).

Consequently, the recurrence of brittle deformation episodes influences fracture hydraulics. The present-day permeable fracture network consists in multiphase reactivated fractures or faults (Dezayes et al., 2010). Schematically, fracture permeability can be enhanced or reduced respectively by extensional and compressional stress regimes. Extension tends to favour dilatational stress and create open fractures, whereas compression tends to generate slip and shear stress by developing fault gouge and related cataclastic clay-rich facies (Genter, 1989; Genter et al., 2000; Davatzes and Hickman, 2005). Due to active precipitation and alteration, open fractures are generally sealed by secondary minerals that induce a self-propping effect (Liotta et al., 2020).

The structural inheritance predisposes the organization of fractures in the reservoir, governs the hydrothermal inheritance and then the resulting present-day permeability of the fracture network.

## 7.2. Hydrothermal alteration and its indicators

The hydrothermal alteration of the granitic basement includes an argillic alteration that superimposes on the propylitic alteration in the whole massif and on the supergene alteration at the top granite, related to its outcropping (Glaas et al., 2021a) (see chapter 6.1). The argillic alteration due to the interaction of circulating fluids in the fracture network with the surrounding rock is characterized by the precipitation of illite and I/S ml (illitic material), secondary quartz, as well as carbonates and sulphides (Genter, 1989; Ledésert et al., 1999, 2010). The propylitic alteration due to the interaction between primary minerals and resident fluids during the cooling of the granitic pluton is mainly characterized by the chloritisation of biotite, precipitation of illite and carbonates in replacement of feldspars, and sulphides (Genter and Traineau, 1993; Dubois et al., 1996; Ledésert et al., 1999; C. Glaas et al., 2018; Vidal et al., 2018). The identification and characterization of the secondary minerals resulting from hydrothermal alteration was performed by standard methods such as binocular observations, X-ray diffraction, scanning electron microscope (SEM) coupled with energy dispersive spectrometry (EDS), and chemical analyses of the bulk rocks (ICP-OES). These methods allowed to locate the occurrences of secondary quartz veins and illitized zones in the different wells as well as to define the chemical composition and microstructural properties (crystallinity, mixed layering ...) of the illitic material (Glaas et al., 2021a) (see chapter 6.1). This pointed out that well crystallized illite (WCI) are predominant in the propylitic alteration zones whereas poorly crystallized illite (PCI) and I/S ml are predominant in the argillic alteration zones.

Nevertheless, the use of short-wave infrared (SWIR) spectroscopy demonstrated the reliability of this technique for identifying propylitic and argillic alteration by quantifying the illitic material in the cuttings samples. This provides a new reliable, time-saving and non-expensive method for building petrographic logs of geothermal wells intersecting the granitic basement of the URG, after calibration of the mineralogy by standard petrographic methods Glaas et al., 2019 (see chapter 6.2). The correlation of mineralogical data with geophysical logs provides an overall idea of the alteration intensity in the well. Indeed, the electrical resistivity correlates with the alteration grades: electrically conductive zones are systematically associated with argillic alteration whereas electrically resistive zones are systematically associated with propylitic alteration, excluding “local anomalies” linked to permeable fractures or quartz veins (chapter 6.4). Similarly, increases in porosity and decreases in bulk density are systematically associated with FZ which underwent argillic alteration. The natural radioactivity given by gamma-ray measurements is generally stable in granitic rocks. It is much more scattered in FZs with the alternation of gamma-ray rich zones due to the occurrence of secondary clay minerals bearing potassium (fracture WRs), and zones depleted in gamma ray containing secondary quartz or geothermal brine (fracture core) (Genter et al., 2007). The correlation of geophysical and geological data enables to interpret the alteration distribution in the granite at the well scale.

## 7.3. Permeable fracture zones

In the three sites, all permeable fractures are steeply dipping (85°E and W) and striking sub-parallel to the maximum horizontal stress direction  $\pm 10^\circ$ , suggesting that these fractures are opening in dilatancy or shearing (Evans, 2005; Valley, 2007; Hehn et al., 2016; Azzola et al., 2019). Permeability appears to be mainly controlled by nearly vertical fracture networks intersecting both Triassic sediments and crystalline Palaeozoic basement. These structural characteristics seem favourable for permeability but are not sufficient and other parameters such as secondary mineralogy seem to constrain the fracture permeability.

The distribution of the illitic material resulting from argillic alteration in the fracture zones was found to be a determining factor in the permeability of the reservoir. On a large scale (decametric) the presence of illitic material indicates past or present-permeability and is therefore generally positive for permeability (Vidal et al., 2018; Glaas et al., 2019b). But on a smaller scale, the presence of illitic material in pores can have a negative effect on permeability because it can clog the system (Caine et al., 1996; Faulkner et al., 2010). The use of SWIR spectroscopy allowed to quantify but also to observe the distribution of the illitic material in the FZs. It was found that paleo and present permeable FZs show high SWIR values. Indeed, the same ranges of SWIR values (i.e. the same illitic amounts) were observed in all the argillic alteration zones of URG wells, independently of their current permeability. However, present-day permeable zones display systematically a scattering of values oscillating between local low SWIR values interpreted as quartz veins or permeable pathways such as open fractures, and local high SWIR values interpreted as highly argillized and clogged WRs (min scattering 4 a.u. and average scattering 8 a.u.) (Glaas et al., 2019b).

Attempts were made to identify which are the permeable drains into the permeable FZs, and what are their specific geophysical and geological signatures. Generally, a permeable drain is characterized by a low SWIR peak and a depleted gamma-ray peak due to the absence of clay minerals and the presence of secondary quartz. It is generally signed by a very high electrical conductivity due to conductive brine circulating, a high porosity and a low density due to the presence of fractures (chapter 6.4). Due to intense fluid circulation, fractures of significant thickness or aperture can be observed in the borehole images. Around these permeable drains, an argillized WR is characterized by higher SWIR values and positive gamma-ray peaks. In these argillized WRs, high electrical conductivity values slightly lower than inside the permeable drain are generally observed (Glaas et al., 2019b, chapter 6.4). At the scale of a FZ including both the permeable drain and its argillized WRs, evidenced by scattered SWIR and electrical resistivity values, several indicators of water conducting fractures can be observed like mud losses, temperature anomaly, and gas occurrence.

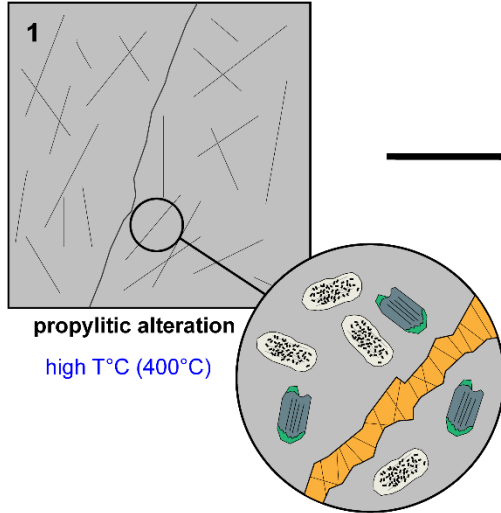
Although all these data do not have the same resolution, they systematically point out anomalies linked to FZ all along the well. The combination of geophysical and mineralogical methods constitutes an added value for the understanding of fluid circulation in the naturally fractured granite of the URG. In fact, it can also distinguish the past from the present-day permeable zones and improve the knowledge of the geometry of the fracture network.

Also, the SWIR method allows the collection of an important dataset with a good resolution, enabling to do multifactorial analyses by coupling the SWIR dataset with other geological or geophysical logs like the electrical resistivity for example.

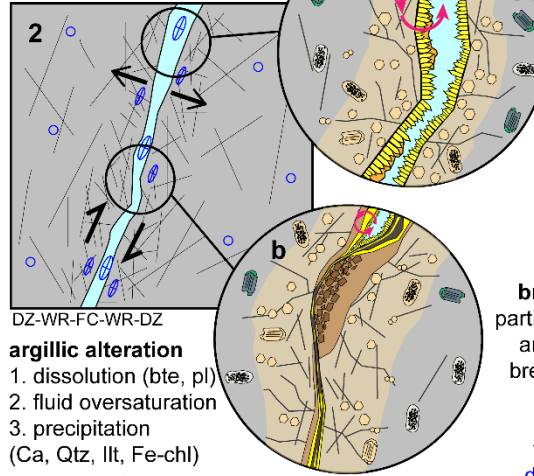
## Conceptual evolution of a fracture zone with time

time →

stress  
microcracks & small-scale fractures



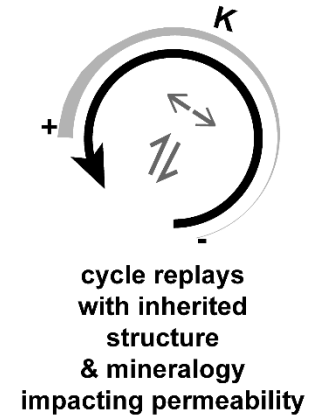
stress  
shear & dilatancy



stress dilatancy  
opening of the fracture  
permeability increase  
fluid circulation in the FC,  
WR and DZ  
increase of fluid/rock ratio

shear stress &  
brittle/ductile deformation  
partial or total clogging of the FC  
and WR due to formation of  
breccia, protomylonite, gouge

permeability drop  
fluid circulation in the DZ  
decrease of fluid/rock ratio

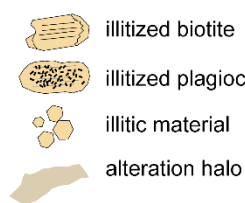


### Legend

propylitic alteration



argillic alteration



deformation



permeability

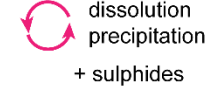
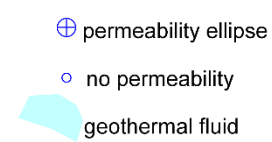


Figure 7.1: Evolution of a permeable fracture zone (KFZ) through time, forming a complex architecture resulting from several deformation and hydrothermal alteration cycles, determining the permeability distribution, DZ: damage zone, WR: wallrock, FC: fault core.

#### 7.4. Towards a revisited conceptual model of FZs

By integrating the main findings of this thesis, a refinement of the conceptual model of fluid circulations in the fracture and fault zones intersected by the URG geothermal wells, which was presented in section 3.3.5., is proposed in Figure 7.1. In fact, the model proposed in section 3.3.5. based on a literature review is a representation of the complexity of fracture zones as it could be observed at a given time. In this revisited model, the evolution through time of a fracture zone is proposed, taking into account the mineralogical and structural controls that build the final complex architecture (Figure 7.1).

1. Right after the emplacement of the pluton, the granite is affected by propylitic alteration. The resident fluids will interact, under decreasing temperatures, with the host rock. It generates the deposition of carbonates, in small-scale fractures and microcracks, the chloritisation of biotite and a weak feldspar illitization in the rock mass. Brittle tectonic activity links microcracks and small-scale fractures, creating larger fractures with irregular geometry (Figure 7.1 1).
2. Stress in dilatancy and in shearing reactivates the pre-existing structures and networks. For ease of representation, the dilatancy and shearing have been shown separately in the zooms a and b respectively.
  - a. Stress dilatancy creates and reopens major structures, allowing the circulation of potassium-rich fluids in their fault core (FC). Drusy quartz and carbonates precipitate on the fault walls. This fluid circulation in the surrounding WRs via the fractures embedded in the damage zone (DZ) induces argillic alteration. Indeed, the increase of fluid-rock ratio in the WR generates higher fluid-rock interactions that result in the dissolution of primary minerals in the rock mass, creating first a secondary porosity partly sealed by the precipitation of secondary minerals. These interactions create an alteration halo around the permeable drain and modify the petrophysical properties of the zone (Figure 7.1 2a).
  - b. In other parts of the FZ, shearing can also crush the altered rock and secondary minerals, creating new fractures but also developing in the FC, cataclasite facies such as gouge, breccia and mylonite. This deformation, at the limit between brittle and ductile, reduces the porphyritic grain size of the granite and clogs the FC and its surrounding. The fluid-rock ratio decreases, and the resulting permeability is mostly located in the distal DZ (Figure 7.1 2b).

This schematic cycle can act repeatedly with this inherited structure and mineralogy. Under dilatancy stress conditions, due to primary mineral dissolution, the fluid is richer in dissolved elements. Thus, in case of oversaturation, it could lead to an intense precipitation of secondary minerals due to changing pressure and temperature conditions, that clogs partially to totally the drains and the secondary porosity previously created. Under shear stress conditions, the FZ can also be partially or totally clogged. However, stress reactivation reactivates the system both by opening and/or shearing and could reopen fluid pathways. Over time, the system is expected to be enriched in clay minerals and the chemical equilibrium between the fluid and the rock closer to equilibrium.



## 8. Major outcomes for industrial exploitation

### 8.1. Conceptual model of the geothermal reservoirs

At Illkirch, the targeted Eschau fault zone at the sediment-basement interface is now a paleodrain (Figure 8.1 and 8.2). The apparent vertical offset of the Eschau fault is of kilometeric scale. The mineralogical study revealed a 200 m thick alteration halo in the granitic footwall of the Eschau fault, characterized by the presence of illitic material that clogged the system in the entire rock mass (Glaas et al., 2021a) (Figure 8.1 and 8.2). This could be due to intense fluid circulations at this interface, resulting from the mixing of salty brine and meteoric waters at the faulted interface as well as bottom basin fluids trapped at the sediments-basement interface. But also, the intense shearing of this normal fault could have tended to clog the structure by crushing the rock. In GIL-1 well, the permeability is located further away from the faulted interface, in the intra-granite faults and fractures system, which is slightly or not affected by the alteration halo of the Eschau fault (Figure 8.2). In the intra-granite section distant from the Eschau fault, 6 permeable FZs were detected from thermal anomalies (Glaas et al., 2020). For example, the zone around 3500 m MD could be linked to a major structure along which the seismic cloud due to injection tests seems to be localized according to ongoing work (Figure 8.1). This could underline the presence of at least one local fault in the intra-granite at Illkirch. Finally, the low productivity of the GIL-1 well despite of its very high fracture density could reflect the presence of fractures that are today mostly paleo-drains. (Glaas et al., 2020, 2021a) (see chapter 5.2).

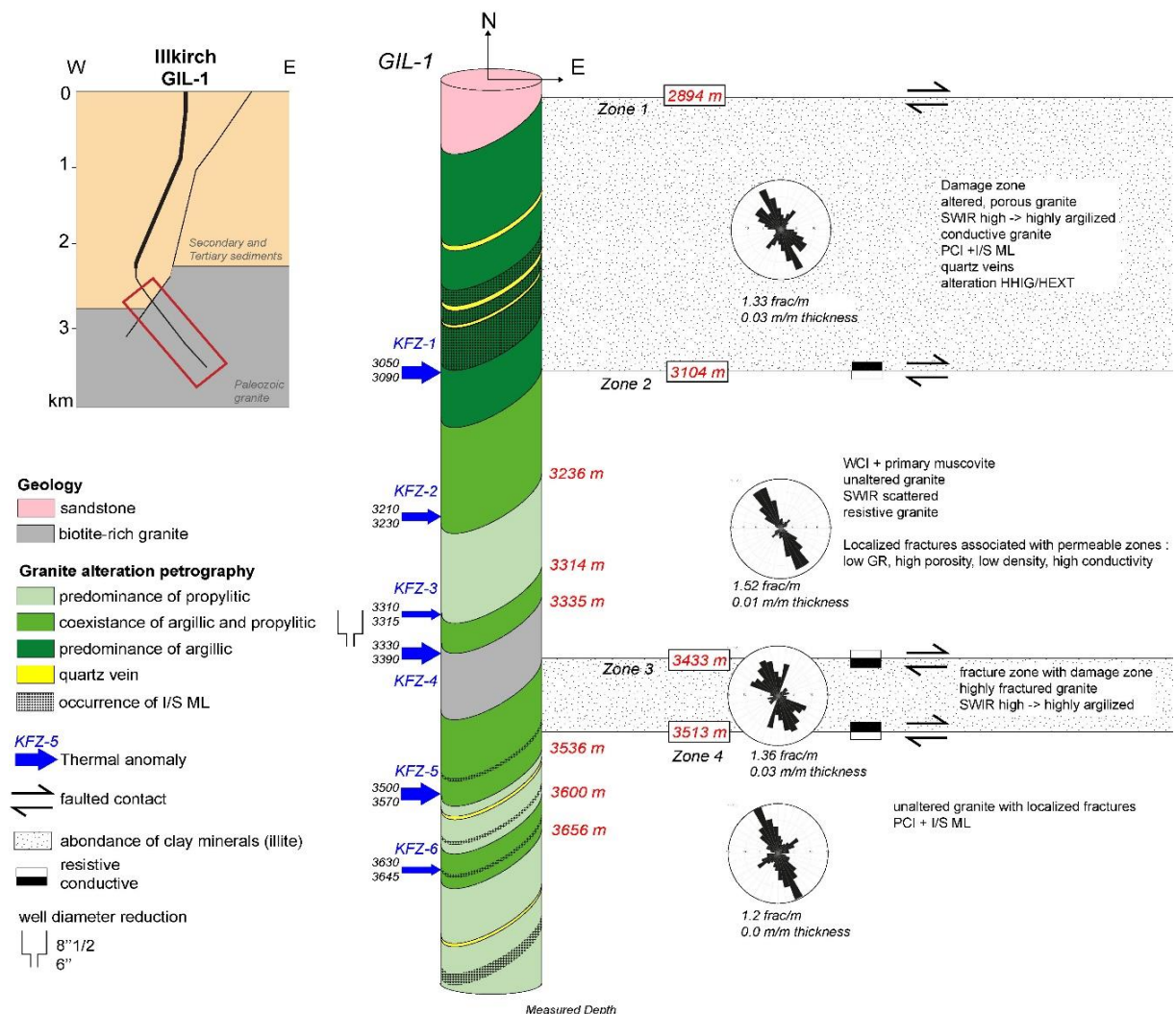


Figure 8.1: Conceptual model of the granitic section intersected by GIL-1 well at Illkirch.

At Rittershoffen and Soultz-sous-Forêts, the geothermal reservoirs are mainly located in the intra-granite fault and fracture system.

Both Rittershoffen wells targeted the Rittershoffen local normal fault in the granite (Figure 8.2). The apparent vertical offset of the Rittershoffen fault is about 200 m. The nearly vertical GRT-1 well intersects the major permeable drain of the Rittershoffen fault core at 2368 m MD (Vidal et al., 2017, 2019). Mineralogical results show a thick altered and fractured halo of 50 m mostly located in the hanging wall above the main fault core, characterized by moderate amounts of illitic material alternating with quartz veins and/or permeable pathways (Vidal et al., 2018; Glaas et al., 2019a, chapter 6.3). The oblique GRT-2 well tangents the local fault over a drilled length of 400 m, and intersects the major permeable drain supposed to be the fault core at 2774 m MD (Figure 8.2) (Vidal et al., 2017, 2019). In GRT-2, the mineralogical results showed a large altered and fractured halo on both sides of the Rittershoffen fault intersection, characterized by large amount of illitic material alternating with quartz veins and/or permeable pathways (Vidal et al., 2018; Glaas et al., 2019b). The GRT-2 well presented the highest natural productivity index before any stimulation, compared to the Soultz-sous-Forêts and Illkirch wells (Baujard et al., 2017a). The hydraulic behaviour of GRT-2 well is controlled by several smaller-scale structures belonging to a local fault.

The Soultz-sous-Forêts wells which initially targeted the massive granite of Soultz-sous-Forêts, intersected local faults and small-scale fractures in the intra-granite (Figure 8.2). Three granite reservoirs were outlined at the top basement (1400-2100 m), at intermediate depth (3200-3900 m) and at great depth (4500-5000 m) (Schill et al., 2017) (Figure 8.2). It was shown that the top reservoir is probably the most permeable but the coldest (Sausse and Genter, 2005). The main permeable fracture zones are intimately associated with argillic hydrothermal alteration and are located at 1820 m in GPK-1, 2120 m in GPK-2 or 2160 m in EPS-1 (Vidal et al., 2019). For example, in GPK-1 well, the SWIR results showed very strong argillic alteration but only locally around the permeable fractures (Glaas et al., 2019b, chapter 6.2). In GPK-4 well, the SWIR results showed that the top of the granitic basement (800 first meters) is highly argillic altered, characterized by high quantities of illitic material alternating with quartz veins and/or permeable pathways (Glaas et al., 2019a, chapter 6.3).

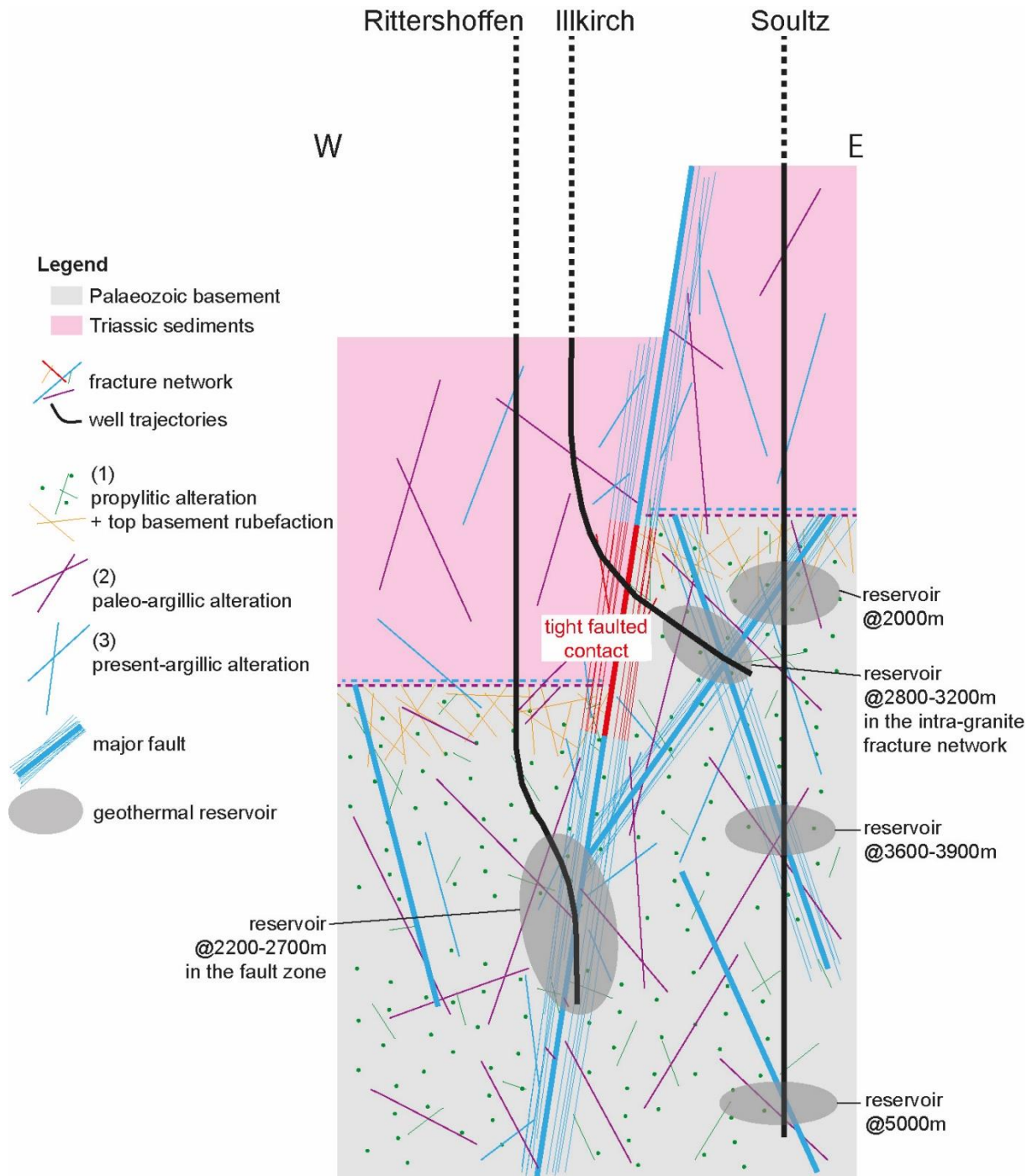


Figure 8.2: 2D conceptual model of the geothermal reservoirs in the Upper Rhine Graben including horst structure and well trajectories.

## 8.2. Implications for the development of the geothermal sector

In the investigated geothermal sites, the geothermal reservoirs are hosted in the naturally fractured granitic basement. However, at Soultz-sous-Forêts and Rittershoffen, geothermal reservoirs are mainly related to local faults whereas at Illkirch the present-day permeable fractures are mainly located far from the horst border fault and are therefore more related to smaller-scale fractures. However, the geothermal reservoir at Illkirch could also be due to local intra-granite faults. In fact, our methods at the well scale do not allow to discriminate if the structure intersected is a major or a small-scale structure. Further complementary studies need to be carried out with methods at the reservoir scale such as microseismicity, that could allow to observe the continuity of structures beyond the well.

In the Central URG, the most promising target for geothermal exploitation is to intersect by drilling and obliquely pass highly dipping local normal faults in the top granite. The application of the SWIR method on the cuttings samples from the geothermal wells in the URG helps to precise the extent of the damage zones associated with local faults intersected by the well. This method if monitored during the drilling could allow to refine the well trajectory in almost real-time in order to obtain a better connection between the well and the natural geothermal reservoir. Innovative drilling techniques inspired from the oil and gas industry should be investigated to see if they can be applied to the geothermal reservoir of the URG in order to optimize the intersection of the nearly vertical faults (Figure 8.3). As an example, horizontal, multilateral and fish bone drilling could be applied to optimize the intersection between the well and the fault zone, or the small-scale fracture network (Figure 8.3) (Li et al., 2013, 2016; Sahu et al., 2020).

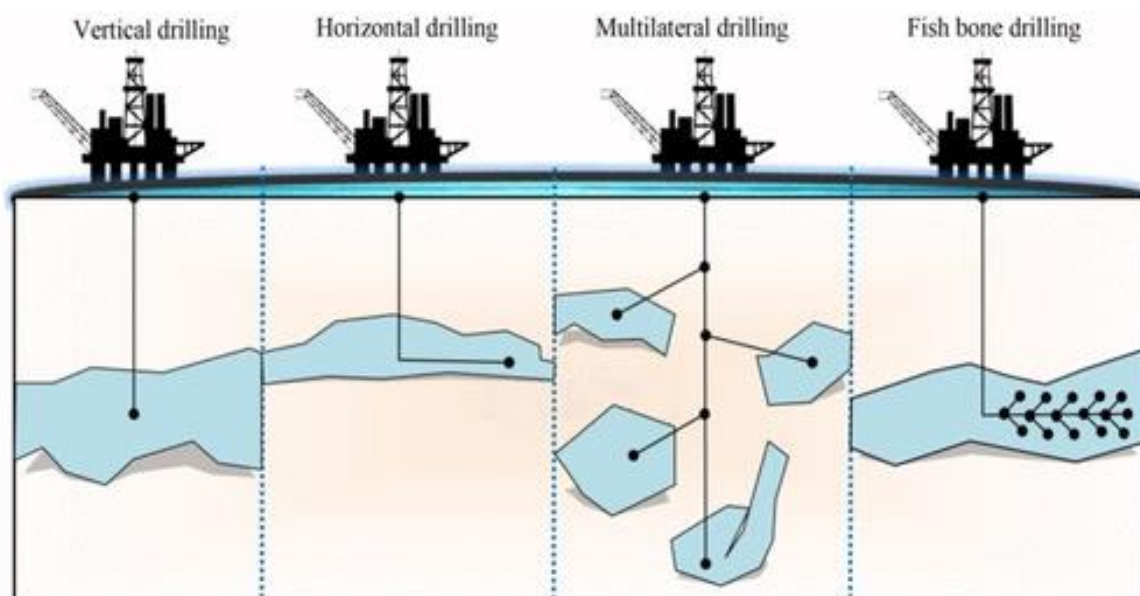


Figure 8.3: Innovative drilling techniques applied in the oil and gas industry (Sahu et al., 2020).

The correlation between SWIR results and electrical resistivity allows to detect centimetric fluid pathways inside decametric KFZs. This resolution is more precise than the one given by thermal anomalies. The identification of these centimetric fluid pathways enable to link their occurrence with major fracture or smaller-scale fractures observed on the borehole imageries

Although the complexity and heterogeneity of FZs do not enable to predict the distribution of permeability with a fine resolution, its understanding was approached. The FZ complexity in terms of mechanical behaviour should also be taken into account for diverse reservoir studies. For example, for seismological studies, the role of clay minerals as fracture filling is of high importance, as clay smearing could limit the occurrence of induced seismic events and could create aseismic movement (Cornet et al., 1997; Meller and Kohl, 2014; Meller et al., 2014a; Cornet, 2019). This phenomenon was observed at many geothermal sites including Rittershoffen where induced seismicity occurred few days after injection tests (Lengliné et al., 2017; Köpke, 2020; Maurer et al., 2020). At Illkirch, this was not observed yet, hence, very few seismic events were recorded during and after the injection tests.

The collection of in-situ data for the characterization of the basement geology could be improved by using conveyed logging techniques which consists in running logging tools inside

the drill pipes. Indeed, it is possible to collect high quality datasets from fracture study and geological characterization in highly deviated wells. At Illkirch, such innovative technique was applied successfully by minimizing the possible risk of losing standard logging tool by using conventional wireline logging techniques.

Also, besides the geological and geophysical considerations for finding the appropriate geothermal target, very often the site implantation is also constrained by other socio-economic parameters. Indeed, the local demand for heat and electricity, the public acceptance in the neighbouring region, but also the land available for sale, and political relations are also factors that can limit the implantation of a geothermal project. Thus, the challenge is to find the best compromise by targeting the geothermal reservoir that is available according to the socio-economic constraints described hereabove.



## 9. Perspectives

From the observations generalized in 8 wells intersecting the fractured granitic basement of the URG, the present-day permeable zones are systematically argillic alteration zones characterized by illite and I/S ml with <10% smectite. The presence of this main alteration phase (illite) produces a homogeneous SWIR signal. The application of the SWIR method to other existing boreholes in the URG targeting granitic basement and where cuttings samples are available, could be interesting to evaluate if the illitization of the crystalline basement is a general process at the basin scale. Several sites could be investigated like Vendenheim in France, or Landau and Insheim in Germany.

Furthermore, as the SWIR signal is homogeneous, the illitic material could be precisely quantified by preliminarily building mixing curves, provided that the grain size is controlled. This quantification could be very useful if the SWIR method is tested on sedimentary formations, where the matrix permeability will be linked the clay amount in the matrix.

In this research study, the analysis of the SWIR results focused on the area of the absorption band at 2200 nm, however other studies focus on the analysis of the intensity or even the slight variation of the position of this absorption band (Simpson and Rae, 2018; Kraal et al., 2021). This could be tested with the SWIR results from the Soultz-sous-Forêts, Rittershoffen and Illkirch wells but requires an improvement of the software developed by Hébert (2018).

To understand the link between the electrical signal, the alteration and the circulating brine, the electrical resistivity could be investigated in-depth by inverting and modelling the resistivity response. This kind of research could be carried out on electrical induction logs and the dual laterolog respectively from Illkirch and Soultz-sous-Forêts geothermal wells.

From a structural point of view, the vertical extension of the fracture network and more precisely of the local faults rooted in the granite could be investigated. Thus, the way the fault architecture evolves with decreasing depth in the Triassic layers would be an interesting challenge. Indeed, these faults could be potential geothermal targets in the sedimentary layers of the Muschelkalk and the Buntsandstein. This concept of multi-aquifers exploitation is already applied in the URG at Landau and Insheim (Germany). In fact, water-conducting fractures were found in the Muschelkalk limestone, Buntsandstein sandstone or Rotliegend sandstone in many wells at Illkirch, Merckwiller, Rittershoffen, Soultz-sous-Forêts, Bruhl, Bruchsal, Insheim, and Landau. If the primary and secondary mineralogy of these sedimentary Triassic formations is well known, the SWIR method coupled to other geophysical methods could also be applied to sedimentary formations to investigate permeability.



## References

- Agemar, T., Schellschmidt, R., Schulz, R., 2012. Subsurface temperature distribution in Germany. *Geothermics* 44, 65–77. <https://doi.org/10.1016/j.geothermics.2012.07.002>
- Aichholzer, C., 2019. Le log complet de la stratigraphie de la zone rhénane ainsi que les modalités stratigraphiques, sédimentaires et structurales de la transition “socle-couverture”. Application à la géothermie profonde. PhD, Université de Strasbourg, France.
- Aichholzer, C., Düringer, Ph., Genter, A., 2019. Detailed descriptions of the lower-middle Triassic and Permian formations using cores and gamma-rays from the EPS-1 exploration geothermal borehole (Soultz-sous-Forêts, Upper Rhine Graben, France). *Geothermal Energy* 7, 34. <https://doi.org/10.1186/s40517-019-0148-1>
- Aksoy, N., Mutlu, H., Solak, Ö.G., Kilinc, G., 2015. CO<sub>2</sub> Emission from Geothermal Power Plants. *Proceedings World Geothermal Congress 2015*. Presented at the World Geothermal congress 2015, Melbourne, Australia, 8.
- Altherr, R., Henes-Klaiber, U., Hegner, E., Langer, C., 1999. Plutonism in the Variscan Odenwald (Germany): from subduction to collision. *International Journal of Earth Sciences* 422–443.
- Altherr, R., Holl, A., Hegner, E., Langer, C., Kreuzer, H., 2000. High-potassium, calc-alkaline I-type plutonism in the European Variscides: northern Vosges (France) and northern Schwarzwald (Germany). *Lithos* 50, 51–73.
- Anderson, B.I., 2001. Modeling and Inversion Methods for the Interpretation of Resistivity Logging Tool Response. PhD, Technische Universiteit Delft, Netherlands.
- Anderson, J.L., Osborne, R.H., Palmer, D.F., 1983. Cataclastic rocks of the San Gabriel fault—an expression of deformation at deeper crustal levels in the San Andreas fault zone. *Tectonophysics* 98, 209–251. [https://doi.org/10.1016/0040-1951\(83\)90296-2](https://doi.org/10.1016/0040-1951(83)90296-2)
- Aquilina, L., Brach, M., Foucher, J.C., De Las Heras, A., Braibant, G., 1993. deepening of GPK-1 HDR borehole 2000-3600m (Soultz-sous-Forêts, France) Geochemical monitoring of drilling fluids. Open File report No. R36 619. BRGM-IMRG, Orléans.
- Archie, G.E., 1942. The Electrical Resistivity Log as an Aid in Determining Some Reservoir Characteristics. *Transactions of the AIME* 146, 54–62. <https://doi.org/10.2118/942054-G>
- Azzola, J., Valley, B., Schmittbuhl, J., Genter, A., 2019. Stress characterization and temporal evolution of borehole failure at the Rittershoffen geothermal project. *Solid Earth* 10, 1155–1180. <https://doi.org/10.5194/se-10-1155-2019>
- Baatartsoyt, B., Schwinn, G., Wagner, T., Taubald, H., Beitter, T., Markl, G., 2007. Contrasting paleofluid systems in the continental basement: a fluid inclusion and stable isotope study of hydrothermal vein mineralization, Schwarzwald district, Germany. *Geofluids* 7, 123–147. <https://doi.org/10.1111/j.1468-8123.2007.00169.x>
- Bacci, E., Gaggi, C., Lanzillotti, E., Ferrozzi, S., Valli, L., 2000. Geothermal power plants at Mt. Amiata (Tuscany–Italy): mercury and hydrogen sulphide deposition revealed by vegetation. *Chemosphere* 40, 907–911. [https://doi.org/10.1016/S0045-6535\(99\)00458-0](https://doi.org/10.1016/S0045-6535(99)00458-0)
- Baillieux, P., 2012. Multidisciplinary approach to understand the localization of geothermal anomalies in the Upper Rhine Graben from regional to local scale. PhD, University of Neuchâtel, Neuchâtel, Switzerland.
- Baillieux, P., Schill, E., Abdelfettah, Y., Dezayes, C., 2014. Possible natural fluid pathways from gravity pseudo-tomography in the geothermal fields of Northern Alsace (Upper Rhine Graben). *Geothermal Energy* 2, 16. <https://doi.org/10.1186/s40517-014-0016-y>

- Baillieux, P., Schill, E., Edel, J.-B., Mauri, G., 2013. Localization of temperature anomalies in the Upper Rhine Graben: insights from geophysics and neotectonic activity. *International Geology Review* 55, 1744–1762. <https://doi.org/10.1080/00206814.2013.794914>
- Baria, R., Baumgaertner, J., Teza, D., Bennett, T., Glass, H., Jupe, A., 2016. Development of geothermal technology to address the climate change issue in the densely populated areas of the world. European Geothermal Congress 2016. Presented at the European Geothermal Congress 2016, Strasbourg, France, 8.
- Bartier, D.L., Meunier, A., Liewig, N., Morvan, G., Addad, A., 2008. Hydrothermal alteration of the Soultz-sous-Forêts granite (Hot Fractured Rock geothermal exchanger) into a tosudite and illite assemblage. *European Journal of Mineralogy* 20, 131–142. <https://doi.org/10.1127/0935-1221/2008/0020-1787>
- Barton, C.A., Zoback, M.D., Moos, D., 1995. Fluid flow along potentially active faults in crystalline rock. *Geology* 23, 683–686. [https://doi.org/10.1130/0091-7613\(1995\)023<0683:FFAPAF>2.3.CO;2](https://doi.org/10.1130/0091-7613(1995)023<0683:FFAPAF>2.3.CO;2)
- Bauer, J.F., Meier, S., Philipp, S.L., 2015. Architecture, fracture system, mechanical properties and permeability structure of a fault zone in Lower Triassic sandstone, Upper Rhine Graben. *Tectonophysics* 132–145. <https://doi.org/10.1016/j.tecto.2015.02.014>
- Baujard, C., Genter, A., Cuenot, N., Mouchot, J., Maurer, V., Hehn, R., Ravier, G., Seibel, O., Vidal, J., 2018a. Experience learnt from a successful soft stimulation and operational feedback after 2 years of geothermal power and heat production in Rittershoffen and Soultz-sous-Forêts plants (Alsace, France). GRC Transactions. Presented at the Geothermal Resources Council 2018, Reno, Nevada, USA, 12.
- Baujard, C., Genter, A., Cuenot, N., Mouchot, J., Maurer, V., Hehn, R., Ravier, G., Seibel, O., Vidal, J., 2018b. Experience from a successful soft stimulation and operational feedback after 2 years of geothermal power and heat production in Rittershoffen and Soultz-sous-Forêts plants (Alsace, France). Presented at the Geothermal Resource Council, Reno, Nevada, USA, 2241–2252.
- Baujard, C., Genter, A., Dalmais, E., Maurer, V., Hehn, R., Rosillette, R., Vidal, J., Schmittbuhl, J., 2017a. Hydrothermal characterization of wells GRT-1 and GRT-2 in Rittershoffen, France: Implications on the understanding of natural flow systems in the Rhine Graben. *Geothermics* 65, 255–268. <https://doi.org/10.1016/j.geothermics.2016.11.001>
- Baujard, C., Hehn, R., Genter, A., Teza, D., Baumgartner, J., Guinot, F., Martin, A., Steinlechner, S., 2017b. Rate of penetration of geothermal wells: a key challenge in hard rocks. Workshop on Geothermal Reservoir Engineering. Stanford University, USA.
- Baumgärtner, D.J., Lersch, 2013. Geothermie 2.0 The Geothermal Power Plant Insheim. *EGR*. 21.
- Beaufort, D., Papapanagiotou, P., Patrier, P., Fouillac, A.M., Traineau, H., 1996. I/S and C/S mixed layers, some indicators of recent physical-chemical changes in active geothermal systems: the case study of Chipilapa (El Salvador). Presented at the Twenty-first Workshop on Geothermal Reservoir Engineering, Stanford University, California, USA.
- Beaufort, D., Rigault, C., Billon, S., Billault, V., Inoue, A., Inoue, S., Patrier, P., 2015. Chlorite and chloritization processes through mixed-layer mineral series in low-temperature geological systems – a review. *Clay Minerals* 50, 497–523. <https://doi.org/10.1180/claymin.2015.050.4.06>
- Belghoul, A., 2007. Caractérisation pétrophysique et hydrodynamique du socle cristallin. PhD. Montpellier II, France.

- Bense, V.F., Gleeson, T., Loveless, S.E., Bour, O., Scibek, J., 2013. Fault zone hydrogeology. *Earth-Science Reviews* 127, 171–192. <https://doi.org/10.1016/j.earscirev.2013.09.008>
- Berg, S.S., Øian, E., 2007. Hierarchical approach for simulating fluid flow in normal fault zones. *Petroleum Geoscience* 13, 25–35. <https://doi.org/10.1144/1354-079305-676>
- Bergerat, F., 1985. Déformations cassantes et champs de contrainte tertiaires dans la plate-forme européenne. PhD, Paris VI.
- Bertani, R., 2018. European Technology and Innovation Platform on Deep Geothermal. Vision for Deep Geothermal ETIP-DG.
- Bertani, R., 2015. Geothermal Power Generation in the World - 2010–2015 Update Report. *Proceedings World Geothermal Congress 2015*. Presented at the World Geothermal Congress 2015, Melbourne, Australia, 19.
- Bertrand, L., Gavazzi, B., Mercier de Lépinay, J., Diraison, M., Géraud, Y., Munsch, M., 2020. On the Use of Aeromagnetism for Geological Interpretation: 2. A Case Study on Structural and Lithological Features in the Northern Vosges. *Journal of Geophysical Research: Solid Earth* 125. <https://doi.org/10.1029/2019JB017688>
- Bettison, L.A., Schiffman, P., 1988. Compositional and structural variations of phyllosilicates from the Point Sal ophiolite, California. *American Mineralogist* 73, 62–76.
- Boiron, M.-C., Cathelineau, M., Richard, A., 2010. Fluid flows and metal deposition near basement /cover unconformity: lessons and analogies from Pb-Zn-F-Ba systems for the understanding of Proterozoic U deposits. *Geofluids* 10, 270–292. <https://doi.org/10.1111/j.1468-8123.2010.00289.x>
- Bonciani, R., Lenzi, A., Luperini, F., Sabatelli, F., 2013. Geothermal power plants in Italy: increasing the environmental compliance. *Proceedings of the European Geothermal Congress 2013*. Presented at the European Geothermal Congress 2013, Pisa, Italy, 6.
- Bons, P.D., Fusswinkel, T., Gomez-Rivas, E., Markl, G., Wagner, T., Walter, B., 2014. Fluid mixing from below in unconformity-related hydrothermal ore deposits. *Geology* 1035–1038.
- Bosia, C., Mouchot, J., Ravier, G., Seibel, O., Genter, A., 2021. Evolution of Brine Geochemical Composition During Operation of EGS Geothermal Plants (Alsace, France). *PROCEEDINGS, 46th Workshop on Geothermal Reservoir Engineering*. Presented at the Workshop on Geothermal Reservoir Engineering, Stanford University, California, USA, 21.
- Bossennec, C., Géraud, Y., Bertrand, L., Mattioni, L., Moretti, I., 2020. Insights on fluid sources and pathways in geothermal sandstone reservoir by structural and geochemical characterization of fractures infills. Presented at the World Geothermal Congress 2020, Reykjavik, 12.
- Bouchet, A., Morin, C., Parneix, J.C., 2017. Mesure de la C.E.C. de onze échantillons. Internal Report ESG. ERM, Poitiers.
- Bradford, J., McLennan, J., Moore, J., Glasby, D., Waters, D., Kruwells, R., Bailey, A., Rickard, W., Bloomfield, K., King, D., 2013. Recent developments at the Raft River geothermal field. Presented at the Thirty-Eighth Workshop on Geothermal Reservoir Engineering, Stanford University, California, USA.
- Brindley, G.W., Brown, G., 1980. X-Ray Diffraction procedures for clay mineral identification. In: *Crystal structures of clay minerals and their X-ray identification*, Brindley G.W. and Brown G. ed. European Mineralogical Union, London, Great Britain.
- Brockamp, O., Clauer, N., Zuther, M., 2003. Authigenic sericite record of a fossil geothermal system: the Offenburg trough, central Black Forest, Germany. *International Journal of Earth Sciences* 843–851.

- Brockamp, O., Schlegel, A., Clauer, N., 2011. Mesozoic hydrothermal impact on Rotliegende and Bunter immature sandstones of the High Rhine trough and its adjacent eastern area (southern Black Forest, Germany). *Sedimentary Geology* 234, 76–88. <https://doi.org/10.1016/j.sedgeo.2010.12.001>
- Brogi, A., 2011. Variation in fracture patterns in damage zones related to strike-slip faults interfering with pre-existing fractures in sandstone (Calcione area, southern Tuscany, Italy). *Journal of Structural Geology* 33, 644–661. <https://doi.org/10.1016/j.jsg.2010.12.008>
- Brogi, A., 2008. Fault zone architecture and permeability features in siliceous sedimentary rocks: Insights from the Rapolano geothermal area (Northern Apennines, Italy). *Journal of Structural Geology* 30, 237–256. <https://doi.org/10.1016/j.jsg.2007.10.004>
- Brown, S.R., 1987. Fluid flow through rock joints: The effect of surface roughness. *Journal of Geophysical Research* 92, 11.
- Bruhn, R.L., Parry, W.T., Yonkee, W.A., Thompson, T., 1994. Fracturing and hydrothermal alteration in normal fault zones. *Pure and Applied Geophysics* 142, 36.
- Buatier, M.D., Chauvet, A., Kanitpanyacharoen, W., Wenk, H.R., Ritz, J.F., Jolivet, M., 2012. Origin and behavior of clay minerals in the Bogd fault gouge, Mongolia. *Journal of Structural Geology* 34, 77–90. <https://doi.org/10.1016/j.jsg.2011.10.006>
- Burg, J.P., Matte, Ph., Leyreloup, A., Marchand, J., 1984. Inverted metamorphic zonation and large-scale thrusting in the Variscan Belt: an example in the French Massif Central. *Geological Society, London, Special Publications* 14, 47–61. <https://doi.org/10.1144/GSL.SP.1984.014.01.05>
- Burisch, M., Gerdes, A., Walter, F.B., Neumann, U., Fettel, M., Markl, G., 2017a. Methane and the origin of five-element veins: Mineralogy, age, fluid inclusion chemistry and ore forming processes in the Odenwald, SW Germany. *Ore Geology Reviews* 81, 42–61.
- Burisch, M., Walter, B.F., Gerdes, A., Lanz, M., Markl, G., 2017b. Late-stage anhydrite-gypsum-siderite-dolomite-calcite assemblages record the transition from a deep to a shallow hydrothermal system in the Schwarzwald mining district, SW Germany. *Geochimica et Cosmochimica Acta* 223, 259–278. <https://doi.org/10.1016/j.gca.2017.12.002>
- Byerlee, J., 1993. Model for episodic flow of high-pressure water in fault zones before earthquakes. *Geology* 21, 303–306.
- Caine, J.S., Evans, J.P., Forster, C.B., 1996. Fault zone architecture and permeability structure. *Geology* 24, 1025–1028. [https://doi.org/10.1130/0091-7613\(1996\)024<1025:FZAAPS>2.3.CO;2](https://doi.org/10.1130/0091-7613(1996)024<1025:FZAAPS>2.3.CO;2)
- Caine, J.S., Manning, A.H., Berger, B.R., 2010. Characterization of Geologic Structures and Host Rock Properties Relevant to the Hydrogeology of the Standard Mine in Elk Basin, Gunnison County, Colorado. Open-File Report No. Open-File Report 2010–1008, Open-File Report. U.S. Department of the Interior & U.S. Geological Survey, Reston, Virginia, USA.
- Carignan, J., Hild, P., Mevelle, G., Morel, J., Yeghicheyan, D., 2001. Routine analyses of trace elements in geological samples using flow injection and low pressure on-line liquid chromatography coupled to ICP-MS: a study of geochemical reference materials BR, DR-N, UB-N, AN-G and GH. *Geostandards Newsletter* 25, 187–198. <https://doi.org/10.1111/j.1751-908X.2001.tb00595.x>
- Cathelineau, M., Boiron, M.-C., 2010. Downward penetration and mixing of sedimentary brines and dilute hot waters at 5km depth in the granite basement at Soultz-sous-Forêts (Rhine graben, France). *Comptes Rendus Geoscience* 342, 560–565. <https://doi.org/10.1016/j.crte.2009.08.010>

- Cathelineau, M., Boiron, M.-C., Fourcade, S., Ruffet, G., Clauer, N., Belcourt, O., Coulibaly, Y., Banks, D.A., Guillocheau, F., 2012. A major Late Jurassic fluid event at the basin/basement unconformity in western France:  $^{40}\text{Ar}/^{39}\text{Ar}$  and K–Ar dating, fluid chemistry, and related geodynamic context. *Chemical Geology* 322–323.
- Cathelineau, M., Fourcade, S., Clauer, N., Buschaert, S., Rousset, D., Boiron, M.-C., Meunier, A., Lavastre, V., Javoy, M., 2004. Dating multistage paleofluid percolations: A K–Ar and  $^{18}\text{O}/^{16}\text{O}$  study of fracture illites from altered Hercynian plutonites at the basement/cover interface (Poitou High, France). *Geochimica et Cosmochimica Acta* 68, 2529–2542. <https://doi.org/10.1016/j.gca.2003.10.037>
- Cautru, J.-P., 1987. Coupe géologique passant par le forage GPK-1 calée sur la sismique réflexion. Report IMRG.
- Chester, F.M., Logan, M., 1987. Composite planar fabric of gouge from the Punchbowl Fault, California. *Journal of Structural Geology* 9, 621–634.
- Chèvremont, Ph., Genter, A., 1989. Etude pétrologique des échantillons de granite de Soultz-sous-Forêts, forage GPK-1. No. Report 89/IRG.
- Choi, J.-H., Edwards, P., Ko, K., Kim, Y.-S., 2016. Definition and classification of fault damage zones: A review and a new methodological approach. *Earth-Science Reviews* 152, 70–87. <https://doi.org/10.1016/j.earscirev.2015.11.006>
- Clauer, N., Liewig, N., Ledesert, B., Zwingmann, H., 2008. Thermal history of Triassic sandstones from the Vosges Mountains-Rhine Graben rifting area, NE France, based on K–Ar illite dating. *Clay Minerals* 43, 363–379. <https://doi.org/10.1180/claymin.2008.043.3.03>
- Clauer, C., Villinger, H., 1990. Analysis of conductive and convective heat transfer in a sedimentary basin, demonstrated for the Rheingraben. *Geophysical Journal International* 100, 393–414. <https://doi.org/10.1111/j.1365-246X.1990.tb00693.x>
- Cocherie, A., Guerrot, C., Fanning, C.M., Genter, A., 2004. Datation U–Pb des deux faciès du granite de Soultz (Fossé rhénan, France). *Comptes Rendus Geoscience* 336, 775–787pp. <https://doi.org/10.1016/j.crte.2004.01.009>
- Comparon, L., 2005. Experimental study of the electrical and dielectric properties of consolidated clayey materials. PhD. Institut de Physique du Globe de Paris, France.
- Cornet, F.H., 2019. The engineering of safe hydraulic stimulations for EGS development in hot crystalline rock masses. *Geomechanics for Energy and the Environment* 100151. <https://doi.org/10.1016/j.gete.2019.100151>
- Cornet, F.H., Helm, J., Poitrenaud, H., Etchecopar, A., 1997. Seismic and aseismic slips Induced by large-scale fluid injections. *Pure Applied Geophysics* 150, 563–583.
- Crain, E.R., 1998. *The Log Analysis Handbook*, Petroleum Engineering. United States.
- Curewitz, D., Karson, J.A., 1997. Structural settings of hydrothermal outflow: Fracture permeability maintained by fault propagation and interaction. *Journal of Volcanology and Geothermal Research* 149–168.
- Dalmais, E., Genter, A., Vidal, J., Baujard, C., Vuataz, F.-D., 2015. Permeability assessment based on drilling data in EGS projects. Case study of Muschelkalk fracture in GRT-1 well for ECOGI Project (Rittershoffen, Alsace, France). *European Geothermal Workshop 2015*. Presented at the European Geothermal Workshop 2015, Strasbourg, France, 4.
- Davatzes, N.C., Hickman, S.H., 2005. Controls on fault-hosted fluid flow; Preliminary results from the Coso Geothermal Field, CA. Presented at the Geothermal Resources Council Transactions, Geothermal Resources Council, Davis, California, 343–348.
- Davison, C.C., Wang, C.Y., 1988. Hydrogeologic characteristics of major fracture zones in a large granite batholith of the Canadian shield. *Proceedings, 4th Canadian-American*

- Conference on Hydrogeology. Presented at the 4th Canadian-American Conference on Hydrogeology, Banff, Canada.
- De Lima, O., Sharma, M., 1990. A grain conductivity approach to shaly sandstones. *Geophysics* 55, 1347–1356. <https://doi.org/10.1190/1.1442782>
- Degouy, M., Villeneuve, B., Weber, R., 1992. logistical support and development of the Soultz hot dry rock site: - seismic observation wells -wellEPS-1 1990-1991 Soultz-sous-Forets (France) Final report. No. Final Report. BRGM, Orléans.
- Dezayes, C., Chèvremont, P., Tourlière, B., Homeier, G., Genter, A., 2005. Geological study of the GPK4 HFR borehole and correlation with the GPK3 borehole (Soultz-sous-Forêts, France). Report. BRGM, Orléans, France.
- Dezayes, C., Genter, A., Valley, B., 2010. Structure of the low permeable naturally fractured geothermal reservoir at Soultz. *C. R. Geoscience* 342, 517–530. <https://doi.org/10.1016/j.crte.2009.10.002>
- Dezayes, C., Lerouge, C., 2019. Reconstructing paleofluid circulation at the Hercynian basement/Mesozoic sedimentary cover interface in the Upper Rhine Graben. *Geofluids* 2019, 1–30. <https://doi.org/10.1155/2019/4849860>
- Dezayes, C., Lerouge, C., Sanjuan, B., 2012. Projet TECITUR, relation tectonique/anomalies thermiques: rôle des circulations de fluides dans le fossé rhénan. Rapport d'avancement No. RP-60702-FR.
- Dezayes, C., Sanjuan, B., Gal, F., Lerouge, C., Brach, M., 2013. Forage d'exploration géothermique GRT-1. Suivi géochimique des fluides et caractérisation des zones fracturées. No. RP-62546-FR. BRGM.
- Dèzes, P., Schmid, S.M., Ziegler, P.A., 2004. Evolution of the European Cenozoic Rift System: interaction of the Alpine and Pyrenean orogens with their foreland lithosphere. *Tectonophysics* 389, 1–33. <https://doi.org/10.1016/j.tecto.2004.06.011>
- Doehl, F., 1967. The Tertiary and Pleistocene sediments of the Northern and Central part of the Upper Rhinegraben. *Abh. Geol. Landesans., The Rhinegraben Progress Report* 1967 6, 48–54.
- Drüppel, K., Stober, I., Grimmer, J.C., Mertz-Kraus, R., 2020. Experimental alteration of granitic rocks: Implications for the evolution of geothermal brines in the Upper Rhine Graben, Germany. *Geothermics* 88, 101903. <https://doi.org/10.1016/j.geothermics.2020.101903>
- Dubois, M., Ayt Ougougdal, M., Meere, P., Royer, J.-J., Boiron, M.-C., Cathelineau, M., 1996. Temperature of paleo- to modern self-sealing within a continental rift basin: The fluid inclusion data (Soultz-sous-Forêts, Rhine graben, France). *European Journal of Mineralogy* 8, 1065–1080. <https://doi.org/10.1127/ejm/8/5/1065>
- Duckworth, J.H., 1998. *Spectroscopic Quantitative Analysis. Academic Press Applied Spectroscopy: A Compact Reference for Practitioners.*
- Duringer, P., Aichholzer, C., Orciani, S., Genter, A., 2019. The complete lithostratigraphic section of the geothermal wells in Rittershoffen (Upper Rhine Graben, eastern France): a key for future geothermal wells. *BSGF - Earth Sciences Bulletin* 190, 13. <https://doi.org/10.1051/bsgf/2019012>
- Edel, J.B., Maurer, V., Dalmais, E., Genter, A., Richard, A., Letourneau, O., Hehn, R., 2018. Structure and nature of the Palaeozoic basement based on magnetic, gravimetric and seismic investigations in the central Upper Rhinegraben: Focus on the deep geothermal project of Illkirch-Graffenstaden. *Geothermal Energy* 6. <https://doi.org/10.1186/s40517-018-0099-y>

- Edel, J.-B., Schulmann, K., 2009. Geophysical constraints and model of the “Saxothuringian and Rhenohercynian subduction - magmatic arc system” in NE France and SW Germany. *Bulletin de La Société Géologique de France* 6, 545–558.
- Edel, J.-B., Schulmann, K., Rotstein, Y., 2007. The Variscan tectonic inheritance of the Upper Rhine Graben: evidence of reactivations in the Lias, Late Eocene–Oligocene up to the recent. *International Journal of Earth Sciences* 2, 305–325. <https://doi.org/10.1007/s00531-006-0092-8>
- Edel, J.-B., Whitechurch, H., Diraison, M., 2006. Seismicity wedge beneath the Upper Rhine Graben due to backwards Alpine push? *Tectonophysics* 428, 49–64. <https://doi.org/10.1016/j.tecto.2006.08.009>
- Edenhofer, O., Madrugá, R.P., Sokona, Y., Seyboth, K., Matschoss, P., Kadner, S., Zwickel, T., Eickemeier, P., Hansen, G., Schlömer, S., von Stechow, C., 2012. Renewable energy sources and climate change mitigation: special report of the Intergovernmental Panel on Climate Change. Cambridge University Press 49, 49-6309-49–6309. <https://doi.org/10.5860/CHOICE.49-6309>
- European Commission, 2016. SET Plan - Declaration of intent on Strategic Targets in the context of an Initiative for Global Leadership in Deep Geothermal Energy.
- Evans, K.F., 2005. Permeability creation and damage due to massive fluid injections into granite at 3.5 km at Soultz: 2. Critical stress and fracture strength. *Journal of Geophysical Research: Solid Earth* 110. <https://doi.org/10.1029/2004JB003169>
- Evans, K.F., Genter, A., Sausse, J., 2005. Permeability creation and damage due to massive fluid injections into granite at 3.5 km at Soultz: 1. Borehole observations. *Journal of Geophysical Research: Solid Earth* 110. <https://doi.org/10.1029/2004JB003168>
- Evans, K.F., Zappone, A., Kraft, T., Deichmann, N., Moia, F., 2012. A survey of the induced seismic responses to fluid injection in geothermal and CO<sub>2</sub> reservoirs in Europe. *Geothermics* 41, 30–54. <https://doi.org/10.1016/j.geothermics.2011.08.002>
- Faulds, J.E., Hinz, N.H., Coolbaugh, M.F., Cashman, P.H., Kratt, C., Dering, G., Edwards, J., Mayhew, B., McLahan, H., 2011. Assessment of favorable structural settings of geothermal systems in the Great Basin, western USA. Presented at the Geothermal Resources Council Transactions, 777–784.
- Faulkner, D.R., Jackson, C.A.L., Lunn, R.J., Schlische, R.W., Shipton, Z.K., Wibberley, C.A.J., Withjack, M.O., 2010. A review of recent developments concerning the structure, mechanics and fluid flow properties of fault zones. *Journal of Structural Geology* 32, 1557–1575. <https://doi.org/10.1016/j.jsg.2010.06.009>
- Faulkner, D.R., Lewis, A.C., Rutter, E.H., 2003. On the internal structure and mechanics of large strike-slip fault zones: field observations of the Carboneras fault in southeastern Spain. *Tectonophysics* 367, 235–251.
- Faulkner, D.R., Rutter, E.H., 2001. Can the maintenance of overpressured fluids in large strike-slip fault zones explain their apparent weakness? *Geological Society of America* 29, 503–506.
- Forster, C.B., Evans, J.P., 1991. Hydrogeology of thrust faults and crystalline thrust sheets: Results of combined field and modeling studies. *Geophysical Research Letters* 18, 979–982. <https://doi.org/10.1029/91GL00950>
- Freymark, J., Bott, J., Cacace, M., Ziegler, M., Scheck-Wenderoth, M., 2019. Influence of the main border faults on the 3D hydraulic field of the Central Upper Rhine Graben. *Geofluids* 2019, 1–21. <https://doi.org/10.1155/2019/7520714>
- Fridriksson, T., Mateos, A., Orucu, Y., Audinet, P., 2017. Greenhouse Gas Emissions from Geothermal Power Production. Proceedings, 42nd Workshop on Geothermal Reservoir Engineering. Presented at the 42nd Workshop on Geothermal Reservoir Engineering, Stanford University, Stanford, California, 12.

- Fulignati, P., 2020. Clay minerals in hydrothermal systems. *Minerals* 10. <https://doi.org/doi:10.3390/min10100919>
- Gailler, L.-S., Bouchot, V., Martelet, G., Thinon, I., Coppo, N., Baltassat, J.-M., Bourgeois, B., 2014. Contribution of multi-method geophysics to the understanding of a high-temperature geothermal province: The Bouillante area (Guadeloupe, Lesser Antilles). *Journal of Volcanology and Geothermal Research* 275, 34–50. <https://doi.org/10.1016/j.jvolgeores.2014.02.002>
- Gallé, C., 1994. Neutron porosity logging and core porosity measurements in the Beauvoir granite, Massif Central Range, France. *Journal of Applied Geophysics* 32, 125–137.
- Gardien, V., Rabinowicz, M., Vignerresse, J.-L., Dubois, M., Boulvais, P., Martini, R., 2016. Long-lived interaction between hydrothermal and magmatic fluids in the Soultz-sous-Forêts granitic system (Rhine Graben, France). *Lithos* 246–247, 110–127.
- Garnish, J.D., 1985. Hot Dry Rock - A European perspective. Geothermal Research Council Hawai.
- Genter, A., 1989. Géothermie roches chaudes sèches : le granite de Soultz-sous-Forêts (Bas-Rhin, France). Fracturation naturelle, altérations hydrothermales et interaction eau-roche. PhD. Université d'Orléans, France.
- Genter, A., Bujard, C., Cuenot, N., Hehn, R., Maurer, V., Mouchot, J., Seibel, O., Vidal, J., 2018. Exploiting fractured granites for producing heat or electricity: dream or reality? 80th EAGE Conference & Exhibition 2018. Presented at the EAGE.
- Genter, A., Castaing, C., Dezayes, C., Tenzer, H., Traineau, H., Villemin, T., 1997a. Comparative analysis of direct (core) and indirect (borehole imaging tools) collection of fracture data in Hot Dry Rock Soultz reservoir (France). *Journal of Geophysical Research* 102, 15,419-15,431.
- Genter, A., Cuenot, N., Dezayes, C., Sausse, J., Valley, B., Baumgartner, J., Fritsch, D., 2007. How a better characterization of a deep crystalline reservoir can contribute to improve EGS performance at Soultz. First European Geothermal Review, Geothermal Energy for Electric Power Production. Presented at the First European Geothermal Review, Geothermal Energy for Electric Power Production, Abstracts and Papers, Mainz, Rhineland Palatinate, Germany, 34–40.
- Genter, A., Evans, K., Cuenot, N., Fritsch, D., Sanjuan, B., 2010. Contribution of the exploration of deep crystalline fractured reservoir of Soultz to the knowledge of enhanced geothermal systems (EGS). *Comptes Rendus Geoscience* 342, 502–516. <https://doi.org/10.1016/j.crte.2010.01.006>
- Genter, A., Homeier, G., Chèvremont, Ph., Tenzer, H., 1999. Deepening of GPK-2 HDR borehole, 3880-5090m (Soultz-sous-Forêts, France). Geological Monitoring. Report. BRGM.
- Genter, A., Martin, P., Montaggioni, P., 1992. Application of FMS and BHTV tools for evaluation of natural fractures in the Soultz geothermal borehole GPK-1. *Geothermal Energy in Europe - The Soultz Hot Dry Rock Project*, Sur GR j'ai Que 69–82.
- Genter, A., Tenzer, H., 1995. Geological monitoring of GPK-2 HDR borehole, 1420-3880 m (Soultz-sous-Forêts, France). Report BRGM No. R38629. Orléans.
- Genter, A., Traineau, H., 1996. Analysis of macroscopic fractures in granite in the HDR geothermal well EPS-I, Soultz-sous-Forêts, France. *Journal of Volcanology and Geothermal Research* 121–141.
- Genter, A., Traineau, H., 1993. Deepening of GPK-1 HDR borehole 2000-3600m (Soultz-sous-Forêts). Geological monitoring. Report. BRGM, Orléans.
- Genter, A., Traineau, H., 1992. Hydrothermally altered and fractured granite as an HDR reservoir in the EPS-1 borehole, Alsace, France. *PROCEEDINGS*, Seventeenth

- Workshop on Geothermal Reservoir Engineering. Presented at the Workshop on Geothermal Reservoir Engineering, Stanford University, California, USA, 6.
- Genter, A., Traineau, H., Artignan, D., 1997b. Synthesis of geological and geophysical data of Soultz-sous-Forêts (France). OpenFile Report. BRGM.
- Genter, A., Traineau, H., Dezayes, C., Elsass, P., Ledésert, B., Meunier, A., Villemin, T., 1995. Fracture analysis and reservoir characterization of the granitic basement in the HDR Soultz project (France). *Geothermal Sciences and Technologies* 4, 189–214.
- Genter, A., Traineau, H., Ledésert, B., Bourguine, B., Gentier, S., 2000. Over 10 years of geological investigations within the HDR Soultz project, France. Presented at the World Geothermal Congress, Kyushu, Japan, 3707–3712.
- Gentier, S., Rachez, X., Dezayes, C., Blaisonneau, A., Genter, A., 2005. How to Understand the Effect of the Hydraulic Stimulation in Terms of Hydro-Mechanical Behavior at Soultz-sous-Forêts (France). *GRC Transactions*.
- GeOrg, T., 2017. EU-Projekt GeORG - Geoportal [WWW Document]. URL <http://www.geopotenziale.org/home?lang=3>
- Gérard, A., Genter, A., Kohl, T., Lutz, P., Rose, P., Rummel, F., 2006. The deep EGS (Enhanced Geothermal System) project at Soultz-sous-Forêts (Alsace, France). *Geothermics* 35, 473–483.
- Gérard, A., Kappelmeyer, O., 1987. The Soultz-sous-Forêts project. *Geothermics* 16, 393–399.
- Gérard, A., Menjot, A., Schwoerer, P., 1984. L'anomalie thermique de Soultz-sous-Forêts. *Géothermie Actualités* 35–42.
- Géraud, Y., Rosener, M., Surma, F., Place, J., Le Garzic, É., Diraison, M., 2010. Physical properties of fault zones within a granite body: Example of the Soultz-sous-Forêts geothermal site. *Comptes Rendus Geoscience* 342, 566–574. <https://doi.org/10.1016/j.crte.2010.02.002>
- Ghorbani, A., Revil, A., Coperey, A., Soueid Ahmed, A., Roque, S., Heap, M.J., Grandis, H., Viveiros, F., 2018. Complex conductivity of volcanic rocks and the geophysical mapping of alteration in volcanoes. *Journal of Volcanology and Geothermal Research* 357, 106–127. <https://doi.org/10.1016/j.jvolgeores.2018.04.014>
- Gillespie, P.A., Walsh, J.J., Watterson, J., Bonson, C.G., Manzocchi, T., 2001. Scaling relationships of joint and vein arrays from The Burren, Co. Clare, Ireland. *Journal of Structural Geology* 183–201.
- Glaas, C., Genter, A., Girard, J.-F., Patrier, P., Vidal, J., 2018. Permeability approach in deep fractured reservoirs of the Upper Rhine Graben. Hydrothermal alteration (clays) and electrical logs analyze in the geothermal wells of Alsace (France). 9th European Geothermal PhD Days. ETH, Zürich.
- Glaas, C., Genter, A., Girard, J.F., Patrier, P., Vidal, J., 2018. How do the geological and geophysical signatures of permeable fractures in granitic basement evolve after long periods of natural circulation? Insights from the Rittershoffen geothermal wells (France). *Geothermal Energy* 6. <https://doi.org/10.1186/s40517-018-0100-9>
- Glaas, C., Patrier, P., Vidal, J., Beaufort, D., Genter, A., 2021a. Clay mineralogy: a signature of granitic geothermal reservoirs of central Upper Rhine Graben. Submitted to *Minerals Journal*.
- Glaas, C., Patrier, P., Vidal, J., Beaufort, D., Girard, J.F., Genter, A., 2021b. Hydrothermal Alteration in the New Deep Geothermal Well GIL-1 (Strasbourg Area, France). Presented at the World Geothermal Congress 2020, Reykjavik, 11.

- Glaas, C., Vidal, J., Genter, A., 2020. Structural characterization of naturally fractured geothermal reservoirs in the central Upper Rhine Graben. Submitted to *Journal of Structural Geology*.
- Glaas, C., Vidal, J., Patrier, P., Beaufort, D., Genter, A., 2019a. Contribution of SWIR to the clay signature of permeable fracture zones in the granitic basement. Overview of Soultz and Rittershoffen wells. Presented at the European Geothermal Congress, Den Haag, The Netherlands, 11-14 June, 11.
- Glaas, C., Vidal, J., Patrier, P., Girard, J.-F., Beaufort, D., Petit, S., Genter, A., 2019b. How do secondary minerals in granite help distinguish paleo- from present-day permeable fracture zones? Joint interpretation of SWIR spectroscopy and geophysical logs in the geothermal wells of Northern Alsace. *Geofluids* 2019, 1–20. <https://doi.org/10.1155/2019/8231816>
- Gleeson, S.A., Yardley, B.W.D., 2002. Extensional Veins and Pb-Zn Mineralisation in Basement Rocks: The Role of Penetration of Formation Brines. *Water-Rock Interaction, Water Science and Technology Library* 40, 189–205. [https://doi.org/10.1007/978-94-010-0438-1\\_8](https://doi.org/10.1007/978-94-010-0438-1_8)
- Griffiths, L., Heap, M.J., Wang, F., Daval, D., Gilg, H.A., Baud, P., Schmittbuhl, J., Genter, A., 2016. Geothermal implications for fracture-filling hydrothermal precipitation. *Geothermics* 64, 235–245. <https://doi.org/10.1016/j.geothermics.2016.06.006>
- Gudmundsson, A., Fjeldskaar, I., Brenner, L.S., 2002. Propagation pathways and fluid transport of hydrofractures in jointed and layered rocks in geothermal fields. *Journal of Volcanology and Geothermal Research* 116, 257–278. [https://doi.org/10.1016/S0377-0273\(02\)00225-1](https://doi.org/10.1016/S0377-0273(02)00225-1)
- Guillou-Frottier, L., Carré, C., Bourguin, B., Bouchot, V., Genter, A., 2013. Structure of hydrothermal convection in the Upper Rhine Graben as inferred from corrected temperature data and basin-scale numerical models. *Journal of Volcanology and Geothermal Research* 256, 29–49. <https://doi.org/10.1016/j.jvolgeores.2013.02.008>
- Haas, I.O., Hoffmann, C.R., 1929. Temperature gradient in Pechelbronn oil bearing region, lower Alsace: its determination and relation to oil reserves. *Bull. Am. Assoc. Petr. Geol.* 13, 1257–1273.
- Hagedorn, B., Lippolt, H.J., 1994. Isotopische Alter von Zerrüttungszonen als Alterschranken der Freiamt-Sexau-Mineralisation (Mittlerer Schwarzwald). *Abhandlungen Der Geologie Des Landesamt Baden-Württemberg* 205–219.
- Häring, M.O., Schanz, U., Ladner, F., Dyer, B.C., 2008. Characterisation of the Basel 1 enhanced geothermal system. *Geothermics* 37, 469–495. <https://doi.org/10.1016/j.geothermics.2008.06.002>
- Heap, M.J., Kushnir, A.R.L., Gilg, H.A., Wadsworth, F.B., Reuschlé, T., Baud, P., 2017. Microstructural and petrophysical properties of the Permo-Triassic sandstones (Buntsandstein) from the Soultz-sous-Forêts geothermal site (France). *Geothermal Energy* 5. <https://doi.org/10.1186/s40517-017-0085-9>
- Hébert, B., 2018. Approche quantitative par spectrométrie Vis-NIR des minéraux argileux et uranifères dans les sables du gisement de Tortkuduk, Kazakhstan. PhD, Université de Poitiers, Poitiers.
- Hébert, R.L., Ledésert, B., Bartier, D., Dezayes, C., Genter, A., Grall, C., 2010. The Enhanced Geothermal System of Soultz-sous-Forêts: A study of the relationships between fracture zones and calcite content. *Journal of Volcanology and Geothermal Research* 196, 126–133. <https://doi.org/10.1016/j.jvolgeores.2010.07.001>
- Hehn, R., Genter, A., Vidal, J., Baujard, C., 2016. Stress field rotation in the EGS well GRT-1 (Rittershoffen, France). Presented at the European Geothermal Congress, Strasbourg.

- Heynekamp, M.R., Goodwin, L.B., Mozley, P.S., Haneberg, W.C., 1999. Controls on faultzone architecture in poorly lithified sediments, Rio Grande Rift, NewMexico: implications for fault-zone permeability and fluid flow. *AGU Geophysical Monograph* 113, 27–51. <http://dx.doi.org/10.1029/GM113p0027>
- Hooijkaas, G.R., Genter, A., Dezayes, C., 2006. Deep-seated geology of the granite intrusions at the Soultz EGS site based on data from 5km-deep boreholes. *Geothermics, The Deep EGS (Enhanced Geothermal System) Project at Soultz-Sous-Forêts, Alsace, France* 35, 484–506. <https://doi.org/10.1016/j.geothermics.2006.03.003>
- Housse, B.A., 1984. Reconnaissance du potentiel géothermique du Buntsandstein à Strasbourg-Cronembourg. *Géothermie Actualités* 36–41.
- Huang, W.L., Bishop, A.M., Brown, R.W., 1986. The effect of fluid/rock ratio on feldspar dissolution and illite formation under reservoir conditions. *Clay Minerals* 21, 585–601. <https://doi.org/10.1180/claymin.1986.021.4.10>
- Hunt, G.L., Salisbury, J.W., 1970. Visible and Near Infrared Spectra of Minerals and Rocks: I. Silicic Minerals. *Modern Geology* 1, 283–300.
- Hurtig, E., Cermak, V., Haenel, R., Zui, V., 1992. *Geothermal Atlas of Europe*. Hermann Haack Verlagsgesellschaft MbH, Germany.
- Huttrer, G.W., 2020. *Geothermal Power Generation in the World 2015-2020 Update Report*. Proceedings World Geothermal Congress 2020. Presented at the World Geothermal Congress 2020, Reykjavik, Iceland, 17.
- Ikari, M.J., Saffer, D.M., Marone, C., 2009. Frictional and hydrologic properties of clay-rich fault gouge. *Journal of Geophysical Research* 114, B05409. <https://doi.org/10.1029/2008JB006089>
- Illies, J.H., 1972. The Rhine graben rift system-plate tectonics and transform faulting. *Geophysical Surveys* 1, 27–60. <https://doi.org/10.1007/BF01449550>
- Illies, J.H., Greiner, G., 1979. Holocene movements and state of stress in the Rhinegraben rift system. *Tectonophysics* 52, 349–359.
- Inoue, A., 1995. Formation of clay minerals in hydrothermal environments. In: *Origin and mineralogy of clays*, Velde B. ed. Springer, Berlin, Germany.
- International Renewable Energy Agency, European Commission, 2019. *Renewable power generation costs in 2018*. International Renewable Energy Agency 88.
- International Renewable Energy Agency, European Commission, 2018. *Renewable Energy Prospects for the European Union*.
- Ishibashi, M., Yoshida, H., Sasao, E., Yuguchi, T., 2016. Long term behavior of hydrogeological structures associated with faulting: An example from the deep crystalline rock in the Mizunami URL, Central Japan. *Engineering Geology* 208, 114–127. <https://doi.org/10.1016/j.enggeo.2016.04.026>
- Jacquemont, B., 2002. *Etude des interactions eaux-roches dans le granite de Soultz-sous-Forêts. Quantification et modélisation des transferts de matière par les fluides*. PhD. Université de Strasbourg, France.
- Jung, R., 1992. Connecting a Borehole to a Nearby Fault by Means of Hydraulic Fracturing. Presented at the Geothermal Resources Council, 6.
- Jung, R., Schindler, M., Nami, P., Tischner, T., 2010. Determination of flow exits in the Soultz borehole GPK2 by using the brine displacement method. *Comptes Rendus Geoscience* 342, 636–643. <https://doi.org/10.1016/j.crte.2009.06.002>
- Just, J., Kontny, A., 2011. Thermally induced alterations of minerals during measurements of the temperature dependence of magnetic susceptibility: a case study from the

- hydrothermally altered Soultz-sous-Forêts granite, France. *International Journal of Earth Sciences* 21. <https://doi.org/10.1007/s00531-011-0668-9>
- Kamineni, D.C., Dugal, J.J.B., 1982. A study of rock alteration in the Eye—Dashwa lakes pluton, Atikokan, northwestern Ontario, Canada. *Chemical Geology* 36, 35–57. [https://doi.org/10.1016/0009-2541\(82\)90038-9](https://doi.org/10.1016/0009-2541(82)90038-9)
- Kappelmeyer, O., 1991. European HDR project at Soultz-sous-Forêts general presentation. *Geothermal Sciences and Technologies* 263–289.
- Koltzer, N., Scheck-Wenderoth, M., Bott, J., Cacace, M., Frick, M., Sass, I., Fritsche, J.-G., Bär, K., 2019. The effects of regional fluid flow on deep temperatures (Hesse, Germany). *Energies* 12, 2081. <https://doi.org/10.3390/en12112081>
- Kominou, A., Yardley, B.W.D., 1997. Fluid-rock interactions in the Rhine Graben: A thermodynamic model of the hydrothermal alteration observed in deep drilling. *Geochimica et Cosmochimica Acta* 61, 515–531. [https://doi.org/10.1016/S0016-7037\(96\)00358-4](https://doi.org/10.1016/S0016-7037(96)00358-4)
- Köpke, R., 2020. Fracture network characterization in enhanced geothermal systems by induced seismicity analysis. PhD, Karlsruhe Institute of Technology (KIT) & Université de Strasbourg.
- Kraal, K.O., Ayling, B.F., Blake, K., Hackett, L., Perdana, T.S.P., Stacey, R., 2021. Linkages between hydrothermal alteration, natural fractures, and permeability: Integration of borehole data for reservoir characterization at the Fallon FORGE EGS site, Nevada, USA. *Geothermics* 89, 101946. <https://doi.org/10.1016/j.geothermics.2020.101946>
- Kushnir, Alexandra R.L., Heap, M.J., Baud, P., 2018. Assessing the role of fractures on the permeability of the Permo-Triassic sandstones at the Soultz-sous-Forêts (France) geothermal site. *Geothermics* 74, 181–189. <https://doi.org/10.1016/j.geothermics.2018.03.009>
- Kushnir, Alexandra R. L., Heap, M.J., Baud, P., Gilg, H.A., Reuschlé, T., Lerouge, C., Dezayes, C., Düringer, P., 2018. Characterizing the physical properties of rocks from the Paleozoic to Permo-Triassic transition in the Upper Rhine Graben. *Geothermal Energy* 6. <https://doi.org/10.1186/s40517-018-0103-6>
- Lacirignola, M., Blanc, I., 2013. Environmental analysis of practical design options for enhanced geothermal systems (EGS) through life-cycle assessment. *Renewable Energy* 50, 901–914. <https://doi.org/10.1016/j.renene.2012.08.005>
- Lagarde, J.-L., Capdevila, R., Fourcade, S., 1992. Granites et collision continentale : l'exemple des granitoïdes carbonifères dans la chaîne hercynienne ouest-européenne. *Bulletin de La Société Géologique de France* 163, 597–610.
- Lampe, C., Person, M., 2000. Episodic hydrothermal fluid flow in the Upper Rhinegraben (Germany). *Journal of Geochemical Exploration* 69–70, 37–40. [https://doi.org/10.1016/S0375-6742\(00\)00049-2](https://doi.org/10.1016/S0375-6742(00)00049-2)
- Ledésert, B., Berger, G., Meunier, A., Genter, A., Bouchet, A., 1999. Diagenetic-type reactions related to hydrothermal alteration in the Soultz-sous-Forets Granite, France. *European Journal of Mineralogy* 11, 731–741.
- Ledésert, B., Dubois, J., Genter, A., Meunier, A., 1993. Fractal analysis of fractures applied to Soultz-sous-Forets hot dry rock geothermal program. *Journal of Volcanology and Geothermal Research* 57, 1–17. [https://doi.org/10.1016/0377-0273\(93\)90028-P](https://doi.org/10.1016/0377-0273(93)90028-P)
- Ledésert, B., Hebert, R., Genter, A., Bartier, D., Clauer, N., Grall, C., 2010. Fractures, hydrothermal alterations and permeability in the Soultz Enhanced Geothermal System. *Comptes Rendus Geoscience* 342, 607–615. <https://doi.org/10.1016/j.crte.2009.09.011>

- Ledésert, B., Hébert, R.L., Grall, C., Genter, A., Dezayes, C., Bartier, D., Gérard, A., 2009. Calcimetry as a useful tool for a better knowledge of flow pathways in the Soultz-sous-Forêts Enhanced Geothermal System. *Journal of Volcanology and Geothermal Research* 181, 106–114. <https://doi.org/10.1016/j.jvolgeores.2009.01.001>
- Ledésert, B., Joffre, J., Amblès, A., Sardini, P., Genter, A., Meunier, A., 1996. Organic matter in the Soultz HDR granitic thermal exchanger (France): natural tracer of fluid circulations between the basement and its sedimentary cover. *Journal of Volcanology and Geothermal Research* 70, 235–253. [https://doi.org/10.1016/0377-0273\(95\)00058-5](https://doi.org/10.1016/0377-0273(95)00058-5)
- Lengliné, O., Boubacar, M., Schmittbuhl, J., 2017. Seismicity related to the hydraulic stimulation of GRT1, Rittershoffen, France. *Geophysical Journal International* 208, 1704–1715. <https://doi.org/10.1093/gji/ggw490>
- Lévy, L., Fridriksson, T., Findling, N., Lanson, B., Fraisse, B., Marino, N., Gibert, B., 2020. Smectite quantification in hydrothermally altered volcanic rocks. *Geothermics* 85, 101748. <https://doi.org/10.1016/j.geothermics.2019.101748>
- Lévy, L., Gibert, B., Sigmundsson, F., Flóvenz, Ó., Hersir, G., Briole, P., Pezard, P., 2018. The role of smectites in the electrical conductivity of active hydrothermal systems: electrical properties of core samples from Krafla volcano, Iceland. *Geophysical Journal International* 215, 1558–1582. <https://doi.org/10.1093/gji/ggy342>
- Li, B., Liang, Y.-P., Li, X.-S., Zhou, L., 2016. A pilot-scale study of gas production from hydrate deposits with two-spot horizontal well system. *Applied Energy* 176, 12–21. <https://doi.org/10.1016/j.apenergy.2016.05.061>
- Li, X.-S., Yang, B., Duan, L.-P., Li, G., Huang, N.-S., Zhang, Y., 2013. Experimental study on gas production from methane hydrate in porous media by SAGD method. *Applied Energy* 112, 1233–1240. <https://doi.org/10.1016/j.apenergy.2013.02.007>
- Liotta, D., Brogi, A., Ruggieri, G., Rimondi, V., Zucchi, M., Helgadóttir, H.M., Montegrossi, G., Friðleifsson, G.Ó., 2020. Fracture analysis, hydrothermal mineralization and fluid pathways in the Neogene Geitafell central volcano: insights for the Krafla active geothermal system, Iceland. *Journal of Volcanology and Geothermal Research* 391, 106502. <https://doi.org/10.1016/j.jvolgeores.2018.11.023>
- Lippolt, H.J., Kirsch, H., 1994. Isotopic investigation of post-Variscan plagioclase sericitization in the Schwarzwald gneiss massif. *Chemie Der Erde* 54, 179–198.
- Lippolt, H.J., Seibel, W., 1991. Evidence for multistage alteration of Schwarzwald lamprophyres. *European Journal of Mineralogy* 3, 587–601.
- Lockner, D.A., Beeler, N.M., 2002. Rock Failure and Earthquakes. In: Lee, W.H.K., International Association of Seismology and Physics of the Earth's Interior (Eds.), *International Handbook of Earthquake and Engineering Seismology: A Project of the Committee on Education International Association of Seismology and Physics of the Earth's Interior.*, International Geophysics Series. Academic Press, Amsterdam.
- Lund, J.W., Boyd, T.L., 2020. Global geothermal direct use update. *Proceedings World Geothermal Congress 2020*. Presented at the World Geothermal Congress 2020, Reykjavik, Iceland.
- Madejová, J., Balan, E., Petit, S., 2010. Application of Vibrational Spectroscopy to the Characterization of Phyllosilicates and other Industrial Minerals. In: Ferraris, G., Christidis, G.E. (Eds.), *Advances in the Characterization of Industrial Minerals*. European Mineralogical Union, 171–226. <https://doi.org/10.1180/EMU-notes.9.6>
- Madejová, J., Gates, W.P., Petit, S., 2017. IR Spectra of Clay Minerals. *Developments in Clay Science*. Elsevier, 107–149. <https://doi.org/10.1016/B978-0-08-100355-8.00005-9>

- Manning, C.E., Ingebritsen, S.E., 1999. Permeability of the continental crust: Implications of geothermal data and metamorphic systems. *Reviews of Geophysics* 37, 127–150. <https://doi.org/10.1029/1998RG900002>
- Mas, A., Guisseau, D., Patrier Mas, P., Beaufort, D., Genter, A., Sanjuan, B., Girard, J.P., 2006. Clay minerals related to the hydrothermal activity of the Bouillante geothermal field (Guadeloupe). *Journal of Volcanology and Geothermal Research* 158, 380–400. <https://doi.org/10.1016/j.jvolgeores.2006.07.010>
- Mas, A., Patrier, P., Beaufort, D., Genter, A., 2003. Clay-mineral signatures of fossil and active hydrothermal circulations in the geothermal system of the Lamentin Plain, Martinique. *Journal of Volcanology and Geothermal Research* 124, 195–218. [https://doi.org/10.1016/S0377-0273\(03\)00044-1](https://doi.org/10.1016/S0377-0273(03)00044-1)
- Masanet, E., Chang, Y., Gopal, A.R., Larsen, P., Morrow, W.R., Sathre, R., Shehabi, A., Zhai, P., 2013. Life-Cycle Assessment of electric power systems. *Annual Review of Environment and Resources* 38, 107–136. <https://doi.org/10.1146/annurev-environ-010710-100408>
- Maurer, V., Gaucher, E., Grunberg, M., Koepke, R., Pestourie, R., Cuenot, N., 2020. Seismicity induced during the development of the Rittershoffen geothermal field, France. *Geothermal Energy* 8, 5. <https://doi.org/10.1186/s40517-020-0155-2>
- Mégel, T., Rybach, L., 2000. Production capacity and sustainability of geothermal doublets. *Proceedings World Geothermal Congress 2000*. Presented at the World Geothermal Congress 2000, Kyushu - Tohoku, Japan, 6.
- Meier, S., Bauer, J.F., Philipp, S.L., 2015. Fault zone characteristics, fracture systems and permeability implications of Middle Triassic Muschelkalk in Southwest Germany. *Journal of Structural Geology* 70, 170–189. <https://doi.org/10.1016/j.jsg.2014.12.005>
- Meller, C., Genter, A., Kohl, T., 2014a. The application of a neural network to map clay zones in crystalline rock. *Geophysical Journal International* 196, 837–849. <https://doi.org/10.1093/gji/ggt423>
- Meller, C., Kohl, T., 2014. The significance of hydrothermal alteration zones for the mechanical behavior of a geothermal reservoir. *Geothermal Energy* 2. <https://doi.org/10.1186/s40517-014-0012-2>
- Meller, C., Kontny, A., Kohl, T., 2014b. Identification and characterization of hydrothermally altered zones in granite by combining synthetic clay content logs with magnetic mineralogical investigations of drilled rock cuttings. *Geophysical Journal International* 199, 465–479. <https://doi.org/10.1093/gji/ggu278>
- Meller, C., Ledésert, B., 2017. Is there a link between mineralogy, petrophysics, and the hydraulic and seismic behaviors of the Soultz-sous-Forêts granite during stimulation? A review and reinterpretation of petro-hydronechanical data toward a better understanding of induced seismicity and fluid flow. *Journal of Geophysical Research: Solid Earth* 122, 9755–9774. <https://doi.org/10.1002/2017JB014648>
- Meunier, A., 1982. Superposition de deux altérations hydrothermales dans la syénite monzonitique du Bac de Montmeyre (Sondage INAG 1, Massif Central, France). *Bulletin de Minéralogie* 105, 386–394. <https://doi.org/10.3406/bulmi.1982.7633>
- Meunier, A., Velde, B., 1989. Solid solutions in I/S mixed-layer minerals and illite. *American Mineralogist* 74, 1106–1112.
- Michon, L., Van Balen, R.T., Merle, O., Pagnier, H., 2003. The Cenozoic evolution of the Roer Valley Rift System integrated at a European scale. *Tectonophysics* 367, 101–126. [https://doi.org/10.1016/S0040-1951\(03\)00132-X](https://doi.org/10.1016/S0040-1951(03)00132-X)
- Mitchell, T.M., Faulkner, D.R., 2012. Towards quantifying the matrix permeability of fault damage zones in low porosity rocks. *Earth and Planetary Science Letters* 339–340, 24–31. <https://doi.org/10.1016/j.epsl.2012.05.014>

- Moeck, I.S., 2014. Catalog of geothermal play types based on geologic controls. *Renewable and Sustainable Energy Reviews* 37, 867–882. <https://doi.org/10.1016/j.rser.2014.05.032>
- Moore, D.M., Reynolds, R.C., 1997. X-Ray Diffraction and the identification and analysis of clay minerals, Oxford University Press. ed. Oxford, New York.
- Moreno, L., Neretnieks, I., 1993. Fluid flow and solute transport in a network of channels. *Journal of Contaminant Hydrology* 14, 163–192. [https://doi.org/10.1016/0169-7722\(93\)90023-L](https://doi.org/10.1016/0169-7722(93)90023-L)
- Mouchot, J., Genter, A., Cuenot, N., Seibel, O., Scheiber, J., Bosia, C., Ravier, G., 2018. First Year of Operation from EGS Geothermal Plants in Alsace, France: Scaling Issues. PROCEEDINGS, 43rd Workshop on Geothermal Reservoir Engineering. Presented at the 43rd Workshop on Geothermal Reservoir Engineering, Stanford University, Stanford, California, 12.
- Mouchot, J., Ravier, G., Seibel, O., Pratiwi, A., 2019. Deep Geothermal Plants Operation in Upper Rhine Graben: Lessons Learned. European Geothermal Congress 2019. Presented at the European Geothermal Congress 2019, Den Haag, The Netherlands, 8.
- Neuman, S.P., 2008. Multiscale relationships between fracture length, aperture, density and permeability. *Geophysical Research Letters* 35, L22402. <https://doi.org/10.1029/2008GL035622>
- Nishimoto, S., Yoshida, H., 2010. Hydrothermal alteration of deep fractured granite: Effects of dissolution and precipitation. *Lithos* 115, 153–162. <https://doi.org/10.1016/j.lithos.2009.11.015>
- Niwa, M., Shimada, K., Tamura, H., Shibata, K., Sueoka, S., Yasue, K., Ishimaru, T., Umeda, K., 2016. Thermal Constraints on Clay Growth in Fault Gouge and Their Relationship with Fault-zone Evolution and Hydrothermal Alteration: Case Study of Gouges in the Kojaku Granite, Central Japan. *Clays and Clay Minerals* 64, 86–107. <https://doi.org/10.1346/CCMN.2016.0640202>
- Numelin, T., Marone, C., Kirby, E., 2007. Frictional properties of natural fault gouge from a low-angle normal fault, Panamint Valley, California: Frictional strength of natural fault gouge. *Tectonics* 26, n/a-n/a. <https://doi.org/10.1029/2005TC001916>
- Odling, N.E., Gillespie, P., Bourguin, B., Castaing, C., Chiles, J.-P., Christensen, N.P., Fillion, E., Genter, A., Olsen, C., Thrane, L., Trice, R., Aarseth, E., Walsh, J.J., Watterson, J., 1999. Variations in fracture system geometry and their implications for fluid flow in fractured hydrocarbon reservoirs. *Petroleum Geoscience* 5, 373–384.
- Parneix, J.-C., Meunier, A., 1982. Les transformations et la microfissuration du granite de Mayet-de-Montagne (Allier, France) sous l'influence des réactions minérales d'altération hydrothermale. 38, 203–210.
- Patrier, P., Bruzac, S., Pays, R., Beaufort, D., Bouchot, V., Verati, C., Gadalia, A., 2013. Occurrence of K-feldspar-bearing hydrothermal breccias in the Bouillante geothermal field (Basse Terre – Guadeloupe). *Bulletin de La Société Géologique de France* 184, 119–128. <https://doi.org/10.2113/gssgfbull.184.1-2.119>
- Patrier, P., Papapanagiotou, P., Beaufort, D., Traineau, H., Bril, H., Rojas, J., 1996. Role of permeability versus temperature in the distribution of the fine (< 0.2  $\mu\text{m}$ ) clay fraction in the Chipilapa geothermal system (El Salvador, Central America). *Journal of Volcanology and Geothermal Research* 72, 101–120. [https://doi.org/10.1016/0377-0273\(95\)00078-X](https://doi.org/10.1016/0377-0273(95)00078-X)
- Peters, T., Hofmann, B., 1984. Hydrothermal clay mineral formation in a biotite-granite in northern Switzerland. *Clay Minerals* 19, 579–590. <https://doi.org/10.1180/claymin.1984.019.4.05>

- Petit, S., 1999. Characterization of Octahedral Substitutions in Kaolinities Using Near Infrared Spectroscopy. *Clays and Clay Minerals* 47, 103–108. <https://doi.org/10.1346/CCMN.1999.0470111>
- Pfaff, K., Hildenbrandt, L.H., Leach, D.L., Jacob, D.E., Markl, G., 2010. Formation of the Wiesloch Mississippi Valley-type Zn-Pb-Ag deposit in the extensional setting of the Upper Rhinegraben, SW Germany. *Mineral Deposits* 45, 647–666. <https://doi.org/10.1007/s00126-010-0296-5>
- Pontual, S., Merry, N., Gamson, P., 1997. G-Mex Vol.1, Spectral interpretation field manual. AusSpec international Pty. Ltd., Kew, Victoria 3101, Australia.
- Pratiwi, A., Ravier, G., Genter, A., 2018. Life-cycle climate-change impact assessment of enhanced geothermal system plants in the Upper Rhine Valley. *Geothermics* 75, 26–39. <https://doi.org/10.1016/j.geothermics.2018.03.012>
- Pribnow, D., Clauser, C., 2000. Heat and fluid flow at the Soultz Hot Dry Rock system in the Rhine Graben. *Proceedings World Geothermal Congress 2000*. Presented at the World Geothermal Congress 2000, Kyushu - Tohoku, Japan, 6.
- Pribnow, D., Schellschmidt, R., 2000. Thermal tracking of upper crustal fluid flow in the Rhine graben. *Geophysical Research Letters* 27, 1957–1960. <https://doi.org/10.1029/2000GL008494>
- Ravier, G., Baujard, C., Dalmais, E., Maurer, V., Cuenot, N., 2016. Towards a comprehensive environmental monitoring of a geothermal power plant in the Rhine graben. Presented at the European Geothermal Congress 2016, Strasbourg, France, 9.
- Ravier, G., Harders, V., El Aoud, M., 2017. Rittershoffen geothermal heat plant. First geothermal heat plant for industrial uses worldwide. *EuroHeat&Power*.
- Rawling, G.C., Goodwin, L.B., 2006. Structural record of the mechanical evolution of mixed zones in faulted poorly lithified sediments, Rio Grande rift, New Mexico, USA. *Journal of Structural Geology* 17.
- Rawling, G.C., Goodwin, L.B., Wilson, J.L., 2001. Internal architecture, permeability structure, and hydrologic significance of contrasting fault-zone types. *Geological Society of America* 29, 46–46.
- Ray, D., 2019. Lazard's Levelized Cost of Energy Analysis - Version 13.0. 20.
- Reinecker, J., Hochschild, T., Kraml, M., Löschan, G., Kreuter, H., 2019. Experiences and challenges in geothermal exploration in the Upper Rhine Graben. Presented at the European Geothermal Congress, 8.
- Revil, A., Cathles III, L.M., Losh, S., Nunn, J.A., 1998. Electrical conductivity in shaly sands with geophysical applications. *Journal of Geophysical Research* 103, 23925–23936. <https://doi.org/10.1029/98JB02125>
- Revil, A., Murugesu, M., Prasad, M., Le Breton, M., 2017. Alteration of volcanic rocks: A new non-intrusive indicator based on induced polarization measurements. *Journal of Volcanology and Geothermal Research* 341, 351–362. <https://doi.org/10.1016/j.jvolgeores.2017.06.016>
- Richard, A., Gillot, É., Maurer, V., Cuenot, N., Klee, J., 2019. Upper Rhine Graben: the largest exploration by 3D seismic reflection. Presented at the European Geothermal Congress, Den Haag, Netherlands.
- Richard, A., Maurer, V., Edel, J.-B., Genter, A., Baujard, C., Dalmais, E., 2016. Towards targeting geothermal reservoir: exploration program for a new EGS project in urban context in Alsace. *European Geothermal Congress*. Strasbourg, France.
- Rigault, C., Patrier, P., Beaufort, D., 2010. Clay minerals related to circulation of near neutral to weakly acidic fluids in active high energy geothermal systems. *Bulletin de La Société Géologique de France* 181, 337–347. <https://doi.org/10.2113/gssgfbull.181.4.337>

- Rotstein, Y., Edel, J.-B., Gabriel, G., Boulanger, D., Schaming, M., Munsch, M., 2006. Insight into the structure of the Upper Rhine Graben and its basement from a new compilation of Bouguer Gravity. *Tectonophysics* 425, 55–70. <https://doi.org/10.1016/j.tecto.2006.07.002>
- Saffer, D.M., Marone, C., 2003. Comparison of smectite- and illite-rich gouge frictional properties: application to the updip limit of the seismogenic zone along subduction megathrusts. *Earth and Planetary Science Letters* 215, 219–235. [https://doi.org/10.1016/S0012-821X\(03\)00424-2](https://doi.org/10.1016/S0012-821X(03)00424-2)
- Sahu, C., Kumar, R., Sangwai, J.S., 2020. Comprehensive Review on Exploration and Drilling Techniques for Natural Gas Hydrate Reservoirs. *Energy & Fuels* 34, 11813–11839. <https://doi.org/10.1021/acs.energyfuels.0c02202>
- Sanjuan, B., Millot, R., Dezayes, C., Brach, M., 2010. Main characteristics of the deep geothermal brine (5km) at Soultz-sous-Forêts (France) determined using geochemical and tracer test data. *Comptes Rendus Geoscience* 342, 546–559. <https://doi.org/10.1016/j.crte.2009.10.009>
- Sanjuan, B., Millot, R., Innocent, Ch., Dezayes, C., Scheiber, J., Brach, M., 2016. Major geochemical characteristics of geothermal brines from the Upper Rhine Graben granitic basement with constraints on temperature and circulation. *Chemical Geology* 428, 27–47. <https://doi.org/10.1016/j.chemgeo.2016.02.021>
- Sanjuan, B., Négrel, G., Lous, M.L., Poulmarch, E., Gal, F., Damy, P.-C., 2021. Main geochemical characteristics of the deep geothermal brine at Vendenheim (Alsace, France) with constraints on temperature and fluid circulation. *Proceedings World Geothermal Congress 2021*. Presented at the World Geothermal Congress 2021, Reykjavik, Iceland, 12.
- Sanner, B., 2019. Summary of EGC 2019 Country Update Reports on Geothermal Energy in Europe. *European Geothermal Congress 2019*. Presented at the European Geothermal Congress 2019, Den Haag, The Netherlands, 14.
- Sausse, J., Dezayes, C., Dorbath, L., Genter, A., Place, J., 2010. 3D model of fracture zones at Soultz-sous-Forêts based on geological data, image logs, induced microseismicity and vertical seismic profiles. *Comptes Rendus Geoscience* 342, 531–545. <https://doi.org/10.1016/j.crte.2010.01.011>
- Sausse, J., Fourar, M., Genter, A., 2006. Permeability and alteration within the Soultz granite inferred from geophysical and flow log analysis. *Geothermics* 544–560.
- Sausse, J., Genter, A., 2005. Types of permeable fractures in granite. *Geological Society, London, Special Publications* 240, 1–14. <https://doi.org/10.1144/GSL.SP.2005.240.01.01>
- Sausse, J., Genter, A., Leroy, J.L., 1998. Description et quantification des altérations filoniennes : paléoécoulements fluides dans le granite de Soultz-sous-Forêts (Bas-Rhin, France). *Bulletin de La Société Géologique de France* 28.
- Schellschmidt, R., Clauser, C., 1996. The thermal regime of the Upper Rhine Graben and the anomaly at Soultz. *Z. Angew. Geologie* 42, 40–44.
- Schellschmidt, R., Schulz, R., 1992. Hydrogeothermic Studies in the Hot Dry Rock Project at Soultz-sous-Forêts. *Geothermal Energy in Europe, The Soultz Hot Dry Rock Project 3*, 217–238.
- Schill, E., Genter, A., Cuenot, N., Kohl, T., 2017. Hydraulic performance history at the Soultz EGS reservoirs from stimulation and long-term circulation tests. *70*, 110–124. <https://doi.org/10.1016/j.geothermics.2017.06.003>
- Schleicher, A.M., Warr, L.N., Kober, B., Laverret, E., Clauer, N., 2006. Episodic mineralization of hydrothermal illite in the Soultz-sous-Forêts granite (Upper Rhine Graben, France). *Contributions to Mineralogy and Petrology* 349–364.

- Schlumberger, 2018. HRLA High-Resolution Laterolog Array | Schlumberger [WWW Document]. URL [https://www.slb.com/services/characterization/petrophysics/wireline/legacy\\_services/high\\_res\\_array.aspx](https://www.slb.com/services/characterization/petrophysics/wireline/legacy_services/high_res_array.aspx) (accessed 12.3.18).
- Schlumberger, 1993. Schlumberger Wireline and Testing. Houston, Texas 77252-2175.
- Schmidt, R.B., Bucher, K., Stober, I., 2018. Experiments on granite alteration under geothermal reservoir conditions and the initiation of fracture evolution. *European Journal of Mineralogy* 30, 899–916. <https://doi.org/10.1127/ejm/2018/0030-2771>
- Schnaebeler, R., 1948. Monographie géologique du champ pétrolifère de Péchembronn. *Mémoire Du SCGAL* 7, 254.
- Scholz, C.H., Anders, M.H., n.d. The permeability of faults. US Geological Survey Open-File Report No. 94–228, The mechanical involvement of fluids in faulting.
- Schulte, T., Zimmermann, G., Vuataz, F.-D., Portier, S., Tischner, T., Junker, R., Jatho, R., Huenges, E., 2010. Enhancing geothermal reservoirs. *Geothermal Energy Systems - Exploration, Development, and Utilization*. Weiheim, Germany, 173–243.
- Schumacher, M.E., 2002. Upper Rhine Graben: Role of preexisting structures during rift evolution. *Tectonics* 21, 6-1-6–17. <https://doi.org/10.1029/2001TC900022>
- Schwinn, G., Wagner, T., Baatartsogt, B., Markl, G., 2006. Quantification of mixing processes in ore-forming hydrothermal systems by combination of stable isotope and fluid inclusion analyses. *Geochimica et Cosmochimica Acta* 70, 965–982. <https://doi.org/10.1016/j.gca.2005.10.022>
- Serra, O., 1984. *Fundamentals of Well-Log Interpretation*, Elsevier. ed. ELF Aquitaine, Pau, France.
- Serra, O., Serra, L., 2000. *Diagraphies, Acquisition et applications*, Serralog. ed.
- Shipton, Z.K., Cowie, P.A., 2001. Damage zone and slip-surface evolution over  $\mu\text{m}$  to km scales in high porosity Navajo sandstone, Utah. *Journal of Structural Geology* 1825–1844.
- Sibson, R.H., 1977. Fault rocks and fault mechanisms. *Journal of the Geological Society* 133, 191–213. <https://doi.org/10.1144/gsjgs.133.3.0191>
- Simpson, M.P., Rae, A.J., 2018. Short-wave infrared (SWIR) reflectance spectrometric characterisation of clays from geothermal systems of the Taupō Volcanic Zone, New Zealand. *Geothermics* 73, 74–90. <https://doi.org/10.1016/j.geothermics.2018.01.006>
- Sittler, C., 1992. Illustration de l'histoire géologique du Fossé rhénan et de l'Alsace. *N Jb Geol Paläont Abh* 186, 255–282.
- Sittler, C., 1985. Les hydrocarbures d'Alsace dans le contexte historique et géodynamique du fossé Rhénan. *Bull. Cent. Rech. Elf Explor. Prod.* 9, 335–371.
- Sizun, J.-P., 1995. Modification des structures de porosité de grès lors de transformations pétrographiques dans la diagenèse de l'hydrothermalisme. Application au Trias de la marge Ardéchoise et du fossé Rhénan. Université de Strasbourg.
- Smith, M.P., Savary, V., Yardley, B.W.D., Valley, J.W., Royer, J.J., Dubois, M., 1998. The evolution of the deep flow regime at Soultz-sous-Forêts, Rhine Graben, eastern France: Evidence from a composite quartz vein. *Journal of Geophysical Research: Solid Earth* 103, 27223–27237.
- Socomine, 1995. GPK2 Final Report, European Hot Dry Rock Program. Southern International Inc.
- Solum, J.G., Davatzes, N.C., Lockner, D.A., 2010. Fault-related clay authigenesis along the Moab Fault: Implications for calculations of fault rock composition and mechanical and

- hydrologic fault zone properties. *Journal of Structural Geology* 32, 1899–1911. <https://doi.org/10.1016/j.jsg.2010.07.009>
- Solum, J.G., van der Pluijm, B.A., Peacor, D.R., 2005. Neocrystallization, fabrics and age of clay minerals from an exposure of the Moab Fault, Utah. *Journal of Structural Geology* 27, 1563–1576. <https://doi.org/10.1016/j.jsg.2005.05.002>
- Staněk, M., Géraud, Y., 2019. Granite microporosity changes due to fracturing and alteration: secondary mineral phases as proxies for porosity and permeability estimation. *Solid Earth* 10, 251–274. <https://doi.org/10.5194/se-10-251-2019>
- Staupe, S., Mordhorst, T., Nau, S., Pfaff, K., Brüggmann, G., Jacob, D.E., Markl, G., 2012. Hydrothermal carbonates of the Schwarzwald ore district, southwestern Germany: Carbon source and conditions of formation using  $\delta^{18}\text{O}$ ,  $\delta^{13}\text{C}$ ,  $^{87}\text{Sr}/^{86}\text{Sr}$ , and fluid inclusions. *The Canadian Mineralogist* 50, 1401–1434.
- Stober, I., Bucher, K., 2015. Hydraulic conductivity of fractured upper crust: insights from hydraulic tests in boreholes and fluid-rock interaction in crystalline basement rocks. *Geofluids* 15, 161–178. <https://doi.org/10.1111/gfl.12104>
- Stober, I., Bucher, K., 2007. Hydraulic properties of the crystalline basement. *Hydrogeology Journal* 15, 213–224. <https://doi.org/10.1007/s10040-006-0094-4>
- Stober, I., Jodocy, M., 2009. Characteristics of geothermal reservoirs in the Upper Rhine Graben of Baden-Württemberg and France. *Grundwasser* 127–137. <https://doi.org/10.1007/s00767-009-0103-3>
- Storey, B.C., Lintern, B.C., 1981. Alteration, fracture infills and weathering of the Strath Halladale granite. No. ENPU--81-13. Institute of Geological Sciences, London.
- Stussi, J.-M., Cheilletz, A., Royer, J.-J., Chèvremont, P., Féraud, G., 2002. The hidden monzogranite of Soultz-sous-Forêts (Rhine Graben, France). *Mineralogy, petrology and genesis. Géologie de La France* 45–64.
- Swanson, E., Sussman, A., Wilson, J., 2019. Rapid clay precipitation in explosion-induced fractures. *Geology* 47, 1176–1180. <https://doi.org/10.1130/G46957.1>
- Tappert, M.C., 2013. The mineral chemistry, near-infrared, and mid-infrared reflectance spectroscopy of phengite from the Olympic Dam IOCG deposit, South Australia. *Ore Geology Reviews* 13.
- Toby, B.H., 2006. R factors in Rietveld analysis: How good is good enough? *Powder Diffraction* 21, 67–70. <https://doi.org/10.1154/1.2179804>
- Traineau, H., Genter, A., Cautru, J.-P., Fabriol, H., Chèvremont, Ph., 1992. Petrography of the granite massif from drill cutting analysis and well log interpretation in the geothermal HDR borehole GPK-1 (Soultz, Alsace, France). *Geothermal Energy in Europe - The Soultz Hot Dry Rock Project*. Bresee, James C., Montreux, Switzerland, 1–29.
- Valley, B., 2007. The relation between natural fracturing and stress heterogeneities in deep-seated crystalline rocks at Soultz-sous-Forêts (France). PhD. Université de Neuchâtel, Switzerland.
- Valley, B., Evans, K.F., 2007. Stress State at Soultz-Sous-Forêts to 5 Km Depth from Wellbore Failure and Hydraulic Observations. 10.
- Velde, B., 1977. Clays and clay minerals in natural and synthetic systems, *Development in sedimentology*. Elsevier, Amsterdam.
- Vernoux, J.F., Genter, A., Razin, P., Vinchon, C., 1995. Geological and petrophysical parameters of a deep fractured sandstone formation as applied to geothermal exploitation. public No. R 38622. BRGM Orléans, France.

- Vidal, J., Genter, A., 2018. Overview of naturally permeable fractured reservoirs in the central and southern Upper Rhine Graben: Insights from geothermal wells. *Geothermics* 74, 57–73. <https://doi.org/10.1016/j.geothermics.2018.02.003>
- Vidal, J., Genter, A., Chopin, F., 2017. Permeable fracture zones in the hard rocks of the geothermal reservoir at Rittershoffen, France. *Journal of Geophysical Research: Solid Earth* 122, 4864–4887. <https://doi.org/10.1002/2017JB014331>
- Vidal, J., Genter, A., Chopin, F., Dalmais, E., 2016a. Natural fractures and permeability at the geothermal site Rittershoffen, France. Presented at the European Geothermal Congress, Strasbourg, France.
- Vidal, J., Genter, A., Schmittbuhl, J., 2016b. Pre- and post-stimulation characterization of geothermal well GRT-1, Rittershoffen, France: insights from acoustic image logs of hard fractured rock. *Geophys J Int* 845–860.
- Vidal, J., Genter, A., Schmittbuhl, J., 2015. How do permeable fractures in the Triassic sediments of Northern Alsace characterize the top of hydrothermal convective cells? Evidence from Soultz geothermal boreholes (France). *Geothermal Energy* 3, 8. <https://doi.org/10.1186/s40517-015-0026-4>
- Vidal, J., Hehn, R., Glaas, C., Genter, A., 2019. How can temperature logs help identify permeable fractures and define a conceptual model of fluid circulation? An example from deep geothermal wells in the Upper Rhine Graben. *Geofluids* 14. <https://doi.org/10.1155/2019/3978364>
- Vidal, J., Patrier, P., Genter, A., Beaufort, D., Dezayes, C., Glaas, C., Lerouge, C., Sanjuan, B., 2018. Clay minerals related to the circulation of geothermal fluids in boreholes at Rittershoffen (Alsace, France). *Journal of Volcanology and Geothermal Research* 349, 192–204. <https://doi.org/10.1016/j.jvolgeores.2017.10.019>
- Villemin, T., Alvarez, F., Angelier, J., 1986. The Rhinegraben: Extension, subsidence and shoulder uplift. *Tectonophysics* 128, 47–59. [https://doi.org/10.1016/0040-1951\(86\)90307-0](https://doi.org/10.1016/0040-1951(86)90307-0)
- Villemin, T., Bergerat, F., 1987. L'évolution structurale du fossé rhénan au cours du Cénozoïque : un bilan de la déformation et des effets thermiques de l'extension. *Bull. Soc. Géol. France* 8, 245–255.
- Vuataz, F.-D., Brach, M., Criaud, A., Fouillac, C., 1990. Geochemical monitoring of drilling Fluids: A powerful tool to forecast and detect formation waters. *SPE Formation Evaluation* 5, 177–184. <https://doi.org/10.2118/18734-PA>
- Walter, B.F., Burisch, M., Fusswinkel, T., Marks, M.A.W., Steele-MacInnis, M., Wälle, M., Apukhtina, O.B., Markl, G., 2018. Multi-reservoir fluid mixing processes in rift-related hydrothermal veins, Schwarzwald, SW-Germany. *Journal of Geochemical Exploration* 186, 158–186. <https://doi.org/10.1016/j.gexplo.2017.12.004>
- Walter, B.F., Burisch, M., Markl, G., 2016. Long-term chemical evolution and modification of continental basement brines - a field study from the Schwarzwald, SW Germany. *Geofluids* 16, 604–623. <https://doi.org/10.1111/gfl.12167>
- Walter, B.F., Burisch, M., Marks, M.A.W., Markl, G., 2017. Major element compositions of fluid inclusions from hydrothermal vein-type deposits record eroded sedimentary units in the Schwarzwald district, SW Germany. *Mineralium Deposita* 52, 1191–1204.
- Walter, B.F., Kortenbruck, P., Scharrer, M., Zeitvogel, C., Wälle, M., Mertz-Kraus, R., Markl, G., 2019. Chemical evolution of ore-forming brines – Basement leaching, metal provenance, and the redox link between barren and ore-bearing hydrothermal veins. A case study from the Schwarzwald mining district in SW-Germany. *Chemical Geology* 506, 126–148.

- Waxman, M.H., Smits, L.J.M., 1968. Electrical Conductivities in Oil-Bearing Shaly Sands. Presented at the 42nd Annual Fall Meeting, Journal of Society of Petroleum Engineers, 107–122.
- Wilson, M.J., 2013. Rock Forming minerals. Sheet silicates: clay minerals., Deer, Howie and Zussman. ed. Geological Society.
- Wojdyr, M., 2010. Fityk: a general-purpose peak fitting program. Journal of Applied Crystallography 43, 1126–1128. <https://doi.org/10.1107/S0021889810030499>
- Zemanek, J., Glen, E.E.J., Norton, L.J., Cardwell, R.L., 1970. Formation evaluation by inspection with the borehole televiewer. Geophysics 2, 254–269.
- Ziegler, P.A., 1992. European Cenozoic rift system. Case history studies on rifts: European and Asian. Tectonophysics 91, 11.
- Ziegler, P.A., Schumacher, M.E., Dèzes, P., Van Wees, J.-D., Cloetingh, S., 2006. Post-Variscan evolution of the lithosphere in the area of the European Cenozoic Rift System. Geological Society, London, Memoirs 32, 97–112.
- Zuther, M., Brockamp, O., 1988. The fossil geothermal system of the Baden-Baden trough (northern Black Forest, F.R. Germany). Chemical Geology 71, 337–353. [https://doi.org/10.1016/0009-2541\(88\)90058-7](https://doi.org/10.1016/0009-2541(88)90058-7)



# APPENDICES



## APPENDIX 1

### Original paper

The Appendix 1 presents a conjoint work that was conducted and published in the peer reviewed *Geofluids Journal*, to refine the interpretation of the thermal signature of permeable fractures, based on data from Soultz-sous-Forêts and Rittershoffen wells. Temperature logs measured at equilibrium and during production coupled with flow logs, were analysed to improve the interpretation of temperature anomalies and fluid circulations at the well scale.

Vidal, J., Hehn, R., Glaas, C., Genter, A., 2019. How can temperature logs help in identifying permeable fractures and define a conceptual model of fluid circulation? An example from deep geothermal wells in the Upper Rhine Graben. *Geofluids Journal* 14. <https://doi.org/10.1155/2019/3978364>



## Research Article

# How Can Temperature Logs Help Identify Permeable Fractures and Define a Conceptual Model of Fluid Circulation? An Example from Deep Geothermal Wells in the Upper Rhine Graben

Jeanne Vidal , Régis Hehn, Carole Glaas , and Albert Genter

*ES-Géothermie, Bat Le Belem 5 rue de Lisbonne, 67300 Schiltigheim, France*

Correspondence should be addressed to Jeanne Vidal; [jeannevidal@ing.uchile.cl](mailto:jeannevidal@ing.uchile.cl)

Received 7 November 2018; Revised 25 January 2019; Accepted 19 February 2019; Published 10 July 2019

Guest Editor: Fabrizio Agosta

Copyright © 2019 Jeanne Vidal et al. This is an open access article distributed under the Creative Commons Attribution License, which permits unrestricted use, distribution, and reproduction in any medium, provided the original work is properly cited.

Identifying fluid circulation in fracture zones (FZs) is a key challenge in the extraction of deep geothermal heat from natural reservoirs in the Upper Rhine Graben. This study focuses on permeable FZs present within the granitic basement penetrated by deep geothermal well GPK-1 at Soultz and GRT-1 and GRT-2 at Rittershoffen (France). The various temperature (T) log datasets acquired from these wells during production and at equilibrium, with the associated flow logs, allow for the unique opportunity to interpret fluid circulation at the borehole scale. All permeable FZs identified by permeability indicators measured during drilling operations and from image logs spatially coincide with positive or negative T anomalies observed in the T logs during production and/or at equilibrium. However, within the FZs, partially open fractures act as narrower paths for circulation at different temperatures. These temperatures can even be estimated with confidence if the associated flow log is available. The polarity of the T anomalies correlates with the state of equilibrium of the well and thus can change over the well history. During production, the temperature of the water inflow through the fractures can be estimated relative to the mixture of water circulating below the fractures. At thermal equilibrium, the water temperature is estimated with respect to the temperature of the surrounding rock formation. Because temperature fluxes and geothermal fluids are intimately linked, T logs are a useful, reliable, and very sensitive tool to localize the inflow of geothermal water through FZs.

## 1. Introduction

In the Upper Rhine Graben (URG), the underground temperature distribution is spatially heterogeneous, and a series of local anomalies with temperatures above 140°C at a 2 km depth are observed at the regional scale [1–4]. These temperature anomalies are interpreted as convective cells circulating along vertical local faults (Figure 1) [2, 5, 6]. Hot upwellings are mainly concentrated around N-S-striking local faults on the western side of the URG. These N-S-striking local faults, which originate in the Paleozoic granitic basement and extend through the sedimentary cover, channelize these deep fluids. Over more than 30 years, 18 deep geothermal wells have targeted these faults in Germany (Landau, Insheim, Bruchsal, and Brühl) and France (Soultz-sous-Forêts, Rittershoffen and, most recently, Illkirch and Vendenheim) (Figure 1) [7–12]. Temperature (T) logs obtained from these

wells confirm the presence of hydrothermal convection and assert the roles of faults and fracture zones (FZs) as preferential pathways for geothermal brine [12–15]. The top of the granitic basement, which is highly fractured and affected by hydrothermal alteration, presents a low geothermal gradient associated with the vertical flow of brine and is locally affected by temperature anomalies interpreted as the thermal signatures of the FZs (Figures 2–4) [14–16].

Thus, the characterization of permeable fracture zones that act as primary potential paths for fluid flow is a key challenge for the development of geothermal reservoirs in granitic rocks. Experience shows that the characterization of permeable FZs by flow logs (obtained with a spinner tool) is difficult because flow logs are hard to obtain and interpret in these reservoirs. In contrast, T logs are cheap and easily acquired. T anomalies are interpreted as the thermal expressions of permeable FZs in several deep wells in geothermal

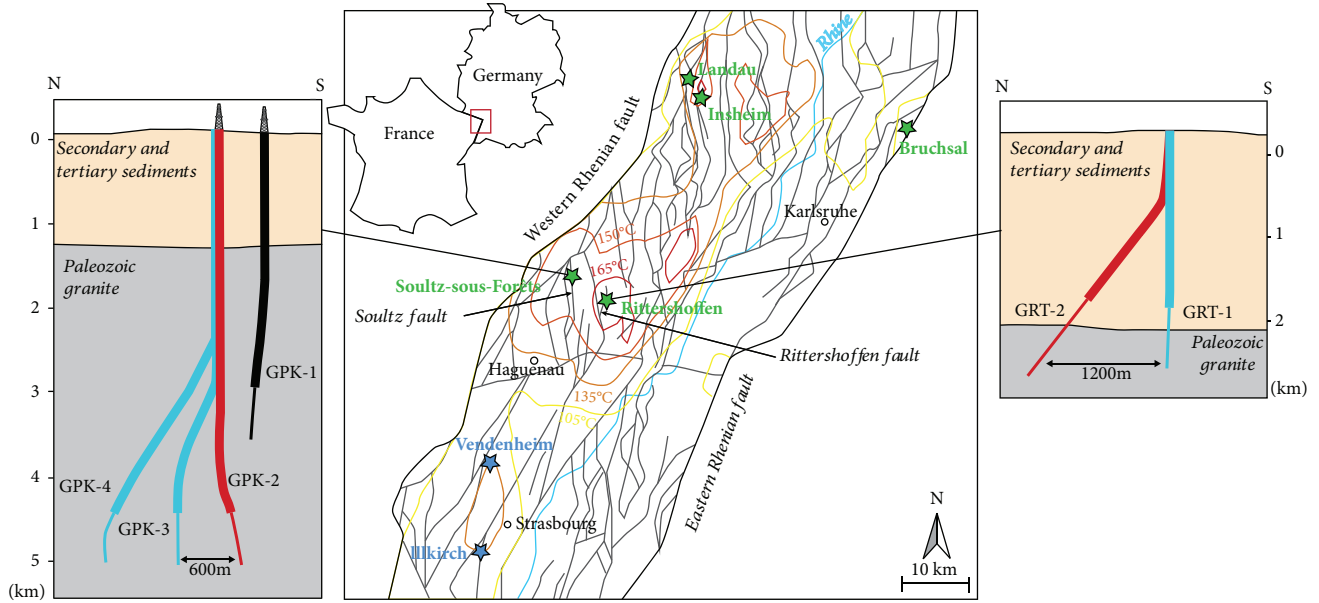


FIGURE 1: Structural map of the center of the Upper Rhine Graben with isotherms at a 2 km depth from the geoportal GeORG [55]. The geothermal anomaly in the Strasbourg area is from the dataset of Baillieux et al. [1]. Geothermal power plants in operation are represented by green stars, and the geothermal projects under drilling operations are represented by blue stars. On the left: N-S section through the geothermal wells of the Soultz-sous-Forêts power plant with a simplified geology. On the right: N-S section through the geothermal wells of the Rittershoffen power plant with a simplified geology. The thick line represents the casing section of the well, whereas the thin one represents the open hole. Production wells are in red, and injection wells are in blue. The GPK-1 well is represented in black because it is now used as an observation well.

systems worldwide [13, 14, 17–19]. However, in this paper, the datasets of the T logs acquired from wells at equilibrium and during production, combined with flow logs when they are available, offer a unique chance to further interpret T logs at the borehole scale. The reinterpretation of T logs at equilibrium and during production and their comparison with the permeability indicators and structural data from the FZs in well GPK-1 at Soultz and wells GRT-1 and GRT-2 at Rittershoffen provide a new perspective to better understand brine circulation through FZs in the granitic basement.

After a structural analysis of the main permeable fracture network that has channelized geothermal brines at the first order, the attention is focused on a comparison of T logs obtained at equilibrium and during production with flow logs if they are available from the wells. Finally, a conceptual model of fluid circulations through the FZs and the associated T anomalies is proposed at the borehole scale.

## 2. Soultz and Rittershoffen Geothermal Sites

Both projects exploit the hot upwelling of geothermal brine concentrated around the Soultz and the Rittershoffen faults (Figure 1). Extensive studies have identified convection associated with these hot upwellings; these studies have used numerical models on both the regional scale [4, 20] and local scale [21]. The role of faults as preferential fluid pathways is evident in other geothermal systems [22–25].

The pilot project of Soultz-sous-Forêts was initiated in the late 1980s. The target of the project was the development, hydraulic testing, and modeling of two Enhanced Geothermal System (EGS) heat exchangers within the granitic

basement at depths of 3.5 and 5 km [15, 26, 27]. In 1987, exploration well GPK-1 was drilled to a depth of 2 km and extended to a depth of 3.6 km in 1992 after hydraulic stimulation (Figure 1). At Soultz, geothermal water was pumped from the production well (GPK-2) and reinjected at a lower temperature into the injection wells (GPK-3 and GPK-4) after delivering geothermal energy through a heat exchanger to a binary power plant [10].

The geothermal project in Rittershoffen was initiated in 2008 and advised by lessons learned in Soultz. It is located less than 10 km east of Soultz (Figure 1). Injection well GRT-1 was drilled to a depth of 2.5 km in 2012 and thermally, chemically, and hydraulically stimulated in 2013. Production well GRT-2 was drilled to a depth of 2.5 km and is highly deviated accordingly to the geometry of the Rittershoffen fault (Figure 1). Well GRT-2 was not stimulated and thus, is defined as a hydrothermal well. The geothermal reservoir is mainly located in the granitic basement.

Geochemical studies indicate that the same brine is circulating within the large-scale fractured reservoir between Soultz and Rittershoffen [28, 29]. The reservoir was thoroughly investigated with a large amount of data (obtained from core samples, image logs, geophysical logs, microseismic data, vertical seismic profile, seismic reflection, etc.); these data were used to develop structural models of the multiscale fracture network associated with the Soultz and Rittershoffen faults [13, 30–33] as well as models of hydraulic circulation [34].

At the borehole scale, structural information from the granitic basement indicates that the highest density of fractures occurs in the first hundred meters of the

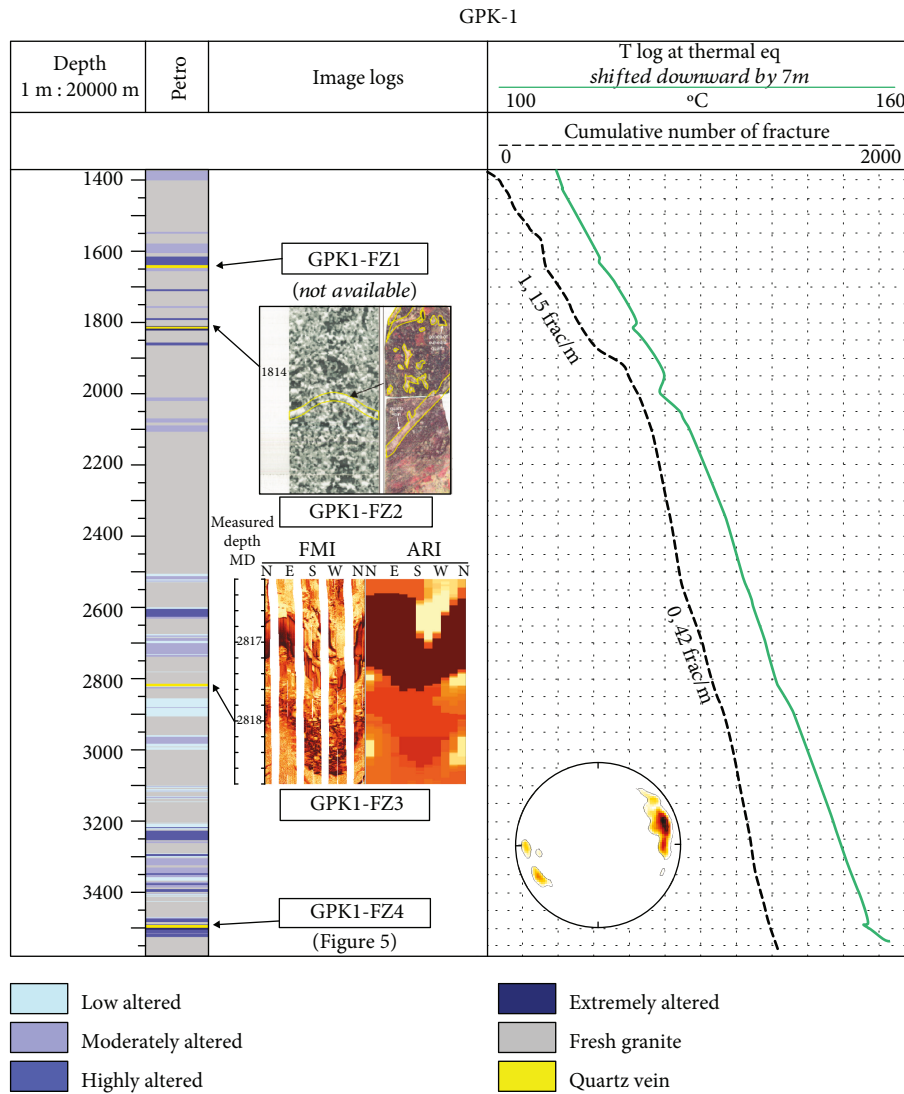


FIGURE 2: T logs from the granitic basement at thermal equilibrium in GPK-1 (Mar 1993, five months after the last hydraulic tests). T anomalies are associated with the permeable FZs observed in the image logs. The structural data of these FZs are presented in Table 1. Depth is expressed in Measured Depth (MD). T logs and flow logs were shifted manually to fit the anomalies with the fracture zones. Petrographic results are from Genter and Traineau [38]. Schmidt diagrams (lower hemisphere) and the cumulative number of fractures in the granitic basement are from Genter et al. [35].

hydrothermally altered granite. Data from acoustic image logs indicate values of 1,15 frac/m in GPK-1 in the first 500 m (data from a BoreHole TeleViewer, [35]) (Figure 2), 1,15 frac/m in GRT-1 in the first 200 m (Figure 3), and 0,75 frac/m in the deviated well GRT-2 (data from ultrasonic borehole images, [36]) (Figure 4). The fractures are mainly oriented NNW-SSE, with a steep dip mainly westward in GPK-1 (data from BHTV, [35]). In well GRT-1, the fractures strike mainly N10°E and dip approximately 60°W, whereas they are more scattered in GRT-2, with the main set oriented N160° to N-S and dipping 60°W (data from UBI, [36]). Hydraulic tests in GPK-1 indicate that 95% of the fluid flow enters the rock mass at only 10 discrete flow points [14]. These tests are consistent with cores from the permeable FZ, where a high density of partially open fractures promotes fluid circulation. These partially open fractures are

centimeters thick and are mainly filled by geodic quartz [37, 38]. An investigation of a quartz vein in the exploration borehole EPS-1 revealed at least seven generations of quartz, indicating a pulsed system of circulation [39]. Surrounding the core is a damage zone, with a width that ranges from centimeters to tens of meters. In this altered and porous zone, primary minerals are partly dissolved, and illite precipitation dominates the granite matrix [38, 40]. The degrees of alteration in the granite were determined based on the observations of the illitization amount in the core samples or cuttings [37, 41–43].

These permeable FZs mainly intersected in the granitic section, which is dominated by low temperature gradients associated with convection. The T gradients are approximately 20°C/km in GPK-1, nearly in GRT-1, and 18°C/km in GRT-2 (Figures 2–4). All permeable FZs have T anomalies

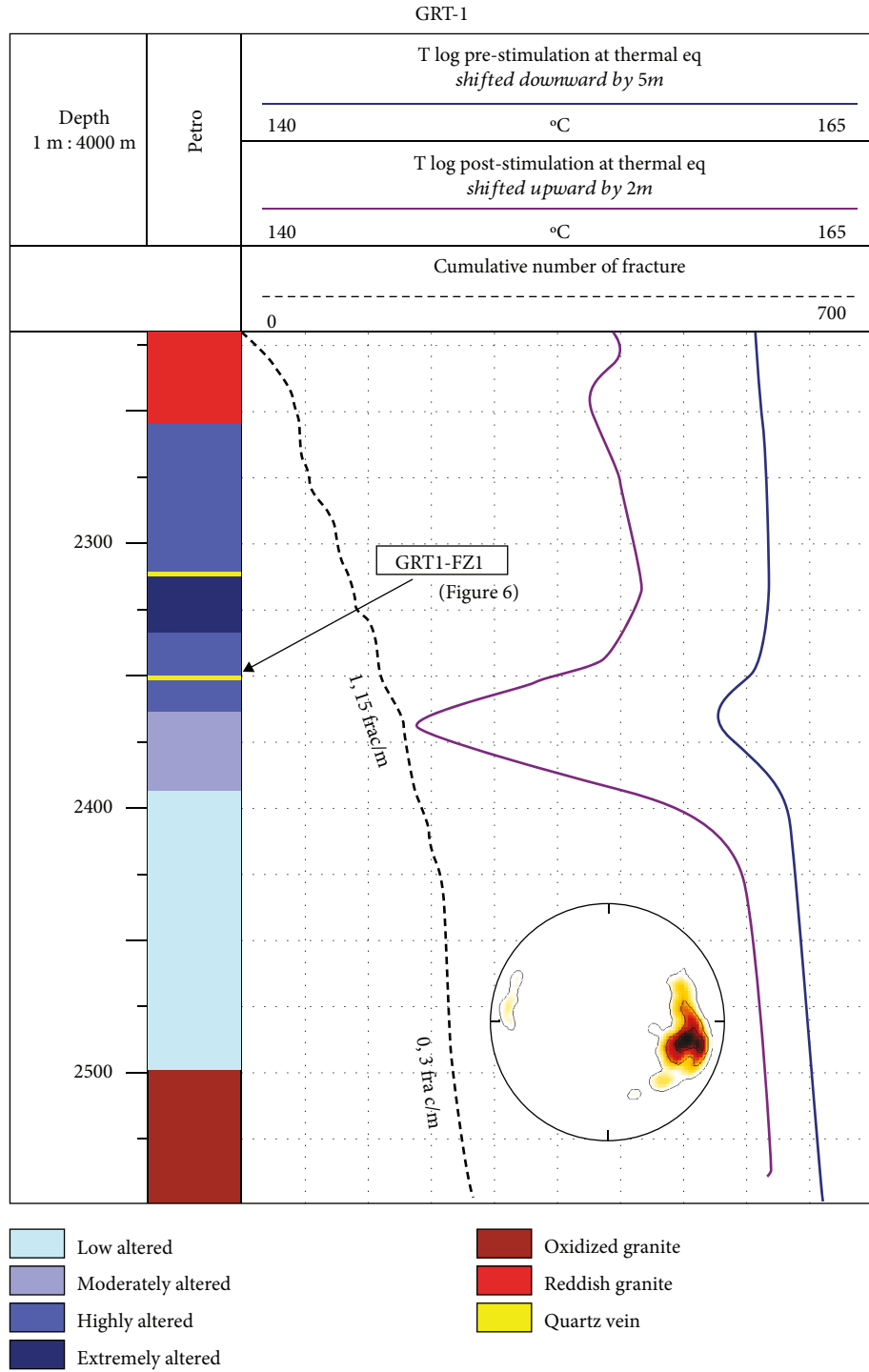


FIGURE 3: T logs from the granitic basement at thermal equilibrium in GRT-1 prestimulation (Apr 2013, four months after hydraulic tests) and poststimulation (Dec 2013, five months after hydraulic stimulation). T anomalies are associated with the permeable FZs observed in the image logs. The structural data of these FZs are presented in Table 1. Depth is expressed in Measured Depth (MD). T logs and flow logs were shifted manually to fit the anomalies with the fracture zones. Petrographic results are from Vidal et al. [44] and Glaas et al. [41]. Schmidt diagrams (lower hemisphere) and the cumulative number of fractures in the granitic basement are from Vidal et al. [36].

that spatially correlate with null observations in the T logs (Figures 2–4) [13–16]. Negative T anomalies are interpreted as the remnant cooling of porous damage zones after mud invasions during drilling operations and water injection

during stimulation operations [15]. However, is this interpretation still true several months after drilling operations and hydraulic tests, when the well is at thermal equilibrium? Could we propose another interpretation based on the

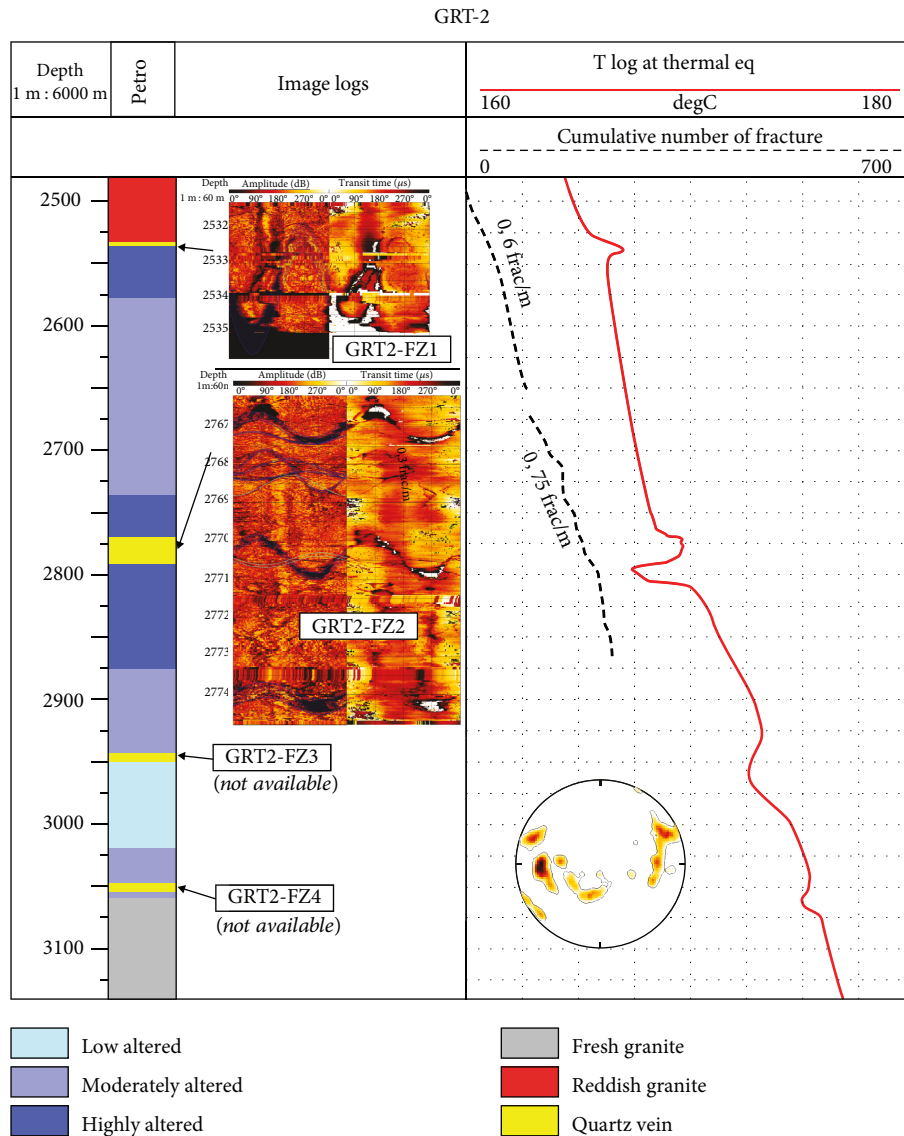


FIGURE 4: T logs from the granitic basement at thermal equilibrium in GRT-2 (September 2014, one month after drilling). T anomalies are associated with the permeable FZs observed in the image logs. The structural data of these FZs are presented in Table 1. Depth is expressed in Measured Depth (MD). T logs and flow logs were shifted manually to fit the anomalies with the fracture zones. Petrographic results are from Vidal et al. [44] and Glaas et al. [41]. Schmidt diagrams (lower hemisphere) and the cumulative number of fractures in the granitic basement are from Vidal et al. [36].

internal organization of the FZs? Is the intensity of the anomaly linked with the degree of permeability of the FZs? How could we explain the polarity and variations in the intensity of T anomalies over time?

### 3. Materials and Methods

3.1. *Permeable FZs from Mud Logs and Image Logs.* FZs that correspond to clusters of fractures partially open at the borehole scale and surrounded by a halo of hydrothermal alteration were identified in previous studies in Soultz and Rittershoffen [16, 44]. The core of the FZ is composed of opened fractures and quartz veins, and the damage zone is composed of illitic minerals [38]. Other secondary

minerals could be present (carbonates, sulfates, sulfides, and Fe-oxides).

Permeable FZs were identified using permeability indicators from several mud logs as follows:

- (i) Drilling mud losses and brine outflow are linked to permeable FZs [13–15, 33, 38, 45, 46]
- (ii) The occurrence of alkanes, as well as other gases such as helium, CO<sub>2</sub>, and radon, indicates permeable fracture zones [47, 48]
- (iii) The mineralogical investigation of rock cuttings or core samples, when available, is an efficient method for identifying hydrothermally altered zones in the

granite [13, 49]. Brine circulation through a permeable fracture zone leads to partial sealing by secondary geodic quartz and clay mineral deposits, which are easily detectable in cuttings by visual inspection and in the laboratory by XRD [39, 40, 43, 50]. When cuttings are not available or reliable, gamma ray (GR) logging, which measures natural radioactivity, is a good indicator of hydrothermal alteration [42]. In GR, the occurrence of geodic quartz is associated with sharp localized negative anomalies, whereas clay minerals, which are K-bearing minerals, are associated with positive anomalies that can extend several meters

Finally, once the permeability indicators are identified, acoustic image logs allow for the identification of the geometry of the FZs and the acoustic aperture of the fractures at the borehole scale.

**3.2. T Logs and Flow Logs.** The T anomalies observed in a temperature profile are considered the most reliable of the permeability indicators [14, 16, 18, 24]. T logs can be acquired at thermal equilibrium, i.e., after several weeks without well operations, or during production. When T logs are acquired during production, a flow log can also be acquired, and the flow is measured based on the speed of the rotation of the helix (spinner tool). T logs acquired at equilibrium are acquired downward; T logs and flow logs acquired during production are acquired upward. T logs acquired during production allow for temperature estimation of the water circulating into the fracture zone with the following equation (assuming a first-order approximation) (Figure 5):

$$T_r \times Q_r + T_f \times Q_f = T_m \times Q_m, \quad (1)$$

where  $T_r$  is the temperature of the water coming from below the fracture,  $Q_r$  is the flowrate of the water coming from below the fracture,  $T_f$  is the temperature of the water coming from the fracture,  $Q_f$  is the flowrate of the water coming from the fracture,  $T_m$  is the temperature of the mix of water above the fracture, and  $Q_m$  is the flowrate of the mix of water above the fracture.

At equilibrium, T anomalies were identified primarily with T logs acquired before stimulation (Figures 2–4). Thermal equilibrium must not be influenced by cold mud or cold water stored in fractures after drilling and hydraulic operations. Poststimulation T logs were compared to prestimulation T logs. It is possible to observe some vertical depth shifts between T anomalies and fracture zones from core samples and image logs. These shifts could have several explanations. All logs were not acquired at the same time, and the process of depth matching among all logs is complicated. Moreover, temperature variations led to cable elongations that were not corrected for the well-logging data. The logs were shifted downward or upward based on the depths of the main open fractures observed in the acoustic logs.

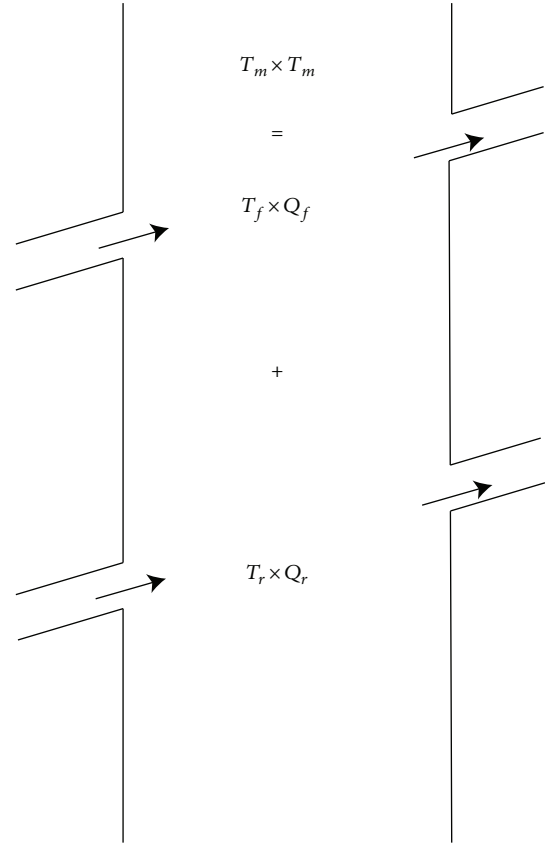


FIGURE 5: Scheme of the mixture of fluids coming from fractures into a permeable FZ.

## 4. Results

**4.1. Permeable FZs from T Logs at Thermal Equilibrium.** Four permeable FZs are identified in GPK-1, and they are all associated with negative thermal anomalies at thermal equilibrium (Table 1 and Figure 2). The borehole images of GPK1-FZ2 and GPK1-FZ3 are available in Vidal et al. [16, 43, 44]. Another negative anomaly is visible at a depth of 2100 m, but based on hydraulic tests, the FZ was identified as permeable after stimulation [51].

In GRT-1, one FZ was identified as permeable after stimulation and is associated with a negative anomaly at thermal equilibrium (Table 1 and Figure 3). GRT1-FZ1 includes the two permeable fractures observed in the granitic basement, as described in Vidal et al. [16]. A poststimulation anomaly is observed in the T log at 2236 m MD, but it is not spatially correlated with permeability indicators obtained before stimulation. Four permeable FZs are identified in GRT-2; two are associated with positive anomalies (GRT2-FZ1 and GRT2-FZ2), and two are associated with negative anomalies (GRT2-FZ3 and GRT2-FZ4) (Figure 4). GRT2-FZ1 includes the two uppermost permeable fractures observed in the table 1 of Vidal et al. [16], and GRT2-FZ2 includes the five deepest fractures. The borehole images of GRT-1 and GRT-2 are available in Vidal et al. [16].

Permeable fractures are mainly oriented N170°E and dip westward (Figure 6). Fractures that dip westward are associated with positive or negative T anomalies. Fractures that dip

TABLE 1: Temperature anomalies in well GPK-1 in Soultz and GRT-1 and GRT-2 in Rittershoffen. Structural data from the main open fractures in the FZs, as well as the polarity and depth of the anomalies, are presented. Structural data in italics indicate that acoustic images are not available. For GRT-2, values are calculated from oriented calipers [41].

Name	Main open fracture			Temperature anomaly	
	MD m	Strike Deg	Dip Def	MD m	Signal
GPK1-FZ1	1645	N155°E	76°W	1623	-
GPK1-FZ2	1814	N120°E	47°E	1815	-
GPK1-FZ3	2817	N150°E	75°W	2818	-
	2818.5	N140°E	70°X		
GPK1-FZ4	3489	N160°E	60°W	3495	-
	3496	N170°E	70°W		
GRT1-FZ1	2328	N20°E	50°W	2380	-
	2368	N170°E	55°W		
GRT2-FZ1	2534	N00°E	80°E	2537	+
	2540	N10°E	72°E		
	2767	N154°E	83°W		
GRT2-FZ2	2770.5	N160°E	87°W	2775	+
	2774	N170°E	64°W		
	2787	N45°E	57°E		
GRT2-FZ3	2788	N00°E	55°W	2970	-
	2950	<i>N170°E</i>	<i>90°E</i>		
GRT2-FZ4	3050	<i>N00°E</i>	<i>70°W</i>	3060	-

eastward are also associated with T anomalies that are positive or negative. The polarity of T anomalies is not directly linked to the fracture orientation or the dip direction. Thus, it is not possible to anticipate the polarity of the anomalies with respect to the fracture geometry.

4.2. Fluid Circulation from T Logs during Production

4.2.1. GPK-1. The permeable FZ in GPK1-FZ4 is presented in Figure 7. In September 1996, during production at 10.8 L/s, a flow log and a T log were acquired. The first inflow of water into the well was observed at 3496 m MD, with a measured flow of 1.5 L/s. This inflow depth corresponds with a negative T anomaly (148°C) in the T logs acquired during production. These anomalies are spatially correlated with an open fracture, which is visible in the acoustic image log, striking N170°E and dipping westward 70° at 3496 m MD. Then, several small positive anomalies are observed and associated with a flow increase at the same depth as the open fracture, striking N160°E and dipping 60°W at 3489 m MD. All of these small anomalies are assumed to originate from the same fracture. Above this, the flow is 2.7 L/s, and the measured temperature is 149°C. Following the equation described in Section 3.2, the temperature of the water that arrives in this major fracture is approximately 150°C:

$$\frac{149 \times 2.7 - 148 \times 1.5}{(2.7 - 1.5)} = 150.2. \quad (2)$$

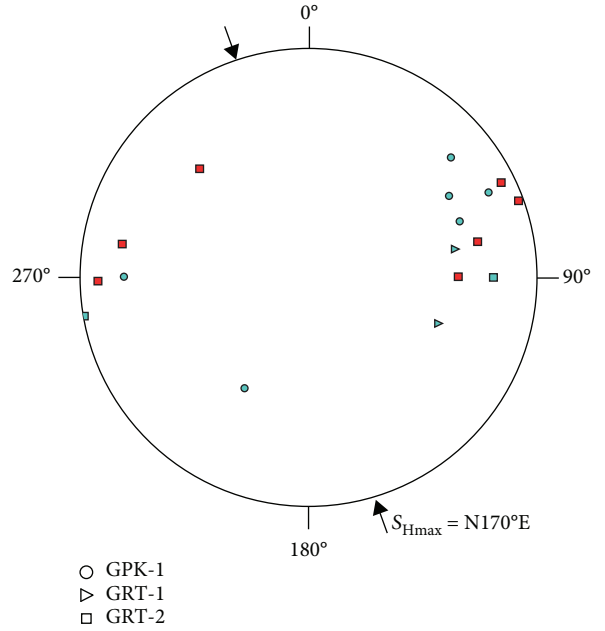


FIGURE 6: Stereoplot of the permeable fractures identified in acoustic image logs from GPK-1 (circle), GRT-1 (triangle), and GRT-2 (square). Blue symbols indicate fractures associated with negative anomalies, and red symbols indicate positive anomalies. Orientations and dips are detailed in Table 1. The maximum horizontal stress is from [56] for Soultz and from [57] for Rittershoffen.

At equilibrium (five months after the hydraulic tests), the water inflow through GPK1-FZ4 is associated with a negative anomaly in the T log acquired in March 1993.

The subsequent T logs acquired from well GPK-1 during production are more affected by hydraulic circulation than the other wells and thus are less reliable.

4.2.2. GRT-1. In GRT-1, during hydraulic tests in January 2013, a T log and a flow log were acquired during airlift production at 12,3 L/s. However, the flow log is not entirely useful; anomalies are observed but are barely quantifiable. T logs at equilibrium were acquired pre- and poststimulation in April and December of 2013, respectively (Figure 8).

In the production T log, a small negative anomaly is observed at 2233 m MD, which is not correlated with the flow anomaly (Figure 8(a)). This T anomaly is not observed in the prestimulation T log at thermal equilibrium. However, a T anomaly is observed in the poststimulation T log at 2235.5 m MD. This anomaly corresponds with an open fracture striking N180°E and dipping 60° westward at 2236.5 m MD.

The main permeable FZ of GRT1-FZ1 extends from 2325 to 2368 m MD. Two major open fractures associated with mud losses were also identified. The first one, which is found at the top of the FZ, strikes N20°E and dips 50° westward and is located at 2326 m MD [16]. Although mud losses were observed during drilling operations, no T anomaly was observed during production at this depth. A small negative anomaly is observed in the poststimulation T log (Figure 3).

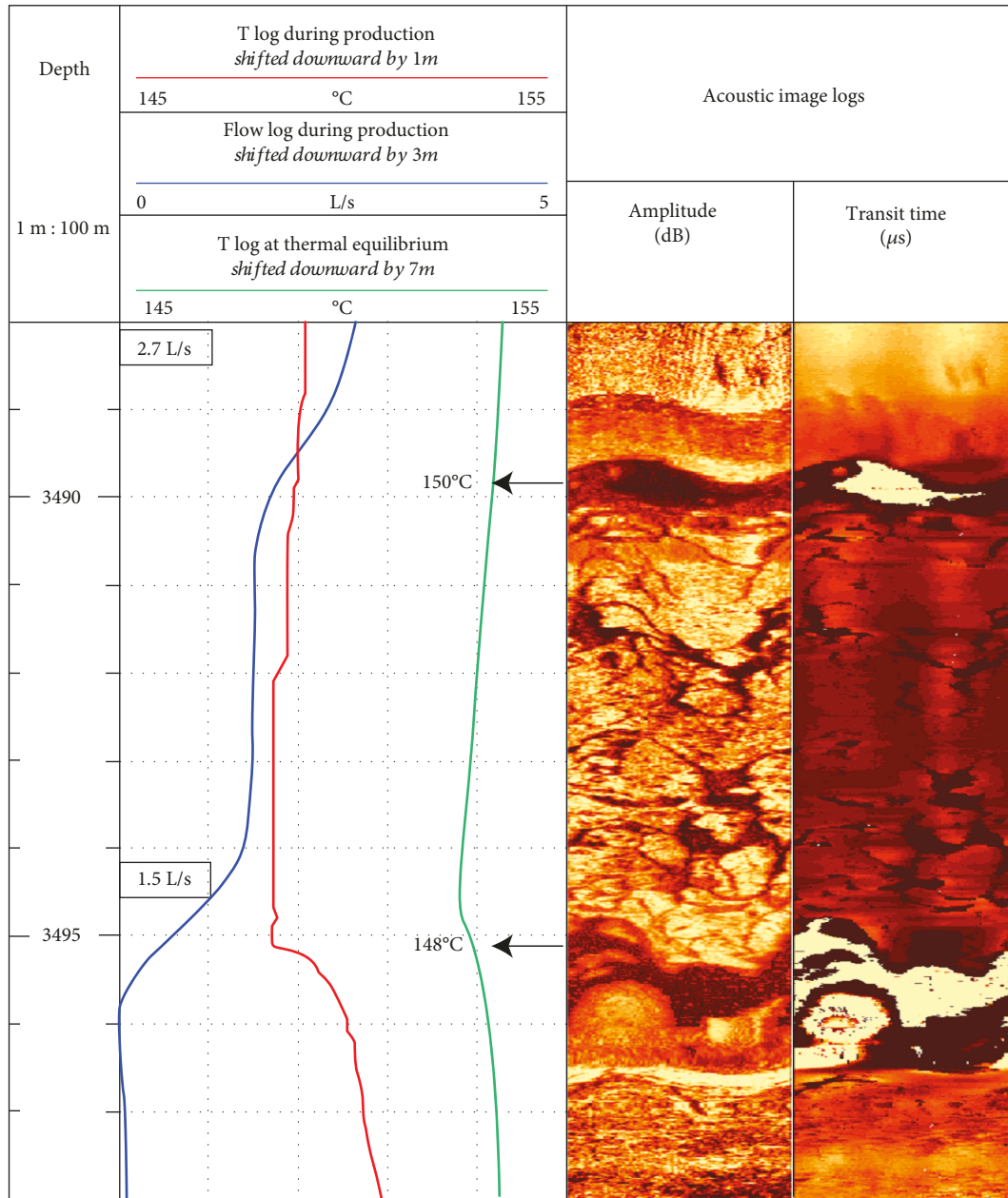
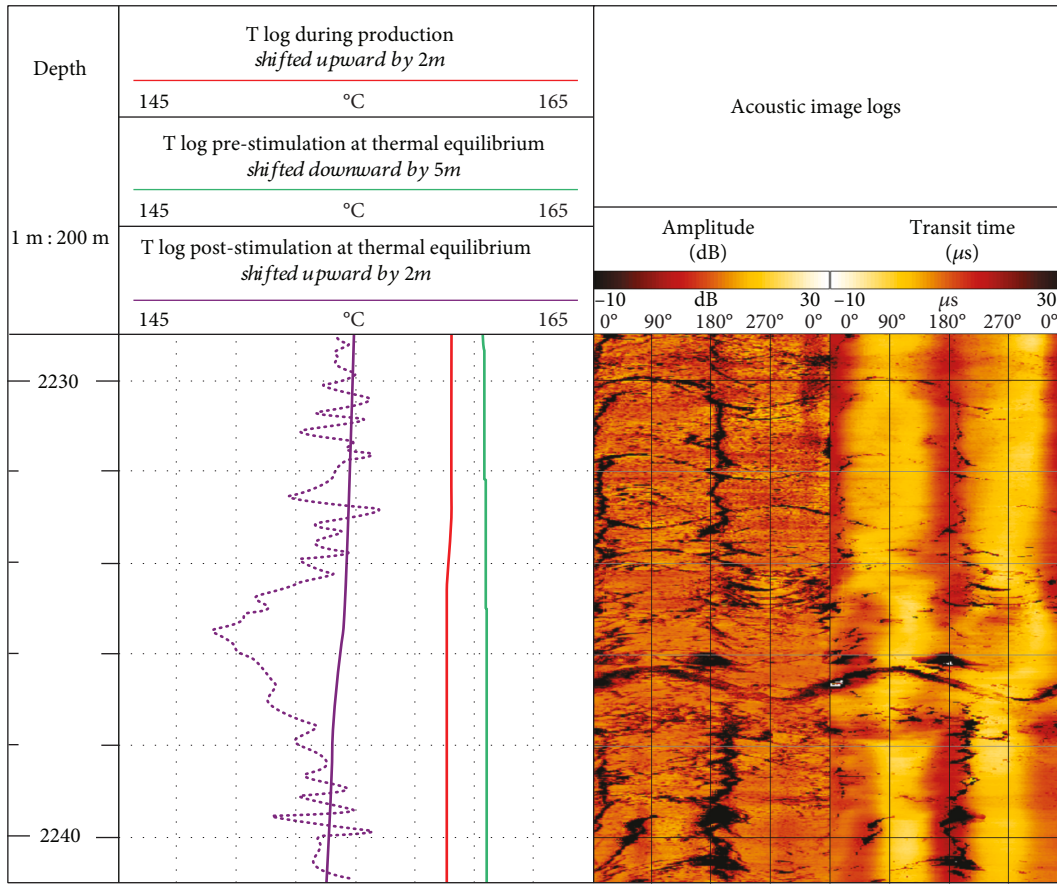


FIGURE 7: T logs from well GPK-1 at thermal equilibrium (Mar 1993, five months after the last hydraulic tests) and during production, with the corresponding flow log (Sept 1996, production test at 11 L/s). T and flow anomalies are associated with the open fractures observed in the acoustic image logs at 3490 and 3495 m MD, respectively. Arrows indicate inflows of geothermal water through the fractures. Depth is expressed in MD. The T logs and flow logs were shifted manually to fit the anomalies with fracture zones in all wells.

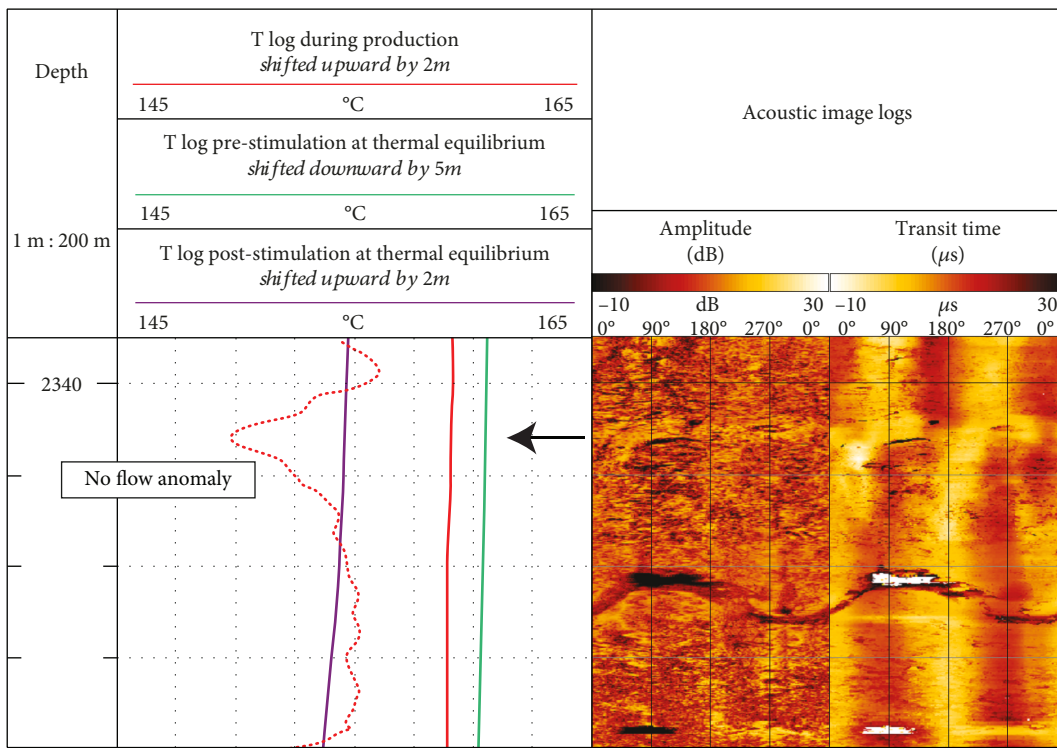
In the production T log, a small negative anomaly is observed at 2341 m MD that is not correlated with a flow anomaly (Figure 8(b)). This T anomaly is incorporated into a larger anomaly evident in the prestimulation T log at thermal equilibrium and in the poststimulation T log (Figure 3). These anomalies correlate with an open fracture striking N25°E and dipping 60° westward at 2345 m MD (Figure 8(b)).

The second open fracture of GRT1-FZ1 is associated with mud losses and is located at 2368 m MD. It is striking N175°E and dipping 65° westward. This fracture controls 2/3 of the total flowrate and is at the interface between highly altered

and fractured granite above and low altered granite below [16]. Thus, this fracture permits the first inflow of water into the well. Surprisingly, the flow log is not consistent with this observation and is thus considered unreliable for the evaluation of the absolute flow associated with the fractures in the well. The flow anomaly is associated with a T anomaly (+3°C) at 2364 m MD (Figure 8(c)). A second T anomaly (+5°C) at 2350 m MD is observed. This positive T anomaly is not clearly associated with an open fracture but is associated with a cluster of thin fractures. However, the calculation of the water temperature at this depth is not possible because the flow log is not reliable. At equilibrium,

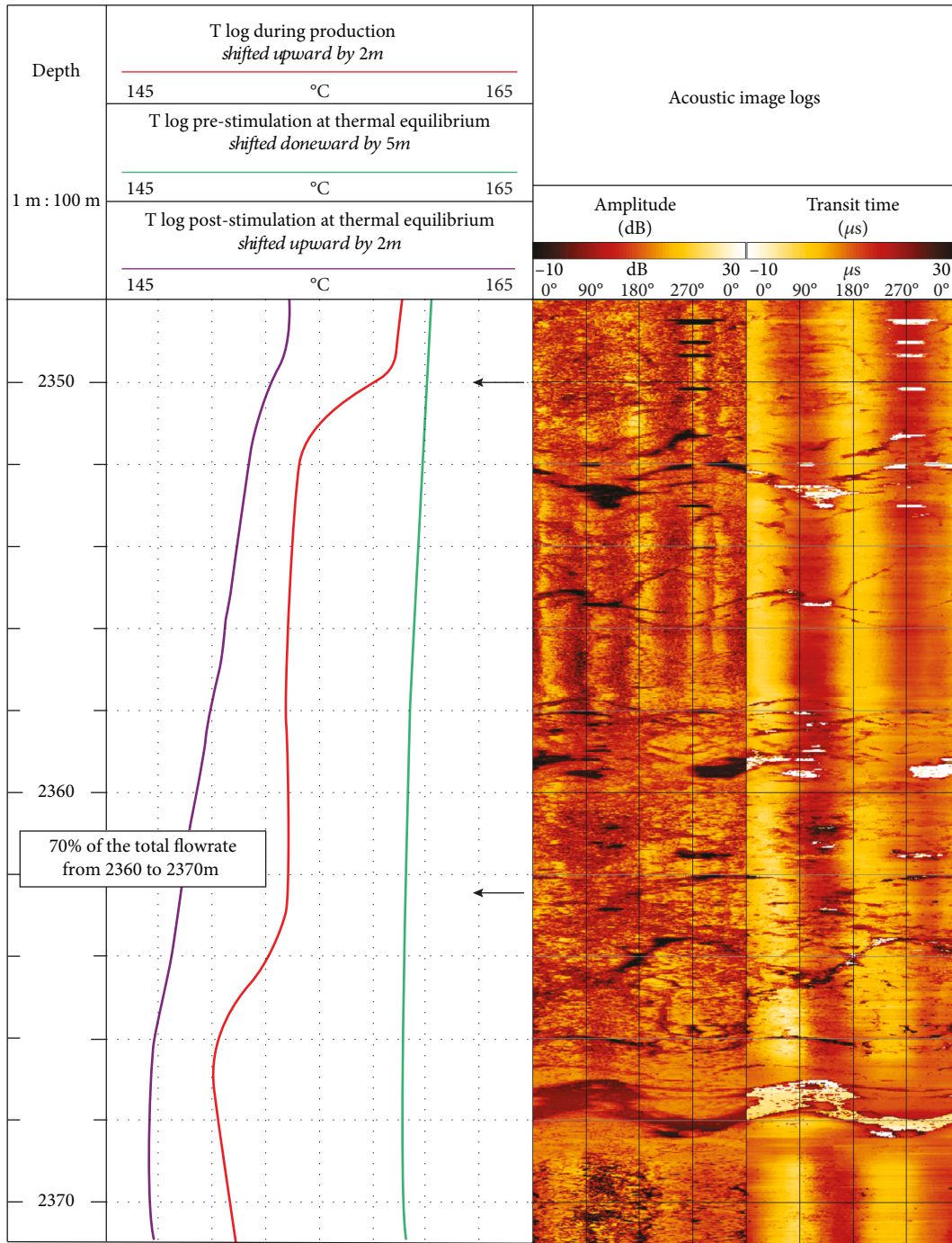


(a)



(b)

FIGURE 8: Continued.



(c)

FIGURE 8: T logs obtained from well GRT-1 during production (Jan 2013, airlift production), at thermal equilibrium prestimulation (Apr 2013, four months after hydraulic tests) and poststimulation (Dec 2013, five months after hydraulic stimulation). Dotted lines indicate the gradient of the T logs during production (red) and poststimulation (purple). T anomalies are associated with open fractures observed in acoustic image logs at (a) 2236 m MD, (b) 2345 m MD, and (c) 2368 m MD. Arrows indicate inflows of geothermal water through fractures. Depth is expressed in MD. T logs and flow logs were shifted manually to match anomalies with fracture zones.

the prestimulation log indicates a large negative T anomaly, whereas the poststimulation T log indicates two negative anomalies that correspond with those observed during production (Figure 3).

4.2.3. GRT-2. Only one temperature log at thermal equilibrium was acquired in this well in September 2014. Two positive T anomalies are observed for GRT2-FZ1 and GRT2-FZ2 (Figure 4). These anomalies are the only positive

ones observed in the well, but as they are observed at thermal equilibrium, without previous injection into the well, they are considered reliable. They indicate water inflows hotter than the surrounding rock formation. Unfortunately, the temperature of this water cannot be precisely calculated because flow logs and T logs acquired during production are not available. Both anomalies are associated with open fractures at the borehole scale, which mainly strike N170°E and dip westward [16].

## 5. Discussion

**5.1. Thermal Signature of Permeable FZs.** GPK1-FZ4 corresponds to the first inflow of water into the well and thus marks the beginning of thermal convection. The first inflow of water into the well is at 148°C through a fracture at 3496 m MD (Figure 7). The negative anomaly in the production T log is explained by an inflow of water colder than the deeper reservoir during production. The positive anomaly described above is interpreted as the inflow of water from a fracture at 3489 m MD, which is hotter (150°C) than water from the fracture at 3496 m MD (148°C). At thermal equilibrium, GPK1-FZ4 is associated with a negative anomaly because the water inflows have temperatures of 148°C and 150°C and are probably colder than the temperature of the deep granite at equilibrium (Figure 2).

GRT1-FZ1 also corresponds to the first inflow of water into the well and thus to the beginning of thermal convection. Positive T anomalies are observed in the bottom part of the FZ at 2365 and 2350 m MD because geothermal water that comes from the fractures is hotter than the water coming from the underlying reservoir (Figure 8(c)). At thermal equilibrium, these hot water inflows are no longer observed, but the negative T anomaly does not suggest that hot water does not circulate. This means that the circulating water is probably colder than the reservoir at equilibrium. These fractures correlate with a flow anomaly. However, T anomalies during production at 2341 m MD and 2235 m MD indicate inflows of water colder than the mix of water below, a trend not seen in the flow log (Figures 8(a) and 8(b)). The T anomaly at 2231 m MD is associated with an FZ enhanced after stimulation at 2236 m MD because it is associated with a negative T anomaly in the poststimulation T log (Figure 8(a)).

GRT2-FZ1 and GRT2-FZ2 exhibit the only two positive T anomalies at equilibrium observed in the wells of Rittershoffen. Positive T anomalies are probably less common than negative T anomalies at equilibrium because the reservoir at equilibrium is generally hotter than the circulating water. Fractures are direct paths for cold mud or water during drilling and hydraulic operations and thus cool faster than the rest of the rock formation. The greater the quantity of cold water that is injected, the fewer positive anomalies visible. Because well GRT-2 was not stimulated, positive anomalies are probably more common in that well than in the stimulated well GRT-1 and GPK-1.

As observed by Evans et al. [14], temperature flux and geothermal fluid flow are intimately linked. T logs are better tools than flow logs for examining water circulation because T logs are more sensitive to small water inflows than flow

logs, which require massive water inflow to produce an observable modification in the rotation speed of the helix. However, the estimation of the absolute water temperature circulating in a fracture requires a reliable associated flow log, which is often not available.

**5.2. Water Circulation through Permeable FZs.** Based on T and flow logs, most of the water circulation in the wells occurs in the first hundreds of meters of the granitic basement, where a high density of permeable FZs is observed: in the first 500 meters of the Soultz basement (1400 to 2100 m MD in GPK-1) and in the first 200 meters of the Rittershoffen basement (2200 to 2400 m MD in GRT-1 and 2500 to 2800 m MD (i.e., 2200 to 2400 m TVD) in the deviated well GRT-2) (Figures 2–4). The partially open fractures are several centimeters wide inside the FZs and are probably interconnected to each other over short distances, leading to a rather complex 3D organization that has channelized the water circulation [45, 46]. Inside a permeable FZ, geothermal water can circulate at different temperatures through different partially open fractures, representing multichannel pathways for geothermal fluids, as observed in GPK-1, where the water coming from the upper fracture is hotter (Figure 7). In this case, water coming from fractures less than 10 m apart circulates at different temperatures, which is surprising because circulations coming from narrow fractures should reach a state of equilibrium and a homogeneous temperature. Water may circulate through the FZs too fast to reach equilibrium. From the dataset presented in this article, the velocity and direction of these circulations cannot be determined.

The orientations and dips of the fractures cannot be linked to the polarity of the T anomalies at equilibrium (Figure 6). Negative T anomalies at equilibrium are observed more often than positive ones in the Soultz and Rittershoffen wells, but the negative anomalies are linked to the contrast between the temperature of the fluid circulating through the FZs and the temperature of the reservoir at equilibrium, which is generally hotter than the circulating water. During production, a positive T anomaly indicates an inflow of water hotter than the mix of water circulating below (Figure 9). At equilibrium, this anomaly could be positive if the geothermal water coming from the fracture is hotter than the surrounding rock formation or negative if the geothermal water is colder than the surrounding rock formation. T logs acquired during production are representative of the mix of water present during circulation, whereas T logs at thermal equilibrium reflect the temperature of the water leaching through the FZs relative to the temperature of the surrounding rock formations.

Contrary to the interpretation proposed by Genter et al. [15], the negative T anomalies in T logs at equilibrium are not a result of cooling of the FZs but only indicate that the circulation of water is colder than the surrounding formation. However, equilibrium could be difficult to identify depending on the volume of cold water previously injected and the time since the last injection.

The recurrence of negative anomalies could also be influenced by hydrothermal alteration (Figure 9). As modeled by Gentier et al. [52], during cold injection, thermal

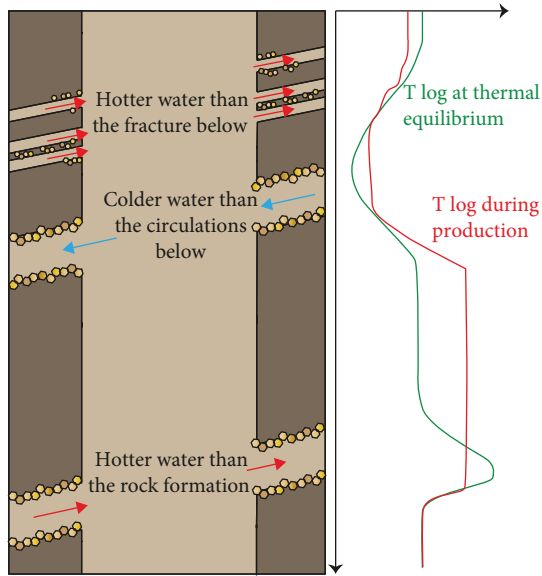


FIGURE 9: Conceptual model of fluid circulation in an FZ partly plugged with quartz and illite and the associated T anomalies measured during production and at thermal equilibrium.

microcracking of quartz within the FZ is observed, which creates preferential flow paths and thus leads to preferential cooling in these fractures. All permeable fractures are associated with quartz veins, which could enhance the thermal effect of cold reinjection through the FZs (Figures 2–4). Moreover, Tung et al. [53] and Alevizos et al. [54] suggested that occurrences of illite could enhance fault creeping, which can release fluid and trigger endothermic chemical reactions. In the case of GPK-1, Sausse et al. [33] identified the correlation between GPK1-FZ4 and the fault zone imaged in the reservoir. The influence of clay minerals, particularly illite, on the fault movements at Soultz was already proposed by Meller et al. [49]. In the case of GRT-1 and GRT-2, preliminary geometrical modeling suggests a possible correlation between GRT1-FZ1 and GRT2-FZ2 and a fault zone imaged in the reservoir [7, 16]. The influence of these endothermic reactions on permeable FZs and the associated T anomalies should be investigated in further studies.

## 6. Concluding Remarks

In this study, a network of permeable FZs was identified in well GPK-1 at Soultz and wells GRT-1 and GRT-2 at Rittershoffen based on the reinterpretation of T logs obtained during production and at thermal equilibrium; these T logs were correlated with permeability indicators measured during drilling operations, acoustic image logs, and flow logs obtained during hydraulic tests. All permeable FZs present similar characteristics as follows:

- (1) They are composed of cm thick fractures partly filled by quartz
- (2) They are associated with T anomalies during production and/or at thermal equilibrium

This study presents a unique dataset of T logs and associated flow logs (if available) acquired during production and at thermal equilibrium at different times in well histories. T logs are useful and inexpensive tools for the localization of permeable FZs because they are more sensitive to small water inflows into wells than flow logs. Moreover, the comparison of T logs acquired in production and at thermal equilibrium provides a new interpretation of temperature anomalies. Based on these data, the temperature of water coming from partially open fractures was estimated. The study shows that geothermal water could circulate at different temperatures and in different fractures a few meters apart within the same FZ, which suggests a new interpretation of T anomalies. At temperature equilibrium, T anomalies are positive or negative with respect to the temperature of the surrounding rock formations. Because the surrounding formations are often hotter than the fractures, which are direct paths for fluid and thus cool faster than the surrounding rocks, negative anomalies are more often observed than positive ones. The nature of secondary deposits could also enhance the cooling effect observed in the T logs. In contrast, during production, anomalies are positive or negative with respect to the mix of water circulating below the fracture and not with respect to the surrounding formation. Therefore, anomaly polarity could change over time depending on the equilibrium state.

## Data Availability

Please contact ES-Géothermie for data requests at [geothermie@es.fr](mailto:geothermie@es.fr).

## Conflicts of Interest

The authors declare that there are no conflicts of interest regarding the publication of this paper.

## Acknowledgments

This work received funding from the European Union's Horizon 2020 research and innovation programme under grant agreement no. 792037 (MEET project). The study was partly funded by ADEME (French Agency of Energy and Environment) in the framework of the DEEP-EM project. The authors acknowledge the GEIE EMC and ECOGI for providing the data. The authors appreciate the helpful and constructive remarks of the two anonymous reviewers and the lead guest editor of this special issue, Dr Fabrizio Agosta.

## References

- [1] P. Baillieux, E. Schill, J.-B. Edel, and G. Mauri, "Localization of temperature anomalies in the Upper Rhine Graben: insights from geophysics and neotectonic activity," *International Geology Review*, vol. 55, no. 14, pp. 1744–1762, 2013.
- [2] Y. Benderitter and P. Elsass, "Structural control of deep fluid circulation at the Soultz HDR site, France: a review, France," *Geothermal Science and Technology*, vol. 4, pp. 227–237, 1995.
- [3] D. Pribnow and C. Clauser, "Heat and fluid flow at the Soultz Hot Dry Rock system in the Rhine Graben," in *Proceedings of*

- World Geothermal Congress 2000*, Kyushu - Tohoku, Japan, 2000.
- [4] D. Pribnow and R. Schellschmidt, "Thermal tracking of upper crustal fluid flow in the Rhine Graben," *Geophysical Research Letters*, vol. 27, no. 13, pp. 1957–1960, 2000.
- [5] D. Bächler, T. Kohl, and L. Rybach, "Impact of graben-parallel faults on hydrothermal convection-Rhine Graben case study," *Physics and Chemistry of the Earth*, vol. 28, no. 9–11, pp. 431–441, 2003.
- [6] P. Baillieux, E. Schill, Y. Abdelfettah, and C. Dezayes, "Possible natural fluid pathways from gravity pseudo-tomography in the geothermal fields of northern Alsace (Upper Rhine Graben)," *Geothermal Energy*, vol. 2, no. 1, 2014.
- [7] C. Baujard, A. Genter, E. Dalmais et al., "Hydrothermal characterization of wells GRT-1 and GRT-2 in Rittershoffen, France: implications on the understanding of natural flow systems in the Rhine graben," *Geothermics*, vol. 65, pp. 255–268, 2017.
- [8] J. Baumgärtner and C. Lerch, "Geothermal 2.0: the Insheim geothermal power plant. The second generation of geothermal power plants in the Upper Rhine Graben," in *Proceedings of third European geothermal review*, Mainz, Germany, 2013.
- [9] J. Baumgärtner, D. Teza, T. Hettkamp, G. Homeier, R. Baria, and S. Michelet, "Electricity production from hot rocks," in *Proceedings of World Geothermal Congress 2005*, Antalya, Turkey, 2005.
- [10] A. Genter, C. Baujard, N. Cuenot et al., "Geology, geophysics and geochemistry in the Upper Rhine Graben: the frame for geothermal energy use," in *Proceedings of European Geothermal Congress 2016*, Strasbourg, France, 2016.
- [11] T. Hettkamp, J. Baumgärtner, D. Teza, and C. Lerch, "Experiences from 5 years operation in Landau," in *Proceedings of Third European Geothermal Review*, Mainz, Germany, 2013.
- [12] J. Vidal and A. Genter, "Overview of naturally permeable fractured reservoirs in the central and southern Upper Rhine Graben: insights from geothermal wells," *Geothermics*, vol. 74, pp. 57–73, 2018.
- [13] C. Dezayes, A. Genter, and B. Valley, "Structure of the low permeable naturally fractured geothermal reservoir at Soultz," *Comptes Rendus Geoscience*, vol. 342, no. 7–8, pp. 517–530, 2010.
- [14] K. F. Evans, A. Genter, and J. Sausse, "Permeability creation and damage due to massive fluid injections into granite at 3.5 km at Soultz: 1. Borehole observations," *Journal of Geophysical Research: Solid Earth*, vol. 110, no. B4, 2005.
- [15] A. Genter, K. Evans, N. Cuenot, D. Fritsch, and B. Sanjuan, "Contribution of the exploration of deep crystalline fractured reservoir of Soultz to the knowledge of enhanced geothermal systems (EGS)," *Comptes Rendus Geoscience*, vol. 342, no. 7–8, pp. 502–516, 2010.
- [16] J. Vidal, A. Genter, and F. Chopin, "Permeable fracture zones in the hard rocks of the geothermal reservoir at Rittershoffen, France," *Journal of Geophysical Research: Solid Earth*, vol. 122, no. 7, pp. 4864–4887, 2017.
- [17] C. A. Barton, M. D. Zoback, and D. Moos, "Fluid flow along potentially active faults in crystalline rock," *Geology*, vol. 23, no. 8, pp. 683–686, 1995.
- [18] J. Bradford, J. McLennan, J. Moore et al., "Recent developments at the Raft River geothermal field," in *Proceedings of Thirty-Eighth Workshop on Geothermal Reservoir Engineering*, Stanford University, California, USA, 2013.
- [19] A. Mas, D. Guisseau, P. Patrier Mas et al., "Clay minerals related to the hydrothermal activity of the Bouillante geothermal field (Guadeloupe)," *Journal of Volcanology and Geothermal Research*, vol. 158, no. 3–4, pp. 380–400, 2006.
- [20] C. Le Carlier, J.-J. Royer, and E. L. Flores, "Convective heat transfer at the Soultz-sous-Forêts geothermal site: implications for oil potential," *First Break*, vol. 12, no. 1285, 1994.
- [21] V. Magnenet, C. Fond, A. Genter, and J. Schmittbuhl, "Two-dimensional THM modelling of the large scale natural hydrothermal circulation at Soultz-sous-Forêts," *Geothermal Energy*, vol. 2, no. 1, 2014.
- [22] S. Bellani, A. Brogi, A. Lazzarotto, D. Liotta, and G. Ranalli, "Heat flow, deep temperatures and extensional structures in the Larderello geothermal field (Italy): constraints on geothermal fluid flow," *Journal of Volcanology and Geothermal Research*, vol. 132, no. 1, pp. 15–29, 2004.
- [23] D. Curewitz and J. A. Karson, "Structural settings of hydrothermal outflow: fracture permeability maintained by fault propagation and interaction," *Journal of Volcanology and Geothermal Research*, vol. 79, no. 3–4, pp. 149–168, 1997.
- [24] N. C. Davatzes and S. H. Hickman, "Controls on fault-hosted fluid flow; preliminary results from the Coso geothermal field, CA," in *Geothermal Resources Council Transactions*, pp. 343–348, Geothermal Resources Council, Davis, California, 2005.
- [25] J. E. Faulds and N. H. Hinz, "Favorable tectonic and structural settings of geothermal systems in the Great Basin region, Western USA: proxies for discovering blind geothermal systems," in *Proceedings of World Geothermal Congress 2015*, Melbourne, Australia, 2015.
- [26] C. Dezayes, A. Genter, and S. Gentier, *Deep geothermal energy in Western Europe: the Soultz Project - Final Report (open file no. BRGM/RP-54227-Fr)*, BRGM, Orléans, France, 2005.
- [27] A. Gérard, A. Genter, T. Kohl, P. Lutz, P. Rose, and F. Rummel, "The deep EGS (enhanced geothermal system) project at Soultz-sous-Forêts (Alsace, France)," *Geothermics*, vol. 35, no. 5–6, pp. 473–483, 2006.
- [28] B. Sanjuan, R. Millot, C. Dezayes, and M. Brach, "Main characteristics of the deep geothermal brine (5 km) at Soultz-sous-Forêts (France) determined using geochemical and tracer test data," *Comptes Rendus Geoscience*, vol. 342, no. 7–8, pp. 546–559, 2010.
- [29] B. Sanjuan, J. Scheiber, F. Gal, S. Touzelet, A. Genter, and G. Villadangos, "Interwell chemical tracer testing at the Rittershoffen site (Alsace, France)," in *Proceedings of European Geothermal Congress 2016*, Strasbourg, France, 2016.
- [30] A. Genter and H. Traineau, "Analysis of macroscopic fractures in granite in the HDR geothermal well EPS-1, Soultz-sous-Forêts, France," *Journal of Volcanology and Geothermal Research*, vol. 72, no. 1–2, pp. 121–141, 1996.
- [31] O. Lengliné, M. Boubacar, and J. Schmittbuhl, "Seismicity related to the hydraulic stimulation of GRT1, Rittershoffen, France," *Geophysical Journal International*, vol. 208, no. 3, pp. 1704–1715, 2017.
- [32] J. Place, M. Diraison, C. Naville, Y. Géraud, M. Schaming, and C. Dezayes, "Decoupling of deformation in the Upper Rhine Graben sediments. Seismic reflection and diffraction on 3-component vertical seismic profiling (Soultz-sous-Forêts area)," *Comptes Rendus Geoscience*, vol. 342, no. 7–8, pp. 575–586, 2010.

- [33] J. Sausse, C. Dezayes, L. Dorbath, A. Genter, and J. Place, “3D model of fracture zones at Soultz-sous-Forêts based on geological data, image logs, induced microseismicity and vertical seismic profiles,” *Comptes Rendus Geoscience*, vol. 342, no. 7-8, pp. 531–545, 2010.
- [34] S. Gentier, X. Rachez, T. D. T. Ngoc, M. Peter-Borie, and C. Souque, “3D flow modelling of the medium-term circulation test performed in the deep geothermal site of Soultz-sous-Forêts (France),” in *Proceedings of World Geothermal Congress 2010*, Kyushu - Tohoku, Japan, 2010.
- [35] A. Genter, C. Castaing, C. Dezayes, H. Tenzer, H. Traineau, and T. Villemin, “Comparative analysis of direct (core) and indirect (borehole imaging tools) collection of fracture data in the Hot Dry Rock Soultz reservoir (France),” *Journal of Geophysical Research*, vol. 102, no. B7, pp. 15419–15431, 1997.
- [36] J. Vidal, A. Genter, F. Chopin, and E. Dalmais, “Natural fractures and permeability at the geothermal site Rittershoffen, France,” in *Proceedings of European Geothermal Congress 2016*, Strasbourg, France, 2016.
- [37] H. Traineau, A. Genter, J.-P. Cautru, H. Fabriol, and P. Chèvremont, “Petrography of the granite massif from drill cutting analysis and well log interpretation in the geothermal HDR borehole GPK-1 (Soultz, Alsace, France),” in *Geothermal Energy in Europe—The Soultz Hot Dry Rock Project*, J. C. Bresee, Ed., pp. 1–29, Gordon and Breach Science Publishers S.A., Montreux, Switzerland, 1992.
- [38] A. Genter, H. Traineau, B. Ledésert, B. Bourguine, and S. Gentier, “Over 10 years of geological investigations within the HDR Soultz project, France,” in *Proceedings of World Geothermal Congress 2000*, Kyushu - Tohoku, Japan, 2000.
- [39] M. P. Smith, V. Savary, B. W. D. Yardley, J. W. Valley, J. J. Royer, and M. Dubois, “The evolution of the deep flow regime at Soultz-sous-Forêts, Rhine Graben, eastern France: evidence from a composite quartz vein,” *Journal of Geophysical Research: Solid Earth*, vol. 103, no. B11, pp. 27223–27237, 1998.
- [40] B. Ledésert, G. Berger, A. Meunier, A. Genter, and A. Bouchet, “Diagenetic-type reactions related to hydrothermal alteration in the Soultz-sous-Forêts Granite, France,” *European Journal of Mineralogy*, vol. 11, no. 4, pp. 731–742, 1999.
- [41] C. Glaas, A. Genter, J. F. Girard, P. Patrier, and J. Vidal, “How do the geological and geophysical signatures of permeable fractures in granitic basement evolve after long periods of natural circulation? Insights from the Rittershoffen geothermal wells (France),” *Geothermal Energy*, vol. 6, no. 1, p. 14, 2018.
- [42] G. R. Hooijkaas, A. Genter, and C. Dezayes, “Deep-seated geology of the granite intrusions at the Soultz EGS site based on data from 5 km-deep boreholes,” *Geothermics*, vol. 35, no. 5-6, pp. 484–506, 2006.
- [43] J. Vidal, P. Patrier, A. Genter et al., “Clay minerals related to the circulation of geothermal fluids in boreholes at Rittershoffen (Alsace, France),” *Journal of Volcanology and Geothermal Research*, vol. 349, pp. 192–204, 2018.
- [44] J. Vidal, A. Genter, C. Glaas, R. Hehn, N. Cuenot, and C. Baujard, *Temperature Signature of Permeable Fracture Zones in Geothermal Wells of Soultz-sous-Forêts in the Upper Rhine Graben*, GRC Transactions, Reno, Nevada, USA, 2018.
- [45] J. Sausse, C. Dezayes, A. Genter, and A. Bisset, “Characterization of fracture connectivity and fluid flow pathways derived from geological interpretation and 3D modelling of the deep seated EGS reservoir of Soultz (France),” in *Proceedings of Thirty-Third Workshop on Geothermal Reservoir Engineering*, Stanford University, California, USA, 2008.
- [46] J. Sausse, M. Fourar, and A. Genter, “Permeability and alteration within the Soultz granite inferred from geophysical and flow log analysis,” *Geothermics*, vol. 35, no. 5-6, pp. 544–560, 2006.
- [47] L. Aquilina, M. Brach, J. C. Foucher, A. De Las Heras, and G. Braibant, *Deepening of GPK-1 HDR Borehole 2000-3600 m (Soultz-sous-Forêts, France)*, *Geochemical Monitoring of Drilling Fluids (open file no. R36619)*, BRGM, Orléans, France, 1993.
- [48] F.-D. Vuataz, M. Brach, A. Criaud, and C. Fouillac, “Geochemical monitoring of drilling fluids: a powerful tool to forecast and detect formation waters,” *SPE Formation Evaluation*, vol. 5, no. 2, pp. 177–184, 1990.
- [49] C. Meller, A. Kontny, and T. Kohl, “Identification and characterization of hydrothermally altered zones in granite by combining synthetic clay content logs with magnetic mineralogical investigations of drilled rock cuttings,” *Geophysical Journal International*, vol. 199, no. 1, pp. 465–479, 2014.
- [50] M. Dubois, B. Ledésert, J. L. Potdevin, and S. Vançon, “Détermination des conditions de précipitation des carbonates dans une zone d’altération du granite de Soultz (soubassement du fossé Rhénan, France) : l’enregistrement des inclusions fluides,” *Comptes Rendus de l’Académie des Sciences - Series IIA - Earth and Planetary Science*, vol. 331, no. 4, pp. 303–309, 2000.
- [51] R. Jung, “Hydraulic fracturing and hydraulic testing in the granitic section of borehole GPK-1, Soultz-sous-Forêts,” in *Geothermal Energy in Europe - The Soultz Hot Dry Rock Project*, J. C. Bresee, Ed., pp. 149–198, Gordon and Breach Science Publishers S.A., Montreux, Switzerland, 1992.
- [52] S. Gentier, A. Hosni, C. Dezayes, and A. Genter, *Projet GEFRAc: modélisation du comportement hydro-thermo-mécanique des milieux fracturés (module 1) (Open file report No. BRGM/RP-52702-FR)*, BRGM, 2004.
- [53] R. Tung, T. Poulet, M. Peters, M. Veveakis, and K. Regenauer-Lieb, “Explaining high permeability on localised fault zones through THMC feedbacks - a Soultz-sous-Forêts inspired approach,” in *Proceedings of 40th New Zealand Geothermal Workshop. Presented at the New Zealand Geothermal Workshop*, Taupo, New Zealand, 2018.
- [54] S. Alevizos, T. Poulet, and E. Veveakis, “Thermo-poro-mechanics of chemically active creeping faults. 1: theory and steady state considerations,” *Journal of Geophysical Research: Solid Earth*, vol. 119, no. 6, pp. 4558–4582, 2014.
- [55] GeORG Team, “EU-Projekt GeORG - Geoportail [WWW Document],” 2017, June 2017, <http://www.geopotenziale.org/home?lang=3>.
- [56] B. C. Valley and K. F. Evans, “Stress state at Soultz-sous-Forêts to 5 km depth from wellbore failure and hydraulic observations,” in *Proceedings of Thirty-Second Workshop on Geothermal Reservoir Engineering*, Stanford University, California, USA, 2007.
- [57] R. Hehn, A. Genter, J. Vidal, and C. Baujard, “Stress field rotation in the EGS well GRT-1 (Rittershoffen, France),” in *Proceedings of European Geothermal Congress 2016*, Strasbourg, France, 2016.





## APPENDIX 2

### Original paper

The Appendix 2 presents a conjoint work that was conducted and published in the peer reviewed *Journal of Volcanology and Geothermal Research*, during my master internship as a contribution to the PhD thesis of Jeanne Vidal. It is about the mineralogical characterization of the granitic basement intersected by Rittershoffen GRT-1 and GRT-2 wells.

Vidal, J., Patrier, P., Genter, A., Beaufort, D., Dezayes, Ch., Glaas, C., Lerouge, C., Sanjuan, B., 2018. Clay minerals related to the circulation of geothermal fluids in boreholes at Rittershoffen (Alsace, France). *Journal of Volcanology and Geothermal Research* 349, 192-204. <https://doi.org/10.1016/j.jvolgeores.2017.10.019>





## Clay minerals related to the circulation of geothermal fluids in boreholes at Rittershoffen (Alsace, France)



Jeanne Vidal <sup>a,\*</sup>, Patricia Patrier <sup>b</sup>, Albert Genter <sup>c</sup>, Daniel Beaufort <sup>b</sup>, Chrystel Dezayes <sup>d</sup>, Carole Glaas <sup>c</sup>, Catherine Lerouge <sup>d</sup>, Bernard Sanjuan <sup>d</sup>

<sup>a</sup> University of Strasbourg, CNRS UMR 7516 IPGS, 1 rue Blessig, F-67084 Strasbourg Cedex, France

<sup>b</sup> University of Poitiers, CNRS UMR 7285 IC2MP, HydrASA, Bat B8, Rue Albert Turpain, TSA51106, F-86073 Poitiers Cedex 9, France

<sup>c</sup> ES-Géothermie, 5 rue Lisbonne, 67300 Schiltigheim, France

<sup>d</sup> BRGM, 3 Av. Claude Guillemin, BP6009, 45060 Orléans Cedex 02, France

### ARTICLE INFO

#### Article history:

Received 13 October 2017

Accepted 31 October 2017

Available online 20 November 2017

#### Keywords:

Clay minerals

Hydrothermal parageneses

Chemical composition

Geothermal field

Rittershoffen

Upper Rhine Graben

### ABSTRACT

Two geothermal wells, GRT-1 and GRT-2, were drilled into the granite at Rittershoffen (Alsace, France) in the Upper Rhine Graben to exploit geothermal resources at the sediment–basement interface. Brine circulation occurs in a permeable fracture network and leads to hydrothermal alteration of the host rocks. The goal of the study was to characterize the petrography and mineralogy of the altered rocks with respect to the permeable fracture zones in the granitic basement. As clay minerals are highly reactive to hydrothermal alteration, they can be used as indicators of present-day and paleo-circulation systems. Special attention has been paid to the textural, structural and chemical properties of these minerals. The fine-grained clay fraction (<5 μm) was analyzed around the originally permeable fracture zones to observe the crystal structure of clay minerals using X-ray diffraction. Chemical microanalysis of the clay minerals was performed using scanning electron microscopy coupled with energy dispersive X-ray spectroscopy. The occurrences of mixed layers illite-smectite (~10% smectite) provide a promising guide for identifying the fracture zones that control the present-day circulation of geothermal fluids in the Rittershoffen wells. However, multistage paleo-circulation systems could lead to an abundance of heterogeneous and fine-grained illitic minerals that could plug the fracture system. The permeability of fracture zones in the GRT-1 well was likely reduced because of an intense illitization, and the well was stimulated. The occurrence of chlorite in the permeable fracture zones of GRT-2 is indicative of less intense illitization, and the natural permeability is much higher in GRT-2 than in GRT-1.

© 2017 The Authors. Published by Elsevier B.V. This is an open access article under the CC BY-NC-ND license (<http://creativecommons.org/licenses/by-nc-nd/4.0/>).

### 1. Introduction

In geothermal systems, alteration minerals provide useful information about the physico-chemical conditions of both past and present hydrothermal activity. This is particularly the case with clay minerals, which have been investigated as markers of circulation zones based on their reactivity to changes in physico-chemical conditions (Beaufort et al., 1992, 1996; Browne and Ellis, 1970; Flexser, 1991; Mas et al., 2006; Patrier et al., 1996; Reyes, 1990). The properties of clay minerals are affected by temperature in addition to several other factors, such as rock and fluid chemistries, time and the fluid/rock ratio. This study focused on the argillic alteration of permeable fracture zones related to a hydrothermal system located in the Upper Rhine Graben at Rittershoffen in France (Fig. 1). Two deep geothermal wells - GRT-1, which has a vertical trajectory, and GRT-2, which has a deviated trajectory - intersect natural, permeable fracture zones in the

sandstones and granitic basement beneath Rittershoffen (Baujard et al., 2017; Vidal et al., 2017). The influence of argillic alteration on the permeability of fracture zones at the borehole scale is an important milestone for an industrial project because fracture zones channel hot geothermal fluids that are exploited for high-temperature (>160 °C) heat applications at the surface.

Geothermal systems are dynamic systems that are constantly evolving; thus, the observed secondary minerals potentially consist of several superimposed alteration assemblages. In Rittershoffen boreholes, the mineral products of the existing hydrothermal circulation system (160 °C) appear to be superimposed upon previous secondary minerals formed during earlier circulations events. Abundance of secondary minerals may lead to plugging and the transformation of fracture zones from conduits into barriers to fluid flow. As the nature of fracture permeability is an important aspect of this geothermal project, most of the cutting samples were collected along the open-hole sections of wells around the originally permeable (OP) fracture zones in both wells. Cutting samples from both GRT-1 and GRT-2 were investigated to identify the alteration mineralogies, and special attention was paid

\* Corresponding author.

E-mail address: [j.vidal@unistra.fr](mailto:j.vidal@unistra.fr) (J. Vidal).

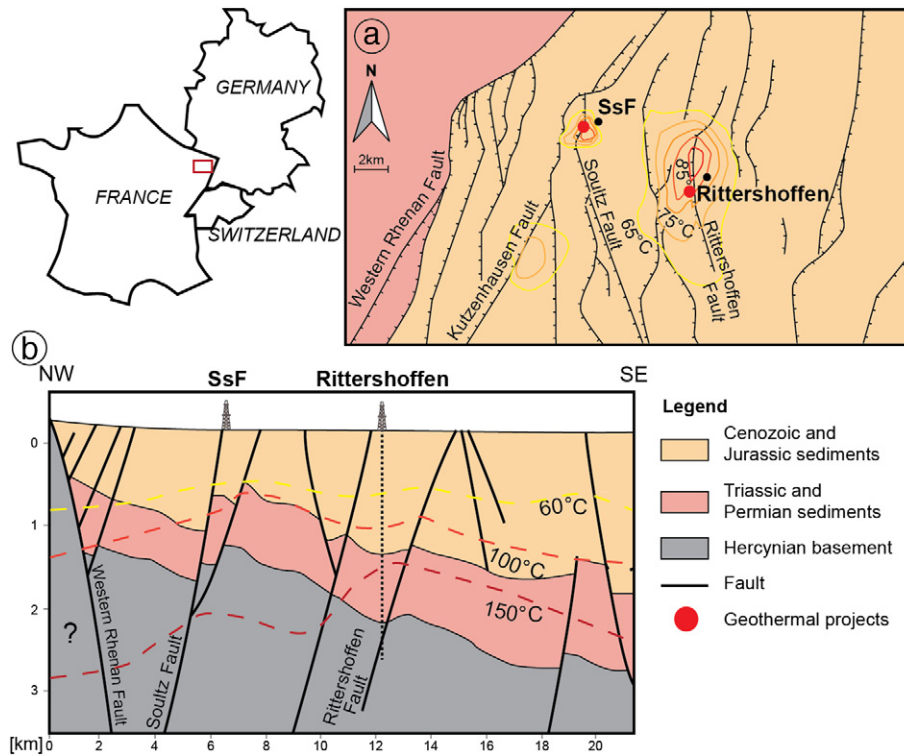


**Fig. 1.** Location of the Rittershoffen geothermal site. a) Geological and structural map of the Rittershoffen and Soutz-sous-Forêts (SsF) area. Isotherms at the top of the basement are from Baillieux et al. (2014). b) Geological cross section through the Rittershoffen and Soutz-sous-Forêts geothermal sites after *Geoportail of EU-Project GeORG - INTERREG IV Upper Rhine* (2012). The dashed line is an interpreted trajectory of the geothermal well GRT-1.

to the clay fraction. The fine-grained fraction of cuttings (<5 μm) was analyzed using X-ray Diffraction (XRD) to identify well-crystallized illite, poorly crystallized illite and mixed layers illite-smectite. Then, scanning electron microscopy (SEM) coupled with energy-dispersive X-ray spectroscopy (EDS) was used to analyze the chemical compositions of the clay minerals.

**2. Geological context**

The geothermal site at Rittershoffen is located in the Upper Rhine Graben (URG), approximately 15 km east of the Western Rhenan fault and less than 10 km from the well-known Soutz-sous-Forêts geothermal site (Alsace, France) (Fig. 1a). In the URG, the underground temperature distribution is spatially heterogeneous, and several geothermal anomalies are concentrated throughout the western side of the URG in the areas of Soutz-sous-Forêts and Rittershoffen (Baillieux et al., 2013; Pribnow and Schellschmidt, 2000; Schellschmidt and Clauser, 1996). Temperature anomalies at the top of the granitic basement indicated by several temperature measurements are concentrated along the Soutz and Kutzenhausen normal faults that dip toward the west (Fig.

1a) (Baillieux et al., 2014). These zones are attributed to the upwelling of hot geothermal fluids through fault zones within the crystalline basement and Triassic and Permian sandstones (Fig. 1b) (Benderitter et al., 1995; Pribnow and Clauser, 2000; Pribnow and Schellschmidt, 2000). Geothermal reservoirs in the granitic basement at Rittershoffen are quite similar to the reservoir at Soutz. Both deep fluids are of the NaCl type with total dissolved solids (TDS) values close to 100 g/L (Table 1) (Sanjuan et al., 2014, 2016). The pH values of the fluids in both reservoirs are close to 5.0. The fluids are interpreted as having originated from the mixing of primary marine brine with water of meteoric origin (Sanjuan et al., 2010, 2016). The estimated temperature of the deep reservoir calculated by primary cationic geothermometers (Na-K, Na-K-Ca, Na-K-Ca-Mg, K-Mg, Na-Li and Mg-Li) and by a δ<sup>18</sup>O<sub>H<sub>2</sub>O-SO<sub>4</sub> isotope geothermometer was 225 ± 25 °C at Soutz and at Rittershoffen (Sanjuan et al., 2016).</sub>

Alteration episodes of the granitic reservoir are well known to have occurred in deep wells at Soutz (Genter, 1989; Hooijkaas et al., 2006; Ledésert et al., 1999; Traineau et al., 1992). Early propylitic alteration of the whole granitic batholith is characterized by the formation of epidote, the partial transformation of primary biotite into Fe,Mg-chlorite

**Table 1**

Chemical compositions of geothermal fluid sampled in the Paleozoic granite at Soutz-sous-Forêts in the well GPK-2 at a measured depth of 5000 m (Sanjuan et al., 2014) and at Rittershoffen in the well GRT-1 at a measured depth of 2580 m (Sanjuan et al., 2016).

Location	T <sub>Bottom</sub> °C	pH	TDS g/L	Na mg/L	K mg/L	Ca mg/L	Mg mg/L	Cl mg/L	SO <sub>4</sub> mg/L	SiO <sub>2</sub> mg/L	Br mg/L	Li mg/L	Gas
Soutz-sous-Forêts	200	4.98	99	28,140	3195	7225	131	58,559	157	201	216	173	CO <sub>2</sub> N <sub>2</sub> CH <sub>4</sub>
Rittershoffen	>160	6.27	101	28,451	3789	7200	138	59,900	220	146	251	190	unknown

and the partial replacement of primary potassic feldspar with small crystallites of illite. Then, hydrothermal alterations dominated by illite, quartz and calcite occur around fracture zones after fluid circulations. Several alteration facies were identified by Hooijkaas et al. (2006). The same granitic batholith was encountered at Rittershoffen. As geothermal fluids are similar, alterations observed at Soultz could be a reasonable reference for petrographical studies at Rittershoffen.

### 3. OP fracture zones, thermal profile and hydraulic yield of the geothermal wells at Rittershoffen

At Rittershoffen, two wells, GRT-1 and GRT-2, penetrate the Cenozoic, Mesozoic and Permian sediments overlying the Paleozoic basement. The wells were drilled to a true vertical depth of 2.6 km in the southeastern end of a horst and targeted the so-called Rittershoffen normal fault at the top of the basement (Baujard et al., 2017). Based on a seismic reflection interpretation of the sedimentary cover, this fault strikes N-S, dips 45° westward and displays an apparent vertical offset of approximately 200 m (Fig. 1b) (Baujard et al., 2017). Wells intersect the fracture network associated with the Rittershoffen fault in Buntsandstein and

Permian sandstones (from ~245 Ma to ~255 Ma) and in the Carboniferous granite (~340 Ma) (Baujard et al., 2017). The fracture network was investigated in the open-hole sections using acoustic image logs correlated with standard geophysical logs (e.g., gamma ray, neutron porosity), cutting observations and permeability indicators (i.e., mud losses, gas occurrences), and temperature logs (Vidal et al., 2017). If fracture zones present indications of permeability or temperature anomalies at the borehole scale after drilling operations without any stimulation operations, they are qualified as OP fracture zones (Vidal et al., 2017). In GRT-1, one main OP fracture zone was observed in the granitic basement from measured depths (MD) of 2325 to 2368 m (Fig. 2) (Vidal et al., 2016a, 2017). In GRT-2, four OP fracture zones were observed in the granitic basement (Fig. 3) (Baujard et al., 2017; Vidal et al., 2017). The main OP fracture zone is located at 2766–2800 m MD (Fig. 3). Others OP fracture zones are located at approximately 2535 m MD, approximately 2950 m MD and approximately 3050 m MD (Vidal et al., 2017).

The thermal profiles of two wells are divided into two parts (Baujard et al., 2017).

- The uppermost part is associated with a linear geothermal gradient of 95 °C/km indicative of conductive heat transfer (Baujard et al., 2017).

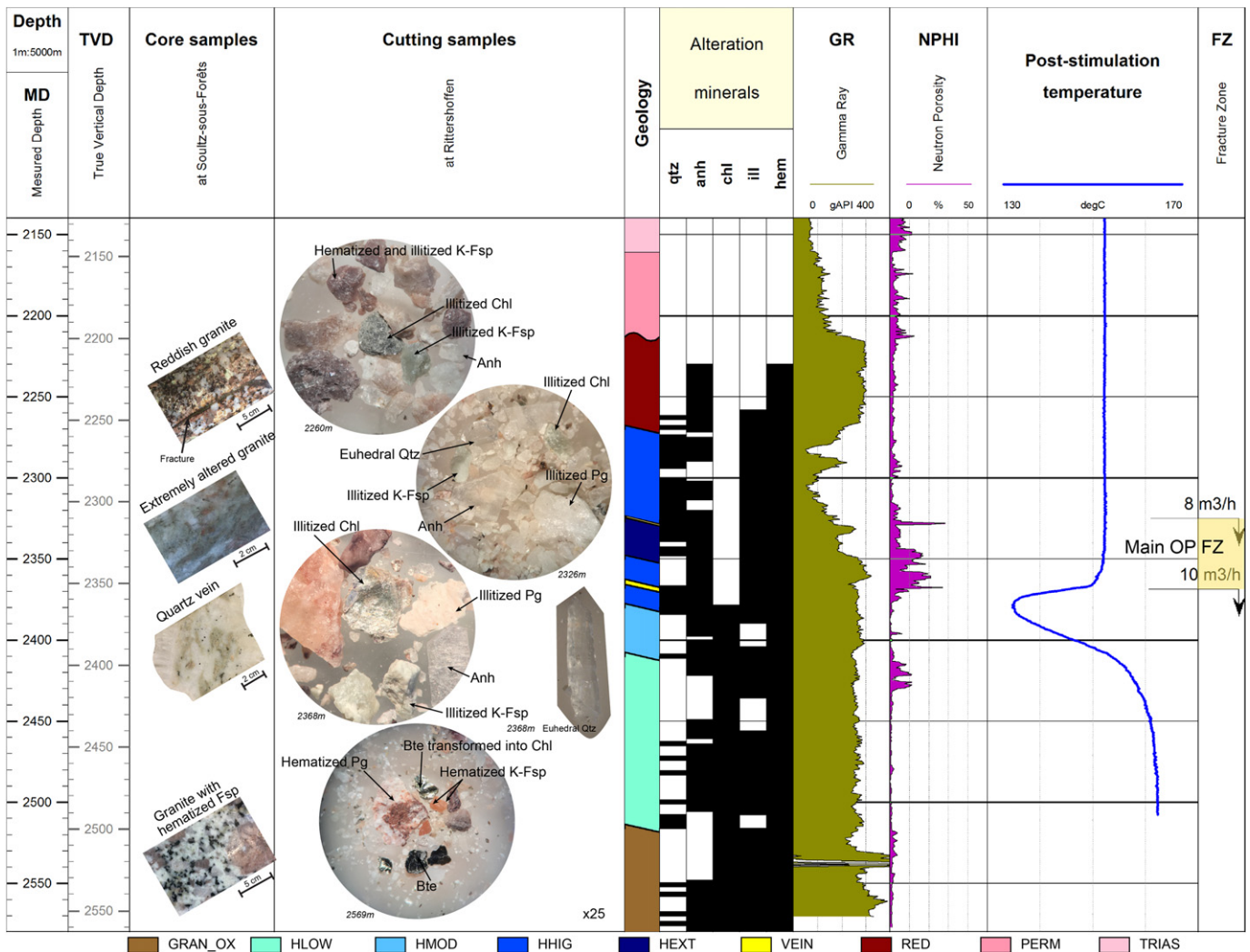
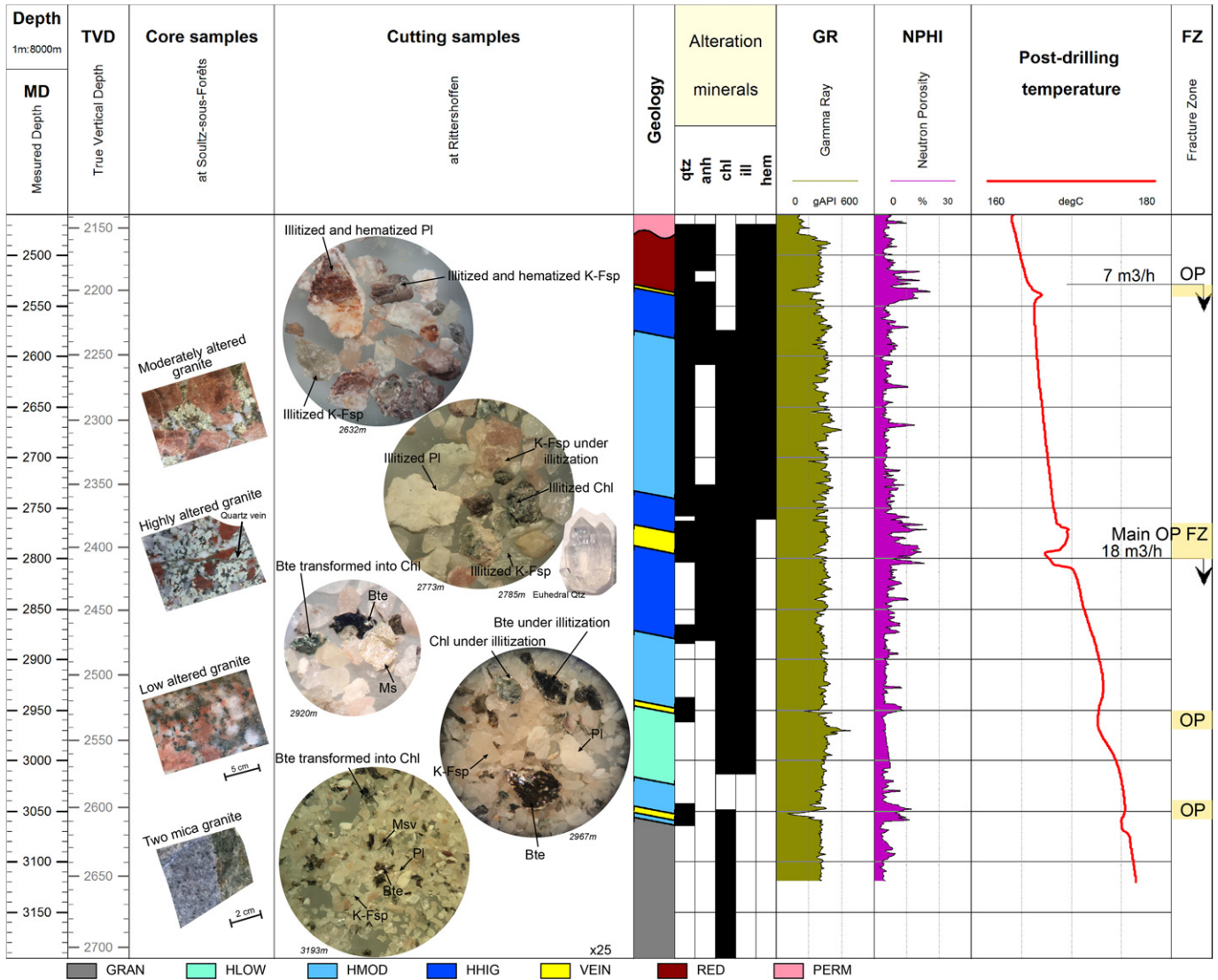


Fig. 2. Temperature log in the granitic basement of GRT-1 correlated with cutting sample observations, occurrences of alteration minerals, and gamma ray (GR) and neutron porosity (NPHI) data. The light-yellow interval is an originally permeable (OP) fracture zone identified from a structural analysis (Vidal et al., 2016a, 2017). Core samples from Soultz-sous-Forêts are indicated as potential analogs of the alteration grades observed in the cuttings. Black in the alteration mineral columns indicates the presence of the minerals in cuttings. Cuttings observed with a hand lens are magnified 25×. Qtz = quartz, anh = anhydrite, chl = chlorite, ill = illite, hem = hematite, bte = biotite, pg = plagioclase feldspar, K-Fsp = potassic feldspar. GRAN\_OX = propylitic alteration and hematite precipitation, HLOW = low degree of argilization, HMOD = moderate degree of argilization, HHIG = high degree of argilization, HEXT = extreme degree of argilization, VEIN = quartz vein, RED = reddish granite affected by paleoweathering, PERM = Permian sediments, TRIAS = Triassic sediments.



**Fig. 3.** Temperature log in the granitic basement of GRT-2 correlated with cutting sample observations, occurrences of alteration minerals, and gamma ray (GR) and neutron porosity (NPHI) data. Light-yellow intervals are originally permeable (OP) fracture zones identified from a structural analysis (Vidal et al., 2017). Core samples from Soultz-sous-Forêts are indicated as potential analogs of the alteration grades observed in the cuttings. Black in the alteration mineral columns indicates the presence of the minerals. Cuttings observed with a hand lens are magnified 25×. Qtz = quartz, anh = anhydrite, chl = chlorite, ill = illite, hem = hematite, bte = biotite, pg = plagioclase feldspar, K-Fsp = potassic feldspar, ms = muscovite. GRAN = propylitic alteration, HLOW = low degree of argilization, HMOD = moderate degree of argilization, HHIG = high degree of argilization, VEIN = quartz vein, RED = reddish granite affected by paleoweathering, PERM = Permian sediments.

The sedimentary formations from the Cenozoic and Mesozoic (Lower Jurassic and Upper Triassic) may serve as cap rocks that insulate the active hydrothermal system below.

- The deepest part exhibits a null geothermal gradient in GRT-1 (Fig. 2) and a low geothermal gradient of 18 °C/km in GRT-2 (Fig. 3) (Baujard et al., 2017). Heat and matter transfer in these hard, fractured sandstones (of the Buntsandstein and the Permian formations) and the fractured granitic basement are dominated by convective processes. This section has positive and negative deviations from the geothermal gradient, which are positive or negative anomalies interpreted as the thermal signature of the OP fracture zones (Baujard et al., 2017; Vidal et al., 2017). Each OP fracture zone is associated with thermal anomalies that may be caused by the outflow of hot geothermal fluids (positive anomalies) or by remnant cooling of porous damage zones after mud invasion during drilling operations and the massive injection of water during stimulation operations (negative anomalies) (Barton et al., 1995; Bradford et al., 2013; Davatzes and Hickman, 2005; Genter et al., 2010; Vidal et al., 2017).

The bottom-hole temperatures are 166 °C in GRT-1 and 177 °C in GRT-2 (Baujard et al., 2017). The hydraulic behavior of the vertical well GRT-1 is controlled by the main OP fracture zone in the granitic basement from 2325 to 2368 m MD (Fig. 2), and its natural permeability was deemed too low for industrial exploitation (Baujard et al., 2017; Vidal et al., 2016a). The well was thermally, chemically and hydraulically (TCH) stimulated with success, and its hydraulic yield was enhanced from 0.5 L/s/bar to 2.5 L/s/bar (Baujard et al., 2017). The hydraulic behavior of the deviated well GRT-2 is controlled by several OP fracture zones. The natural permeability of the well was high enough for industrial exploitation and presented a good hydraulic yield (higher than 3 L/s/bar) and therefore was not stimulated (Baujard et al., 2017). These OP fracture zones in the granitic basement host the fracture-controlled circulation of fluids that generate the observed hydrothermal alterations. The study focused on the hydrothermal alteration in the granitic basement inferred from observations of clay minerals. Associated minerals such as silicates (i.e., quartz and other forms of silica) and carbonates also provide information about the hydrothermal alteration, but they were not part of the study.

## 4. Methodology

### 4.1. Evaluation of argilization from observations of cutting

The first part of the study involved the investigation of the alteration petrography of the cutting samples by hand-lens examination at 3-m depth intervals. With cutting samples, spatial resolution is low and textural relations between minerals are not studied. Moreover, minerals from the fractures and the surrounding granitic protolith are commonly mixed within each cutting sample. The degree of argilization of the primary minerals and the occurrence of chlorite were investigated by hand-lens examination of the granitic samples. The degrees of alteration of the granitic cuttings were determined based on observations of analogue core samples from Soultz (core samples in Figs. 2 and 3) (Genter and Traineau, 1992; Hooijkaas et al., 2006). The whole granitic basement affected by propylitic alteration is designated GRAN (core sample in Fig. 3). The top of the granitic basement is affected by paleo-weathering related to Permian exhumation of the basement. This facies is associated with hematization and designated reddish granite (RED) (core sample in Fig. 2). Moreover, four types of granitic facies were determined to show increasing levels of argilization of the primary minerals:

- A facies with a low degree of argilization (HLOW) is characterized by the persistence of weakly argilized biotite and chlorite and by unaltered plagioclase and potassic feldspars. The texture of the granitic protolith is preserved (core sample in Fig. 3);
- A facies with a moderate degree of argilization (HMOD) is characterized by the total argilization of biotite and the preservation of unaltered plagioclase and potassic feldspars (core sample in Fig. 3);
- A facies with a high degree of argilization (HHIG) is characterized by the total argilization of biotite and the partial to total replacement of plagioclase and potassic feldspars with clay minerals (core samples in Fig. 3);
- A facies with an extremely high degree of argilization (HEXT) is characterized by the total argilization of primary minerals (i.e., biotite and the plagioclase and potassic feldspars). The overall texture of the core sample is completely modified compared with that of the granitic protolith (core samples in Fig. 2).

The macroscopic observations were correlated with the geophysical logs (i.e., gamma ray and neutron porosity) to provide supplementary information about the vertical distribution of the clay minerals identified in the cuttings. The gamma ray log involves the measurement of the potassium, thorium and uranium contents used to detect the leaching of radioactive primary minerals (negative anomaly) or the presence of clay minerals that incorporate radioactive chemical elements within the fracture zones (positive anomaly). The neutron porosity log is based on the response of a formation to the emission of fast neutrons by a given source; in granite, that response is positive if there is a fracture or if clays and hydrated minerals occur in the formation.

Then, thin sections made from mount cuttings in epoxy were observed by microscopy in approximately fifty cutting samples from both wells. The degree of illitization of the primary minerals was estimated from microscopic observations of the replacement rate of the K-feldspars by illite in thin sections.

### 4.2. Identification of clay minerals

The second part of the study focused on the identification of clay minerals. Twenty-one and thirty-eight cuttings samples were collected from GRT-1 and GRT-2, respectively. The sampling was concentrated in the permeable and altered fracture zones, which were identified within the granitic basement using acoustic image and temperature logs. Some

of the samples were located in lightly altered zones and were used as reference materials, as they are believed to be representative of rocks preserved from present-day fluid circulation properties. Samples were not ground; they were dispersed in distilled water by ultrasonic vibration to disintegrate the particles. Oriented powders on glass slides were prepared with a < 5  $\mu\text{m}$  clay suspension, obtained by sedimentation. Clay minerals were identified by XRD of air-dried and ethylene-glycol (EG)-saturated oriented powders carried out on a Bruker D8 Advance diffractometer (CuK $\alpha$  radiation, 40 kV, 40 mA). The analytical conditions were as follows: angular domain: 2.5–30° 2 $\theta$ ; step increment: 0.025 2 $\theta$ ; and counting time per step: 3 s. XRD data acquisition and treatment were conducted using the X'Pert HighScore software (PANalytical B.V.). The clay minerals were identified according to the literature (Brindley and Brown, 1980) (Fig. 4). When present, the (001) reflection from the illitic minerals was deconvoluted into poorly crystallized illite (PCI), well-crystallized illite (WCI) and ordered illite-rich mixed layered illite/smectite (I/S) using the Fityk software (Fig. 4c). The full width at half maximum (FWHM) intensity of the typical (001) reflections of WCI and PCI at 10 Å is a good indicator of the crystallinity along the c axis (Kubler, 1968). The crystallinity along the c axis of the chlorite was estimated from the FWHM intensity of the (002) reflection at 7 Å.

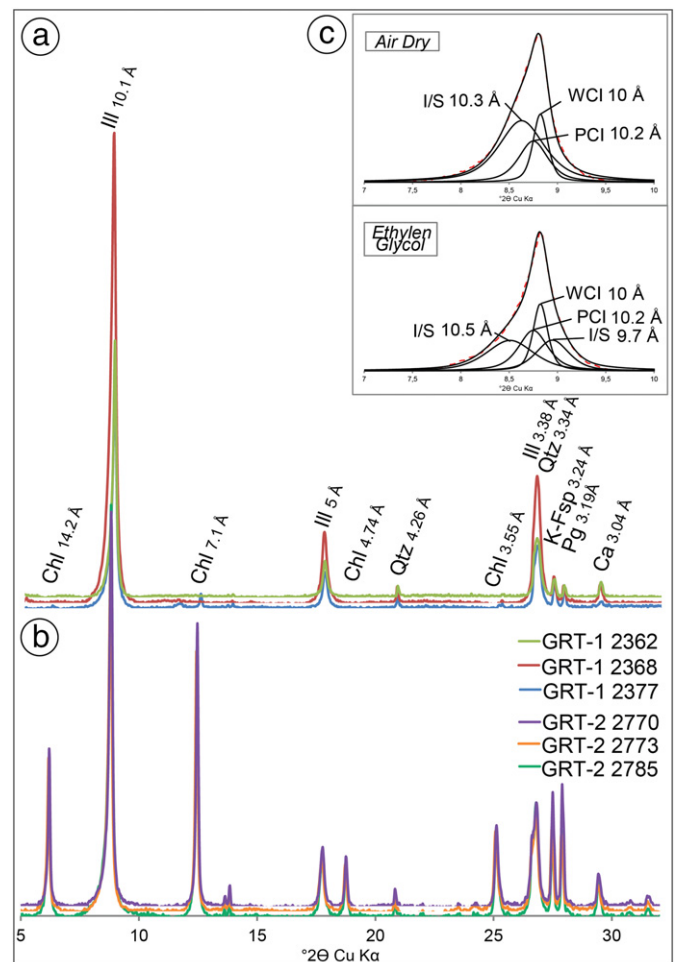


**Fig. 4.** X-ray diffractograms of the clay fraction as observed in the main OP FZ a) in GRT-1 (samples 2362, 2368 and 2377) and b) in GRT-2 (samples 2770, 2773 and 2785). Ill = illite, Chl = chlorite, Qtz = quartz, Pg = plagioclase feldspar, K-Fsp = potassic feldspar, Ca = calcite. c) deconvolution of the 7–10° 2 $\theta$  CuK $\alpha$  domain of the X-ray diffractograms (<5  $\mu\text{m}$  clay fraction) of air-dried and EG-saturated oriented powder of an example sample. I/S: ordered illite/smectite mixed layer; WCI: well-crystallized illite, PCI: poorly crystallized illite. Dashed red line represents the data.

4.3. Analysis of chemical composition of clay minerals

Finally, the third part of the study involved the investigation of the chemical compositions of clay minerals using a JEOL 5600LV SEM,

which was equipped with a BRUKER XFlash 4030 Silicon Drift Detector (accompanied by the SPIRIT software). The analytical conditions were as follows: 15 kV; 1 nA; counting time: 60 s; and working distance: 16.5 mm. The analyzed elements were Si, Al, Fe, Mg, Mn, Ti, Ca, Na

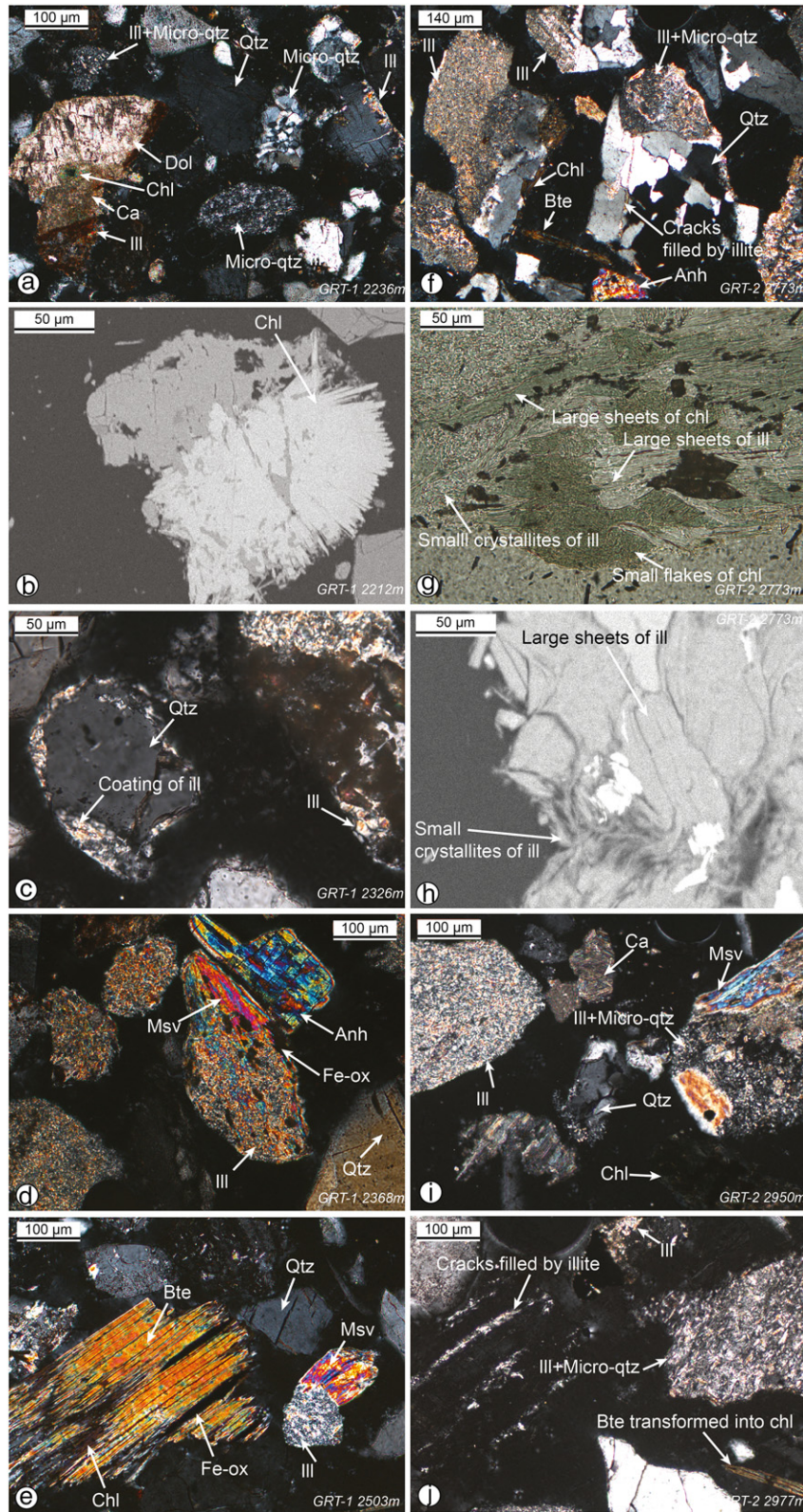


**Fig. 5.** Microscopic observations of thin sections of cuttings fixed in epoxy in GRT-1 at a) 2236 m MD (PPL), b) 2212 m MD (SEM observations), c) 2326 m MD (PPL), d) 2368 m MD (PPL), and e) 2503 m MD (plane polarized light, PPL); and in GRT-2 at f) 2773 m MD (PPL), g) 2773 m MD (crossed polarized light, XPL), h) 2273 m MD (SEM), i) 2950 m MD (PPL) and j) 2977 m MD (PPL) Qtz = quartz, Bte = biotite, Chl = chlorite, Ill = illite, Py = pyrite, Anh = anhydrite, Dol = dolomite, Ca = calcite, Fe-ox = iron oxides.

and K. The system was calibrated with a variety of synthetic oxide and natural silicate standards. The reproducibilities of the standard analyses were approximately 1%, except for Na, which had a reproducibility of 1.5%.

## 5. Alteration petrography in the geothermal wells at Rittershoffen

### 5.1. Observations in GRT-1

The top of the granitic basement is encountered at 2212 m MD in GRT-1. The first granitic facies intersected is the RED facies down to 2270 m MD (Fig. 2). Cuttings near the contact with the overlying sediments are reddish because of the intense precipitation of hematite (cuttings in Fig. 2). Fractures into reddish granite contain a large amount of illitic minerals associated with micro-quartz (Fig. 5a). Carbonates such as calcite and dolomite as well as sulfate are prevalent in fractures. Some green chlorite minerals are observed (Fig. 5a). More microscopy images of the cutting samples in GRT-1 are provided in the Supplementary material S1. SEM observations indicate epitaxial growth of the large chlorite (>50  $\mu\text{m}$ ) that likely crystallized from hydrothermal circulations (Fig. 5b). The RED facies is correlated with a well-known pattern of gamma rays that is characteristic of the reddish granite in the area (Fig. 2) (Vidal et al., 2016b). At the top of the granitic basement, the gamma ray intensity decreases abruptly in the sedimentary cover.

Below the RED facies, an HHIG facies is intersected down to 2326 m MD (cuttings in Fig. 3).

The main OP fracture zone presents abundant euhedral quartz from 2326 to 2329 m MD and from 2365 to 2368 m MD that could indicate the presence of quartz veins (cuttings in Fig. 2). These quartz veins are associated with a sharply negative anomaly of gamma ray radiation (Fig. 2) and have already been observed in acoustic image logs (Vidal et al., 2017). Small crystallites of illitic minerals occur as grain coatings of quartz (Fig. 5c). At the top of the main OP fracture zone, a HEXT facies is observed from 2329 to 2350 m MD (Fig. 2) in which cuttings are highly bleached in response to intense hydrothermal alteration (cuttings in Fig. 2). Anhydrite and pyrite are abundant in the main OP fracture zone of GRT-1. Chlorite is seldom observed within the main OP fracture zone of GRT-1. At the bottom of the main OP fracture zone, an HHIG facies is observed down to 2380 m MD (cuttings in Fig. 2), and primary biotite and local feldspars are completely replaced by small crystallites of illitic minerals (Fig. 5d). Neutron porosity values confirm the significant argilization of the main OP fracture zone, with values between 10 and 20% from 2340 to 2370 m MD and maxima of nearly 40% at 2325 and 2370 m MD.

Below the main OP fracture zone, from 2380 to 2410 m MD, an HMOD facies is encountered, and then from 2410 to 2516 m MD, an HLOW facies is observed (Fig. 2). The deep granitic samples from 2516 to 2580 m MD are affected by propylitic alteration with the partial transformation of primary biotite into chlorite and the partial replacement of primary potassic feldspar or muscovite with small crystallites of illitic minerals (Fig. 5e). Cuttings exhibit a reddish colour, and this facies is designated GRAN\_OX (Fig. 2).

### 5.2. Observations in GRT-2

The top of the granitic basement is encountered at 2480 m MD in GRT-2. The first granitic facies is RED down to 2533 m MD (Fig. 3). At the base of the RED facies, the abundance of euhedral quartz from 2533 to 2536 m MD suggests the presence of quartz veins associated with the presence of an OP fracture zone at the same depth. Then, an HHIG facies is observed from 2536 to 2578 m MD, and an HMOD facies is observed from 2578 m MD to 2737 m MD (Fig. 3).

The main OP fracture zone in GRT-2 is associated with an HHIG facies observed from 2737 to 2875 m MD. The top of the main OP fracture zone is associated with neutron porosity values between 10% and 20% from 2760 to 2810 m MD, which are correlated with the significant

argilization of the cuttings (Fig. 3). In thin sections, primary minerals are replaced by illitic minerals but are still identifiable compared with the main OP fracture zone in GRT-1 (Fig. 5f). The microscopic observations indicate at least two different sizes of illitic minerals that are likely associated with different hydrothermal events. Illitic minerals are present as large sheets (>50  $\mu\text{m}$ ) as well as small crystallites (<5  $\mu\text{m}$ ) and are sometimes present as the infill of cracks (Fig. 5f, g and h). At least two sizes of chlorite are also observed. Chlorite derived from the transformation of biotite is observed as large sheets (>50  $\mu\text{m}$ ), and another population of chlorite in the form of small flakes (<5  $\mu\text{m}$ ) is also observed (Fig. 5h). More microscopy images of the cutting samples in GRT-2 are provided in the Supplementary material S2. In the main OP fracture zone, cuttings from 2770 to 2791 m MD indicate euhedral quartz, which is interpreted as the occurrence of quartz veins (Fig. 3). These cuttings correlate with quartz veins observed in acoustic image logs (Vidal et al., 2017).

Below the main OP fracture zone, an HMOD facies is observed until the OP fracture zone at 2944 m MD. Locally, primary minerals are completely transformed into small crystallites of illitic minerals, while primary muscovite could be preserved (Fig. 5i). Green chlorite and calcite are also found at these depths. The OP fracture zone is associated with an abundance of euhedral quartz from 2944 to 2950 m MD correlated with a sharply negative anomaly of gamma ray radiation (Fig. 3). Below the OP fracture zone, from 2950 to 3020 m MD, an HLOW facies is associated with primary quartz minerals intersected by microcracks filled with illitic minerals or with an assemblage of microquartz and illitic minerals (Fig. 5j). Then, the increase in neutron porosity until 13% suggests an increase in the argilization of cuttings. Cuttings from 3020 to 3046 m MD confirm this increase in argilization and are associated with an HMOD facies (Fig. 3). The deepest OP fracture zone is associated with an abundance of euhedral quartz from 3046 to 3061 m MD correlated with a sharp negative anomaly of gamma ray radiation (Fig. 3). The deepest cuttings, from 3061 to 3196 m MD, are light gray (Fig. 3). They are associated with the propylitic alteration and are designated GRAN.

In conclusion, four main facies of argilization were observed in GRT-1, and three were observed in GRT-2 (Figs. 2 and 3 and Supplementary material 3). An HEXT facies is not observed in the main OP fracture zones of GRT-2, the primary minerals are not completely transformed into illitic minerals in the OP fracture zones of GRT-1, and Fe-rich chlorite is much more abundant. The highest levels of alteration (HHIG and HEXT) are observed in the main OP fractures zones of GRT-1 and GRT-2 (Figs. 2 and 3 and Supplementary material 3). Euhedral quartz is always observed in abundance within the OP fracture zones.

## 6. Identification of clay minerals

X-ray diffractograms indicate that the clay alteration products are dominated by illite and chlorite in the Rittershoffen wells (Fig. 4). The (001) reflections of the illitic minerals at 10 Å are complex. The (001) reflections were deconvolved into two or three Gaussian peaks (Fig. 4c). Two peaks that correspond to the index peaks of WCI and PCI are consistently observed at approximately 10 Å and 10.2 Å, respectively (Fig. 4c). The WCI peak corresponds to a d-value of 10 Å and is characterized by a narrow FWHM that ranges from 0.08 to 0.24°2 $\theta$  in GRT-1 and from 0.09 to 0.18°2 $\theta$  in GRT-2. The PCI peak corresponds to a d-value of 10.2 Å and is characterized by a broader FWHM (between 0.26 and 0.48°2 $\theta$  in GRT-1 and between 0.18 and 0.44°2 $\theta$  in GRT-2). Microscopic observations reveal that illitic minerals occur as large sheets and as small crystallites. Deconvolution is therefore based on a first-order approximation with well-crystallized illitic minerals and poorly crystallized illitic minerals. However, there are likely more illitic populations.

Mixed layers I/S (~10% smectite) were identified in some of the samples. In air-dried samples, the layers are characterized by a broad peak near 10.3 Å that splits into two peaks near 10.5 Å and 9.7 Å after EG

saturation (Fig. 4c) (Lanson et al., 1995). The WCI and PCI peaks do not shift after EG saturation. Chlorites were identified by their non-expandability and their harmonic peaks at 14 Å and 7 Å. The FWHM of the peak at 7 Å varies between 0.08 and 0.12°2θ in GRT-1 and between 0.09 and 0.18°2θ in GRT-2. Chlorite is less abundant in the diffractograms of GRT-1 than in those of GRT-2 (Fig. 4).

6.1. Observations in GRT-1

Based on the crystallographic properties of the illitic minerals, two zones can be observed in the granite (Fig. 6a).

The shallowest zone is composed of samples from 2212 to 2338 m MD that are associated with the first three alteration facies intersected by the well GRT-1, RED, HHIG and HEXT. In this zone, the average proportion of WCI (%Int WCI) is 0.43, and the average FWHM of WCI is 0.15°2θ. The average proportion of PCI (%Int PCI) is 0.31, and the average

FWMH of PCI is 0.34°2θ. Mixed layers I/S are systematically present in this section, with an average %Int I/S of 0.26.

The deepest zone is composed of samples from 2347 to 2503 m MD that are associated with the last three alteration facies intersected by the well GRT-1, HHIG, HMOD and HLOW. In this zone, the %Int WCI is 0.72, and the average FWHM of WCI is 0.15°2θ. The average %Int PCI is 0.40, and the average FWHM of PCI is 0.28°2θ. Mixed layers I/S layers are no longer present in this section.

The crystallographic properties of chlorite are more strongly influenced by the main OP fracture zone than by the limits of alteration facies, as observed for illitic minerals (Fig. 6a).

From the top of the granitic basement (2212 m MD) to the top of the main OP fracture zone (2326 m MD), the average proportion of chlorite (%Int Chl) is 0.05 (Fig. 6a). Chlorite is only observed in one sample of the main OP fracture zone at 2354 m MD, wherein the highest proportion of chlorite in GRT-1 (0.97) is observed. From the base of the main OP

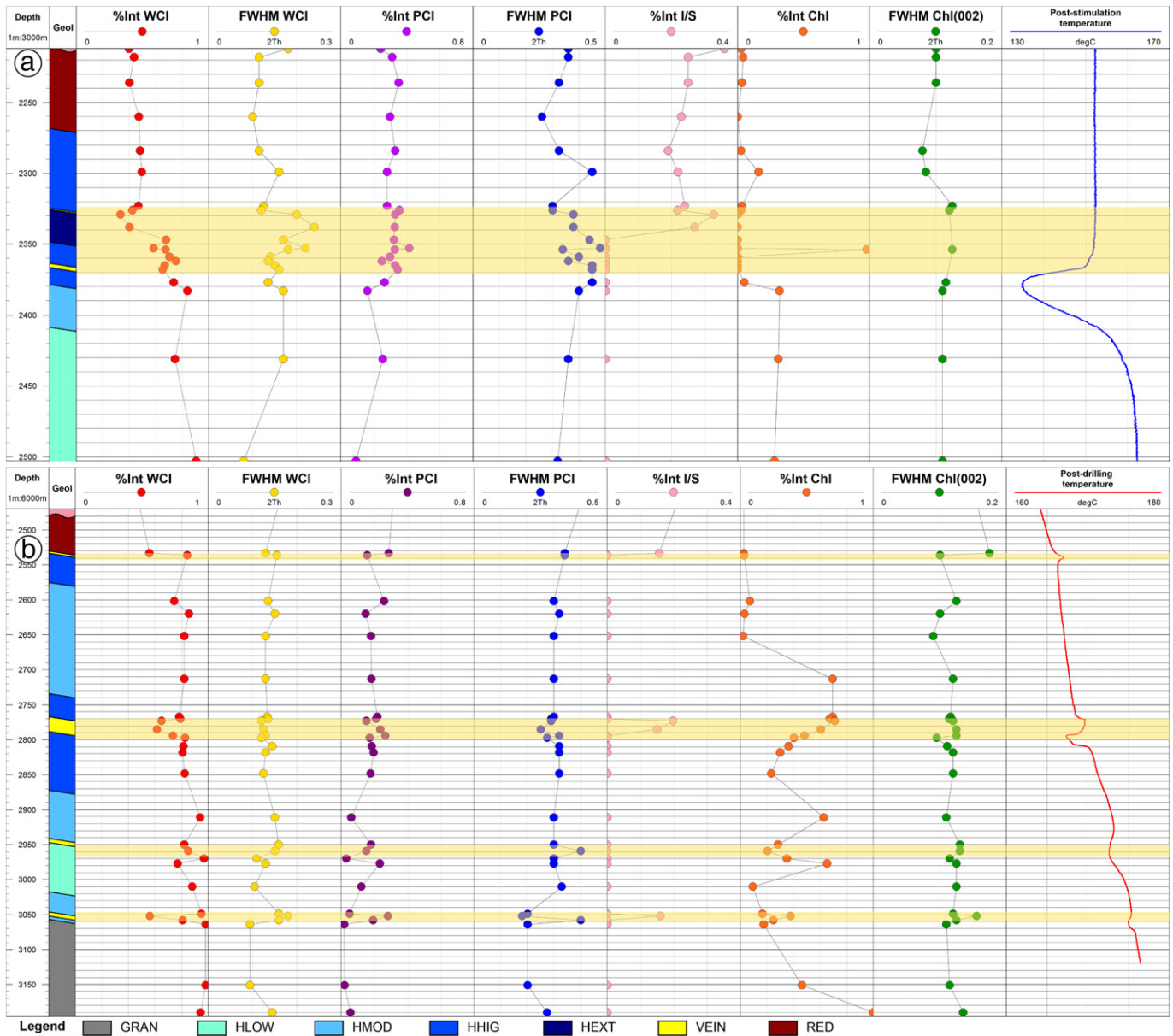


Fig. 6. Crystal structure properties of the illitic minerals and chlorite measured using XRD of the <5 μm clay fraction versus depth a) in GRT-1 and b) in GRT-1. Relative proportion of WCI: %Int WCI = WCI int/(WCI int + PCI int + I/S int), where WCI int = the intensity of the peak deconvolved from the (001) reflection of the illitic minerals. Relative proportion of Chl: %Int Chl = (Chl int)/(Chl int + WCI int + PCI int + I/S int), where Chl int = the intensity of the peak of the (002) reflection of the chlorite. Light-yellow intervals represent originally permeable (OP) fracture zones from a structural analysis (Vidal et al., 2017, 2016a).

fracture zone (2377 m MD) to the bottom of the granitic basement (2503 m MD), chlorite is observed with an average %Int Chl of 0.24. With an average value of  $0.10^{\circ}2\theta$ , the FWHM values of chlorite do not vary significantly with depth.

## 6.2. Observations in GRT-2

The crystallographic properties of illitic minerals are more strongly influenced by the occurrence of the OP fracture zone than by limits of alteration facies, as observed for GRT-1 (Fig. 6b).

From the top of the granitic basement (2480 m MD) to the bottom of the granitic basement (3196 m MD), %Int WCI tends to increase with depth (Fig. 6b). The average %Int WCI is 0.78, with an average FWHM of  $0.13^{\circ}2\theta$ . Locally, the %Int WCI decreases in OP fracture zones:

- %Int WCI is 0.56 for the sample at 2533 m MD;
- %Int WCI is 0.65 and 0.61 for samples at 2773 and 2785 m MD;
- %Int WCI is 0.56 for the sample at 3052 m MD.

From the top of the granitic basement (2480 m MD) to the bottom of the granitic basement (3196 m MD), %Int PCI tends to decrease with depth (Fig. 6b). The average %Int PCI is 0.16, with an average FWHM of  $0.30^{\circ}2\theta$ . Locally, %Int PCI increases at each OP fracture zones:

- %Int PCI is 0.29 for the sample at 2533 m MD;
- %Int PCI is 0.23 and 0.27 for samples at 2785 and 2794 m MD;
- %Int PCI is 0.18 and 0.15 for samples at 2950 and 2959 m MD;
- %Int WCI is 0.28 for the sample at 3052 m MD.

Mixed layers I/S are observed in samples at 2533, 2773, 2785 and 3052 m MD and are associated with OP fracture zones (Fig. 6b). Outside OP fracture zones, mixed layers I/S are no longer observed.

Chlorite is observed in all samples from the granitic basement of GRT-2 (Fig. 6b). The average %Int Chl is 0.38, and the FWHM is relatively constant, with an average value of  $0.12^{\circ}2\theta$  (Fig. 6b). In the main OP fracture zone, the %Int Chl decreases from 0.71 at 2773 m MD to 0.23 at 2848 m MD.

In conclusion, the granitic basement is characterized by a general increase in %Int WCI and a decrease in %Int PCI with depth. However, local variations are associated with OP fracture zones in both wells. Each OP fracture zone is associated with a decrease in %Int WCI, an increase in %Int PCI and the occurrences of mixed layers I/S. These variations are more strongly correlated with the alteration facies limit in GRT-1 than in GRT-2. In GRT-1, the main OP fracture zone appears to act as an interface between two zones that are quite distinct, with occurrences of mixed layers I/S above and no longer mixed layers I/S below.

## 7. Chemical compositions of clay minerals

The structural formulae of the illitic minerals were calculated relative to a structure containing 11 oxygen atoms and assuming that the total iron content was composed of  $\text{Fe}^{3+}$  (Supplementary material 4). The structural formulae of the chloritic minerals were calculated relative to a structure containing 14 oxygen atoms and assuming that the total iron content was composed of  $\text{Fe}^{2+}$  (Supplementary material 4).

### 7.1. Observations in GRT-1

The chemical analyses of the illitic minerals (WCI + PCI + ml I/S) in GRT-1 do not demonstrate major variations with depth (Fig. 7a). The interlayer charge is between 0.83 and 0.90, and the average octahedral Al content is  $1.67 \pm 0.05$  per  $\text{O}_{10}(\text{OH})$  (Supplementary material 4). Samples above the main OP fracture zone (i.e. from 2212 to 2329 m MD) present an XFe ratio  $< 0.5$ , whereas samples in the main OP fracture

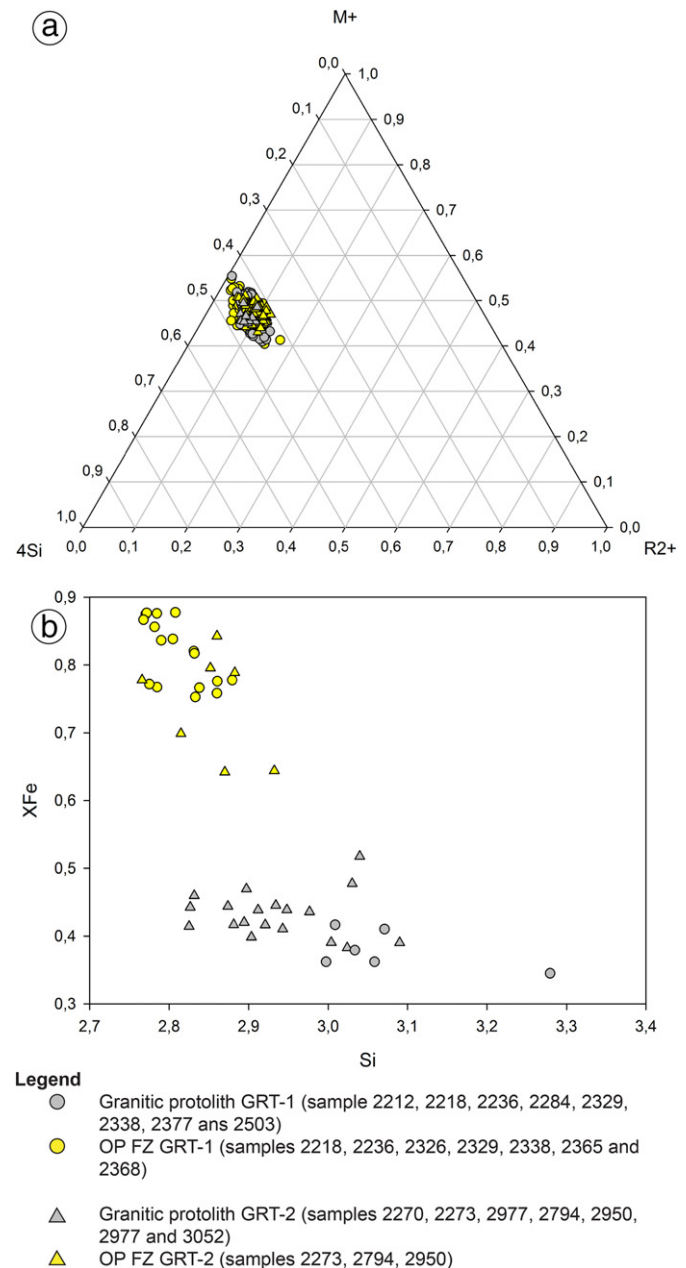


Fig. 7. Plot of the structural formulae of a) the illitic minerals in a  $M+ - R2+ - 4Si$  ternary diagram and b) chlorite in a diagram of XFe versus Si for wells GRT-1 and GRT-2. XFe =  $\text{Fe}/(\text{Fe} + \text{Mg})$ . The average structural formula for each sample is presented in Supplementary material 4.

zone and below (i.e. from 2329 to 2503 m MD) present an XFe ratio  $\geq 0.5$ .

Two types of chlorite were distinguished based on their structural formulae. Samples associated to sealed fracture zone at the top of the granitic basement, at 2218 m MD, and in the main OP fracture zone, at 2368 m MD, contain Fe-rich chlorite with XFe  $> 0.80$  (Fig. 7a). The deepest sample in GRT-1 associated to granitic protolith, at 2503 m MD, contains ferromagnesian chlorite with XFe = 0.38.

### 7.2. Observations in GRT-2

The chemical analyses of the illitic minerals (WCI + PCI + ml I/S) in GRT-2 do not demonstrate major variations with depth (Fig. 7b). The interlayer charge varies between 0.85 and 0.91, and the average octahedral Al content is  $1.63 \pm 0.07$  per  $\text{O}_{10}(\text{OH})$  (Supplementary material

4). Samples in OP fracture zones, i.e. at 2270, 2773, 2950, and 3052 m MD, present an XFe ratio (~0.5) similar to that of samples associated to the granitic protolith, i.e. at 2794 and 2977 m MD.

Two types of chlorite were distinguished based on their structural formulae. Samples in OP fracture zones, i.e. at 2773, 2794 and 2950 m MD, contain Fe-rich chlorites with XFe > 0.60 (Fig. 7b). Ferromagnesian chlorite with XFe < 0.5 is observed in samples in OP fracture zones, i.e. at 2770, 2773, 2950, and 3052 m MD, as well as in the sample at 2977 m MD associated to the granitic protolith (Fig. 7b).

In conclusion, the illitic minerals in both wells exhibit similar compositions regardless of the size of the illitic minerals, the occurrences of OP fracture zones or the alteration facies of the granitic basement (Fig. 7a). Chlorite occurs as two distinct populations: Fe,Mg-chlorite, which corresponds to the large sheets observed by microscopy, resulting from the alteration of biotite (Fig. 5g); and Fe-chlorite, which forms aggregates of small flakes or epitaxial growths along pore walls, formed during later hydrothermal events (Fig. 5g and b). Fe-chlorite is associated with OP fracture zones, whereas Fe,Mg-chlorite is observed regardless of the occurrence of OP fracture zones and the alteration facies of the granitic basement.

**8. Discussion**

*8.1. Interpretation of the alteration assemblages in the granitic basement*

The characterizations of the alteration petrography and of the secondary mineralogies of the cuttings collected from the two wells investigated in this study help to refine the hydrothermal history of the granitic basement at Rittershoffen (Fig. 8).

*8.1.1. Early alteration stage in the poorly fractured granitic basement*

Petrographic observations of the basement rocks from the parts of the wells that preserve the characteristics of strong fracture-controlled

alteration features reveal that the entire granitic batholith has been affected by an earlier alteration stage consisting of the pervasive replacement of biotite and primary calc-silicate minerals with an assemblage of Fe,Mg-chlorite, epidote and illite (Fig. 8). This type of alteration and its consequent mineral assemblage correspond to the propylitic alteration facies reported in the literature (Lowell and Guilbert, 1970). Propylitic alteration is very common in magmatic intrusive bodies. This alteration occurs during the cooling of an igneous intrusion, and results from interactions, at moderate to high temperatures (200 to 400 °C), of the most reactive igneous minerals with fluids of diverse origins that are stagnant in pores or microcracks (Reyes, 1990; Thomasson and Kristmannsdottir, 1972). Consequently, propylitic alteration can affect large volumes of intrusive rocks, and it is representative of hydrothermal alteration in inactive flow regimes (Beaufort et al., 1990).

*8.1.2. Subsequent alteration stages in the highly fractured granitic basement*

The OP fracture zones identified within the two boreholes during the drilling operations and from the subsequent geophysical monitoring were characterized. In the well GRT-1, OP fracture zones correlate with HEXT and HHIG facies, whereas in the well GRT-2, they correlate with HHIG and HMOD facies (Figs. 2 and 3 and Supplementary material 3). According to petrographic observations of cuttings from these facies, three different mineral assemblages can be distinguished based on the following parageneses:

- Illite + quartz + hematite ± calcite
- Illite + Fe-chlorite ± pyrite
- Illite + ml I/S + hematite ± calcite

These three parageneses crystallized under different physico-chemical conditions and reveal typical multistage hydrothermal crystallization (Fig.

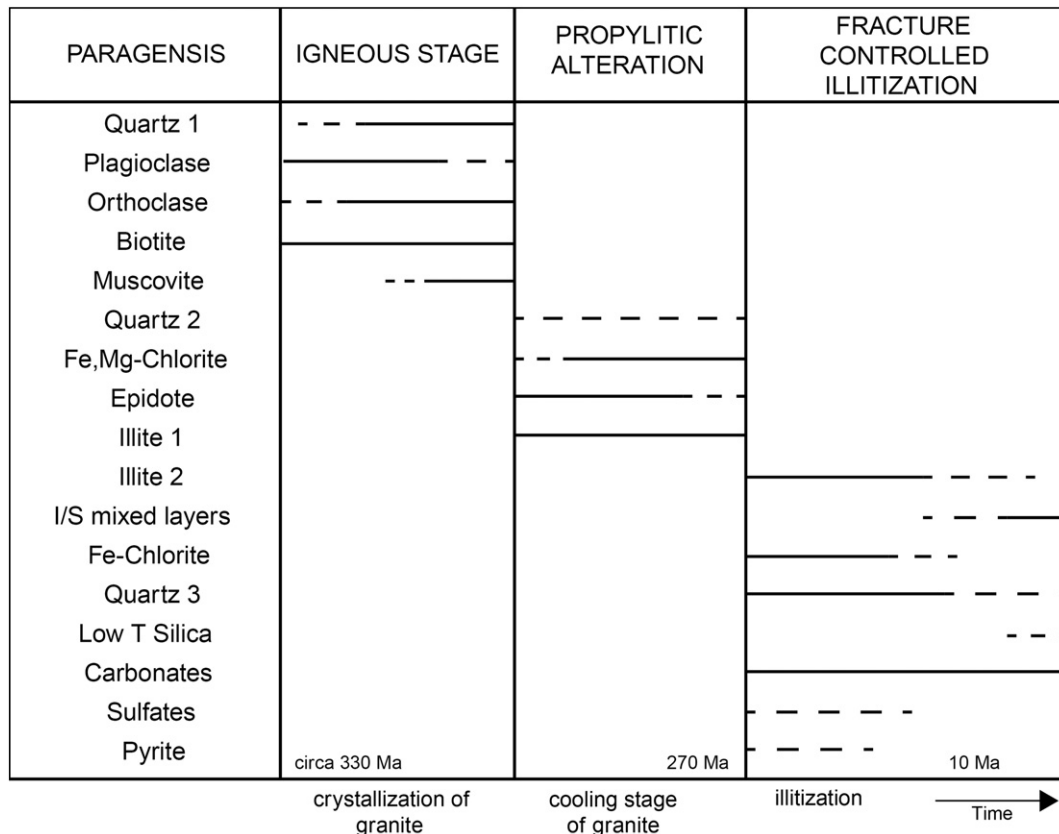


Fig. 8. Paragenesis sequence and alteration history of the granitic basement at Rittershoffen.

8). The strong illitization of the wall rock in these facies could completely obliterate the features of the earlier propylitic alteration, and in some cases, strong illitization dominated by mixed layers I/S could even obliterate minerals from earlier hydrothermal parageneses (Fig. 8). For example, in HEXT facies in the well GRT-1, chlorite is no longer observed and was likely replaced completely by illite and mixed layers I/S. The relative timing of the hydrothermal events that promoted these mineral assemblages is not strictly constrained due to the absence of core samples.

It is important to note that similar mineral parageneses have been observed in the geothermal wells of Soultz (Genter, 1989; Genter and Traineau, 1992; Jacquemont, 2002; Ledéseret et al., 1999), in which the occurrence of illitic minerals in fractures of core samples has been dated to more than five different geological ages from the Permian to the Eocene (Bartier et al., 2008; Clauer et al., 2008; Schleicher et al., 2006). Moreover, these clay minerals were not found at isotopic equilibrium within the currently circulating fluids at either Soultz or Rittershoffen (Table 1). Only calcite was found to be in isotopic equilibrium with the existing fluids (Fouillac and Genter, 1992). Nevertheless, the isotopic composition of the mixed layers I/S has not yet been determined because of the difficulty in separating these phases from other illitic minerals and because their relationship with the subsurface geothermal fluids is still questionable.

### 8.2. Illitic signature of paleo-circulation systems and OP fracture zones

Illitic minerals are known to be potential indicators of fluid circulation and paleo-circulation systems (Flexser, 1991; Harvey and Browne, 1991; Patrier et al., 1996; Teklemariam et al., 1996; Mas et al., 2003, 2006).

Observations of cuttings, macroscopically by a hand lens and microscopically in thin sections, reveal that the highest illitization occurs

above 2380 m TVD in the well GRT-1 (HEXT and HHIG) and above 2470 m TVD in the well GRT-2 (HHIG and HMOD). These sections of strong illitization suggest that intense paleo-circulation systems were concentrated in the first 200 m of the granitic basement in GRT-1 and in the first 300 m of the granitic basement in GRT-2. Both sections of strong illitization are delimited at the base by main OP fracture zones in both wells.

XRD results obtained for the well GRT-1 confirm the observations of cuttings. The main OP fracture zone acts as an interface between two highly distinct sections. The uppermost section is associated with a low proportion of WCI correlated with the occurrence of mixed layers I/S that suggest intense paleo-circulations. This uppermost section correlates with HEXT and HHIG facies. The deepest section is associated with a high proportion of WCI correlated with the absence of mixed layers I/S. This deepest section correlates with HHIG, HMOD and HLOW facies.

The XRD results obtained for the well GRT-2 do not indicate two sections delimited by the main OP fracture zone, as observed for cuttings and GRT-1. XRD results reveal local variations that correlate with the three OP fracture zones in the granitic basement. The three OP fracture zones are associated with a local decrease in WCI, a local increase in PCI and occurrences of mixed layers I/S regardless of the alteration facies. These variations in the XRD results could be linked to local variations in the physico-chemical conditions in OP fracture zones. In an OP fracture zone that channels ascending geothermal fluids that are strongly oversaturated with respect to the surrounding clay minerals, abrupt changes in the flow regime, including the mixing of geothermal fluids, can lead to the explosive nucleation of small clay crystallites and promote the occurrence of heterogeneous mineral assemblages, such as mixed layers I/S (Beaufort et al., 1996; Patrier et al., 1996).

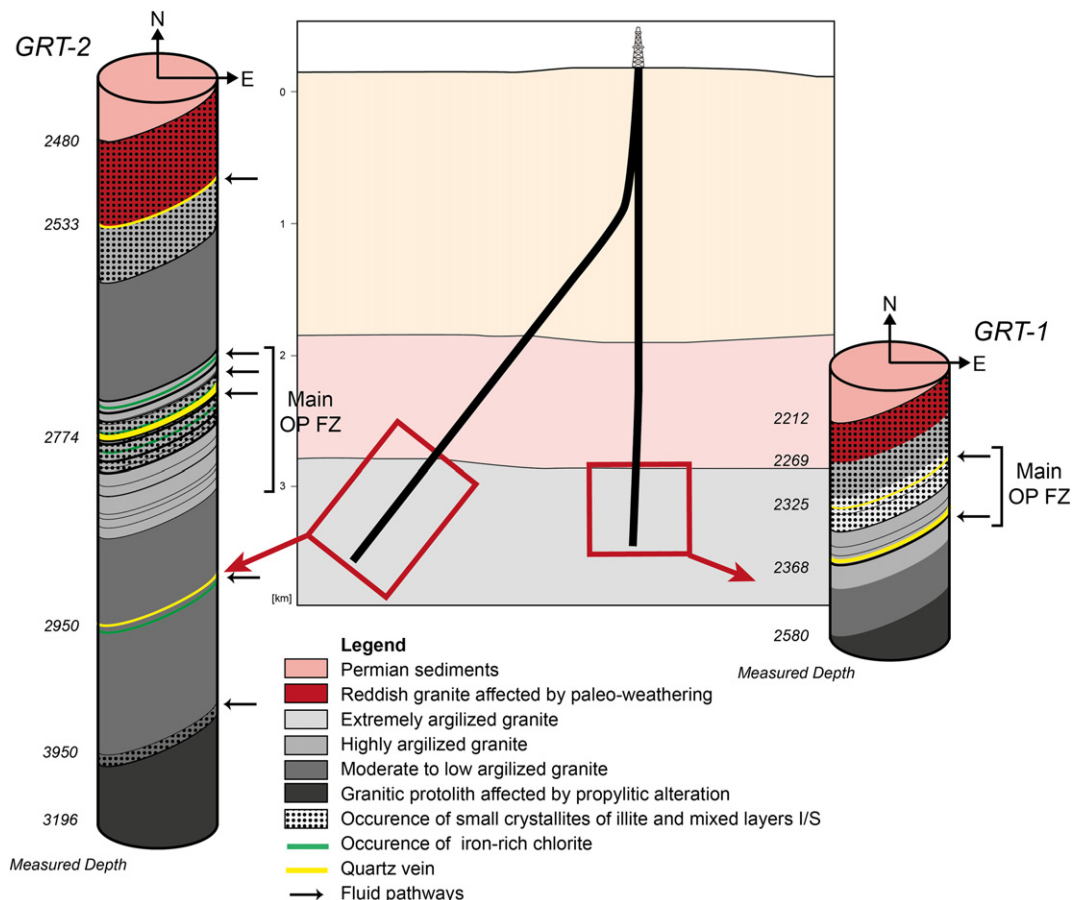


Fig. 9. Conceptual model of alteration from the clay minerals along open-holes of wells GRT-1 and GRT-2.

The chemical analyses of the illitic minerals in the Rittershoffen wells are quite consistent, and thus, we can suppose that the fluid did not evolve over time (Fig. 7a).

Even if mixed layers I/S can result from both past and present-day hydrothermal events, the occurrence of mixed layers I/S appears to be the signature of the OP fracture zones in the Rittershoffen wells (Fig. 9). Mixed layers I/S occur in the main OP fracture zone in the well GRT-1 and in three OP fracture zones in the well GRT-2. However, extensive precipitations of mixed layers I/S could lead to plugging of the OP fracture zones, thereby decreasing their natural permeability. In the well GRT-1, for example, primary and earlier secondary minerals are completely replaced by mixed layers I/S in the main OP fracture zone, and the permeability is reduced to the point that the well needs to be stimulated to bring it into production.

### 8.3. Chlorite signature in OP fracture zones

Two populations of chlorite were observed in the wells GRT-1 and GRT-2 (Fig. 7b). Ferromagnesian chloritic minerals associated with propylitic alteration occur throughout the granitic batholith. These minerals originate from the alteration of biotite under oxidizing conditions. It has been demonstrated that the chemistries of chloritic minerals are rock-dominated during propylitic alteration (Beaufort et al., 1992; López-Munguira et al., 2002; Mas et al., 2006) and that the incorporation of magnesium is promoted within the structure of chlorite, which crystallizes with iron oxides such as hematite under oxidizing conditions (Beaufort et al., 1992). It has also been demonstrated that the chemistry of Fe-chlorite is likely controlled by fluids circulating in the permeable fracture zones under reducing conditions (Beaufort et al., 2015; Mas et al., 2006; Patrier et al., 1996). Both of these chlorites are associated with higher temperatures than those in the present-day wells, and they do not represent current hydrothermal circulation. However, the persistence of Fe-chlorite in the OP fracture zones of GRT-2 indicates that these minerals have yet to be completely destabilized by oxidizing fluids, which are currently crystallizing mixed layers I/S (Fig. 9). The OP fracture zones of GRT-2 show higher natural permeabilities than the main OP fracture zone in GRT-1.

## 9. Conclusions

The alteration petrography within the granitic basement of two deep geothermal wells at Rittershoffen, GRT-1 and GRT-2, was investigated with a special focus on the clay minerals and their influence on permeability. The whole granitic basement was affected by a pervasive early stage of propylitic alteration, with the crystallization of Fe,Mg-chlorite, illite and epidote. Several stages of fluid circulation occurred later within OP fracture zones and led to subsequent alteration of the granite. These stages can be identified based on several mineral assemblages dominated by illitic minerals that formed successively. OP fracture zones in both wells are associated with occurrences of small crystallites of illite and mixed layers I/S (~10% smectite) that are the clay signatures of zones of circulation at Rittershoffen. However, the abundance of small crystallites of illite and mixed layers I/S could lead to plugging of the fracture network. When small crystallites of illite and mixed layers I/S do not completely obliterate minerals from previous hydrothermal parageneses, as observed for the well GRT-2, the natural permeability of OP fracture zones is higher and the corresponding well does not require stimulation.

## Acknowledgments

This work was based on data from the geothermal project at Rittershoffen, France. The authors acknowledge the ECOGI project, the ES-Géothermie company and the owners of the geological and geophysical log data and the cutting samples. The authors also acknowledge GEIE EMC for providing the Soultz core samples. This work was

performed under the framework of the LabEx G-Eau-Thermie Profonde, which is overseen by the French National Research Agency (ANR) under the program "Investissements d'Avenir". This manuscript was prepared as a contribution to the PhD thesis of Jeanne Vidal and was co-funded by the ADEME (French Agency for Environment and Energy Management) and the LabEx G-Eau-Thermie Profonde. The research leading to these findings received funding from the ANR Programme under the grant agreement ANR-15-CE06-0014 (Project CANTARE-Alsace) and was also supported by the EGS Alsace project co-funded by the ADEME and Electricité de Strasbourg company. The authors acknowledge the use of the Move Software Suite granted by Midland Valley's Academic Software Initiative.

## Supplementary data

Supplementary data to this article can be found online at <https://doi.org/10.1016/j.jvolgeores.2017.10.019>.

## References

- Baillieux, P., Schill, E., Edel, J.-B., Mauri, G., 2013. Localization of temperature anomalies in the Upper Rhine Graben: insights from geophysics and neotectonic activity. *Int. Geol. Rev.* 55:1744–1762. <https://doi.org/10.1080/00206814.2013.794914>.
- Baillieux, P., Schill, E., Abdelfettah, Y., Dezayes, C., 2014. Possible natural fluid pathways from gravity pseudo-tomography in the geothermal fields of northern Alsace (Upper Rhine Graben). *Geotherm. Energy* 2. <https://doi.org/10.1186/s40517-014-0016-y>.
- Bartier, D., Ledésert, B., Clauer, N., Meunier, A., Liewig, N., Morvan, G., Addad, A., 2008. Hydrothermal alteration of the Soultz-sous-Forêts granite (hot fractured rock geothermal exchanger) into a tosudite and illite assemblage. *Eur. J. Mineral.* 20:131–142. <https://doi.org/10.1127/0935-1221/2008/0020-1787>.
- Barton, C.A., Zoback, M.D., Moos, D., 1995. Fluid flow along potentially active faults in crystalline rock. *Geology* 23:683–686. [https://doi.org/10.1130/0091-7613\(1995\)023<0683:FFAPAF>2.3.CO;2](https://doi.org/10.1130/0091-7613(1995)023<0683:FFAPAF>2.3.CO;2).
- Baujard, C., Genter, A., Dalmais, E., Maurer, V., Hehn, R., Rosillette, R., Vidal, J., Schmittbuhl, J., 2017. Hydrothermal characterization of wells GRT-1 and GRT-2 in Rittershoffen, France: implications on the understanding of natural flow systems in the Rhine graben. *Geothermics* 65:255–268. <https://doi.org/10.1016/j.geothermics.2016.11.001>.
- Beaufort, D., Westercamp, D., Legendre, O., Meunier, A., 1990. The fossil hydrothermal system of Saint Martin, Lesser Antilles: geology and lateral distribution of alterations. *J. Volcanol. Geotherm. Res.* 40:219–243. [https://doi.org/10.1016/0377-0273\(90\)90122-V](https://doi.org/10.1016/0377-0273(90)90122-V).
- Beaufort, D., Patrier, P., Meunier, A., Ottaviani, M.M., 1992. Chemical variations in assemblages including epidote and/or chlorite in the fossil hydrothermal system of Saint Martin (Lesser Antilles). *J. Volcanol. Geotherm. Res.* 51:95–114. [https://doi.org/10.1016/0377-0273\(92\)90062-1](https://doi.org/10.1016/0377-0273(92)90062-1).
- Beaufort, D., Papapanagiotou, P., Patrier Mas, P., Fouillac, A.M., Traineau, H., 1996. I/S and C/S mixed layers, some indicators of recent physical-chemical changes in active geothermal systems: The case study of Chipilapa (El Salvador). *Proceedings of Seventeenth Workshop on Geothermal Reservoir Engineering*. Stanford University, California, USA.
- Beaufort, D., Rigault, C., Billon, S., Billault, V., Inoue, A., Inoue, S., Patrier, P., 2015. Chlorite and chloritization processes through mixed-layer mineral series in low-temperature geological systems – a review. *Clay Miner.* 50:497–523. <https://doi.org/10.1180/claymin.2015.050.4.06>.
- Benderitter, Y., Tabbagh, A., Elsass, P., 1995. Calcul de l'effet thermique d'une remontée hydrothermale dans le socle fracturé. Application à l'anomalie géothermique de Soultz-sous-Forêts (Nord Alsace). *Bull. Soc. Geol. Fr.* 1, 37–48.
- Bradford, J., McLennan, J., Moore, J., Glasby, D., Waters, D., Kruwells, R., Bailey, A., Rickard, W., Bloomfield, K., King, D., 2013. Recent developments at the Raft River geothermal field. *Proceedings of Thirty-Eighth Workshop on Geothermal Reservoir Engineering*. Stanford University, California, USA.
- Brindley, G.W., Brown, G., 1980. X-ray Diffraction procedures for clay mineral identification. In: Brindley, G.W., Brown, G. (Eds.), *Crystal Structures of Clay Minerals and Their X-Ray Identification*, pp. 305–360 London, Great Britain.
- Browne, P.R.L., Ellis, A.J., 1970. The Ohaki-Broadlands hydrothermal area, New Zealand: mineralogy and related geochemistry. *Am. J. Sci.* 269:97–131. <https://doi.org/10.2475/ajs.269.2.97>.
- Clauer, N., Liewig, N., Ledésert, B., Zwingmann, H., 2008. Thermal history of Triassic sandstones from the Vosges Mountains-Rhine Graben rift area, NE France, based on K-Ar illite dating. *Clay Miner.* 43:363–379. <https://doi.org/10.1180/claymin.2008.043.3.03>.
- Davatzes, N.C., Hickman, S.H., 2005. Controls on fault-hosted fluid flow: Preliminary results from the Coso Geothermal Field, CA. In: *Geothermal Resources Council Transactions* (Ed.), Geothermal Resources Council, Davis, California, pp. 343–348.
- Flexser, S., 1991. Hydrothermal alteration and past and present thermal regimes in the western moat of Long Valley caldera. *J. Volcanol. Geotherm. Res.* 48:303–318. [https://doi.org/10.1016/0377-0273\(91\)90048-5](https://doi.org/10.1016/0377-0273(91)90048-5).
- Fouillac, A.M., Genter, A., 1992. An O, D, C isotopic study of water/rock interactions in the sSoultz-sous-Forêts granite. Drillhole GPK-1, HDR Site, Alsace. In: Bresee, James C.

- (Ed.), *Geothermal Energy in Europe - The Soultz Hot Dry Rock Project*, pp. 105–117 Montreux, Switzerland.
- Genter, A., 1989. *Géothermie roches chaudes sèches: le granite de Soultz-sous-Forêts (Bas-Rhin, France). Fracturation naturelle, altérations hydrothermales et interaction eau-roche*. (PhD thesis). Université d'Orléans, France.
- Genter, A., Traineau, H., 1992. Hydrothermally altered and fractured granite as an HDR reservoir in the EPS-1 borehole, Alsace, France. *Proceedings of Seventeenth Workshop on Geothermal Reservoir Engineering*. Stanford University, California, USA.
- Genter, A., Evans, K., Cuenot, N., Fritsch, D., Sanjuan, B., 2010. Contribution of the exploration of deep crystalline fractured reservoir of Soultz to the knowledge of enhanced geothermal systems (EGS). *Compt. Rendus Geosci.* 342:502–516. <https://doi.org/10.1016/j.crte.2010.01.006>.
- Geoportail of EU-Project GeORG - INTERREG IV Upper Rhine. [WWW Document]. <http://www.geopotenziale.org>, Accessed date: 14 April 2016.
- Harvey, C.C., Browne, P.R.L., 1991. Mixed-layer clay geothermometry in the Wairakei geothermal field, New Zealand. *Clay Clay Miner.* 39:614–621. <https://doi.org/10.1346/ccmn.1991.0390607>.
- Hooijkaas, G.R., Genter, A., Dezayes, C., 2006. Deep-seated geology of the granite intrusions at the Soultz EGS site based on data from 5 km-deep boreholes. *Geothermics* 35:484–506. <https://doi.org/10.1016/j.geothermics.2006.03.003>.
- Jacquemont, B., 2002. *Etude des interactions eaux-roches dans le granite de Soultz-sous-Forêts; Quantification et modélisation des transferts de matière par les fluides*. (PhD thesis). Université de Strasbourg, France.
- Kubler, B., 1968. Evaluation quantitative du métamorphisme par la cristallinité de l'illite: Etat des progrès réalisés ces dernières années. *Bull. Cent. Rech. Pau-SNPA* 2, 385–397.
- Lanson, B., Beaufort, D., Berger, G., Petit, S., Lachapagne, J.-C., 1995. Evolution of clay minerals crystallographic structure in the dutch Rotliengende sandstone reservoir. *Bull. Centres Rech. Explor. Prod. Elf-Aquitaine* 19, 243–265.
- Ledésert, B., Berger, G., Meunier, A., Genter, A., Bouchet, A., 1999. Diagenetic-type reactions related to hydrothermal alteration in the Soultz-sous-Forêts Granite, France. *Eur. J. Mineral.* 11:731–741. <https://doi.org/10.1127/ejm/11/4/0731>.
- López-Munguira, A., Nieto, F., Morata, D., 2002. Chlorite composition and geothermometry: a comparative HRTEM/AEM-EMPA-XRD study of Cambrian basic lavas from the Ossa Morena Zone, SW Spain. *Clay Clay Miner.* 37:267–281. <https://doi.org/10.1180/0009855023720033>.
- Lowell, J.D., Guilbert, J.M., 1970. Lateral and vertical alteration-mineralization zoning in porphyry ore deposits. *Econ. Geol.* 65:373–408. <https://doi.org/10.2113/gsecongeo.65.4.373>.
- Mas, A., Patrier, P., Beaufort, D., Genter, A., 2003. Clay-mineral signatures of fossil and active hydrothermal circulations in the geothermal system of the Lamentin Plain, Martinique. *J. Volcanol. Geotherm. Res.* 124:195–218. [https://doi.org/10.1016/S0377-0273\(03\)00044-1](https://doi.org/10.1016/S0377-0273(03)00044-1).
- Mas, A., Guisseau, D., Patrier Mas, P., Beaufort, D., Genter, A., Sanjuan, B., Girard, J.P., 2006. Clay minerals related to the hydrothermal activity of the Bouillante geothermal field (Guadeloupe). *J. Volcanol. Geotherm. Res.* 158:380–400. <https://doi.org/10.1016/j.jvolgeores.2006.07.010>.
- Patrier, P., Papapanagiotou, P., Beaufort, D., Traineau, H., Bril, H., Rojas, J., 1996. Role of permeability versus temperature in the distribution of the fine (<0.2 μm) clay fraction in the Chipilapa geothermal system (El Salvador, Central America). *J. Volcanol. Geotherm. Res.* 72:101–120. [https://doi.org/10.1016/0377-0273\(95\)00078-X](https://doi.org/10.1016/0377-0273(95)00078-X).
- Pribnow, D., Clauser, C., 2000. Heat and fluid flow at the Soultz Hot Dry Rock system in the Rhine Graben. *Proceedings of World Geothermal Congress 2000. Kyushu - Tohoku, Japan*.
- Pribnow, D., Schellschmidt, R., 2000. Thermal tracking of upper crustal fluid flow in the Rhine graben. *Geophys. Res. Lett.* 27.
- Reyes, A.G., 1990. Petrology of Philippine geothermal systems and the application of alteration mineralogy to their assessment. *J. Volcanol. Geotherm. Res.* 43:279–309. [https://doi.org/10.1016/0377-0273\(90\)90057-M](https://doi.org/10.1016/0377-0273(90)90057-M).
- Sanjuan, B., Millot, R., Dezayes, C., Brach, M., 2010. Main characteristics of the deep geothermal brine (5 km) at Soultz-sous-Forêts (France) determined using geochemical and tracer test data. *Compt. Rendus Geosci.* 342:546–559. <https://doi.org/10.1016/j.crte.2009.10.009>.
- Sanjuan, B., Millot, R., Ásmundsson, R., Brach, M., Giroud, N., 2014. Use of two new Na/Li geothermometric relationships for geothermal fluids in volcanic environments. *Chem. Geol.* 389:60–81. <https://doi.org/10.1016/j.chemgeo.2014.09.011>.
- Sanjuan, B., Millot, R., Innocent, C., Dezayes, C., Scheiber, J., Brach, M., 2016. Major geochemical characteristics of geothermal brines from the Upper Rhine Graben granitic basement with constraints on temperature and circulation. *Chem. Geol.* 428:27–47. <https://doi.org/10.1016/j.chemgeo.2016.02.021>.
- Schellschmidt, R., Clauser, C., 1996. The thermal regime of the Upper Rhine Graben and the anomaly at Soultz. *Z. Für Angew. Geol.* 42, 40–44.
- Schleicher, A.M., Warr, L.N., Kober, B., Laverret, E., Clauser, N., 2006. Episodic mineralization of hydrothermal illite in the Soultz-sous-Forêts granite (Upper Rhine Graben, France). *Contrib. Mineral. Petrol.* 152:349–364. <https://doi.org/10.1007/s00410-006-0110-7>.
- Teklemariam, M., Battaglia, S., Gianelli, G., Ruggieri, G., 1996. Hydrothermal alteration in the Aluto-Langano geothermal field, Ethiopia. *Geothermics* 25:679–702. [https://doi.org/10.1016/S0375-6505\(96\)00019-3](https://doi.org/10.1016/S0375-6505(96)00019-3).
- Thomasson, J., Kristmannsdottir, H., 1972. High temperature alteration minerals and thermal brines, Reykjanes, Iceland. *Contrib. Mineral. Petrol.* 36:123–134. <https://doi.org/10.1007/bf00371183>.
- Traineau, H., Genter, A., Cautru, J.-P., Fabriol, H., Chèvremont, P., 1992. *Petrography of the granite massif from drill cutting analysis and well log interpretation in the geothermal HDR borehole GPK-1 (Soultz, Alsace, France)*. In: Bresee, James C. (Ed.), *Geothermal Energy in Europe - The Soultz Hot Dry Rock Project*, pp. 1–29 Montreux, Switzerland.
- Vidal, J., Genter, A., Schmittbuhl, J., 2016a. Pre- and post-stimulation characterization of geothermal well GRT-1, Rittershoffen, France: insights from acoustic image logs of hard fractured rock. *Geophys. J. Int.* 206:845–860. <https://doi.org/10.1093/gji/ggw181>.
- Vidal, J., Ulrich, M., Whitechurch, H., Genter, A., Schmittbuhl, J., Dalmis, E., Girard-Berthet, V., 2016b. Hydrothermal Alteration of the Hidden Granite in the Geothermal Context of the Upper Rhine Graben. *Proceedings of Forty-First Workshop on Geothermal Reservoir Engineering*. Stanford University, California, USA.
- Vidal, J., Genter, A., Chopin, F., 2017. Permeable fracture zones in the hard rocks of the geothermal reservoir at Rittershoffen, France. *J. Geophys. Res. Solid Earth* 122. <https://doi.org/10.1002/2017JB014331>.



## APPENDIX 3

### Extended Abstract

The Appendix 3 present the preliminary work conducted on the Illkirch GIL-1 well that was accepted for presentation at the *World Geothermal Congress 2020*. This work is the preliminary mineralogical characterization of the granitic basement of the GIL-1 well, then completed and submitted to Minerals Journal.

Glaas, C., Patrier, P., Vidal, J., Beaufort, D., Girard, J.-F., Genter, A., 2021. Hydrothermal alteration in the new deep geothermal well GIL-1 (Strasbourg area, France). Presented at the World Geothermal Congress 2020, Reykjavik, 11.



## Hydrothermal Alteration in the New Deep Geothermal Well GIL-1 (Strasbourg Area, France)

Carole Glaas<sup>1,2</sup>, Patricia Patrier<sup>3</sup>, Jeanne Vidal<sup>1,4</sup>, Daniel Beaufort<sup>3</sup>, Jean-François Girard<sup>2</sup>, Albert Genter<sup>1</sup>

<sup>1</sup>ES-Géothermie, Bat Le Belem 5 rue de Lisbonne, 67300 Schiltigheim, France, <sup>2</sup>University of Strasbourg, CNRS, UMR 7516 IPGS, 5 Rue René Descartes, 67084 Strasbourg Cedex, France, <sup>3</sup>University of Poitiers, CNRS UMR 7285 IC2MP, HydrASA, Bat B8 rue Albert Turpain, TSA51106, F-86073 Poitiers Cedex 9, France, <sup>4</sup>University of Chile, FCFM, Dept. of Geology, Andean Geothermal Center of Excellence (CEGA), Plaza Ercilla 803, Santiago, Chile

[carole.glaas@es.fr](mailto:carole.glaas@es.fr)

**Keywords:** illite, clay minerals, fracture zone, granitic reservoir, X-ray diffraction (XRD), Short Wave Infrared (SWIR), Illkirch, Upper Rhine Graben (URG)

### ABSTRACT

The first geothermal well of Illkirch located South of Strasbourg (France), GIL-1, has been drilled to 3.8 km deep in a granitic basement. Drill cuttings and geophysical logs from basement were investigated in terms of hydrothermal alteration and natural fractures respectively. Petrographic observations of the 250 cuttings samples between 2900 and 3800 m MD were conducted on-site during the drilling with binocular loupe and enabled to identify the hydrothermal alteration grades in the open-hole granitic section of the well. From binocular examination, secondary minerals like drusy quartz, carbonates and anhydrite were spatially correlated to the occurrences of natural fractures. In the granitic section corresponding to propylitic alteration, phyllosilicates include primary biotite, muscovite and secondary chlorite. Then, 48 cuttings samples were analyzed by X-ray diffraction (XRD) to identify the secondary clay mineralogy corresponding to poorly crystallized illite (PCI) and illite-rich illite-smectite mixed layers (I/S ML) which generally takes place within fractured zones (FZs). Mud logging and geophysical logs acquired in the granitic section of GIL-1 well have been used for characterizing fracture location (calimetry, temperature log) and fracture orientation (electrical image logs). The granitic section of the well is characterized by a dense network of natural fractures. From 2900 to 3300 m MD, about 220 electrical conductive fractures have been observed on the image logs. From temperature logs, three main permeable zones have been identified and correlated with the occurrences of natural conductive fractures. From 2900 to 3200 m MD, the clay signature is mainly governed by the occurrences of PCI and I/S ML which are correlated to permeable FZs. In the deepest part of the granitic section, secondary chlorite and possible secondary well crystallized illite (WCI) have been observed. In parallel, an innovative short-wave infrared (SWIR) spectroscopy method was developed for characterization of clay minerals in those fractured reservoirs. It was first applied to the granitic section of the Soultz and Rittershoffen geothermal wells (Alsace, France). This time-saving method allows the quantification of illitic hydrothermal alteration and indirectly the recognition of permeable FZs. In perspective, SWIR data acquired in GIL-1 will also be analyzed in order to confirm the applicability of this routine and cheap method for deep geothermal well in the Upper Rhine Graben (URG).

### 1. INTRODUCTION

Since more than 30 years, a geothermal rush was observed in the Upper Rhine Graben (URG). The pioneer project of Soultz-sous-Forêts investigated the naturally fractured granitic reservoir within four geothermal deep wells (5 km). The nearby Rittershoffen project took then advantage of the lessons learned from Soultz by drilling two deep geothermal wells (3km) in the granitic basement targeting the multiscale network of fractures. Two more geothermal projects are under drilling operations in the Strasbourg area, in Vendenheim and in Illkirch. This contribution focuses on the preliminary geological results (petrography, secondary mineralogy, natural fractures) collected in the granitic section of the Illkirch GIL-1 well drilled to 3.8 km. The mid-Carboniferous granitic basement of the URG has been affected by several extensional and compressional tectonic phases which developed a multi-scale fracture network (Schumacher, 2002; Villemin and Bergerat, 1987). In deep geothermal projects, the target is to cross these natural fracture zones (FZs) which are today the seat of hydrothermal circulations and act as the main pathways for the natural brine through wide convection cells (Baillieux et al., 2013; Dezayes and Lerouge, 2019; Schellschmidt and Clauser, 1996). At the top of the highly fractured granitic basement, several temperature anomalies localized along the main faults are the expression of the fluid circulation in the FZs (Figure 1). In these complex FZs, specific mineralogical assemblages are evidences of paleo or present hydrothermal circulations. Clay minerals like illite, chlorite and tosudite are very sensitive to the fluid/rock (F/R) ratio, to the pH and to the temperature and are systematically precipitated in FZs (Ledésert et al., 2010). But the occurrence of other secondary minerals like drusy quartz, carbonates, barite, and anhydrite is also associated to fracture infillings (Smith et al., 1998; Traineau et al., 1992). Hence, this study will investigate the alteration mineralogy in the granitic section of the deviated GIL-1 well drilled between 2.9 and 3.8 km. Alteration mineralogy from about 250 cuttings will be derived from petrographic observation with binocular loupe and with X-ray diffraction (XRD). These petrographic results will be linked to the FZs occurrences on the electrical image logs. The goal will be to identify the clay signature of FZs in the granitic basement. These preliminary results aim to calibrate the short-wave infrared (SWIR) data acquired in the GIL-1 well. This innovative SWIR method already demonstrated its applicability to the granitic basement of the URG with the Soultz and Rittershoffen case studies whose examples will also be presented (Glaas et al., 2019; Vidal et al., 2018a).

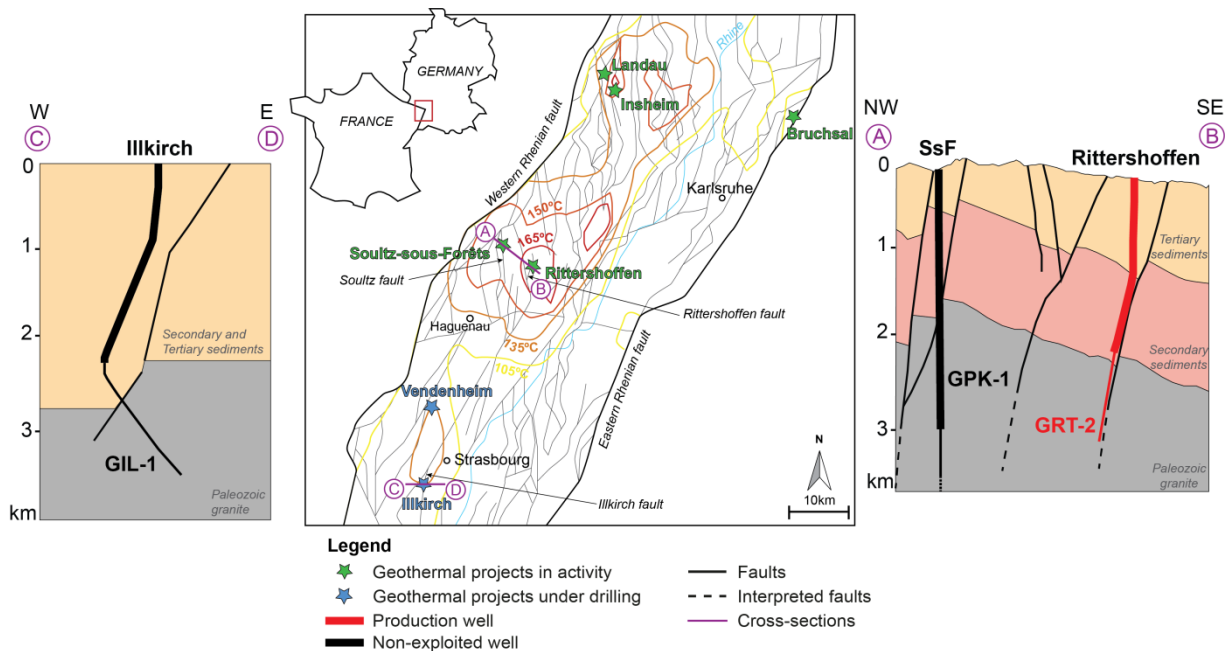


**Figure 1:** Structural map of the center of the Upper Rhine Graben with isotherms at 2 km depth after Vidal et al., (2019) and the geoportail GeOrg (GeOrg, 2017). The geothermal anomaly in the Strasbourg area is from the dataset of Baillieux et al., (2013). On the left: W-E cross section through the geothermal well of the Illkirch geothermal well with a simplified geology. On the right: NW-SE cross-section through the geothermal wells of Soutz and Rittershoffen. The thick line represents the casing section of the well, whereas the thin one represents the open hole.

## 2. GEOLOGICAL SETTING

### 2.1 The fractured and altered granitic basement in the URG

All the deep wells drilled into the granitic basement of Soutz and Rittershoffen provide a wide knowledge of the multiscale fracture network intersected (Dezayes et al., 2010; Genter and Traineau, 1996; Sausse and Genter, 2005). Core samples available at Soutz show small-scale fractures with no evidence of displacement, filled by carbonates, chlorite, iron oxides, epidote and sulphides. Intersections of faults were also observed with a filling of drusy quartz, carbonates, barite and clay minerals. Nowadays, in the URG, the target for geothermal projects is the permeable FZs lying in the first hundred meters of the hydrothermally altered granitic reservoir (Vidal and Genter, 2018). Investigation of the alteration parageneses could be a good indicator of the paleo and present-day circulations in the well and thus, of the localization of the permeable FZs intersected. During the cooling of the crystalline pluton, the granite underwent a pervasive alteration which presents the petrographic and mineralogical features of the propylitic facies. Today, it exhibits several grades of hydrothermal alteration related to fluid circulation in natural fractures (Ledésert et al., 2010; Traineau et al., 1992). The unaltered crystalline granitic basement at Rittershoffen and Soutz-sous-Forêts geothermal sites (located tens of kms North of Strasbourg) is composed of primary muscovite, biotite, K-feldspar, plagioclase, and quartz (Stussi et al., 2002; Traineau et al., 1992). This primary mineralogy is affected by hydrothermal alteration, and specific mineralogical associations are reflecting the several alteration grades encountered. According to the previous studies on the Soutz-sous-Forêts geothermal wells, the hydrothermal alteration grades in the granite are well known from core observations (Ledésert et al., 1999; Meller et al., 2014; Meller and Kohl, 2014; Meller and Ledésert, 2017; Sausse et al., 2006; Traineau et al., 1992). The core mineralogy and hydrothermal alteration grades were then cross-referenced with the minerals observed in the cuttings at Rittershoffen, although the texture information and the mineral assemblage were not reflected in the cuttings (Figure 2). The low hydrothermal alteration (HLOW) grade is characterized by more chlorite than primary biotite, the absence or minor amount of secondary illite, and unaltered primary plagioclase and K-feldspars. The moderate hydrothermal alteration (HMOD) grade is characterized by the presence of illite due to the further alteration of chlorite, plagioclase and K-feldspar (weakly altered); fresh and weakly altered biotite is observed in minor amounts. The high hydrothermal alteration (HHIG) grade is associated with abundant illitic material, very low amounts of chlorite, strongly altered plagioclase and K-feldspar, and relics of altered biotite. The extreme hydrothermal alteration (HEXT) grade is characterized by the total depletion of biotite, abundant illitic material replacing primary biotite, plagioclase and K-feldspar, as well as drusy quartz prisms linked to hydrothermal circulation (Genter et al., 1997; Nishimoto and Yoshida, 2010; Traineau et al., 1992). The VEIN facies defines the core of the fracture zone identified by the highest amounts of secondary drusy quartz and its association with a high calcite content (Hébert et al., 2010; Ledésert et al., 2009). The granitic facies identified in the cuttings include an “unaltered” granite (GRAN), which is characterized by the presence of biotite, hematite, calcite, and affected by a propylitic alteration related to the cooling of the pluton (Genter et al., 2000; Jacquemont, 2002), and locally reddish granite (RED), which contains a large amount of red K-feldspar megacrysts oxidized through intense exposure to weathering fluids. In Soutz and Illkirch the GRAN shows facies variations with high amounts of muscovite named two-mica granite (GR2M) (Cocherie et al., 2004). The presence of illite in the granitic basement as a major signature of hydrothermal alteration was also confirmed by complementary laboratory analyses. In previous studies on the Rittershoffen wells, (XRD) was performed on the <5  $\mu\text{m}$  fraction of selected cuttings, from which three groups of illitic minerals (well-crystallized illite (WCI), poorly crystallized illite (PCI), and illite-rich illite/smectite mixed layers (I/S ML)) were identified (Vidal et al., 2018b). The chemical compositions of the clay minerals were obtained using a scanning electron microscope (SEM) coupled with energy-dispersive X-ray spectroscopy (EDS). This study showed that permeable FZs were associated with the occurrence of poorly PCI

and I/S ML crystallized during hydrothermal circulation (Vidal et al., 2018b). XRD measurements in the Soultz wells also evidenced the presence of illite in fractured and altered zones as well as the presence of chlorite and biotite in HLOW and GRAN.

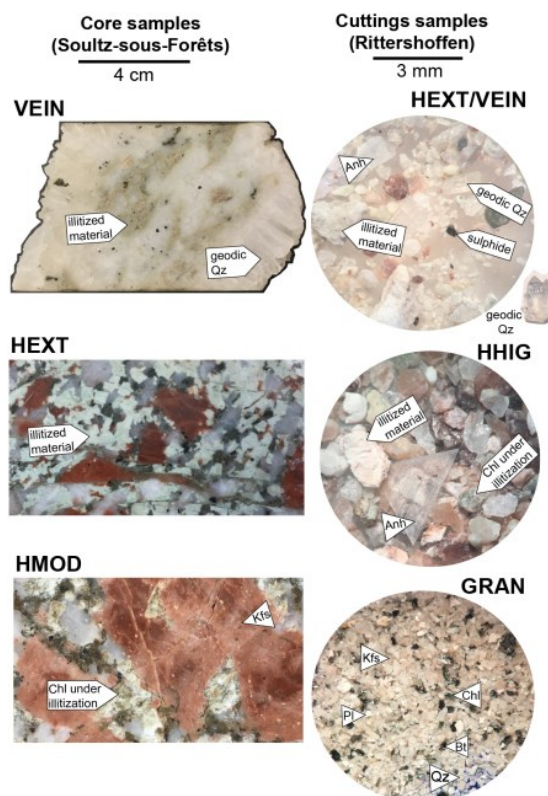


**Figure 2:** Examples of mineralogical assemblages of the granitic basement observed in cores (left) and observed in cuttings (right), defining the several hydrothermal alteration grades from Glaas et al., (2019). GRAN: unaltered granite, HMOD: moderately hydrothermally altered granite, HHIG: highly hydrothermally altered granite, HEXT: extremely hydrothermally altered granite, VEIN: secondary drusy quartz vein.

## 2.2 Illkirch site

The main objective of this geothermal project is to generate electricity and to supply yearly about 50 GWh of heat to a neighboring district heating network in the suburb of Strasbourg. Exploration works were carried out between 2013 and 2016: gravimetric surveys, aeromagnetic survey, reprocessing of vintage 2D seismic data, new 2D seismic data acquisition (35k m in 2015) and all available data, including numerous oil and geothermal exploration well data, which could be integrated to get a detailed picture of the deep underground around the project's location (Edel et al., 2018; Richard et al., 2016). The defined geothermal target was a major fault zone with a normal off-set of 800 m located at the interface between sedimentary cover (clastic Triassic sandstone) and crystalline basement (Figure 1). Expected temperature is 150°C with a nominal flow rate of 70 l/s. The drilling of the first deviated well GIL-1 ended in July 2019 at the total depth of 3.8 km. The GIL-1 well reached the top basement at 2.9 km which corresponds to the target fault zone oriented N20°E and dipping, 70°W from electrical image logs.

## 3. MATERIALS AND METHODS

### 3.1 Materials

The cuttings (chip samples) collected during the drilling of the wells are first washed and then dried on-site. Depending on the well section and on the sampling distance of the cuttings, the sample will represent a variable volume of rock (Table 1). The average size of the cutting grains varies between 0.5 and 2 mm in each sample. This cuttings grain size can be highly influenced by the drilling tool wearing and thus could influence the SWIR absorption feature.

**Table 1:** various rock volumes represented by the cuttings samples for different sections of the GIL-1 well.

well	section	depth interval	sampling distance	volume of rock
GIL-1	8"1/2	2894-3324mMD	5m	160L
	6"	3324-2694mMD	5m	90L

### 3.2 Methods

This petrographic study is based on a multi-approach methodology correlating datasets with different scales from sample to drill hole scale and various techniques (Figure 3). This methodology is about to be applied to the GIL-1 well, where the binocular loupe observations and XRD analyses were already performed. Electrical image logs were also acquired and this study will focus on the first part of the methodology presented in the Figure 3 by correlating the results from these methods before interpreting the SWIR results.

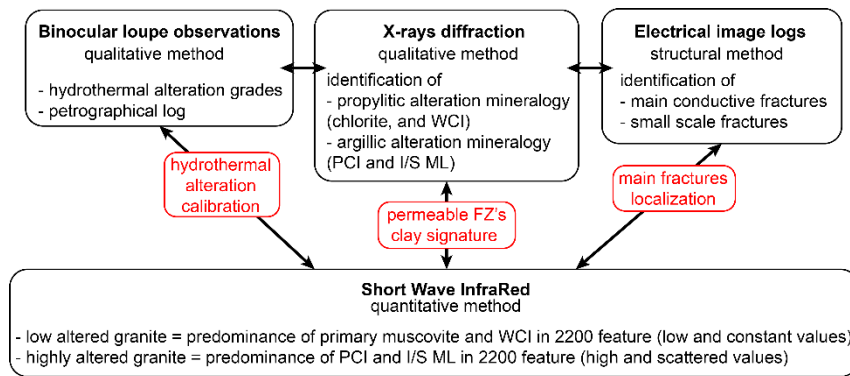


**Figure 3: Workflow used for characterizing hydrothermal mineralogy in the granitic basement of URG geothermal wells. Abbreviations: well crystallized illite (WCI), poor crystallized illite (PCI), illite-smectite mixed layers (I/S ML).**

### 3.2.1 X-ray diffraction method

XRD was made on selected cuttings samples of the GIL-1 well to identify clay minerals. In total, 48 cuttings samples were collected from the GIL-1 well. The sampling was concentrated in the permeable and altered FZs but also in the GRAN and GR2M which serve as reference materials as it is believed to be representative of rocks preserved from actual fluid circulation properties. 15 samples were prepared as disoriented powders of the bulk rock to analyze the whole rock mineralogy. The cuttings were grinded using a ring and agate mills. Analyses were carried out on a Phillips diffractometer (CuK $\alpha$  radiation, 40kV, 40mA). The analytical conditions were as follow: angular domain: 2-65° 2 $\theta$ ; step increment: 0.0235 2 $\theta$  and counting time per step: 0.90 s. Then, 48 samples including the 15 samples that were analyzed for bulk rock mineralogy were dispersed in distilled water by ultrasonic vibration without any preliminary grinding to avoid contamination of the <5 $\mu$ m fraction by primary micas. Oriented powders were prepared from the <5 $\mu$ m fraction size separated from suspension in water by sedimentation. Clay minerals were identified by XRD of air-dried (AD) and ethylene-glycol (EG)-saturated oriented powders carried out on a Phillips diffractometer (CuK $\alpha$  radiation, 40kV, 40mA). The analytical conditions were as follow: angular domain: 2-35° 2 $\theta$ ; step increment: 0.0235 2 $\theta$  and counting time per step: 0.73 s. XRD data acquisition and treatment were conducted using the X'Pert HighScore software (PANalytical B.V.). The clay minerals were identified according to the literature (Brindley and Brown, 1980; Moore and Reynolds, 1997). In this study, we measure the full width at half maximum (FWHM) and intensities of the 7 Å and 10 Å reflections as well as the ratio between the intensity of the d<sub>002</sub> and the d<sub>001</sub> reflections (noted I<sub>002</sub>/I<sub>001</sub>) on the oriented powders diffractograms. The 10 Å reflection observed on the diffractograms is in our study the integration of the intensities diffracted by the micas and illitic minerals (illite and illite-rich I/S ML). However, it is possible to identify the dominant phyllosilicate from the following parameters.

- The ratio I<sub>002</sub>/I<sub>001</sub> is lower than 0,10 for trioctahedral micas (biotite), whether dioctahedral clays (muscovite and illite) will have a ratio between 0,37 and 0,55.

- The FWHM of the 10 Å reflection enables to differentiate the contribution between muscovite and illite: higher the FWHM, lower the crystallinity along the c axis. The muscovite presents a FWHM lower than the one of illite (Figure 4).

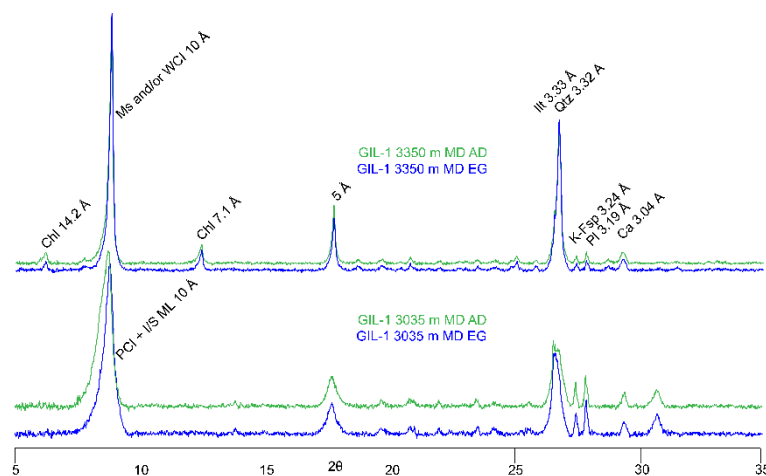


**Figure 4: XRD results in the GIL-1 well of oriented samples of the fraction <5  $\mu$ m from GIL-1. Comparison between air dried (AD) and ethylene-glycol (EG) conditions. The sample at 3035 m MD presents a predominance of illite-rich illite-smectite mixed layers (I/S ML) and poor crystallized illite (PCI) whereas the sample at 3350 m MD presents a predominance of muscovite and/or well crystallized illite (WCI).**

### 3.2.2 Temperature anomalies

Temperature (T) anomalies are interpreted as the signature of circulations between the well and the formation (Barton et al., 1995; Bradford et al., 2013; Davatzes and Hickman, 2005; Vidal et al., 2019). In the case of T profiles acquired at equilibrium and computing negative and positive T anomalies, positive anomalies are interpreted as open FZs where hotter brine than the formation

circulates, whereas negative anomalies are interpreted as open FZs where colder water than the formation circulates (Vidal et al., 2019). In the GIL-1 well, the T profiles were not acquired at equilibrium but 12 hours after injection. This implies that the open FZs are cooled by the injected fluid inducing only negative T anomalies. Thus, in the GIL-1 well, only the localized depth sections of the T anomalies were represented in the Figure 5, showing in blue sections the occurrence of T anomalies.

### 3.2.3 Electrical image logs

Image logs have been intensively used in the Soultz and Rittershoffen wells mainly with acoustic logs (Genter et al., 1995; Vidal et al., 2019). The open-hole section of the GIL-1 well was completely imaged by electrical image logs. Composed of 8 pads the electrical imager tool measures the resistivity of the borehole wall providing an unwrapped image of the borehole wall. On this unwrapped image, sinusoids are the trace of natural conductive fractures. A low conductivity is expressed by light colours (yellow to white) whereas a high conductivity is expressed by darkest colours (black). In the data presented in this study (Figure 6), the static image on the left is normalized over the complete depth interval of the well and thus the contrast responds to large-scale variations in lithology, porosity and saturation whereas the dynamic image on the right is normalized using a sliding window of 0.5 m; this highlights small-scale variations in contrast due to bedding, fractures, and changes in porosity. In the Figure 5 and Figure 6, very conductive fractures (appearing black on both dynamic and static images) were reported in red dots along depth. As both the very saline brine and the clay minerals are very conductive, a black fracture on both static and dynamic images could even be interpreted as an open fracture with very saline and conductive brine, or as a clogged fracture filled by conductive secondary clay minerals.

## 4. RESULTS: HYDROTHERMAL ALTERATION FACIES AND PERMEABLE FZS IN GIL-1

### 4.1. Petrographical log from binocular loupe observations

The petrographical log of the granitic section of the GIL-1 well is composed of three main zones:

- **2900-3100 m MD.** The first zone, highly altered and fractured, is observed at the top of the granitic basement from 2900 to 3100 m MD (Figure 5). The binocular observations revealed the absence of primary biotite, the presence of illitic material identified by the dusty aspect of the cuttings samples, as well as the occurrence of hematite and small amounts of calcite. Locally, hydrothermal drusy quartz was also observed in this zone at 3012 and 3022 m MD and anhydrite from 3050 to 3100 m MD (Figure 5).
- **3100-3350 m MD.** The second zone, fractured but less altered, is then observed from 3100 to 3350 m MD where primary biotite was commonly observed. The top of this zone from 3100 to 3200 m MD revealed the presence of hydrothermal drusy quartz, anhydrite and hematite, yielding a moderate hydrothermal alteration (HMOD). A small section of low hydrothermally altered granite described as a two-mica granite rich in muscovite is present from 3200 to 3220 m MD (Figure 5).
- **>3350 m MD.** The third zone, from 3350 to 3703 m MD is characterized by low hydrothermal alteration grades and the presence of unaltered two-mica granite clearly visible from 3357 to 3445 m MD and at the bottom from 3683 to 3703 m MD. Biotite, muscovite and chlorite were regularly observed in considerable amounts in these sections. On the contrary, between 3500 and 3650 m MD moderate to high hydrothermal alteration are associated with drusy quartz as well as anhydrite and hematite.

### 4.2 XRD results

The first zone from 2900 to 3100 m MD where illitic material was identified from binocular loupe observations is characterized by the predominance of illite and illite-rich I/S ML. Illite is characterized by the reflections at 10, 5 and 3.33 Å in AD and EG without any shift. Illite-rich I/S ML differ from illite by presenting a slight change of the profile after EG saturation (light blue dots in the Figure 5). FWHM of  $d_{001}$  reflection at 10 Å is scattered between 0.25 and 0.6 °2 $\theta$ .

The second zone from 3100 to 3350 m MD is characterized by the predominance of micas and/or WCI. The FWHM of  $d_{001}$  reflection at 10 Å varies between 0.15 and 0.3 °2 $\theta$ . The ratio  $I_{002}/I_{001}$  of the lower FWHM 10 Å reflections suggests the predominance of biotite (in the <5 $\mu$ m fraction). Its occurrence in the fine fraction can be due to its partial destabilization into chlorite. The  $d_{060}$  at 1.49 Å observed on the disoriented pattern evidences also the occurrence of muscovite in these samples.

The third zone from 3350 to 3700 m MD is quite heterogeneous with occurrence of both illite-rich I/S ML (at 3492 m MD) with a FWHM higher than 0.4 °2 $\theta$  and PCI (at 3582 m MD) with a FWHM close to 0.4 °2 $\theta$  associated with micas/WCI in the fine fraction. This third zone is also characterized by the occurrence of chlorite.

Some supplementary mineralogical analyses are needed to differentiate propylitic chlorite resulting from the alteration of the primary biotite during the cooling of the granitic pluton, from potential ferrous chlorite which could occur in the FZs, as a result of the hydrothermal alteration of the granite (Vidal et al., 2018b).

If we focus on the permeable FZs intersected by the well at 3080, 3225 and 3365 m MD evidenced by T anomalies, different clay properties from the XRD results associated to these T anomalies are observed.

- **T-anomaly at 3050-3090 m MD.** From 3000 to 3100 m MD, the XRDs associated to the T anomaly evidence illitic material characterized by the systematic occurrence of illite-rich I/S ML. This is conveyed by high values of FWHM up to 0.6 °2 $\theta$ .
- **T-anomaly at 3210-3230 m MD.** From 3210 to 3230 m MD, the XRDs associated to the T anomaly evidence illitic material composed of WCI (FWHM up to 0.3 °2 $\theta$ ) associated with primary micas (FWHM close to 0.15 °2 $\theta$ ).

- T-anomaly at 3330-3390 m MD.** From 3300 to 3360 m MD, the XRDs associated to the T anomaly are not presenting the same signature than the two precedents permeable FZs. The FWHM values at 10 Å are homogeneous and very low (0.15 °2θ). The variations the ratio  $I_{002}/I_{001}$  (for the <5µm fraction) and the occurrence of  $d_{060}$  at 1.49 Å suggest the persistence of both di- and trioctahedral micas. These observations could suggest that natural permeability takes also place in fractures cross-cutting low hydrothermally altered granite.

More generally, it is observed that the FWHM of the 10 Å peak at depths of T anomalies are systematically expressed by scattered values. This scattering reflects the presence of illitic material containing +/- illite-rich I/S ML which could indicate changes in the physico-chemical conditions and/or a pulsed system with several generations of clayey material. The presence of illite-rich I/S ML in agreement with the temperatures measured in the drill-hole (minimum 155°C) are probably reflecting the latest stage of argilization related to fluid circulation in the fracture system.

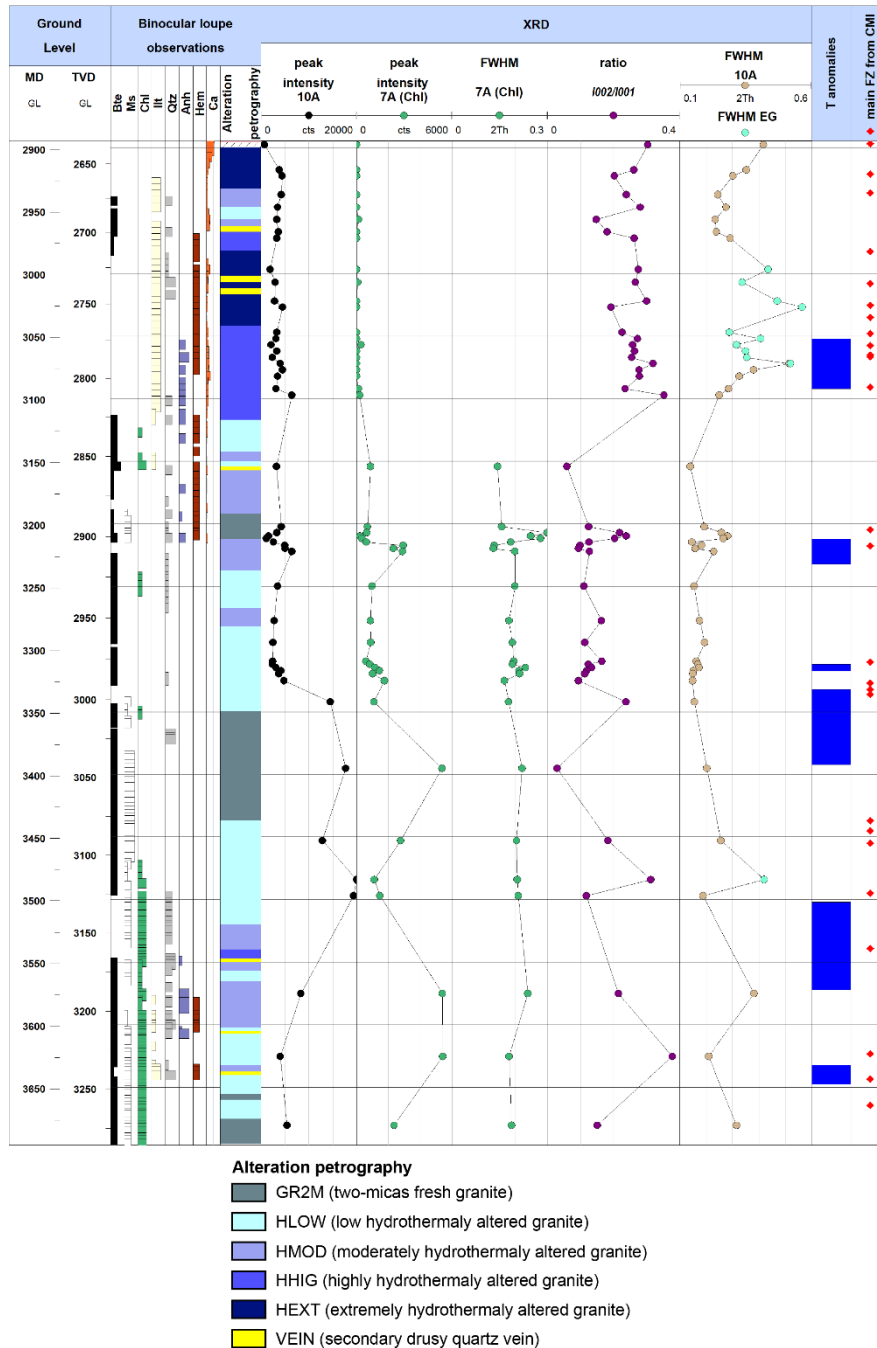


**Figure 5: Composite log from GIL-1 presenting from left to right the alteration mineralogy and the alteration petrography from binocular loupe observation, the XRD results from the oriented fractions < 5 µm, ratios 060/001 and 002/001 are related to the 001 peak at 10 Å and the ratio 060/001 is from disoriented bulk powders. Blue dots in the FWHM at 10 Å are underlying the samples where a shift between the AD and EG diffractograms was observed. T anomalies are from thermal logs realized post injection, in dark blue intense and in light blue less intense T anomalies. Main conductive fractures in red dots (right) were observed on the electrical image logs.**

### 4.3 FZs derived from image logs in GIL-1

About 30 main conductive fractures have been analyzed from electrical image logs in GIL-1. They are not regularly distributed over the well but they are mainly concentrated between 2900-3100 m MD, around 3200 m MD, around 3350 m MD and deeper than 3450 m MD but with a more sparse distribution (Figure 6). T anomalies are located at 3051-3090, 3210-3230, 3330-3390, 3500-3570, and 3630-3645 m MD (Figure 6). These T anomalies systematically correlate with the conductive fractures visible (Figure 6). Surprisingly, all the conductive fractures visible on the electrical image logs do not present T anomalies. This could be explained by the fact that fractures appearing as conductive on both static and dynamic images could be due to the presence of conductive clay minerals which will tend to seal the fracture. For example, the conductive electrical fractures located from the top basement to 3050 m MD, do not match spatially with T log anomalies as well as those located around 3450 m MD (Figure 6).

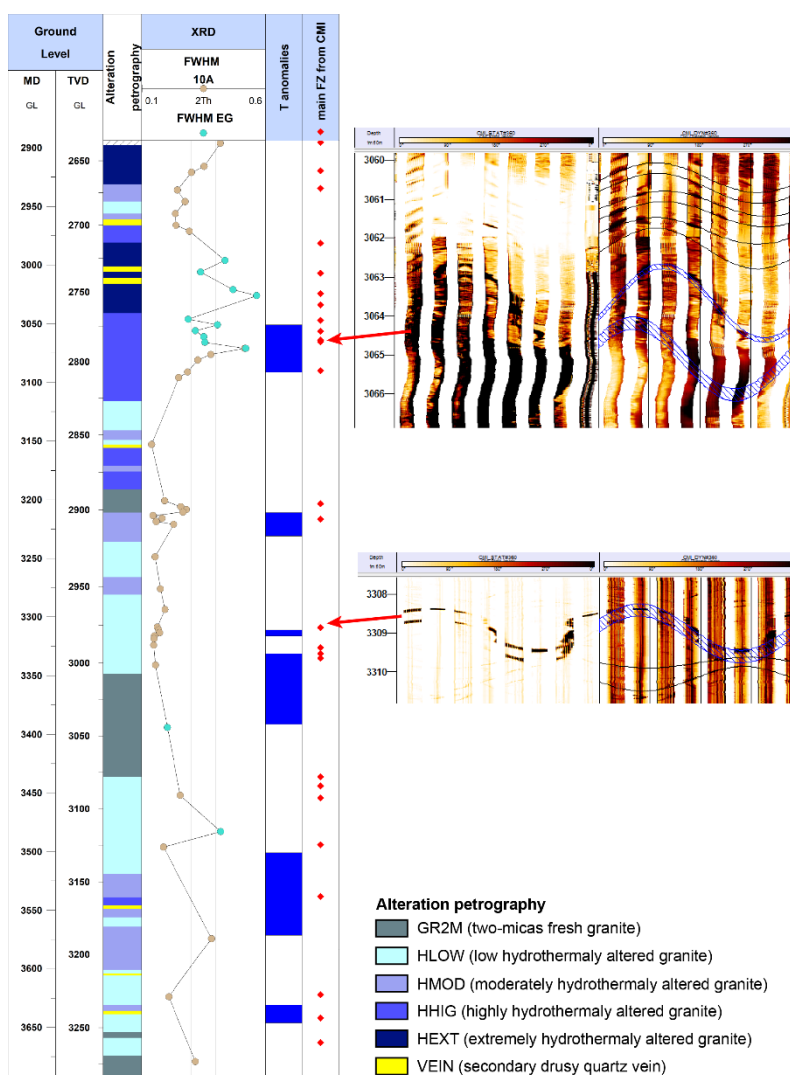


**Figure 6: Composite log of the GIL-1 well presenting the alteration petrography, the FWHM of the 10 Å peak where blue dots in the FWHM at 10 Å are underlying the samples where a shift between the AD and EG diffractograms was observed. T anomalies are from thermal logs realized post injection, in dark blue intense and in light blue less intense T anomalies. Main conductive fractures in red dots (right) were observed on the electrical image logs. Two electrical image show conductive fractures associated to the T anomalies.**

## 5. DISCUSSION

In the granitic part of the GIL-1 well, two main stages of hydrothermal alteration were observed. Outside the FZs, propylitic alteration which corresponds to the cooling of the granitic pluton is observed and characterized by the occurrence of secondary chlorite +/- WCI. This paragenetic association needs to be confirmed by further petrographic observations, nevertheless it is quite common in the Soultz and Rittershoffen granite. This first alteration stage is superimposed by alteration parageneses linked to the fracture network. The most symptomatic secondary minerals associated with permeable reservoirs seem to be located between 2900 and 3100 m MD, where permeable FZs are characterized by PCI and illite-rich I/S ML which display scattered and high values of the 10 Å FWHM. The occurrence of both illite and illite-rich I/S ML traduces changes in the physico-chemical conditions of crystallization. This could be explained by crystallization kinetics linked to variable oversaturation of the fluids, changes in water-rock ratio, or pulsed fluids. The structure of FZs described in Soultz and Rittershoffen wells seems to be encountered in the Illkirch GIL-1 well as well, systematically characterized by secondary drusy quartz in the core zone and clay minerals like illite in the surrounding damage zone. The electrical image logs present a highly fractured granitic basement with a major conductive fracture located at the contact between the sedimentary cover and the granite. Image logs show a dense small-scale fracture network which could present a potential contribution to permeability, especially in the lowest part of the well from 3200 to 3700 m MD.

Conductive fractures are not always associated to T anomalies thus are not always permeable. Temperature signature in GIL-1 must be interpreted more in-depth and carefully until a temperature log at thermal equilibrium is acquired. The limits of the electrical image logs in terms of permeability interpretation also need to be considered. This rich structural dataset needs to be further investigated.

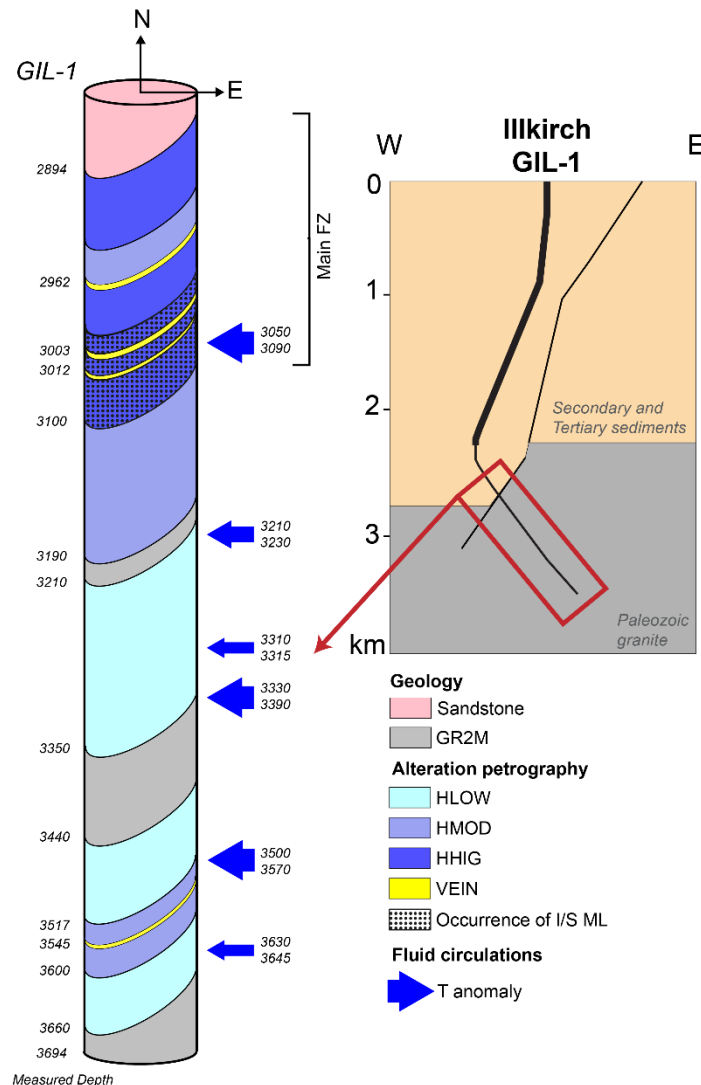


**Figure 7: Conceptual model of hydrothermal alteration from the clay minerals along the granitic open-hole of GIL-1 well.**

## 6. CONCLUSION

The combination of these methods helps to identify the hydrothermal alteration halos associated to the several temperature anomalies in a newly drilled geothermal well in the Strasbourg area. The binocular loupe observation enables to have a global description of the alteration granitic facies in the well, as well as a qualitative petrographic description. The XRD method enables to have a qualitative description of 48 samples in the well to describe the clay signature of the alteration facies observed with the binocular loupe, but also of permeable FZs observed on the T log. In GIL-1, the most permeable structure seems to be located between 2900 and 3100 m MD. The upper part of the well (2900-3100 m MD) is characterized by the occurrence of clay minerals related to vein alteration (PCI, I/S ML). The HLOW zone from 3100-3350 m MD is characterized by the occurrences of clay minerals related to propylitic alteration (chlorite, +/- WCI). The downiest part seems more complex with alternation of HLOW to HHIG associated with the presence of polyphasic illitic material. The clay mineralogy of this zone needs to be further investigated by considering the structural data from electrical image logs.

The next step will be the quantification of the illitisation linked to the fluid circulation in the fracture network. That for, complementary investigations of the clay minerals will be done based on the SWIR data acquired in GIL-1. In Soultz and Rittershoffen wells, this method allowed identifying the alteration halo around the major permeable FZs and gave quantitative information about the illitic material quantity. In the URG granitic context, SWIR spectroscopy is an efficient method to quantify the alteration, once it has been calibrated with other mineralogical analyses like XRD as experienced at Soultz and Rittershoffen. In the Illkirch GIL-1 well, SWIR were acquired on the 250 cuttings samples of the granitic section and their interpretation will be done applying the methodology already used in Soultz and Rittershoffen wells.

The well GIL-1 intersected a dense fracture network composed of major conductive fractures observed on electrical image logs but also clusters of a small-scale conductive fracture network. Investigations of this fracture network are at the preliminary stage and will be deepened in the future in order to better conceptualize the model of circulations at the borehole scale.

## ACKNOWLEDGMENTS

This work was realized in the framework of the PhD of Carole Glaas which is jointly supported by the ANRT (French Agency for Research and Technology) and ES-Géothermie. The authors acknowledge the EGS Alsace project co-funded by ADEME (French Agency for Environment) and ES SA, as well as ESIG, GEIE EMC, ECOGI for providing geoscientific data for Illkirch, Soultz and Rittershoffen respectively.

## REFERENCES

- Baillieux, P., Schill, E., Edel, J.-B., Mauri, G., 2013. Localization of temperature anomalies in the Upper Rhine Graben: insights from geophysics and neotectonic activity. *International Geology Review* 55, 1744–1762. <https://doi.org/10.1080/00206814.2013.794914>
- Barton, C.A., Zoback, M.D., Moos, D., 1995. Fluid flow along potentially active faults in crystalline rock. *Geology* 23, 683–686. [https://doi.org/10.1130/0091-7613\(1995\)023<0683:FFAPAF>2.3.CO;2](https://doi.org/10.1130/0091-7613(1995)023<0683:FFAPAF>2.3.CO;2)
- Baujard, C., Genter, A., Cuenot, N., Mouchot, J., Maurer, V., Hehn, R., Ravier, G., Seibel, O., Vidal, J., 2018. Experience from a successful soft stimulation and operational feedback after 2 years of geothermal power and heat production in Rittershoffen and Soultz-sous-Forêts plants (Alsace, France). Presented at the Geothermal Resource Council, Reno, Nevada, USA, pp. 2241–2252.
- Baujard, C., Genter, A., Dalmais, E., Maurer, V., Hehn, R., Rosillette, R., Vidal, J., Schmittbuhl, J., 2017. Hydrothermal characterization of wells GRT-1 and GRT-2 in Rittershoffen, France: Implications on the understanding of natural flow systems in the Rhine Graben. 65, 255–268pp. <https://doi.org/10.1016/j.geothermics.2016.11.001>
- Bradford, J., McLennan, J., Moore, J., Glasby, D., Waters, D., Kruwells, R., Bailey, A., Rickard, W., Bloomfield, K., King, D., 2013. Recent developments at the Raft River geothermal field. Presented at the Thirty-Eighth Workshop on Geothermal Reservoir Engineering, Stanford University, California, USA.
- Brindley, G.W., Brown, G., 1980. *Crystal Structures of Clay Minerals and their X-Ray Identification*, Mineralogical Society of Great Britain and Ireland.
- Cocherie, A., Guerrot, C., Fanning, C.M., Genter, A., 2004. Datation U–Pb des deux faciès du granite de Soultz (Fossé rhénan, France). *Comptes Rendus Geoscience* 336, 775–787pp. <https://doi.org/10.1016/j.crte.2004.01.009>
- Davatzes, N.C., Hickman, S.H., 2005. Controls on fault-hosted fluid flow; Preliminary results from the Coso Geothermal Field, CA. Presented at the Geothermal Resources Council Transactions, Geothermal Resources Council, Davis, California, pp. 343–348.
- Dezayes, C., Genter, A., Valley, B., 2010. Structure of the low permeable naturally fractured geothermal reservoir at Soultz. *C. R. Geoscience* 342, 517–530. <https://doi.org/10.1016/j.crte.2009.10.002>
- Dezayes, C., Lerouge, C., 2019. Reconstructing Paleofluid Circulation at the Hercynian Basement/Mesozoic Sedimentary Cover Interface in the Upper Rhine Graben. *Geofluids* 2019, 1–30. <https://doi.org/10.1155/2019/4849860>
- Edel, J.B., Maurer, V., Dalmais, E., Genter, A., Richard, A., Letourneau, O., Hehn, R., 2018. Structure and nature of the Palaeozoic basement based on magnetic, gravimetric and seismic investigations in the central Upper Rhinegraben: Focus on the deep geothermal project of Illkirch-Graffenstaden. *Geothermal Energy* 6. <https://doi.org/10.1186/s40517-018-0099-y>
- Garnish, J.D., 1985. Hot Dry Rock - A European perspective. *GRC Hawaiï*.
- Genter, A., Evans, K., Cuenot, N., Fritsch, D., Sanjuan, B., 2010. Contribution of the exploration of deep crystalline fractured reservoir of Soultz to the knowledge of enhanced geothermal systems (EGS). *Comptes Rendus Geoscience* 342, 502–516. <https://doi.org/10.1016/j.crte.2010.01.006>
- Genter, A., Traineau, H., 1996. Analysis of macroscopic fractures in granite in the HDR geothermal well EPS-1, Soultz-sous-Forêts, France. *Journal of Volcanology and Geothermal Research* 121–141.
- Genter, A., Traineau, H., Artignan, D., 1997. Synthesis of geological and geophysical data at Soultz-sous-Forêts (France) (No. 39440). BRGM, Orléans, France.
- Genter, A., Traineau, H., Dezayes, C., Elsass, P., Ledéser, B., Meunier, A., Villemin, T., 1995. Fracture Analysis and Reservoir Characterization of the Granitic Basement in the HDR Soultz Project (France). *Geotherm. Sci. & Tech.* 4, 189–214.
- Genter, A., Traineau, H., Ledéser, B., Bourguin, B., Gentier, S., 2000. Over 10 years of geological investigations within the HDR Soultz project, France. Presented at the World Geothermal Congress, Kyushu, Japan, pp. 3707–3712.
- GeOrg, T., 2017. EU-Projekt GeORG - Geoportail [WWW Document]. URL <http://www.geopotenziale.org/home?lang=3>
- Gérard, A., Kappelmeyer, O., 1987. The Soultz-sous-Forêts project. *Geothermics* 16, 393–399.
- Gérard, A., Menjot, A., Schwoerer, P., 1984. L'anomalie thermique de Soultz-sous-Forêts. *Géothermie Actualités* 35–42.
- Glaas, C., Genter, A., Girard, J.F., Patrier, P., Vidal, J., 2018. How do the geological and geophysical signatures of permeable fractures in granitic basement evolve after long periods of natural circulation? Insights from the Rittershoffen geothermal wells (France). *Geothermal Energy* 6. <https://doi.org/10.1186/s40517-018-0100-9>
- Glaas, C., Vidal, J., Patrier, P., Beaufort, D., Genter, A., 2019. Contribution of SWIR to the Clay Signature of Permeable Fracture Zones in the Granitic Basement. Overview of Soultz and Rittershoffen wells. Presented at the European Geothermal Congress, Den Haag, The Netherlands, 11-14 June, p. 11.

- Hébert, B., 2018. Approche quantitative par spectrométrie Vis-NIR des minéraux argileux et uranifères dans les sables du gisement de Tortkuduk, Kazakhstan. Université de Poitiers, Poitiers.
- Hébert, R.L., Ledésert, B., Bartier, D., Dezayes, C., Genter, A., Grall, C., 2010. The Enhanced Geothermal System of Soultz-sous-Forêts: A study of the relationships between fracture zones and calcite content. *Journal of Volcanology and Geothermal Research* 196, 126–133. <https://doi.org/10.1016/j.jvolgeores.2010.07.001>
- Hunt, G.L., Salisbury, J.W., 1970. Visible and Near Infrared Spectra of Minerals and Rocks: I. Silicate Minerals. *Modern Geology* 1, 283–300.
- Jacquemont, B., 2002. Etude des interactions eaux-roches dans le granite de Soultz-sous-Forêts. Quantification et modélisation des transferts de matière par les fluides. (PhD). Université de Strasbourg, France.
- Kappelmeyer, O., 1991. European HDR project at Soultz-sous-Forêts general presentation. *Geotherm. Sci. & Tech.* 263–289.
- Ledésert, B., Berger, G., Meunier, A., Genter, A., Bouchet, A., 1999. Diagenetic-type reactions related to hydrothermal alteration in the Soultz-sous-Forêts Granite, France. *European Journal of Mineralogy* 11, 731–741.
- Ledésert, B., Hébert, R., Genter, A., Bartier, D., Clauer, N., Grall, C., 2010. Fractures, hydrothermal alterations and permeability in the Soultz Enhanced Geothermal System. *Comptes Rendus Geoscience* 342, 607–615. <https://doi.org/10.1016/j.crte.2009.09.011>
- Ledésert, B., Hébert, R.L., Grall, C., Genter, A., Dezayes, C., Bartier, D., Gérard, A., 2009. Calcimetry as a useful tool for a better knowledge of flow pathways in the Soultz-sous-Forêts Enhanced Geothermal System. *Journal of Volcanology and Geothermal Research* 181, 106–114. <https://doi.org/10.1016/j.jvolgeores.2009.01.001>
- Madejová, J., Gates, W.P., Petit, S., 2017. IR Spectra of Clay Minerals, in: *Developments in Clay Science*. Elsevier, pp. 107–149. <https://doi.org/10.1016/B978-0-08-100355-8.00005-9>
- Mas, A., Guisseau, D., Patrier, P., Beaufort, D., Sanjuan, B., Girard, J.P., 2006. Clay minerals related to the hydrothermal activity of the Bouillante geothermal field (Guadeloupe). *Journal of Volcanology and Geothermal Research* 158, 380–400.
- Meller, C., Genter, A., Kohl, T., 2014. The application of a neural network to map clay zones in crystalline rock. *Geophysical Journal International* 196, 837–849. <https://doi.org/10.1093/gji/ggt423>
- Meller, C., Kohl, T., 2014. The significance of hydrothermal alteration zones for the mechanical behavior of a geothermal reservoir. *Geothermal Energy* 2. <https://doi.org/10.1186/s40517-014-0012-2>
- Meller, C., Ledésert, B., 2017. Is There a Link Between Mineralogy, Petrophysics, and the Hydraulic and Seismic Behaviors of the Soultz-sous-Forêts Granite During Stimulation? A Review and Reinterpretation of Petro-Hydromechanical Data Toward a Better Understanding of Induced Seismicity and Fluid Flow. *Journal of Geophysical Research: Solid Earth* 122, 9755–9774. <https://doi.org/10.1002/2017JB014648>
- Moore, D.M., Reynolds, R.C., 1997. X-Ray Diffraction and the Identification and Analysis of Clay Minerals.
- Nishimoto, S., Yoshida, H., 2010. Hydrothermal alteration of deep fractured granite: Effects of dissolution and precipitation. *Lithos* 115, 153–162. <https://doi.org/10.1016/j.lithos.2009.11.015>
- Patrier, P., Papapanagiotou, P., Beaufort, D., Traineau, H., Bril, H., Rojas, J., 1996. Role of permeability versus temperature in the distribution of the fine (< 0.2 μm) clay fraction in the Chipilapa geothermal system (El Salvador, Central America). *Journal of Volcanology and Geothermal Research* 72, 101–120. [https://doi.org/10.1016/0377-0273\(95\)00078-X](https://doi.org/10.1016/0377-0273(95)00078-X)
- Pontual, S., Merry, N., Gamson, P., 1997. G-Mex Vol.1, Spectral interpretation field manual. Ausspec international Pty. Ltd., Kew, Victoria 3101, Australia.
- Richard, A., Maurer, V., Edel, J.-B., Genter, A., Baujard, C., Dalmais, E., 2016. Towards targeting geothermal reservoir: exploration program for a new EGS project in urban context in Alsace, in: *European Geothermal Congress*. Strasbourg, France.
- Sausse, J., Fourar, M., Genter, A., 2006. Permeability and alteration within the Soultz granite inferred from geophysical and flow log analysis. *Geothermics* 544–560.
- Sausse, J., Genter, A., 2005. Types of permeable fractures in granite. Geological Society, London, Special Publications 240, 1–14. <https://doi.org/10.1144/GSL.SP.2005.240.01.01>
- Schellschmidt, R., Clauer, 1996. The thermal regime of the upper rhine graben and the anomaly at Soultz. *Z. Angew. Geologie* 42, 40–44.
- Schumacher, M.E., 2002. Upper Rhine Graben: Role of preexisting structures during rift evolution. *Tectonics* 21, 6-1-6–17. <https://doi.org/10.1029/2001TC900022>
- Smith, M.P., Savary, V., Yardley, B.W.D., Valley, J.W., Royer, J.J., Dubois, M., 1998. The evolution of the deep flow regime at Soultz-sous-Forêts, Rhine Graben, eastern France: Evidence from a composite quartz vein. *Journal of Geophysical Research: Solid Earth* 103, 27223–27237.
- Stussi, J.-M., Cheilletz, A., Royer, J.-J., Chèvremont, P., Féraud, G., 2002. The hidden monzogranite of Soultz-sous-Forêts (Rhine Graben, France). *Mineralogy, petrology and genesis. Géologie de la France* 45–64.

- Traineau, H., Genter, A., Cautru, J.-P., Fabriol, H., Chèvremont, Ph., 1992. Petrography of the granite massif from drill cutting analysis and well log interpretation in the geothermal HDR borehole GPK-1 (Soultz, Alsace, France), in: *Geothermal Energy in Europe - The Soultz Hot Dry Rock Project*. Bresee, James C., Montreux, Switzerland, pp. 1–29.
- Vidal, J., Genter, A., 2018. Overview of naturally permeable fractured reservoirs in the central and southern Upper Rhine Graben: Insights from geothermal wells. *Geothermics* 74, 57–73. <https://doi.org/10.1016/j.geothermics.2018.02.003>
- Vidal, J., Glaas, C., Hébert, B., Patrier, P., Beaufort, D., 2018a. Use of SWIR spectroscopy for the exploration of permeable fracture zones in geothermal wells at Rittershoffen (Alsace, France). Presented at the Geothermal Resources Council, Reno, USA, p. 10.
- Vidal, J., Hehn, R., Glaas, C., Genter, A., 2019. How can temperature logs help identify permeable fractures and define a conceptual model of fluid circulation? An example from deep geothermal wells in the Upper Rhine Graben. *Geofluids* 14. <https://doi.org/10.1155/2019/3978364>
- Vidal, J., Patrier, P., Genter, A., Beaufort, D., Dezayes, C., Glaas, C., Lerouge, C., Sanjuan, B., 2018b. Clay minerals related to the circulation of geothermal fluids in boreholes at Rittershoffen (Alsace, France). *Journal of Volcanology and Geothermal Research* 349, 192–204. <https://doi.org/10.1016/j.jvolgeores.2017.10.019>
- Villemin, T., Bergerat, F., 1987. L'évolution structurale du fossé rhénan au cours du Cénozoïque : un bilan de la déformation et des effets thermiques de l'extension. *Bull. Soc. géol. France* 8, 245–255.

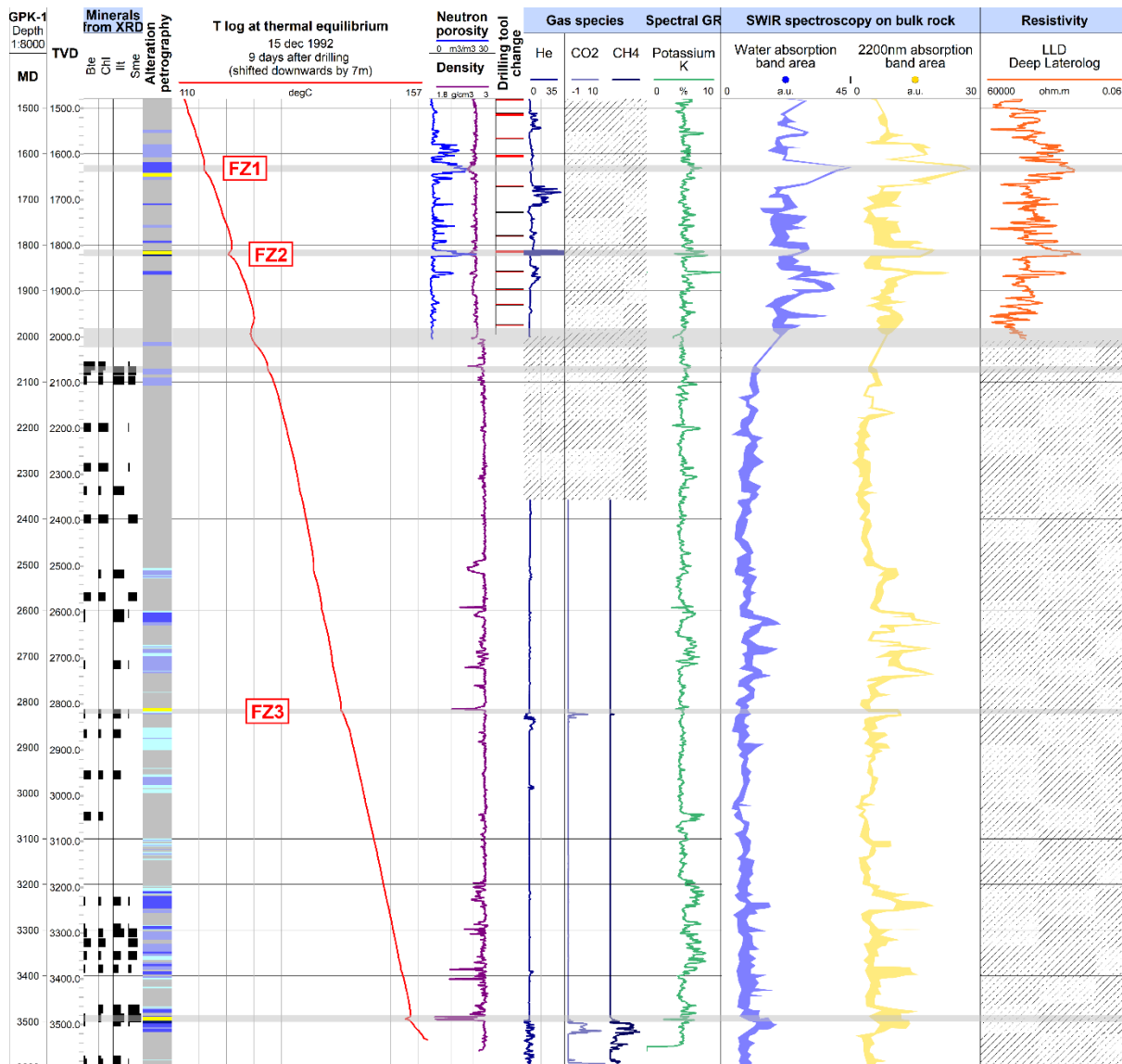


## APPENDIX 4

Supporting SWIR spectroscopy results

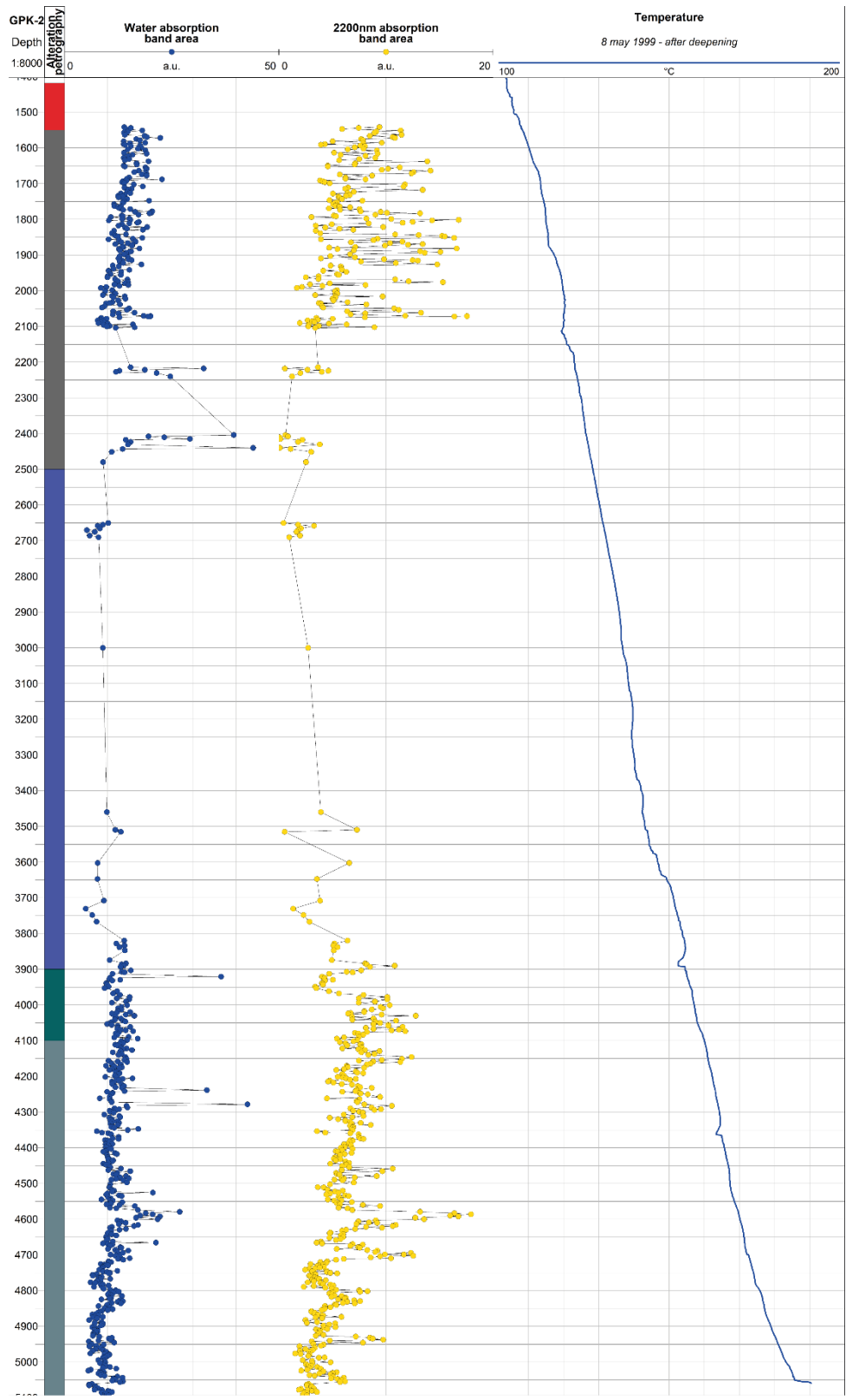


# SWIR results in the Soultz-sous-Forêts wells



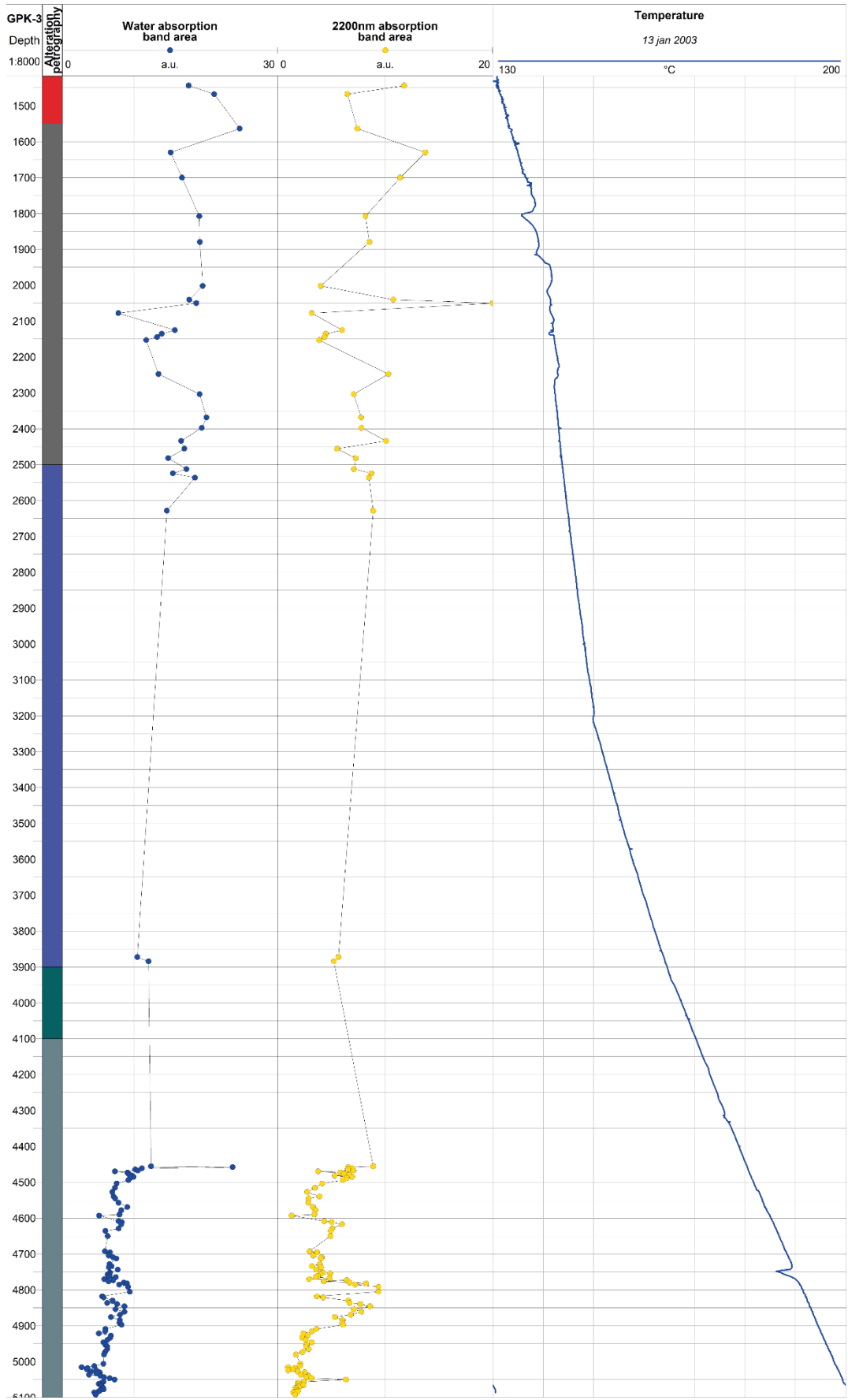
**Legend**

- GRAN
- HLOW
- HMOD
- HHIG
- HEXT
- VEIN
- permeable zones
- no data available



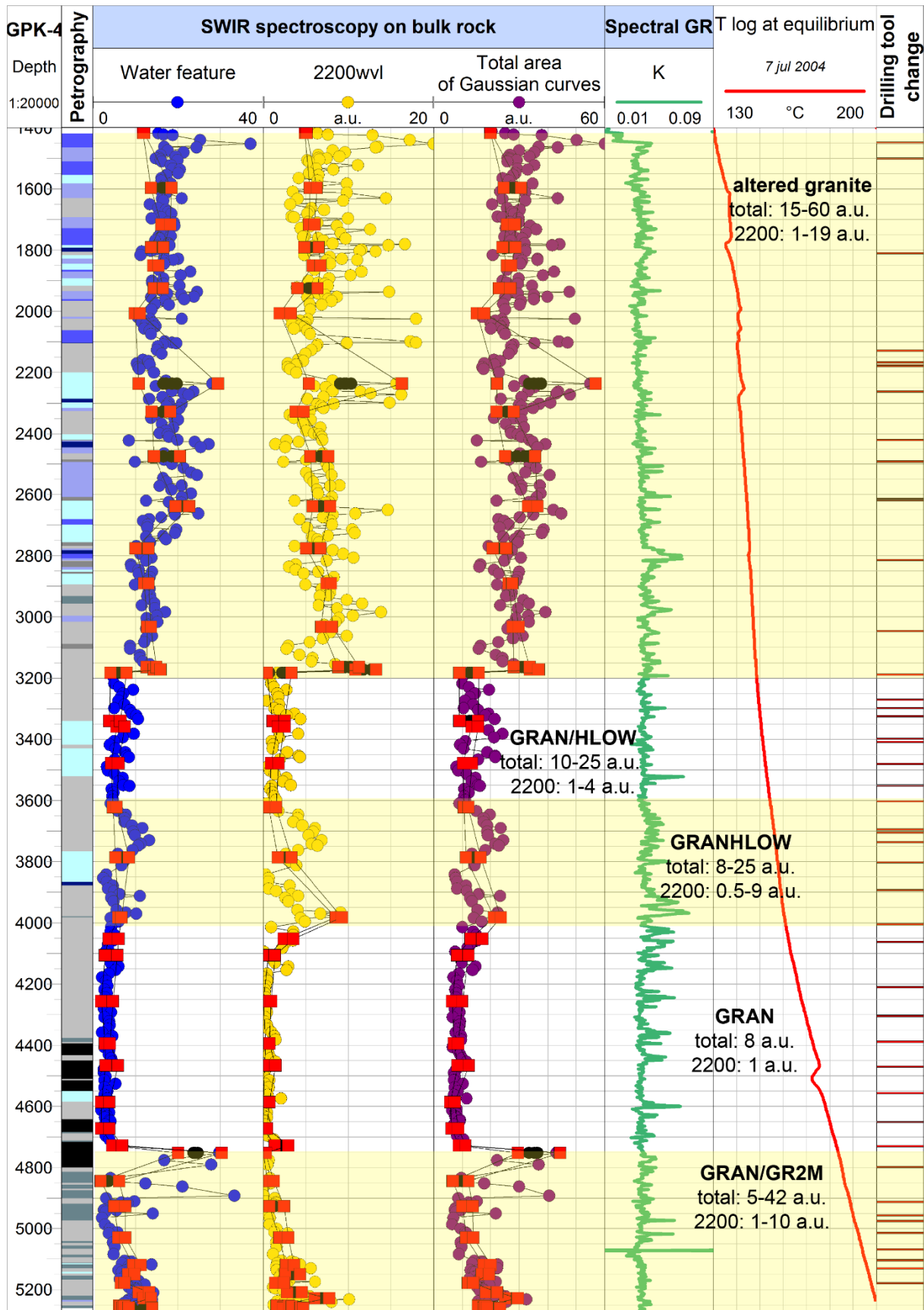
**Legend**

- reddish granite
  - porphyric granite
  - porphyric granite with intense argillic alteration
- biotite and amphibole-rich granite
  - two-mica granite

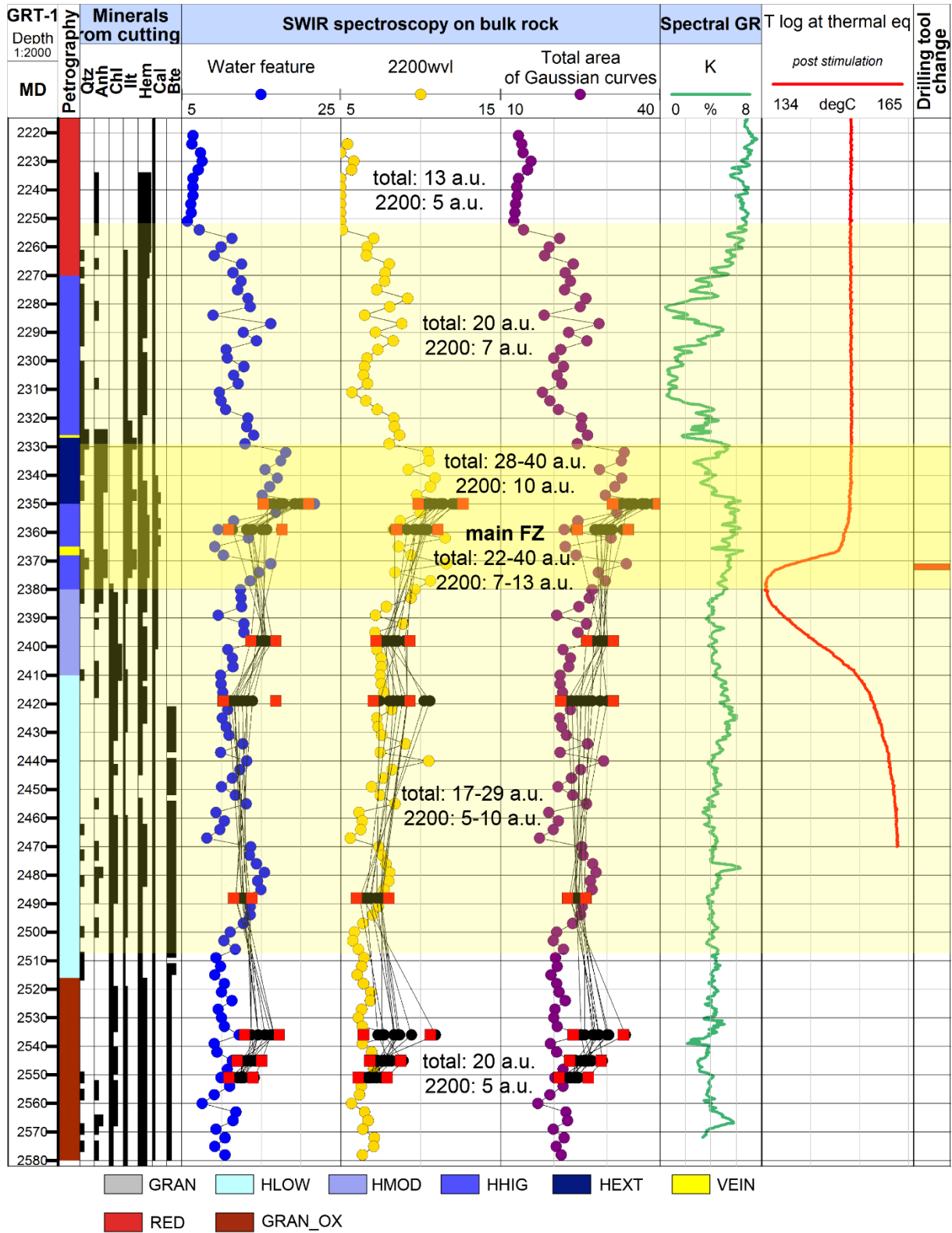


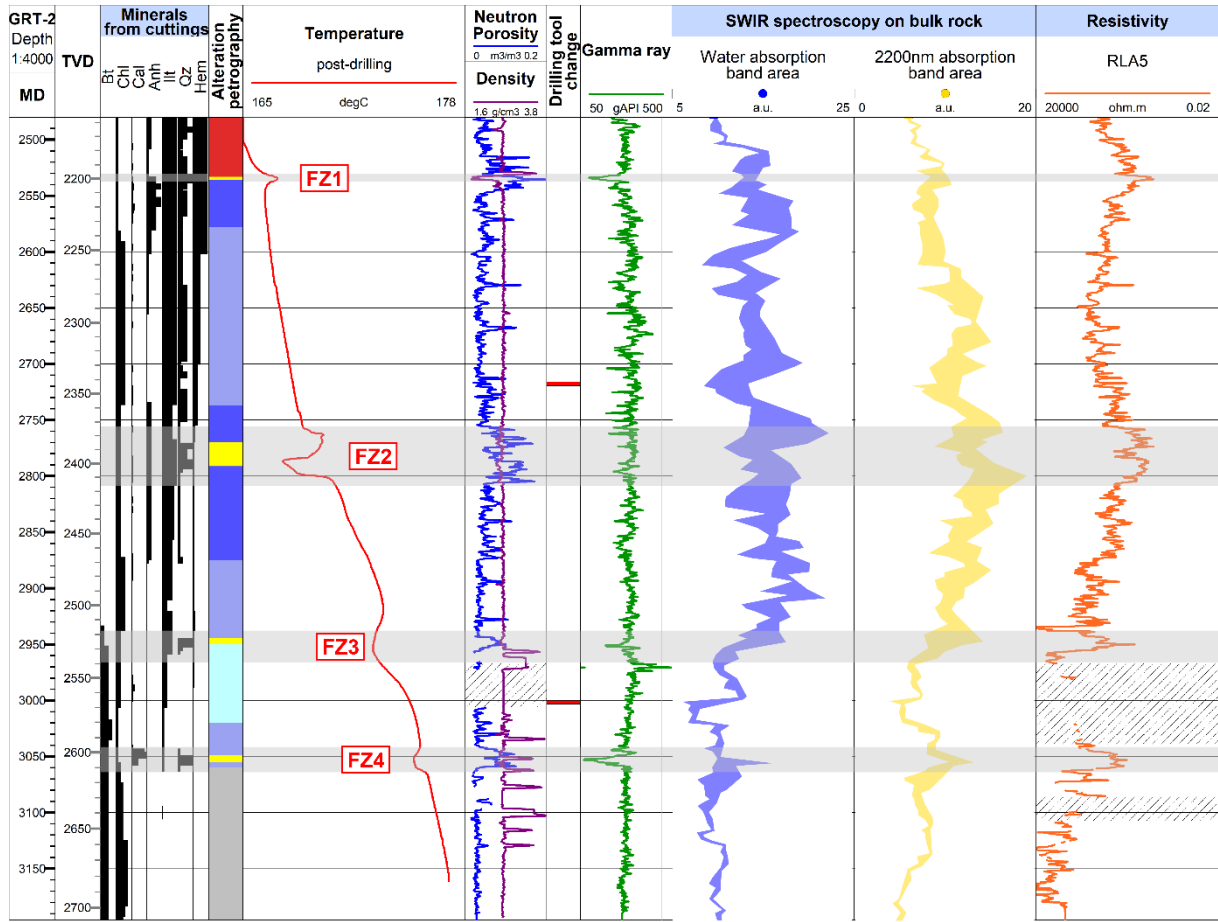
**Legend**

- reddish granite
- porphyric granite
- porphyric granite with intense argillic alteration
- biotite and amphibole-rich granite
- two-mica granite



# SWIR results in the Rittershoffen wells

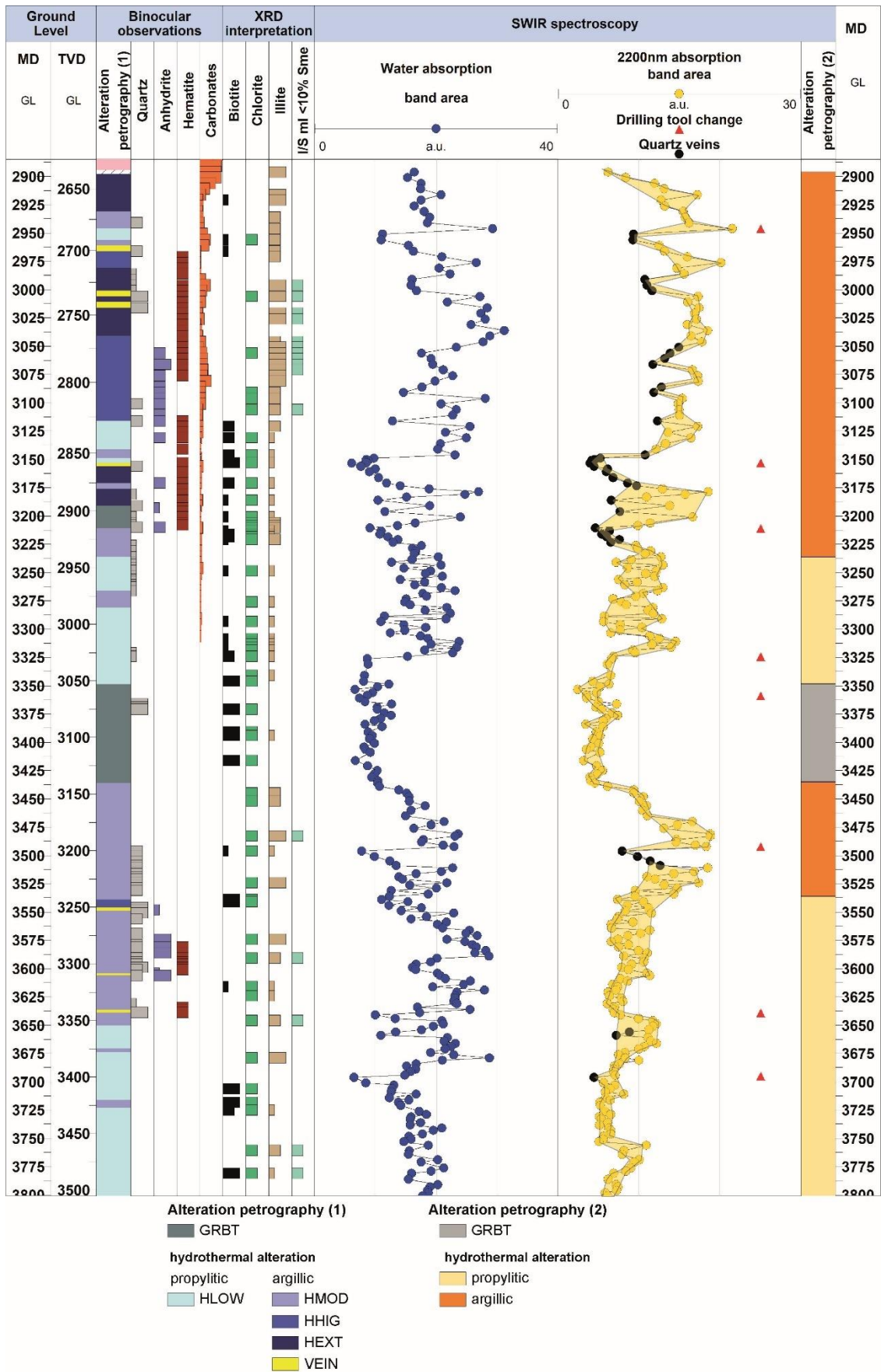




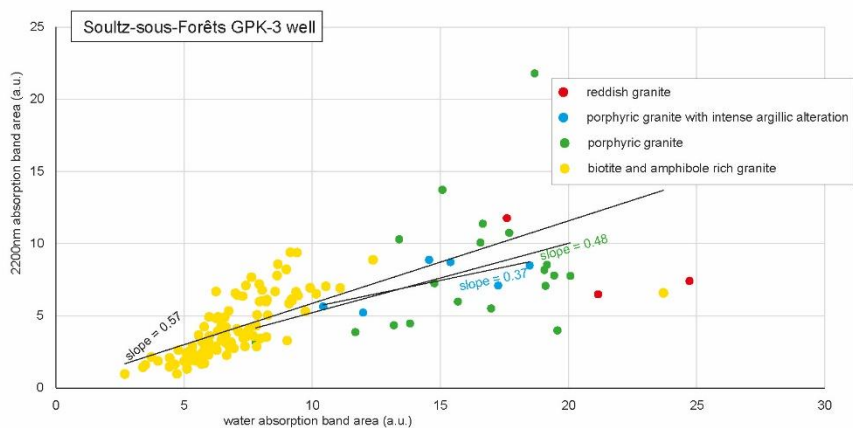
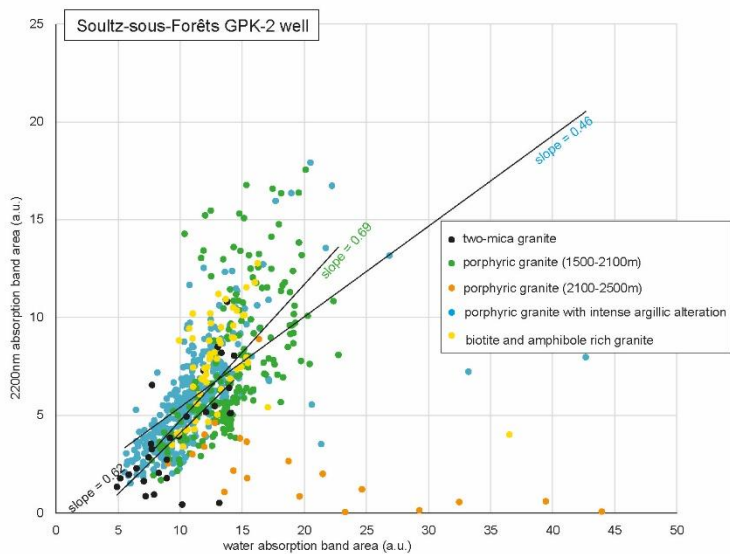
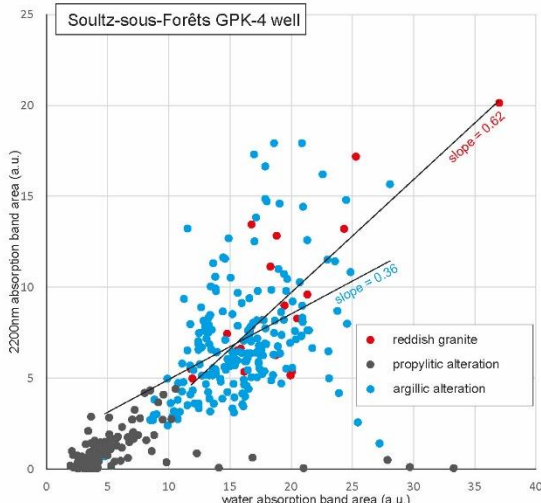
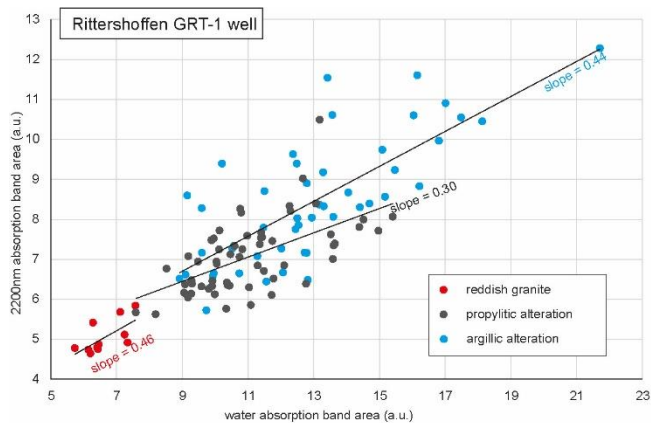
**Legend**

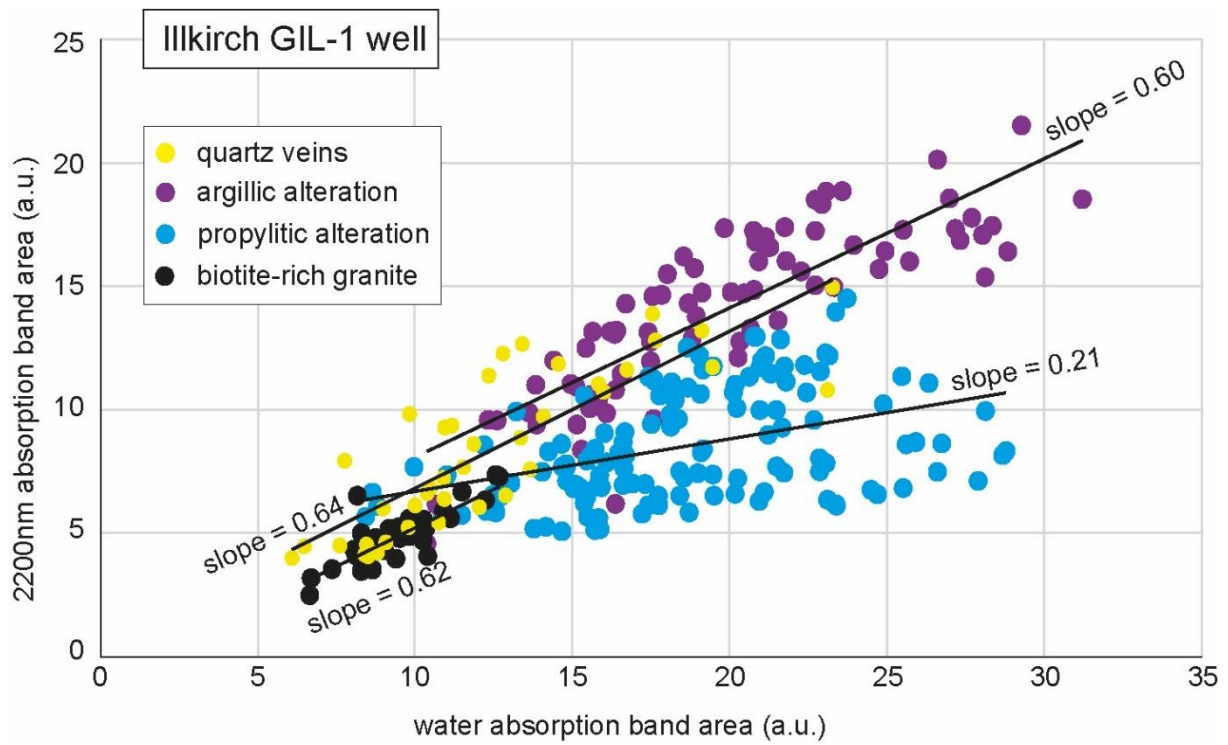
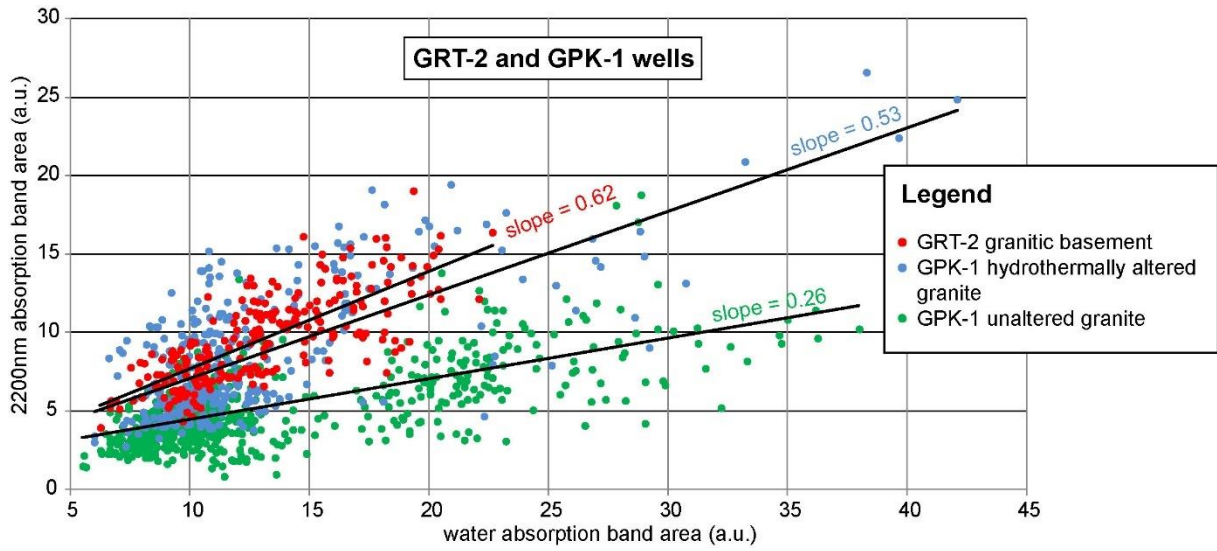
GRAN	HLOW	HHIG	permeable zones
RED	HMOD	VEIN	no data available

# SWIR results in the Illkirch well



# SWIR correlation in the Soultz-sous-Forêts, Rittershoffen and Illkirch wells







## APPENDIX 5

Supporting mineralogical results of Illkirch GIL-1 well



## Structural formulae of primary minerals from the granite of the Illkirch GIL-1 well

Structural formulae (based on 11 oxygens), of biotite from various depths in GIL-1 well. n.a.: number of analyses; An. Av.: analytical average; s.d.: standard deviation; OCT: octahedral occupancy; INTCH: interlayer charge; XFe: Fe/(Fe+Mg+Mn).

Samples	GIL-1 3070m		GIL-1 3482m		GIL-1 3573m		GIL-1 3678m
n.a.	3		7		3		1
	An. Av.	s.d.	An. Av.	s.d.	An. Av.	s.d.	
Si	2.81	0.01	2.80	0.02	2.78	0.03	2.81
Al IV	1.19	0.01	1.20	0.02	1.22	0.03	1.19
Al VI	0.07	0.01	0.05	0.01	0.42	0.59	0.10
Fe <sup>2+</sup>	1.20	0.01	1.21	0.02	1.11	0.26	1.20
Mg	1.32	0.01	1.29	0.03	1.15	0.31	1.26
Ti	0.24	0.00	0.27	0.01	0.14	0.12	0.25
Mn	0.04	0.01	0.04	0.01	0.06	0.01	0.06
OCT	2.87	0.01	2.85	0.03	2.88	0.12	2.87
Ca	0.00	0.00	0.00	0.00	0.01	0.00	0.01
Na	0.01	0.00	0.01	0.00	0.01	0.01	0.01
K	0.90	0.00	0.90	0.03	0.73	0.17	0.83
INTCH	0.92	0.01	0.91	0.03	0.76	0.18	0.85
XFe	0.47	0.00	0.48	0.00	0.48	0.01	0.48

Structural formulae (based of 8 oxygens), of potassic feldspar from various depths in GIL-1 well. n.a.: number of analyses; An. Av.: analytical average; s.d.: standard deviation.

Samples	GIL-1 3015m		GIL-1 3080m		GIL-1 3350m		GIL-1 3492m		GIL-1 3583m		GIL-1 rock1	
n.a.	18		9		2		19		5		4	
	An. Av.	s.d.										
Si	2.99	0.00	2.99	0.00	2.98	0.02	2.98	0.01	2.98	0.01	2.99	0.01
Al	1.01	0.01	1.01	0.01	1.02	0.01	1.01	0.01	1.02	0.01	1.01	0.01
Fe <sup>2+</sup>	0.00	0.00	0.00	0.00	0.00	0.00	0.00	0.00	0.01	0.00	0.00	0.00
Mg	0.01	0.00	0.01	0.00	0.01	0.00	0.01	0.00	0.00	0.00	0.01	0.00
Ti	0.00	0.00	0.00	0.00	0.01	0.01	0.00	0.00	0.00	0.00	0.00	0.00
Mn	0.00	0.00	0.00	0.00	0.00	0.00	0.00	0.00	0.00	0.00	0.00	0.00
Ca	0.00	0.00	0.00	0.00	0.00	0.00	0.00	0.00	0.00	0.00	0.00	0.00
Na	0.05	0.04	0.03	0.04	0.09	0.01	0.03	0.01	0.08	0.06	0.06	0.04
K	0.93	0.05	0.96	0.04	0.89	0.03	0.96	0.02	0.91	0.07	0.94	0.05

Structural formulae (based on 8 oxygens), of albite from various depths in GIL-1 well. n.a.: number of analyses; An. Av.: analytical average; s.d.: standard deviation.

Samples	GIL-1 3015m		GIL-1 3080m	GIL-1 3350m		GIL-1 3492m		GIL-1 3583m		GIL-1 rock1
n.a.	5		1	3		6		8		1
	An. Av.	s.d.		An. Av.	s.d.	An. Av.	s.d.	An. Av.	s.d.	
Si	3.01	0.00	3.02	3.01	0.02	3.01	0.01	2.99	0.06	3.01
Al	1.02	0.01	1.01	1.02	0.02	1.03	0.01	1.05	0.07	1.04
Fe2+	0.00	0.00	0.02	0.00	0.00	0.00	0.00	0.00	0.00	0.00
Mg	0.01	0.00	0.00	0.01	0.00	0.01	0.00	0.01	0.00	0.00
Ti	0.00	0.00	0.00	0.00	0.00	0.00	0.00	0.00	0.00	0.00
Mn	0.00	0.00	0.00	0.00	0.00	0.00	0.00	0.00	0.00	0.00
Ca	0.00	0.00	0.00	0.02	0.01	0.01	0.01	0.02	0.03	0.01
Na	0.87	0.02	0.82	0.81	0.01	0.84	0.02	0.79	0.08	0.80
K	0.00	0.00	0.01	0.01	0.01	0.01	0.01	0.04	0.06	0.01

Structural formulae (based on 8 oxygens), of oligoclase from 3583 m in GIL-1 well. An. Av.: analytical average; s.d.: standard deviation.

Sample	GIL-1 3583m	
n.a.	4	
	An. Av.	s.d.
Si	2.84	0.05
Al	1.19	0.06
Fe2+	0.00	0.00
Mg	0.01	0.00
Ti	0.00	0.00
Mn	0.00	0.00
Ca	0.14	0.06
Na	0.71	0.06
K	0.04	0.05

Structural formulae (based on 2 oxygens), of calcite from various depths in GIL-1 well. n.a.: number of analyses; An. Av.: analytical average; s.d.: standard deviation.

Samples	GIL-1 3015m		GIL-1 3080m		GIL-1 3492m		GIL-1 3583m		GIL-1 3688m	GIL-1 rock1	
n.a.	9		9		6		2		1	3	
	An. Av.	s.d.		An. Av.	s.d.						
Si	0.02	0.01	0.03	0.01	0.02	0.01	0.03	0.00	0.03	0.03	0.00
Al	0.01	0.01	0.01	0.00	0.01	0.01	0.02	0.00	0.01	0.01	0.00
Fe2+	0.02	0.02	0.01	0.00	0.02	0.02	0.00	0.00	0.02	0.00	0.00
Mg	0.02	0.00	0.01	0.00	0.01	0.01	0.02	0.00	0.01	0.01	0.00
Ti	0.00	0.00	0.00	0.00	0.00	0.00	0.00	0.00	0.00	0.00	0.00
Mn	0.01	0.01	0.01	0.01	0.02	0.02	0.00	0.00	0.01	0.00	0.00
Ca	1.88	0.01	1.89	0.03	1.90	0.04	1.87	0.01	1.87	1.89	0.01
Na	0.01	0.01	0.01	0.01	0.00	0.01	0.02	0.00	0.01	0.01	0.01
K	0.01	0.01	0.01	0.01	0.02	0.01	0.00	0.00	0.01	0.01	0.00

Calculations of structural formulae on the basis of 2 oxygens, of some ankerite (population 1) at various depths in GIL-1 well. n.a.: number of analyses; An. Av.: analytical average; s.d.: standard deviation.

Samples	GIL-1 3015m		GIL-1 3080m	GIL-1 3583m		GIL-1 rock1	
n.a.	6		1	2		3	
	An. Av.	s.d.		An. Av.	s.d.	An. Av.	s.d.
Si	0.01	0.00	0.02	0.01	0.00	0.01	0.01
Al	0.01	0.00	0.01	0.01	0.00	0.01	0.00
Fe2+	0.41	0.03	0.34	0.31	0.1	0.35	0.01
Mg	0.42	0.03	0.51	0.51	0.13	0.43	0.02
Ti	0.00	0.00	0.00	0.00	0.00	0.00	0.00
Mn	0.03	0.00	0.03	0.03	0.00	0.03	0.00
Ca	1.11	0.05	1.07	1.12	0.03	1.16	0.01
Na	0.00	0.00	0.01	0.01	0.00	0.00	0.00
K	0.01	0.00	0.01	0.00	0.00	0.01	0.00

Calculations of structural formulae on the basis of 2 oxygens, of some ankerite (population 2) at 3080 m in GIL-1 well. n.a.: number of analyses; An. Av.: analytical average; s.d.: standard deviation.

Samples	GIL-1 3080m	
n.a.	2	
	An. Av.	s.d.
Si	0.01	0.00
Al	0.00	0.00
Fe2+	0.17	0.22
Mg	0.71	0.16
Ti	0.00	0.00
Mn	0.03	0.01
Ca	1.06	0.05
Na	0.00	0.00
K	0.01	0.00





## Contrôles minéralogiques et structuraux sur la perméabilité de réservoirs cristallins profonds naturellement fracturés.

Application aux puits géothermiques du fossé Rhénan supérieur.

### Résumé

La compréhension de la distribution de la perméabilité dans le granite naturellement fracturé du fossé Rhénan supérieur est un défi clé pour les projets géothermiques. Les zones de faille et de fracture (FZ) qui contrôlent les circulations naturelles de fluides ont été étudiées à partir de données de puits géophysiques et géologiques des trois sites de géothermie de Soultz-sous-Forêts, Rittershoffen et Illkirch (France). Les fractures naturelles intersectées par les puits géothermiques ont été investiguées à partir d'imageries de paroi et de diagraphies géophysiques. L'analyse structurale du socle intégrée sur ces trois sites du fossé Rhénan supérieur montre l'existence de deux principaux ensembles conjugués de fractures sub-verticales orientées N-S à NNE-SSW. A partir de plusieurs milliers de cuttings, les altérations hydrothermales ont été analysées par des méthodes pétrographiques classiques ainsi qu'avec la méthode innovante de spectroscopie infra-rouge à courte longueur d'onde (SWIR). Les minéraux argileux secondaires liés aux circulations anciennes et actuelles dans les fractures correspondent à du matériel argillique de type illitique. La comparaison des ensembles de données sur les trois sites a permis de souligner que la distribution des altérations hydrothermales permet de préserver ou non la perméabilité dans les FZ. Pour atteindre des débits exploitables, la connexion entre les puits et le réseau de fractures perméables peut être maximisée par des trajectoires de puits recoupant les failles locales au toit du socle granitique de manière optimisée

**Mots-clés :** altération argillique, fractures naturelles, réservoir granitique, spectroscopie infra-rouge à courte longueur d'onde (SWIR), circulation de fluides, puits géothermiques, fossé Rhénan supérieur.

### Abstract

The understanding of permeability distribution in the naturally fractured granitic basement of the Upper Rhine Graben (URG) is a key challenge for geothermal projects. Fault and fracture zones (FZ) controlling the natural fluid flow were investigated from geophysical and geological well data from the three geothermal sites of Soultz-sous-Forêts, Rittershoffen and Illkirch (France). Natural fractures intersecting the geothermal wells were investigated based on borehole image logs, and geophysical logs. A detailed structural comparison in the basement of the three geothermal sites from the URG shows two main, conjugate, nearly vertical fracture sets oriented N-S to NNE-SSW. Based on several thousands of cutting samples, hydrothermal alterations were investigated with classical petrographic methods as well as innovative Short-Wave InfraRed (SWIR) spectroscopy. The secondary clay minerals most intimately associated to paleo or present fluid circulations in fractures correspond to argillic materials and mainly consist in illitic material. Dataset comparison highlighted that the distribution of hydrothermal alteration allows to preserve or not permeability in FZs. To achieve suitable flowrates, the connection between the wells and the permeable fracture network should be maximised by smart well trajectories cross-cutting local faults at the top basement. The application of SWIR method on basement rocks demonstrated that it could be a real innovative tool to be integrated in future deep geothermal exploration wells drilled in the URG.

**Keywords:** argillic alteration, natural fractures, granite reservoir, Short-Wave InfraRed (SWIR) spectroscopy, fluid circulation, geothermal wells, Upper Rhine Graben.